

AD-A279 883

Volume
41

G

Grain Boundaries and Interfacial Phenomena
in Electronic Ceramics

Levinson • Hirano



The
American
Ceramic
Society

Grain Boundaries

and

Interfacial Phenomena

in

Electronic Ceramics

DTIC
ELECTE
JUN 03 1994

▼▲▼

S G D

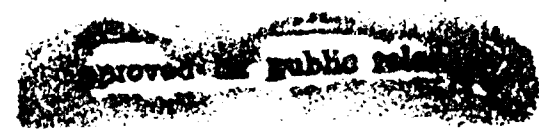
Edited by

Lionel M. Levinson

and

Shin-ichi Hirano

▲▼▲



This Document Contains
Missing Page/s That Are
Unavailable In The
Original Document

Geramic
Transactions
Volume 41

0

Grain Boundaries
and
Interfacial Phenomena
in
Electronic Ceramics

Accesion For	
NTIS	CRA&I
DTIC	TAB
Unannounced	
Justification	
By _____	
Distribution /	
Availability Codes	
Dist	Avail and / or Special
A-1	

DTIC
ELECTE
JUN 03 1994
S G D

02 0 0 03T

94-16444



Related titles published by the American Ceramic Society:

Experimental Techniques of Glass Science
Edited by Catherine J. Simmons and Osama H. El-Bayoumi
© 1993, ISBN 0-944904-58-0

Handbook on Characterization Techniques for the Solid-Solution Interface
Edited by James H. Adair, Jon A. Casey, and Sridhar Venigalla
© 1993, ISBN 0-944904-67-X

Ceramic Transactions, Volume 38: Advances in Ceramic-Matrix Composites
Edited by Narottam P. Bansal
© 1993, ISBN 0-944904-69-6

Ceramic Transactions, Volume 36: Microwaves: Theory and Application in Materials Processing II
Edited by David E. Clark, Wayne R. Tinga, and Joseph R. Laia, Jr.
© 1993, ISBN 0-944904-66-1

Ceramic Transactions, Volume 34: Functionally Gradient Materials
Edited by J. Birch Holt, Mitsue Koizumi, Toshio Hirai, and Zuhair A. Munir
© 1993, ISBN 0-944904-64-5

Ceramic Transactions, Volume 31: Porous Materials
Edited by Kozo Ishizaki, Laurel Sheppard, Shojiro Okada, Toyohiro Hamasaki, and Ben Huybrechts
© 1993, ISBN 0-944904-59-9

Ceramic Transactions, Volume 30: Nucleation and Crystallization in Liquids and Glasses
Edited by Michael C. Weinberg
© 1993, ISBN 0-944904-57-2

Ceramic Transactions, Volume 26: Forming Science and Technology for Ceramics
Edited by Michael J. Cima
© 1991, ISBN 0-944904-48-3

Ceramic Transactions, Volume 24: Point Defects and Related Properties of Ceramics
Edited by Thomas O. Mason and Jules L. Routbort
© 1991, ISBN 0-944904-46-7

Ceramic Transactions, Volume 22: Ceramic Powder Science IV
Edited by Shin-ichi Hirano, Gary L. Messing, and Hans Hausner
© 1991, ISBN 0-944904-44-0

Advances in Ceramics, Volume 28: Failure Analysis of Brittle Materials
Edited by V.D. Frechette
© 1990, ISBN 0-944904-30-0

For information on ordering titles published by the American Ceramic Society, or to request a publications catalog, please call 614-890-4700, or write to Customer Service Department, 735 Ceramic Place, Westerville, OH 43081.

Grain Boundaries
and
Interfacial Phenomena
in
Electronic Ceramics



Edited by
Lionel M. Levinson
General Electric Corporate Research and Development
Shin-ichi Hirano
Nagoya University



DTIC QUALITY IMPROVED 2

Ceramic
Transactions
Volume 41

Published by
The American Ceramic Society
735 Ceramic Place
Westerville, Ohio 43081

*Proceedings of the International Symposium on Grain Boundaries and Interfacial Phenomena,
presented at the PAC RIM Meeting, held in Honolulu, HI, November 8-10, 1993.*

Library of Congress Cataloging-in-Publication Data

International Symposium on Grain Boundaries and Interfacial Phenomena
in Electronic Ceramics (1993 : Honolulu, Hawaii)
Grain boundaries and interfacial phenomena in electronic ceramics
/ edited by Lionel M. Levinson, Shin-ichi Hirano.
p. cm. -- (Ceramic transactions, ISSN 1042-1122 ; v. 41)
Proceedings of the International Symposium on Grain Boundaries and
Interfacial Phenomena in Electronic Ceramics, held in Honolulu,
Hawaii Nov. 7-10, 1993, in conjunction with the PAC RIM Meeting.
Includes index.
ISBN 0-944904-73-4
1. Electronic ceramics--Surfaces--Congresses. 2. Grain
boundaries--Congresses. 3. Surface chemistry--Congresses.
I. Levinson, Lionel M. II. Hirano, Shin'ichi, 1942-
III. Title. IV. Series.
TK7871.15.C4158 1993
621.381--dc20

94-4933
CIP

Copyright © 1994, The American Ceramic Society. All rights reserved.

No part of this book may be reproduced, stored in a retrieval system, or transmitted in
any form or by any means, electronic, mechanical, photocopying, microfilming,
recording, or otherwise, without written permission from the publisher.

Permission to photocopy for personal or internal use beyond the limits of Sections 107
and 108 of the U.S. Copyright Law is granted by the American Ceramic Society,
provided that the base fee of US\$5.00 per copy, plus US\$.50 per page, is paid directly to
the Copyright Clearance Center, 27 Congress Street, Salem MA 01970, USA. The fee code
for users of the Transactional Reporting Service for *Ceramic Transactions Volume 41* is 0-
944904-73-4/94 \$5.00+\$0.50. This consent does not extend to other kinds of copying, such
as copying for general distribution, for advertising or promotional purposes, or for
creating new collective works. Requests for special photocopying permission and reprint
requests should be directed to the Director of Publications, The American Ceramic
Society, 735 Ceramic Place, Westerville OH 43081, USA.

This work relates to Department of Navy Grant N00014-93-1-0366 issued by the Office of
Naval Research. The United States Government has a royalty-free license throughout the
world in all copyrightable material contained herein.

Printed in the United States of America.

1 2 3 4-98 97 96 95 94

ISSN 1042-1122
ISBN 0-944904-73-4

Contents

Preface	ix
---------------	----

Overview

Grain Boundary Segregation in Semiconducting Oxides	3
Yet-Ming Chiang and Jeri Ann S. Ikeda	
Electrical Activity at Individual Grain Boundaries and Interfaces in Semiconducting Oxides	19
H.L. Tuller and K-K. Baek	
Chemically Induced Interface Migration in Oxides.....	35
Jae Ho Jeon, Suk-Joong L. Kang, Sang Chul Han, and Duk Yong Yoon	
Nano/Microstructure Design for Improving Thermoelectric Characteristics of Porous Silicon Carbide	53
K. Koumoto, W.S. Seo, and C.H. Pai	
Grain Boundary Characteristics in PZLT, GBBLC, and High-T _c Superconducting Ceramics and Their Relation to Properties	65
M.Y. Zhao, Z.W. Yin, and B.M. Xu	

Ferrites and Titanates

Grain Boundary Microstructure and Magnetic Properties of Low- Temperature-Fired Ni-Zn-Cu Ferrite	81
Masayuki Fujimoto	
Dependence of Magnetic Properties of (Co,Fe) ₃ O ₄ Film on Microstructure Control Through Phase Separation.....	93
Shin-ichi Hirano, Toshinobu Yogo, Ko-ichi Kikuta, and Hiroshi Yamamoto	
Low-Temperature-Sintered Ferrite for Multilayer Chip Components.....	101
Jen-Yan Hsu, Wen-Song Ko, Hsiao-Miin Sung, Meei-Lin Suen, and Chi-Jen Chen	
Influence of Process Parameters on Power Losses Minimum vs. Temperature of Mn-Zn Ferrites	111
M.J. Tsay, C.S. Liu, M.J. Tung, and C.J. Chen	
Grain Boundary Layered PTCR Ceramics Based on PbTiO ₃ -TiO ₂	119
M. Okada, M. Homma, and S. Iwashita	

Grain Core-Grain Shell Structure in Nb-Doped BaTiO ₃ Capacitor Ceramics	129
X.Y. Song, D.R. Chen, and Z.W. Yin	
The V-Shape Characteristics of (Pb _{0.6} Sr _{0.4})TiO ₃ Ceramics.....	135
T.D. Tsai, C.T. Hu, and I.N. Lin	
Effect of BN Addition on the Sintering and Electrical Properties of Y-Doped BaTiO ₃ Ceramics.....	145
Seh-Jin Park, Joon-Hyung Lee, and Sang-Hee Cho	
Effects of Grain Boundary Structure on the Resistivity Phenomenon in Doped BaTiO ₃	153
R.C. Buchanan, R.D. Roseman, and J. Kim	
Microstructural and Compositional Analyses on Grain Boundary of Low-Temperature-Sintered Pb(Zr,Ti)O ₃ Ceramics	161
Dunzhuo Dong, Kenji Murakami, Nagaya Okada, and Shoji Kaneko	
Particle Size Effect on the Room Temperature Structure of Barium Titanate	169
B.D. Begg, E.R. Vance, D.J. Cassidy, J. Nowotny, and S. Blairs	
Influence on the Grain Boundary Interfacial Trap Levels in Ba _{0.76} Sr _{0.24} TiO ₃ -Based PTCR Ceramics by Oxidative Annealing	177
Myung Chul Kim, Soo Hyung Hur, and Soon Ja Park	
Role of Porosity on PTCR Characteristics of Semiconducting BaTiO ₃ Ceramics.....	185
Joon-Hyung Lee, Jeong-Joo Kim, and Sang-Hee Cho	

Varistors and Conductors

Interface States at Grain Boundaries and Their Effects on the I-V Characteristics in ZnO:Pr Varistors—Theoretical Calculation.....	195
Kazuo Mukae and Koichi Tsuda	
Cryogenic Behavior of ZnO Varistors	207
Lionel M. Levinson and William N. Schutz	
Modeling the Electrical Characteristics of Polycrystalline Varistors Using Individual Grain Boundary Properties	217
Qingzhe Wen and David R. Clarke	
VDR Effect in Bi-Diffused SrTiO ₃ -Based Ceramics	231
N. Ichinose and M. Watanabe	

Sub-Grain-Boundary Phenomenon in ZnO Varistor Ceramics During Sintering	239
Xiaolan Song and Fuyi Liu	
The Polynuclear Hydroxy Metal Cations Pillared Zirconium Phosphates and Their Proton Conductivity.....	245
Y. Ding, J. Rozière, and D. Jones	
Li Deintercalation in Lithium Transition Metal Nitride, Li_3FeN_2.....	253
M. Nishijima, Y. Takeda, N. Imanishi, O. Yamamoto, and M. Takano	
Positive Hole-Type Charge Carriers in Oxide Materials.....	263
Friedemann Freund, Eun-Joo Whang, François Batllo, Lionel Desranges, Corinne Desranges, and Minoru M. Freund	
Characterization of Electroconductive TiN/Al-O-N Composites	279
J.L. Hoyer, J.A. Clark, and J.P. Bennett	

High-Temperature Superconductors

Grain Boundary Degradation of YBCO Superconductors Sintered in CO_2-Containing Atmospheres.....	289
U. Balachandran, K.L. Merkle, J.N. Mundy, Y. Gao, C. Zhang, D. Xu, and G. Selvaduray	
Interface Effects in Bi-“2212”/Ag and Bi-“2223”/Ag Superconductors...	299
S.J. Golden, T. Yamashita, A. Bhargava, J.C. Barry, and I.D.R. Mackinnon	
Film/Substrate Thermal Boundary Resistance for Er-Ba-Cu-O High-T_c Thin Films	307
P.E. Phelan, Y. Song, and M. Kelkar	
Effect of Impregnation of ZrO_2 on the Chemical Stability and the Superconductivity of Y and Bi Systems.....	315
Masaaki Muroya and Hideaki Minamiyama	

Processing and Characterization

Cofire Technology: Quantifying Glass Infiltration in the Ceramic-Metal Interfacial Region.....	325
K.S. Venkataraman, L.D. Martin, and D.A. Weirauch, Jr.	
Zirconia Hydrogel Casting of PZT Ceramics.....	337
T.E. Petroff, S.A.M. Hesp, and M. Sayer	
Interface and Microstructure Development of Coated Alumina Powders During Heating.....	345
H. Yokoi and W.D. Kingery	

High Q-Factor Tri-Plate Resonator with an Inner Conductor of Melted Silver.....	355
M. Kobayashi, K. Kawamura, and K. Suzuki	
Sintering and Microstructure of $\text{Sr}_{0.6}\text{Ba}_{0.4}\text{Nb}_2\text{O}_6$ Ceramics	363
Junichi Takahashi, Shiro Nishiwaki, and Kohei Kodaira	
Interfacial Phenomena and Dielectric Properties of $\text{Pb}(\text{Mg}_{1/3}\text{Nb}_{2/3})\text{O}_3$ Ceramics with Excess PbO	371
K.H. Yoon, Y.S. Cho, D.H. Lee, and D.H. Kang	
Characterization of Bridgman Crystal Growth Using Radiographic Imaging.....	379
S.E. Sorokach, R.T. Simchick, A.L. Fripp, W.J. Debnam, and P.G. Barber	
Index	387

P*reface*

This volume contains the proceedings of the International Symposium on Grain Boundaries and Interfacial Phenomena in Electronic Ceramics, held in Honolulu November 7-10, 1993, in conjunction with the PAC RIM Meeting. The meeting was cosponsored by 10 ceramic societies and associations from countries bordering the Pacific Ocean. The symposium participants included ceramists from the United States, Japan, Korea, Taiwan, Canada, People's Republic of China, and India.

The symposium cochairs were fortunate to have the support of an international organizing committee: Janusz Nowotny (Australian Science and Technology Organization, Australia), Soon Ja Park (Seoul National University, Korea), Michael Sayer (Queen's University, Canada), and Zhiwen Yin (Shanghai Institute of Ceramics, China). We would also like to express our appreciation to the symposium session chairs, R. Pohanka, M. Sayer, Z. Yin, and J. Nowotny, who also ably assisted in coordinating the manuscript reviews.

This symposium and therefore this proceedings was organized to bring together worldwide expertise in grain boundary and interfacial phenomena in electronic ceramics. These issues are key to understanding technological advances in fields as diverse as ferroelectrics, sensors, PTCRs, packaging ceramics, varistors, thick films, magnetic ceramics, titanates, capacitors, and multilayer and composite materials. Interfacial phenomena often determine the sintering and densification behavior of ceramics, as well as contact and joint functionality.

Finally, it was the goal of the meeting organizers to bring together experts in these various areas to provide a forum to promote the exchange of ideas that will occur when workers in diverse materials concentrate on the common interfacial and grain boundary phenomena underlying their specialized applications.

Lionel M. Levinson
Shin-ichi Hirano

Overview

GRAIN BOUNDARY SEGREGATION IN SEMICONDUCTING OXIDES

Yet-Ming Chiang and Jeri Ann S. Ikeda*

Dept. of Materials Science and Engineering, Massachusetts Institute of Technology,
Cambridge, Massachusetts, USA

ABSTRACT

Solute and defect segregation at grain boundaries and surfaces in electroceramics and other oxides controls a broad range of interfacial properties. Model experiments in acceptor- and donor-doped TiO_2 show that in a semiconducting oxide with complex defect structure, including mixed electronic and ionic compensation, the equilibrium space charge potential corresponds to that expected from ionic space charge theory. As a result, the potential and the interfacial density of charged defects can be quantitatively predicted on the basis of lattice defect structure, and can be varied by control of doping, temperature, and oxygen activity. Implications of these results for the control of defect segregation at electrically active grain boundaries in complex oxides are discussed.

INTRODUCTION

Semiconducting oxides are used in a broad range of applications in which the defect chemistry of interfaces provide important chemical or electrical functionalities. The most well-known of these are perhaps grain boundary barrier-layer electroceramics such as zinc oxide varistors and barium titanate positive-temperature-coefficient (PTC) resistors, but interfacial defect properties also play a critical role in oxides used for a variety of other applications, including for example catalysts and surface and heterojunction-based gas and chemical sensors. The high temperature properties of grain boundaries and surfaces are clearly important in microstructure development processes such as creep, sintering, and grain growth as well. While the lattice defect properties of many of the important semiconducting oxides have been extensively studied, comparatively little is known about their interfacial defect chemistry (which, in this context, includes the nonstoichiometry of the interface and near-interface region, as well as solute segregation).

The relationship between lattice defects and interfacial defects in ionic systems is in large part defined by the space-charge interaction. As first formulated by Frenkel [1], Lehovec [2], and Kliewer and Koehler [3], an ionic space charge results when the

* now at Norton Company, Worcester, Massachusetts

To the extent authorized under the laws of the United States of America, all copyright interests in this publication are the property of The American Ceramic Society. Any duplication, reproduction, or republication of this publication or any part thereof, without the express written consent of The American Ceramic Society or fee paid to the Copyright Clearance Center, is prohibited.

formation of defects at the interface differs energetically from those in the bulk, resulting at equilibrium in a variation in ionic defect concentration at the interface, and a corresponding electrical potential difference between the interface and the bulk. The interface charge is balanced by an oppositely-charged space-charge layer penetrating the crystal. The magnitude of the potential difference is determined by the formation energy of lattice defects at the interface, temperature and lattice defect concentration. Numerous studies in alkali- and silver halides [4-7] leave little doubt as to the existence of the space-charge potential in simple ionic systems. In MgO, the segregation [8] and spatial distribution [9] of aliovalent cations at grain boundaries likewise provide convincing evidence for a space-charge mode of segregation which is distinct from Gibbsian adsorption at the grain boundary. In more complex oxides, including MgAl₂O₄ [10], MnZn ferrites [11], SrTiO₃ [12,13], and BaTiO₃ [13-15], deviations in both cation and anion stoichiometry have been observed at grain boundaries and surfaces. In instances where experimental procedures suggest a preservation of high temperature equilibrium, these seem clearly related to existence of a space charge. However, a quantitative interpretation of the segregation in terms of the lattice defect structure has not been achieved in these systems. Dynamic effects during processing causing redistribution of solutes and defects often complicate the picture, although such effects can be of critical importance in real electroceramic systems since they determine what is retained after cooling to room temperature.

In TiO₂ (rutile phase), a system with defect properties which are representative of a broad range of semiconducting oxides, a more systematic approach has been possible [16-18]. The ability to access a number of Brouwer defect regimes by varying doping, temperature, and oxygen activity, renders this system ideal for exploring the variation in interfacial chemistry as a function of lattice defect chemistry. We have conducted systematic studies of space charge segregation using model experiments in which the accumulation of aliovalent solutes is measured. Observations of the variation in space charge potential with temperature and doping were recently reported [17-18]. Here we briefly review those results, and discuss new results on the pO₂ dependence of the space charge potential.

DEFECT AND SPACE CHARGE MODEL

The lattice nonstoichiometry of TiO₂ is well-characterized as a function of temperature and oxygen activity, as are the regimes of crystallographic shear phase (CSP) and defect cluster formation. For simplicity we have concentrated efforts on the high temperature ($T > 1473\text{K}$), low defect concentration ($\delta < 0.005$) regime within which experimental studies (summarized by Bursill et al. [19,20]) find CSP's as well as smaller defect clusters to be absent. In this regime, transport properties have been found to be well-described by dilute point-defect models (for recent reviews see refs. 19-22).

The defect model used here has been discussed in detail in ref. 17. In brief, defect chemical equilibrium constants from the literature have been used to calculate the lattice concentrations of the relevant defects as a function of doping, temperature, and oxygen activity. Some of the calculated results are shown in Fig. 1(A) as plots of defect concentrations against solute doping, for a temperature of 1350°C and air atmosphere.

Figure 1(B) shows a similar calculation plotted against oxygen partial pressure, in a material doped with 1% pentavalent donor (e.g., Nb⁵⁺, Ta⁵⁺), at 1350°C. Together, a family of curves of this type map the variation of point defect concentration with the

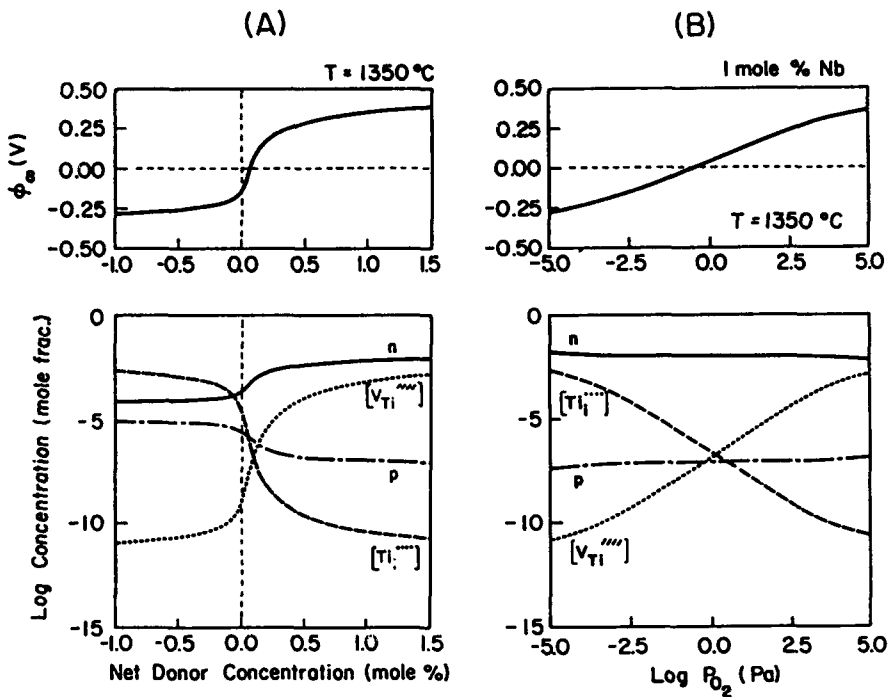
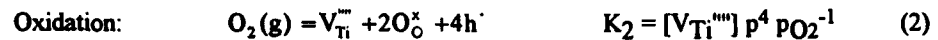
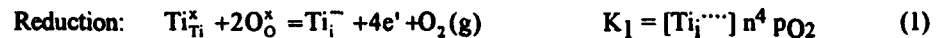


Figure 1. Calculated lattice defect concentrations in TiO_2 at 1350°C , plotted against (A) solute doping at constant pO_2 (air); and (B) pO_2 at constant donor doping. Corresponding space charge potential curves are shown above the respective diagrams.

important experimental variables of temperature, oxygen activity, and doping. The defect model includes six point defects: A_{Ti}^+ (substitutional trivalent acceptors), D_{Ti}^+ (substitutional pentavalent donors), Ti_i^{4+} , $\text{V}_{\text{Ti}}^{3+}$, n and p . Implicit is the assumption, in accordance with recent analyses of literature data [21-23], that reduction is accommodated by the formation of Ti_i^{4+} at higher temperatures, and that the cation Frenkel is the lowest-energy intrinsic ionic defect mechanism in ideal, stoichiometric TiO_2 . Defect association has been assumed negligible at the temperatures and doping levels of interest, based on estimates of electrostatic binding energies [17,24]. (This is in large part due to the screening afforded by the high dielectric constant of TiO_2 , $\epsilon=120$.) The following quasi-chemical defect reactions and corresponding mass-action equilibrium constants are necessary to solve for the lattice concentration of defects:



(Notice that the product $K_1 K_2 / K_i^4$ equals the Frenkel equilibrium constant, K_f .) The electroneutrality condition (in compositions co-doped with acceptor and donor solutes) is given by

$$[A_{Ti}']_{\infty} + n_{\infty} + 4[V_{Ti}'''']_{\infty} = [D_{Ti}']_{\infty} + 4[Ti_i^{...}]_{\infty} + p_{\infty} \quad (4)$$

and can be rewritten in terms of the above equilibrium constants as

$$[A_{Ti}']_{\infty} + n + \frac{4K_2}{K_i^4} p_{\infty} n^4 = [D_{Ti}']_{\infty} + \frac{4K_1}{p_{\infty} n^4} + \frac{K_i}{n} \quad (4A)$$

Using Eqs. 1-4, the concentrations of all defects can be calculated for given conditions of dopant concentration, temperature, and p_{O_2} , using available values for the constants K_1 , K_2 , and K_i . The accuracy of the calculation obviously depends on the accuracy of the equilibrium constants. Unfortunately, neither absolute accuracy nor error limits are usually reported for defect equilibrium constants. Upon analysing several sources of literature data for the value of K_1 (in which experiments appear to have been carefully conducted) [21,23,25-28], we find that the reported values agree with one another to within a factor of 2 over the temperature range of 1273-1623K. Evaluating K_i separately, the value of K_2 can also be separated from experimental data in donor-doped compositions which provide a value for the combined equilibrium constant K_2/K_i^4 [23,25,26]. Upon doing so, the value of K_2 also varies by less than a factor of 2 amongst three sources of data. This gives some confidence in the reliability of the equilibrium constants. In calculating Figures 1 and 2, constants obtained by Baumard and Tani [25] have been used, as these values self-consistently describe the experimentally observed variation in electrical conductivity of a single set of donor-doped materials over a wide range of temperature and oxygen activity.

Having calculated the concentration of lattice defects for various defect conditions representative of the actual experiments conducted, the space-charge potential at interfaces can then be calculated assuming an equilibration of these defects with the interface. According to the formalism developed by Lebovec [2] and Kliwer and Koehler [3], the free energy of a crystal containing point defects is minimized at finite temperature by balancing the configurational entropy gained for dispersing defects within the lattice with the free energy gained upon segregating defects to sites of lower energy at the surface. In principle all defects can have an interaction with the interface (i.e., the very surface layer of a crystal, or the disordered "core" region at grain boundaries). For the host ionic defects, V_{Ti}''' and $Ti_i^{...}$, the interaction energy is equivalent to a defect formation energy, defined as the energy to form the defect within the lattice by moving an ion to or from the interface. For solutes this interaction energy is essentially a Gibbsian adsorption energy, and for electrons and holes, a trapping energy. In the present study we simplify matters by considering only solutes of fixed aliovalency, and which are very close in ionic radius to the host, Ti^{4+} . Estimated elastic-misfit strain energy for segregation are thus small compared to the electrostatic driving force resulting from the space charge model [18]. At the high temperatures of interest in this study ($T > 1200^{\circ}C$), we also assume that electron and hole trapping are negligible. This is equivalent to assuming that all ionic defects remain fully ionized throughout the crystal. (At lower temperatures, electrons and holes may be trapped at interfacial defects of both intrinsic and extrinsic types; indeed, at room

temperature, it is this trapping which gives rise to grain boundary barriers in electroceramics.)

With these simplifying assumptions, the space charge potential is determined by the formation energy of the host ionic defects ($g_{V_{Ti}}$ and g_{Ti_i}), their lattice defect concentration, and temperature. Choosing a reference point for the space charge potential which is zero at the surface, the potential varies with distance as $\phi(x)$, reaching a bulk potential value of ϕ_∞ . Upon minimizing the free energy of the defective crystal, the condition of thermal equilibrium is one in which the concentration of each defect varies with potential in the space charge layer as

$$n_i(x) = n_{i,\infty} \exp \left[\frac{-z_i e [\phi(x) - \phi_\infty]}{kT} \right]. \quad (5)$$

where $n_{i,\infty}$ is the lattice defect concentration (per cm^{-3}) and $z_i e$ is the effective charge of the defect. (Eq. 5 assumes that the Debye length of the space charge layer is sufficiently large and the defect concentrations sufficiently small that a continuum description is applicable. This seems to be a reasonable approximation for the present system [17,18].) Far from the interface, the host defects $V_{Ti}^{'''}$ and $Ti_i^{''''}$ are formed against a potential value of ϕ_∞ and with an energy expenditure of $g_{V_{Ti}}$ or g_{Ti_i} , giving the lattice concentrations:

$$[V_{Ti}^{''''}]_\infty = \exp \left[\frac{-(g_{V_{Ti}} - 4e\phi_\infty)}{kT} \right] \quad (6)$$

$$[Ti_i^{''''}]_\infty = \exp \left[\frac{-(g_{Ti_i} + 4e\phi_\infty)}{kT} \right] \quad (7)$$

in which the concentrations are in mole fraction relative to the lattice density of Ti sites. Since the lattice concentrations are known from the defect model, the net potential difference between the interface and bulk, equivalent to ϕ_∞ , can be obtained directly. Using relations (5) and (6), the variation in space charge potential with lattice defect chemistry is shown at the top of Fig. 1 (in this example $g_{V_{Ti}}=2.4$ eV and $g_{Ti_i}=2.1$ eV). Notice that a "titration" of the potential from positive to negative, through an isoelectric point (zero potential difference), is expected as a function of lattice defect chemistry. Notice also that this isoelectric point falls very close to the *stoichiometric* point in the defect diagrams (e.g., where $[V_{Ti}^{''''}] = [Ti_i^{''''}]$). However, the stoichiometric point and the isoelectric are not precisely coincident unless $g_{V_{Ti}}=g_{Ti_i}$.

Combining results such as those shown in Fig. 1, a complete space charge potential surface can be calculated as a function of the experimental variables, as shown in Fig. 2. Here the variation in ϕ_∞ with doping and oxygen activity has been calculated for a temperature of 1350°C; other surfaces result at other temperatures. These results give the direct correspondence between the lattice defect chemistry of TiO_2 and the space charge potential. Notice that regimes of negative ϕ_∞ essentially correspond to where $TiO_{2-\delta}$ is understoichiometric (oxygen deficient, $\delta>0$), whereas regimes of positive ϕ_∞ correspond to where the lattice is overstoichiometric (cation deficient, $\delta<0$).

Furthermore, for each value of the space charge potential, there exists a unique value of the interfacial charge density, σ (which is balanced by the space charge). While the value of ϕ_∞ is determined by the interaction of $V_{Ti}^{'''}$ and $Ti_i^{....}$ with the interface, all charged defects are free to accumulate or deplete in the resulting space charge layer (according to Eq. 5). By choosing solutes (e.g., Al^{3+} , Ga^{3+} , and Nb^{5+}) with minimal adsorption driving force, we have in essence introduced *charge tracers* which can freely segregate or deplete in the space charge layer in response to the electrical potential. Their net accumulation in the space charge layer is therefore equivalent to σ . In the experiments discussed below, we use the accumulation and depletion of the aliovalent solutes to determine σ . The relationship between σ and ϕ_∞ is obtained by solving Gauss' law and Poisson's equation [18], giving

$$\sigma = -\left\{ \frac{ekT}{2\pi} \sum_i n_i \infty \left[\exp\left(\frac{z_i e \phi_\infty}{kT}\right) - 1 \right] \right\}^{1/2} \quad (8)$$

where the summation is over all charged defects in the system. As discussed in ref. 17, the contribution of minority defects to the charge density becomes negligible when the defect structure is clearly dominated by extrinsic doping, and Eq. 8 can be simplified with little error to include only the defects showing the greatest absolute change in concentration in the space charge layer, which are the acceptor and donor solutes.

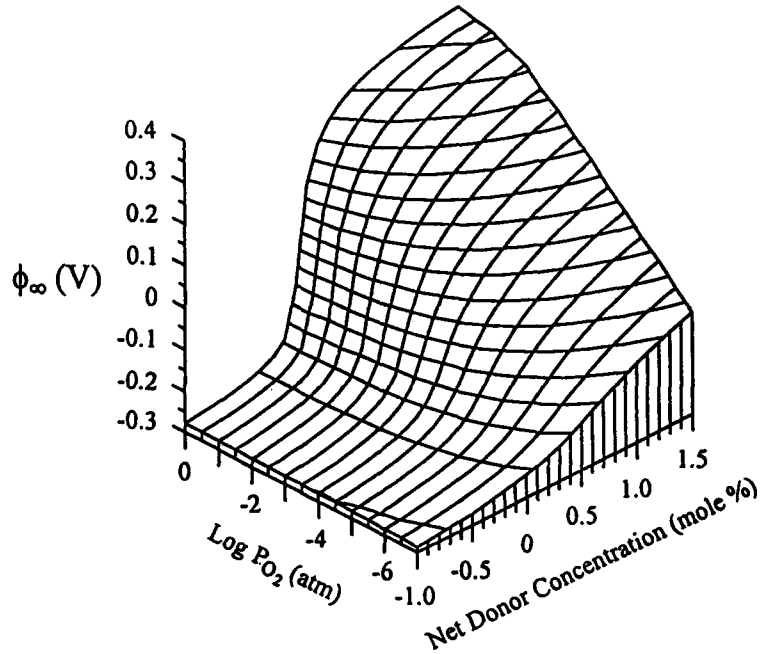


Figure 2. Space charge potential as a function of solute doping and p_{O_2} , calculated using defect model in text and experimentally determined values of defect formation energies, $g_{V_{Ti}}=2.4$ eV and $g_{Ti_i}=2.6$ eV.

EXPERIMENTS

We studied the grain boundary segregation in polycrystalline samples co-doped with Al^{3+} or Ga^{3+} as an acceptor and Nb^{5+} as a donor, equilibrated under conditions of temperature and oxygen partial pressure spanning the defect regimes shown in Figs. 1-3. Homogeneously doped TiO_2 powders were prepared by coprecipitation from aqueous chloride solutions, and the compositions analysed using inductively coupled plasma (ICP) emission spectroscopy. Polycrystalline samples were sintered and annealed for several hours at the desired temperatures, in air or CO/CO_2 mixtures giving the desired oxygen partial pressure, and quenched by rapidly withdrawing from the furnace hot zone to room temperature ambient gas. Quench rate experiments [18] showed that in donor-doped compositions, even leisurely cooling is sufficient to preserve the high temperature solute distribution, while in acceptor-doped compositions, solute segregation during cooling must be taken into account due to much faster diffusion kinetics.

Segregation was studied using scanning transmission electron microscopy (STEM, Vacuum Generators model HB5). Conventional segregation profiles were obtained by stepping the ~ 1 nm electron beam at close intervals across grain boundaries oriented parallel to the beam, accumulating point-by-point analyses of composition. These profiles provided qualitative results showing solute segregation as well as depletion, and also provide indications of the width of the segregated layers. For quantitative analyses of space charge, a different method was used in which the excess coverage of each aliovalent solute, Γ_i (concentration per unit boundary area) was measured. Both segregation and depletion (negative Γ_i) were taken into account. The details of the method are discussed elsewhere [18]. In brief, a volume in the shape of a rectangular parallelepiped, containing the grain boundary plane, is defined by rastering the nanometer-sized probe of the Vacuum Generators HB5 STEM across the surface of the specimen (Fig. 3).

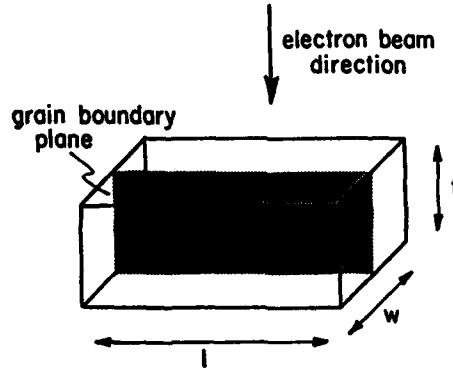


Figure 3. Schematic of STEM analysed volume used to measure grain boundary solute coverage.

The scanned area ($l \times w$) is made large enough with respect to the probe size and associated beam broadening (which is thickness-dependent) that the incident electron intensity is uniform across the analysed volume, but small enough for a high sensitivity to any segregated solute. The width w is chosen to be sufficiently large to include the boundary and both space charge layers. Typical scanned areas were 26.5×34.0 nm or 13.3×17.0

nm, in specimens of 60-150 nm thickness. Using energy-dispersive x-ray analysis (Link Systems windowless detector), the excess solute concentration within this volume is measured, using the grains on either side as internal standards (assumed to be of the ICP-analysed bulk composition). The excess (or deficit) concentration of each aliovalent solute is related to its coverage by:

$$\Gamma_i = C_i^{\text{excess}} \cdot N \cdot w \quad (9)$$

where N is the cation site density in the lattice ($3.21 \times 10^{22} \text{ cm}^{-3}$ for rutile). For measurement of interfacial coverage, this method gives both high precision (due to the ease of accumulating data for long times and good counting statistics) and high accuracy (assuming good compositional standards) since the analyzed volume need not be deconvolved from the segregation profile. A number of interfacial segregation studies have recently been performed using this method, including characterization of grain size-dependent segregation in TiO_2 [29], the composition and "chemical width" of thin glassy films at grain boundaries in ruthenate thick-film resistors [30], and Bi solute coverage at ZnO grain boundaries [31].

Assuming that all aliovalent solute segregation or depletion takes place in the space-charge layers, and that the segregation is symmetric about the grain boundary plane, the boundary charge density compensating a single space charge layer, σ , is one-half the total aliovalent solute coverage measured:

$$\sigma = \frac{1}{2} \sum_i \Gamma_i \quad (10)$$

The electrical potential difference, ϕ_{∞} , at the boundary in question is determined from the measured value of σ using Eq. 8, and the calculated defect concentrations.

TITRATION OF THE SPACE CHARGE POTENTIAL

Segregation profiles showed that the segregation or depletion of aliovalent solutes varied with dopant concentration, temperature, and oxygen activity, in agreement with the space charge model. Figures 4 and 5 show examples where the effective charge of the segregated solute has changed sign as each of the experimental variables are independently varied, demonstrating a reversal in the sign of the space charge potential. In Fig. 4, the horizontal sequence shows (A) the segregation of Al acceptor and depletion of Nb donor when the sample has a net acceptor doping, (B) no observed segregation at slight donor doping, near the isoelectric point, and (C) Nb segregation and Al depletion, when the sample has a net donor doping. This sequence represents a variation of ϕ_{∞} from negative to positive values, as shown in Fig. 1. Proceeding vertically from D-B-E, on the other hand, the potential in a sample of constant composition is titrated from negative to positive with decreasing temperature. In Fig. 5, a sample of fixed net donor level (0.51% Nb) shows reduced Nb segregation when the oxygen partial pressure is reduced from 0.21 atm to 5.8×10^{-4} atm, and then a change to acceptor segregation (with slight donor depletion seen) as the p_{O_2} is further reduced to 8.7×10^{-7} atm. This sequence clearly demonstrates the titration of ϕ_{∞} from positive to negative sign with decreasing p_{O_2} , as calculated in Fig. 1(B).

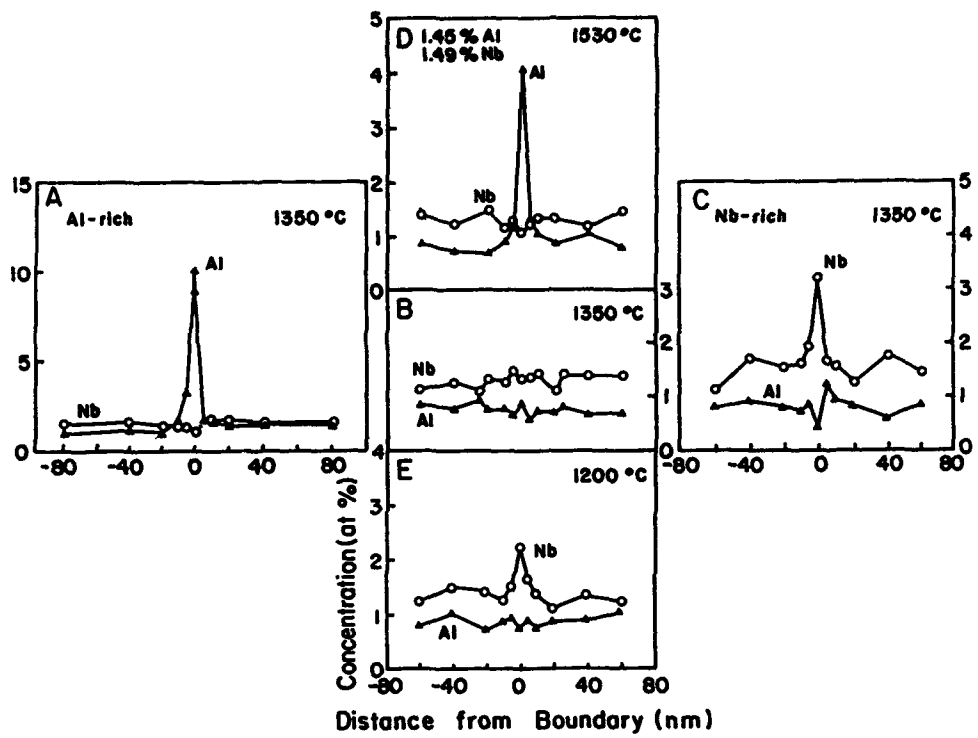


Figure 4. Segregation profiles in co-doped TiO_2 at 1350°C showing accumulation and depletion of aliovalent solutes at grain boundaries in TiO_2 , and "titration" in the effective charge of the segregated solute as doping and temperature are varied.

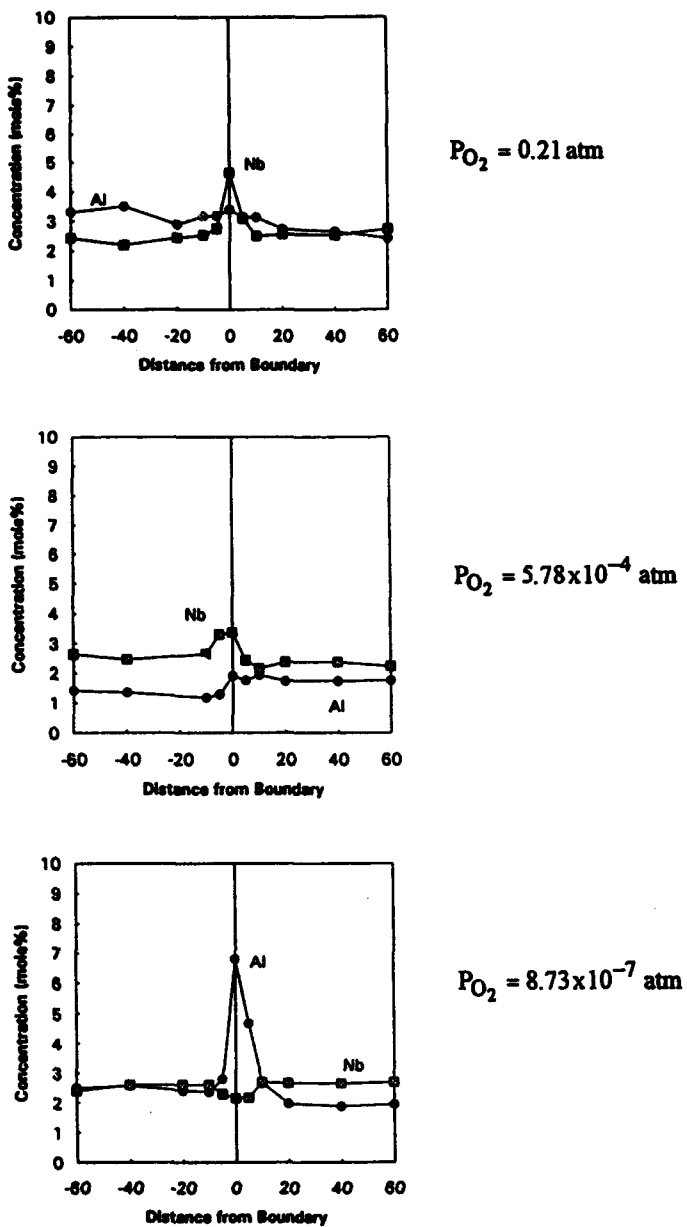


Figure 5. Oxygen partial pressure dependence of segregation in a co-doped sample with 0.51% net donor doping, at 1350°C, showing change from donor to acceptor segregation as p_{O_2} is reduced.

QUANTIFICATION OF SPACE CHARGE PARAMETERS

Quantitative measurements of the space charge potential are shown in Figs. 6 and 7. In these results, each datum represents a single grain boundary, at which the net accumulation of aliovalent solute was measured and the potential calculated from Eq. 8. The boundaries were randomly selected, with the only criterion being suitability for STEM analysis (i.e., the region was not overly thick, and the grain boundary could be tilted parallel to the electron beam, with neither grain in a strongly diffracting condition). The results are therefore representative of the distribution of boundaries in a polycrystal. In all samples, an occasional boundary with virtually no detectable segregation is observed. These are believed to be special boundaries of high coincidence misorientations; in fact, one such boundary was found using high resolution transmission electron microscopy to be a {101} twin boundary [18]. Even excluding these "special" boundaries, a significant variation in ϕ_{∞} from boundary to boundary is observed, which further analysis has shown lies outside the counting statistics errors of the measurements, and are probably related to details of boundary structure.

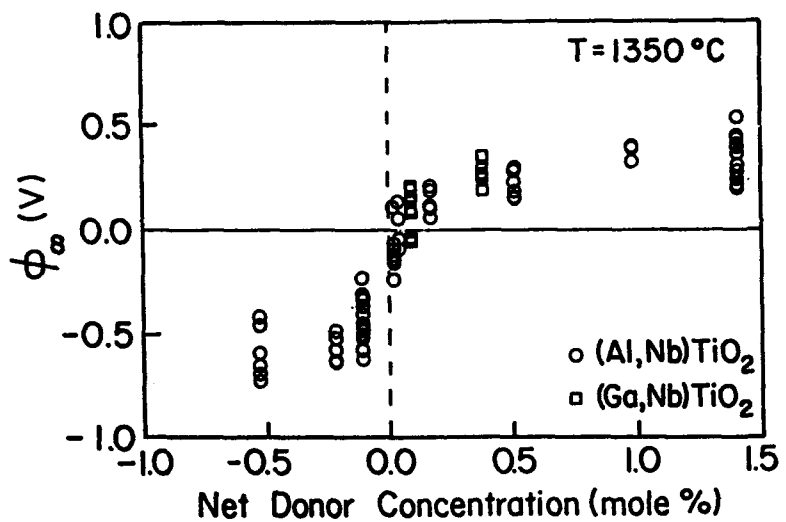


Figure 6. Space charge potential determined from aliovalent solute coverage at grain boundaries, excluding "special" boundaries with virtually no segregation.

In acceptor-doped samples, a factor contributing to the larger spread in observed values is nonequilibrium segregation upon cooling. This is particularly significant at higher acceptor concentrations, due to an increase in lattice diffusion rates. The σ and ϕ_{∞} values in acceptor-doped samples are therefore be regarded as upper limits. Upon fitting the space charge model to the ϕ_{∞} values in Fig. 6, we obtained a cation vacancy formation energy, gV_{Ti} , of 2.4 eV and an upper limit to gTi of 2.6 eV. The sum of these yields a

Frenkel energy of ≤ 5.0 eV, which is in reasonable accord with results from Baumard and Tani [25], Tani and Baumard [26], and Tuller [23] of 4.4-4.6 eV. (Notice that whereas the separate terms in E_f can be obtained from the space charge interaction, only the sum of energies is possible from transport studies.) The appearance of the isoelectric point in the donor-doped regime (Figs. 1 and 6) is due to the contribution of native reduction to the defect structure at high temperature; a slight donor doping is necessary to compensate for the defects introduced by reduction. With increasing temperature, or decreasing p_{O_2} , increasing amounts of lattice reduction cause the isoelectric to move to higher donor concentrations [18].

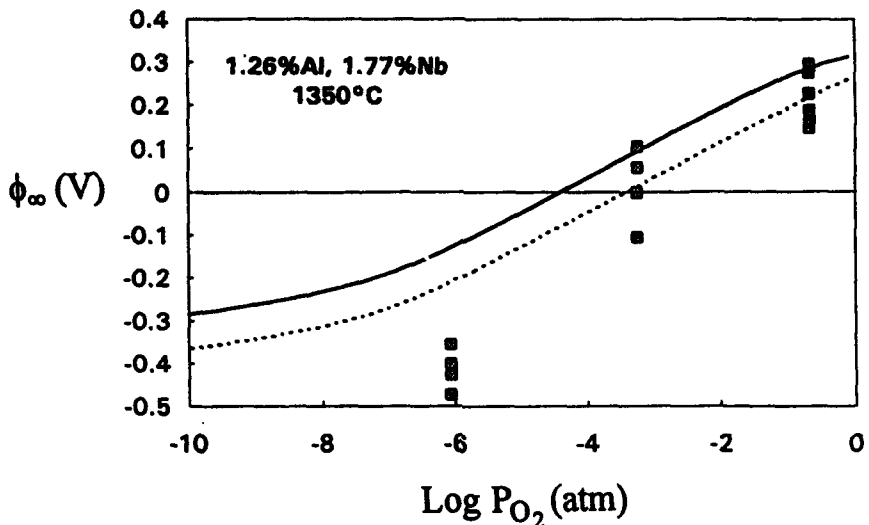


Figure 7. Experimental and calculated results for the space charge potential as a function of oxygen partial pressure, in a sample containing 0.51% net donor doping.

Results as a function of p_{O_2} (Fig. 7) also show the "titration" of the potential from positive to negative values (for a donor doped sample) as predicted by the model (e.g., Fig. 1B). With respect to the detailed fit between model and data, it should first be noted that segregation of Al during cooling is likely for the sample annealed at the lowest p_{O_2} . This is because the lattice is understoichiometric, as in the case of acceptor doped compositions. The two samples in Fig. 7 showing a near-zero and a positive potential are adequately quenched, however, and the model can be fitted to these data assuming a preservation of high temperature equilibrium. The solid curve in Fig. 7 is calculated using the defect energies and equilibrium constants which were discussed earlier. While it shows a noticeable discrepancy with the data, the variation in the parameters necessary to produce a better fit is small. For example, the dashed curve shows a better fit obtained using a factor-of-5 lower value for the product of equilibrium constants, K_2/K_1^4 . Variability of this order in the equilibrium constants would not be surprising (e.g., only a factor of 1.5 error in K_i .) If the equilibrium constants are not changed, a variation in the defect formation energies of ~ 0.2 eV produces a similar result. These small variations in the

fitting parameters notwithstanding, the level of quantitative agreement between the model and the data is excellent, and strongly supports the interpretation that the ionic space charge is the primary cause of the boundary segregation. Limited observations of surface segregation in these samples using Auger electron spectroscopy are qualitatively consistent with the STEM results for grain boundaries, suggesting that other types of interfaces, and perhaps dislocations as well, behave similarly.

IMPLICATIONS FOR ELECTROCERAMICS

The results illustrate a clear and quantitative link between a complex lattice defect chemistry and the space charge potential, suggesting that the defect chemistry of interfaces in semiconducting oxides can be predicted on the basis of lattice properties. In this model system, despite high electronic carrier concentrations, it appears to be the equilibration of ionic defects with the interface which determines the interfacial chemistry. The results also imply that interfaces in semiconducting oxides will generally be nonstoichiometric. If valences of cations and anions are indeed fixed, in the presence of a space charge potential the interfacial charge σ is an ionic charge, and must arise from a grain boundary nonstoichiometry. Thus the potential surface in Fig. 3 also corresponds to a stoichiometry surface for the interface. In the present system, regardless of whether the lattice defect structure is varied as a consequence of changes in doping, temperature, or oxygen activity, *understoichiometric* $\text{TiO}_2\text{-}\delta$ ($\delta>0$) has an oxygen deficient interface, while *overstoichiometric* $\text{TiO}_2\text{-}\delta$ ($\delta<0$) has a cation deficient interface. An exactly stoichiometric interface can exist, but is a singularity in defect space and would seem to be of limited importance. This deviation in interfacial stoichiometry is much larger than the parallel variation in lattice nonstoichiometry. At the bulk defect concentrations and temperatures examined in this study, the interfacial charge densities reach monolayer proportions [18], corresponding to interfacial ionic defect concentrations (of unknown specific identity) which are several tens of percent. It would be remarkable if such large changes did not have an impact on the physical structure of surfaces and grain boundaries, or their chemical and electronic properties. However, the details of these relationships remain to be elucidated.

It is important to emphasize that the present results are concerned with *equilibrium* defect and solute distributions. While these have an obvious and direct relevance to high temperature equilibrium boundary phenomena, they are only one aspect of the complex defect behavior of electrically active boundaries. In a variety of electroceramics including ZnO varistors, BaTiO_3 PTC thermistors, and soft magnetic ferrites, the optimization of boundary properties often involves both a high temperature firing step and a controlled, oxidative cooling step. While equilibrium segregation may be achieved during the former, nonequilibrium defect creation processes and additional solute segregation are likely during the latter. In addition to segregation during cooling, exemplified by the acceptor-doped and reduced TiO_2 studied here, demixing and defect formation processes can occur in the presence of local pO_2 gradients. Oxidation-driven solute segregation, which has been observed at TiO_2 surfaces [32], and cation vacancy creation at PTC boundaries [33] as the bulk strives towards a new defect equilibrium, are two specific processes of this kind. To fully understand the relationship between interfacial defects and electrical properties, results such as those discussed here combined with studies correlating additives with the appearance of specific interface states [34] are clearly necessary.

CONCLUSIONS

From defect and space-charge modeling and the quantitative measurement of aliovalent solute segregation at grain boundaries, the functional dependence of the space-charge potential in TiO_2 on lattice defect structure has been clarified. Throughout a broad range of bulk defect conditions, an ionic space-charge is maintained. Correspondingly, it is inferred that the grain boundaries and surfaces of TiO_2 are generally nonstoichiometric; and regardless of whether the lattice defect structure is varied as a consequence of changes in doping, temperature, or oxygen activity, understoichiometric $TiO_{2-\delta}$ ($\delta > 0$) bears a positive interfacial charge, implying an oxygen deficiency at the interface, while overstoichiometric $TiO_{2+\delta}$ ($\delta < 0$) bears a negative interfacial charge, i.e., a cation deficiency at the interface. The interfacial and space charge defect densities are often a large fraction of a monolayer. It is expected that such dramatic changes in interfacial defect concentration have a significant influence on the electrical, chemical, and structural characteristics of surfaces and grain boundaries, and that similar behavior occurs in other semiconducting oxides.

Acknowledgments

We are grateful to Professors H.L. Tuller and J.B. Vander Sande, and Dr. A.J. Garratt-Reed, for many useful discussions. The support of U.S. Department of Energy Grant No. DE-FG02-87ER45307 and NSF/MRL Grant No. DMR 90-22933 is acknowledged.

References

1. J. Frenkel, Kinetic Theory of Liquids, Oxford University Press, New York, 1946.
2. K. Lehouc, "Space-Charge Layer and Distribution of Lattice Defects at the Surface of Ionic Crystals," *J. Chem. Phys.* **21** [7] 1123 (1953).
3. K.L. Kliewer and J.S. Koehler, "Space Charge in Ionic Crystals. I. General Approach with Application to NaCl," *Phys. Rev.* **140** [4A] A1226 (1965).
4. J.M. Blakely and S. Danyluk, "Space Charge Regions at Silver Halide Surfaces: Effects of Divalent Impurities and Halogen Pressure," *Surf. Sci.* **40** 37 (1973).
5. S. Danyluk and J.M. Blakely, "Space Charge Regions at Silver Halide Surfaces: Experimental Results for Undoped AgCl," *Surf. Sci.* **41** 359 (1974).
6. M.F. Yan, R.M. Cannon, and H.K. Bowen, "Space Charge, Elastic Field, and Dipole Contributions to Equilibrium Solute Segregation at Interfaces," *J. Appl. Phys.* **54** [2] 764 (1983).
7. R.A. Hudson, G.C. Farlow, and L.M. Slifkin, "Individual Formation Parameters of Charged Point Defects in Ionic Crystals: Silver Chloride," *Phys. Rev. B* **36** [9] 4651 (1987).
8. J.R.H. Black and W.D. Kingery, "Segregation of Aliovalent Solutes Adjacent to Surfaces in MgO," *J. Am. Cer. Soc.* **62** [3-4] 176 (1979).

9. Y.M. Chiang, A.F. Henriksen, W.D. Kingery, and D. Finello, "Characterization of Grain-Boundary Segregation in MgO," *J. Am. Cer. Soc.* **64** [7] 385 (1981).
10. Y.-M. Chiang and W.D. Kingery, "Grain Boundary Migration in Nonstoichiometric Solid Solutions of Magnesium Aluminate Spinel: II, Effect of Grain Boundary Nonstoichiometry," *J. Am. Cer. Soc.* **73** [5] 1153-58 (1990).
11. Y.-M. Chiang and W.D. Kingery, "Grain Boundary Composition in MnZn Ferrites," Advances in Ceramics, Vol. 6, edited by M.F. Yan and A.H. Heuer, pp. 300-311, The American Ceramic Society, Columbus, Ohio, 1983.
12. C.J. Peng and Y.-M. Chiang, "Grain Growth in Donor-Doped Strontium Titanate," *J. Mat. Res.*, **5**[6], 1237-45 (1990).
13. Y.-M. Chiang and T. Takagi, "Grain Boundary Chemistry of Barium Titanate and Strontium Titanate: I, High Temperature Equilibrium Space Charge," *J. Am. Ceram. Soc.*, **73**[11], 3278-85 (1990).
14. Y.-M. Chiang and T. Takagi, "Grain Boundary Chemistry of Barium Titanate and Strontium Titanate: II, Origin of Electrical Barriers in Positive-Temperature-Coefficient Thermistors," *J. Am. Ceram. Soc.*, **73**[11], 3286-91 (1990).
15. S.B. Desu and D.A. Payne, "Interfacial Segregation in Perovskites: II, Experimental Evidence," *J. Am. Ceram. Soc.*, **73**[11], 3398-406 (1990).
16. J.A.S. Ikeda, Y.-M. Chiang and C.G. Madras, "Grain Boundary Electrostatic Potential as a Function of Acceptor and Donor Doping in TiO₂," pp. 341-8 in Ceramic Transactions vol. 24: Point Defects and Related Properties of Ceramics, Ed. by T.O. Mason and J.L. Routbort, Am. Ceram. Soc., Cincinnati, OH, 1991.
17. J.A.S. Ikeda and Y.-M. Chiang, "Space Charge Segregation at Grain Boundaries in Titanium Dioxide: I, Relationship between Lattice Defect Chemistry and Space Charge Potential," *J. Am. Ceram. Soc.*, **76**[10] 2437-46 (1993).
18. J.A.S. Ikeda, Y.-M. Chiang, "Space Charge Segregation at Grain Boundaries in Titanium Dioxide: II, Model Experiments," *J. Am. Ceram. Soc.*, **76**[10] 2447-59 (1993).
19. L.A. Bursill, M.G. Blanchin, and D.J. Smith, "Precipitation in Non-Stoichiometric Oxides. II, {100} Platelet Defects in Reduced Rutiles," *Proc. R. Soc. Lond. A*, **391**, 373-91 (1984).
20. L.A. Bursill, G.-J. Shen, D.J. Smith, and M.G. Blanchin, "Emergence of Small Defect Contrast within HREM Images of Nonstoichiometric Rutile," *Ultramicroscopy*, **13**, 191-204 (1984).
21. J. Sasaki, N.L. Peterson and K. Hoshino, "Tracer Impurity Diffusion in Single-Crystal Rutile (TiO_{2-x})," *J. Phys. Chem. Solids* **46** [11] (1985).

22. K. Hoshino, N.L. Peterson and C.L. Wiley, "Diffusion and Point Defects in TiO_{2-x} ," *J. Phys. Chem. Solids* **46** 1397 (1985).
23. H.L. Tuller, unpublished work.
24. J.A.S. Ikeda, "Grain Boundary Defect Chemistry and Electrostatic Potential in Acceptor- and Donor-Doped Titanium Dioxide," Ph.D. Thesis, MIT, Cambridge, Massachusetts, June 1992.
25. J.F. Baumard and E. Tani, "Thermoelectric Power in Reduced Pure and Nb-Doped TiO_2 Rutile at High Temperature," *Phys. Stat. Sol. A* **39** 373 (1977), and J.F. Baumard and E. Tani, "Electrical Conductivity and Charge Compensation in Nb Doped TiO_2 Rutile," *J. Chem. Phys.* **63** [3] 857 (1977).
26. E. Tani and J.F. Baumard, "Electrical Properties and Defect Structure of Rutile Slightly Doped with Cr and Ta," *J. Solid State Chem.*, **32**, 105-113 (1980).
27. G. Levin and C.J. Rosa, "The Defect Structure, Nonstoichiometry and Electrical Conductivity of MO_2 Oxides Doped by Pentavalent Oxides, Part II: The Defect Structure and Electrical Conductivity of Pure and Doped TiO_2 (Rutile) at 1273K," *Z. Metallkde.*, **70**, 646-652 (1979).
28. J.F. Marucco, J. Gautron, P. Lemasson, "Thermogravimetric and Electrical Study of Non-stoichiometric Titanium Dioxide TiO_{2-x} between 800 and 1100°C," *J. Phys. Chem. Solids* **42** 363 (1981).
29. C.D. Terwilliger, "Determination of Grain Boundary Properties in Nanocrystalline Materials," Ph. D. Thesis, MIT, Cambridge, Massachusetts, September 1993.
30. Y.-M. Chiang, L.A. Silverman, R.H. French, and R.M. Cannon, "The Thin Glass Film between Nanocrystalline Conductor Particles in Thick Film Resistors," to appear in *J. Am. Ceram. Soc.*.
31. J.-Q. Lee and Y.-M. Chiang, unpublished.
32. J.A.S. Ikeda, Y.-M. Chiang and B.D. Fabes, "Non-Equilibrium Surface Segregation in Al-doped TiO_2 under an Oxidizing Potential: Effects on Redox Color-Boundary Migration," *J. Am. Cer. Soc.* [6] 1633 (1990).
33. J. Daniels and R. Wernicke, "Defect Chemistry and Electrical Conductivity of Doped Barium Titanate Ceramics: Part V. New Aspects of An Improved PTC Model," *Philips Res. Repts.*, **31**[6], 544-59 (1976).
34. H.L. Tuller and K.-K. Baek, these proceedings.

ELECTRICAL ACTIVITY AT INDIVIDUAL GRAIN BOUNDARIES AND INTERFACES IN SEMICONDUCTING OXIDES

H.L. Tuller and K-K. Baek
Center for Materials Science & Engineering
Massachusetts Institute of Technology
Cambridge, MA 02139

ABSTRACT

Grain boundaries and other interfaces often control the electrical properties of devices. A clearer understanding of the chemistry-structure-property correlations of such boundaries can be achieved by examining individual electrically active boundaries. Following a review of earlier such work, we report recent results on active boundaries isolated in ZnO ceramics by an in-diffusion method. Breakdown voltages and nonlinearity coefficients are examined as a function of processing conditions and dopant types. DLTS measurements are used to identify interface states and other deep levels in the vicinity of the boundaries. Directions for future work are proposed.

INTRODUCTION

It is well known that the unique abilities of semiconductor electronics to rectify, modulate, switch and amplify electrical signals derive from the existence of many individual, highly controlled electrically active junctions. The most important of these are the p-n, metal-semiconductor and metal-insulator-semiconductor (MIS) interfaces. In some applications, particularly solar photovoltaic and display technologies, polycrystalline semiconductors are utilized which, by their nature, introduce additional interfaces, i.e. grain boundaries, some of which are electrically active. The electrical activity of these boundaries and their dependence on processing conditions, even in silicon, remain poorly understood.

In contrast to conventional semiconductor technology, in which the use of single crystalline semiconductors predominates, electro-ceramics, for historic and cost reasons, are largely polycrystalline. Consequently grain boundaries often control the electronic properties of these devices. This can result in increased resistance and non-ohmic behavior of the device as well as difficulty in reproducing desired device characteristics. Grain boundaries which block

To the extent authorized under the laws of the United States of America, all copyright interests in this publication are the property of The American Ceramic Society. Any duplication, reproduction, or republication of this publication or any part thereof, without the express written consent of The American Ceramic Society or fee paid to the Copyright Clearance Center, is prohibited.

electronic transport between the grains in negative temperature coefficient (NTC) thermistors, for example, are to be avoided. On the other hand, electrically active interfaces are essential to the operation of the ZnO varistor, the BaTiO₃ positive temperature coefficient (PTC) thermistor, the SrTiO₃ barrier layer capacitor and the SnO₂ gas sensor, to name a few.

While both electro-ceramic polycrystalline devices and integrated circuits contain hundreds or thousands of individual boundaries, only in integrated circuits, where one uses parallel planar processes, can many junctions be fabricated simultaneously with near identical characteristics. In the sintering processes used to make electro-ceramics, inhomogeneities are the rule rather than the exception. Such materials are characterized by non-uniform grain size, porosity, second phase distribution, impurity segregation and grain-grain misorientation.

In this paper, we focus our attention on attempts to investigate individual electrically active interfaces in ZnO-based structures with varistor-like properties. First, we summarize earlier investigations and comment on both their strengths and limitations. Then, we present some of our recent work on in-diffused structures which include some comprehensive deep level transient spectroscopy (DLTS) data as a function of dopants. Last, we conclude with suggestions for future work.

VARISTOR CHARACTERISTICS

A varistor is a device whose resistance decreases sharply at a characteristic breakdown potential. It may be used as an over-voltage protection device when placed in parallel with the circuit to be protected. A schematic of the I-V characteristics of a varistor is presented in Fig. (1). One generally distinguishes three regimes. At low voltage in the "prebreakdown regime" (Region I) the device shows ohmic-like characteristics with an effective resistivity of the order of 10¹⁰-10¹² ohm-cm and a so-called "leakage current" which is thermally activated. In the vicinity of the breakdown voltage (Regime II) the current increases orders of magnitude with small increases in voltage. The slope of this curve is given by the nonlinearity factor α with values between 30-60 typical for commercial devices. Ultimately, the resistance of the device is limited by the resistivity of the grains leading to the "up-turn" regime (Region III) where the device is again ohmic. "Up-turn" refers to the shape of the curve when plotted on a V vs. I plot.

From both a theoretical and practical standpoint, one wishes to understand the relationship between the magnitude and temperature dependence of the leakage current, the breakdown voltage V_B , the non-linearity factor, α , the device stability and the chemistry and structure of the grain boundary.

Perhaps the most widely accepted model of the grain boundary junction is the double back-to-back Schottky barrier model proposed by a number of

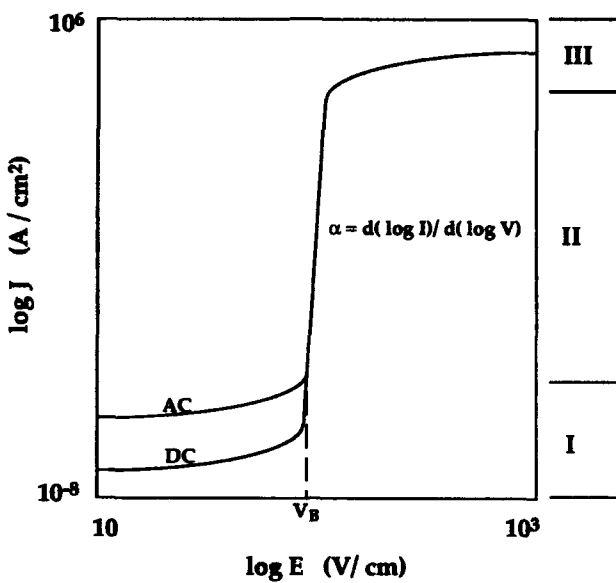


Figure 1: A schematic logJ-logE curve of a ZnO varistor. Region I is the prebreakdown regime; Region II is the breakdown regime; and Region III is the upturn regime.

investigators(1-4) over the years and summarized most recently by Greuter et al.(5) Key features of the model include (1) a distribution of interface states at the boundary which serve as electron traps, (2) corresponding positively charged depletion layers on either side of the boundary for charge compensation, (3) shallow donor levels in the grains to render them conductive and (4) additional deep levels in the bulk which are believed important in enhancing the depletion process, and (5) the resultant potential barrier Φ_B which blocks electron transport between grains at low voltage and contributes to the high resistivity in Region I. At voltages near V_B , electrons promoted above the barrier experience high accelerating potentials and, via an avalanche process, lead to significant electron-hole generation at the reverse biased junction. The resultant holes are swept towards the interface by the built-in field where they deplete the electron traps leading to a collapse of the barrier and a sharp increase in current density-Region II. The shape and magnitude of the I-V characteristics of Fig. 1 must depend on the initial barrier height Φ_{B0} at zero applied bias and the voltage dependence of the barrier height $\Phi_B(V)$. These in turn can be expected to depend on the density and distribution of the interface traps $N_t(E)$ and the densities and energies of the shallow and deep bulk levels N_o and N_i .

From a practical standpoint, three criteria, in addition to having conductive grains, must be met in order for polycrystalline ZnO to exhibit desirable varistor qualities. These include:

1. Deep donors, e.g. Mn
2. Segregants, e.g. Bi, Pr
3. Oxidative anneal

The obvious question which arises is how do these three factors influence the nature, density and distribution of interface and bulk states and in turn the barrier dependence on applied voltage? We look to individual interfaces to clarify these issues.

SINGLE BOUNDARY STUDIES

The idealized polycrystalline varistor is shown schematically in Fig. 2a in which each small square symbolizes a grain and each gray region between the grains, the depletion region. The dark strips at top and bottom of the figure represent the electrodes. The breakdown voltage per grain boundary is calculated by dividing the measured breakdown voltage of the device by the number of grain boundaries in series between the electrodes. The latter number is commonly obtained by dividing the device thickness D by the average grain size d.

However, it is difficult to understand the characteristics of a single grain boundary by measuring the overall electrical properties of a polycrystalline ZnO varistor, as the actual varistor consists of numbers of grain boundaries with varying characteristics connected, both in series and in parallel, thus forming rather complex three-dimensional networks.

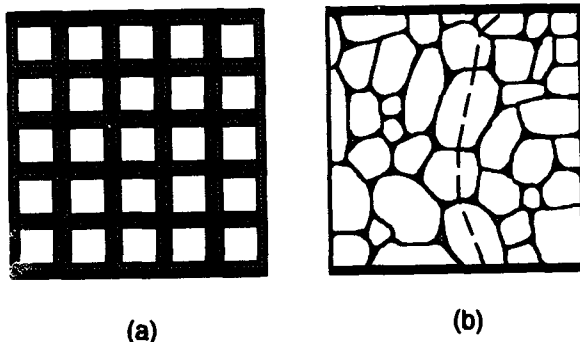


Figure 2 A schematic 2-dimensional diagram of an idealized ZnO polycrystalline varistor (a) and realistic representation of the same ZnO varistor (b).

A more realistic representation of a varistor is given in Fig. 2b which contains a distribution of grain sizes and shapes. The current path, illustrated by the dashed line, intercepts four possibly unequal grain boundary barriers. One can easily imagine others which intercept six or seven boundaries. Obviously the overall electrical characteristics are not representative of any individual boundary and can, at best, be used to obtain some average picture which may, with the appropriate models, be used to ascertain the degree of homogeneity of the system.(2)

An obvious way around these difficulties is to examine the properties of individual boundaries. Two general approaches have been taken to achieve this goal. The first involves interrogating individual boundaries in a polycrystalline mass by the use of micro-electrodes while the second requires the fabrication of structures which include only single active interfaces. These are reviewed below.

SINGLE GRAIN JUNCTION MEASUREMENT ON POLYCRYSTALLINE ZnO VARISTORS

Several studies have reported on the electrical characterization of single grain-to-grain junctions in polycrystalline ZnO varistors. Generally, three different experimental approaches have been used to accomplish this purpose. The first involves achieving microcontacts on two adjacent grains with the help of very sharp metallic needles (radius of curvature $\ll 1\text{mm}$) This arrangement is illustrated on the upper part of Fig. (3). Varistor-like characteristics with breakdown voltages of 4V were reported by Einzinger(6) using Bi-doped commercial ZnO varistors.

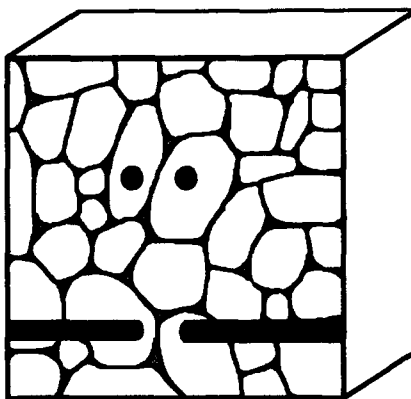


Figure 3 Microcontacts for single boundary I-V measurements

In a related approach, varistor specimens with very large grain size (diameter of about 150 μm) were prepared to accommodate the microwelding of lead wires (diameter of about 25 μm) on either side of single grain boundary on a surface treated polycrystalline varistor.⁽⁷⁾ Single boundary I-V characteristics with maximum α of 45, and V_B values of 3.1V were obtained. A near zero voltage barrier height (Φ_{B0}) was estimated to be approximately 0.57 eV from the temperature dependence of the leakage current.

In the second approach, improved electrical contacts are established by evaporating a pair of opposing aluminum⁽⁸⁾ or gold⁽⁹⁾ electrodes on the polished surface of a polycrystalline varistor disk. (See the lower part of Fig. 3) A breakdown voltage of ~3.3V was obtained from the I-V characteristics at room temperature according to Mahan et al⁽⁸⁾ and 3.6 V according to Van Kemenade.⁽⁹⁾

Einzinger performed similar measurements with Cr and Au sputtered-electrodes but on thin polished sheets (~0.2mm) of commercial ZnO varistor material.⁽¹⁰⁾ The surrounding ZnO material was removed with a micro-manipulator to isolate a 'true' single boundary.. The I-V characteristics of nominally second phase-free single boundaries were found to exhibit the well defined varistor behavior. Measurements taken on boundaries with and without Bi-rich intergranular layers indicated that the intergranular layers have a strong deleterious effects on the degree of nonlinearity.

Most recently, Dunlop and Olsson⁽¹¹⁾ reported single boundary DC I-V measurements on boundaries which were also investigated by TEM. This represents the first report which attempts to characterize both the electrical and chemistry of a individual boundary. The study showed that a distribution of types of boundaries with different I-V characteristics and phase distributions exist in ZnO varistors.

The microcontact method thus provides means, in principle, of studying many individual boundaries in a single device and thereby developing a statistical basis for understanding the overall characteristics of the device. Nevertheless, a number of important limitations remain. First, it is difficult to control the chemistry of individual boundaries. Second, due to the contact method, there is limited ability to examine the electrical properties at elevated tempearture and controlled atmosphere. Finally, unless the specimens are thinned, the current pathways remain difficult to control.

SYNTHETIC SINGLE BOUNDARY STUDIES

Thin Film Varistor

Some investigators have simulated a varistor structure by forming two layer structures in which one layer is ZnO and the other, a material which is typically a second phase found at the triple point between grains.

Suzuoki et al(12) studied a ZnO-Bi₂O₃ two-layer thin film varistor prepared by RF sputtering as a model system representing a single grain boundary in the ZnO varistor. The two-layer thin film structure showed highly non-linear, asymmetrical I-V characteristics whose nonlinearity coefficient for reverse bias equals or exceeds those of ZnO based varistors (maximum value of α ~ 60-90). The device, however, also exhibited a decrease in low voltage resistance after voltage application reflecting a degradation of the device.

A similar study of a thin film junction based on a ZnO-Pr/Co oxide two-layer thin film varistor has also been reported.(13) The junction showed highly nonlinear I-V characteristics with a maximum value of α around 30, when the ZnO layer was positively biased. The depletion region formed in the ZnO layer adjacent to the ZnO-PrCo oxide interface was attributed to be the main source of the electrical characteristics of the thin film junction.

The advantages of the thin film approach include the ability to readily form single barriers and control the interfacial chemistry. However, these studies show that the junctions do not accurately replicate the ZnO grain boundary, the barriers tend to be unstable upon biasing and dopants tend to become volatile during fabrication.

Bi-Crystal Varistors

Among the possible approaches to study an individual grain boundary, a ZnO bi-crystal with controlled dopants at the interface would appear to be the most ideal material for study. The inherent difficulties in fabricating such bi-crystals have, however, remained a major obstacle. Part of the difficulty is related to ZnO's high volatility, and high thermal expansion anisotropy. Because ZnO sublimates at the melting temperature, techniques for ZnO bi-crystal fabrication based on melt growth methods cannot be utilized.

Bi-crystal-like structures have however been fabricated by utilizing low melting interlayers. Schwing et al(14) fabricated such structures by sandwiching an intermediate layer of common varistor additives (Bi₂O₃, MnO₂, Co₃O₄, and Cr₂O₃) between undoped ZnO single crystal plates. The microstructure of the "sandwiches" fired at 900C for 1 hour consisted of two single crystals well separated by a 5 μ m thick intergranular layer. For the structures fired at 1100C, the microstructure was similar except that the ZnO single crystals were in direct contact at certain points along the interface. The sandwiches fired at 900C in general exhibited superior varistor I-V characteristics which was attributed directly to the presence of a continuous Bi₂O₃ rich layer at the interface absent in specimens fired at 1100C. However, ac measurements showed that the potential barriers at the sandwich interface were due to depletion regions adjacent to the additive oxide interfacial layers rather than to the layer themselves, which were shown to have resistivities much lower than for those calculated for the depletion layers.

Summarizing the bi-crystal work, the approach enables the investigation of a single boundary with a simplified current pathway and well controlled interfacial chemistry. However, since a continuous second phase at the interface is apparently necessary to obtain good varistor-like properties, the results may not be representative of actual grain boundaries.

Surface In-Diffusion

Non-ohmic grain boundary properties can also be obtained by diffusing oxides such as Bi_2O_3 and/or Sb_2O_3 into the grain boundaries of undoped ZnO as first demonstrated by Matsuoka.⁽¹⁵⁾ This approach relies on the fact that the diffusion of ions is more rapid along the grain boundaries, and thus the grain boundaries act as short circuit paths for diffusion. Sukkar and Tuller⁽¹⁶⁾ reported that single electrically active ZnO grain boundaries were successfully prepared by using a surface in-diffusion method. In this technique, a "sandwich" composed of undoped polycrystalline ZnO discs with dopants added to the interface is sintered at 1400-1440°C for 12-24 hours. Dopants with different nominal concentrations, either as single, double or triple additions were applied to the interface. As a result, single electrically active grain boundaries were successfully fabricated in Mn/Pr -, Co/Pr -, Mn/Co/Pr -doped ZnO samples.

Chiou et al⁽¹⁷⁾ also reported that low voltage ZnO varistors may be fabricated by metal surface in-diffusion of Bi_2O_3 into a ZnO pellet predoped with transition metal cations. In this case, the diffusion source was prepared by pressing the powder into a thin disc shape, and annealing at 950°C-1350°C for 1 hour. The prepared varistors showed a smaller non-linearity parameter (α max = 7-15) and a larger dielectric constant than commercial varistors.

The authors have followed on the work of Sukkar and Tuller by extending the so called Surface In-Diffusion (SID) method to include more extensive characterization methods including DLTS and transmission electron microscopy.⁽¹⁸⁾ Sandwich structures including Pr/Co , Pr/Mn , Pr/Ni , Pr/Co/Mn , and Pr/Mn/Ni have been investigated.

Typical I-V characteristics of a Pr/Co -doped SID sample at room temperature are shown in Fig. (4). Symmetric varistor like I-V characteristics with a breakdown voltage of ~3V were obtained. Also included is the incremental nonlinearity coefficient (α). These I-V characteristics confirm that a single electrically active boundary is formed in the direction perpendicular to current flow. Other SID specimens sometimes exhibit multiple active boundaries reflected in larger V_B 's. For evaluation of the potential barrier height (Φ_B), the modified thermionic model based on the double-Schottky barrier model proposed by Pike and Seager⁽¹⁹⁾ may be employed. The thermionic emission current across a single grain boundary potential barrier is given by

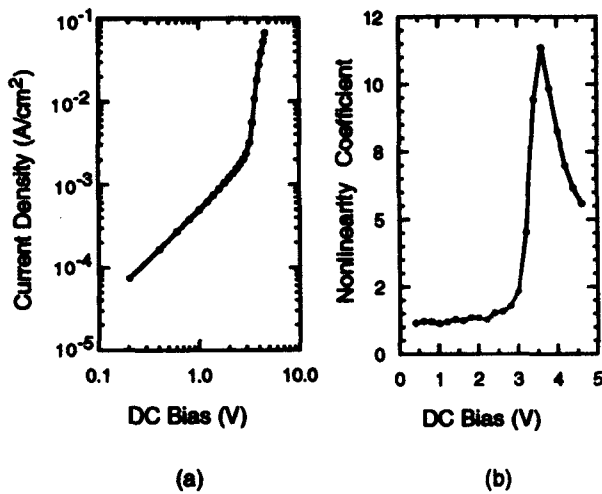


Figure 4 Typical electrical characteristics of a Pr/Co-doped SID ZnO varistor, (a) log-logV, (b) nonlinearity coefficient.

$$J = A^* T^2 \exp\{-(L+\Phi_B)/kT\} \{1-\exp(-eV/kT)\} \quad (1)$$

where Φ_B is the voltage dependent potential barrier height, A^* , the Richardson constant, and L the energy difference between the fermi energy and conduction band edge. At $V \approx 0$, equation (1) reduces to

$$J = A^* T eV / k (N_D / N_C) \exp\{-\Phi_B(V)/kT\} \quad (2)$$

where N_D is the donor density, N_C the conduction band effective density of states and $\Phi_B(0)$ the near zero bias barrier height. Thus, a plot of $\ln(G_0 T^{1/2})$ vs. $1/T$, where G_0 is the near-zero bias conductance, should yield a linear curve with a slope of $-\Phi_B(0)/k$ for a temperature-independent barrier height.

A plot of $\ln(G_0 T^{1/2})$ vs. $1/T$ for a Pr/Co/Mn-doped specimen yields an activation energy, ΔE , of 0.24 eV. Other specimens with a variety of dopants also measured over the same temperature range of 196-250°C yielded even lower activation energies in the range of 0.01 - 0.08 eV. These values are much smaller than ~1 eV normally obtained from C-V measurements of Pr-based, polycrystalline ZnO varistors.(20)

One may evaluate the barrier height as a function of voltage at a given temperature by rearrangement of equation (1);

$$\Phi_B(V) = kT \ln\{ A^* AT^2 ND/I NC \} \{ 1 - \exp(-eV/kT) \} \quad (3)$$

where I and V are the measured currents and voltages, respectively and A the cross-sectional area.

Specimens with different dopants exhibit similar Φ_B vs. V characteristics as shown in Fig. (5). Generally, Φ_B initially drops rapidly at low voltage (< 1 V), then more slowly as the applied voltage increases and again more rapidly as the voltage approaches the breakdown voltage. The Pr/Ni- and Pr/Co/Mn-doped SID samples do not exhibit the sharp drop at ~ 3 V exhibited by the others.

Estimated Φ_{BO} values obtained from Fig. 5 range from 0.55 eV (Pr/Ni-doped SID sample) to 0.70 eV (Pr/Co/Mn-doped SID sample). These values are much larger than those estimated from the temperature dependent I-V measurements and come much closer to the expected value of ~ 1 eV. The results of the DC measurements are summarized in Table 1.

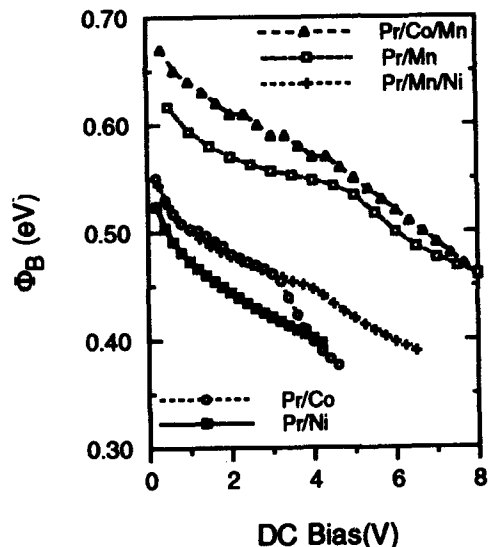


Figure 5 Plot of Φ_B vs. V , SID ZnO varistors at 20C.

Table 1 Summary of DC I-V characteristics of SID samples

Dopants	J (leakage) (mA/cm ²)	V _B (V)	α_{max}	ΔE^* (eV)	Φ_{BO}^{**} (eV)
Pr/Co	0.5	3.0	11	0.02	0.60
Pr/Mn	0.015	4.0	9	0.08	0.65
Pr/Ni	1.5	4.0	4	0.01	0.54
Pr/Co/Mn	0.007	-	13	0.24	0.70
Pr/Mn/Ni	0.5	3.8	5	0.02	0.57

(*) :from thermionic model (V=constant)

(**) :from thermionic model (T=constant)

While the breakdown voltages of around 3-4 V indicate that single electrically active layers are formed in these specimens, the leakage currents in the prebreakdown regime are much higher (by a factor of 10^2 - 10^3) than expected from other studies of single barrier ZnO based varistors.(6-11) These features, common to all SID samples regardless of the dopant type, suggest that parallel leakage paths in the structure mask the true I-V characteristics of the electrically active barriers formed therein.

To confirm this hypothesis, microcontact measurements were performed which showed that a certain fraction of the boundaries did not attain full electrical activity thereby forming "poor" barriers. In other words, each SID sample apparently consists of varistor-like, electrically active barriers and nearly linear, resistive barriers connected in parallel. We suspect that the 'poor' barriers are either due to a poor distribution of the dopants during the annealing steps, inhomogeneous oxygen distribution during the oxidation step or degradation of some barriers due to inhomogeneous current flow. These features require further study.

The double Schottky barrier model relates the potential barrier height to density of charges trapped in the localized interface states. Furthermore, the density and distribution of these interface states determine the voltage dependence of Φ_B and thus the value of the non-linearity factor α . Characterization of these interface states, therefore, is required to properly understand the electrical activity of the boundaries, and their dependence on the boundary chemistry and structure.

Deep Level Transient Spectroscopy (DLTS) measurements were carried out for each SID sample from -196°C to 450°C to determine the distribution of interface states. Higher temperatures were required for these specimens to detect emission rates from deep interface states (~1 eV) believed to exist in ZnO structures.

DLTS spectra obtained for a Pr/Co-doped SID sample are shown in Fig. (6). The pulse height was set to 4.0 V which is slightly larger than the breakdown voltage of the sample. In the low temperature DLTS, one sharp peak was observed at $-105^{\circ}\text{C} \sim -80^{\circ}\text{C}$, with indication of another shallow peak at lower temperature. DLTS results from other Pr/Co-doped SID samples showed two well defined peaks, confirming the existence of another trap at a lower temperature of around -140°C . These two levels are believed to be bulk traps. At high temperatures, another sharp, well defined peak is observed at $280^{\circ}\text{C} \sim 300^{\circ}\text{C}$.

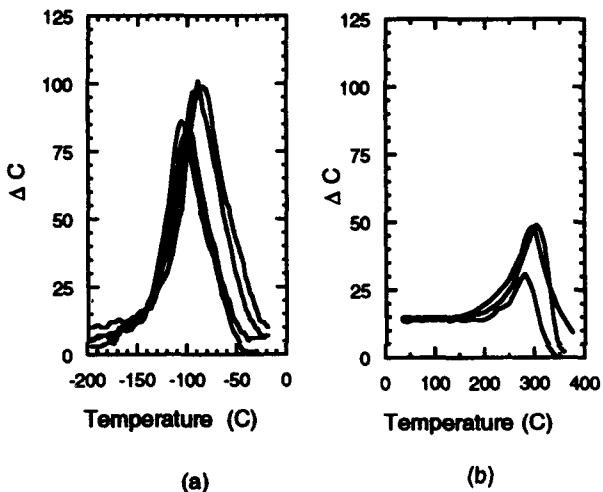


Figure 6 DLTS spectra of a Pr/Co-doped SID sample at low temperature (a), and at high temperature (b); signature temperature (T_p) increased with increase of the emission rate of each spectrum which was set to 22.5, 45, 112.5, 225 sec^{-1} for (a), 112.5, 225, 450 sec^{-1} for (b).

From each DLTS spectrum a set of peak temperatures, T_p , and emission rates, e_m , are obtained. Applying the expression for e_m given by

$$e_m = \sigma N_c V_{th} \exp \{-(E_C - E)/kT_p\} \quad (4)$$

the energy level of the trap, E , relative to the conduction band edge, E_C can be obtained from a plot of $\ln e_m$ vs. $1/T$. In this equation, σ is the capture cross section, N_C the effective density of states, and V_{th} the thermal velocity. A plot of $\ln(e_m T_p^2)$ vs. (T_p^{-1}) derived from the DLTS spectra in Fig. (6) is shown in Fig. (7). The resulting data fit the Arrhenius plot well. Overall, DLTS measurements on Pr/Co-doped samples showed that there are two separate bulk states; E_1 ($= 0.27$ eV), E_2 ($= 0.39$ eV), and two interface states; E_3 ($= 0.62$ - 0.7 eV), E_4 ($= 1.13$ eV) in these materials.

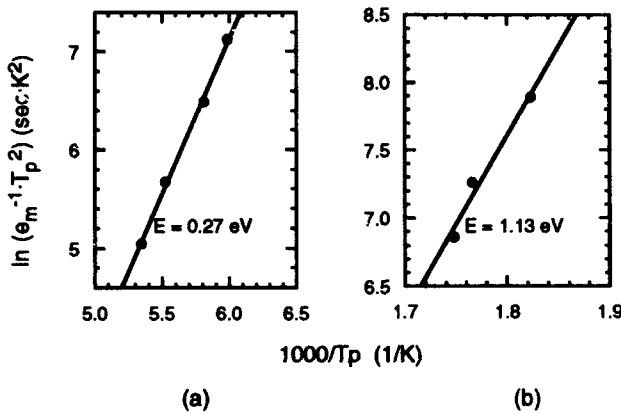


Figure 7 Plot of the emission rate as a function of signature temperature (T_p). From the DLTS spectra of the Pr/Co-doped SID sample at low temperature (a), and at high temperature (b). See Fig. (6).

The other SID samples, with different dopants, also exhibited two or three well defined DLTS peaks. The results of the DLTS measurement are summarized in Fig. (8). Additional DLTS measurements with different pulse shape confirmed that the deeper levels, E_3 and E_4 are interface levels,(21) while E_1 and E_2 are bulk states. At least, on a preliminary basis, if we compare these results with those of Table 1, the deep interface state, E_4 ($= 1.13$ eV) seems to correlate with a high α value. Such results, however, require further study before such conclusions can be confirmed.

In summary, while the in-diffusion process for forming individual active boundaries, to date, suffers from leakage problems, it has provided the opportunity to obtain well defined DLTS spectra for a series of dopant combinations. Such information about the interface state distributions allows for modeling of the I-V characteristics, which are now in progress. Further work is necessary to refine the in-diffusion process to minimize or eliminate the high

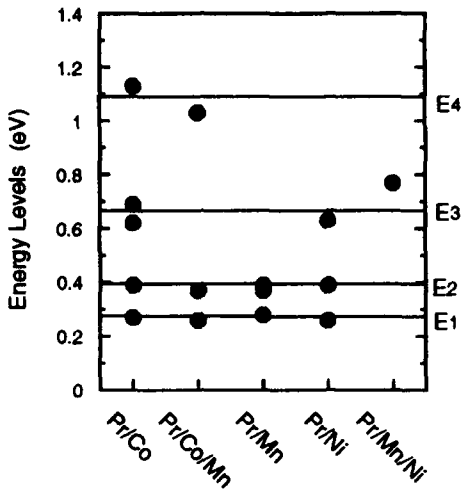


Figure 8 Trap energy levels obtained from DLTS measurements of SID samples, where E₁ and E₂ are bulk traps, E₃ and E₄ are interface states.

leakage paths. Micro-electrodes, in combination with high resolution analytical tools such as scanning transmission electron microscopy (STEM), applied to such structures, may provide the desired correlations between structure and properties. Other approaches, such as fabrication of bi-crystal structures provide an additional important factor, i.e. control of boundary structure, assuming fabrication difficulties can be overcome. New instrumentation, which enables fabrication of interfaces under highly controlled environments, e.g. molecular beam epitaxy (MBE), laser ablation, etc., hold out promise for further important advances in this field.

CONCLUSION

Single boundary studies promise to shed new light on the relationship between boundary chemistry and structure and the resultant electrical properties of grain boundaries. To be of the most significance however, they must (1) be representative of boundaries in polycrystalline ceramics, 2) provide simple current pathways, 3) enable adequate control of local chemistry and structure as well as (4) microscopic analysis by high resolution analytical techniques.

ACKNOWLEDGEMENTS

The support of this work by the MIT Center of Materials Science and Engineering under Contract # DMR-9022933 is most appreciated.

REFERENCES

1. K. Eda, "Conduction mechanism of nonohmic ZnO ceramics", *J. Appl. Phys.* **49** (1978) 2964-29.
2. G. D. Mahan, L. M. Levinson and H. R. Philipp, "Theory of conduction in ZnO varistors", *J. Appl. Phys.* **50** (1979) 2799-2812.
3. P. L. Hower and T. K. Gupta, "A barrier model for ZnO varistors", *J. Appl. Phys.* **50** (1979) 4847-4855.
4. G. E. Pike, "Electronic properties of ZnO varistors: a new model", in *Grain Boundaries in Semiconductors*, Ed. H. J. Leamy, G. E. Dike, and C. H. Seager, North-Holland, New York, (1982) 369-380.
5. F. Greuter, G. Blatter, F. Stucki and M. Rossinelli, "Conduction mechanism in ZnO varistors: an overview", in *Advances in Varistor Technology*, Ed. L. M. Levinson, Am. Ceram. Soc., (1989) 31-53.
6. R. Einzinger, "Metal oxide varistor action - A Homojunction breakdown mechanism", *App. Surf. Sci.* **1** (1978) 329-340.
7. M. Tao, B. Ali, O. Dorlanne and A. Loubiere, "Different 'single grain junctions' within a ZnO varistor", *J. Appl. Phys.* **61** (1987) 1562-1567.
8. G. D. Mahan, L. M. Levinson and H. R. Philipp, "Single grain junction studies of ZnO varistors- theory and experiment", *App. Phys. Lett.*, **33** (1978) 830-832.
9. J. T. C. Van Kemenade and R. K. Eijntshoven, "Direct determination of barrier voltage in ZnO varistors", *J. Appl. Phys.* **50** (1979) 938-832.
10. R. Einzinger, "Grain boundary properties in ZnO varistors", in *Advances in Ceramics*, vol.1, Ed. L. M. Levinson and D. C. Hill, Am. Ceram. Soc., Columbus, OH (1981) 359-374.
11. E. Olsson and G. L. Dunlop, "Characterization of individual interfacial barriers in a ZnO varistor material", *J. Appl. Phys.* **66** (1989) 3666-3675.
12. Y. Suzuki, A. Ohki, T. Mizutani and M. Ieda, "Electrical properties of ZnO-Bi₂O₃ thin film varistors", *J. Phys. (D: Appl. Phys.)*, **20** (1987) 511-517.
13. H. Morooka, Y. Yano, and Y. Shirakawa, "Electrical properties of sputtered ZnO-PrCo oxide thin film varistors," *Ceram. Bull.* **69** (1990) 520.
14. U. Schwing and B. Hoffmann, "New approach to the measurement of the single-contact varistor", in *Advances in Ceramics*, vol.1, Ed. L. M. Levinson and D. C. Hill, Am. Ceram. Soc., Columbus, OH (1981) 383-393.
15. M. Matsuoka, "Progress in research and development of ZnO varistors", in *Advances in Ceramics*, vol.1, Ed. L. M. Levinson and D. C. Hill, Am. Ceram. Soc., Columbus, OH (1981) 290-308.

16. M.H. Sukkar and H.L. Tuller, "ZnO Interface Electrical Properties-Role of Oxygen Chemisorption," in *Nonstoichiometric Compounds-Surfaces, Grain Boundaries, and Structural Defects*, Eds., J. Nowotny and W. Weppner, Kluwer Academic Publ., Dordrecht, The Netherlands (1989) 237-263.
17. B. -S. Chiou, T. -C. Chen and J. -G. Duh, "A ZnO varistor derived from metal oxide diffusion", *J. Phys. (D ; Appl. Phys.)*, **22** (1989) 844-847.
18. I.G. Solorzano, J.B. VanderSande, K-K. Baek, and H.L. Tuller, "Compositional Analysis and High Resolution Imaging of Grain Boundaries in Pr-Doped ZnO Ceramics," in the *Proc. of The Symp. on Atomic Scale Imaging of Surfaces and Interfaces* (Vol. 295), Eds., D.K. Biefelson, D.J. Smith, and D.S. Y. Tong, Materials Research Society, Pittsburgh, PA (1993) 189-194.
19. G. E. Pike and C. H. Seager, "The DC voltage dependence of semiconductor grain boundary resistance", *J. Appl. Phys.* **50** (1979) 3414-3422
20. K. Mukae and I. Nagasawa, "Effect of Pr oxide and donor concentration in the grain boundary region of ZnO varistors", in *Advances in Ceramics*, vol.1, Ed. L. M. Levinson and D. C. Hill, Am. Ceram. Soc., Columbus, OH (1981) 331-342.
21. K. Tsuda and K. Mukae, "Interface states of ZnO varistors", in *High Tech Ceramics*, Ed. P. Vincenzini, Elsevier Science Publishers B. V., Amsterdam, (1987) 1781-1790.

CHEMICALLY INDUCED INTERFACE MIGRATION IN OXIDES

Jae Ho Jeon and Suk-Joong L. Kang

Department of Ceramic Science and Engineering, Korea Advanced Institute of Science and Technology, Taejon 305-701, Korea

Sang Chul Han and Duk Yong Yoon

Department of Materials Science and Engineering, Korea Advanced Institute of Science and Technology, Taejon 305-701, Korea

ABSTRACT

Grain boundaries and intergranular liquid films in metals and oxides migrate upon adding or removing solute atoms. Behind the migrating boundaries form new solid solutions either enriched with or depleted of the solute atoms. The characteristics of the boundary migration behavior are described in Mo-Ni, alumina, and SrTiO₃ as examples. Critical experiments with two solute species show that the driving force for the migration stems from the coherency strain energy in the diffusion zone in front of the migrating boundaries. In SrTiO₃ doped with Nb₂O₅ and sintered in a reducing atmosphere, the liquid films formed by infiltrating with CuO, PbO, and Bi₂O₃ migrate during the heat-treatment in air. The driving force is attributed to the lattice parameter change associated with the formation of Sr ion vacancies and the change of Ti ion valency.

INTRODUCTION

During the processing of polycrystalline materials at high temperatures, solute atoms may be added to or removed from them. During sintering, for instance, a specimen can gain some solute species from the surrounding atmosphere, or lose others by evaporation. The solute species can be deliberately added by coating the specimen surface before heat-treatment as in grain boundary diffusion studies. Under certain conditions the composition change can occur within solid solution ranges.

It has been commonly believed that such a composition change in a polycrystalline material will occur by grain boundary diffusion and symmetric lattice diffusion from the

To the extent authorized under the laws of the United States of America, all copyright interests in this publication are the property of The American Ceramic Society. Any duplication, reproduction, or republication of this publication or any part thereof, without the express written consent of The American Ceramic Society or fee paid to the Copyright Clearance Center, is prohibited.

grain boundaries. But it was discovered, initially in metals, that when polycrystalline specimens were brought into contact with a solute source or sink, the grain boundaries migrated, leaving behind them new solid solutions either enriched with or depleted of the solute atoms.^{1,2} The phenomenon has been referred to as chemically or diffusion induced grain boundary migration, and was observed to occur also in oxides and compounds. Intergranular liquid films were also observed to migrate under similar experimental conditions.³⁻⁸ The liquid films can be present between the grains in liquid phase sintered specimens, or can be produced by partial melting. The liquid film migration (LFM) has been extensively studied in metal and oxide specimens prepared by liquid phase sintering.

Various theories have been proposed for the driving force of this phenomenon. Hillert^{9,10} proposed, extending Sulonen's idea for discontinuous precipitation,¹¹ that solute diffusion could occur in front of the migrating boundaries and the coherency strain energy in the diffusion zone could drive the migration. Experiments in both metals and oxides showed that the driving force stemmed from the lattice parameter change with composition in agreement with the coherency strain hypothesis.^{4-6,12-16} But recent observations of the boundary migration induced by interstitial solute atoms indicate that the coherency strain theory may not apply generally.^{17,18}

In this report we will briefly review the observations of the chemically induced interface migration (CIIM) with examples in a metal and two oxides, and describe the coherency strain model and its implications on the migration behavior. We will then present the results of a recent study on the liquid film migration in SrTiO_3 induced by defects produced during oxidation. These results will be analyzed in terms of the coherency strain model.

OBSERVATIONS IN METALS AND OXIDES

The chemically induced grain boundary migration was first observed by Rhines and Montgomery¹⁹ in 1938 during the diffusion of Zn into Cu. The phenomenon was rediscovered in 1970s by den Broeder in a Cr-W diffusion couple,²⁰ by Tu in a Pb-AgPd diffusion couple,²¹ and by Hillert and Purdy during the diffusion of Zn from its vapor into Fe.²² Since then it has been observed to occur in many metal alloy systems, as listed in a review by Handwerker.² Because most of these observations were made with either solid or vapor solute sources in contact with polycrystalline specimens, the composition changes during the boundary migration were difficult to control.

The chemically induced migration of intergranular liquid films was first observed by Yoon and Huppmann³ during the sintering of W grains separated by Ni melt films. It has been extensively investigated in liquid phase sintered Mo-Ni alloys with various solute species.^{4-6,13} It was observed to occur also during partial melting.^{23,24} The liquid phase sintered Mo-Ni specimens had typical microstructures of spherical Mo-Ni grains separated by either liquid films or grain boundaries from its neighbors.¹³ When the sintered specimen was heat-treated again after placing a compact of Co powder on its top, Co quickly dissolved and spread in the liquid matrix, and the intergranular liquid films and

grain boundaries migrated as shown in Fig. 1. The solid formed behind the migrating boundaries was more lightly etched than the initial solid formed during the liquid phase sintering treatment. Microprobe analysis across the region indeed showed that the newly formed solid was uniformly enriched with about 0.9 at.% Co and slightly depleted of Ni.

There are numerous advantages in using the liquid phase as a medium for the solute source as in these experiments. The liquid composition can be systematically varied by adding different solute species at varying concentrations, and because the solid formed during sintering or heat-treatment has the composition in equilibrium with the liquid matrix, the solid composition can be also varied systematically. It is thus possible to vary systematically the driving force for the migration as will be discussed shortly. Another advantage is that each grain boundary or liquid film is in close contact with the liquid solute source. In contrast, a solid or vapor solute source is in contact with a specimen only at its surface.

Initial attempts to observe the chemically induced interface migration in ceramic systems by Handwerker *et al.*²⁵ were not apparently successful. The first observation of CIIM in an oxide was made during the sintering of PLZT.⁷ The driving force for the migration was attributed to the evaporation of PbO. Since then grain boundary migration has been observed in ZrO_2 -(CaO, MgO),²⁶ $SrTiO_3$ -(CaO, BaTiO₃),^{15,27} Al_2O_3 -(Fe_2O_3),²⁸ and Al_2O_3 -(Cr_2O_3)²⁹ where the solute species are shown in the parenthesis. It was also observed in other compounds such as CdS -($ZnCl_2$),³⁰ and $CaCO_3$ -($BaCO_3$, $SrCO_3$),^{31,32} The liquid film migration was observed in ZrO_2 -(Y_2O_3),^{33,34} ZrO_2 - Y_2O_3 -(MgO),¹⁴ and MgO - V_2O_5 -(NiO, CoO)³⁵ as well as in PLZT.⁷

The grain boundary migration in Al_2O_3 is shown in Fig. 2 as an example.²⁹ Commercially produced translucent Al_2O_3 specimens were polished and thermally etched to mark the initial grain boundaries. They were then heat-treated at 1500°C in air in containers with Al_2O_3 - Cr_2O_3 powder mixtures. The volatile Cr_2O_3 in the surrounding atmosphere diffused along the grain boundaries, which migrated, leaving behind Al_2O_3 - Cr_2O_3 solid solutions. The composition profiles across the grain boundaries indeed showed that the regions swept by the moving grain boundaries were enriched with Cr_2O_3 . The average migration distance initially increased linearly with the heat-treatment time, and the migration rate increased with the Cr_2O_3 concentration in the Al_2O_3 - Cr_2O_3 source powder mixture. The observations at sections perpendicular to the specimen surfaces showed that the migration was limited to layers of a few grains at the surface with the migration rate decreasing away from the surface. The segments of some grain boundaries were observed to move in opposite directions as indicated by an arrow in Fig. 2.

DIFFUSIONAL COHERENCY STRAIN THEORY

Because new solid solutions that are close to equilibrium (in the presence of the solute source) are formed during the boundary migration, the chemical free energy has been suggested as the driving force for the migration. But the chemical free energy decreases in all equilibration processes, and hence the key question is whether the entire chemical free



Fig. 1. The microstructure of 85Mo-15Ni (wt%) alloy sintered at 1460°C for 20 h and heat-treated at 1460°C for 1 h after embedding in a Mo-Ni-Co powder mixture of 20 wt% Co. (The single and double full arrows indicate the migrating grain boundary and liquid film, respectively, and the dotted arrows indicate the initial boundary locations.)

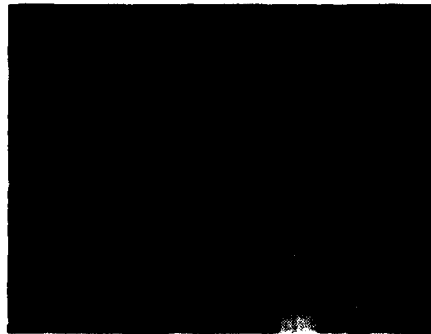


Fig. 2. An Al_2O_3 specimen heat-treated at 1500°C for 6 h with a 75 Al_2O_3 -25 Cr_2O_3 (wt%) powder mixture. (The grain boundaries were initially grooved deeply by thermal etching.)

energy is used to drive the boundary migration. As an attempt to resolve this, Sulonen¹¹ and Hillert^{9,10} proposed the diffusional coherency strain model, initially for discontinuous precipitation. As illustrated in Fig. 3, when a boundary moves over a small distance, the new solid enriched with the solute atoms behind the moving boundary will be initially coherent with the parent grain, but upon exceeding a critical thickness the coherency will be broken, producing misfit dislocations at the initial location. The growth of the new solid solution is thus identical to the epitaxial growth on a substrate. The growing solid will hence have the strain-free lattice parameter a' corresponding to its composition C' . In front of the moving boundary, solute diffusion can occur over a short distance, dissipating a large part of the chemical free energy. This frontal diffusion layer can be so thin that it can remain coherent with the receding parent grain, and the coherency strain energy can drive the atoms to jump across the boundary, which will move in the opposite direction as illustrated in Fig. 3. The solution of Fick's diffusion equations with a moving boundary shows³⁶ that the thickness of the frontal diffusion layer will be approximately equal to the ratio of the lattice diffusivity D to the boundary velocity v , and the values of D/v estimated for the observed migrations are often

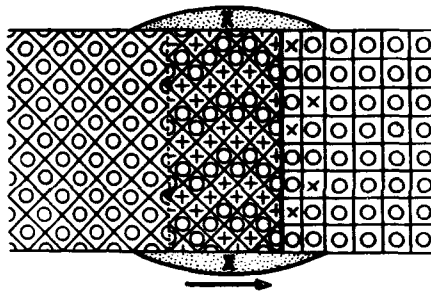


Fig. 3. The diffusional coherency strain model of a boundary migrating to the right from its initial location indicated by a dotted line.

considerably larger than the lattice spacings but small enough to maintain the coherency.

The coherency strain theory can be applied to the liquid film migration in a straightforward way. The rate can be described in terms of diffusion across a liquid film between one interface in equilibrium with a strain-free solid and another in equilibrium with a coherently strained solid.^{37,38} The analysis shows that in the limit of small coherency strain, most of the chemical free energy will be dissipated in the lattice diffusion in front of the moving boundary, and the limiting composition C_c of the coherent diffusion layer at the boundary will be nearly equal to C' of the strain-free solid across the liquid film. Because the migration occurs by dissolution at the surface of the coherent diffusion layer and reprecipitation at the surface of the growing strain-free solid, the driving force is equal to the coherency strain energy ΔG_c .

$$\Delta G_c = VY\delta^2. \quad (1)$$

where V is the molar volume, Y the orientation dependent elastic constant, and δ the coherency strain. For a binary system, if Vegard's law applies,

$$\delta = \eta (C_c - C_0). \quad (2)$$

where C_0 is the composition of the initial solid, and η is the lattice misfit parameter, which is equal to the fractional lattice parameter change with composition. Because the low strain limit applies to most of the solid solutions, as shown for a typical alloy,³⁹ C_c can be taken to be equal to C' , which can be readily measured. The values of ΔG_c can then be estimated from Eq. (1).

On the other hand, the application of the coherency strain theory to the grain boundary migration is not straightforward, because the limiting composition of the coherent layer at the boundary cannot be determined in terms of thermodynamic principles. It can only be assumed in analogy to the liquid film that the relationship $C_c = C'$ holds also for grain boundaries (in most solid solutions).

Critical tests for the coherency strain theory were performed in liquid phase sintered Mo-Ni alloys by Yoon and co-workers.^{4-6,13} If Vegard's law is valid in a multicomponent system with solute atoms indicated by i ,

$$\delta = \sum \eta_i \Delta C_i, \quad (3)$$

where ΔC_i is the concentration change of the i th solute species (assuming that the low

strain limit applies). For a ternary system with solute species 1 and 2,

$$\delta = \eta_1 \Delta C_1 + \eta_2 \Delta C_2. \quad (4)$$

This relationship shows the physically obvious possibility that in ternary system—as well as in higher order systems—the magnitude and sign of δ can be readily varied. Its value can be, in particular, reduced close to 0 even at (with) finite composition changes. Under such conditions, no migration of either liquid film or grain boundaries was observed in liquid phase sintered Mo-Ni alloys,^{5,13} demonstrating fairly definitively that the driving force for the migration arose from the diffusional coherency strain energy. A similar experiment was performed on partially stabilized cubic ZrO_2 .¹⁴ Such experiments on $SrTiO_3$ will be described in the following section.

The other observed characteristics of CIIM were also shown to be consistent with the coherency strain theory. In $Cu-(Zn)$ ⁴⁰ and $Al_2O_3-(Fe_2O_3)$ ⁴¹ the migrations occurred to the direction of the grains with larger Y in agreement with the prediction of the coherency strain theory for the initiation of the migration.³⁷ The suppression of the migration at high temperatures could be attributed to the coherency loss in the frontal diffusion zone because of high lattice diffusivity relative to the migration velocity,^{13,42} and the migration reversal with increasing boundary curvature was also attributed to the same effect.^{43,44} The faceting of the migrating liquid films was observed to be in accord with the strain energy variation arising from the elastic anisotropy,³⁹ but the faceting of the grain boundaries, as shown for example in Fig. 2, could not be explained on the basis of the coherency strain model.^{1,45-51}

Although the coherency strain theory thus appears to be valid in general for the solid solutions of substitutional atoms, recent observations of grain boundary migration induced by interstitial atoms (O in Ag¹⁷ and C in Ni¹⁸) at relatively high temperatures cast some doubt on its generality. In these cases, the lattice diffusivities were so high that the lengths of the frontal diffusion zones were estimated to exceed the critical values for coherency breaking. The frontal diffusion implies, however, that the entire chemical free energy cannot be the driving force for the migration.

BOUNDARY MIGRATION IN $SrTiO_3$ INDUCED BY Ca and Ba

When sintered $SrTiO_3$ specimens were heat-treated at 1200°, 1300°, and 1400°C in contact with $BaTiO_3$ or CaO powder, Yoon and co-workers²⁷ observed that the grain boundaries migrated, forming behind them $SrTiO_3-BaTiO_3$ or $SrTiO_3-CaTiO_3$ solid solutions. Although the occurrence of the grain boundary migration and possibly recrystallization at a high temperature (1400°C) was clearly demonstrated, the microstructures were not clear enough for a quantitative analysis of the observations. Because the lattice parameter increases or decreases upon replacing a part of Sr with Ba or

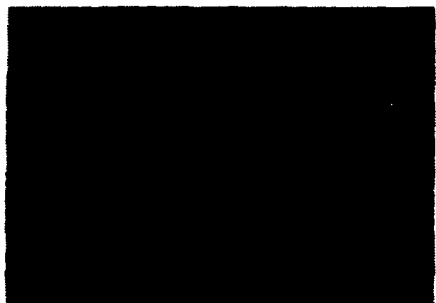
Ca, respectively, the migration was attributed to the compressive or tensile coherency strain produced by the diffusion of Ba or Ca.

Subsequently, Yoon and Kang¹⁵ attempted to test the coherency strain in SrTiO₃ by heat-treating sintered SrTiO₃ specimens in contact with BaTiO₃–CaTiO₃ powder mixtures of varying concentration ratios. While the structures characteristic of chemically induced grain boundary were observed when the mole ratio of BaTiO₃ to CaTiO₃ deviated from 1, no migration occurred at the mole ratio of 1. Attributing the slight deviation of this value from the estimated iso-lattice parameter diagram of this ternary system⁵² to the difference in the diffusivities of BaTiO₃ and CaTiO₃, Yoon and Kang¹⁵ concluded that the results provided an evidence for the coherency strain as the driving for the migration.

Although their interpretation of the observations is largely correct, it is difficult to achieve the condition of the nearly 0 coherency strain in such a ternary solid system of complete mutual solubility, because the composition of the diffusion zone at the grain boundary is not fixed by any thermodynamic condition. This difficulty can be overcome by using another phase (such as liquid) as a source of Ba and Ca. Therefore, CuO liquid which formed films between the SrTiO₃ grains was used as a medium for supplying BaTiO₃ and CaTiO₃ at various concentrations.

In this experiment, the specimens were prepared by ball milling in ethylalcohol SrTiO₃ powder of about 99.8 wt% purity to which 0.2 mol% Nb₂O₃ was added. The compacts were sintered in air at 1480°C for 5 h. The sintered specimens had densities of about 90 % with some pores within the grains as well as between the grains. They were heat-treated again in air at 1300°C for 4 h after pasting powder mixtures of 80CuO–20[xCaO–(1-x)BaO] in mol% on the flat surfaces with x = 1, 0.7, 0.54, 0.5, 0.3, 0.25, 0.2, and 0. At this heat-treatment temperature the CuO–CaO–BaO mixtures are expected to melt and quickly penetrate along the grain boundaries of the sintered SrTiO₃ specimens to form intergranular liquid films. With x=0, the liquid films migrated extensively as shown in Fig. 4(a). As x increased to 0.2 and 0.25, the migration rate decreased as shown in Fig. 4(b), and with x=0.3 and 0.5, no migration occurred, with the initial sintered structure remaining intact as shown in Fig. 4(c). As x increased further to 0.54, 0.7, and 1, the migration rate increased again with x until with x=1, the migration was as extensive as that shown in Fig. 4(a) with x=0.

The composition profiles (measured by wavelength dispersive microprobe analysis) across the migrating liquid films in the specimens with 80CuO–20CaO or 80CuO–20BaO indeed confirmed that Ca or Ba partially replaced Sr in the regions swept by the liquid films as shown in Fig. 5. When the mixture contained both CaO and BaO, a part of Sr would have been replaced by both Ca and Ba. The Ca content in the newly formed solid with the 80CuO–20CaO mixture was about 17 at.% of the cation species, which was more than twice larger than about 6.4 at.% for Ba with the 80CuO–20BaO mixture. These results show that the solubility of Ca in SrTiO₃ in equilibrium with the CuO-rich liquid is much higher than that of Ba. Assuming that the Ca and Ba contents in the solid solutions with SrTiO₃ increased linearly with their contents in the CuO-rich liquids, their values were estimated for various ratios of CaO/BaO in the liquid phase.



4-(a)



4-(b)



4-(c)

Fig. 4. The microstructures of SrTiO_3 specimens heat-treated at 1300°C for 4 h in air after infiltrating with (a) 80CuO-20BaO (mol%), (b) 80CuO-5CaO-15BaO, and (c) 80 CuO-6CaO-14BaO.

Because the low strain limit is expected to apply, the values of the coherency strain δ driving the migration for various ratios of CaO/BaO can then be estimated from Eq. (4) using the measured η for Ca and Ba in SrTiO_3 .⁵² This analysis shows that δ will be 0 when x for the liquid mixture is 0.32. This falls between $x=0.3$ and 0.5 where no migration is observed. The results thus show that when the coherency strain is reduced nearly to 0, the boundary migration does not occur in spite of the chemical instability in the system. The driving force for the migration therefore arises from the coherency strain energy. The experimental scheme and analysis are identical to those used

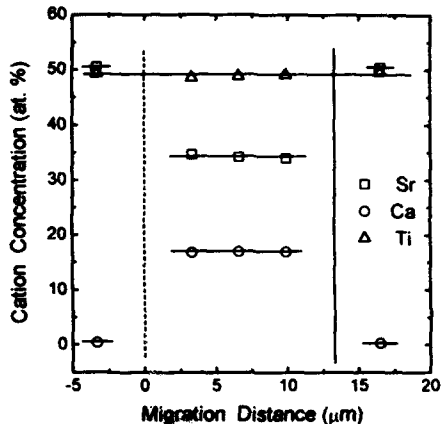


Fig. 5. The measured composition profile across a migrating liquid film in a SrTiO_3 specimen heat-treated at 1300°C for 4 h in air after infiltrating with 80CuO-20CaO (mol%). (The dotted and full vertical lines, respectively, indicate the initial and final locations of the liquid film.)

for the migrations in Mo-Ni^{5,13} and cubic ZrO₂.¹⁴ There may be a range of x (0.3 and 0.5) for the absence of the migration, because a minimum driving force is required for a finite migration rate.¹³

There are intrinsic uncertainties in estimating δ from Eq. (4). The values of η are obtained from the lattice parameter change with composition which has been measured at room temperature. The values at the heat-treatment temperatures should be used, but usually they are not readily available. The composition change of the solid in the absence of the migration can be only obtained by extrapolating the values measured when the migration occurs. Therefore, there is some uncertainty in the values of ΔC when the migration is very slow or absent. But for the migration in the presence of a liquid phase, there is in principle no limit to the accuracy that can be attained. In contrast, as noted earlier, when only solid sources are used for the grain boundaries in a system with unlimited solubility, the composition even at the junction between the source and the grain boundary is undetermined. Therefore, although the results obtained here with the CuO-rich liquid are similar to those obtained by Yoon and Kang¹⁵ with the solid source, there is a basic difference between the two experiments for the ultimate accuracy and reproducibility that can be obtained.

When the composition changes estimated for the absence of the migration did not exactly correspond to $\delta=0$, or, likewise, if the migration was observed even with δ estimated to be 0, it was suggested that other types of driving forces arising, for example, from space charge effect in oxides may also operate in addition to the coherency strain energy.^{14,15} If the total driving force ΔG_t takes the form,

$$\Delta G_t = \Delta G_c + \Delta G_e, \quad (5)$$

with ΔG_e representing the additional driving force, both ΔG_c and ΔG_e will be greater than 0. Then, with any combination of two solute species, of which each alone can induce the migration, the migration will always occur, unless both driving forces are simultaneously reduced to 0. Therefore, the absence of migration with certain combinations of two solute species shows that there cannot be a driving force of significantly large magnitude in addition to ΔG_c .

The other possibility is that the additional energy appears in a form which is directly linked to both the magnitude and sign of the coherency strain produced by each solute species. In such a case, ΔG_c can be reduced by the additional energy effect, but a significantly large driving force of such a form appears to be highly unlikely. Therefore, if no boundary migration is observed under the condition that the coherency strain arising from two solute species is close to 0, the result can be taken as an evidence that only the coherency strain energy is the significant driving force. Any discrepancy is likely to be due to the inherent uncertainties noted previously. In this sense, the results obtained by Yoon and Kang¹⁵ on the grain boundary migration with solid sources is still significant.

Because they showed that the migration did not occur under a certain combination of the concentrations of two solute atoms, the coherency strain energy is likely to be the sole driving force for grain boundaries.

DEFECT INDUCED BOUNDARY MIGRATION IN SrTiO_3

Grain boundary barrier layer capacitors are often made by sintering $(\text{Ba, Sr})\text{TiO}_3$ with additives such as Al_2O_3 and SiO_2 to form a liquid phase. Small amounts of Nb_2O_5 or La_2O_3 are also added and reducing sintering atmospheres are used in order to make semiconducting grains. In some processes⁵³ CuO , MnO_2 , Te_2O_3 , or Bi_2O_3 are infiltrated into the grains boundaries of the sintered pieces in a subsequent heat-treatment in air to produce insulating intergranular layers. It has been suggested⁵⁴ that defect diffusion layers also form adjacent to the grain boundaries.

A careful observation of the microstructures of the boundary layer capacitors produced by these methods often show peculiar grain boundary structures depending apparently on the etching condition.⁵⁵ There are thick regions between the grains which etch differently from the grains. Li and co-workers⁵⁶ indeed observed recently that the boundaries in SrTiO_3 sintered with Nb_2O_5 migrated during the infiltration with $50\text{PbO}-45\text{Bi}_2\text{O}_3-5\text{B}_2\text{O}_3$ (wt%) melt. Detecting some Pb and Bi in the region swept by the moving boundaries, they suggested that the boundary migration was induced by these solute atoms. This suggestion was, however, puzzling, because neither Pb nor Bi was known to be soluble in SrTiO_3 .

In view of the possibly important effect of the boundary migration on the properties of this material, a systematic study was undertaken to verify and characterize the boundary migration. Thin disks of SrTiO_3 with 0.2 mol% Nb_2O_5 were prepared by sintering at 1480°C for 5 h. Normally a flowing $5\text{H}_2-95\text{N}_2$ atmosphere was used for the sintering, but for comparison some specimens were sintered in air. The sintered specimens were infiltrated with CuO , Bi_2O_3 , PbO , or $50\text{PbO}-45\text{Bi}_2\text{O}_3-5\text{B}_2\text{O}_3$ (wt%) by heat-treating at 1200°C for 1 h in air. The sections perpendicular to the flat surfaces were polished and etched in a $50\text{H}_2\text{O}-45\text{HNO}_3-5\text{HF}$ (vol%) solution for about 10 to 30 s.

After the infiltrating treatment, the liquid phases had penetrated along the grain boundaries to the interior of the specimens and the intergranular boundaries were observed to have migrated as shown in Fig. 6 at interior regions of the specimen infiltrated with CuO . These intergranular boundaries are likely to be thin liquid films as shown in earlier studies.⁵⁷ The migration appeared to be slightly more rapid near the surfaces of the specimens which were in contact with the infiltrants. In Fig. 6(b) the segments of the same boundaries migrated in opposite directions.

The boundary migration was observed also with PbO , Bi_2O_3 , and $50\text{PbO}-45\text{Bi}_2\text{O}_3-5\text{B}_2\text{O}_3$ infiltrants, and the migration behavior including the migration distances appeared to be independent of the type of the infiltrant material. The composition analysis was performed extensively across the migration regions with both wave length and energy dispersive microprobe analysis, and no trace of any of the additive elements was found in

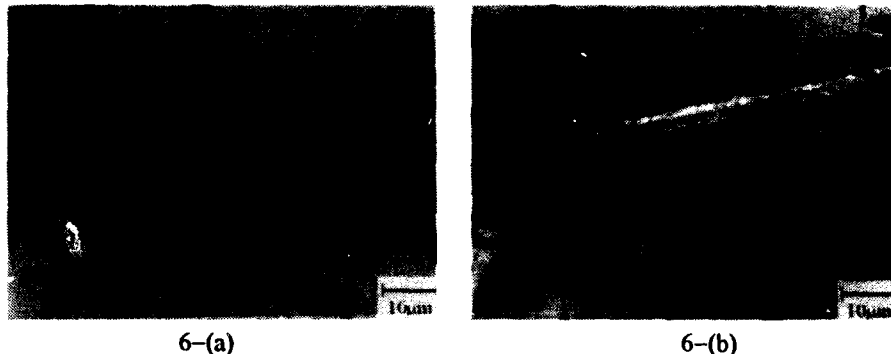


Fig. 6. Two different areas (a and b) at the interior of a SrTiO_3 -0.2 mol% Nb_2O_5 specimen sintered at 1480°C for 5 h in 5H_2 - 95N_2 atmosphere and heat-treated at 1200°C for 1 h in air after infiltrating with CuO . (The arrows indicate some of the initial boundary locations.)

the regions swept by the migrating boundaries. These observations indicated that the migration was not induced by the infiltrant materials contrary to the suggestion of Li *et al.*⁵⁶

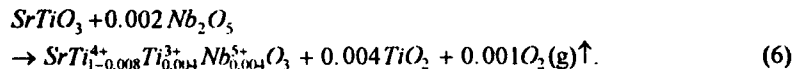
Because these results were puzzling, the possibility of the migration induced by defects associated with the atmosphere change from the sintering to the infiltration treatments was explored. When both the sintering and infiltration treatments were done in air, the grain boundaries appeared to have been infiltrated with the liquids but did not show the migration with any of the infiltrants as shown, for example, in Fig. 7. It was thus concluded that the migration was induced by the change from the reducing to the oxidizing atmosphere. It appeared that with thin liquid films of the infiltrants between the grains, the migration kinetics was enhanced, producing rapid migrations. When the specimens were heat-treated with the atmosphere change but without any infiltrants, no boundary migration was observed, probably because of the lower mobility of the grain boundaries than that of the liquid films. Previously, Yoon and co-workers¹⁵ also observed very slow grain boundary migration at 1200°C under probably much higher driving forces induced by BaTiO_3 or



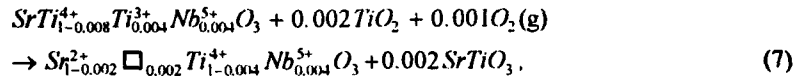
Fig. 7. A SrTiO_3 -0.2 mol% Nb_2O_5 specimen sintered at 1480°C for 5 h in air and heat-treated at 1200°C for 1 h in air after infiltrating with CuO .

CaTiO_3 . It is possible that at higher temperatures even the grain boundaries will migrate at relatively high rates after the atmosphere change.

Even with the atmosphere change, no liquid film migration was observed if Nb_2O_5 was not added to the SrTiO_3 powder before sintering. The driving force for the migration thus appeared to arise from the defects associated with the Nb_2O_5 additive and the atmosphere. When SrTiO_3 is doped with compounds such as La_2O_3 or Nb_2O_5 , the charge compensation mechanism is known to vary with atmosphere.^{58,59} In a reducing atmosphere, the electronic compensation causes the oxide to become semiconducting with a reaction,



There is thus an excess TiO_2 , which is likely to remain at grain boundaries. In an oxidizing atmosphere the self-compensation occurs, causing the oxide to become insulating. According to the results obtained by Cho,⁶⁰ the likely reaction is,



where \square denotes Sr^{2+} vacancies. The TiO_2 and O_2 will thus diffuse into and the SrTiO_3 out of the crystal lattice, producing 0.002 fraction of Sr^{2+} vacancies and converting the Ti^{3+} ions, which correspond to about 0.004 fraction of the Ti ions, to Ti^{4+} .

This reaction will cause a change of the lattice parameter, because the effective size of an ion is usually different from that of its vacancy⁶¹ and the ionic radii of Ti^{3+} and Ti^{4+} have been reported to be 0.81 and 0.745 Å, respectively.⁶² The lattice parameters of the specimens sintered in 5H₂-95N₂ and in air were measured by X-ray at room temperature. Although the resolution was about 10⁻⁴ Å, no lattice parameter difference between the two specimens could be measured. It thus appears that the lattice parameter change associated with the atmosphere change as measured at room temperature is quite small, but at the heat-treatment temperature (1200°C) the lattice parameter change could be larger. Thus it could not be ruled out that the coherency strain energy in the frontal diffusion zone caused by the defects was the driving force for the liquid film migration.

In order to test this possibility the SrTiO_3 specimens sintered in 5H₂-95N₂ atmosphere were heat-treated in air after infiltrating them with 80CuO-20[xCaO-(1-x)BaO] of varying x. The experiments were thus identical to those described in the previous section except the atmosphere change between the sintering and the heat-treatment. In this case the migration was observed to occur at all values of x including

0.54 and 0.4, but no migration occurred at $x=0.3$. This observation that the migration could be stopped by introducing solute atoms of different sizes is significant, because it indicates that there is no driving force for the migration in addition to the coherency strain as discussed in the previous section.

CONCLUSIONS

In most of the previous studies, the migration of grain boundaries and intergranular liquid films was induced by the addition or removal of substitutional solute atoms. Many of these systems formed solid solutions over wide composition ranges, and from the measured variation of the lattice parameter with composition the magnitude and sign of the coherency strain could be calculated. Using two solute species of different sizes, the coherency strain energy was shown to be the driving force for the migration in a number of systems.

The interface migration induced by defects as described in this report for SrTiO_3 is more complex, because the type and amount of the defects have to be first known accurately. The lattice parameter change associated with the defects has to be also known to obtain the coherency strain. Often such data are not readily available. The diffusional processes in the frontal coherent zones will be also complex. Nevertheless, the observation of LFM with the atmosphere change in SrTiO_3 shows that CIIM is a general phenomenon which can occur in a variety of systems and conditions.

In various material processes ranging from welding and heat-treatment to sintering, CIIM is being found to be important for the microstructural and compositional changes. The liquid film migration in the processing of the boundary layer capacitor is one of the examples.

ACKNOWLEDGMENT

This was supported in part by the Korea Science and Engineering Foundation through the Center for Interface Science and Engineering of Materials and by the Agency for Defense Development, Republic of Korea.

KEY WORDS

Al_2O_3 – Cr_2O_3 , SrTiO_3 , grain boundary migration, liquid film migration, coherency strain, boundary layer capacitor

REFERENCES

¹A. H. King, "Diffusion Induced Grain Boundary Migration," *Inter. Met. Rev.*, 32[4] 173-89 (1987).

²C. A. Handwerker, "Diffusion Induced Grain Boundary Migration in Thin Films"; pp. 245-322 in *Diffusion phenomena in Thin Film and Microelectronic Materials*. Edited by D. Gupta and P. S. Ho. Noyes Publications, Park Ridge, New Jersey, 1988.

³D. N. Yoon and W. J. Huppman, "Chemically Induced Driven Growth of Tungsten Grains during Sintering in Liquid Nickel," *Acta Metall.*, 27[6] 973-7 (1979).

⁴Y.-J. Baik and D. N. Yoon, "Migration of Liquid Film and Grain Boundary in Mo-Ni Induced by Temperature Change," *Acta Metall.*, 33[10] 1911-7 (1985).

⁵W.-H. Rhee, Y.-D. Song, and D. N. Yoon, "A Critical Test for the Coherency Strain Effect on Liquid Film and Grain Boundary Migration in Mo-Ni-(Co-Sn) Alloy," *Acta Metall.*, 35[1] 57-60 (1987).

⁶H.-K. Kang, S. Hackney, and D. N. Yoon, "Migration of Liquid Film and Grain Boundary in Mo-Ni Induced by W Diffusion," *Acta Metall.*, 36[3] 695-9 (1988).

⁷J.-J. Kim, B.-M. Song, D.-Y. Kim, and D. N. Yoon, "Chemically Induced Grain Boundary Migration and Recrystallization in PLZT Ceramics," *Am. Ceram. Soc. Bull.*, 65[10] 1390-2 (1986).

⁸J.-W. Jeong, D. N. Yoon, and D.-Y. Kim, "Migration of Intergranular Boundaries in Cubic Zirconia-Yttria Induced by Magnesia Addition," *J. Am. Ceram. Soc.*, 73 [7] 2063-7 (1970).

⁹M. Hillert, "On the Theories of Growth during Discontinuous Precipitation," *Metall. Trans.*, 3[11] 2729-41 (1972).

¹⁰M. Hillert, "On the Driving Force for Diffusion Induced Grain Boundary Migration," *Scr. Metall.*, 17[2] 237-40 (1983).

¹¹M. S. Sulonen, "On the Driving Force of Discontinuous Precipitation and Dissolution," *Acta Metall.*, 12[6] 749-53 (1964).

¹²D. N. Yoon, "Chemically Induced Interface Migration in Solids," *Annu. Rev. Mater. Sci.*, 19, 43-58 (1989).

¹³W.-H. Rhee and D. N. Yoon, "The Grain Boundary Migration Induced by Diffusional Coherency Strain in Mo-Ni Alloy," *Acta Metall.*, 37[1] 221-8 (1989).

¹⁴J.-W. Jeong, D. N. Yoon, and D.-Y. Kim, "Chemically Induced Instability at Interfaces of Cubic ZrO_2 - Y_2O_3 Grains in a Liquid Matrix," *Acta Metall. Mater.*, 39[6] 1275-9 (1991).

¹⁵K.-J. Yoon and S.-J. L. Kang, "Chemical Control of the Grain Boundary Migration of $SrTiO_3$ in the $SrTiO_3$ - $BaTiO_3$ - $CaTiO_3$ System," *J. Am. Ceram. Soc.*, 76[6] 1641-4 (1993).

¹⁶J.-H. Jeon and S. -J. L. Kang, "Effect of Sintering Atmosphere on Interface Migration of Nb-doped Strontium Titanate during Infiltration of Oxide Melts" ; unpublished work.

¹⁷C.-Y. Yoo, "Grain Boundary Migration Induced by Oxygen in Silver and Thermal Etching of Silver"; Ph.D. Thesis. Korea Advanced Institute of Science and Technology, Seoul, Korea, 1993.

¹⁸T.-W. Jang, "Grain Boundary Migration and Recrystallization in Nickel Induced by Carbon Addition"; M.S.Thesis. Korea Advanced Institute of Science and Technology,

Seoul, Korea, 1993.

¹⁹F. N. Rhines and A. M. Montgomery, "A New Type of Structure in the Alpha Copper-Zinc Alloy," *Nature* 141[3] 413 (1938).

²⁰F. J. A. den Broeder, "Interface Reaction and a Special Form of Grain Boundary Diffusion in the Cr-W System," *Acta Metall.*, 20[3] 319-32 (1972).

²¹K. N. Tu, "Kinetics of Thin-Film Reactions between Pb and AgPd Alloys," *J. Appl. Phys.*, 48[8] 3400-4 (1977).

²²M. Hillert and G. R. Purdy, "Chemically Induced Grain Boundary Migration," *Acta Metall.*, 26[2] 333-40 (1978).

²³T. Muschik, W. A. Kaysser, and T. Hohenkamp, "Melting of Cu-In Solid Solutions at Small Superheating by Droplet Formation and Liquid Film Migration," *Acta Metall.*, 37[2] 603 (1989).

²⁴R. G. Thompson, D. E. Mayo, and B. Radhakrishnan, "The Relationship between Carbon Content, Microstructure, and Intergranular Liquation Cracking in Cast Nickel Alloy 718," *Metall. Trans.*, 22A[2] 557-67 (1991).

²⁵C. A. Handwerker, R. L. Coble, and J. E. Blendell, "Diffusion-Induced Grain Boundary Migration and Discontinuous Precipitation Experiments in Ceramic Systems"; pp.213-23 in *Advances in Ceramics*, vol 6, *Character of Grain Boundaries*. Edited by M. F. Yan and A. H. Heuer. American Ceramic Society, Columbus, OH, 1983.

²⁶E. P. Butler and A. H. Heuer, "Grain Boundary Phase Transformation during Aging of a Partially Stabilized ZrO_2 -A Liquid Phase Analogue of Diffusion-Induced Grain Boundary Migration (DIGM)," *J. Am. Ceram. Soc.*, 68[4] 197-202 (1985).

²⁷K. -J. Yoon, D. N. Yoon, and S.-J. L. Kang, "Chemically Induced Grain Boundary Migration in $SrTiO_3$," *Ceram. Int.*, 16[3] 151-5 (1990).

²⁸H.-Y. Lee and S.-J. L. Kang, "Chemically Induced Grain Boundary Migration and Recrystallization in Al_2O_3 ," *Acta Metall. Mater.*, 38[7] 1307-12 (1990).

²⁹S.-C. Han, "Chemically Induced Grain Boundary Migration in Alumina-Chromia"; M.S.Thesis. Korea Advanced Institute of Science and Technology, Seoul, Korea, 1990.

³⁰Y.-S. Yoo, "Chemically Induced Interface Migration in Cadmium-Sulfide System"; M.S.Thesis. Korea Advanced Institute of Science and Technology, Seoul, Korea, 1989.

³¹B. Evans, R. S. Hay, and N. Shimizu, "Diffusion Induced Grain Boundary Migration in Calcite," *Geology*, 14[1] 60-3 (1986).

³²R. S. Hay and B. Evans, "Chemically Induced Migration in Low and High Angle Calcite Grain Boundaries," *Acta Metall.*, 35[8] 2049-62 (1987).

³³R. Chain, M. Ruhle, and A. H. Heuer, "Microstructural Evolution in ZrO_2 -12 wt% Y_2O_3 Ceramics," *J. Am. Ceram. Soc.*, 68[9] 427-31 (1985).

³⁴R. Chain, A. H. Heuer, and D. G. Brandon, "Phase Equilibration in ZrO_2 - Y_2O_3 Alloys by Liquid Film Migration," *J. Am. Ceram. Soc.*, 69[3] 243-8 (1986).

³⁵J. E. Blendell, C. A. Handwerker, C. A. Shem, and N.-D. Dang, "Diffusion Induced Interface Migration in Ceramics"; pp. 541-8 in *Ceramic Microstructures '86 Role of Interfaces*. Edited by J. A. Pask and A. G. Evans. Plenum Press, New York/London, U.K. 1987.

³⁶W. A. Tiller, K. A. Jackson, J. W. Rutter, and B. Chalmers, "The Redistribution of Solute during the Solidification of Metals," *Acta Metall.*, 1[7] 428-37 (1953).

³⁷D. N. Yoon, J. W. Cahn, C. A. Handwerker, J. E. Blendell, and Y.-J. Baik, "Coherency Strain Induced Migration of Liquid Films through Solid"; pp. 19-31 in *Interface Migration and Control of Microstructure*. Edited by C. S. Pande, D. A. Smith, A. H. King, and J. Walter. American Society for Metals, Metals Park, OH, 1985.

³⁸C. A. Handwerker, J. W. Cahn, D. N. Yoon, and J. E. Blendell, "The Effect of Coherency Strain on Alloy Formation : Migration of Liquid Films"; pp. 275-92 in *Diffusion in Solid : Recent Developments*. Edited by M. A. Dayananda and G. E. March. The Metallurgical Society, Warrendale, PA, 1985.

³⁹Y.-J. Baik, J. K. Kim, and D. Y. Yoon, "The Effect of Elastic Anisotropy on the Migration of Intergranular Liquid Films and the Precipitation of a Liquid Phase in a Co-Cu Alloy," *Acta Metall. Mater.*, 41[8] 2385-93 (1993).

⁴⁰F. S. Chen, G. Dixit, A. J. Aldykiewicz, and A. H. King, "Bicrystal Studies of Diffusion-Induced Grain Boundary Migration in Cu/Zn," *Metall. Trans.*, 21A[9] 2363-7 (1990).

⁴¹H.-Y. Lee, S.-J. L. Kang, and D. Y. Yoon, "The Effect of Elastic Anisotropy on the Direction and Faceting of Chemically Induced Grain Boundary Migration in Al_2O_3 ," *Acta Metall. Mater.*, 41[8] 2497-502 (1993).

⁴²J. K. Kim and D. Y. Yoon, "The Suppression of Chemically Induced Liquid Film Migration in Co-Cu at High Temperature," *Acta Metall. Mater.*, in press.

⁴³Y.-J. Baik and D. N. Yoon, "The Effect of Curvature on the Grain Boundary Migration Induced by Diffusion Coherency Strain in Mo-Ni Alloy," *Acta Metall.*, 35[9] 2265-71 (1987).

⁴⁴L. Chongmo and M. Hillert, "A Metallographic Study of Diffusion Induced Grain Boundary Migration in the Fe-Zn System," *Acta Metall.*, 29[12] 1949-60 (1981).

⁴⁵S.-C. Han, D. Y. Yoon, and M. Brun, "Migration of Grain Boundaries in Alumina Induced by Chromia Addition"; unpublished work.

⁴⁶M. A. Hofmann, W. A. Kaysser, and G. Petzow, "Grain Boundary Migration in Recrystallized Mo Foils in the Presence of Ni," *J. Phys. Colloq. C4*, 46[4] 545-52 (1985).

⁴⁷S. A. Hackney, F. S. Biancaniello, D. N. Yoon, and C. A. Handwerker, "Observations on Crystal Defects Associated with Diffusion Induced Grain Boundary Migration in Cu-Zn," *Scr. Metall.*, 20[6] 937-42 (1986).

⁴⁸F. S. Chen and A. H. King, "The Misorientation Dependence of Diffusion Induced Grain Boundary Migration," *Scr. Metall.*, 20[10] 1401-4 (1986).

⁴⁹R. Schmelzle, B. Giakupian, T. Muschik, W. Gust, and R. A. Fournelle, "Diffusion Induced Grain Boundary Migration of Symmetric and Asymmetric $\langle 011 \rangle \{011\}$ Tilt Boundaries during the Diffusion of Zn into Cu," *Acta Metall. Mater.*, 40[5] 997-1007 (1992).

⁵⁰R. S. Hay and B. Evans, "The Coherency Strain Driving Force for CIGM in Non-Cubic Crystals:Comparison with In Situ Observations in Calcite," *Acta Metall. Mater.*, 40[10] 2581-93 (1992).

⁵¹F. S. Chen and A. H. King, "Misorientation Effects upon Diffusion Induced Grain

Boundary Migration in the Copper-Zinc System," *Acta Metall.*, 36[10] 2827-39 (1988).

⁵²M. McQuarrie, "Structural Behavior in the System (Ba, Ca, Sr)TiO₃ and Its Relation to Ceramic Dielectric Characteristics," *J. Am. Ceram. Soc.*, 38[12] 444-9 (1955).

⁵³A. Yamaji and S. Waku, "Studies on SrTiO₃ Boundary Layer Dielectrics," *Rev. Electr. Commun. Lab.*, 20[7-8] 747-63 (1972).

⁵⁴R. Wernicke, "Formation of Second-phase Layers in SrTiO₃ Boundary Layer Capacitors"; pp. 261-71 in *Advances in Ceramics*, Vol. 1, *Grain Boundary Phenomena in Electronic Ceramics*. Edited by L. M. Levinson. American Ceramic Society, Columbus, Ohio, 1981.

⁵⁵G. Goodman, "Capacitor Based on Ceramic Grain Boundary Barrier Layers—a Review"; pp. 215-31 in *Advances in Ceramics*, Vol. 1, *Grain Boundary Phenomena in Electronic Ceramics*. Edited by L. M. Levinson. American Ceramic Society, Columbus, Ohio, 1981.

⁵⁶L. T. Li, X. J. Zhou, X. L. Shi, and X. W. Zhang, "Study of Microstructure and Properties of SrTiO₃-based Grain Boundary Layer Capacitor"; pp 563-6 in *Advanced Structural Materials*, Vol. 2. Edited by Y. F. Han. Elsevier Science Publishers, Amsterdam, 1991.

⁵⁷M. Fujimoto and W. D. Kingery, "Microstructures of SrTiO₃ Internal Boundary Layer Capacitors during and after Processing and Resultant Electrical Properties," *J. Am. Ceram. Soc.*, 68[4] 169-73 (1985).

⁵⁸N. G. Eror and U. Balachandran, "Self-Compensation in Lanthanum-doped Strontium Titanate," *J. Solid State Chem.*, 40[1] 85-91 (1981).

⁵⁹B. F. Flandermeyer, A. K. Agarwal, H. U. Anderson, and M. M. Nasrallah, "Oxidation-Reduction Behavior of La-doped SrTiO₃," *J. Mater. Sci.*, 19[8] 2593-8 (1984).

⁶⁰S. G. Cho, "Microstructure and Electrical Properties of Undoped and Nb-doped SrTiO₃"; Ph. D. Thesis. Alfred University, New York, 1989.

⁶¹B. Henderson, "Some Experimental Techniques"; pp. 29-52 in *The Structures and Properties of Solids*, vol 1, *Defects in Crystalline Solids*. Edited by B. R. Coles. Crane, Russak & Company, Inc., New York, 1972.

⁶²O. Muller and R. Roy, "Introduction"; pp. 1-14 in *Crystal Chemistry of Non-Metallic Materials*, vol 4, *The Major Ternary Structural Families*. Edited by R. Roy. Springer-Verlag, Berlin, 1974.

NANO/MICRO STRUCTURE DESIGN FOR IMPROVING THERMOELECTRIC CHARACTERISTICS OF POROUS SILICON CARBIDE

K. Koumoto, W. S. Seo

**Department of Applied Chemistry, School of Engineering,
Nagoya University, Furo-cho, Chikusa-ku, Nagoya, 464-01 Japan**

C. H. Pai

**Korea Academy of Industrial Technology,
371-36, Garibong-dong, Guro-gu, Korea**

Porous SiC has been proposed as a candidate material for high-temperature thermoelectric energy conversion. Nearly ideal nano/micro structure was deduced from our previous experimental work and we attempted to realize such a structure to improve its thermoelectric properties by means of fine hollow particles synthesized by chemical vapor deposition. Reaction sintering of polycarbosilane(PCS)-impregnated compacts of hollow particles gave rise to porous microstructures with the hollow shape remaining. The repetition of the PCS-impregnation and sintering process resulted in only a slight increase in density but in a great improvement in thermoelectric properties. Porous ceramics having various porosities were further fabricated by sintering the mixture of hollow particles and commercial powder, showing bimodal grain size distributions. Both electrical and thermal conductivities as functions of porosity were successfully simulated by a percolation theory, while Seebeck coefficient showed a maximum at specific porosity.

Introduction

Environmental destruction has become a crucial issue in a global scale, which is closely related to the manner of energy consumption taken by the humankind. Mass production of

To the extent authorized under the laws of the United States of America, all copyright interests in this publication are the property of The American Ceramic Society. Any duplication, reproduction, or republication of this publication or any part thereof, without the express written consent of The American Ceramic Society or fee paid to the Copyright Clearance Center, is prohibited.

carbon dioxide by consuming fossil fuels, for example, possibly leads to a green-house effect, and by-products such as NO_x and SO_x cause acid rain. Accordingly, for the future insurance of energy utilization and environmental preservation, technological development in suppressing the fossil fuel consumption through improving the energy utilization efficiency is urgently required.

We have been attempting, from the standpoint of materials scientists, to develop thermoelectric materials in order to contribute to the improvement in efficiency of our energy utilization by means of the recovery of wasted heat which is widely dispersed at various temperature levels. Especially, ceramic semiconductors have been investigated for this purpose to be applied to high-temperature thermoelectric energy conversion, since they have high thermal stability and corrosion resistance, in general.

Recently, porous ceramics of silicon carbide have been found to show fairly good thermoelectric properties[1-3]. We have pointed out that microstructural inhomogeneities have significant effects on their thermoelectric properties and nano as well as micro structure control would be inevitable to further improve their thermoelectric figure of merit, Z , which is expressed as

$$Z = \sigma\alpha^2/\kappa \quad (1)$$

where σ denotes electrical conductivity, α Seebeck coefficient, and κ thermal conductivity.

In this article, thermoelectric characteristics of porous β -SiC ceramics whose nano/micro structure was controlled by using fine hollow particles of β -SiC[4,5] will be presented and discussed in relation to their structure.

Nano/Micro Structure Design

Guiding principles so far obtained from our previous investigations[3] to improve thermoelectric energy conversion efficiency of n-type β -SiC can be summarized as follows;

(1) High grain-to-grain connectivity should be achieved through grain growth to increase electrical conductivity, maintaining a porous structure to keep low thermal conductivity.

(2) Stacking faults should be eliminated to increase Seebeck coefficient.

In Fig. 1 is shown the methodology to be taken in a normal sintering process. Namely, sintering temperature ought to be as high as possible to promote sufficient grain growth to occur and the powder compaction pressure should also be high to make better grain-to-grain connectivity, while porous structure is maintained. Fortunately, such a procedure can be easily taken for SiC to fabricate its porous bodies, since SiC is a well-known material hard to sinter densely with no additives under normal pressures. In order to obtain high n-type conductivity, sintering is carried out under a N₂ atmosphere so that nitrogen atoms dissolve into SiC grains during sintering and behave as electron donors.

These considerations would further lead us to construct an image of an ideal structure to realize optimum thermoelectric characteristics, and a model microstructure close to a possibly

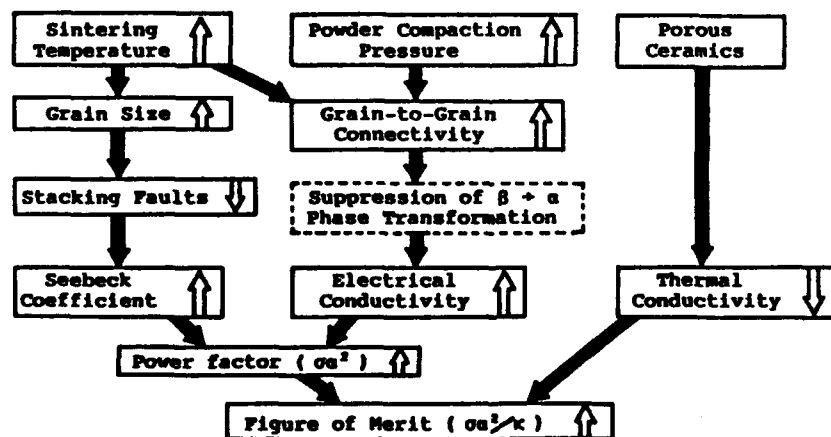


Fig. 1. Guiding principles for microstructure-control in porous β -SiC ceramics.

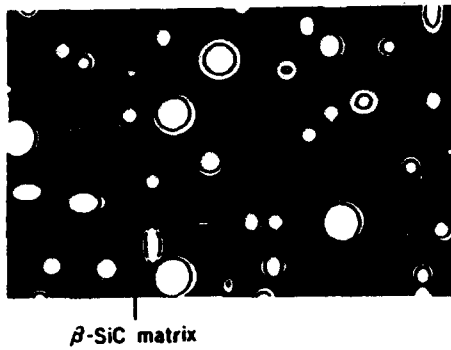


Fig. 2. Nearly ideal structure of porous ceramics; micropores are dispersed in β -SiC matrix.

ideal one is depicted in Fig. 2. The ideal structure must be composed of a single crystalline matrix with no lattice defects, such as stacking faults and dislocations, and yet with optimum donor dopants, with a large number of micropores uniformly dispersed.

Although this kind of microstructure cannot be easily fabricated by currently available processing techniques, we attempted to make microstructures resembling that shown in Fig. 2 by means of reaction sintering of CVD-synthesized hollow particles and polycarbosilane(PCS)[4,5].

Reaction-sintering of Hollow β -SiC Particles and Polycarbosilane

Hollow particles whose average size was $0.06 \mu\text{m}$ were synthesized by a thermal CVD (chemical vapor deposition) method employing SiH_4 and CH_4 as reaction gases and H_2 as a carrier gas. Detailed description of this process can be found in our previous papers[4,6]. A transmission electron micrograph of the hollow particles is shown in Fig. 3(A).

Hollow particles were put in a *n*-hexane solution containing PCS (Nippon Carbon Co., Ltd., Tokyo) and further mixed; the *n*-hexane was evaporated on a hot stirrer. The obtained powder

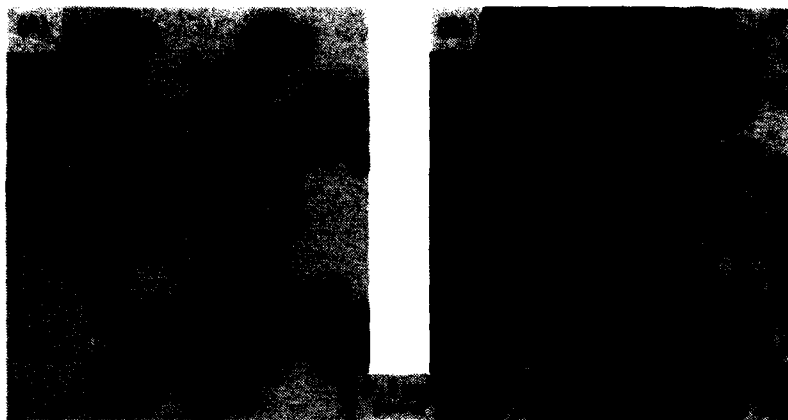


Fig. 3. TEM micrographs of (A) synthesized SiC hollow particles and (B) specimen S1 reaction-sintered at 1580°C for 3 h under N₂.

was crushed, hydrostatically press-formed into a compact, and sintered at 1580°C for 3 h under N₂.

Variation of the composition ratio (weight ratio) of hollow particles to PCS (1:1, 2:1, 4:1, 10:1) showed that the optimum ratio to give the highest mechanical strength was 4:1 when sintered at 1400°C. Higher sintering temperature, for example 1580°C, also gave improved mechanical strength, while the hollow shape of the particles was completely maintained (Fig. 3(B)). However, the resultant sintered bodies always contained large cracks which must have been introduced as the paths for escaping gases produced by pyrolysis of PCS.

To impregnate these cracks with SiC and hence densify the matrix, the reaction-sintered body was further impregnated with PCS, followed by sintering at 1580°C for 3 h under N₂, and this process was repeated. Figure 4 shows the microstructures of the specimens thus obtained for the initial weight ratio of hollow particles to PCS of 4:1. Figure 4 shows that the cracks gradually disappeared with repetition of the impregnation-sintering process. The relative densities of

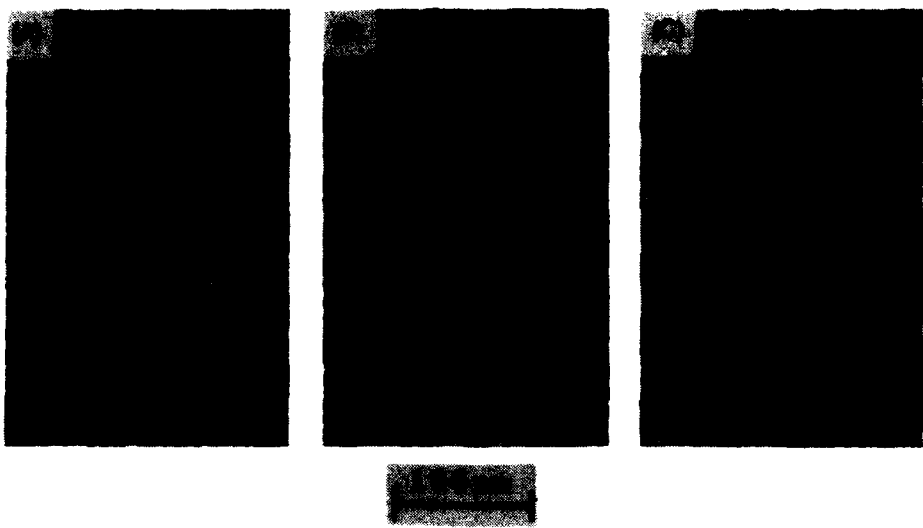


Fig. 4. SEM micrographs of the surfaces of specimens fabricated by (A) only reaction-sintering the 4:1 powder mixture (specimen S1), (B) impregnating specimen S1 with PCS, followed by sintering under the same conditions (specimen S2), and (C) further impregnating specimen S2 with PCS, followed by sintering (specimen S3).

specimens S1, S2, and S3 were 36.3%, 38.9%, and 40.4%, respectively.

Figure 5 shows the temperature dependences of the Seebeck coefficient, electrical conductivity, and power factor for sintered bodies. The Seebeck coefficient was always negative, and as the temperature increased, its absolute value increased. The n-type semiconduction (negative Seebeck coefficient) indicated that nitrogen has been incorporated into the SiC lattice during sintering. The observed anomalous temperature dependence of Seebeck coefficient has already been analyzed in terms of the phonon-drag effect[2]. That is, a decrease in the stacking fault density accompanied by grain growth and crystallite growth[7] increased the phonon mean free path, enhancing the phonon-drag effect, and hence leading to an apparently larger Seebeck coefficient[3]. Actually, the crystallite sizes calculated by the Scherrer equation for (111)

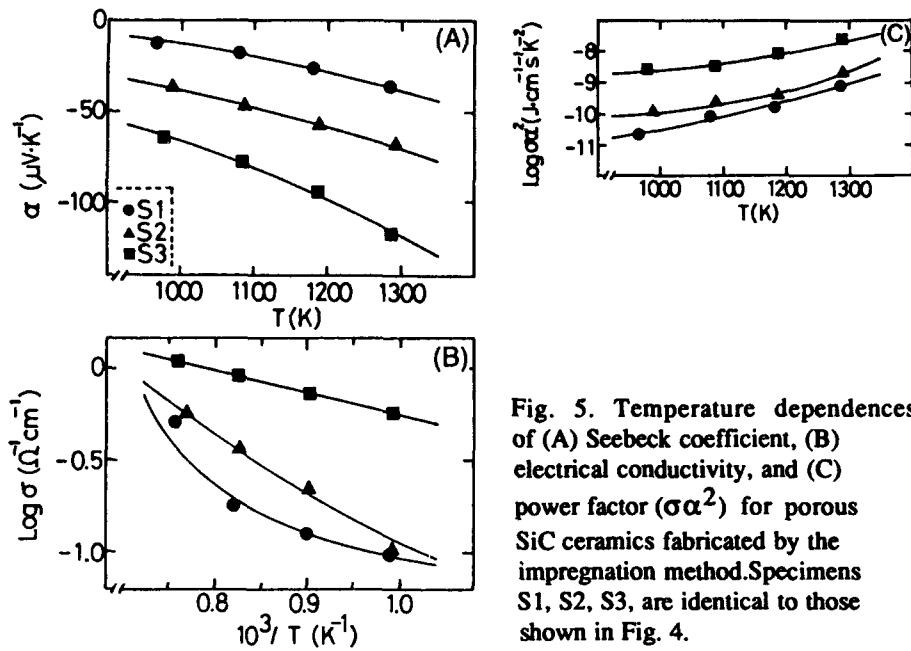


Fig. 5. Temperature dependences of (A) Seebeck coefficient, (B) electrical conductivity, and (C) power factor ($\sigma\alpha^2$) for porous SiC ceramics fabricated by the impregnation method. Specimens S1, S2, S3, are identical to those shown in Fig. 4.

reflections of specimens S1, S2, and S3 were 1550, 1640, and 2700 nm, respectively.

Figure 5 shows that the electrical conductivity also increases with repetition of the impregnation-sintering process, which must be due to the change in microstructure, namely the improved connectivity of SiC grains and the decrease in the crack volume. Electrical conductivity for the specimens fabricated by PCS impregnation is 1 to 2 orders of magnitude lower than that of the porous SiC ceramics fabricated by conventional sintering of commercial powders[3].

The power factor which reflects the thermoelectric conversion efficiency firmly increases with repetition of the impregnation-sintering process. It can be stated that thermoelectric conversion efficiency of SiC ceramics fabricated by the present impregnation method could be further improved by precise control of microstructure and carrier density.

Sintering of the Mixture of Hollow Particles and Commercial Powder

The gas evolving during decomposition of PCS forms large cracks, and a very complicated troublesome procedure is needed to fill them up with solid SiC in a reaction-sintering method. Accordingly, in our next attempt, fine hollow particles were simply mixed with commercial high-purity powder and were sintered to porous bodies with various porosities.

In this section, thermoelectric properties of these porous ceramics are discussed in relation to their microstructure. Our preliminary experimental work[3] indicated that the optimum figure of merit is obtained when the powder compact is sintered at and slightly above 2000°C under N₂, so that specimens employed for discussion here were all obtained by sintering at 2000°C for 3 h and further sintered at 2100°C for 3 h under N₂.

High sintering temperatures presently employed caused the collapse of hollow particles. Then, we expected that the hollow particles would provide the initial packing state with a bimodal size distribution of particles and the sintering process with micropores, hence giving rise to very porous microstructures with unique grain size distributions.

For the sintering process in SiC, it is widely accepted that surface diffusion controls the growth of intergranular necks leading to the grain coarsening[8]. Mass transport from the grain surface to the neck via surface diffusion does not lead to the shrinkage; in other words, the distance between the grains stays unchanged and only pores grow larger. It is also known that stacking faults initially present in each grain become annihilated simultaneously with the grain growth during sintering, which is controlled also by surface diffusion[5]. Therefore, in the present case, collapse of the hollow particles during sintering would leave pores behind, resulting in grain growth, increased porosity, and decreased stacking fault

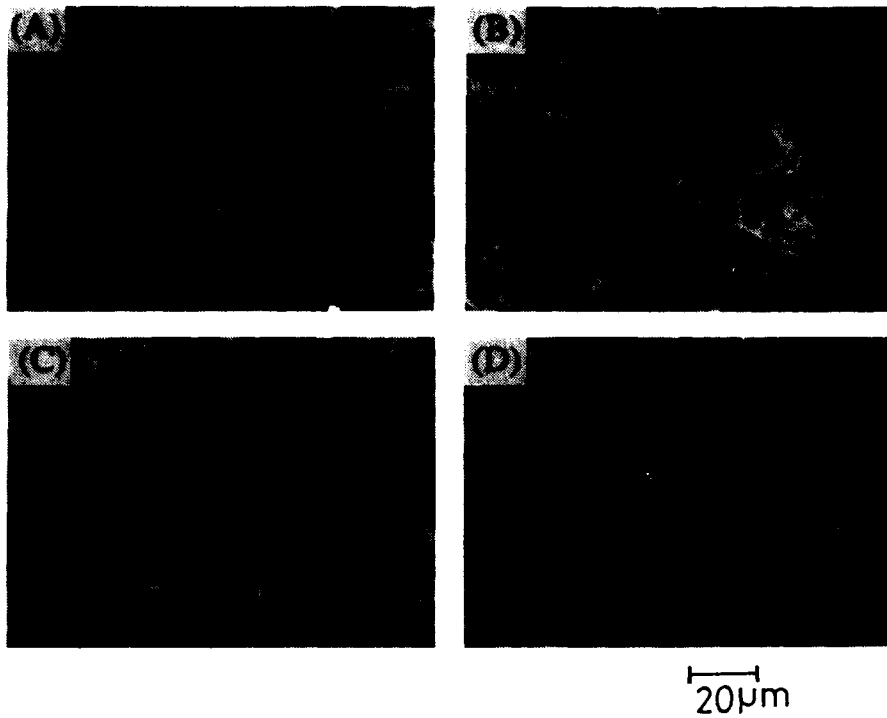


Fig. 6. SEM micrographs of fracture surfaces of sintered specimens; initial contents of hollow particles are (A) 0 vol%, (B) 20 vol%, (C) 55 vol%, and (D) 70 vol%.

density. The expected microstructure can be seen clearly in Fig. 6 where SEM photographs of the fracture surfaces of the sintered specimens initially having various amounts of hollow particles are shown.

Figure 6 reveals that the abnormal (exaggerated) grain growth has taken place in all the specimens initially possessing hollow particles((b)-(e)) giving rise to bimodal grain size distributions. The average size of grains abnormally grown apparently decreased with increasing porosity, while those small grains normally grown are all similar in size. This observation can be rationalized as follows; the increase in porosity, especially the growth of large pores, would have suppressed the contact between small grains and abnormally

grown grains inhibiting the mass transport via surface diffusion.

Figure 7 shows electrical conductivity decreases with increasing fractional porosity. In order to fully understand the change in microstructure and electrical conductivity, the percolation theory was applied to analyzing the data.

The generalized effective medium equation proposed by McLachlan[9,10] can be modified and expressed as;

$$\sigma_m/\sigma_h = (1-f/f_c)^t \quad (2)$$

where f is the volume of the low-conductivity component and f_c is the critical low-conductivity volume fraction at which the high-conductivity component first forms a continuous percolation path across the medium. σ_m is the conductivity of the medium itself and σ_h is the conductivity of the high-conductivity component.

The solid line in Fig. 7 was obtained for the data acquired at 700°C by a curve-fitting technique using Eq. (2). The parameters σ_h , f_c , and t to give the best-fit curve were 636 Scm⁻¹, 0.9, and 2.0, respectively. In general, the value of t for a composite is most often found to lie in the universal range of 1.65 to 2.0, though it is sometimes found to be somewhat below this range or often shows an excess value of 2.0 depending on the microstructural morphology[9]. A rather large value of t (=2.0) obtained here would indicate that porous SiC ceramics

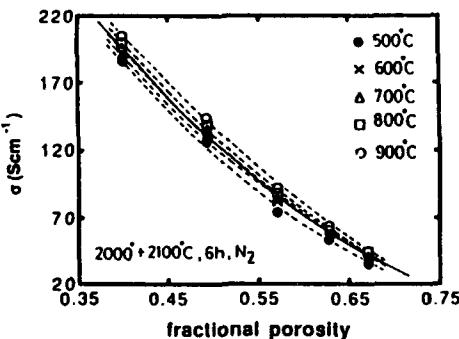


Fig. 7. Electrical conductivity vs. fractional porosity.

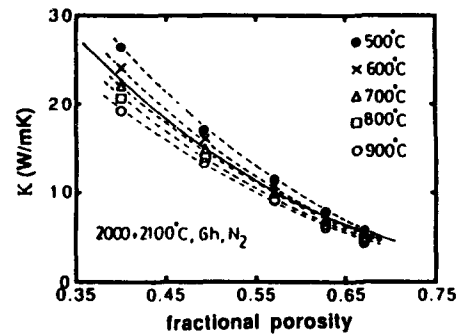


Fig. 8. Thermal conductivity vs. fractional porosity.

fabricated in this work have extraordinary geometries of conducting matrices[9] possibly due to the presence of large pores.

Figure 8 shows thermal conductivity obtained at 500-900°C decreases with increasing fractional porosity. The dashed lines are drawn through the measured points and the solid line shows the fitting result for 700°C data obtained again using Eq. (2) with the following parameters; $\kappa=73$ W/mK, $f_c=0.9$, $t=2.0$. The solid line is fairly well fitted with the measured data, indicating that the relationship between electrical conductivity or thermal conductivity and porosity can be expressed by a similar equation. Then, the following relation would result;

$$\sigma_m / \kappa_m = \sigma_h / \kappa_h \quad (3)$$

These results obviously suggest that the changes in microstructure and porosity during sintering have little effect on the ratio, σ/κ of β -SiC. Therefore, to improve the figure of merit of β -SiC maximization of Seebeck coefficient, α , by controlling the structure is inevitable.

As shown in Fig. 9, the absolute value of Seebeck coefficient increases with increasing temperature in all cases, which is advantageous for increasing the energy conversion efficiency at high temperatures. It can also be seen in the figure that Seebeck coefficient shows maximum values for the fractional porosity of *ca.* 0.6. This result is very interesting because the

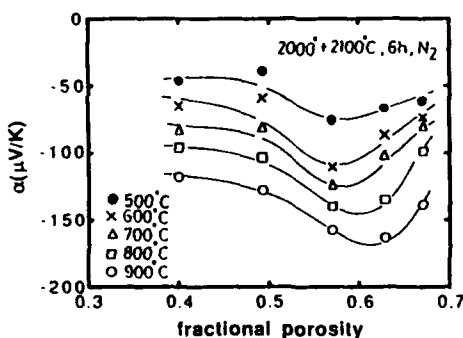


Fig. 9. Seebeck coefficient vs. fraction porosity

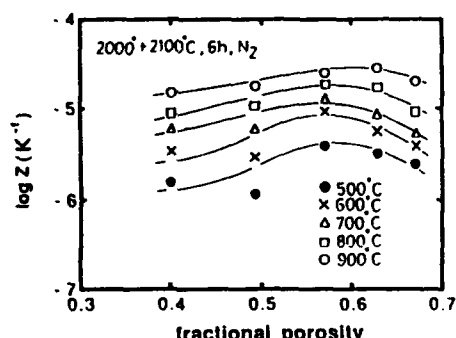


Fig. 10. Figure of merit vs. fraction porosity

figure of merit depends on the porosity and moreover the Seebeck coefficient changes with the change in microstructural features. This is more fully discussed in our recent publication [11].

Figure 10 shows the calculated figures of merit for the porous SiC as functions of fractional porosity. Since σ/κ remains almost constant in spite of the change in porosity, maximum values of Z are found for the porosity giving rise to the maximum Seebeck coefficients (ca. 0.6 fractional porosity). Through the present microstructure regulation, about twice as large a figure of merit as that commonly obtained by sintering commercial powders was realized. Since both σ/κ and Seebeck coefficient increase with increasing temperature accelerating the increase in the figure of merit, porous β -SiC ceramics seem to be highly potential for high-temperature thermoelectric energy conversion.

References

- [1] K. Koumoto, M. Shimohigoshi, S. Takeda, and H. Yanagida, J. Mat. Sci. Lett., 6, 1453(1987).
- [2] K. Koumoto, M. Shimohigoshi, S. Takeda, and H. Yanagida, Ceram. Trans., 2, 501(1989).
- [3] K. Koumoto, C. H. Pai, S. Takeda, and H. Yanagida, Proc. 8th ICT & 2nd ECT, edited by H. and S. Scherrer, Nancy, France(1989)pp.107.
- [4] C. H. Pai, K. Koumoto, S. Takeda, and H. Yanagida, J. Mat. Sci., 24, 3679(1989).
- [5] C. H. Pai, Y. Sasaki, K. Koumoto, and H. Yanagida, J. Am. Ceram. Soc., 74, 2922(1991).
- [6] K. Koumoto and C. H. Pai, Proc. 11th ICT, edited by K. R. Rao, University of Texas, Arlington, Texas(1992)pp.102.
- [7] W. S. Seo, C. H. Pai, K. Koumoto, and H. Yanagida, J. Ceram. Soc. Japan, 99, 443(1991).
- [8] C. Greskovich and J. H. Rosolowski, J. Am. Ceram. Soc., 59, 336(1976).
- [9] N. Deprez and D. S. McLachlan, Solid State Commun., 66, 869(1988).
- [10] D. S. McLachlan, M. Blaszkiewicz, and R. E. Newnham, J. Am. Ceram. Soc., 73, 2187(1990).
- [11] W. S. Seo, K. Watari, and K. Koumoto, Proc. 12th ICT, to be published.

GRAIN BOUNDARY CHARACTERISTICS IN PLZT, GBBLC AND HIGH T_c SUPERCONDUCTING CERAMICS AND THEIR RELATION TO PROPERTIES

M. Y. Zhao, Z. W. Yin and B. M. Xu
Shanghai Institute of Ceramics, Chinese Academy of Sciences, Shanghai 200050,
China

ABSTRACT

Many properties of functional ceramics are originated from their grain boundary effects. In this paper, the authors summarized their works on the grain boundary characteristics and microstructures of different types of functional ceramics with emphasis on (1) transparent PLZT ferroelectric ceramics (insulator), (2) SrTiO₃-based GBBLC ceramics (semiconductor) and (3) YBCO high T_c superconducting ceramics. Experimental results showed that the different grain boundary characteristics or microstructures in these ceramics will give rise to big change in their properties, the electro-optic properties of PLZT ceramics, the barrier characteristics and dielectric properties of GBBLC and the current density J_c in YBCO superconducting ceramics.

Keywords: grain boundary, PLZT, GBBLC, YBCO

INTRODUCTION

The great influence of grain boundary of ceramic materials on their properties was a well-known fact to ceramic scientists for a long time. However, the great majority of ceramic materials contains certain amount of pores, impurities and glass phase, which gave difficulties to study the grain boundary effect of these ceramic materials. Besides, the experimental methods and equipments are also important, the rapid development of modern structural analysis instruments made the research work becoming possible. In present paper, the authors summarized their works on the grain boundary characteristics and microstructures of three different types of functional ceramics, namely transparent PLZT ferroelectric ceramics, SrTiO₃-based GBBLC ceramics and YBCO high T_c superconducting ceramics, and their relation to properties.

To the extent authorized under the laws of the United States of America, all copyright interests in this publication are the property of The American Ceramic Society. Any duplication, reproduction, or republication of this publication or any part thereof, without the express written consent of The American Ceramic Society or fee paid to the Copyright Clearance Center, is prohibited.

TRANSPARENT PLZT FERROELECTRIC CERAMICS

Transparent PLZT ferroelectric ceramic materials are insulators, free of pores, very few impurities and can be considered as a single phase material. Their grains are granular with good roundness. In certain range of their compositions, they are ferroelectric or antiferroelectric, so, their properties are very sensitive to the change of external conditions (temperature, stress, electric field etc). Therefore, the transparent PLZT ferroelectric ceramics is one of the most relevant material to study the grain boundary effect in functional ceramics^[1-9].

Grain Boundary Structure Based on TEM Observation

Fig. 1 shows the HREM image photomicrographs taken near the grain boundary from a JEOL 200cx high resolution electron microscope. Most grain boundaries are very thin, about 6 Å (Fig. 1a). Some are only 2-3 Å. However, in some places, broader ones (dozens angstroms) can also be found as amorphous structure (Fig. 1b, segment c).

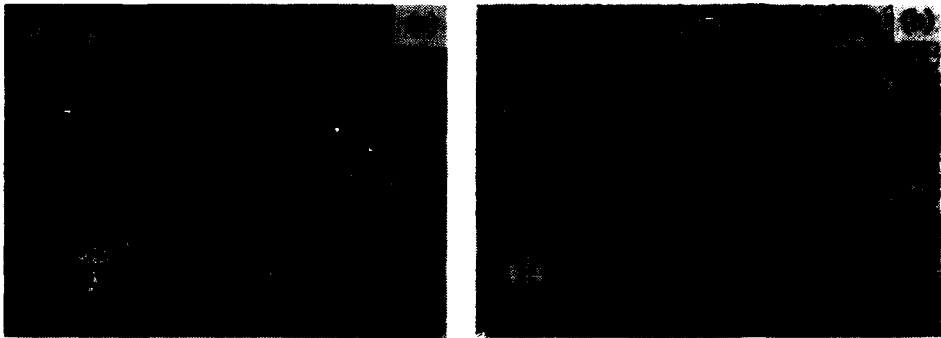


Figure 1 HREM image of two grains and their boundary
(a)one grain along [111] and the other along [100]
(b)two grains both along [110]

The thin boundaries can be either coherent or incoherent. Fig. 2 demonstrates the structure model of grain boundary of segment AB in Fig. 1b. It belongs to coherent boundary. There are shared atoms by the two adjacent grains. The distance between the shared atoms is 4 Ti-O octahedra in grain A or 3 Ti-O octahedra in grain B. However, the grain boundary shown in Fig. 1a belongs to incoherent one. It could be assumed that in ordinary case the grain boundaries in PLZT ceramics should be very fine, of the order of several angstroms. However, when impurities entered into the grain boundaries or triple junctions, second phase

formed and boundary broadened. The thin grain boundary structure of PLZTs explains well why its cubic α phase has good transparency and why the domains in ferroelectric β phase could penetrate the grain boundary from one grain to the other.

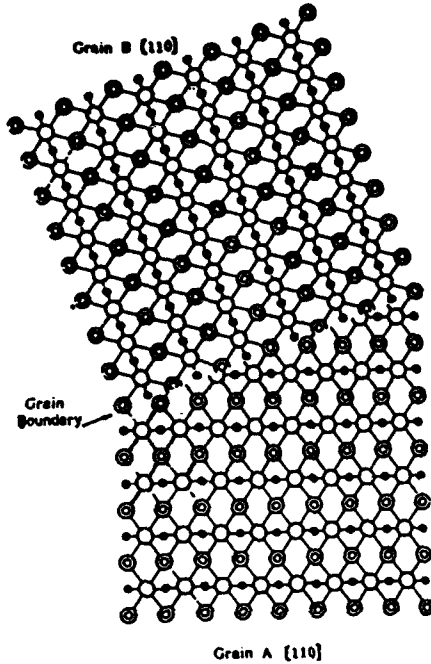


Figure 2 Atomic structure model of grain boundary of segment AB in Fig. 1(b)

Grain Boundary Effect in PLZT Ceramics

The PLZT composition 7.9/70/30 was selected for studying the grain boundary effect on the electro-optical properties of the transparent ceramics. Hot pressing in flowing oxygen atmosphere was used for making the transparent ceramic slugs. The grain-grown specimen at different grain sizes were prepared by reheating the hot-pressed slug in PbO atmosphere to 1340°C–1350°C for 72–168 hours. Fig. 3 shows the microphotographs of 7.9/70/30 PLZT ceramics after heat treatment and compared with its original hot-pressed specimen. The image analyses and stereology studies on above specimens were carried out by means of a Quantimat 900 Micro-Image Automatic Quantitative Analyzer made by Cambridge Instrument Ltd. The total interface area in unit volume of ceramic material, S_v was determined equal to 0.463mm²/mm³ for hot-pressed specimen as shown in

Fig. 3(a) and $0.160\text{mm}^2/\text{mm}^3$ for heat treated specimen as shown in Fig. 3(b) respectively. Fig. 4 gives the longitudinal electric controlled light scattering at different temperatures of the above two specimens. Fig. 4 tells us that the change of grain size distribution of a ceramic material will certainly affect the properties of the material. The grains in hot-pressed PLZT ceramics are small, the

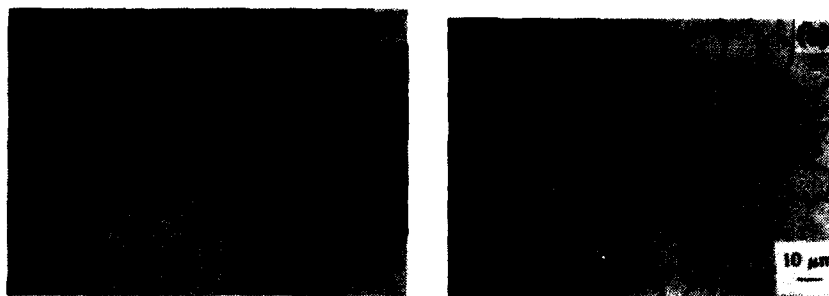


Figure 3 Microphotographs of 7.9/70/30 PLZT ceramics after heat treatment and compared with its original hot-pressed specimen. (a) hot-pressed (b) hot-pressed, and heat treated at 1340°C for 72 hours.

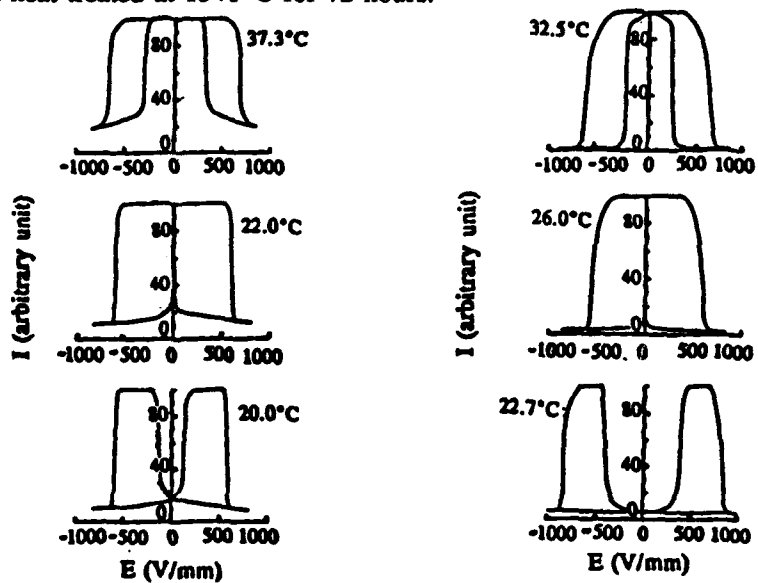


Figure 4 The longitudinal electric controlled light scattering at different temperatures of the hot-pressed and grain-grown specimens of 7.9/70/30 PLZT ceramics (a) hot-pressed, $S_v=0.463\text{mm}^2/\text{mm}^3$, (b) heat-treated, $S_v=0.160\text{mm}^2/\text{mm}^3$

volumetric fraction of the grain boundary region is high, sometimes reaches 25 %, even more of the total volume of the ceramic. High energy state in hot-pressed PLZT ceramics tends to block the development of macro-domain structure at its ferroelectric state, which results in less scattering at the domain walls and so gives lower contrast.

SINGLE-STEP, LOW-TEMPERATURE SINTERED SrTiO_3 GBBL CAPACITOR CERAMICS

SrTiO_3 grain boundary barrier layer (GBBL) capacitors have been rapidly developed in recent years because of their excellent properties. However, the two-step firing process and high sintering temperature (usually higher than 1400°C) not only increase the commercial cost of the capacitors, but also are the main obstacles to fabricate monolithic GBBL capacitors^[10,11]. The authors have found^[12,13] that by doping a kind of sintering aid mainly consisting of Li_2O and SiO_2 , SrTiO_3 GBBL capacitors can be single-fired between 1100 and 1200°C in reducing atmosphere, which is favourable for fabricating monolithic GBBL capacitors with base metal inner electrodes. Fig. 5 shows the schematic diagram of the microstructure development of this new kind of capacitor materials.

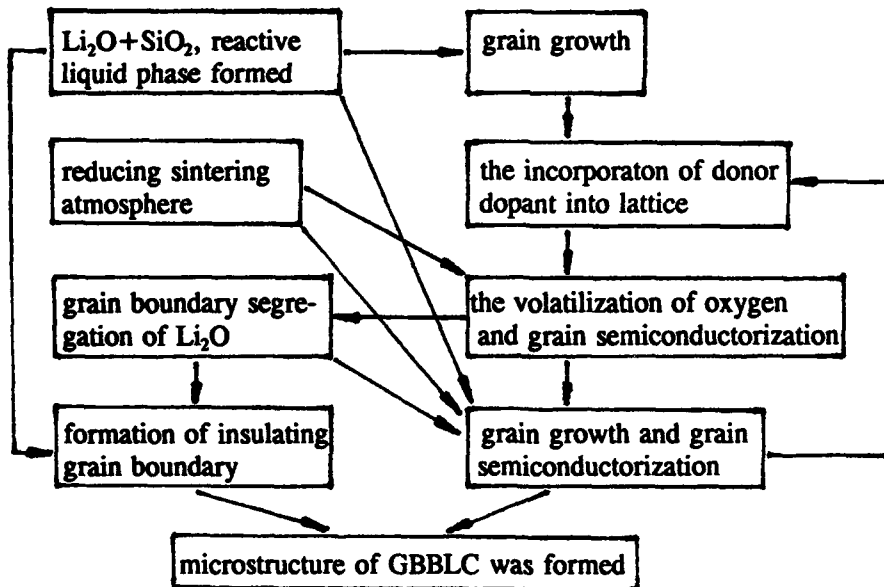


Figure 5 Schematic diagram of the microstructure development of the single-step, low-temperature sintered SrTiO_3 , GBBL capacitor materials

The Grain Boundary Characteristics of One-step, Low-temperature Sintered SrTiO₃ GBBL Capacitor Ceramics

Based on HREM, four different types of grain boundaries were observed in the one-step, low-temperature sintered SrTiO₃ GBBL capacitor ceramics namely (1) broad crystalline grain boundary, (2) broad non-crystalline grain boundary, (3) narrow non-crystalline grain boundary and (4) "clean" grain boundary. They are shown in Figure 6.

The width of grain boundary in Fig. 6(a) and (b) is in the range of 100-1000Å, close to that of two-step fired GBBL ceramics. The narrow non-crystalline grain boundary in Fig. 6(c), its width is several to ten angstroms and its structure is something like the grain boundary as shown in Fig. 1(a) for PLZT. The width of "clean" grain boundary as shown in Fig. 6(d) is only 2-3Å, its structure is very similar to the coherent boundary of PLZT as shown in Fig. 2.

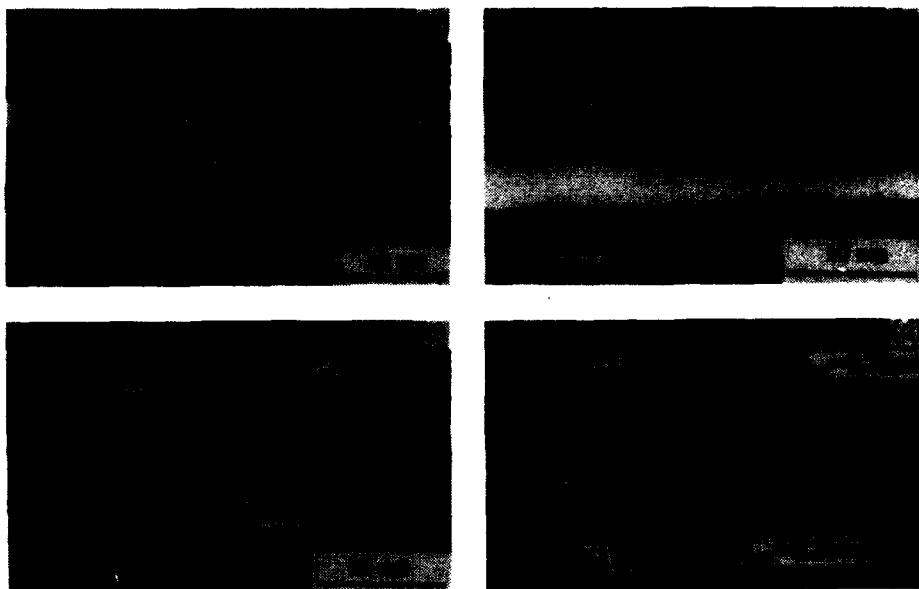


Figure 6 HREM image of two grains and their boundary

- (a)broad crystalline grain boundary
- (b)broad non-crystalline grain boundary
- (c)narrow non-crystalline grain boundary
- (d)"clean" grain boundary

As for the two-step fired SrTiO_3 GBBL ceramics, their grain boundary characteristics have been fully studied^[14,15]. Since the second-step firing process, namely diffusion process, was carried out at temperatures quite lower than the temperature used for first-step sintering process. The driving force of formation of new grain boundary is the thermal diffusion of molten impurity ions along the original grain boundaries, so a continuous broad grain boundary phase can be formed, which is independent of sintering process and the orientation of the grains. However, as for one-step fired GBBL ceramics, the formation of grain boundary phase is almost simultaneous with the sintering and is intimately correlated with the grain growth and the orientation of the grains. It is clear that different fabrication technology will give different grain boundary characteristics and result in quite different properties of the materials.

Current-Voltage Relation and Grain Boundary Barrier Model in SrTiO_3 GBBL Capacitor Ceramics

The difference in grain boundary characteristics between one-step low-temperature sintered and two-step fired SrTiO_3 GBBL capacitor ceramics will certainly lead to their different properties, especially their I-V relations. Fig. 7 shows the I-V characteristics of these two materials. It can be seen from Fig. 7 that the non-linear behaviour of the I-V curve of one-step sintered ceramic is

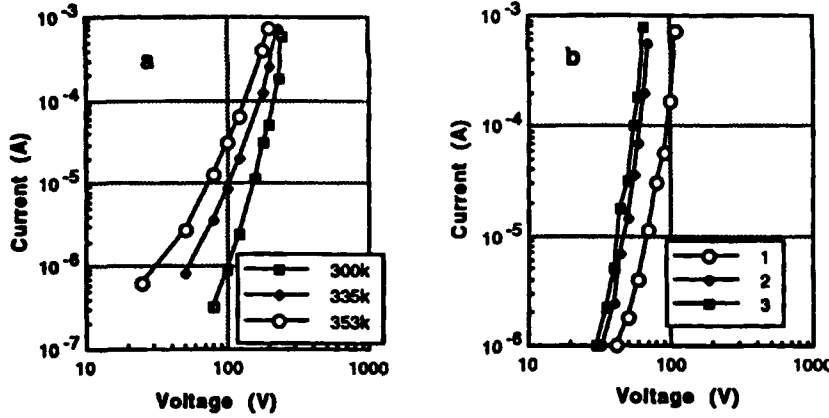


Figure 7 I-V curves of SrTiO_3 GBBL capacitor ceramics

(a) two-step fired
 (b) one-step sintered:

- (1) low donor content (about 0.1 mol% Nb_2O_5), at 288k and 358k (overlapped)
- (2) high donor content (about 0.5 mol% Nb_2O_5), at 288k
- (3) high donor content (about 0.5 mol% Nb_2O_5), at 358k

more pronounced than that of two-step fired sample. For low donor content sample, its I-V behaviour is independent on temperature. However, for high donor content sample, its I-V curve moves to lower voltage side along with the increase of the temperature.

One of the authors has systematically studied the grain boundary barrier and grain boundary breakdown of the two-step fired SrTiO_3 GBBL capacitor ceramics^[16]. They concluded that due to the presence of a continuous broad grain boundary phase in this material a model of grain boundary Schottky barrier with an intergranular insulating layer was proposed as shown in Fig. 8. With this model, the current-voltage relation and capacitance-voltage relation were theoretically analyzed and derived. When using this model for GBBL capacitors

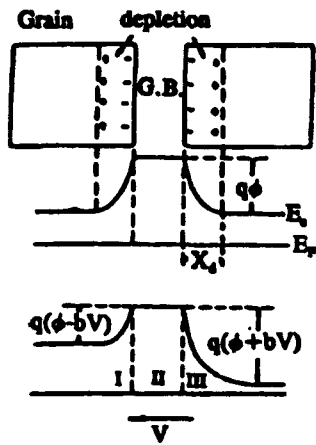


Figure 8 Grain boundary Schottky barrier with an intergranular layer

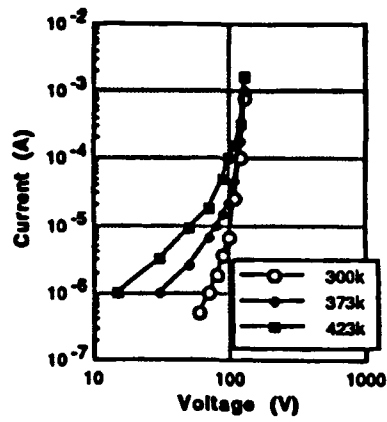


Figure 9 I-V characteristics of ZnO varistor

compared with the Schottky barrier model for ZnO varistor^[17,18], two different breakdown mechanisms were found: the avalanche breakdown for the former which is temperature dependent and the tunnelling breakdown for the latter which is temperature independent. Fig. 9 shows the non-linear characteristics of a ZnO varistor in breakdown region. As for the one-step, low-temperature sintered GBBL capacitor ceramics, there are four different types of grain boundaries. Among them the broad crystalline or non-crystalline grain boundary phases play the same role as that in the two-step fired materials. High donor contents is of advantage to broaden the grain boundaries, which makes these two types of grain boundary to dominate the properties of the material. However low donor content is profitable to form the narrow and "clean" grain boundaries. The grain boundary structure and characteristics of these two types of grain boundary are

in YBCO ceramics perpendicular to the grain boundary and along the grain boundary are shown in Fig. 10. Fig. 10(a) shows that the profile taken across the boundary has a copper rich zone, which is typically asymmetric with respect to the boundary plane. A composition profile obtained along the boundary is shown in Fig. 10(b). It showed that the most notable feature of the composition variation in the grain boundary is their regular oscillatory nature. These heterogeneities might be an intrinsic feature of the boundary and would give a pronounced effect on the nature of electrical transport in polycrystalline YBCO superconductors.

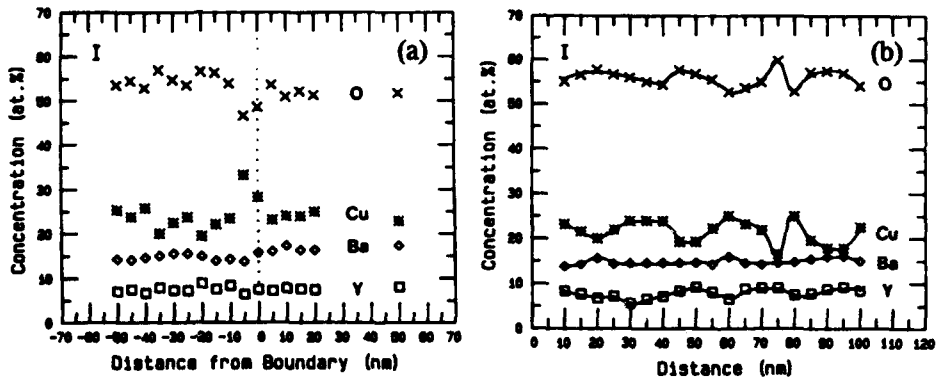


Figure 10 Composition profile of grain boundaries in YBCO ceramics^[20]
(a) perpendicular to the boundary, (b) along a boundary

Many research groups have identified the grain boundary phases in YBCO ceramics, including CuO, BaCuO₂, Cu₂O, BaCO₃ and Y₂O₃. They were presented probably as a result of non-stoichiometry of the starting powder mixture or incorrect processing. Besides, other impurities, such as Sr, Zr or Al ions were also found at highly misoriented grain boundaries. It is said that^[21] Cooper pairs can only tunnel over a nonsuperconducting region of 5 angstroms (parallel to the c-axis) and 20 angstroms (perpendicular to the c axis), so the impurity layers along the grain boundaries with thickness more than 20 Å would form weak links.

The anisotropy behaviour, especially the anisotropy of the current density in bulk YBCO superconductors is an important property and has been analyzed by magnetization measurement and pulse method. Magnetization measurement for single crystal has shown a factor of 20 between J_c^{ab} measured along the a-b plane (i.e. Cu-O plane) to that measured perpendicular to the a-b plane J_c^c ^[22]. V. Selvamanickam and K. Salama studied the intergrain transport current density and its anisotropy by the pulse method with the oriented-grain YBCO superconducting ceramics^[23]. They were performed on the oriented-grain samples with the transport current aligned at different angles to the a-b plane. Table 2 lists their

rather similar to the grain boundaries in ZnO varistors, so the Schottky barrier play the important role on the properties of the materials.

YBCO HIGH T_c SUPERCONDUCTING CERAMICS

The discovery of high T_c superconducting oxides, such as YBCO superconductors has stimulated enormous research works because of their potentially immense technological applications. However, the use of bulk YBCO superconductors in high-current devices has met troubles due to the low transport critical current density J_c and its severe degradation in magnetic fields. The limited J_c in YBCO superconducting ceramics has been attributed largely to the weak link behaviour of grain boundaries.

Critical Current Density of Grains and Their Grain Boundaries

A direct measurement of the transport current density of individual grains and grain boundaries in YBCO superconductors has been successfully made by P. Chaudhari et al as shown in Tabel 1^[19].

Table 1 Critical current density J_c of individual grains at 4.2-5K^[19]

Grain 1	Grain 2	Grain boundary ($10^3 A/cm^2$)
> 500	> 500	50
> 100	70	18
250	220	12
390	130	3.1
260	14	0.7
8.5	0.5	0.7

Weak Link Behaviour of Grain Boundary

The specific features of the grain boundary in YBCO ceramics which results in formation of weak links may be as follows: (1) composition variation at grain boundary regions, (2) segregation of second phase and other impurities at grain boundary areas, (3) anisotropy ---- high angle grain boundaries and (4) defect structure at grain boundaries ---- microcracks, pores and dislocations.

The local composition profile variation within YBCO grain boundaries was studied by S. E. Babcock et al^[20]. The composition profiles of grain boundaries

results. A current density anisotropy ratio (J_c^{ab}/J_c^c) of 25 was estimated. Thus, the severe anisotropy in conductivity would cause weak connections at high-angle grain boundaries.

Table 2 Details of samples used in transport current anisotropy measurements^[23]

Angle between current and a-b plane (degree)	Room-temperature resistivity (mΩ·cm)	No. of grain boundaries between current contacts	Critical current density (A/cm ²) (T=77K, H=0)
0	0.4	0	75000
16	2.12	70	18000
34	13.08	140	3560
70	25.96	260	3330

The defect structure of grain boundaries, such as microcracks, pores and dislocations are other factors to form weak links^[24,25]. Fig. 11 shows the HREM image of microcracks at the grain boundary region of YBCO ceramics and the width of the microcracks is in the range of 6-7nm. It was assumed that the presence of microcracks were resulted from the severely anisotropic thermal expansion along different crystallographic directions.



Figure 11 HREM image of microcracks at grain boundaries

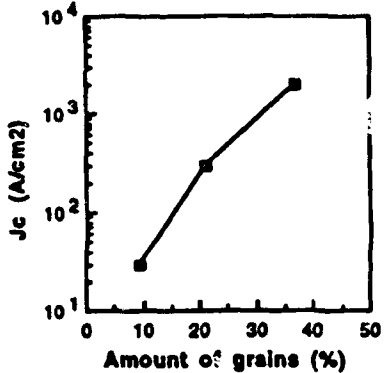


Figure 12 The correlation between J_c and amount of grains containing coherent GBs in YBCO ceramics

Besides, the coherent grain boundaries with the intergranular region being 5--

10Å and the influence of their amounts on J_c have also been studied in detail by the authors^[26]. The result showed that the coherent grain boundary is narrow and straight and no grain boundary phase presented. The authors found that the coherent grain boundaries are frequently parallel to the a-b plane of the adjacent grains. The critical current density J_c of the ceramics will increase along with the increase of the amount of grains containing coherent grain boundaries in the material as shown in Fig. 12.

REFERENCES

1. Z. W. Yin, X. M. He, C. E. Li, Z. Y. Wei, and H. Y. Ni, "Phase Transition and Properties of 7.9/70/30 PLZT Ferroelectric Ceramic Materials", Proc. of the First China-US Seminar on Microstructure and Properties of Ceramic Materials, May, 1983, Science Press, Beijing, China, 410, 1984
2. B. H. Chu, H.K. Ngao, X. S. Zhen and Z. W. Yin, "Grain Boundary Phenomena in PLZT Transparent Ferroelectric Ceramic Materials", *ibid*, 192
3. Z. W. Yin, "Recent Development of PLZT Ceramics Research in Shanghai Institute of Ceramics", Proc. of ISAF'86, 8-11, June, 1986, Lehigh University, 139-45
4. D. N. Huang, Z.W. Yin, and L. E. Cross, "Electrical Properties of Grain Grown PLZT Ceramics", *ibid*, 159-64
5. X. T. Chen, D, N, Huang and Z. W. Yin, "Optical and Electro-Optical Properties of PLZT Ceramics with Different Grain Size", *ibid*, 62-65
6. Z. W. Yin, D. N. Huang, X. T. Chen, X. Q. Chen and X. L. Zhou, "Stereology Studies on Grain Growth of PLZT Ceramics", *J. Inorg. Mat.*, 1 [2] 97-101 (1986)
7. Z. W. Yin, X. Y. Song and J. W. Feng, "Grain Boundary Structures in PLZT Ceramics", *Ferroelectrics*, 94 [2] 269-274 (1989)
8. Z. W. Yin, "Studies on Microstructure and Microproperties of PLZT Ceramics", *Ceramics International*, 15 [4] 311-15 (1989)
9. P. C. Wang and Z. W. Yin, "Some Aspects of PLZT research in Shanghai Institute of Ceramics", *Ferroelectrics*, 123 [1-4] 131-130 (1992)
10. G. Goodman, "Capacitors Based on Ceramic Grain Boundary Barrier Layers-- A Review", pp. 215-31 in *Advances in Ceramics*, Vol. 1, Edited by L. M. Levinson. The American Ceramic Society, Columbus, Ohio, 1981
11. M. F. Yan and W. W. Rhode, "Ultrahigh Dielectric Capacitance in TiO_2 Ceramics", pp. 226-38 in *Advances in Ceramics*, Vol. 7, Edited by M. F. Yan and A. H. Heuer. The American Ceramic Society, Columbus, Ohio, 1983
12. B. M. Xu, H. Wang and Z. W. Yin, " Study on Sintering $SrTiO_3$, GBBL Capacitors at Low Temperatures", *J. Chin. Ceram. Soc.*, 19 [4] 354-360 (1991)

13. B. M. Xu, H. Wang and Z. W. Yin, "The Doping Analysis of SrTiO_3 GBBL Capacitors Sintered at Low Temperatures", *J. Chin. Ceram. Soc.*, 20 [1] 16-22 (1992)
14. M. Fujimoto and W. D. Kingery, "Microstructure of SrTiO_3 Internal Boundary Layer Capacitor During and After Processing and Resultant Electrical Properties", *J. Am. Ceram. Soc.*, 68 [4] 169-73 (1985)
15. N. Stenton and M. P. Harmer, "Electron Microscopy Studies of a Strontium Titanate Based Boundary-Layer Material", pp. 156-65 in Ref. 11
16. J. P. Zhong, H. Wang and Z. W. Yin, "The Grain Boundary Barrier of Semiconducting Ceramics", *Ferroelectrics*, 101 81-86 (1990)
17. O. A. Clarke, "The Microstructural Location of the Intergranular Metal-Oxide Phase in a Zinc Oxide Varistor", *J. Appl. Phys.*, 49 [4] 2407-11 (1978)
18. L. M. Levinson and H. R. Philipp, "The physics of Metal Oxide Varistors", *J. Appl. Phys.*, 46 [2] 1332-40 (1975)
19. P. Chaudhari, J. Mannhart, D. Dimos, C.C. Tsuei, J. Chi, M. M. Oprysko, and M. Scheuermann, "Direct Measurement of the Superconducting Properties of Single Grain Boundaries in $\text{YBa}_2\text{Cu}_3\text{O}_{7-\delta}$ ", *Phys. Rev. Lett.* Vol. 60 [16] 1653-56 (1988)
20. S. E. Babcock and D. C. Larbalestier, "Evidence for Local Composition Variations within $\text{YBa}_2\text{Cu}_3\text{O}_{7-\delta}$ Grain Boundaries", *Appl. Phys. Lett.*, 55 [4] 392-95 (1989)
21. S. L. Wen, "The Relationship of Atomic Structure with T_c and Microstructure with J_c in High T_c Superconductors", International Symposium on Electron Microscopy, Ed. Kehsim Kuo, Beijing, China, 1990, 319
22. T. R. Dinger, T. K. Worthington, W. J. Gallagher and R. L. Sandstrom, "Direct Observation of Electronic Anisotropy in Single-Crystal $\text{Y}_1\text{Ba}_2\text{Cu}_3\text{O}_{7-\delta}$ ", *Phys. Rev. Lett.*, 58 [25] 2687-94 (1987)
23. V. Selvamanickam and K. Salama, "Anisotropy and Intergrain Current Density in Oriented Grained Bulk $\text{YBa}_2\text{Cu}_3\text{O}_x$ Superconductor", *Appl. Phys. Lett.*, 57 [15] 1535-77 (1990)
24. J. W. Feng, S. L. Wen, M. Y. Zhao and C. E. Li, "TEM Observation of Structure Defects in Y(Eu)-Ba-Cu-O Superconductor", *J. Chin. Ceram. Soc.*, 17 (5) 462-66 (1989)
25. S. Nakahara, G. J. Fisanick, M. F. Yan, R. B. VanDover and T. Boone, "On the Defect Structure of Grain Boundaries on $\text{Ba}_2\text{YCu}_3\text{O}_{7-\delta}$ ", *J. Crys. Growth*, 85 [2] 639-51 (1987)
26. X. Y. Song, S. L. Wen, Z. X. Zhao, M. Y. Zhao, C. E. Li and D. L. Jin, "Effect of Microstructures on Properties of YBCO", *Chin. Sci.*, 35A [8] 834-37 (1992)

Ferrites and Titanates

**GRAIN BOUNDARY MICROSTRUCTURE
AND MAGNETIC PROPERTIES OF
LOW-TEMPERATURE-FIRED
NI-ZN-CU FERRITE**

Masayuki Fujimoto
Taiyo Yuden Co., Ltd.
1660 Kamisatomi, Haruna-machi, Gunma 370-33 Japan

Slowly cooled and rapidly cooled multilayer chip inductors each containing a Ag internal electrode and low-temperature-fired Ni-Zn-Cu ferrite but exhibiting different inductance were characterized using analytical electron microscopy. Elastic strain fields were observed at the grain boundaries in the rapidly cooled sample, causing degradation of the inductance. The strain field arising from a decrease in the effective permeability of the ferrite was found to be due to Cu precipitates. The occurrence of Cu metal precipitates at grain boundaries was dependent on the starting chemical composition, oxygen partial pressure, and thermal equilibrium during cooling after the sintering.

I. INTRODUCTION

The multilayer chip inductor has many strong points. Besides its shape compatibility with the chip resistor and multilayer chip capacitor, it has merits such as no need for core processing, potential of miniaturization, and no cross-talk due to leakage of magnetic flux because of circulation patterns set within magnetic elements.^{1,2)} With these excellent characteristics, and with the development of high density surface mounting, it has been expanding its market in the field of not only consumer electronics such as video cameras, liquid crystal TV's, and head-phone stereos, but also industrial devices such as hard disks, personal wireless communication systems, and automobile telephones.

For constructing internal circulation patterns in ferrite material, common through-holes are made through ferrite green sheets of prescribed thickness and 3/4 circular conductor pattern is printed, and simultaneously, the through-holes are filled with conducting paste and adjacent 3/4 circular patterns are connected. By repeating this process, the prescribed internal circulation pattern (coil) is formed. To obtain a Q

To the extent authorized under the laws of the United States of America, all copyright interests in this publication are the property of The American Ceramic Society. Any duplication, reproduction, or republication of this publication or any part thereof, without the express written consent of The American Ceramic Society or fee paid to the Copyright Clearance Center, is prohibited.

(quality factor; $1/t_{\text{ane}}$) as high as inductor high-conductivity material must be used in the internal circulation pattern. Silver is one of the best materials its properties include low resistivity for Q value as high as for an inductor, low price compared with other noble metals which can be used in mass-production, and sinterability under air atmosphere which allows for the use of simple sintering furnace without specific atmosphere such as N_2 or H_2 . However its low melting point ($960^\circ C$) prevents use of conventional ferrite powder which requires high temperature for sintering (about $1300^\circ C$). For decreasing the sintering temperature, not only non-stoichiometric starting chemical composition with a small excess of Ni-Zn-Cu which is well known to improve solid-phase sintering of ferrite using formation of oxygen vacancies as a diffusion path, but also small-grain-size, high pure raw materials must be adopted.

It is also well known that the permeability of spinel ferrite is strongly affected by the inner stress related to the microstructure, i.e., it is a somewhat microstructure-sensitive material.

In this study, high-resolution analytical electron microscopy (HR-AEM) was used to characterize the grain boundary microstructure of multilayer chip inductors. Samples were prepared so as to minimize the residual stress of the internal electrode and ferrite body, and to produce variations in the magnetic properties by altering the sintering process. Here, the relationship between the observed and analyzed grain boundary microstructures inducing inner stress and the resulting magnetic properties are reported.

II. EXPERIMENTAL

The raw materials, submicron-order Fe_2O_3 , NiO , ZnO and CuO powders, were ball-milled with distilled water with a starting chemical composition of $(Ni_{0.34}Cu_{0.22}Zn_{0.40}O)[Fe_2O_3]_{0.98}$, that is, a small excess of Ni-Zn-Cu chemical composition (shortage of Fe_2O_3). A slurry was cast into a green sheet for fabrication of multilayer chip inductors. Common through-holes were made in the ferrite green sheets, and a 3/4 circular pattern of the silver conductor paste was printed. At the same time, silver paste was introduced into the through-hole to fill it and connect the adjacent 3/4 circular pattern by lamination. the laminated block was cut into chips. The samples were the sintered at $880^\circ C$ under air atmosphere at different cooling rates, either slowly ($-300^\circ C/h$) or rapidly ($-900^\circ C/h$). Finally, silver external electrodes were formed on both sides of the chips for electrical measurements.

III. L-Q PROPERTIES

The frequency dependence of L (inductance) and Q properties of the samples are shown in Fig. 1. Both the rapidly cooled and slowly cooled samples, exhibiting a high Q value and constant L value up to the high frequency region, were available for use as inductive elements in electronic circuits. However, in spite of their identical Q values, the L value of the slowly cooled sample was much larger than that of the rapidly cooled one.

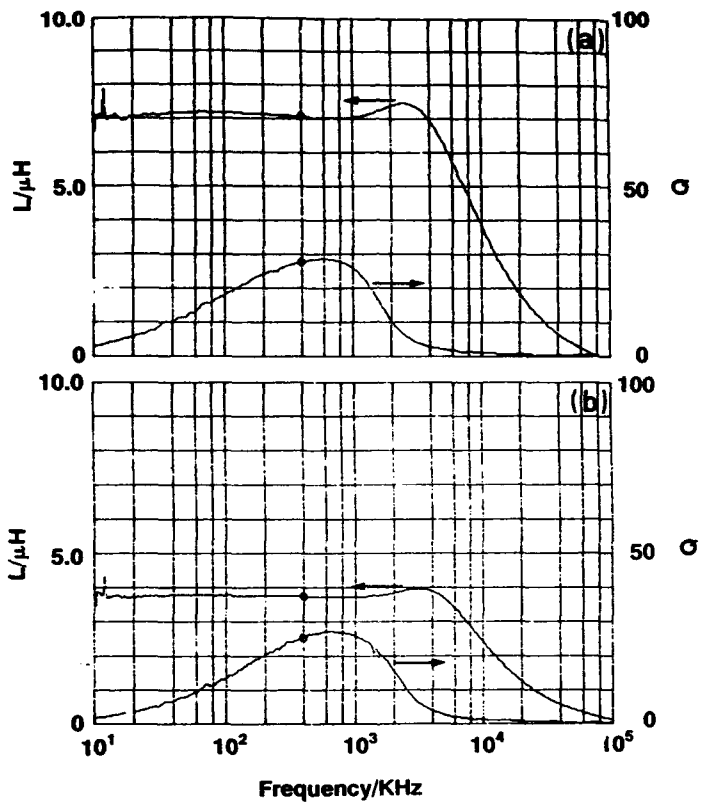


Fig.1. Frequency dependence of L (inductance) and Q (quality factor) properties for the a) slowly cooled sample, and b) rapidly cooled sample.

IV HR-AEM ANALYSIS

Figure 2 shows TEM bright-field images of the samples. Both the samples show precipitates at the multiple grain junction with a pore. The rapidly quenched sample showed a number of interference fringes near the grain boundaries, while the slowly cooled one did not. The small-sized fringes located near the grain boundaries were obviously different from thickness extinction fringes, but similar to the contrast arising from elastic strain around coherent or incoherent precipitates.³⁾ More precise observation revealed that the centers of the strain field image were not located on the grain boundary but adjacent to it, and that the center line of the strain field images was oriented in one direction, as if it had some crystallographic relationship with the matrix grains (Fig. 3). Figure 4 shows a high-resolution image of the center of the strain field near the edge of the specimen, which was thin enough for lattice image formation. A black swollen line about 5 nm long was clearly recognized between the spinel ferrite lattices. Several similar swollen black lines were also observed at the other center of the strain field. EDX spectra were obtained from the center of the strain field located in a relatively thick region of the specimen (indicated by arrow in Fig. 3), and in the matrix grain, respectively, and these are overlapped and compared in Fig. 5. The spectra indicated a higher Cu concentration at the center of the interference fringe, and Ag was not detectable. Therefore the observed black swollen lines were interstitial Cu between the ferrite spinel lattices, which could be an intermediate stage between grain boundary segregation and precipitation. The equation for initial permeability of ferrite is usually expressed as follows,

$$\mu_i = \frac{M_s^2}{aK + b\lambda\sigma}$$

μ_i : initial permeability

M_s : saturation magnetization

K : crystal magnetic anisotropy

λ : magnetostriction constant

σ : inner stress

a, b : constant

Thus the initial permeability is strongly influenced by the inner stress, which can be induced by exaggerated grain growth, or impurity precipitation at the grain boundaries

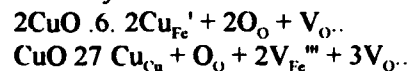
and inside the grains as inclusions. Therefore the degradation of inductance in the rapidly cooled sample was most likely due to inner stress, lattice distortion induced by lattice interstitial-type Cu precipitation adjacent to the grain boundary. Whereas the spherical precipitates at the multiple grain junction with pores in this sample did not contribute to lattice distortion, since they were not located at the grain boundaries, multiple grain junctions with pores without the lattice distortion of ferrite grains did introduce inner stress. In addition, the pores themselves already play a part in reducing the initial permeability of ferrite as air gap, and thus the small precipitation of non-ferromagnetic or ferromagnetic materials, the precipitates do not change the magnetic properties.



Fig. 2. TEM low-magnification bright field image of the a) slowly cooled sample, and b) rapidly cooled sample.

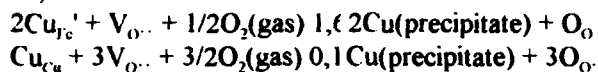
We carefully analyzed and characterized the precipitates at the multiple grain junction in both of the samples using electron diffraction and EDX with HR-AEM. An example of a Cu precipitate at the multiple grain junction in the slowly cooled sample is shown in Fig. 6. The diffraction pattern obtained from the precipitate and the

interpretation of the pattern are shown in Fig. 7. The diffraction spots indicating strong intensity can be indexed as that of f.c.c. metal Cu, and the spots indicating weak intensity can be indexed as that of Cu₂O. In addition, they were located along the same line direction indicating a small lattice misfit, the diffraction spots of Cu and Cu₂O indicating an epitaxial growth-type crystallographic relationship, (110)Cu₂O/(211)Cu. Since Cu₂O epitaxial growth on Cu metal by oxidation was reported previously in deposited Cu metal thin film, it could be deduced that the Cu₂O layer was formed by oxidation of Cu metal precipitates.^{4,5)} The EDX spectrum obtained from the precipitate is shown in Fig.8, in comparison with the EDX spectrum from the matrix grain adjacent to the precipitate. In spite of the presence of a Cu L line peak, no OK α peak was detected in the spectrum from the precipitate, whereas the OK α peak with Fe, Ni, Cu and Zn L line peaks were found in the spectrum from the grain. The Cu₂O oxidation layer on a Cu metal precipitate is very thin, as would be expected from the diffraction spot intensity. Previously, we reported the existence of a Cu metal Dh MTP (Decahedral Multiple Twinned Particle) at the multiple grain junction in low-temperature-fired ferrite with a multilayer chip inductor of Ni-Zn-Cu small excess chemical composition.⁶⁾ Since MTP are not found in large crystals, they are structural anomalies due to a size effect. The MTP occurring in the nucleation stage of crystal growth is not derived from the residue of non-reacted CuO after the calcination process. The situation of Cu ions in calcined powder before the sintering process is still not clear. However, considering the Ni-Zn-Cu ferrite general formula together with the tetrahedral site of Zn²⁺ and octahedral site occupancy of Ni²⁺ and Cu²⁺ in the spinel structure (the possibility of a small amount of Cu²⁺ and Cu⁺ transition at high temperature being neglected), such as [Fe³⁺_{1-x}Zn²⁺_x][Fe³⁺_{1-y-z}Ni²⁺_yCu²⁺_zFe³⁺]O₄ (x+y+z=1.0) and a small excess of Ni-Zn-Cu starting chemical composition, the observed MTP Cu should be precipitated from the Ni-Zn-Cu ferrite matrix during the cooling process after sintering, corresponding to a Cu solid solution with the ferrite. If the CuO occupancy of the Fe³⁺ site or Cu²⁺ (or Ni²⁺ and Zn²⁺) site forms in the above mentioned spinel structure during the sintering process, then the negatively charged defect Cu_{Fe}⁺ and V_{Fe}²⁺ will be formed, respectively, and the corresponding number of positively charged oxygen vacancies will be required to satisfy the site balance and charge neutrality condition:



For the electrical compensation, oxygen vacancies could be formed, which would accelerate grain growth working as part of the diffusion path. After sintering, and

during the cooling process, oxygen vacancies were preferentially filled with oxygen, and then Cu site would be rejected from the spinel structure as metal Cu precipitates, as follows,



In its initial stage, MTP formation occurred at the multiple grain junction. Furthermore, surface oxidation of Cu metal occurred with increasing oxygen partial pressure depending upon the temperature decrease during the cooling process after sintering.

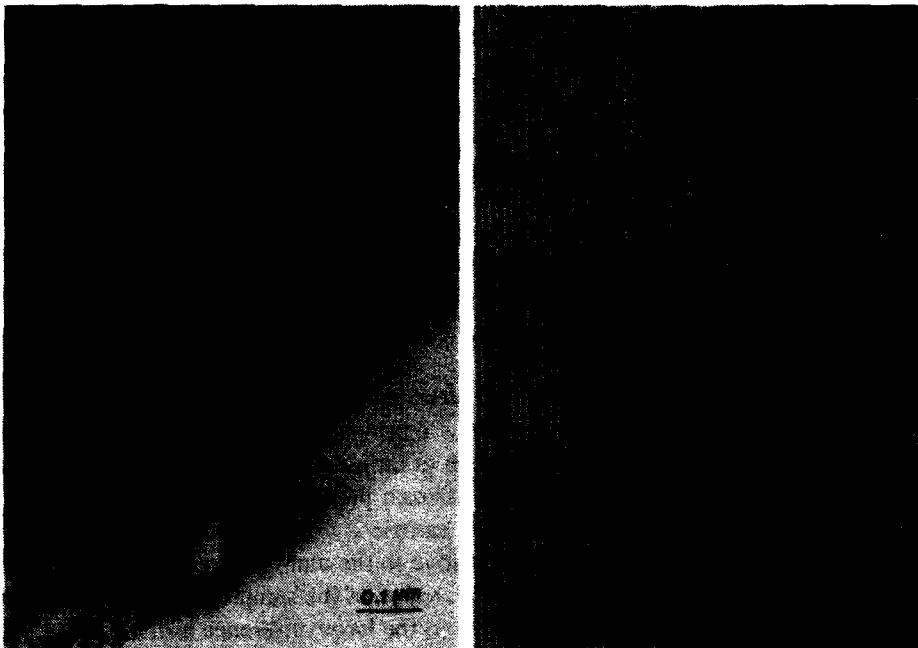


Fig.3. TEM bright-field image of interference fringes located adjacent to the grain boundary. The point of EDX chemical analysis is indicated by the arrow (left).

Fig.4. TEM high-resolution image of the center of interference fringes (right).

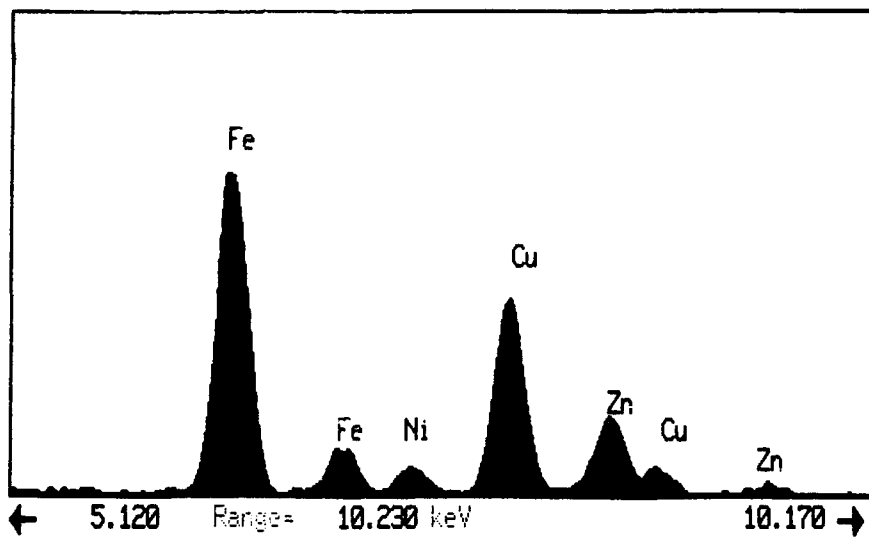


Fig. 5. EDX spectra obtained from the center of interference fringes and the matrix grain, respectively. The spectrum from the center (shaded) and the spectrum from the matrix (black) are overlapped and compared for differences in chemical composition.

Cu dissolved into the grain at the start of the sintering process and precipitated during the cooling process. If the cooling process is a non-equilibrium state, i.e., rapid, then the precipitates cannot move to the multiple grain junction along the grain boundary and are frozen at the grain boundary. The frozen precipitate causes the large lattice distortion, and as a result the L value of the sample is drastically reduced. In contrast, under equilibrium cooling, the precipitates move to the multiple grain junction with the pore, it does not distort the lattice, and the L value of the sample is not reduced. Thus the cooling rate difference after sintering led to the large difference in L value between the rapidly cooled and slowly cooled samples.

Thus the magnetic properties of low-temperature-fired Ni-Zn-Cu ferrite for a multilayer chip inductor strongly depend upon the control of Cu precipitation stemming from the Ni-Zn-Cu small excess in the starting chemical composition for improving the sinterability.

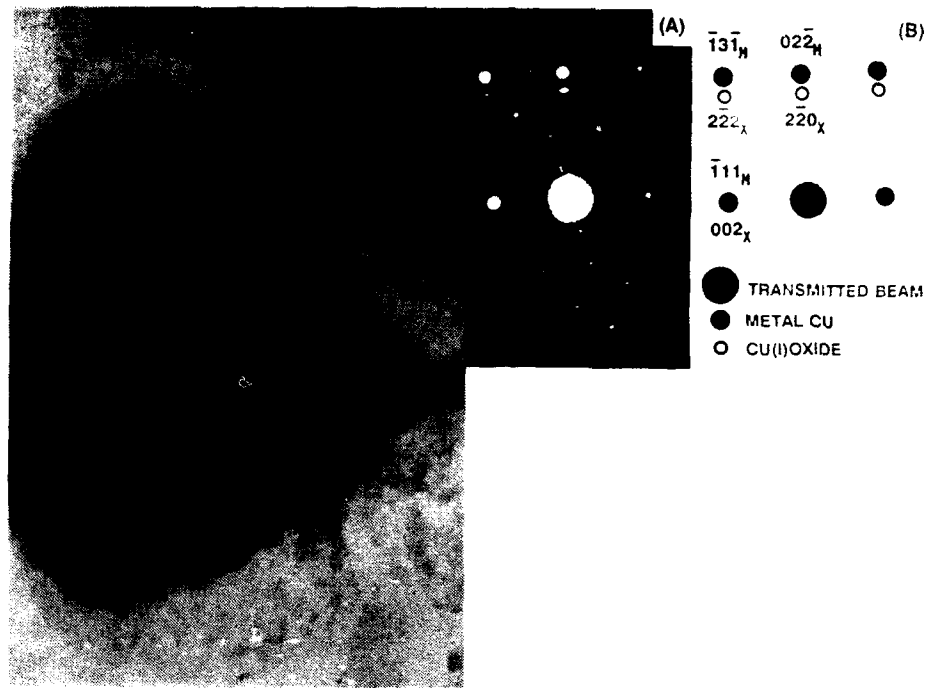


Fig.6. Cu precipitate at the multiple grain junction in the slowly cooled sample (left)

Fig.7 Selected area diffraction pattern obtained from the precipitate shown in Fig.6 (right)

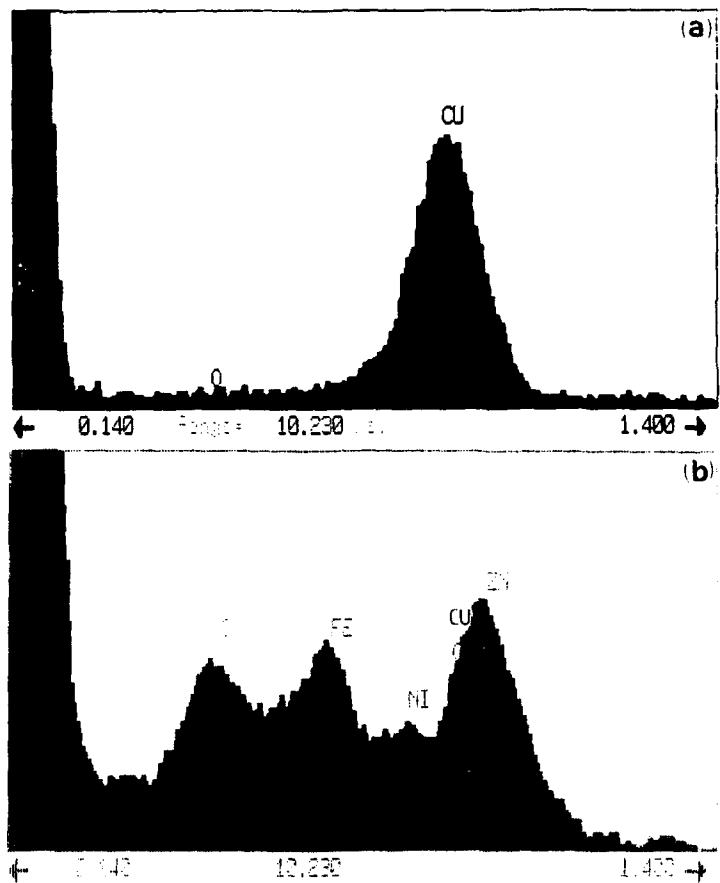


Fig. 8. EDX spectrum obtained from (a) the precipitate shown in Fig. 6, and (b) matrix grain.

V CONCLUSIONS

Slowly cooled and rapidly cooled multilayer chip inductors with an Ag internal electrode and low-temperature-fired Ni-Zn-Cu ferrite exhibiting different inductance values were characterized.

1. Elastic strain fields were observed at the grain boundaries in the rapidly cooled multilayer chip inductor sample exhibiting degradation of inductance. The strain field decreasing the effective permeability of the Ni-Zn-Cu ferrite was due to interstitial-type Cu precipitates.
2. The Cu metal precipitates at the grain boundaries were due to the starting chemical composition and the oxygen partial pressure and thermal equilibrium during cooling after the sintering process.
3. Control of the cooling process is one of the most important factors for obtaining optimal magnetic properties of a multilayer chip inductor.

REFERENCES

1. T. Nothura and M. Takaya, "Passive Components and Hybrid Technology," HYBRIDS, 3 15-19 (1987).
2. M. Takaya, A. Fujisawa, and Y. Mochizuki, "Development of Composite Multilayer Hybrid Components," ; Proc. ISHM '90, Tokyo, 747-751.
3. A. Howie, R.B. Nicholson, P.W. Pashley, and N.J. Whelan, *Electron Microscopy of Thin Crystals*, Butterworths, London, 1965 (revised edition published by Krieger, New York, 1977), p258.
4. T. Homma and T. Yoneoka, "Electron Diffraction Study of the Epitaxy of Cu₂O on the (011) Face of Copper," J. Appl. Phys. 46 [4] 1459-1464 (1975).
5. V.M. Castano and W. Krakow, "Observation of the Epitaxy, Oxidation and Surface Structure of Copper on Thin Gold Films by High Resolution Electron Microscopy," Surface Sci. 191 45-65 (1987).
6. M. Fujimoto, K. Hoshi, M. Nakazawa and S. Sekiguchi, "Cu Multiply Twinned Particle Precipitation in Low-Temperature Fired Ni-Zn-Cu Ferrite," Jpn. J. Appl. Phys., 32 [12] 5532-5536 (1993).

**DEPENDENCE OF MAGNETIC PROPERTIES OF $(Co,Fe)_3O_4$ FILM
ON MICROSTRUCTURE CONTROL THROUGH PHASE
SEPARATION**

**Shin-ichi Hirano, Toshinobu Yogo, Ko-ichi Kikuta
and Hiroshi Yamamoto**

**Department of Applied Chemistry, School of Engineering, Nagoya
University, Furo-cho, Chikusa-ku, Nagoya 464-01, Japan**

ABSTRACT

Homogeneous and dense $(Co,Fe)_3O_4$ films were synthesized on Si(111) substrates by the sol-gel method through metal-organic compounds. $(Co,Fe)_3O_4$ films (Co:Fe=1:1) were heat-treated at 600°C within miscibility gap, resulting in the increase of the coercive force through in-situ microstructure control by phase separation. Similar behavior was observed for $(Co,Fe)_3O_4$ films (Co:Fe=2:1), which undergo the spinodal decomposition at both 600°C and 700°C. The coercive force of the spinodally decomposed films depended upon the microstructure development. The binodally decomposed films showed no increase of coercive force with heat treatment.

INTRODUCTION

There are two types of phase separation behavior: The one is the binodal decomposition, which can separate an uniform phase

To the extent authorized under the laws of the United States of America, all copyright interests in this publication are the property of The American Ceramic Society. Any duplication, reproduction, or republication of this publication or any part thereof, without the express written consent of The American Ceramic Society or fee paid to the Copyright Clearance Center, is prohibited.

into an equilibrium two phases by the nucleation and growth process. The other is the spinodal decomposition, in which there is no thermodynamic barrier to the development of a new phase.

The spinodal decomposition proposed by Cahn et al.¹⁻³ is an interesting and promising method for the in-situ microstructure control of functional ceramics at the nanometer level. Several oxide systems, such as $(Co,Fe)_3O_4$ system⁴⁻⁶, $(Ti,Sn)O_2$ system⁷⁻⁹, and $(Al,Cr)_2O_3$ system¹⁰, have been shown to decompose spinodally.

The spinel-structure region of $(Co,Fe)_3O_4$ system exhibits the miscibility gap below the critical temperature which is about 850°C (Fig. 1). Takahashi et al. proposed that $(Co,Fe)_3O_4$ powder heat-treated within the miscibility gap was spinodally decomposed⁴⁻⁵. Recently, we could synthesize the $(Co,Fe)_3O_4$ films by a sol-gel method from metal-organic compounds⁶. We calculated the locus of spinodal decomposition using the theory of Cook and Hilliard¹¹, as shown with dotted line in Fig. 1. When the $(Co,Fe)_3O_4$ system is spinodally decomposed within the dotted line shown in Fig. 1, the ferri-magnetic phase (Fe-rich phase) and the non-magnetic phase (Co-rich phase) would be controlled at the nanometer level, resulting in the increase of the coercive force due to pinning of the movement of magnetic domain walls.

This paper describes the magnetic property changes of the $(Co,Fe)_3O_4$ films in relation to the development of the modulated structure due to the spinodal decomposition.

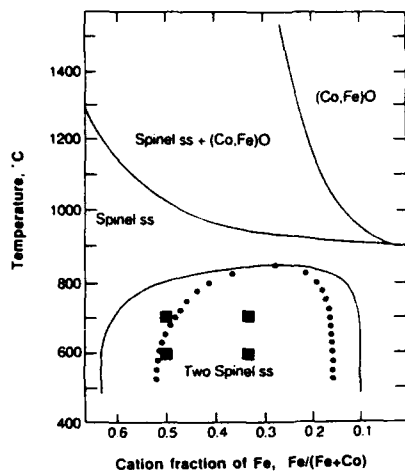


Figure 1 Phase diagram of Co-Fe-O system (■ show the compositions and temperatures of phase separation treatments in this work)

EXPERIMENTAL PROCEDURE

The coating solution for $(\text{Co},\text{Fe})_3\text{O}_4$ films was prepared as follows: Cobalt(II) acetate 4-hydrate was dissolved in 2-methoxyethanol with 2-aminoethanol, which was added as stabilizing agent, and refluxed to form a stable cobalt-containing solution. Separately, iron(III) acetylacetone was dissolved in 2-methoxyethanol with 2,4-pentane-dione (the stabilizing agent), and refluxed to yield a stable iron-containing solution. These solutions were mixed, and then refluxed to form a stable coordination solution. The concentration of the precursor solution was adjusted to be about 0.1 mol/L.

Polished and rinsed Si(111) wafers were used as substrates. The gel films were prepared on Si(111) substrates through a dip coating method. In order to form crystalline solid solution films, the gel films were heat-treated at 900°C for 20 hours in O₂ flow. The dip coating-firing process was repeated several times to increase the film thickness. Then, the solid solution films were annealed in O₂ flow at the temperature shown as ■ in Fig. 1 and then quenched to room temperature.

The phases and the microstructure of the films were analyzed by the X-ray diffraction method (XRD) using CuK α radiation with a graphite monochromator and TEM, respectively. Magnetic properties of the films were measured with a vibrating sample magnetometer (VSM) with maximum applied field of 17.5kOe at room temperature. Nickel metal was used to correct the magnetization. The coercive force (H_c), the saturation magnetization (I_s), and the remanence magnetization (I_r) were evaluated from a hysteresis loop. Thermomagnetic curves were measured using a Faraday type magnetic balance (MB). Curie temperature (T_c) of the $(\text{Co},\text{Fe})_3\text{O}_4$ films was determined from the temperature of zero magnetization. The temperature was calibrated by T_c of Nickel metal.

RESULTS AND DISCUSSION

(1) $(\text{Co},\text{Fe})_3\text{O}_4$ (Co:Fe=1:1) Films

The $(\text{Co},\text{Fe})_3\text{O}_4$ (Co:Fe=1:1) solid solution films were synthesized at 900°C, and then subjected to the phase separation treatment at 700°C and 600°C. Figures 2 and 3 show the changes of XRD profiles of the $(\text{Co},\text{Fe})_3\text{O}_4$ (Co:Fe=1:1) films with heat treatment time at 700°C and 600°C, respectively. Figure 2 reveals clearly that the films heat-treated at 700°C show the characteristic behavior of the binodal decomposition, because no movement of the diffraction peak was observed after Co-rich phase appeared suddenly for 22.5 hrs treatment. On the other hand, the films heat-treated at 600°C show the characteristic behavior of the spinodal decomposition as shown in Fig. 3, from the fact that gradual separation of two side diffraction peaks of Co- and Fe-rich phases was detected by XRD.

The changes of the coercive force along the longitudinal direction of the $(\text{Co},\text{Fe})_3\text{O}_4$ (Co:Fe=1:1) films with heat treatment time at 700°C and 600°C are shown in Fig. 4. The coercive force of the binodally decomposed films heat-treated at 700°C was constant regardless of heat treatment time. However, the coercive force of the spinodally decomposed films heat-treated at 600°C increased remarkably with proceeding the spinodal decomposition.

These phenomena prove that the microstructure developed by the spinodal decomposition leads to the increase of the coercive force, because the non-magnetic domains formed by the spinodal decomposition contributes to the pinning of the movement of magnetic domain walls as reported⁶.

Figure 5 shows the change of the thermomagnetic curves of the $(\text{Co},\text{Fe})_3\text{O}_4$ (Co:Fe=1:1) films with heat treatment time at 700°C in the binodal region. The curie temperature increased suddenly from 370°C to 410°C for 22.5 hrs treatment, and then was kept constant with further heat treatment. The result indicates that the non-magnetic phase nucleates evidently for about 22.5 hrs in the solid solution.

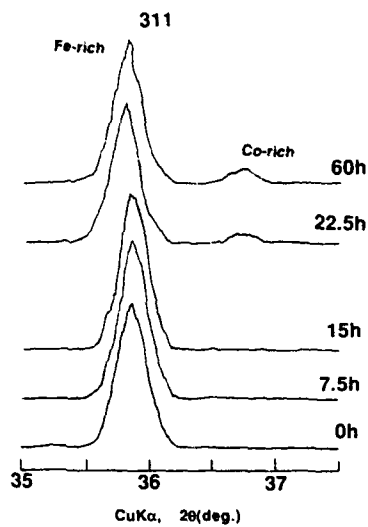


Figure 2 Change of XRD profiles of $(Co,Fe)_3O_4$ films (Co:Fe=1:1) on Si(111) with annealing time at 700°C (prefired at 900°C for 20h.)

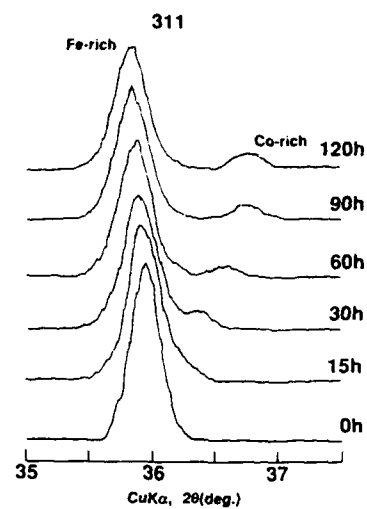


Figure 3 Change of XRD profiles of $(Co,Fe)_3O_4$ films (Co:Fe=1:1) on Si(111) with annealing time at 600°C (prefired at 900°C for 20h.)

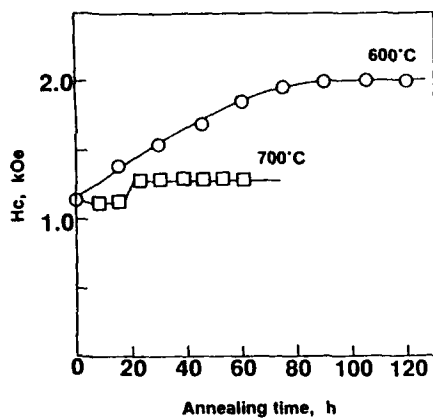


Figure 4 Coercive force of $(Co,Fe)_3O_4$ films (Co:Fe=1:1) on Si(111) heat-treated for various times (prefired at 900°C for 20h.)

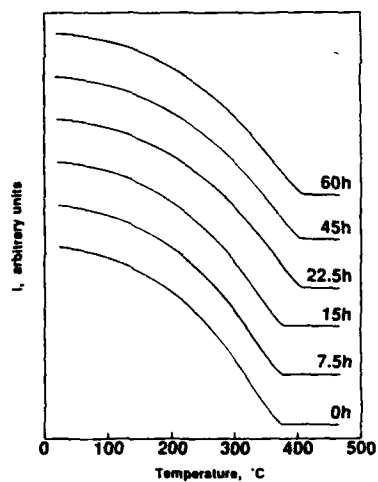


Figure 5 Thermomagnetic curves of $(Co,Fe)_3O_4$ films (Co:Fe=1:1) on Si(111) heat-treated at 700°C for various times (prefired at 900°C for 20h.)

(2) $(\text{Co},\text{Fe})_3\text{O}_4$ (Co:Fe=2:1) Films

The $(\text{Co},\text{Fe})_3\text{O}_4$ (Co:Fe=2:1) solid solution films were prepared at 900°C, and then subjected to the phase separation treatment at 700°C and 600°C. Figures 6 and 7 show the changes of XRD profiles of the $(\text{Co},\text{Fe})_3\text{O}_4$ (Co:Fe=2:1) films with heat treatment time at 700°C and 600°C, respectively. These figures indicate that the films heat-treated at 700°C and 600°C show the characteristic behavior of the spinodal decomposition, revealing the compositional changes of two phases.

The changes of the coercive force along the longitudinal direction of the $(\text{Co},\text{Fe})_3\text{O}_4$ (Co:Fe=2:1) films with heat treatment time at 700°C and 600°C are shown in Fig. 8. The coercive force increases from 0.9 to 2.0kOe with heat treatment time at 700°C and from 0.9 to 2.8kOe with heat treatment time at 600°C. These phenomena suggest that the modulated microstructure by the spinodal decomposition⁶ is effective to control the magnetic properties of the $(\text{Co},\text{Fe})_3\text{O}_4$ films, causing the pinning of the magnetic domain wall movement.

Figure 9 shows the change of the thermomagnetic curves of the $(\text{Co},\text{Fe})_3\text{O}_4$ (Co:Fe=2:1) films with heat treatment time at 700°C. The curie temperature increased gradually from 200°C to 410°C with proceeding the spinodal decomposition. Compared to Fig.5, it is clear that the spinodal decomposition can be distinguished from the binodal decomposition by the difference of the changes of the thermomagnetic curves.

CONCLUSION

Homogeneous and dense $(\text{Co},\text{Fe})_3\text{O}_4$ films were prepared on Si(111) substrates by sol-gel method through metal-organic compounds. The $(\text{Co},\text{Fe})_3\text{O}_4$ films heat-treated within spinodal line was found to be spinodally decomposed. The modulated microstructure developed by the spinodal decomposition leads to the increase of the coercive force due to pinning of the movement of magnetic domain walls.

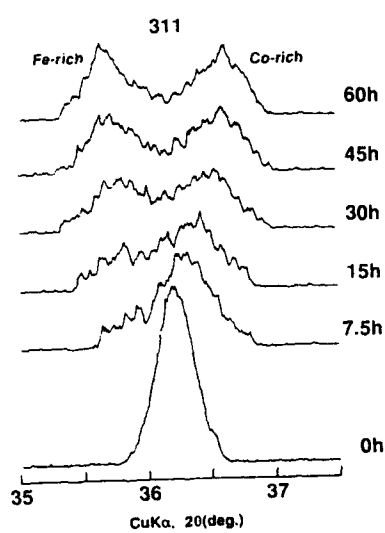


Figure 6 Change of XRD profiles of $(Co,Fe)_3O_4$ films (Co:Fe=2:1) on Si(111) with annealing time at 700°C (prefired at 900°C for 20h.)

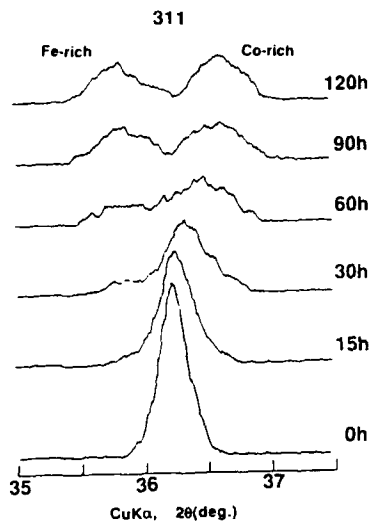


Figure 7 Change of XRD profiles of $(Co,Fe)_3O_4$ films (Co:Fe=2:1) on Si(111) with annealing time at 600°C (prefired at 900°C for 20h.)

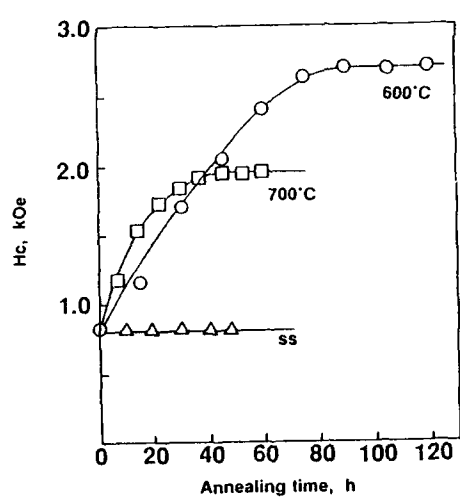


Figure 8 Coercive force of $(Co,Fe)_3O_4$ films (Co:Fe=2:1) on Si(111) heat-treated for various times (prefired at 900°C for 20h.)

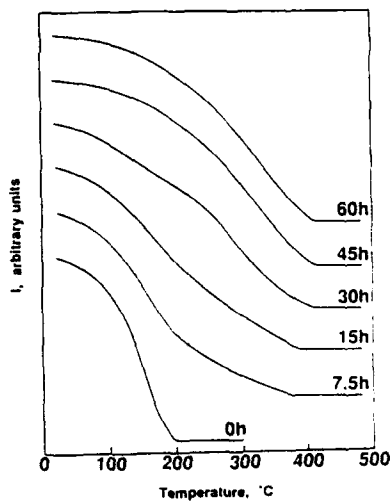


Figure 9 Thermomagnetic curves of $(Co,Fe)_3O_4$ films (Co:Fe=2:1) on Si(111) heat-treated at 700°C for various times (prefired at 900°C for 20h.)

REFERENCES

- 1) J. W. Cahn and J. E. Hilliard, "Free Energy of a Nonuniform System. I. Interfacial Free Energy," *J. Chem. Phys.*, **28** [2] 258-67 (1958)
- 2) J. W. Cahn, "On Spinodal Decomposition," *Acta. Met.*, **9** [9] 795-801 (1961)
- 3) J. W. Cahn, "Spinodal Decomposition," *Trans. AIME*, **242** 166-81 (1968)
- 4) M. Takahashi and M. E. Fine, "Coercive Force of Spinodally Decomposed Cobalt Ferrite with Excess Cobalt," *J. Am. Ceram. Soc.*, **53** [11] 633-34 (1970)
- 5) M. Takahashi, J. R. C. Guimaraes and M. E. Fine, "Spinodal Decomposition in the System CoFe₂O₄-Co₃O₄," *J. Am. Ceram. Soc.*, **54** [6] 291-95 (1971)
- 6) S. Hirano, T. Yogo, K. Kikuta, E. Asai, K. Sugiyama and H. Yamamoto, "Preparation and Phase separation Behavior of (Co,Fe)₃O₄ Films," *J. Am. Ceram. Soc.*, **76** [7] 1788-92 (1993)
- 7) V. S. Stubican and A. H. Schultz, "Spinodal Decomposition in the System TiO₂-SnO₂," *J. Am. Ceram. Soc.*, **51** [5] 290-91 (1968)
- 8) T. C. Yuan and A. V. Virkar, "Kinetics of Spinodal Decomposition in the TiO₂-SnO₂ System : The Effect of Aliovalent Dopants," *J. Am. Ceram. Soc.*, **71** [1] 12-21 (1988)
- 9) S. Hirano, T. Yogo, K. Kikuta, S. Arakawa, Y. Seki and K. Kawamoto, "Processing and Spinodal Decomposition of (Ti,Sn)O₂ and Doped films," *Ceram. Trans.*, **22** 727-32 (1991)
- 10) A. H. Schultz and V. S. Stubican, "Separation of Phases by Spinodal Decomposition in the Systems Al₂O₃-Cr₂O₃ and Al₂O₃-Cr₂O₃-Fe₂O₃," *J. Am. Ceram. Soc.*, **53** [11] 613-16 (1970)
- 11) H. E. Cook and J. E. Hilliard, "A Simple Method of Estimating the Chemical Spinodal," *Trans. AIME*, **233** 142-46 (1965)

Low Temperature Sintered Ferrite for Multilayer Chip Components

Jen-Yan Hsu, Wen-Song Ko, Hsiao-Miin Sung, Meci-Lin Suen and Chi-Jen Chen
Materials Research Labs, Industrial Technology Research Institute, Hsinchu, Taiwan,
R.O.C.

NiCuZn ferrite has been utilized as the material for multilayer chip inductors and chip beads. Bi_2O_3 and lead glass were introduced to the ferrite, respectively, to reduce the sintering temperature of the material to 875°C for co-firing with the printed internal conductor. However, the initial permeability and saturation induction degraded. The quality factor, Q, increased with the addition of either dopants. The additives formed a liquid phase in the grain boundaries and triple points to enhance the densification of the ferrite at lower temperatures. [key Word: ferrite, dopants, multilayer, chip components]

INTRODUCTION

Multilayer chip inductors and chip beads are the passive surface mount devices (SMD) which have increasingly been used in hybrid circuits for products such as video cameras, notebook computers, hard and floppy disk drives, cellular phones, ... and etc.[1,2] The advantage of these devices over the conventional coil-wound chip inductors is the excellent magnetic shield because of their closed magnetic circuits.[3,4] Hence, electro-magnetic interference (EMI) from the devices to the other components in circuits is avoided. In addition, the multilayer chip devices can be miniaturized to a much smaller size than the conventional chip coils, that enables their applications in the electronic circuits of higher density for compact electronic equipments.

Multilayer chip inductors and beads can be fabricated by either screen printing method[5] or lamination of green sheets[6]. The internal electric conductor which is connected among the ferrite layers is printed in a coil manner. Silver is suggested to be the conductor material because of its low resistivity, resulting in the components with higher quality factor, Q.[7] Furthermore, the Ag paste is commercially available and lower cost than the Ag-Pd paste.

NiCuZn ferrite is a relevant magnetic material for this component due to the better magnetic properties at high frequencies and the capability of being sintered at lower temperatures (at about 1000°C or below) than NiZn ferrite. However, the melting point of Ag is 961°C. It requires a further decrease in the sintering temperature of NiCuZn ferrite to below 900°C for preventing the Ag diffusion into the ferrite and causing the increase in

To the extent authorized under the laws of the United States of America, all copyright interests in this publication are the property of The American Ceramic Society. Any duplication, reproduction, or republication of this publication or any part thereof, without the express written consent of The American Ceramic Society or fee paid to the Copyright Clearance Center, is prohibited.

resistivity of the internal conductor. It was also reported that the diffused Ag will enhance the densification of NiCuZn ferrite but provoke the Cu segregation from the ferrite, resulting in the inferior magnetic properties of the material.[7]

The objective of this study is to introduce two additives of low melting point, namely, Bi_2O_3 , and lead glass, into the NiCuZn ferrite, respectively, to promote the densification of the material at the aforementioned temperature range. The effect of the dopants on the magnetic properties of specimens was discussed and their microstructures were characterized and correlated to the fabrication parameters and properties.

EXPERIMENTAL PROCEDURES

The Fe_2O_3 , NiO , CuO and ZnO powders were prepared as the compositions in Table I and mixed by ball milling. The mixed powders were calcined at 750°C and then added with the various amounts of the dopants (Table I). The composition of lead glass is PbO : 80-85 wt%, SiO_2 : 10-15 wt%, B_2O_3 : 5-8 wt%, and Al_2O_3 : 0-3 wt%. A centrifugal ball mill was used to grind the aforementioned powder mixtures at 200 rpm for 1 hour. The average particle size of the ground powders was 1.5 μm , measured by a particle size analyzer¹. The powders were dried in an oven and then added with PVA for granulation. The powders were then dry pressed into toroidal bodies.

Table I. Compositions of NiCuZn ferrite with and without dopants.

(wt%)	Fe_2O_3	NiO	ZnO	CuO	lead glass	Bi_2O_3
No Dopant	65.51	8.91	18.29	7.9	0	0
NG1	64.86	8.82	18.11	7.82	1	0
NG2	62.99	8.57	17.59	7.6	4	0
NB1	63.97	8.64	17.91	7.71	0	1.95
NB2	62.56	8.47	17.57	7.56	0	4.29

The green specimens were sintered at various temperatures from 850°C to 950°C, soaked for 2 hours, and furnace cooled. The density of the sintered samples was measured by the Archimedean method. The magnetic properties, i.e., initial permeability (μ_i), quality factor (Q), and saturation induction (B_s), were measured by the LCR meters² and an AC B-H hysteresis loop tracer³, respectively. The B_s values of the specimens were measured at 0.1 Hz. The microstructure of the sintered specimens was characterized by SEM⁴ and TEM⁵.

¹ Mastersizer E, Malvern Instruments, Ltd., Malvern, UK.

² Model 4284A and 4191A LCR Meters, Hewlette Packard, Rockaway, NJ

³ Model AMH-20 Automatic Hysteresisgraph, Walker Scientific Inc., Worcester, MA

⁴ Model S-360, Cambridge Instrument Ltd., Cambridge, UK

with EDS⁶. The samples for the SEM characterization were prepared by thermal etching for one hour at the temperatures of 100°C lower than the sintering temperatures of the specimens.

RESULTS AND DISCUSSION

1. Properties

Table II shows the sintering temperatures, density and magnetic properties of the five specimens. Bi₂O₃ exhibited better effect on reducing the densification temperature of the ferrite than the lead glass. The NB1 and NB2 specimens, contained 1.95 wt% (0.5 mol%) and 4.29 wt% (1.0 mol%), respectively, can be sintered at 875°C and showed a higher density than that of NG2 sintered at 900°C. The composition (N63) without additives required the highest sintering temperature among the studied formulations.

Table II. Sintering temperatures, density and magnetic properties of the specimens

Sample	Sintering Temperature (°C)	Density (g/cc)	Initial Permeability, μ_i , at 1 MHz	Quality Factor, Q, at 1 MHz	Saturation Induction, B_s (Tesla)
N63	950	5.05	505	69	0.34
NG1	925	5.08	230	104	0.305
NG2	900	5.16	131	99	0.22
NB1	875	5.21	219	104	0.324
NB2	875	5.24	185	103	0.307

The initial permeability, quality factor at 1.0 MHz, and saturation induction are also illustrated in the Table II. The N63 specimen exhibited the highest value of μ_i and B_s among the five samples despite its lowest sintered density. However, it has a lower quality factor compared to the doped ferrites. The additives enhanced the densification of the specimens but deteriorated their permeability. The μ_i values of the four doped specimens are no more than half of the value of N63. The saturation induction of the doped samples was also degraded but to a much less extent except for the NG2 sample, which only has 0.22 Tesla. The NB1 sample shows 0.324 Tesla that is comparable to the B_s value of N63.

Figures 1 and 2 indicate the values of μ_i and Q of the five sintered formulations with respect to the measuring frequencies. The N63 specimen shows a lower resonant frequency than the rest of the formulations (Figure 1). The maximum Q factor of the specimens was at about 300 KHz except for NG2. Its maximum Q value shifted to a higher frequency of

⁵ Model 2000FX, JOEL, Ltd., Tokyo, Japan

⁶ Model LZ5, Link Analytical Ltd. Bucks, UK

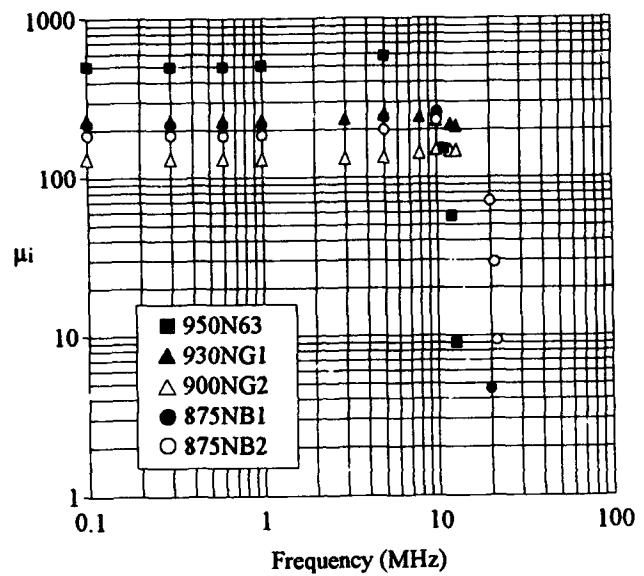


Figure 1. Initial permeability versus measuring frequency of the sintered specimens.

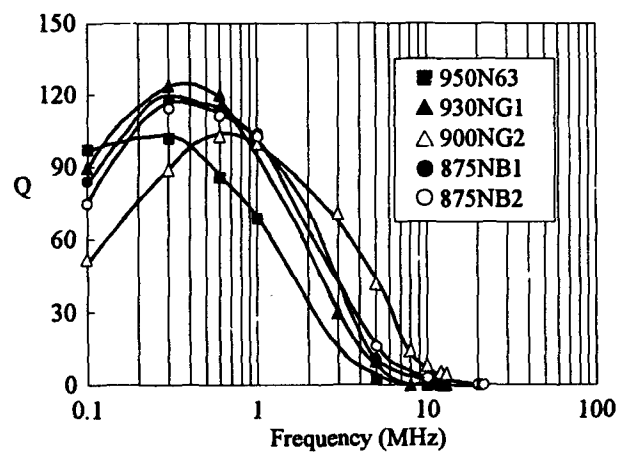


Figure 2. The quality factor of the ferrites versus the measuring frequency.

600 KHz.

2. Microstructure

The microstructure of N63 is shown in Figures 3. The grain size of this specimen varies from less than 1 μm to more than 10 μm . The intragranular porosity was observed in the larger grains. This is a typical microstructure for the iron-deficient ferrites, i.e., the molar content of Fe_2O_3 is less than 50% in the ferrite composition. Since the anion vacancies, i.e., oxygen vacancies, in the lattice are formed so that it enhances the grain boundaries movement during the sintering stage. The pores are easily to be trapped in the grain interior during the grain growth.

With increasing amount of the lead glass in the composition, the intragranular porosity decreased, as shown in Figure 4 and 5. Fewer entangled pores inside the grains were found in the NG1 specimen and no intragranular porosity in NG2. The average grain size of the sintered bodies also decreased with increasing amount of the lead glass content. Figure 5 indicates that the grain size distribution of NG2 is narrow and no grains are larger than 10 μm . By the SEM analysis, no grain boundary phases were observed in these two specimens.

In Figure 6, a bismuth-rich phase was observed in the grain boundaries of the NB1 specimen, identified by EDS. This spherical grain boundary phase is believed to precipitate during the thermal etching process. Intragranular porosity is scarce and the grain size distribution is narrow in this sample. The average grain size is about 5 μm .

Figures 7 and 8 illustrated the microstructures of NG1 and NB1 using TEM. A Pb-rich phase was observed in the triple points of the grain boundaries in NG1, while a Bi-rich phase distributed at triple points as well as the grain boundaries in NB1. The microchemistry of the specimens was characterized by an attached EDS. An even higher magnification, i.e., lattice images, may be required to analyze the distribution of the second phases at the clean grain boundaries in both specimens.

3. Correlation

During the sintering stage, Bi_2O_3 and lead glass form liquid phases in the grain boundaries and triple points to promote the densification of specimens at lower temperatures, 875°C to 900°C. The second phases obstructed the grain boundary movement and avoided the exaggerated grain growth, resulting in the smaller grain size and elimination of the intragranular porosity, as compared Figures 3 to 6. This effect was profound with increasing amount of the additives.

The highest initial permeability of N63 is attributed to the largest grain size among the five specimens. Though, the intragranular pores can pin on the domain wall and hinder its



Figure 3. Microstructure of N63 sintered at 950°C. Intragranular porosity is observed.



Figure 4. Microstructure of NG1 sintered at 930°C with less intragranular pores.



Figure 5. No pores are inside the grains of NG4, sintered at 900°C. The grain size distribution is narrower than the previous two figures.



Figure 6. Microstructure of NB1 sintered at 875°C. The spherical Bi-rich phase is observed in the grain boundaries. That is believed to form during the thermal etching process.



Figure 7. Microstructure of NG1 indicates the Pb-rich phase distributes in the triple points, as shown by the arrows.



Figure 8. Bi-rich second phase, indicated by the arrows, is observed in the grain boundaries and triple points.

movement, causing the deleterious permeability. It was reported[8] the distances between pores rather than grain size account for variations in permeability. Samples with giant grains and included porosity still had higher permeability than those with normally grown grains, provided the distances between pores were the same. In addition, the nonmagnetic ions, i.e., Bi^{3+} , Pb^{2+} , Al^{3+} , Si^{4+} , and B^{3+} , from the two additives may enter the crystal lattice of the ferrites and reduce the saturation magnetization, and hence the initial permeabilities.[9]

The four doped specimens exhibited higher quality factor than that of N63. It is believed due to the higher resistivity of the material. The smaller grain size, i.e., more grain boundaries per unit volume, and the aforementioned grain boundary phases increased the resistivity of the specimens. Besides, the previous substituted nonmagnetic ions in the ferrite lattices reduced the material conductivity.

SUMMARY

Bi_2O_3 demonstrated a better efficiency than the lead glass to reduce the sintering temperature of the studied NiCuZn ferrites. With the addition of 0.5 mol% Bi_2O_3 , the densification temperature of the ferrite was reduced from more than 950°C to 875°C . The initial permeability of the doped specimen was deteriorated, the saturation induction remained comparable, but the quality factor was improved compared to the formulation without any dopant. The variation in the magnetic properties was attributed to the microstructure alteration and chemical modification of the formulation with respect to the addition of the sintering aids.

REFERENCES

1. "In the Chips Component Makers Discover Smaller is Better," *Jpn. Electronic Eng.*, No. 5, 28-33, 1991.
2. "Key of the Portable - Packaging Technology," pp. 10-38 in *Nikkei New Materials* (Japanese), No. 116, June 22, 1992
3. M. Takaya, "The Multilayer Chip Inductor Features Innovative Design," *Jpn. Electronic Eng.*, 38-41, 1986.
4. T. Nomura and A. Nakano, "New Evolution of Ferrite for Multilayer Chip Components," pp. 1198-1201 in *Proceedings of the 6th International Conference on Ferrites*, ed. by T. Yamaguchi and M. Abe, The Japan Society of Powder and Powder Metallurgy, Tokyo and Kyoto, Japan, 1992.
5. A. Ono, T. Muruno and N. Kaihara, "The Technology of Electrode for Multilayer Chip Inductor (I) Terminal Electrode," *ibid*, pp. 1206-1209.

6. US Patent 4,543,553.
7. A. Nakano, H. Momoi, and T. Nomura, "Effect of Ag on Microstructure of the Low Temperature Sintered NiCuZn Ferrites," pp. 1225-1228 in *Proceedings of the 6th International Conference on Ferrites*, ed. by T. Yamaguchi and M. Abe, The Japan Society of Powder and Powder Metallurgy, Tokyo and Kyoto, Japan, 1992.
8. M. Drofenik and S. P. Besenigar, "Reexamination of the Grain Size/Permeability Relation in High Permeability Mn-Zn Ferrites," *Ceram. Bull.*, 65 [4] 656-659, 1986.
9. A. Goldman, "Chemical Aspects of Ferrites," Chapter 3, pp. 87-114 in *Modern Ferrite Technology*, Van Nostrand Reinhold, New York, 1990.

Influence of Process Parameters on Power Losses Minimum Versus Temperature of Mn-Zn ferrites

M.J.Tsay^{*}, C.S.Liu^{}, M.J.Tung^{*}, C.J.Chen^{*}**

*** Materials Research Laboratories, Industrial Technology Research Institute,
Hsinchu, 31015, Taiwan, R.O.C.**

**** Department of Materials Science and Engineering, National Tsing Hua
University, Hsinchu, Taiwan, R.O.C.**

In the study, we found that the power losses minimum versus temperature for a selected composition of Mn-Zn ferrites can be adjusted by presintering and sintering conditions. The results show that presintering condition effectively influence the minimum loss temperature and value of this minimum loss point. Besides, the minimum loss temperature is affected by oxidation degree during sintering. Furthermore, the effect of additives with isovalent or aliovalent cations on minimum loss temperature was also studied. It is found that when MgO is added to Mn-Zn ferrites containing CaO-SiO₂, the minimum loss temperature can be shifted to higher temperature as compared with ferrite with V₂O₅. On the other hand, the effect of V₂O₅ on minimum loss temperature is opposite. That is to say, additives with different cation valence affect the minimum loss temperature of Mn-Zn ferrites. Therefore, we conclude that although the minimum loss temperature is naturally determined by a selected composition, process parameters still play an important role to minimum loss temperature. (Key word: Mn-Zn ferrite, power loss, additives, minimum loss, permeability)

I INTRODUCTION

In Mn-Zn ferrites for power supplies, low loss characteristics is of prime importance. When it is used at high power the exothermic heat becomes a problem. The magnetic loss becomes minimum around the secondary maximum peak temperature T_s of μ_i . Thus, the losses decrease as the temperature rises when a composition having a higher T_s than the operating temperature is selected.

To the extent authorized under the laws of the United States of America, all copyright interests in this publication are the property of The American Ceramic Society. Any duplication, reproduction, or republication of this publication or any part thereof, without the express written consent of The American Ceramic Society or fee paid to the Copyright Clearance Center, is prohibited.

Therefore, our goal in this paper is to investigate the influence of process parameters on minimum loss temperature of Mn-Zn ferrites. Generally, the power loss of Mn-Zn ferrites is dominated by hysteresis loss and eddy current loss as long as operating frequency is lower than the relaxation frequency of wall displacement.^[1,2] When the operating frequency is high(>500kHz), relaxation losses must be taken into account. Based on the above background, the power loss was measured below 500kHz in this study.

II EXPERIMENTAL

Mn-Zn ferrite samples were prepared by conventional powder metallurgical processes. Fe_2O_3 , $MnCO_3$, ZnO powders were weighed and mixed for 4 hrs, and then dried and presintered. The resulting powders, plus CaO - SiO_2 , V_2O_5 , MgO were milled in water for 40 mins. After drying, the powders are granulated through 40-mesh sieve and pressed into toroids. A computer-controlled tube furnace was used to regulate both firing temperature and oxygen partial pressure. The samples were sintered from 1250 °C to 1300 °C for 3 hrs and atmospheric conditions were controlled during cooling to maintain spinel phase equilibrium. The power loss was measured by an apparatus made by Ryowa company. That is to say, power loss was obtained by computing the digital data of primary exciting current and secondary induced voltage detected from coils wound around a toroidal core under sinusoidal excitation. The excitation frequencies were below 500 kHz, and applied magnetic flux density was fixed at 200mT. Specimens were placed in a oven so that its temperature could be controlled. And optical microscope was used to observe the microstructure and addition effect.

III RESULTS AND DISCUSSION

It is well known that the minimum loss temperature decreased with increasing the measured frequency.^[3,4] Figure 1 shows the relationship between power loss and temperature at several frequencies. It is found that the minimum loss temperature is shifted to 60°C, when measuring frequency is increased to 250kHz. In addition, minimum loss temperature is closely related to process parameters. CaO - SiO_2 was generally used as additives for Mn-Zn ferrites^[5,6] to reduce the power loss at high frequency. In Figure 2, it shows the effect of CaO - SiO_2 content on temperature dependence of power loss of Mn-Zn ferrites. Both the power loss at lower temperature and minimum loss temperature become lower, when addition

amounts of CaO-SiO_2 is increased. The more CaO-SiO_2 , the lower the power loss at lower temperature. On the other hand, the minimum loss temperature of Mn-Zn ferrites with less CaO-SiO_2 content shifts higher. Especially, the power loss in the high temperature region reduces obviously.

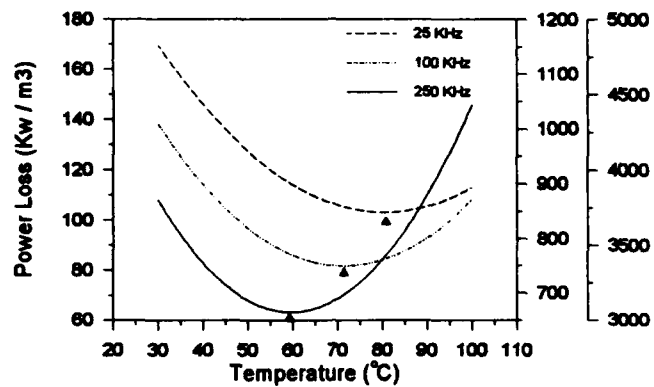


Figure 1 Temperature dependence of power loss for samples measured at various frequencies

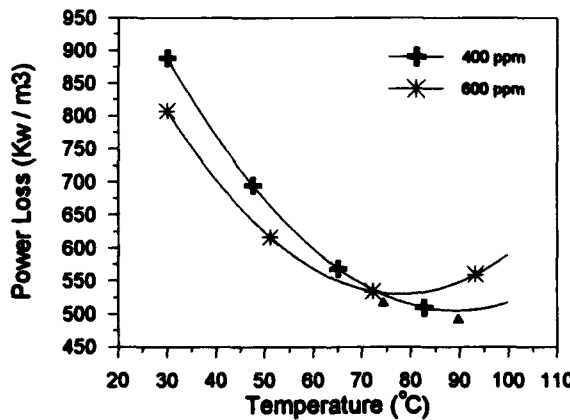


Figure 2 Temperature dependence of power loss for samples containing CaO-SiO_2

Figure 3 clearly shows that Mn-Zn ferrites with less CaO-SiO₂ can keep small grains, on the contrary abnormal grains are observed for sample with higher CaO-SiO₂. From these results, we can deduce that the resistivity of Mn-Zn ferrites with higher CaO-SiO₂ becomes lower at high temperature due to the abnormal grain growth. This makes the power loss at higher temperature increased obviously. But the hysteresis loss at low temperature can be lowered by the large grains. This is why the low power loss was obtained at the lower temperature for sample containing higher CaO-SiO₂.

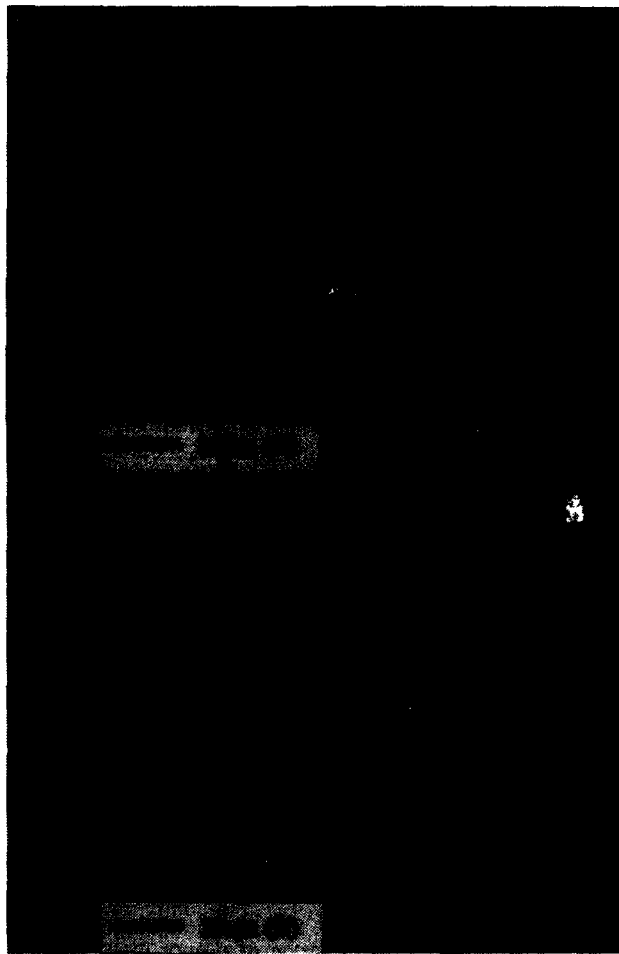


Figure 3 Micrographs by OM for samples added with different amounts of CaO-SiO₂ (A)400ppm (B)600ppm

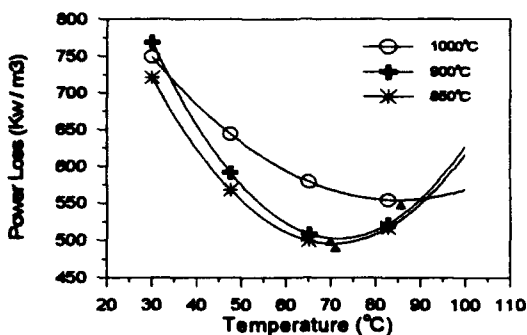


Figure 4 Temperature dependence of power loss for samples presintered at various temperature

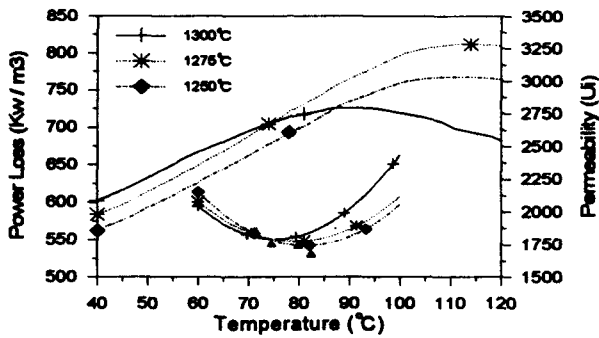


Figure 5 Variation of intial permeability and power loss with temperature for samples sintered at different temperature

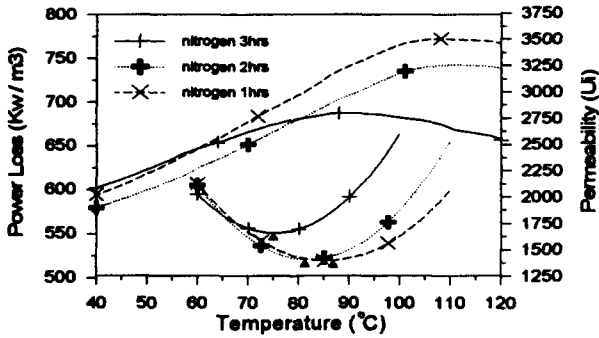


Figure 6 Variation of intial permeability and power loss with temperature for samples sintered at 1250°C for 3hr but annealed oxygen partial pressure with different time

Presintering conditions determine the sinterability of Mn-Zn ferrites. Figure 4 shows the influence of presintering temperature on temperature dependence of power loss. It is shown that the better the presintering temperature (850°C), the lower the minimum value of power loss, because samples with different sintered density and homogeneity were obtained from various presintering temperature. When we examine the minimum loss temperature, it is found that the minimum loss temperature is shifted to lower temperature for sample with lower presintering temperature. In figure 5, each sample was sintered at a different temperature (1250°C ~ 1300°C) for 3hrs and equilibrated with the same oxygen partial pressure (4%). It is found that the lower the sintering temperature, the higher the minimum loss temperature, because when samples were sintered at different temperature and equilibrated with the same oxygen partial pressure, samples sintered at higher temperature will have more Fe⁺² content.^[8,9] These results are compatible with the μ -T curve in Figure 5. It is seen that the secondary maximum peak is shifted to lower temperature for sample sintered at 1300°C due to the increase of Fe⁺². Besides, Figure 6 shows the effect of annealing time used to equilibrate the spinel phase on minimum loss temperature. It is observed that although the sintering time for each sample is equal, the minimum loss point is obviously influenced by annealing time. The shorter annealing time, the higher the minimum loss temperature. As described above, the minimum loss temperature is closely related to both the sintering temperature and annealing time. When an optimum sintering condition is selected, the minimum loss temperature shifts higher and the minimum value remain low.

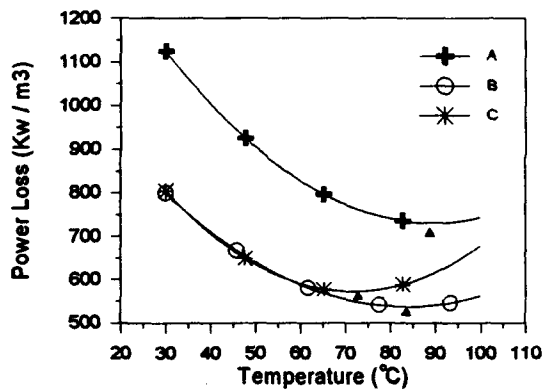


Figure 7 Temperature dependence of power loss for samples added with (A)CaO-SiO₂ (B)CaO-SiO₂-MgO (C)CaO-SiO₂-V₂O₅

Figure 7 shows the effect of additives on minimum loss temperature. We selected V_2O_5 and MgO as additives, they are separately co-added with $CaO-SiO_2$ to Mn-Zn ferrites. It is found that as compared with sample containing $CaO-SiO_2$ sample co-added with $CaO-SiO_2$ and V_2O_5 or MgO exhibits a better temperature dependence of power loss. In addition, it is seen that the minimum loss temperature is reduced remarkably by V_2O_5 . It is deduced that V_2O_5 has the effect of raising the Fe^{+2} content in spinel matrix of Mn-Zn ferrites due to high cation valence.^[10,11,12,13] This cause the secondary maximum peak of μ_i-T curve shift to lower temperature.

IV CONCLUSION

By examining the process parameters on power loss minimum. It is found that although the minimum loss temperature of Mn-Zn ferrites is related to the selected composition, it is also influenced effectively by sintering conditions, such as sintering temperature and oxygen partial pressure during sintering. The minimum value of power loss for temperature is reduced when Mn-Zn ferrites co-added with $CaO-SiO_2$ and MgO is sintered at 1250 °C. Besides, the temperature taking the minimum value shifts higher.

V ACKNOWLEDGEMENTS

The authors would like to thank the Ministry of Economic Affairs, Republic of China, for financial support under contract number 3A92100 to the Industrial Research Institute.

VI REFERENCES

1. Smit.J. and H.P.J.Wijn, 1959, *Ferrites*, pp. 73-75, Philips Technical Library
2. B.D.Cullity, "Introduction to Magnetic Material", 1972, CH12, pp.443-444
3. T.G.W.Stijntjes and J.J.Roelofsma, "Low Loss Power Ferrites for Frequencies up to 500kHz", Proc.ICF-4, pp.493-500
4. T.Mochizuki, I.Sasaki, and M.Torii, "Mn-Zn Ferrite for 400-600kHz Switching Power Supplies", Proc.ICF-4, pp.487-492

5. Tsunco Akashi, "Effect of the addition of CaO and SiO₂ on the Magnetic Characteristics and Microstructures of Manganese-Zinc Ferrites (Mn_{0.68}Zn_{0.21}Fe_{2.11}O_{4+δ})", Trans.Japan. I st. Met.2,pp.171 (1961)
6. I-Nan Lin,R.K.Mishra, and G.Thomas, "CaO Segregation in Mn-Zn Ferrites", IEEE Trans. Mag.MAG-18,pp.1544-1546(1982)
7. H.Haneda,E.Bannai,H.Yamamura,A.Watanabe, and S.Shirasaki, "Oxygen Self-Diffusion and Polycrystalline Zinc Ferrites", *Proceeding of the Fourth International Conference On Ferrites, Advances In Ceramics*, Vol.15,16, Ed. by F. Y. Wang, The American Ceramic Society, Westerville, Ohio, 1984
8. P.E.C.Franken, "The Influence of the Grain Boundary on the Temperature Coefficient of Ti-Substituted Telecommunication Ferrites", IEEE Trans. Mag. MAG-14,pp.898-899(1978)
9. R.C.Sundall, Jr., B.B.Ghate, R.J.Holmes and C.E.Pass, "The Grain boundary Chemistry and Magnetic Properties of Mn_{0.5}Zn_{0.4}Fe_{2.1}O₄", in Ceramic Vol.1: Grain Boundary Phenomena in Electronic Ceramics, ed. L.M.Levinson, Amer. Ceram.Cos.Inc.,Columbus,Ohio,pp.502-511 (1981)
- 10.P.E.Bongers, F.J.A.Den Broege, J.P.M.Damen, P.E.C.Franken and W.T.Stacy, "Defects, Grain Boundary Segregation, and Second Phases of Ferrites in Relation to the Magnetic Properties", in Ferrites Proc. International Conference, Japan(1980), pp.265-271
- 11.P.E.C.Franken and W.T.Stacy, "Examination of Grain Boundaries of Mn-Zn Ferrites by AES and TEM", J.AM.Ceram.63,pp.315-319(1980)
- 12.H.Tsunnekaea, A.Nakata, T.Kamijo, and K.Okutani, "microstructure and Properties of Commercial Grade Manganese Zinc Ferrites", IEEE Trans. Mag. MAG-5,pp.1855-1857(1979)
- 13.T.Akashi, "Precipitation in Grain Boundaries of Ferrites and Their Electrical Resistivities", Part II .NEC Reaserch and Development,8, pp.66-82(1970)

GRAIN BOUNDARY LAYERED PTCR CERAMICS BASED ON $PbTiO_3$ - TiO_2

M.Okada, M.Homma, Dept.of Materials Science,
Faculty of Engineering,Tohoku Univ.,Sendai,Japan

S. Iwashita,Seiko Epson Co, Suwa, Japan.

Abstract

Niobium doped $PbTiO_3$ - TiO_2 ceramics show PTCR properties at the Curie temperature of $490^\circ C$. A new type of $PbTiO_3$ - TiO_2 ceramics with the boundary layer structure is proposed. The microstructure where TiO_2 grains are surrounded by the thin layer of $PbTiO_3$, are prepared by painting PbO on the surface of TiO_2 sintered bodies, followed by annealing, or by conventional powder techniques. Both techniques yield such a microstructure with boundary layer of $PbTiO_3$, which shows PTCR properties. Optimum amount of $PbTiO_3$ at grain boundaries for yielding the good PTCR properties, were studied.

Introduction

It is well known that semiconducting $BaTiO_3$ ceramic show the Positive Temperature Coefficient of Resistivity (PTCR properties) above the Curie temperature ($T_c=120^\circ C$). In order to expand their high temperature applications, PTCR materials with high Curie temperature have been demanded. It was reported that Nb-doped $PbTiO_3$ - TiO_2 composite ceramics showed PTCR properties at the Curie temperature of $PbTiO_3$ ($490^\circ C$), which is the highest temperature among those of available PTCR materials.¹ The Curie temperature of this system is controlled by the addition of $SrTiO_3$ and $CaTiO_3$.²

It was also confirmed that the PTCR properties in $PbTiO_3$ - TiO_2 system was originated from the interface of $PbTiO_3$ and TiO_2 grains in directly measuring the resistivity-temperature characteristics of the $PbTiO_3$ - TiO_2 interface by welding a fine Pt electrode wire on the surface of each grain.³ Based on this observation, a new type of PTCR ceramics with a boundary layer structure is proposed as follows; since PTCR properties occur at the interface between $PbTiO_3$ and TiO_2 grains, it is expected that

To the extent authorized under the laws of the United States of America, all copyright interests in this publication are the property of The American Ceramic Society. Any duplication, reproduction, or republication of this publication or any part thereof, without the express written consent of The American Ceramic Society or fee paid to the Copyright Clearance Center, is prohibited.

the TiO_2 grains surrounded by the thin boundary layer of $PbTiO_3$ phases would enable to show PTCR properties. Then the purpose of the present investigations is to explore the possibility of the formation of $PbTiO_3$ - TiO_2 PTCR ceramics with such boundary layer structure.

Experimental Procedure

Approach for Formation of BL Structure

Figure 1 schematically illustrates two experimental methods for formation of Boundary Layered (BL) structure in $PbTiO_3$ - TiO_2 ceramics.

(1) Painting of PbO on the surface of sintered TiO_2 bodies; The boundary layer of $PbTiO_3$ around TiO_2 is formed by the same method used for the developments of $BaTiO_3$ boundary layer capacitor.¹ Because $PbTiO_3$ is formed by the reaction; $PbO+TiO_2 \rightarrow PbTiO_3$, PbO coated on the surface of Nb-doped TiO_2 sample diffuses into TiO_2 bodies through grain boundaries, particularly above 883°C at which PbO becomes liquid.²

(2) Conventional powder techniques; Decrease of the amount of $PbTiO_3$ in $PbTiO_3$ - TiO_2 system will partially form the BL structure during calcination and firing since $PbTiO_3$ would be formed by the reaction mentioned above. In controlling the amount of PbO , the possibility for forming BL structure with the conventional powder techniques was studied.

Sample Preparations

The specimens were prepared from 99.89% PbO and 99.7% TiO_2 with 99.89% Nb_2O_5 as the doping element.

(1) Painting of PbO on the surface of TiO_2 ; The green compacts of $(Ti_{0.994}Nb_{0.006})O_2$ with a 10mm in diameter and 5mm in thickness, were sintered at 1000~1400°C for 2 hrs in air or Ar atmosphere(1st annealing). The PbO powders with about 200mg were painted on the surface of the sintered TiO_2 disks, which were further annealed at 900~1200°C for 18 hrs in Ar atmosphere(2nd annealing). (2) Conventional powders techniques; The nominal compositions of the specimens are $Pb(Ti_{0.994}Nb_{0.006})O_2$ -(90~95mole%)($Ti_{0.994}Nb_{0.006})O_2$. The green compacts were put in the Al_2O_3 crucible with $(PbCO_3)_2Pb(OH)_2 \cdot 3ZrO_2$ for creating PbO atmosphere. They were fired at 1000~1100°C for 2 hrs in Ar atmosphere without calcination.

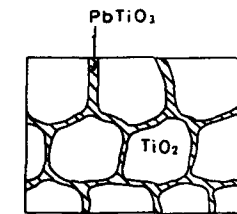
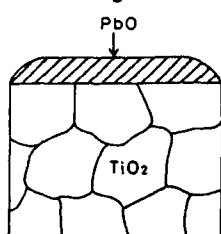
Resistivity Measurements and Microstructural Observations

The microstructures of the samples were observed by using transmission electron microscopy. The microstructural constituent

was analyzed with Energy Dispersion X-ray(EDX) microanalysis. Thin foil specimens were prepared by ion-beam milling.

Using the two probe method, the resistivity of samples was measured from room temperature to 600°C on heating at a rate of 3°C/min in air. In-Ga alloys were used for the electrodes, which were covered with stainless steel sheets.

(a) Painting of PbO



Boundary Layered (BL)
Structure

(b) Conventional Powder
Techniques

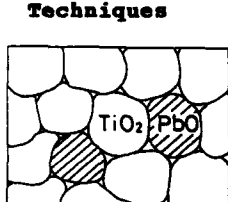


Fig.1 Schematic illustration
how to prepare the BL
structure in $\text{PbTiO}_3\text{-TiO}_2$
system.

Results and Discussion

Formation of BL Structure by Painting and Diffusion of PbO

Figure 2 shows the relative sintered density of TiO_2 before and after 2nd annealing(at 1000°C for 2 hrs) with the increased weight of sintered bodies (corresponding to the diffused amount of PbO) after 2nd annealing versus sintering temperatures of TiO_2 , where the theoretical density of the samples after 2nd annealing is assumed to be that of TiO_2 . The relative sintered density of TiO_2 increases with increasing sintering temperatures, specially up to 95% after sintering at 1300°C. The increased weight of sintered bodies after 2nd annealing, decreased with increasing sintering temperatures of TiO_2 . The high relative density of TiO_2 may make the diffusion of PbO along grain boundaries difficult.

Figure 3 shows the corresponding resistivity temperature characteristics of TiO_2 samples sintered at 1000°C~1300°C in air

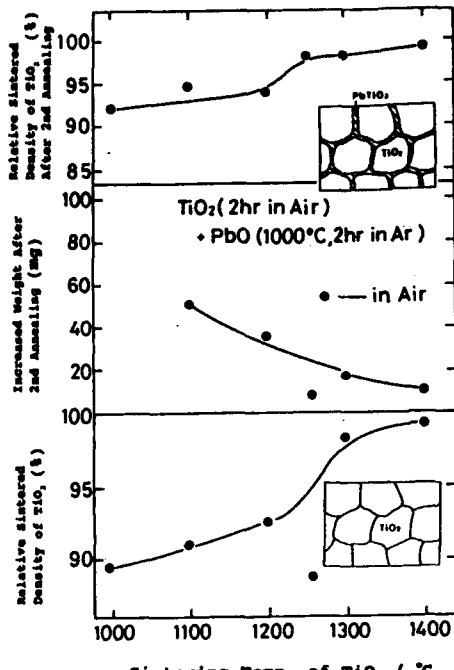


Fig.2 Relative sintered density of TiO_2 before and after 2nd annealing and increased amount of weight after 2nd annealing versus sintering temperatures of TiO_2 .

and followed by 2nd annealing for diffusion of PbO at 1000°C in Ar atmosphere. The samples sintered at $1000^\circ\text{C} \sim 1250^\circ\text{C}$ show PTCR properties at 490°C , but those at 1300°C show no PTCR properties. It seemed that linked TiO_2 grains would form the low resistivity electrical short circuit when the relative density of TiO_2 exceeds 95%.

Figure 4 shows the corresponding electron micrograph of the TiO_2 sample sintered at 1200°C for 2 hrs, followed by 2nd annealing at 1000°C for 2 hrs, (a) bright field and (b) dark field micrograph imaged with the diffraction of grain boundary phase. The grain boundary phase with the thickness of around 12 nm existed along the TiO_2 grain boundary in Fig.4(a), which is more clearly visible in Fig.4(b). EDX analysis detected the M_a radiation of Pb from grain boundary phase. Although the exact

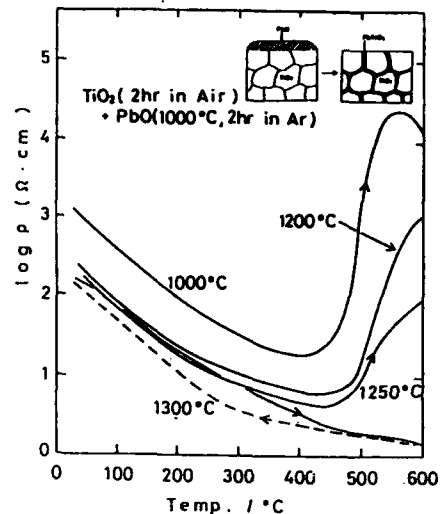


Fig.3

The resistivity-temperature characteristics of TiO_2 samples sintered at $1000 \sim 1300^\circ\text{C}$, followed by annealing at 1000°C for 2 hrs in Ar atmosphere.

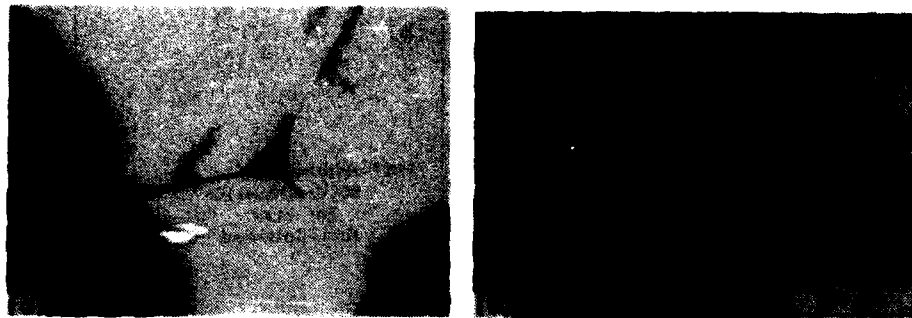


Fig.4 Transmission Electron Micrograph (TEM) of PbO painted TiO_2 samples annealed at 1000°C for 2 hrs. (a)bright field, (b)dark field imaged with diffracted beam of the grain boundary phase.

chemical composition of the thin layer of grain boundary phase could not be determined, it is expected that the grain boundary phase mainly consists of PbTiO_3 . This means that BL structure is formed by painting of PbO on the surface of TiO_2 grains, followed by annealing.

Since PbTiO_3 phase becomes liquid above 1280°C,³ the PbTiO_3 powders were painted on the surface of TiO_2 samples for the formation of BL structure. But it was observed that PbTiO_3 liquid phase did not diffuse along the grain boundary of TiO_2 grains. The wettability between PbTiO_3 and TiO_2 phase turned out to be poor.

Formation of BL Structure by Conventional Powder Techniques

Figure 5 shows the resistivity temperature characteristics of the (a) PbTiO_3 -90% TiO_2 and (b) PbTiO_3 -95% TiO_2 samples, which shows PTCR properties when the sintering temperatures were 1000°C~1025°C. But, the samples sintered over 1050°C show no PTCR properties, which would be due to the formation of electrical short circuits of the linked TiO_2 as discussed above.

Figure 6 shows the relative sintered density, PTCR effects ($\log(\rho_{\text{max}}/\rho_{\text{min}})$) and resistivity at room temperature of the PbTiO_3 -(90~95)mole% TiO_2 samples versus sintering temperatures. The relative sintered density increases with increasing sintering temperatures and becomes to be over 94% above 1050°C where no PTCR properties were observed. But the room temperature resistivity decreases with increasing sintering temperatures. The PbTiO_3 -90% TiO_2 samples show higher PTCR properties than those of PbTiO_3 -95% TiO_2 after sintering at 1000°C.

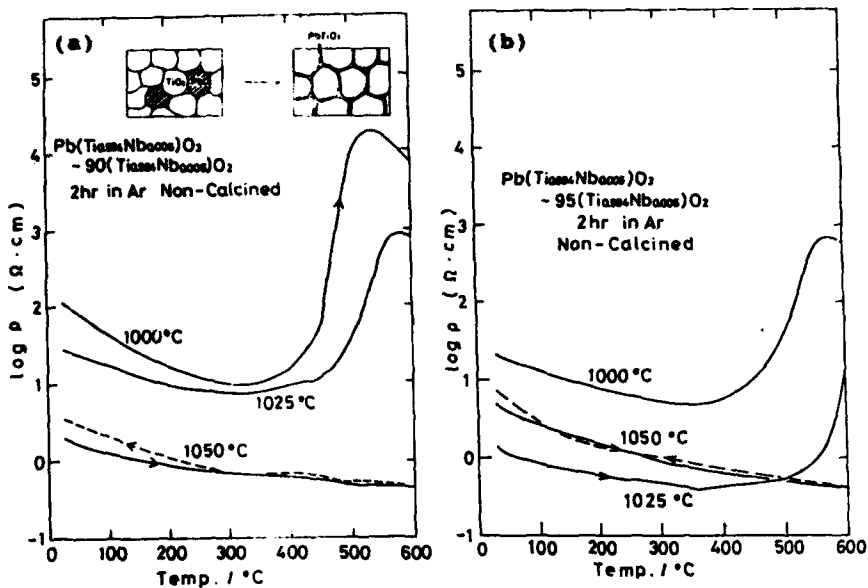


Fig. 5 The resistivity-temp. characteristics of PbTiO_3 -(90~95)mole% TiO_2 samples.

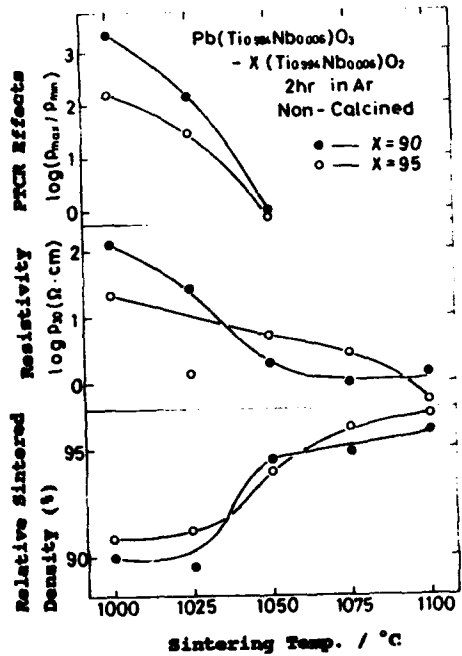


Fig. 6

The relative sintered density, resistivity at R.T. and PTCR properties of PbTiO_3 -(90~95)% TiO_2 samples versus sintering temp..

Figure 7 shows the electron micrograph of this sample sintered at 1000°C. The grain boundary phase with dark contrast was observed. EDX analysis indicated that grain boundary phase would be PbTiO_3 phase. Although grain boundary phase was not enough to cover the TiO_2 grains, the BL structure was formed by conventional powder techniques. The reason why slight increment of sintering temperatures formed the electrical short circuit may be due to the lack of this total amount of PbTiO_3 phases along grain boundaries of TiO_2 grains. Total amount of PbTiO_3 grain boundary phase should increase from 10%, in improving PTCR properties. Optimum amount of PbTiO_3 was further studied as discussed below.

It was found that the TiO_2 grains surrounded by thin boundary layer of PbTiO_3 , enabled to show PTCR properties. The grain boundary layered PTCR ceramics were formed by the painting method or conventional powder techniques in PbTiO_3 - TiO_2 system.

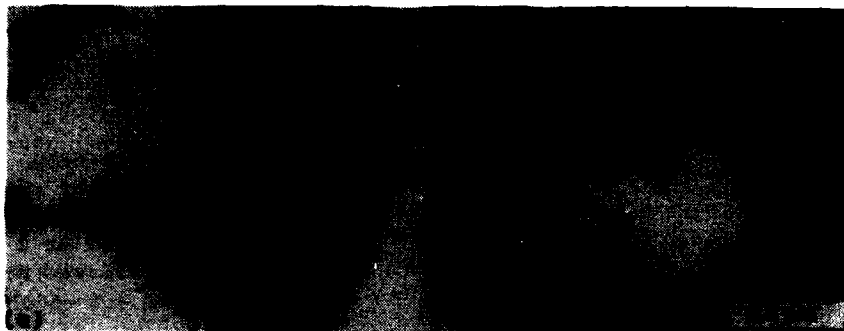


Fig.7 TEM of PbTiO_3 -90% TiO_2 samples sintered at 1000°C for 2 hrs. (a)BF, (b)DF.

Improvements of Thermal Stability of PTCR Properties in BL Structure by Addition of SrTiO_3

The disadvantage of these grain boundary layered PTCR ceramics discussed above is their poor thermal stability. The resistivity of the samples increases after increasing the temperature above 500°C in air. It was reported that the thermal stability of PTCR properties in this system would be improved by the addition of SrTiO_3 to the system.¹ In the next approach, the optimum composition for the stability of PTCR properties was studied in the range of $(\text{Pb}_{0.8}\text{Sr}_{0.1})\text{TiO}_3$ -(85~70)mole% TiO_2 . As a result, it was found that optimum composition was $(\text{Pb}_{0.8}\text{Sr}_{0.1})\text{TiO}_3$ -70mole% TiO_2 .

Figure 8 shows the resistivity temperature characteristics of $(\text{Pb}_{0.8}\text{Sr}_{0.1})\text{TiO}_3$ -70mole% TiO_2 sintered at 965°C for 2 hrs in Ar, followed by annealing at 400~600°C in air. The samples annealed at 400°C increase its resistivity on cooling after heating up to 600°C. But those annealed at 500°C and 600°C show almost no hysteresis on heating and cooling. The resistivity of the samples at room temperature increases with increasing annealing temperature. The addition of SrTiO_3 is very effective for stabilizing the PTCR properties in this system. The optimum composition of the PbTiO_3 was 70mole% for the BL structure which gave almost same PTCR properties as those reported in PbTiO_3 -30mole% TiO_2 samples.

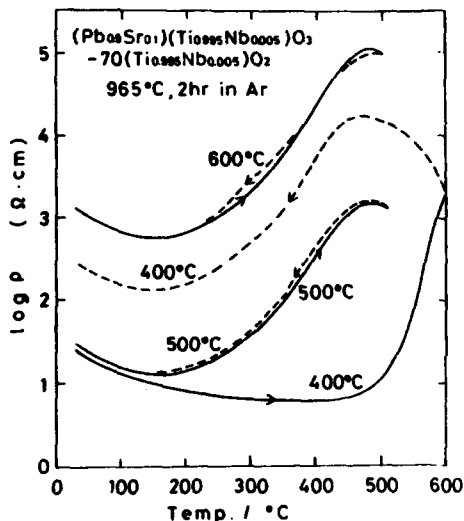


Fig. 8 The resistivity-temp. characteristics of $(\text{Pb}_{0.8}\text{Sr}_{0.1})\text{TiO}_3$ -70% TiO_2 samples sintered at 2 hrs in Ar, followed by annealing at 400~600°C in air.

Conclusion

The grain boundary layered type PTCR ceramics was prepared by using the PbTiO_3 - TiO_2 system. The BL structure in this system was formed by either painting of PbO on the surface of TiO_2 , following by annealing for diffusing PbO along grain boundaries of TiO_2 , or by conventional powder techniques. It was also found that the optimum composition which gave the good thermal stability of PTCR properties was $(\text{Pb}_{0.8}\text{Sr}_{0.1})\text{TiO}_3$ -70mole% TiO_2 .

References

1. M.Okada,T.Iijima, and M.Homma, "New Composite PTC Materials Based on PbTiO₃-TiO₂," Ceramics Microstructure '86, "Role of Interface", Edited by A. Pask and A.G.Evans, Plenum Publishing, (1988) P.697.
2. M.Okada,T.Iijima, and M.Homma, "Curie Temperature Control of PbTiO₃-TiO₂ PTCR Composite Ceramics by Addition of SrTiO₃ and CaTiO₃", Proceeding of Interntl. Institute for the Science of Sintering Symposium, Edited by Sigeru Somiya et al. Elsevier Science Publishers, (1988) P.884.
3. T.Iijima,M.Okada, and M.Homma, "Microstructure-PTCR property Relationships in PbTiO₃-TiO₂ Ceramics", ISIJ International, 29 (1989 P.229.
4. S.Waku, "Studies on the Boundary Layer Ceramic Capacitor" Rev.Elect.Comm.,15,(1967) P. 689.
5. D.E.Rase,B.Jaffe,W.R.Cook and H.Yaffe, "Piezoelectric Ceramics", Academic Press London/ New york, (1971), P.117

GRAIN CORE-GRAIN SHELL STRUCTURE IN Nb-DOPED BaTiO₃ CAPACITOR CERAMICS

X.Y.Song, D.R.Chen and Z.W.Yin
Shanghai Institute of Ceramics, Chinese Academy of Sciences
1295 Ding-Xi Road, Shanghai 200050, China

Key words : shell-core structure, BaTiO₃, capacitor ceramics

ABSTRACT

The grain core-grain shell structure was observed in Nb-doped BaTiO₃ ceramics during our work on fabrication of multi-layer capacitor materials. Studies on analysis electron microscopy and high resolution electron microscopy showed that the core-shell structure is formed due to the inhomogeneous distribution of Nb atoms in BaTiO₃. The grain core which contains less Nb atoms shows to be ferroelectric region with domain structure, whereas the grain shell which is rich in Nb atoms is a non-ferroelectric region. Both regions possess perovskite structure, their interface connects the core and shell having no structure discontinuity, which is different from the grain boundaries or domain boundaries. The amount of grains with core-shell structure in the ceramic and the thickness of the grain shell seems to have quite an effect on the dielectric property of the ceramic materials.

INTRODUCTION

Early in sixties, Okazaki et al [1] had proposed the presence of grain shell-grain core structure in ferroelectric ceramics. In early eighties, Rawal et al first observed the grain shell-grain core phenomena on TEM in Bi-doped PTC type BaTiO₃ ceramics[2]. Later, one of the authors of this paper[3] investigated the crystalline grains and their boundaries in PTC type BaTiO₃ ceramics by TEM and EDAX, and indicated that the shell-core structure may be caused by the nonuniform distribution of silicon impurities in grains. The results also indicated that both shell and core in a grain possess BaTiO₃ structure and their orientations crystallographically remain the same. Hennings et al [4] have worked on the dielectric properties and chemical homogeneity of BaTiO₃ ceramics sintered with additions of the pseudophase

To the extent authorized under the laws of the United States of America, all copyright interests in this publication are the property of The American Ceramic Society. Any duplication, reproduction, or republication of this publication or any part thereof, without the express written consent of The American Ceramic Society or fee paid to the Copyright Clearance Center, is prohibited.

"CdBi₂Nb₂O₉" for materials showing the "X7R" dielectric temperature characteristic. The results showed that their microstructures exhibit the grain core-grain shell structure, and the chemical inhomogeneity emerges during a process of reactive liquid-phase sintering. The solution and precipitation process was assumed as the formation mechanism of chemically inhomogeneous perovskites and the core-shell structure of grains. In recent years, during our work on fabrication of multi-layer capacitor materials, the grain core-grain shell structure was also observed in Nb-doped BaTiO₃ ceramics. In present paper, the characteristics of the grain core- grain shell structure of capacitor type BaTiO₃ ceramics were studied by using AEM and HREM. The effect of shell-core structure on the dielectric properties of the capacitor ceramics was also studied and discussed.

EXPERIMENT

The high-purity, fine grain BaTiO₃ base material was prepared by decomposition of barium oxaltitanate. Its grain size is smaller than 0.5 μm . A specific amounts of Nb₂O₅, CoO and sintering aid were added and conventional electronic ceramic fabricating technology was used to make the multi-layer capacitor ceramics [5]. Doping of Nb and Co plays the role respectively as donor and acceptor, which is of advantage to increase the insulating resistance and decrease the dissipation factor $\tan\delta$ of the materials.

Ceramic samples were cut to small disks of 3mm in diameter and 25 μm in thickness. Then they were thinned by an Argon ion beam till a hole formed in the center. The fringe thickness of the hole was about several hundreds angstroms, which was suitable for electron microscope observation. For all the observations a JEM-200CX AEM and HERM was used.

EXPERIMENTAL RESULTS AND DISCUSSION

Lots of electron microscope observations showed that the grain size of BaTiO₃ ceramic samples prepared by above method is about 1 μm and certain amount of grains possess shell-core structure. The TEM bright-field image and dark-field image of a typical shell-core structure grain are shown in Fig.1.

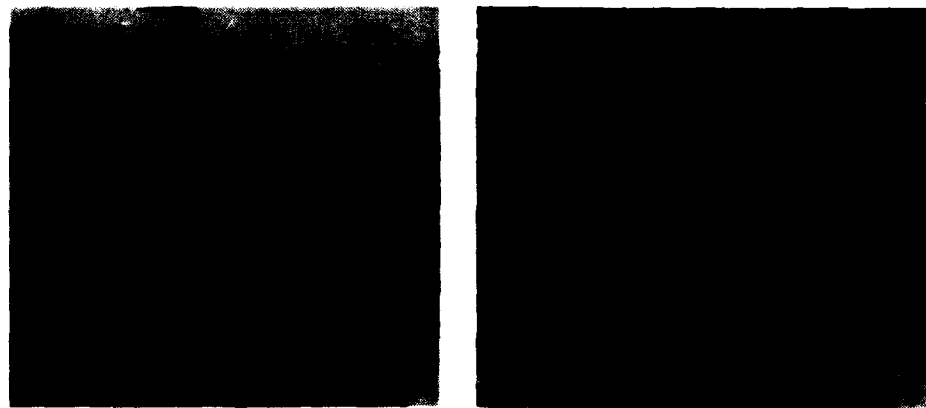


Fig.1. TEM photomicrographs showing grain shell-grain core structure in BaTiO_3 ceramics

- (a) TEM bright-field image. c shows grain core, s grain shell.
- (b) TEM dark-field image. The right part is the result of corresponding selective electron diffraction pattern.

1. Characteristics of shell-core structure and their compositions

The shell-core structure of BaTiO_3 grains in fact are composed of two different forms: the ferroelectric grain core with domain structure and non-ferroelectric grain shell. The experimental results showed that the core and shell in BaTiO_3 grains belong to same crystalline structure, namely ABO_3 perovskite structure. Their interface connects the core and shell and has no structure discontinuity, which is different from the grain boundaries or domain boundaries. The ferroelectric domain characterizing the grain core is a tetragonal ferroelectric phase, whereas the non-ferroelectric grain shell is a paraelectric phase.

The EDAX results on TEM indicate that the occurrence of shell-core structure in BaTiO_3 grains is as a result of inhomogeneous distribution of Nb doping as shown in Fig.2.

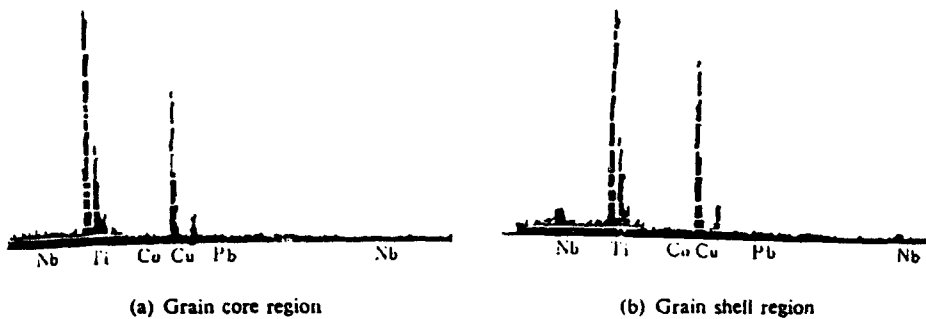


Fig.2. EDAX results of the grain in BaTiO_3 ceramics

- (a) Grain core region
- (b) Grain shell region

The Ba peaks are coincided with the Ti peaks

The Cu peaks due to the Cu specimen grid

From Fig.2a , it shows the grain core is an almost pure BaTiO_3 phase, whereas from Fig.2b, it shows the grain shell is a Nb-rich $\text{Ba}(\text{Ti}_x\text{Nb}_{1-x})\text{O}_3$ phase. During sintering of the ceramics, the Nb ions diffuse from the grain boundaries to the interior of the grains, however, the diffusion rate of Nb^{5+} ions in BaTiO_3 grains is very low [6], this would be the main reason of forming the shell-core structure. The Curie temperature of pure BaTiO_3 is about 120°C , therefore at room temperature it possesses tetragonal ferroelectric phase with domain structure. However, after incorporation of different amount of Nb^{5+} ions into the BaTiO_3 lattice, their Curie temperatures will be drastically lowered accordingly [4]. In view of Nb^{5+} ions to be concentrated at the grain shell, which makes the Curie temperature of the grain shell region below room temperature and possesses paraelectric phase at room temperature. This means that in Nb-doped BaTiO_3 ceramics, there appears a $\text{Ba}(\text{Ti}_x\text{Nb}_{1-x})\text{O}_3$ - BaTiO_3 two-component composite system, where X represents different amount of Nb content and gives different T_c of the new phase. Modification of the Nb content in BaTiO_3 will give different dielectric properties of the ceramic materials, which will be presented in the next section.

2. Effect of shell-core structure on property of the ceramic materials

Fig.3. shows the temperature dependence of capacitance of two Nb-doped BaTiO_3 ceramic samples. The amount of Nb-doping in SX-2

sample is about 0.5 mol.%; whereas in SX-3 sample, more than twice of this amount of Nb was doped. From Fig.3. it can be seen that the temperature dependence of capacitance of SX-3 sample with higher Nb content is better than that of SX-2 sample. TEM observations also show that there are more shell-core structure grains in SX-3 sample than in SX-2 sample. In the mean time, along with the flattening of the capacitance-temperature curve, the shell thickness of the shell-core grain becomes thicker.

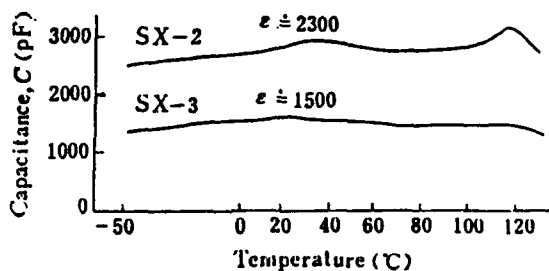


Fig.3. Temperature dependence of capacitance of two Nb-doped BaTiO₃ ceramic samples
 SX-2 sample : lower Nb content
 SX-3 sample : higher Nb content

According to Lichtenecher [7], the dielectric constant k of the shell-core structure ceramics should follow the following formula

$$\log k = V_1 \log k_1 + V_2 \log k_2$$

where V_1 , V_2 and k_1 and k_2 are respectively the volume fraction and dielectric constant of the shell and core. So, in BaTiO₃ ceramics, containing more the shell-core structure grains and thicker the shell thickness will increase the volume fraction of the paraelectric phase which results in decrease of the total amount of the spontaneous polarization vector in the material and leads to decrease the dielectric constant ϵ . This would be the reason why the SX-3 sample has lower ϵ value.

Besides, Nb⁵⁺ ions in BaTiO₃ will replace Ti⁴⁺ to form solid solution. Though this replacement will not change the structure form of the original BaTiO₃, however it will more or less distort the crystalline lattice which will lead to shift the Curie peak to lower

temperature and give effect on the dielectric property of the ceramic material. Owing to that the volume fraction of shell-core structure for different BaTiO_3 grain is different, which will give rise to diffuse the Curie point to a broad temperature range, as a result, to flatten the dielectric constant peak of the material.

CONCLUSION

1. In BaTiO_3 capacitor ceramics, a certain amount of Nb doping will form grains with shell-core structure. The grain core contains almost pure BaTiO_3 ferroelectric phase with domain structure, whereas the grain shell is composed of paraelectric $\text{Ba}(\text{Ti}_x\text{Nb}_{1-x})\text{O}_3$ phase with higher Nb content.
2. Both shell and core regions possess perovskite structure, their interface connects the core and shell having no structure discontinuity, which is different from the grain boundaries or domain boundaries.
3. The amount of grains with shell-core structure in the ceramic and the thickness of the grain shell will play important role on the dielectric constant ϵ and capacitance-temperature characteristics of the capacitor ceramic materials.

REFERENCES

1. K.Okazaki and S.Kashiwabara, J.Jpn.Ceram.Soc 73 (834):60,1965
2. B.S.Rawal and M.Kahn, Advances in Ceramics, Vol.1 Columbus, Ohio, Am.Cer.Soc. Inc. 172, 1981
3. X.Y.Song, S.L.Wen and Y.Yao " AEM Study of PTC BaTiO_3 Ceramics" Jour. Chinese Cer. Soc. 17(1) p.59, 1989 in Chinese
4. D.Hennings and Rosenstein " Temperature-stable Dielectrics Based on Chemically Inhomogeneous BaTiO_3 " Jour. Amer. Cer. Soc. 67(4), P.249, 1984
5. D.R.Chen, M.G.Zhu and X.Y.Song " ϵ_r -T Stability Principle of Nb_2O_5 and CoO Doped BaTiO_3 -Base Dielectric Ceramics" Electronic Devices and Materials 10(1), p.38,1991, in Chinese.
6. W.R.Buessen "Effects of Grain Growth on the Distribution of Nb in BaTiO_3 Ceramics" Jour. Amer. Cer. Soc. 54 (9), p.458, 1971
7. D.K.Lichtenecker, Physikal 2, 27, p.115. 1926

THE V-SHAPE CHARACTERISTICS OF $(\text{Pb}_{0.6}\text{Sr}_{0.4})\text{TiO}_3$ CERAMICS

T.D. Tsai[†], C.T. Hu[†] and I.N. Lin^{*}

[†]Dep. Mater. Sci. and eng. and Mater. Sci. Center
National Tsing-Hua Univ. Taiwan R.O.C.

ABSTRACT

$(\text{Pb}_{1-x}\text{Sr}_x)\text{TiO}_3$ ceramics which possess the marvelous V-shape PTCR characteristics have been successfully synthesized. The concentration of donors need to optimize the minimum resistivity (ρ_{\min}) is around 1.0 mol% Y^{3+} . The electrical properties of these materials vary systematically with the ratio of Pb/Sr . The Curie temperature increases and the resistivity jump decreases markedly, while the resistivity drop varies insignificantly, with the increase of Pb/Sr ratio. The behavior is similar for samples sintered either at 1220°C, 1240°C or 1260°C for 1 hr.

I. INTRODUCTION

The positive temperature coefficient of resistivity (PTCR) of semiconducting barium titanate specimen above the ferroelectric Curie temperature (T_c) was well known since 1955^[1,2]. Much research has since then been conducted on understanding the conduction mechanisms^[3,4] and on developing various applications of these materials^[5,6]. The ceramics in the $(\text{Sr},\text{Ba})\text{TiO}_3$ and $(\text{Pb},\text{Ba})\text{TiO}_3$ series have been most thoroughly developed with the Curie temperature in the range -30°C ~ 360°C^[5,6].

All of those PTCR ceramics possess a low resistivity which is almost constant temperature coefficient of resistivity below T_c . Recently,

To the extent authorized under the laws of the United States of America, all copyright interests in this publication are the property of The American Ceramic Society. Any duplication, reproduction, or republication of this publication or any part thereof, without the express written consent of The American Ceramic Society or fee paid to the Copyright Clearance Center, is prohibited.

another PTCR materials with the behavior distinctly different from the conventional ρ -T properties has been discovered, that is, $(Pb_{1-x}Sr_x)TiO_3$ PTCR ceramics^[7,8]. They exhibit large negative temperature coefficient of resistivity (NTCR) below T_c besides the ordinary PTCR characteristics above Curie temperature. It is called the V-shaped PTCR ceramics.

The synthesis of these materials is still very difficult due to the lack of availability of comprehensive processing datum on $(Pb_{1-x}Sr_x)TiO_3$ PTCR ceramics. A systematic study on the synthesis of the $(Pb_{1-x}Sr_x)TiO_3$ ceramics is, therefore, necessary. This research is aimed to investigate the effects of some processing parameters such as the concentration of donors and the ratio of Pb/Sr etc., on the development of both microstructure and electrical properties of the $(Pb_xSr_{1-x})TiO_3$ PTCR ceramics.

II. EXPERIMENTAL PROCEDURE

One of the problems encountered in the conventional method used for mixing the oxide powders, such as ball milling, is the difficulty in homogeneously dispersing a small amount of semiconductive dopants into the main constituents. For the purpose of improving uniformity in the incorporation of additives, the liquid form of donor, $Y(NO_3)_3 \cdot 5H_2O$, was used. Significant improvements on the microstructure and PTCR properties of the samples are expected.

High purity PbO , TiO_2 , $SrCO_3$, and 5 mole% SiO_2 oxide powders were used as main constituents and sintering aid, respectively. The nominal composition of the samples was $(Pb_xSr_{1-x})Ti_{1.003}O_3$ with $x=0.5$, 0.6 or 0.7. The oxide powders were firstly wet mixed with deionized water, in a plastic jar using plastic-coated iron balls, for 18 hrs. The solution containing Y^{3+} ions (derived from $Y(NO_3)_3 \cdot 5H_2O$), was then added into the pre-milled slurry, and mechanically stirred for 30 minutes. Drops of ammonia were then added into the slurry to gradually adjust the pH value to homogeneously precipitate out the Y^{3+} ions in the form of $Y(OH)_3$, until the pH value of the slurry was higher than 10. The completeness of precipitation was ensured by keeping the content of Y^{3+} ions in the as-filtrated solution below the

detecting sensitivity of the ICP-AES analyzer.

The mixed powders derived from filtrated slurry were dried with IR lamp, sieved through a 60 mesh sieve and then calcined at 1050°C for 1 hr in air. Green pellets of 10 mm diameter were formed by uniaxial pressing with pressure either of 200 kg/cm² or 400 kg/cm² and then sintered at the temperature varied in the range from 1220°C to 1260°C for either 0.5 hr or 1 hr, with the 300°C/hr heating and cooling rates in the stagnant air.

The phase constituents of the calcined powders and the sintered specimens were analyzed using X-ray diffraction technique (Rigaku). The microstructures of polished surfaces of specimens were examined using a scanning electron microscope (SEM). The average grain size was estimated by the linear intersection method. Electrodes were applied on both surfaces of the specimens by rubbing In-Ga alloy to achieve a good ohmic contact. DC resistivity was measured using HP3457A multimeter in the temperature range from room temperature to 500°C.

III. RESULTS

Yttrium ions (Y³⁺) ions were adapted in our study as the semiconducting additives. In order to study the effect of donor concentration on the semiconductivity of (Pb_{0.6}Sr_{0.4})TiO₃ materials, series of samples containing 5.0 mol% SiO₂ and Y³⁺ ions concentrations either of 0.5, 0.8, 1.0, 1.2 or 1.5 mol% were prepared. They were pelletized with the 200 kg/cm² pressure and then sintered at 1220°C for 1hr. The ρ -T characteristics of these samples were shown in Fig.1 to indicate that the incorporation more than 0.8 mol% of Y³⁺ ions could efficiently convert the materials into semiconductive and resulted in marvelous PTCR properties. The samples which contain Y³⁺ ions less than 0.5 mol%, on the other hand, always exhibited high resistivity and no PTCR characteristics at all. The samples containing 0.8 mol% Y³⁺ possessed the most steep resistivity jump above T_c , while those containing 1 mol% Y³⁺ exhibited the lowest resistivity. Increasing the donor concentration beyond the 1 mol% Y³⁺ linearly increased the room temperature resistivity but maintaining the R_{max}/R_{min} ratio about the same order.

The corresponding microstructures indicated that similar microstructures were obtained in samples containing 0.5, 0.8 or 1.0 mol% Y^{3+} . The grain size slightly decreased when the Y^{3+} content was more than 1.0 mol%, which was probably caused by the mechanism that some of the excess Y^{3+} ions stayed at grain boundaries acting as the grain growth inhibitors^[9,10].

The effect of Pb/Sr ratio in $(Pb_{1-x}Sr_x)TiO_3$: 1 mole% Y^{3+} materials on their electrical properties was then examined. The ρ -T characteristics of samples containing 5 mol% SiO_2 and with Pb/Sr ratio equals to 5/5, 6/4 and 7/3, which were labeled as L-50S, M-50S and H-50S, respectively, were shown in Fig.2. Those samples were pressed with 400 kg/cm^2 pressure and then sintered at 1260°C for 0.5hr with 300°C/hr cooling rate. The Curie temperature increased but the electrical resistivity decreased as the Pb content in $(Pb_{1-x}Sr_x)TiO_3$ materials increased. Besides, the table 1 indicated that the amount of SiO_2 content added in these samples showed no effect on shifting T_c temperature.

The resistivity jump, which is $PTC=|\rho_{max}-\rho_{min}|$, decreased markedly but the resistivity drop, which is $NTC=|\rho_{min}-\rho_n|$, varied insignificantly with Pb/Sr ratio (dotted line, Fig.3a). The positive and negative temperature coefficient of resistivity (PTCR and NTCR), which was defined as

$$PTCR \text{ (NTCR)} = \left| \frac{\log \rho_T - \log \rho_{T_c}}{T - T_c} \right|, \quad T=T_c \pm 20^\circ C$$

varied with the Pb/Sr ratio of the samples in a similar manner as resistivity jump (PTC) and resistivity drop (NTC), respectively, as indicated by dotted lines in Fig.3b. The phenomena that the resistivity jump (PTC) and PTCR properties of these samples were lowered as Pb content increased, but the resistivity drop (NTC) and NTCR behavior were influenced insignificantly by Pb/Sr ratio are the same for the samples sintered at 1220°C or 1240°C (Fig.3). Similar results have been reported for $(SrBa)TiO_3$ and $(PbBa)TiO_3$ PTCR ceramics^[4].

The X-ray diffraction patterns for the sintered samples with various Pb/Sr ratios (5/5, 6/4 and 7/3) were shown in Fig.4 to reveal that the materials were of pure tetragonal perovskite phase and the tetragonality of the materials, i.e. the c/a ratio,

increased with the Pb content (Table I).

Table I Curie Temperature and Lattice Parameters of
(Pb_xSr_{1-x})TiO₃ Materials

Pb/Sr Ratio	Curie Temperature		Lattice Parameters		
	T _c ⁽¹⁾	T _c ⁽²⁾	c ₀	a ₀	c/a
5/5	135.4°C	137.9°C	3.954	3.910	1.011
6/4	207.7°C	203.8°C	3.975	3.910	1.017
7/3	262.2°C	264.7°C	4.005	3.910	1.024

(1) SiO₂ = 2.5 mol%; (2) SiO₂ = 5.0 mol%

IV. DISCUSSIONS

The behavior of (Pb_{1-x}Sr_x)TiO₃ materials doped with donors (Y³⁺) is very different from that of conventional PTCR ceramics, such as (Sr_{1-x}Ba_x)TiO₃, BaTiO₃, and (Pb_{1-x}Ba_x)TiO₃ materials. The proportion of donor ions needed to convert the (Pb_{1-x}Sr_x)TiO₃ materials semiconducting is significantly larger than that for other series of PTCR ceramics, which is usually 0.3 mol% donors. No semiconducting properties are obtained when as much as 0.5 mol% Y³⁺-ions have been added, even though the grain growth has already occurred. There are several possibility which could prohibit the 0.5 mol% Y³⁺-doped materials from semiconducting: (1) the Y³⁺-ions have not yet been incorporated into the (PbSr)TiO₃ lattice; (2) large proportion of Y³⁺ ions were dissolved into the liquid phase so that not enough Y³⁺ were incorporated into the lattice; (3) the introducing of cationic vacancies such that the carriers provided by the Y³⁺-ions are compensated; and (4) the Y³⁺ ions simultaneously occupying the A-sites and B-sites of (Pb_{1-x}Sr_x)TiO₃ lattice and acting both as the donors and acceptors.

Among the 4 possibilities, the last one seems to be the most probable cause and the arguments are as follows: The large granular structure shown in Fig. 2a rules out the first two possibilities, since the grain boundaries will be pinned if the Y³⁺-ions are residing at grain boundaries^[9,10,12-14]. Moreover, since the optimum proportion of dopants is still only 1 mol% Y³⁺ even when as much as 10 mol% SiO₂ are

included in $(Pb_{1-x}Sr_x)TiO_3$ materials as liquid phase sintering aids, the dissolving of Y^{3+} ions in liquid phase is concluded to be not significant. The third possibility is also not likely to occur to 0.5 mol% Y^{3+} -doped materials, since cationic vacancies will be induced only when the proportion of donors is so high that electronic charge is highly imbalanced^[15,16].

The simultaneous generation of the donors and acceptors, on the other hand, is possible, since the Y^{3+} ions with the size (0.893 Å) can fit both A-sites (~1.20 Å) and B-sites (0.68 Å) lattices reasonably well. The solubility of Y^{3+} in B-site lattice is, however, expected to be much lower than that in A-site lattice due to the fact that larger strain will be involved when Y^{3+} ions substituting B-site cations. Further increase in the amount of Y^{3+} ions will thus only increase the A-site substitutional defects such that the materials become n-type semiconducting. Similar phenomenon has been observed on $BaTiO_3$ ceramics simultaneously doped with both the Mg^{2+} -ions and the Nb^{5+} -ions^[17], in which more than 0.3 mol% Nb^{5+} ions are needed to convert the materials into semiconducting at the presence of Mg^{2+} -ions. It is concluded, therefore, that the Y^{3+} ions added into the $(Pb_{1-x}Sr_x)TiO_3$ materials will initially occupy both the A-site and B-site lattices such that the electrons supplied by the donors are compensated. The materials are thus still possessing high resistivity when only small amount of Y^{3+} are incorporated. The Y^{3+} ions will act as donors only when A-site substitutions is significantly surpassing the B-site substitutions.

V. CONCLUSION

The semiconductive $(Pb_{1-x}Sr_x)TiO_3$ ceramics with large PTCR (>4 order) and significant NTCR (>2 order) characteristics have been successfully fabricated. The effects on microstructure and electrical properties of some processing parameters are concluded as follow:

- (1) $(Pb_{1-x}Sr_x)TiO_3$ ceramics could be converted into semiconductive by doping 1.0 mol% Y^{3+} ions.
- (2) The Curie point could be shifted by adjusting the Pb/Sr ratio.

IV. REFERENCE

1. O.Saburi, J. Phys. Soc. Japan, 14[9], pp.1159-1174 (1959)
2. O.Saburi, J. Am. Ceram. Soc., 44[2], pp.54-63 (1961)
3. W. Heywang, Solid-State Electronics, Vol.3, pp.51-58 (1961)
4. G.H.Jonker, Solid-State Electronics, Vol.7, pp.895-903 (1964)
5. E.Andrich, Electr. Appl., 26[3], pp.123-144 (1965/66)
6. M.Kuwabara et.al., J. Am. Ceram. Soc., 66[11], pp.c214-c215 (1983)
7. Y.Hamata et.al., J. Electronics Jpn. [5], pp.33-35 (1988)
8. Y.Hamata et.al., Japanese pat.63-280401, Nov.17 (1988)
9. H.F.Cheng, J. Appl. Phys., 66[3], pp.1382-1387 (1989)
10. M.Drofenik et.al., Ceram. Bull., 63[5], pp.702-704 (1984)
11. H.F.Cheng et.al., J. Am. Ceram. Soc., 76[4], pp.827-832 (1993)
12. T.F.Lin et.al., J. Am. Ceram. Soc., 73[3], pp.531-536 (1990)
13. J.S.Chi et.al., J. Mat.Sci., Vol.27, pp.1285-1290 (1992)
14. W.Y.Hwang et.al., Am. Ceram. Soc. Bull., 62[2], pp.231-233 (1983)
15. J.Daniels et.al., Philips Res. Repts, Vol.31 pp.489-559 (1976)
16. J.Daniels et.al., Philips Tech. Rev., 38[3], pp.73-82 (1978/79)
17. B.S. Chiou, G.M. Gou, J. Mater. Sci., (1988)

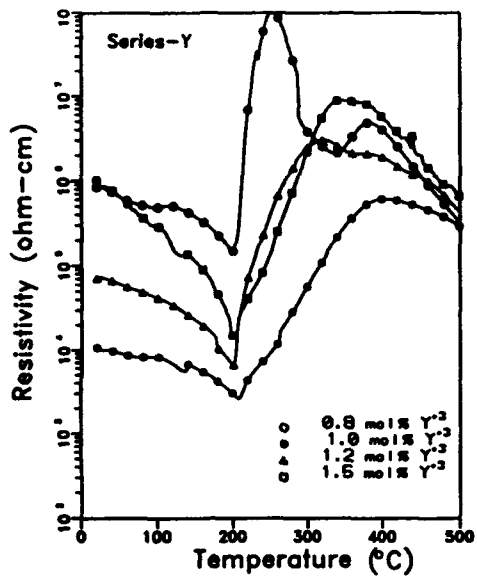


Fig.1 The ρ -T characteristics of the $(\text{Pb}_{0.8}\text{Sr}_{0.2})\text{TiO}_3$ samples with various Y^{3+} content, pressed with 200 kg/cm^2 and sintered at 1220°C for 1hr with 300°C/hr cooling rate.

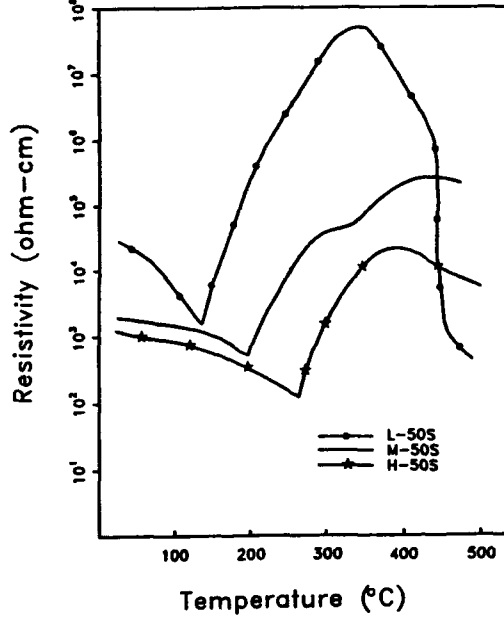


Fig.2 The ρ -T characteristics of the samples with various Pb/Sr ratio. The materials contain 5.0 mol% SiO_2 , pressed with 200 kg/cm^2 , sintered at 1260°C/0.3hr and then cooled at 300°C/hr.

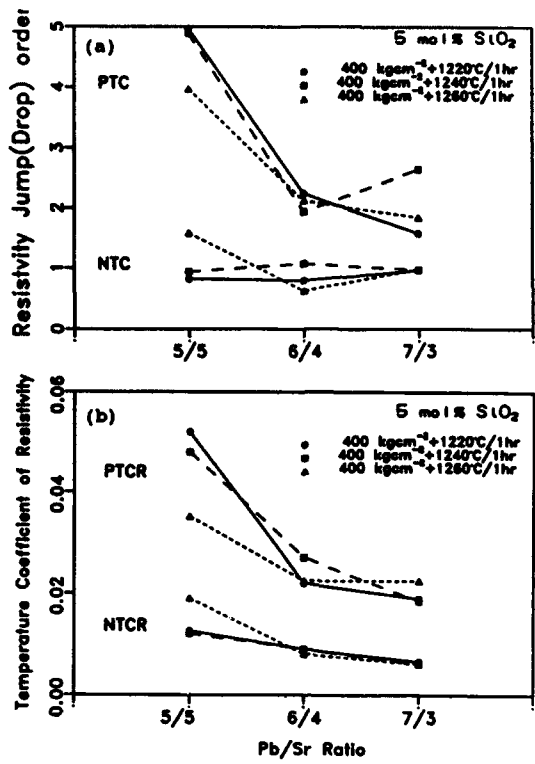


Fig.3 Variations of (a) the resistivity jump (P) and resistivity drop (Q) and (b) the temperature coefficient of resistivity (PTCR and NTCR) with the Pb/Sr ratio.

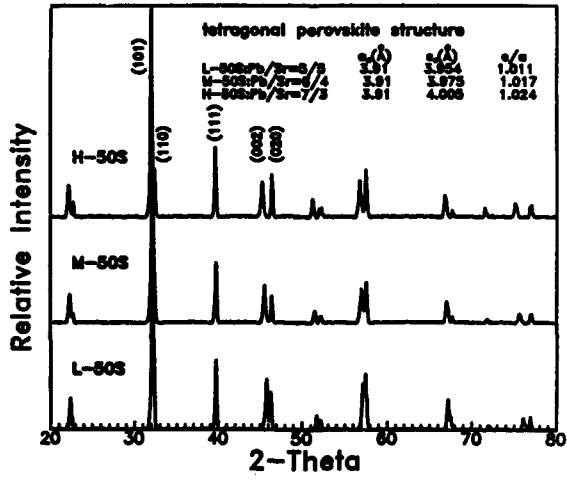


Fig.4 The X-ray diffraction patterns of the samples with various Pb/Sr ratios.

EFFECT OF BN ADDITION ON THE SINTERING AND ELECTRICAL PROPERTIES OF Y-DOPED BaTiO_3 CERAMICS

Seh-Jin PARK, Joon-Hyung LEE and Sang-Hee CHO

Department of Inorganic Materials Engineering
Kyungpook National University, Taegu 702-701, Korea

ABSTRACT

In this study, the effect of BN addition on the sintering and electrical properties of Y-doped BaTiO_3 ceramics were examined. When BN is added to Y-doped BaTiO_3 , BN decomposed to B_2O_3 liquid phase and N_2 gas through BN oxidation. The B_2O_3 -rich liquid phase lowered the starting temperature of densification below 1000°C. Room temperature resistivity of Y-doped BaTiO_3 with addition of BN was decreased and the Curie temperature shifted to higher. These phenomena seem to result from the solid solution of B to Y-doped BaTiO_3 .

[Key Word] : BaTiO_3 , PTCR effect, BN, Curie temperature.

I. INTRODUCTION

BaTiO_3 ceramics is one of the most widely used material as electroceramic components such as dielectrics, capacitors and PTCR devices.¹⁾ Especially, when BaTiO_3 is properly doped with La_2O_3 or Y_2O_3 , it exhibits PTCR (Positive Temperature Coefficient of Resistivity) anomaly near the Curie point,²⁻⁴⁾ and it is used for a variety of purposes, including TV degaussers, temperature sensors, flow sensors, liquid-level sensors, and current-limiting applications.⁵⁻⁷⁾

It is well known that the PTCR effect is greatly affected by the chemical and physical properties of grain boundaries and microstructure of the sintered body,¹¹⁻¹⁴⁾ and this effect has long been established that BaTiO_3 PTCR phenomena is a grain boundary resistive effect.⁸⁻¹⁰⁾ The evidence comes from numerous studies donor-doped single crystal, AC impedance method and cathodoluminescence technique.^{8, 10)}

Besides, for the sintering of BaTiO_3 system, relatively high temperature

To the extent authorized under the laws of the United States of America, all copyright interests in this publication are the property of The American Ceramic Society. Any duplication, reproduction, or republication of this publication or any part thereof, without the express written consent of The American Ceramic Society or fee paid to the Copyright Clearance Center, is prohibited.

above 1350°C is needed. Therefore the low temperature sintering is highly recommended for financial standpoint. Small amount of impurity such as excess TiO_2 , SiO_2 and Al_2O_3 are usually added to $BaTiO_3$ system for low temperature sintering.^{15,16)} These kinds of impurities not only lower sintering temperature but also help the system acquire homogeneous microstructure, and improve reproducibility leading to positive property control.

In this study, effect of BN addition on the evolution of microstructure, defect concentration of grain boundary, sintering and electrical properties of Y-doped $BaTiO_3$ was studied. BN may help the sintering of Y-doped $BaTiO_3$ by forming a liquid phase with oxidation, and act as a lubricant in the forming process.¹⁷⁾

II. EXPERIMENTAL

Specimens were prepared by general ceramic forming process using reagent grade chemicals, $BaCO_3$, TiO_2 , BN and Y_2O_3 . The weighed powders with composition of $(Ba_{0.996}Y_{0.004})TiO_3$ were mixed together with ZrO_2 balls in ethyl alcohol for 28 hours, calcined at 1150°C in air for 1 hour. BN was added to the mixture with different amounts(0~3.2 mol%) and ball-milled again for several hours. The mixture was formed into a pellet by hydrostatic pressing with a pressure of 98MPa. The pellet was sintered in air at 1350°C for 1 hour and cooled down in the furnace with cooling rate of 50°C/h.

Lattice parameter of the sintered specimen was measured by powder X-ray diffraction patterns using $CuK\alpha_1$ radiation. The lattice parameters obtained from these patterns were refined by the Cohen's method on an IBM computer. Sintering behavior was observed by a dilatometer with the same procedure of sintering runs ; the samples were heated at 5°C/min. from room temperature to 1350°C and held at this temperature for 1 hour. Sintered densities were measured to $0.001g\cdot cm^{-3}$ using the Archimedes method with water as the immersion medium. Al electrode was screened on both sides of sintered samples. The DC resistivity versus temperature characteristics of the samples were measured up to 250°C using two-probe method.

III. RESULTS AND DISCUSSION

Fig.1 shows the variation of forming density with addition of BN. The forming density increased greatly as BN was added up to 0.8 mol%, and then slightly increased above 0.8 mol% of BN. It is well known that BN powder has lubrication ability during forming process due to its hexagonal plate-like-shape

similar to graphite.¹⁷⁾ When these BN particles are included in the green body, they can reduce the friction force between mold and compacts. Therefore more homogeneous and higher pressure can act upon the green compacts.

Fig.2 represents the relative density changes as a function of BN contents in the system of Y-doped BaTiO₃ during sintering process. When BN is not added in the specimen, the starting temperature of densification is about 1200°C. As shown in Fig.2, the starting temperature decreases gradually with addition of BN. When 3.2 mol% of BN is added, the densification starts below 1000°C and the maximum density already reaches at 1150°C.

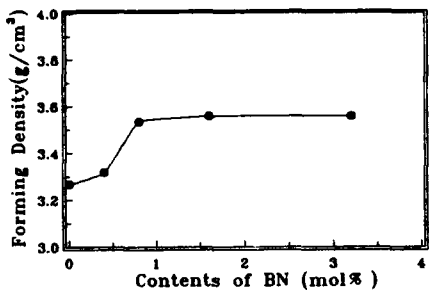


Fig.1 Variation of forming density as a function of BN contents.

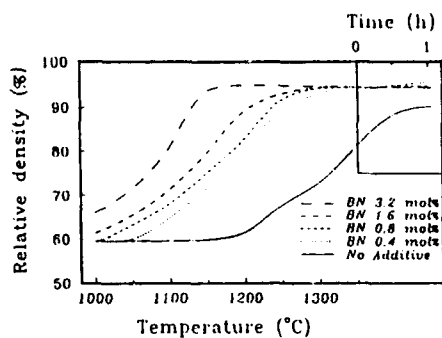


Fig.2 Relative density variation as functions of temperature and BN contents.

Fig.3 shows TG curve of the Y-doped BaTiO₃ specimen with addition of 3.2 mol% of BN. About 1.5 % weight gain was clearly observed around 950°C. This phenomenon seems to result from the formation of B₂O₃ and N₂ gas through BN oxidation. Therefore the lowered starting temperature of densification below 1000°C with addition of BN powders might be due to the formation of B₂O₃ rich liquid phase by BN oxidation.

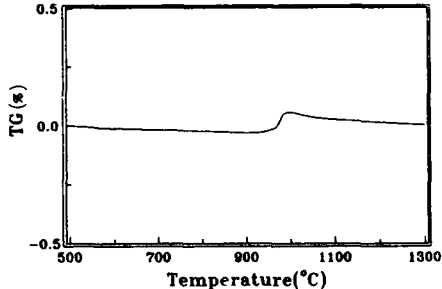


Fig.3 TG curve of a specimen with 3.2 mol% BN addition.

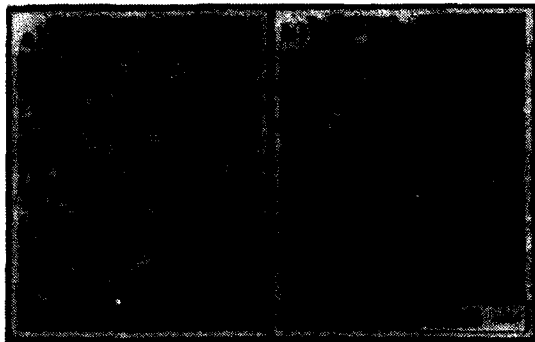


Fig.4 a)SEM and b)its SCI photographs of 3.2 mol% BN added sample.

Fig.4 shows (a) SEM photography and (b) Sample Current Image photography using EPMA of sintered sample of 3.2 mol% BN addition, respectively. Since dark parts signify the existence of light atomic weight material in Fig.4(b), it is quite possible that it includes B or/and O which has light atomic weight among composing atoms. But the analysis shows the even distribution of O atom in the sample. Therefore dark parts along the grain boundaries are believed as the liquid phase composed of B-Ba-Ti-Y-O with large amount of B.

Fig.5 shows the variation of grain size of sintered samples as a function of BN contents. As BN increases, grain size decreases. When small amount of liquid phase forms due to the little addition of BN, grain growth rate increases.

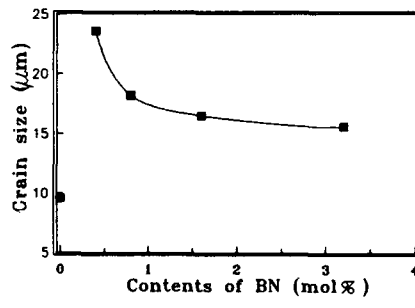


Fig.5 Variation of grain size as a function of BN contents.

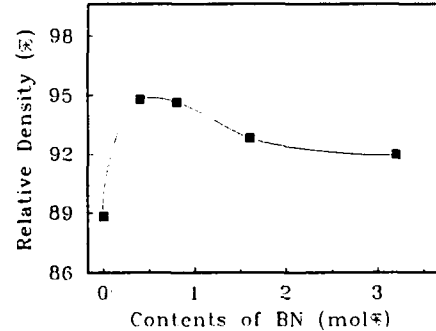


Fig.6 Sintered density variation as a function of BN contents.

It is believed that pore pinning effect was eliminated by accelerated densification. But when BN content increased, grain growth rate decreased due to the enlargement of diffusion length by increased amount of liquid phase.

Fig.6 shows the sintered density of Y-doped BaTiO₃ as a function of BN contents. As BN increases, the sintered density decreases. It is thought that pores are formed by N₂ gas formation during sintering.

Fig.7 represents the changes of room temperature resistivity of Y-doped BaTiO₃ with addition of BN component. As BN increases to 0.4 mol%, the resistivity decreases drastically, and beyond that it decreases gradually. In this system, solid phase of Y-doped BaTiO₃ and liquid phase of B₂O₃ rich B-Ba-Ti-Y-O coexist. Generally, the resistivity of liquid phase, of which the major component is B₂O₃, is very high. Therefore the liquid phase of B-Ba-Ti-Y-O does not seem to contribute to the formation of conduction channel when room temperature resistivity reduces. It seems that small amount of B solute into the perovskite Y-doped BaTiO₃.¹⁸⁾ B as donors might lower room temperature resistivity.

Fig.8 shows lattice constant measured by XRD. Lattice constant does not vary to great extent although the BN contents vary. It seems that the change of lattice constant has not been observed when B³⁺ ions occupy interstitial sites because their ionic radii are too small(0.27Å) to be detected by XRD.

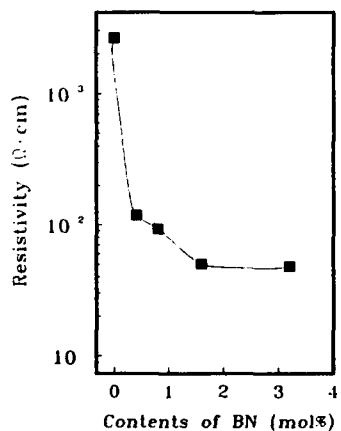


Fig.7 Room temperature resistivity variation as a function of BN contents.

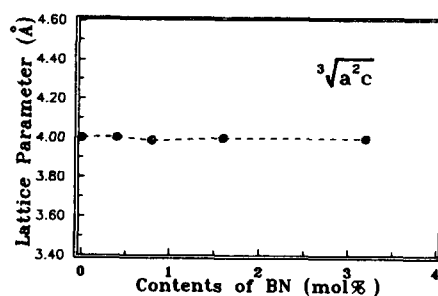


Fig.8 Lattice parameter variation as a function of BN contents

Fig.9 represents PTCR properties as functions of temperature and BN contents. As BN increases, the room temperature resistivity of Y-doped BaTiO_3 drastically decreased and the Curie temperature shifts to higher temperature. These phenomena may result from the solid solution of B to Y-doped BaTiO_3 .

IV. CONCLUSIONS

When BN is added to the Y-doped BaTiO_3 sample, densification started at lower temperature than BN omitted. From TG analysis, weight gain was observed around 950°C. This may seem to result from the formation of B_2O_3 -rich liquid phase and N_2 gas through BN oxidation. Judging from increase of Curie temperature and the decrease of room temperature resistivity B may play role in donors by solution into Y-doped BaTiO_3 .

REFERENCES

1. B.Jaffe, W.R.Cook Jr and H.Jaffe, *Piezoelectric Ceramics*, (Academic Press Inc., 1971), pp.53.
2. S.Ikegami and I.Ueda, "Semiconductive Single Crystal of BaTiO_3 Reduced in Hydrogen Atmosphere," *J.Phys.Soc.Jpn.*, 19[2], 159-166 (1964)
3. E.J.W.Verwey, P.W.Haaijman, F.C.Romeijn, and G.W.Van Oosterhout, "Controlled Valency Semiconductors," *Philips Res.Rep.*, 5[6], 173-187 (1950)
4. O.Saburi, "Properties of Semiconductive Barium Titanates," *J.Phys.Soc.Jpn.*, 14[9], 1157-1174(1959)
5. E.Andrich, "Properties and Applications of PTC Thermistors," *Electron.Appl.*, 26[2] 123-44 (1965/66)

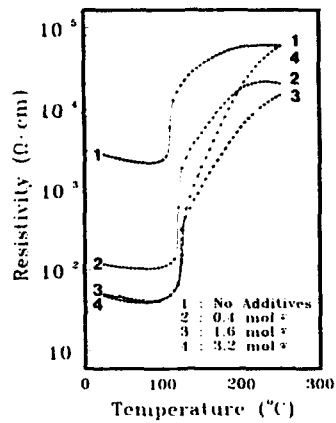


Fig.9 Temperature - Resistivity property as a function of BN contents.

6. E.Andrich,"PTC Thermistors as Self-Regulating Heating Elements," Philips Tech.Rev., 30,170-77(1969)
7. H.Loebl and R.Rossgotterer,"Degaussing Circuits with PTC Resistors," Siemens Rev., 38[11] 520-23(1971)
8. P.Gerthsen and B.Hoffman, "Current-Voltage Characteristics and Capacitance of Single Grain Boundaries in Semiconducting BaTiO₃ Ceramics," Solid State Electron., 16, 617-622(1973)
9. N.Nemoto and J.Oda, "Direct Examinations of PTC Action of Single Grain Boundaries in Semiconducting BaTiO₃ Ceramics," J.Am.Ceram.Soc., 63[7-8], 393-401 (1980)
10. H.Ihrig and M.Klerk,"Visualization of the Grain Boundary Potential Barriers of PTC-Type BaTiO₃ Ceramics by Cathodoluminescence in an Electron-Probe Microanalyzer," Appl.Phys.Lett.,35[4]307-309(1979)
11. M.F.Yan and A.H.Heuer, Additives and Interfaces in Electronic Ceramics, Advances in Ceramics Vol.7 (The American Ceramic Society, Inc., 1983), pp.128-136.
12. M.Kuwabara, Additives and Interfaces in Electronic Ceramics, Advances in Ceramics Vol.7 (The American Ceramic Society, Inc., 1983), pp.137-145.
13. M.Kuwabara, "Effect of Microstructure on the PTCR Effect in Semiconducting Barium Titanate Ceramics" J.Am.Ceram.Soc.,64[11] 639-644 (1981)
14. M.Kuwabara, "Influence of Stoichiometry on the PTCR Effect in Porous Barium Titanate Ceramics," Comm.Am.Ceram.Soc., C-170-171 December (1981)
15. H.Ihrig, "The Positive Temperature Coefficient Resistivity of BaTiO₃ Ceramics as a Function of the Amount of Titanium-Rich Second Phase," Phys.Stat.Sol.(a)47, 437(1978)
16. Y.Matsuo, M.Fujimura, H.Sasaki, K.Nagase and S.Hayakawa, "Semiconducting BaTiO₃ With addition of Al₂O₃, SiO₂, and TiO₂," Ceram. Bull., 47[3] 292-297(1968)
17. Modern Ceramic Engineering 2nd edition, ed. by D.W.Richerson p 428
18. L.M.Castelliz and R.J.Routil,"The Effect of Boric Oxide on the Properties of Barium Titanate Based Ceramics," J.Canadian Ceram.Soc., 38, 69-74 (1969)

EFFECTS OF GRAIN BOUNDARY STRUCTURE ON THE RESISTIVITY PHENOMENON IN DOPED BaTiO₃

R.C. Buchanan, R.D. Roseman and J. Kim, Department of Materials Science and Engineering, University of Cincinnati, Cincinnati, OH 45221-0012

ABSTRACT

Polycrystalline, ferroelectric barium titanate (BaTiO₃) can be made highly conducting through donor doping in low concentrations. The resistivity behavior is dominated by the nature of the grain boundary lattice and domain structure. In this investigation, the factors relating the observed resistivity to the ferroelectric domain and grain boundary structure was achieved by characterization techniques using TEM, SEM and HREM. It was found that structural homogeneity and domain configuration near and across grain boundaries dominate the observed electrical behavior.

INTRODUCTION

BaTiO₃ has an intrinsically high resistivity ($10^{10} \Omega\cdot\text{cm}$) when prepared in an oxidizing atmosphere. Through controlled doping of the A-site perovskite lattice, for example using Y³⁺ or La³⁺ (< 0.3 mol %), n-type polaron conduction can be obtained, generating resistivities $< 10^2 \Omega\cdot\text{cm}$ [1-3]. An important aspect is the observed resistivity differences between samples under various heat treatment conditions. At temperatures below the ferroelectric phase transformation (T_c), non-annealed samples exhibit a significantly lower resistivity than samples which have been annealed (typically 1000°- 1220°C for 30min-10hr) or slow cooled from the sintering temperature [4,5]. These differences have generally been attributed to: 1) Oxygen adsorption along the grain boundaries and diffusion into the grain interior, altering the defect structure [3,6,7]; 2) Time dependent gradient in acceptor barium and titanium vacancy diffusion processes [8-11]; 3) A combination of these theories in which the vacancies are initially present within a grain boundary space-charge layer and are activated when

To the extent authorized under the laws of the United States of America, all copyright interests in this publication are the property of The American Ceramic Society. Any duplication, reproduction, or republication of this publication or any part thereof, without the express written consent of The American Ceramic Society or fee paid to the Copyright Clearance Center, is prohibited.

compensating defects in the grain boundary are neutralized by oxidation [12]; and, 4) The grain boundary potentials are a result of a shift from electronic to vacancy compensation induced by donor segregation, resulting in electron trap sites [13].

Factors which are generally left out of interpretations as to the conduction process between grains are [16]: 1) The lattice and domain structural relationships between and internally within each grain; 2) The actual mode of conduction and necessary elements involved in n-type polaron conduction; and, 3) Generated internal stresses, derived from grain-to-grain structural constraints, modifying and creating potential barriers structurally.

In polycrystalline samples the exact domain patterns and the state of the barriers themselves are complex [16,17]. In this study, direct observations of these type conducting ceramics by SEM and TEM have been performed in order to answer questions concerning alignment of the ferroelectric domain and lattice structure at grain boundaries and their relationship to the conduction process.

EXPERIMENTAL

Donor-doped BaTiO₃ samples were prepared by ball-milling high purity BaTiO₃ (Ba/Ti = 0.997) powders with trivalent dopant additions (La₂O₃, Y₂O₃ < 0.3 mol %) added as a nitrate solution. Milling was carried out using ZrO₂ balls in a solution of isopropyl alcohol / deionized water with fish oil added as a dispersant and a PVA - Carbowax solution added as a binder / lubricant. The dispersed slurry was spray-dried and the powder uniaxially pressed into discs. The heat treatment consisted of a nitrate, binder burnoff at 550°C / 30 min followed by sintering at 1350°C / 2h in air and either: a) cooled at 20°C / min, or b) slow cooled at 5°C / min with an additional annealing step of 1220°C / 6h.

Resistance measurements were made on polished discs with Al evaporated electrodes, using a constant voltage source at 0.01 volts, in series with the sample and picoscale ammeter, between 25° and 250°C at 5°C / min. Foils for TEM analysis were prepared by mechanical grinding and polishing of the samples to a thickness of 40- 90 μ m and ion milling to perforation.

RESULTS AND DISCUSSION

In this study, all samples were processed under identical conditions, except for varying heat treatments. The bulk microstructures developed in each case have similar average grain sizes of $\sim 25 \mu\text{m}$, with an average density of $\sim 93\%$ theoretical. Therefore, the bulk microstructures were not affected by annealing and any variance in electrical properties are grain size independent.

Figure 1 shows annealing effects on the minimum resistivity in lightly donor doped BaTiO_3 . As seen, there is a linear increase in resistivity with time at the anneal temperature of 1220°C , independent of dopant type. For an anneal treatment of 6 hrs, there is a 1 order of magnitude difference in resistivity. These effects are significant when designing sensors, such as PTCR, from these ceramics, as there is a trade off between maximum signal response (abrupt change in resistance near T_c) and accompanying lowest attainable resistivity. An abrupt and large resistivity difference at T_c increases with increasing time at anneal [4,5,16].

The polished and etched SEM micrographs of Figure 2 compare an unmodified BaTiO_3 and a doped (0.24 mol % Y_2O_3) BaTiO_3 sample. The unmodified sample (Figure 2A) shows the random domain alignment typical of BaTiO_3 . The n-type conducting, donor doped sample (Figure 2B) shows the development of a domain structure that is uni-directional throughout each individual grain. This type structure was also independent of heat treatment and occurred in every grain, but, the alignment of the c-axis from grain-to-grain was typically random. Therefore, the directionality of the domain alignment between grains varied, resulting in orientational mismatch at adjoining grain boundaries.

The TEM image of Figure 3 shows a typical grain boundary in the Y-doped non-annealed samples. Domain widths ($\sim 0.8 \mu\text{m}$) from the interior to the grain boundaries are uniform and straight, no splitting or random alignments are found up to the grain boundary. Across a grain boundary the domains often meet and continue with only an angle change and align over a large distance. The TEM image of Figure 4 shows a more complex grain boundary in the Y-doped annealed system. Regions of fine domain widths ($\sim 0.08 \mu\text{m}$) in the near boundary regions are seen to coexist with regions in which no domains are found along with areas in which the domain structure continues unobstructed from the grain interior up to the grain boundary. Fine domain patterns can encompass areas as wide as $2 \mu\text{m}$ and extend into the grain interior 1- 2 μm , before transforming into the coarse domain structure. In these materials a variety of grain boundary situations are

encountered as all three type regions are randomly distributed along the grain boundaries.

Annealing or slow cooling from the sintering temperature allows for cation diffusion and for rapid oxygen adsorption to occur. Acceptor and donor states have been found to segregate to the grain boundaries, along with excess concentrations of dopants [12,13]. Diffusion and segregation effects are considered to be the driving force for formation of the fine and no-domain regions. The more complex grain boundary structures of the annealed systems must also relate to the observed electrical behavior differences compared to the non-annealed, uniform domain structures.

Figure 5 shows HREM images of the immediate grain boundaries in these systems, comparing boundary regions in which domains exist on both sides (Figure 5A), and a boundary region between an area of no-domain across from a domain region (Figure 5B). The grain boundary of Figure 5A shows high coherency between grains and must be considered to be of a very low potential barrier and is suggestive of an easy electron pathway. In these boundaries (domain-to-domain) it is also important to note that no segregated regions or large concentrations of defects are seen. Figure 5B shows a more highly defective and incoherent grain boundary. These regions clearly show a regularly spaced defect in which the periodicity of the barium and titanium atoms are disrupted along the grain boundary. The incoherent boundaries reflect a greater potential barrier to electron flow.

The mode to electronic conduction is considered to be along the unidirectional domain pathways, giving a channeling effect to the electron mobility. Where the interior coarse domain structure extends the length of the grains up to the grain boundaries, an electron pathway is generated from grain-to-grain whenever the alignment is advantageous. In the non-annealed materials, preferentially oriented, coherent boundaries with a minimum potential barrier to electron flow are wide in extent, relating to the lowest resistivity materials. Higher resistivities found in the annealed systems are in part due to the expected low electron mobility through the no-domain regions and corresponding incoherent grain boundaries. Electron transport across grain boundaries is greatly inhibited for domain to no-domain regions and for areas in which no domain regions are common to the boundary. Therefore, the concentration of areas in which electron flow is highly probable (i.e., preferential domain-to-domain alignment) is significantly affected by heat treatment. Annealing greatly reduces this grain boundary concentration, and must be a function of time at anneal.

CONCLUSIONS

The resistivity of these n-type conducting materials is closely related to the specific properties of grain boundaries and near boundary regions, in which the properties are different from the bulk. An important aspect of the uni-directional domain structure is the effect that it has on the grain boundary structure. Each grain is comprised of various potential barriers, of which only certain preferentially aligned grain boundaries allow easy conduction across. A percolation of the conducting electrons along the mutually interacting uni-directional domain pathways creates the low resistivities. An important consideration is that not all boundaries are conducting, and limiting the concentration of conducting grain boundary regions by annealing increases the resistivity below T_c .

REFERENCES

1. W. Heywang, "Semiconducting Barium Titanate," *J. Mat. Sci.*, Vol. 6, pg. 1241-1226 (1971).
2. B. Kulwicki, "PTC Materials Technology, 1955-1980," Grain Boundary Phenomena in Electronic Ceramics, ed., L. Levinson, *Advances in Ceramics*, Vol. 1, pg. 138-154 (1981).
3. G. H. Jonker, "Some Aspects of Semiconducting Barium Titanate," Solid State Electronics, Vol. 7, pg. 895-903 (1964).
4. H. M. Al-Allak, G. J. Russell and J. Woods, "The Effect of Annealing on the Characteristics of Semiconducting BaTiO_3 Positive Temperature Coefficient of Resistance Devices," *J. Phys., D. (London), Appl. Phys.*, Vol. 20, No. 12, pp. 1645-51 (1987).
5. R.D. Roseman, "Influence of Yttria and Zirconia on the Positive Temperature Coefficient of Resistance in Barium Titanate Ceramics," M.S. Thesis, University of Illinois (1992).
6. W. Heywang, "Resistivity Anomaly in Doped Barium Titanate," *Solid State Electron*, Vol. 3, pg 51 (1961).
7. R. W. Newnham, "Structure-Property Relations in Electronic Ceramics," *J. Mat. Ed.*, Vol. 6, No. 5, pg. 806-839 (1984).
8. J. Daniels and R. Wernicke, "Part V. New Aspects Of An Improved PTC Model," *Phillips Research Reports*, Vol. 31, pg. 544-559 (1976).
9. G. V. Lewis and C. R. A. Catlow, "The PTCR Effect in BaTiO_3 ," *Br. Ceram. Proc.*, Vol. 36, pg. 187-199 (1985).
10. G. V. Lewis and C. R. A. Catlow, "Defect Studies of Doped and Undoped Barium Titanate Using Computer Simulation Techniques," *J. Phys. Chem. Solids*, Vol. 47, No. 1, pg 89-97 (1986).

11. H. M. Chan, M. P. Harmer and D. M. Smyth, "Compensating Defect in Highly Donor-Doped BaTiO₃," *J. Am. Ceram. Soc.*, Vol. 69, No. 6, pg. 507-510 (1986).
12. Y. Chiang and T. Takagi, "Grain-Boundary Chemistry of Barium Titanate and Strontium Titanate: I, High Temperature Equilibrium Space Charge," *J. Am. Ceram. Soc.*, Vol. 73, No. 11, pg. 3278-3285 (1990).
13. S. B. Desu and D. A. Payne, "Interfacial Segregation in Perovskites: III, Microstructure and Electrical Properties," *J. Am. Ceram. Soc.*, Vol. 73, No. 11, pg. 3407-3415 (1990).
14. B. M. Kulwicki and A. J. Purdes, "Diffusion Potentials in BaTiO₃ and the Theory of PTC Materials," *Ferroelectrics*, Vol 1, No. 4, pg 253-263 (1970).
15. W. T. Peria, W. R. Bratschun and R. D. Fenity, "Possible Explanation of Positive Temperature Coefficient in Resistivity of Semiconducting Ferroelectrics," *J. Am. Ceram. Soc.*, Vol. 44, No. 5, pg. 249-250 (1961).
16. R.D. Roseman, "Domain And Grain Boundary Structural Effects On The Resistivity Behavior In Donor Doped, PTCR Barium Titanate," Ph.D. Thesis, University of Illinois (1993).
17. H. B. Haanstra and H. Ihrig, "Transmission Electron Microscopy at Grain Boundaries of PTC-Type BaTiO₃ Ceramics," *J. Am. Ceram. Soc.*, Vol. 63, No. 5-6, pg. 288-291 (1980).

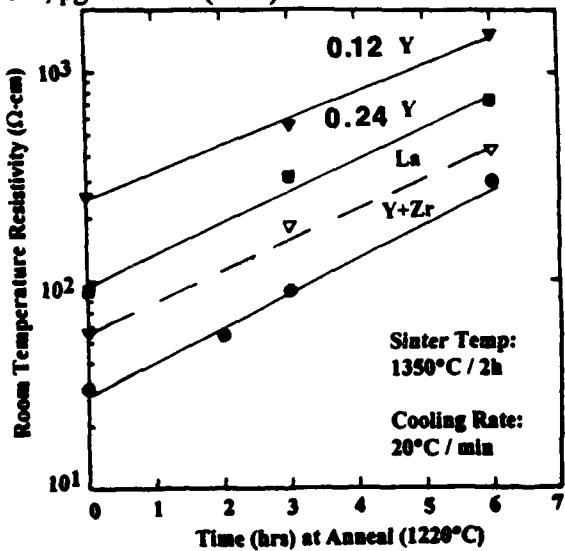


Figure 1. Resistivity below T_c as a function of time at anneal (1220°C), and as a function of dopant type and concentration (mol %).



Figure 2. Polished and etched SEM micrographs comparing the domain structures of: A) unmodified BaTiO₃ and B) donor doped BaTiO₃.

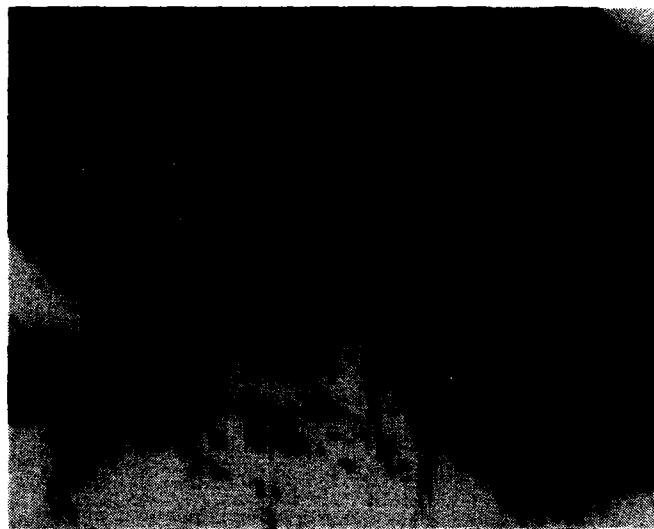


Figure 3. TEM image of non-annealed, donor doped BaTiO₃, showing unidirectional domain structure extending from the grain interior up to the grain boundary.



Figure 4. TEM image of annealed donor doped sample. A complex grain boundary structure in which a finer domain width along with regions of no-domain structure are found.



Figure 5. HREM images of the grain boundary, showing regions in which: (A) the domain structure is common to the boundary; and, (B) an area of no-domain across from a domain region.

MICROSTRUCTURAL AND COMPOSITIONAL ANALYSES ON GRAIN BOUNDARY OF LOW-TEMPERATURE SINTERED Pb(Zr,Ti)O₃ CERAMICS

Dunzhuo Dong,¹ Kenji Murakami,² Nagaya Okada,² and Shoji Kaneko³

¹Graduate School of Electronic Science and Technology, ²Research Institute of Electronics, and ³Department of Materials Science and Technology, Shizuoka University, 3-5-1 Johoku, Hamamatsu 432, Japan

Abstract

The addition of the complex oxides, BiFeO₃ and Ba(Cu_{0.5}W_{0.5})O₃, lowered the sintering temperature and improved the electrical properties of 0.5wt% MnO₂-added Pb(Zr_{0.53}Ti_{0.47})O₃. The characterization of the ceramic bodies using DTA, XRD, SEM, TEM and EPMA suggests an existence of transient liquid phase in the ceramics and this phase may play an important role for lowering the sintering temperature.

INTRODUCTION

Lowering the sintering temperature of Pb(Zr, Ti)O₃ ceramics has been attempted to avoid the volatilization of PbO component which causes the compositional fluctuation and the environmental contamination. Many researchers have reported the low temperature sintering of this ceramics by using the different methods such as the adoptions of additives to form liquid phase¹⁻⁷⁾ and to enhance solid state sintering,^{8, 9)} and fine grained powders as starting material¹⁰⁻¹³⁾ or the hot-pressing sintering¹⁴⁾. Smith et al.¹⁵⁾ have shown that the BiFeO₃-Pb(Zr, Ti)O₃ system was hot-pressed at a temperature between 750°C and 900°C. It has been also reported that another perovskite-type, Ba(Cu_{0.5}W_{0.5})O₃, was used to reduce the sintering temperature of Pb(Fe_{0.5}Nb_{0.5})O₃ ceramics as well as to improve the dielectric properties.¹⁶⁾

The authors have attempted a combined use of two additives, BiFeO₃ (abbreviated as BF) and Ba(Cu_{0.5}W_{0.5})O₃ (BCW), in 0.5wt% MnO₂-added Pb(Zr_{0.53}Ti_{0.47})O₃ (PZT) ceramics and succeeded to lower its sintering temperature down to 935°C.^{17, 18)}

To the extent authorized under the laws of the United States of America, all copyright interests in this publication are the property of The American Ceramic Society. Any duplication, reproduction, or republication of this publication or any part thereof, without the express written consent of The American Ceramic Society or fee paid to the Copyright Clearance Center, is prohibited.

Furthermore, the low-temperature sintered ceramics showed no deterioration of the dielectric and piezoelectric properties, and the addition of extra CuO resulted in the improvement of the piezoelectric properties.

In this paper, the effects of two additives such as BF and BCW on the sintering temperature are discussed. The dielectric and piezoelectric properties of the PZT ceramics, and the results of the microstructural and compositional analyses on the PZT ceramics are also described.

EXPERIMENTAL

Sample Preparation

The samples were prepared by using a conventional method of ceramic engineering. The commercially available Pb_3O_4 , ZrO_2 , TiO_2 , BaCO_3 , CuO , WO_3 , Bi_2O_3 , Fe_2O_3 and MnO_2 (>99.0% purity) were used, and PZT and BCW were separately synthesized by heating the corresponding sources at 870°C for 2h followed by pulverizing. All PZT, BCW, Bi_2O_3 , Fe_2O_3 and CuO were weighed according to the formula: (1-x-y)PZT-xBF-yBCW, and then mixed. Disk samples with 10 mm in diameter and 3 mm in thickness were formed at the pressure of 800 kg/cm² and sintered isothermally at a temperature between 870°C and 1250°C (a heating rate of 5°C/min) for 30 min. Electrical contacts were made with a silver paste. The silver coating was made on both sides of the sample and subsequently fired at 780°C for 20 min.

Measurement

The dielectric and piezoelectric properties of samples were measured after being polarized under 3-4 kV/mm bias at 120°C in a silicone oil bath for 15 min. The electromechanical characteristics were calculated from the resonance measurements,¹⁹⁾ and the dielectric properties were examined by a LCR low-frequency bridge (1kHz). The bulk density, ρ (g/cm³), was measured by the Archimedes method using the following equation:

$$\rho = W_1 / (W_2 - W_3)$$

where W_1 , W_2 and W_3 are the weights of the dry sample, of the same sample saturated with water and of the same sample suspended in water, respectively.

Characterization

A Rigaku RAD-B X-ray diffractometer (XRD) and a Shimadzu DT-30B differential thermal analyzer (DTA) were used to determine the phase relations of sintered

body. The morphology and the composition of the ceramics were analyzed by a JEOL JSM-T330A scanning electron microscope (SEM) and a Shimadzu EPMA-8705 electron probe microanalyzer (EPMA), respectively. The microstructure was observed by a JEOL JEM-2000FX II transmission electron microscope (TEM).

RESULTS

The Effect of BiFeO_3 and $\text{Ba}(\text{Cu}_{0.5}\text{W}_{0.5})\text{O}_3$ Addition

In order to determine the sintering temperature and time of the PZT ceramics, the bulk density of 0.90PZT-0.05BF-0.05BCW ceramics was measured as a function of the sintering time (10-80 min) at different temperatures (880-940°C). The results indicate that the bulk density increases with the sintering time. A saturation effect was observed after 30 min at each temperature, while the saturated value reached maximum above 935°C. Thus, the optimum sintering temperature and time were determined to be 935°C and 30 min, respectively. The sintering time was fixed on 30 min throughout the present experiment.

Firstly, the amount of BCW was fixed on 5 mol% as reported in the case of $\text{Pb}(\text{Fe}_{0.5}\text{Nb}_{0.5})\text{O}_3$ ceramics.¹⁶ The sintering temperature and electrical properties of the ceramics were measured as a function of the amount of BF added and the optimum amount of BF was determined based on the minimum dissipation factor, $\tan \delta$, and maximum values of piezoelectric properties. Secondly, the amount of BF was fixed on the above optimum amount. The amount of BCW was determined in the same way. As a result of this preparation procedure, the optimum composition of the PZT ceramics with complex oxide additives was obtained to be 0.92PZT-0.05BF-0.03BCW (abbreviated as PZT-C) and the sintering temperature was lowered down to 935°C. Finally, the effect of extra CuO addition was investigated because the reaction of CuO in the synthesis of BCW was limited. The piezoelectric properties were very sensitive to a small amount of CuO added, while the dielectric properties were not changed. The results gave the PZT-C with 0.08 wt% CuO

Table I. Summary of the electrical properties of various PZT ceramics.

Sample	Sintering temp., time	$\epsilon^{T_{33}}/\epsilon_0$	$\tan \delta$	T_c	K_p	Q_m	d_{33} ($\times 10^{-12}\text{C/N}$)	Density (g/cm^3)
PZT	1250°C, 30 min	910	1.2	362	51.7	314	210	7.59
PZT-C	935°C, 30 min	847	1.1	290	41.0	670	201	7.65
PZT-C'	935°C, 30 min	850	1.0	290	47.0	950	236	7.66

(PZT-C'). Table I compares the sintering temperature and the electrical properties among PZT, PZT-C and PZT-C' ceramics, where $\epsilon_{33}'/\epsilon_0$ is relative dielectric constant, T_c Curie point, K_p electromechanical coupling factor, Q_m mechanical quality factor and d_{33} piezoelectric constant.

Characterization

The XRD pattern of PZT-C' ceramics corresponds completely to that of $\text{Pb}(\text{Zr}_{0.52}\text{Ti}_{0.48})\text{O}_3$ solid solution,²⁰ as shown in Figure 1. Additional phases originating from BF^{21} , BCW^{22} or CuO^{23} were not observed. This observation is consistent with the PZT-C' ceramics. Figure 2 shows the SEM micrographs of the PZT and PZT-C' ceramics. The micrographs give clear images of grains in the sintered bodies. The PZT-C' ceramics is composed of dense grains with 2 μm to 5 μm in diameter. Surprisingly, the grain size of the PZT-C' is larger than that of the PZT ceramics in spite of the sintering temperature which is lowered to 935°C from 1250°C.

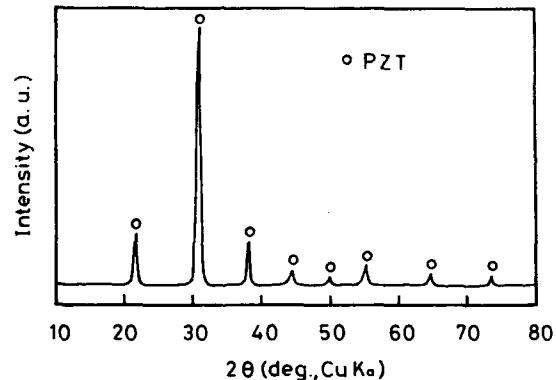


Figure 1 XRD pattern of PZT-C' ceramics.

The elemental analysis of the ceramics using EPMA indicated that no segregation of any element had occurred. Each element seems to distribute homogeneously within a resolution of this method.

Grain boundaries of the PZT-C' ceramics was observed by TEM and its micrographs are shown in Figure 3. The micrographs indicate again the dense grains. More detailed observation (Figure 3 (b)) suggests an existence of the isolated microstructures at the grain boundaries. Furthermore, the qualitative analysis of the composition around the grain boundaries reveals that the lead ion becomes

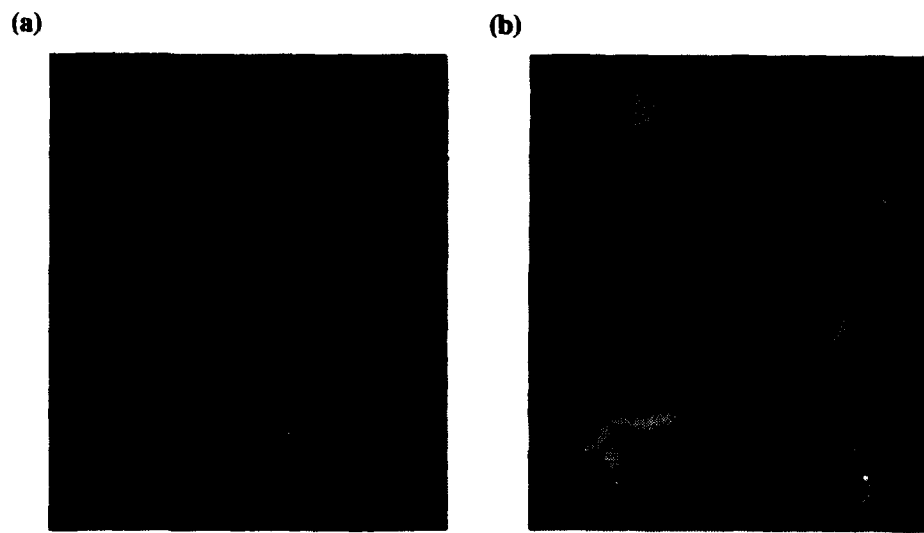


Figure 2 SEM micrographs of (a) PZT and (b) PZT-C' ceramics.

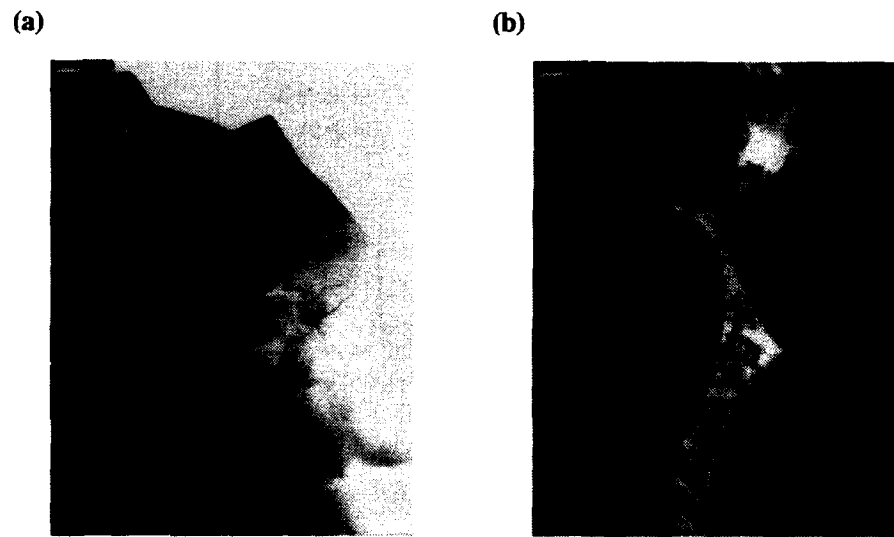


Figure 3 TEM micrographs of PZT-C' ceramics. The grains are clearly imaged in (a) and the detailed microstructure of grain boundaries are shown in (b).

concentrated at the grain boundary and the tendency is more pronounced in the case of the PZT ceramics with complex oxide additives.

DISCUSSION

The addition of the complex oxides caused a drastic reduction in the sintering temperature and an improvement of the properties of the PZT ceramics except for $\epsilon'_{33}/\epsilon_0$, K_p and d_{33} . The extra addition of CuO led to the further improvement of the piezoelectric properties. In order to explain the behavior of BF and BCW in the PZT, the ceramics of different composition, 0.60PZT-0.20BF-0.20BCW, was characterized by XRD and DTA. This ceramics was sintered at a lower temperature (870°C). No XRD pattern was observed originating from BF or other compounds including Bi and/or Fe, as shown in Figure 4, which indicates that the BF forms a solid solution with the PZT ceramics even for the larger concentration of BF, as reported in earlier study.¹⁵⁾ However, the XRD pattern corresponding to BaWO₄ compound²⁴⁾ was detected. The XRD pattern of the synthesized BCW also included the BaWO₄ peaks besides the BCW. Therefore, it seems that in the case of the larger amount of BCW addition, the BaWO₄ compound forms an additional phase besides the PZT ceramics.

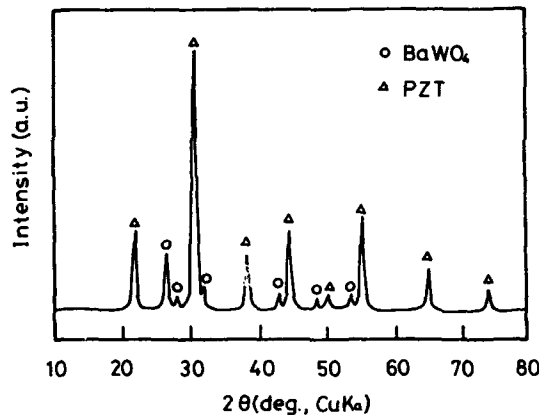


Figure 4 XRD pattern of 0.60PZT-0.20BF-0.20BCW ceramics.

More detailed behavior of BCW is observed in the DTA result of 0.75PZT-0.05BF-0.20BCW ceramics sintered at 875°C. The DTA curve shown in Figure 5 has the broad endothermic peak when heating and exothermic peak when cooling around 920°C. Since the phase diagrams of both PZT and BaWO₄ show that both compounds

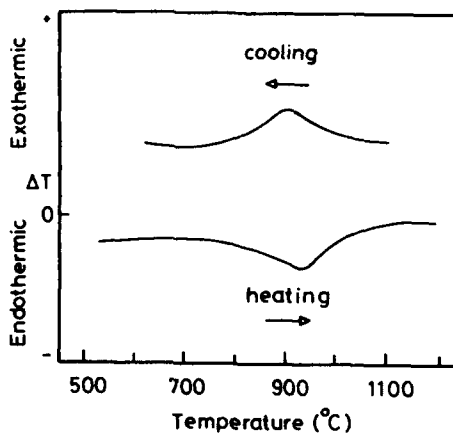


Figure 5 DTA curves of powdered 0.75PZT-0.05BF-0.20BCW ceramics.

are thermally stable at a temperature between 500°C and 1200°C, this result suggests an existence of a different phase, besides the PZT, in the ceramics. It can be deduced that the PZT-C ceramics of the optimum amount of BF and BCW includes the different phase besides the PZT, and that the phase forms the transient phase around 920°C. From the TEM observation, it is also suggested that the different phase is formed at the grain boundaries and includes more lead ions than the grain which is enhanced by the addition of the complex oxides. Thus, the different phase can become the transient liquid phase which may also promote the solidification of the grains even at the lower sintering temperature resulting in the larger grain size, as shown in Figure 2. Therefore, the sintering temperature of the PZT ceramics with the complex oxide is lowered mainly due to the existence of this transient liquid phase.

CONCLUSION

The sintering temperature of the PZT ceramics is successfully lowered by the addition of the complex oxides, BF and BCW, without the deterioration of electrical properties. The XRD and DTA studies indicate that the reduction in this temperature can be related to the existence of the transient liquid phase. The microstructural and compositional analyses reveal that the lead ion becomes concentrated at the grain boundaries and the concentration is enhanced by the addition of the complex oxides. Therefore, the transient phase is formed at the grain boundaries and includes more lead ions than the grains, which may also explain the larger grain size at the lower sintering temperature.

Acknowledgments

The authors wish to thank the Hamamatsu Industrial Research Institute and the Shimadzu Analytical Center for the EPMA measurements. The JEOL is also gratefully acknowledged for the sample preparation of TEM.

References

- 1) D.E. Wittmer and R.C. Buchanan, *J. Am. Ceram. Soc.*, **64**, 485-490 (1981).
- 2) S. Takahashi, *Jpn. J. Appl. Phys.*, **19**, 771-772 (1980).
- 3) S.Y. Cheng, S.L. Fu, C.C. Wei and G.M. Ke, *J. Mater. Sci.*, **21**, 571-576 (1986).
- 4) S.Y. Cheng, S.L. Fu and C.C. Wei, *Ceram. Int'l*, **13**, 223-231 (1987).
- 5) Z. Gui, L. Li, S. Gao and X. Zhang, *J. Am. Ceram. Soc.*, **72**, 486-491 (1989).
- 6) Z. Gui, L. Li, S. Gao and X. Zhang, *Ferroelectrics*, **101**, 93-99 (1990).
- 7) L. Li, X. Zhang and J. Chai, *Ferroelectrics*, **101**, 101-108 (1990).
- 8) R.B. Atkin, R.L. Holman and R.M. Fulrath, *J. Am. Ceram. Soc.*, **54**, 113-115 (1971).
- 9) P.G. Lecuta, F. Constantinescu and D. Brab, *J. Am. Ceram. Soc.*, **68**, 533-537 (1985).
- 10) G. Tomandl, A. Stiegelschmitt and R. Böhner, "Science of Ceramics", Vol. **14**, 305-308, Ed. by D. Tayler, The Institute of Ceramics, Stoke-on-Trent (1988).
- 11) J.F.F. Lozano, P. Durán and C. Moure, "Science of Ceramics", Vol. **14**, 897-902, Ed. by D. Tayler, The Institute of Ceramics, Stoke-on-Trent (1988).
- 12) R. Ral, N.M. Gokhale, R. Krishnan and P. Ramakrishnan, *J. Mater. Sci.*, **24**, 2944-2916 (1989).
- 13) T. Yamamoto, *Am. Ceram. Soc. Bull.*, **71**, 978-985 (1992).
- 14) N.D. Patel and P.S. Nicholson, *Am. Ceram. Soc. Bull.*, **65**, 783-787 (1986).
- 15) R.T. Smith, G.D. Achenbach, R. Gerson and W.J. James, *J. Appl. Phys.*, **39**, 70-74 (1968).
- 16) K. Handa, T. Watanabe, Y. Yamashita and M. Harata, *IEEE Trans. Consum. Electron.*, **CE-30**, 342-347 (1984).
- 17) D. Dong, M. Xiong, K. Murakami and S. Kaneko, *Ferroelectrics*, in press.
- 18) D. Dong, K. Murakami, S. Kaneko and M. Xiong, *J. Ceram. Soc. Jpn.*, **101**, 1090-1094 (1993).
- 19) H. Jaffe, T. Kinsley, T.M. Lambert, D. Schwartz, E.A. Gerber and I.E. Fair, *Proc. IRE*, **49**, 1161-1169 (1961).
- 20) JCPDS File, Card No. 33-784.
- 21) JCPDS File, Card No. 20-169.
- 22) JCPDS File, Card No. 38-1378.
- 23) JCPDS File, Card No. 5-0661.
- 24) JCPDS File, Card No. 8-457.

PARTICLE SIZE EFFECT ON THE ROOM TEMPERATURE STRUCTURE OF BARIUM TITANATE.

B.D. Begg, E.R. Vance, D.J. Cassidy, J. Nowotny and S. Blairs*

ANSTO, Advanced Materials, Menai NSW 2234 Australia

*UNSW, School of Materials Science and Engineering, Kensington NSW 2033 Australia

ABSTRACT

X-ray diffraction and electron microscopy indicated that BaTiO_3 powders $\leq 0.19 \mu\text{m}$ in size were fully cubic whilst those $\geq 0.27 \mu\text{m}$ were completely tetragonal (within a 5 % detection limit for cubic material) at room temperature. The tetragonal to cubic transformation temperature was found to be $121 \pm 3^\circ\text{C}$ by differential scanning calorimetry (DSC) for BaTiO_3 powders with a room temperature (c/a) value > 1.006 . No transformation could be detected using DSC for BaTiO_3 particles with a (c/a) ratio < 1.006 at room temperature. BaTiO_3 powder with a particle size ($0.19 \mu\text{m}$) just too small to be tetragonal at room temperature remained cubic down to 80 K. It is concluded that a model based on surface free energy, as previously discussed for the monoclinic to tetragonal transformation at room temperature of fine ZrO_2 particles, is consistent with the experimental data.

INTRODUCTION

Many room temperature properties of BaTiO_3 , such as permittivity and structure, are known to vary with grain size [1,2]. For instance the peak room temperature permittivity occurs for $0.8 \mu\text{m}$ -sized grains, whilst the extent of tetragonal distortion is known to decrease with decreasing particle size [2-4]. Opinions differ however over whether or not this is accompanied by a second orthorhombic structure [3], and if this decrease in tetragonality leads ultimately to a complete transformation to a cubic [2,5] or "pseudocubic" structure [6] for particles below some critical size. Numerous other workers have reported the stabilisation of the cubic structure in fine grained barium titanate without detailing changes in tetragonality with particle size [7-13].

Two models have been proposed to describe the room temperature stabilisation of the cubic structure in fine grained barium titanate. The first, a phenomenological surface layer model [7] requires that a structural transition exists across a particle at room temperature, from an outer cubic surface layer of a fixed thickness, to a tetragonal core, with a gradient of tetragonality existing between these regions. As the grain size decreases, the influence from the tetragonal core also diminishes, until only a stable cubic particle remains.

In the alternative pure phase model, no coexistence of the cubic and tetragonal structures or indeed any significant gradation of tetragonality occurs in any given crystal. Here, two mechanisms have been proposed to explain the room temperature stabilisation of the cubic structure, the first relates to the strains imposed by the presence of lattice hydroxyl ions whilst the second concerns surface effects, each will be dealt with below.

EXPERIMENTAL PROCEDURE

Two BaTiO_3 powders were examined. The first was a commercially prepared hydrothermal powder whilst the second was hydrothermally grown in the present work to an average particle size (0.28

To the extent authorized under the laws of the United States of America, all copyright interests in this publication are the property of The American Ceramic Society. Any duplication, reproduction, or republication of this publication or any part thereof, without the express written consent of The American Ceramic Society or fee paid to the Copyright Clearance Center, is prohibited.

$\pm 0.05 \mu\text{m}$). Here 0.03 moles each of a hydrolysed titanium alkoxide precursor and barium hydroxide were added to 30 ml of demineralised/deionised water and placed inside a 71 ml unstirred pressure vessel and heated at 5°C/min to a 300°C and held for 5 days. The sample was removed from the vessel after cooling and washed free of BaCO_3 and unreacted Ba(OH)_2 .

Room temperature X-ray diffraction (XRD) of mainly the (002,200) and (004,400) reflections of BaTiO_3 was studied (Co $\text{K}\alpha$ radiation). Low-temperature (80 K) XRD measurements of the same reflections were also performed. Certain XRD profiles were fitted using the XRAYFIT 287 diffraction fitting program [14]. Particle sizes were determined with a JEOL JXA-840 scanning electron microscope running at 15 keV. Fresh commercial hydrothermal BaTiO_3 powder was also examined with a high-resolution JEOL 2000 FX transmission electron microscope run at 200 keV. To obtain a representative average particle size and spread, at least 100 particles were individually measured with the aid of an image analysis program. Differential thermal and thermal gravimetric analysis (DTA/TGA), plus differential scanning calorimetry (DSC), were carried out on ~ 100 mg samples in air with a Setaram TAG-24 Thermal Analyser, using $\alpha\text{-Al}_2\text{O}_3$ as the reference material. A heating rate of 10°C/min to 1200°C was employed. DSC measurements were made on commercial hydrothermal BaTiO_3 powders sintered in air at 900°C for 0.5, 3, 8, 15 and 30 hours or 1200°C for 0.5 hour. The closed nature of the DSC apparatus permitted a slower heating rate of 5°C/min to be used. Infrared emission spectra from the as-received commercial and laboratory-grown hydrothermal BaTiO_3 samples were collected at 100°C intervals between 300°C and 700°C using a modified Digilab FTS-7 spectrometer over the range 4000 - 400 cm^{-1} (nominal resolution of 4 cm^{-1}).

RESULTS AND DISCUSSION

The as-received commercial hydrothermal powder ($0.19 \pm 0.05 \mu\text{m}$) exhibited a symmetrical (200) XRD reflection, characteristic of a cubic structure (see figure 3 below). Sintering this commercial hydrothermal BaTiO_3 powder to larger particle sizes saw the development of an asymmetric (002,200) peak for a $0.27 \pm 0.05 \mu\text{m}$ powder which indicated a slight tetragonal distortion ($c/a = 1.0045$). As the particle size increased further ($0.29 - 0.63 \mu\text{m}$) so too did the level of tetragonal distortion, as seen by the increased splitting of the (002,200) tetragonal peaks.

Whilst the tetragonal distortion ($c/a = 1.0045$) in the $0.27 \mu\text{m}$ commercial hydrothermal BaTiO_3 powder may be seen in the asymmetry of the (002,200) reflections (figure 1), it would be difficult on first glance to exclude the presence of any cubic material in this powder. To determine whether or not this $0.27 \mu\text{m}$ powder was completely tetragonal, the diffraction profile was fitted with two (002,200) tetragonal peaks (figure 1). It was assumed that the XRD powder sample was not preferentially oriented in any manner and so the fitting parameters were constrained such that the area of the (002) peak was half that of the (200) peak.

The excellent nature of the fit indicates that the $0.27 \mu\text{m}$ commercial hydrothermal BaTiO_3 powder was totally tetragonal. Similarly the (202,220) reflections from the same powder were also successfully fitted in a constrained 2:1 ratio which confirmed the random orientation of the powder.

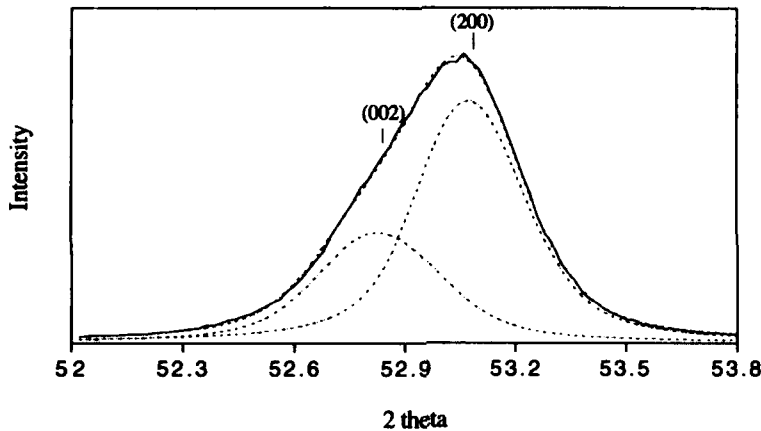


Figure 1. Comparison of the room temperature X-ray diffractogram of (002,200) reflections from commercial hydrothermal BaTiO_3 powder ($c/a = 1.0045$) of $0.27\text{ }\mu\text{m}$ particle size using $\text{Co K}\alpha$ radiation (solid line) with the fitted overall and deconvoluted (002,200) reflections (dotted lines) corresponding to a completely tetragonal powder. The areas of the fitted (002) and (200) peaks were constrained in a 1:2 ratio. All peaks include $\text{K}\alpha 2$ radiation.

The influence of particle size on the room temperature tetragonal distortion of barium titanate has been summarised in figure 2. All commercial hydrothermal barium titanate powders sintered larger than $0.27\text{ }\mu\text{m}$ were completely tetragonal although the extent of the tetragonal distortion varied with particle size. Previously reported data are also shown [2-4].

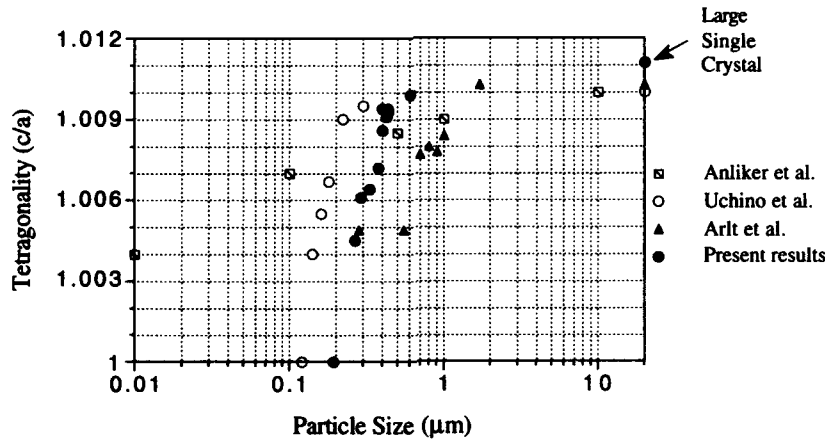


Figure 2. Comparison of the present room temperature tetragonality versus particle size results for commercial hydrothermal barium titanate powder with those previously reported in the literature [2-4].

The present results differ from those of Anliker *et al.* [4] who did not observe room temperature stabilisation of the cubic form and from those of Arlt *et al.* [3] who reported the presence of the orthorhombic structure in fine-grained barium titanate. Our results however are essentially consistent with those of Uchino *et al.* [2] who observed a similar trend of decreasing tetragonality with reducing particle size, with no evidence of the orthorhombic form, leading to the stabilisation of the cubic structure for particles smaller than $0.12\text{ }\mu\text{m}$.

XRD of the (002,200) reflections from our ($\sim 0.28\text{ }\mu\text{m}$) hydrothermally grown (titanium alkoxide-based) BaTiO_3 powder showed that it was tetragonal with $(c/a) = 1.0048$. This result was consistent with the other results obtained from commercial hydrothermal BaTiO_3 powders (figure 2).

The phenomenological surface layer model is now considered. The single-phase nature of individual commercial hydrothermal BaTiO_3 powders (whether totally cubic or completely tetragonal) appears to be in agreement with the proposed pure phase model. However if a cubic surface layer was present, as required by the phenomenological surface layer model, the question of its detection by XRD must be addressed. In the present work the diameter of the largest cubic hydrothermal BaTiO_3 particles was $0.19\text{ }\mu\text{m}$ (see above). Thus the thickness of the proposed [7] cubic surface layer would be $0.095\text{ }\mu\text{m}$. Using a simple volume calculation (based on spherical particles and a cubic surface layer thickness of $0.095\text{ }\mu\text{m}$), the proportion of cubic material in a $0.6\text{ }\mu\text{m}$ BaTiO_3 powder, which the present XRD measurements indicate approaches full tetragonality ($c/a = 1.0099$, figure 2), was calculated to be $\approx 68\%$ cubic.

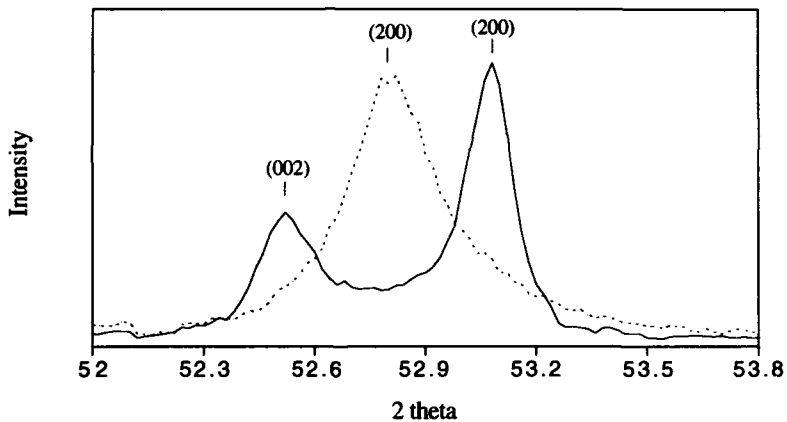


Figure 3. Comparison of room temperature X-ray diffractograms, (002,200) reflections, from $0.61\text{ }\mu\text{m}$ commercial hydrothermal BaTiO_3 powder ($c/a=1.0099$, solid line) and (200) reflection from as-received $0.19\text{ }\mu\text{m}$ cubic powder (dotted line) using $\text{Co K}\alpha$ radiation. Both patterns have been stripped of the $\text{K}\alpha 2$ component. The greater width of the reflection for the cubic powder is due to particle size broadening.

The diffraction patterns from this $0.6\text{ }\mu\text{m}$ tetragonal powder and that of the $0.19\text{ }\mu\text{m}$ fully-cubic hydrothermal material are shown in figure 3. The degeneracy of the symmetrical cubic structure combined with its position between the split (002) and (200) tetragonal peaks should allow the cubic structure to be readily detected in the $0.6\text{ }\mu\text{m}$ powder if it were present at volume percentages $>5\%$. Failure to observe a cubic component in samples $>0.19\text{ }\mu\text{m}$ in size indicates that the cubic

surface layer model as it stands is not a feasible explanation for room temperature stabilisation of the cubic structure. This however does not exclude the absolute existence of a cubic surface layer, but rather only limits its possible influence to the outer particle layers (~ 5 nm). In this connection, it has been postulated from electrical measurements that structural reordering, induced by changes of oxygen activity, takes place in the outermost layers of undoped BaTiO_3 [15] however no effect was observed in parallel XRD measurements, so again the altered layer would have to be very thin.

Possible mechanisms for the room temperature transformation are now discussed.

i) Hydroxyl Ions. Room temperature stabilisation of the cubic structure in fine-grained hydrothermally-prepared barium titanate has been attributed to lattice strains associated with partial retention of hydroxyl ions and their compensating cation vacancies [8]. In the present study the concentration of lattice hydroxyl ions was determined by FTIR and DTA/TGA. In situ FTIR measurements carried out on the as-received cubic commercial BaTiO_3 sample between 300°C and 700°C are shown in figure 4. The peak at a wavenumber of $\sim 1400 \text{ cm}^{-1}$ is characteristic of carbonate whilst the smaller peak at $\sim 3500 \text{ cm}^{-1}$ corresponds to hydroxyl ions. At 300°C the hydroxyl peak is set in a very broad background of hydrogen-bonded water. This broad background is considerably reduced by 400°C and totally removed by 500°C. Carbonate is lost between 600°C and 700°C whilst hydroxyl ions are lost between 400°C and 700°C.

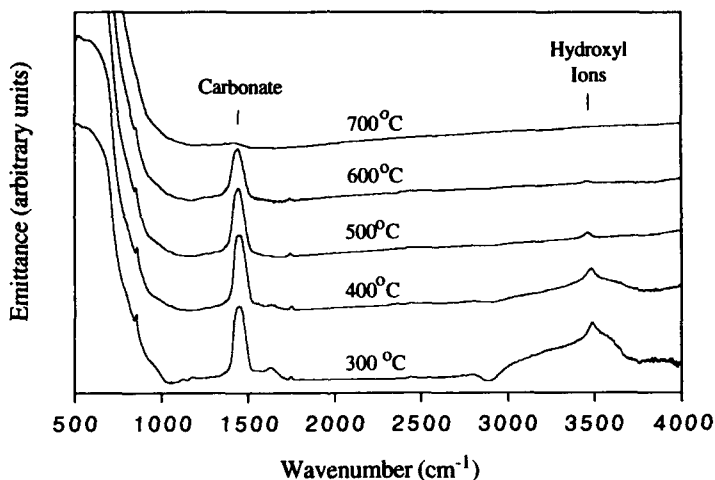


Figure 4. *In situ* FTIR analysis of the as-received commercial hydrothermal BaTiO_3 between 300°C and 700°C.

To quantify these FTIR data, DTA/TGA analysis was carried out on the cubic commercial hydrothermal BaTiO_3 sample (which had subsequently been washed free of carbonate with nitric acid) to determine the weight loss between 400 and 700°C and therefore the concentration of lattice hydroxyl ions. TGA analysis from this BaTiO_3 powder showed a 0.94 % weight loss between 400°C and 700°C may be attributed to the loss of (1.8 %) lattice hydroxyl ions via the $2\text{OH}^- \rightarrow \text{H}_2\text{O}_{(g)} + \text{O}^{2-}$ reaction.

In situ FTIR results from our (nitric acid washed) fresh tetragonal hydrothermally-prepared BaTiO_3 (alkoxide-based) sample indicated that it also contained a significant concentration of hydroxyl

ions, which were similarly removed from the lattice between 400°C and 700°C. TGA results indicated that the concentration of lattice hydroxyl ions was ~2.5 %.

The ability to prepare a tetragonal hydrothermal barium titanate powder with a hydroxyl concentration exceeding that of the commercial cubic-stabilised material (2.5 % and 1.7 % respectively) indicates that hydroxyl ions and associated lattice strains (arising from compensating cation vacancies) are not responsible for room temperature stabilisation of the cubic structure. Vivekandan and Kutty [8] had previously concluded that the stabilisation of the cubic structure resulted from the retention of lattice hydroxyl ions and their compensating cation vacancies, despite the fact that their powders remained cubic after the hydroxyl ions had been removed.

ii) Surface Effects. Surface tension is one size-related mechanism that has been proposed to explain room temperature stabilisation of the cubic structure [2,5]. Here, internal hydrostatic pressure resulting from surface tension in a fine powder (< 0.1 μm) is thought to lower the Curie point to just below room temperature and thereby stabilise the cubic structure [2].

Uchino *et al.* [2] attempted to determine the Curie point of BaTiO_3 using variable-temperature XRD. XRD however is a difficult technique for determining the Curie point when, as in the present case, the tetragonal deformation below the Curie point is very small ($(c/a) = 1.0025$). Subjective judgments must be made to determine when slightly asymmetric peaks (angular splitting $\Delta(2\theta) = 0.12^\circ$ for the (002,200) reflections) become sufficiently symmetrical to indicate a cubic structure. This difficulty is compounded for very fine particles, notably those reputedly exhibiting a drastic decrease in Curie point, where particle size-broadening of XRD peaks is significant $\Delta(2\theta) = 0.08^\circ$ for the powder studied by Uchino *et al.* [2] and which exhibited a supposed Curie point of 75°C.

In the present study, DSC measurements were made in an attempt to resolve the relationship between Curie point and tetragonality (figure 5). The commercial hydrothermal BaTiO_3 powders were sintered to different particle sizes and therefore to different room temperature tetragonality ratios (see figure 2).

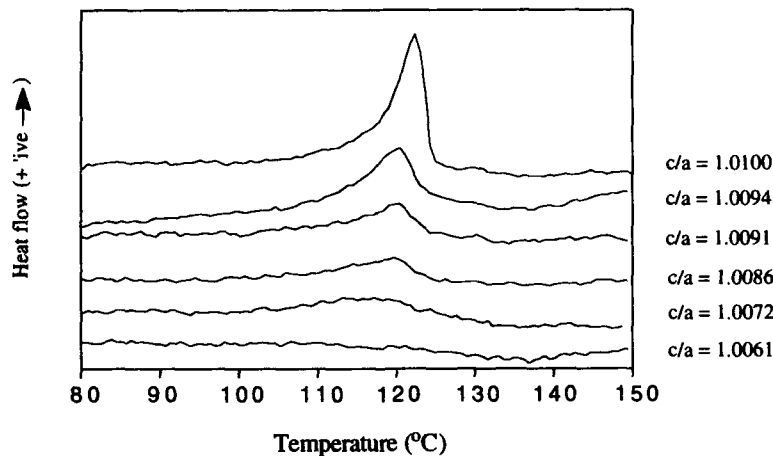


Figure 5. DSC patterns showing transformation temperature of the tetragonal to cubic transformation in commercial hydrothermal BaTiO_3 as a function of tetragonality at room temperature. Each trace has been offset to clarify the diagram.

These DSC results confirm that within experimental error the Curie point remains fixed at $121 \pm 3^\circ\text{C}$ for powders exhibiting a room temperature (c/a) ≥ 1.006 . Unfortunately the present DSC apparatus was not sufficiently sensitive to detect the transformation for materials with (c/a) < 1.006 . The drastic decrease in Curie point with reducing tetragonality reported by Uchino *et al.* [2] for (c/a) ≤ 1.007 could not therefore be confirmed by this method.

Whilst the Curie point was independent of room temperature tetragonality (for powders with a room temperature $c/a > 1.006$), the average enthalpy of the tetragonal to cubic transformation was observed to decrease with decreasing room temperature tetragonal distortion. Since all commercial hydrothermal samples with $c/a > 1.0045$ were completely tetragonal (figure 1), this decrease does not correspond to the proportion of tetragonal material in each sample. Rather it can only refer to the energy required for the tetragonal to cubic transformation to occur, which decreases with decreasing room temperature tetragonality. The transformation enthalpy for the powder with the largest tetragonality ratio compared favourably with the documented value for the BaTiO_3 tetragonal-cubic transformation [16].

A critical experiment to establish the role of surface tension in the room temperature stabilisation of the cubic structure (which Uchino *et al.* [2] did not carry out) was to determine whether the Curie point of cubic BaTiO_3 with a particle size just too small to be tetragonal (in this case $0.19 \mu\text{m}$, figure 2) had been shifted to just below room temperature. Thus XRD at liquid nitrogen temperatures (80 K) was carried out on the as-received $0.19 \mu\text{m}$ commercially-prepared cubic BaTiO_3 powder and the material remained cubic. The Curie point for cubic BaTiO_3 powder (with a particle size just too small to be tetragonal) has not therefore merely been shifted to just below room temperature as proposed by the surface tension mechanism [2]; rather it has decreased drastically to below 80 K or it has vanished altogether.

Surface effects however have also been invoked for stabilising the tetragonal rather than the monoclinic structure at room temperature in very fine-grained zirconia by altering the relative free energies of the two structures [17]. The high specific surface area of very fine particles leads them to possess relatively large amounts of excess surface energy per unit volume when compared to large single crystals. This excess surface energy may differentially contribute to the relative free energies of the tetragonal and cubic structures and possibly lead to room temperature stabilisation of the cubic polymorph. The observed stabilisation of the cubic structure (for a powder $\leq 0.19 \mu\text{m}$) and subsequent increase in tetragonal distortion with increasing particle size for commercial hydrothermal BaTiO_3 at room temperature (figure 2) may be interpreted in terms of the surface energy mechanism.

CONCLUSIONS

The room temperature tetragonality of hydrothermal BaTiO_3 powders which were close to monosized was seen to decrease with decreasing particle size, leading to the stabilisation of the cubic structure at room temperature for particles $0.19 \mu\text{m}$ in size and below. The single phase nature of annealed commercial hydrothermal BaTiO_3 samples irrespective of particle size indicated that the cubic-surface layer model was not appropriate. Whilst XRD is not sensitive enough to rule out the absolute existence of a cubic-surface layer, it does limit its thickness to $< 5 \text{ nm}$.

Hydroxyl ions do not appear to be responsible for stabilising the cubic structure. Present DSC measurements however indicated that the Curie point for powders with a room temperature (c/a) > 1.006 remained fixed at $121 \pm 3^\circ\text{C}$. XRD of a commercial hydrothermal BaTiO_3 powder just too small ($0.19 \mu\text{m}$) to be tetragonal at room temperature revealed that the cubic structure was stable

down to at least 80 K and had not merely been shifted to just below room temperature as proposed elsewhere [2]. Excess surface energy however provides a plausible free energy-based mechanism to explain not only the room temperature stabilisation of the cubic structure in fine-grained BaTiO₃, but also the decreasing relationship between tetragonality and particle size.

ACKNOWLEDGMENTS

We wish to thank R.L. Davis for assistance with the low-temperature X-ray diffraction experiments, K. Finnie for the FTIR results and C.J. Ball for assistance with XRD peak profile fitting.

REFERENCES

1. K. Kinoshita and A. Yamaji, "Grain-size effects on dielectric properties in barium titanate ceramics", *J. Appl. Phys.*, **47** [1] 371-73 (1976).
2. K. Uchino, E. Sadanaga and T. Hirose, "Dependence of the Crystal Structure on Particle Size in Barium Titanate", *J. Am. Ceram. Soc.*, **72** [8] 1555-58 (1989).
3. G. Arlt, D. Hennings and G. de With, "Dielectric properties of fine-grained barium titanate ceramics", *J. Appl. Phys.*, **58** [4] 1619-25 (1985).
4. M. Anliker, H.R. Brugger and W. Kanzig, "Das Verhalten von kolloidalen Seignettelektrika III, Bariumtitanat BaTiO₃", *Hoch. Phys. Acta.*, **27**, 99-124 (1954).
5. K. Uchino, N. Lee, T. Toba, N. Usuki, H. Aburatani and Y. Ito, "Changes in the Crystal Structure of RF-Magnetron Sputtered BaTiO₃ Thin Films", *J. Ceram. Soc. Japan*, **100** [9] 1091-93 (1992).
6. D. Hennings, "Barium Titanate Based Ceramic Materials for Dielectric Use", *Int. J. High Technology Ceramics*, **3**, 91-111 (1987).
7. S. Malbe, J.C. Mutin and J.C. Nippe, "Distribution des paramètres de maille cristalline dans des échantillons pulvérulents de BaTiO₃", *J. Chim. Phys.*, **89**, 825-43 (1992).
8. R. Vivekanandan and T.R.N. Kutty, "Characterization of barium Titanate Fine Powders Formed From hydrothermal Crystallization", *Powder Technology* **57**, 181-92 (1989).
9. F. Yen, C.T. Chang and Y. Chang, "Characterisation of Barium Titanyl Oxalate Tetrahydrate", *J. Am. Ceram. Soc.*, **73** [11] 3422-27 (1970).
10. J.P. Coutures, P. Odier and C. Proust, "Barium Titanate Formation by Organic Resins Formed with Mixed Citrate", *J. Mater. Sci.*, **27** [7] 1849-56 (1992).
11. J.M. Criado, M.J. Díanez, F. Gotor, C. Real, M. Mundi, S. Ramos and J. Del Cerro, "Correlation between Synthesis Conditions, Coherently Diffracting Domain Size and Cubic Phase Stabilisation in Barium Titanate", *Ferroelectric Letters* **14**, 79-84 (1992).
12. S. Naka, F. Nakakita, Y. Suwa and M. Inagaki, "Change from Metastable Cubic to Stable Tetragonal Form of Submicron Barium Titanate", *Bull. Chem. Soc. Jpn.*, **47** [5] 1168-71 (1974).
13. G.H. Jonker and W. Noorlander, "Grain Size of Sintered Barium Titanate", pp. 255-64 in *Science of Ceramics Vol 1*. Edited by G.H. Stewart. Academic Press Inc., New York 1962.
14. R.W. Cheary and A. Coelho, "A fundamental parameters approach to X-ray line-profile fitting", *J. Appl. Cryst.*, **25** [2] 109-21 (1992).
15. J. Nowotny and M. Sloma, "Surface Electrical Properties of BaTiO₃ at Elevated Temperatures", *Solid State Ionics* **49**, 129-133 [1991].
16. I. Barin, *Thermochemical Data of Pure Substances*, VCH, Weinheim, 1989.
17. R.C. Garvie, "The Occurrence of Metastable Tetragonal Zirconia as a Crystallite Size Effect", *J. Phys. Chem.*, **69** [4] 1238-43 (1965).

Influence on the Grain Boundary Interfacial Trap Levels in (Ba_{0.76}Sr_{0.24})TiO₃-based PTCR Ceramics by Oxidative Annealing

Myung Chul Kim, Soo Hyung Hur*, Soon Ja Park*, Department of Materials Science and Engineering, Kunsan National University, Kunsan 573-360, Korea,

*Department of Inorganic Materials Engineering, Seoul National University, Seoul, Korea

<ABSTRACT>

In order to investigate the grain boundary trap levels I-VTS(Isothermal capacitance transient Spectroscopy) measurements were performed at the temperature range of 25 °C and 50 °C for the slowly cooled (Ba_{0.76}Sr_{0.24})TiO₃ based PTCR ceramics. The grain boundary resistivity was greatly increased by slowly oxidative cooling and the grain boundary interfacial traps at -0.36, -0.43 and -0.46 eV below conduction band edge were evaluated. The longer cooling schedule in air leaded to the deepening of trap levels and the increase of trap populations in the grain boundary interface.

1. INTRODUCTION

BaTiO₃-based PTCR ceramics have been extensively used in the practical applications such as thermistor and heater because of its outstanding positive temperature coefficient of resistivity and the cause of PTCR(Positive Temperature Coefficient of Resistivity) property has been

To the extent authorized under the laws of the United States of America, all copyright interests in this publication are the property of The American Ceramic Society. Any duplication, reproduction, or republication of this publication or any part thereof, without the express written consent of The American Ceramic Society or fee paid to the Copyright Clearance Center, is prohibited.

intensively investigated in the aspect of the grain boundary resistive phenomena¹⁻³. The Heywang model, which is the most widely accepted one, attributes this phenomena to the existence of a potential barrier arising from the presence of a surface layer of acceptor states. This potential barrier is due to the existence of back-to back double Schottky barriers formed in the grain boundary interface² and so these phenomena can be also described by thermal emission of majority carrier model. The formation of depletion layer at the grain boundary region is attributed to the existence of carrier traps and the populations of traps at grain boundary interfaces. In order to investigate the grain boundary trap levels ICTS(Isothermal capacitance transient Spectroscopy) measurements were performed at the temperature range of 25 °C and 50 °C for the (Ba_{0.76}Sr_{0.24})TiO₃-based PTCR ceramics slowly cooled down such as 30 °C/hr, 20°C/hr and 15 °C/hr, respectively.

2. EXPERIMENTAL PROCEDURE

Commercially available pure BaTiO₃ powders* with 24 mol% SrCO₃**, 0.2 mol% Sb₂O₃**, 0.04 mol% MnO₂**, 0.2 mol% TiO₂**, 0.2 mol% Al₂O₃**, and 0.4 mol% SiO₂** were ball milled for 24 hrs in ethanol media by using polyethylene jar and zirconia balls. The slurry was dried and powders were isostatically pressed into a disk shape of 1/2 inch diameter. Sintering was performed in a Pt boat with cover at 1320 °C for 1 hour in air after heating up at 600 °C/hr and then the cooling schedules were controlled at 100 °C/hr, 30 °C/hr, 20 °C/hr, 15 °C/hr and 10 °C/hr in air. The colors of sintered ceramics were changed from black into brown according to the longer cooling schedule. The average grain sizes were ~15μm under optical microscopy. The sintered pellets of 0.5mm thickness and 8mm diameter were prepared for the measurement of R-T and ICTS spectra. As an ohmic contact electrode material indium containing Ag paste*** was coated on both surfaces of polished pellet. The grain boundary resistivity was evaluated at 10 °C from Cole-Cole plot through the impedance measurement using HP4192A impedance analyzer. Resistance - temperature curve was measured

* HPBT-1, Fujititan Co., Japan

** Demetron, Degussa Co., Germany

*** Purity 99.99 %, Aldrich Co., USA

using HP4140 picoammeter in a temperature programmable chamber.

The ICTS measurements were performed by using HP 4192A and the details of ICTS measuring system is shown everywhere⁴⁻⁶. ICTS is based on the rapid detection of a capacitance with time after applying a pulse injection, followed by emission or capture of electrons at the deep trap levels. The temperature was controlled within 0.2 °C using a cryostat at 20 °C ~ 50 °C. Transient capacitance $C(t)$ was measured at 1000 KHz under zero biased state after applying -30 V DC bias during 30 seconds.

3. RESULTS AND DISCUSSION

The PTCR effects of $(\text{Ba}_{0.76}\text{Sr}_{0.24})\text{TiO}_3$ based PTCR ceramic samples are plotted in Fig.1, in which different cooling schedules are denoted. The room temperature resistivity is greatly increased by the slower oxidative cooling and as a while the resistivity jump becomes smaller. The increase of the maximum(ρ_{\max}) and the minimum(ρ_{\min}) resistivity resulted from annealing treatment and the temperature(T_{\max}) at ρ_{\max} was decreased. It appears that the value of maximum resistivity is almost saturated at the slow cooling rate(10 °C/hr) as shown in the relationship between ρ_{\max} and T_{\max} of Fig.2.

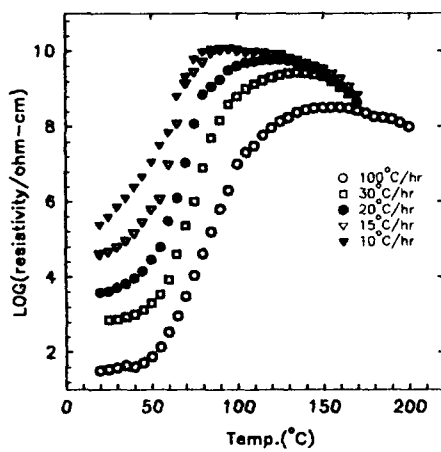


Figure 1. R - T relationship in $(\text{Ba}_{0.76}\text{Sr}_{0.24})\text{TiO}_3$ based PTCR ceramics

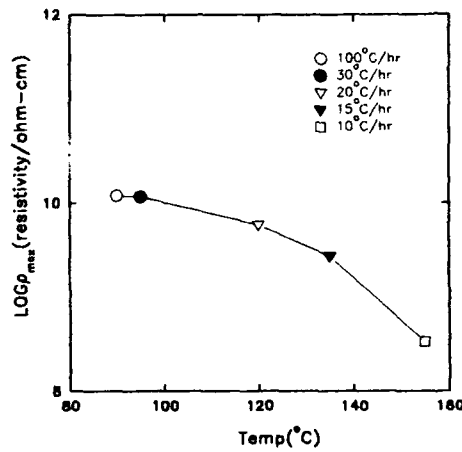


Figure 2. Maximum resistivity versus temperature at the maximum resistivity for the R-T curves of Fig.1.

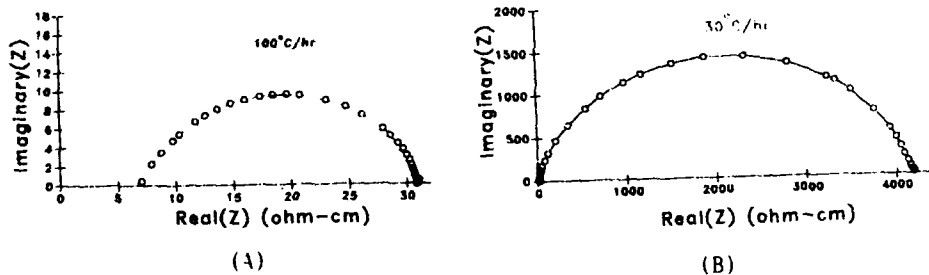
According to Heywang⁷, the resistivity obeys following equation:

$$\rho = \rho_0 \exp(e\phi_0/kT) \quad (1)$$

where ρ_0 is the grain resistivity, α a factor for geometrical configuration, and k the Boltzman constant. For the Heywang model explaining the presence of the two dimensional layer of acceptor states at the grain boundary, the acceptors attract electrons from the bulk resulting in a buildup of a potential barrier. This potential barrier is described by

$$\phi_0 = \frac{eN_s^2}{8\epsilon_0\epsilon_s N_d} \quad (2)$$

where N_s is the number of electrons trapped at the grain boundary, e the electron charge, ϵ_0 the permittivity in free space, ϵ_s the permittivity in the grain boundary region, and N_d the bulk charge carrier concentration. Compared with the previously calculated ρ_{max} vs T_{max} plots for the annealed samples in BaTiO₃-PTCR ceramics by Al-Allak et. al.⁸ these (Ba,Sr)TiO₃ - based PTCR samples show the higher acceptor concentrations and the higher energy levels, indicative to the Mn doping effect.



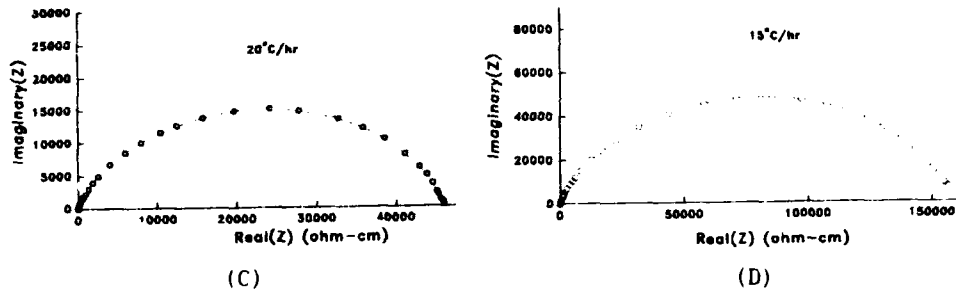


Figure 3. Cole-Cole plots for $(\text{Ba}_{0.76}\text{Sr}_{0.24})\text{TiO}_3$ -based PTCR ceramics cooled down with 100 $^{\circ}\text{C}/\text{hr}$ (A), 30 $^{\circ}\text{C}/\text{hr}$ (B), 20 $^{\circ}\text{C}/\text{hr}$ (C) and 15 $^{\circ}\text{C}/\text{hr}$ (D) in air.

The increase of room temperature resistivity with slow cooling is caused by the increase of grain boundary resistivity as can be seen from impedance plots of Fig. 3. The grain boundary resistivity is evaluated as 24 $\Omega\cdot\text{cm}$ (A) for the sample cooled down as 100 $^{\circ}\text{C}/\text{hr}$, 4.32 $\text{k}\Omega\cdot\text{cm}$ (B) for 30 $^{\circ}\text{C}/\text{hr}$, 45.98 $\text{k}\Omega\cdot\text{cm}$ (C) for 20 $^{\circ}\text{C}/\text{hr}$ and 156.43 $\text{k}\Omega\cdot\text{cm}$ (D) for 15 $^{\circ}\text{C}/\text{hr}$.

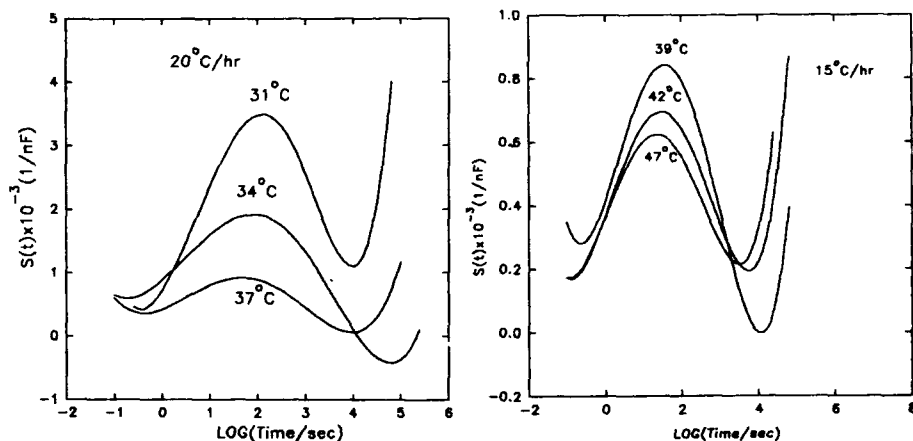


Figure 4. Typical data $S(t)$ of ICTS signal analyzed from transient capacitance data $C(t)$ for the samples which are sintered at 1320 $^{\circ}\text{C}$ for 1 hour and cooled down at 20 $^{\circ}\text{C}/\text{hr}$ (A) and 15 $^{\circ}\text{C}/\text{hr}$ (B) in air.

For the above all samples we could detect the existence of the grain boundary traps which are characterized by the reverse change of transient capacitance $C(t)$ according to the voltage bias sign.⁴ Figure 4(A) and (B) show the typical ICTS spectra $S(t)$ for the samples which are slowly cooled in oxidative atmosphere as 20 °C/hr and 15 °C/hr, respectively. In the temperature range of 20 °C to 50 °C, the acceptor-like interface trap levels are detected as like as can be conformed from the positive curve of $S(t)$. Time constant decreases with temperature increase due to the thermally activated emission of carriers localized in trap centers and the peak value of $S(t)$ spectra also decreases, indicative to the decrease of trap populations.

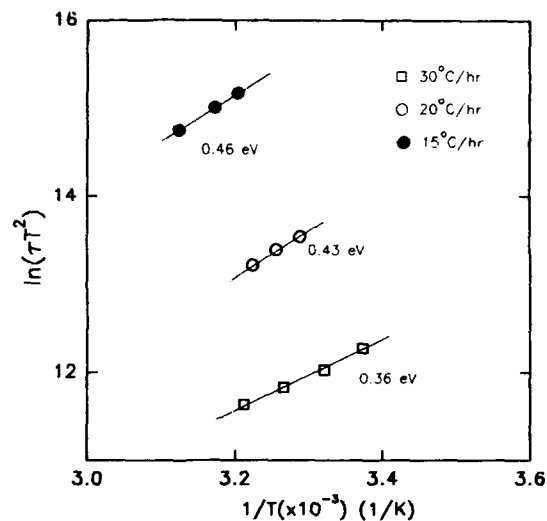


Figure 5. Arrhenius plots of $\ln(\tau T^2)$ vs $1000/T$ for the samples cooled down at 30 °C/hr, 20 °C/hr and 15 °C/hr.

The Arrhenius plots of $\ln(\tau T^2)$ vs $1/T$ are derived from Fig.4 and the slope of Fig.5 gives the activation energy levels of the localized trap. The trap levels of -0.36 eV, -0.43 eV and -0.46 eV below conduction band edge were evaluated at 25 °C ~ 40 °C for the samples at the cooling rate of 30 °C/hr, 20 °C/hr and 15 °C/hr, respectively. The changes of three trap levels with cooling schedules in air show the deepening of trap

levels and the increase of trap concentrations. It has been said⁸⁻¹² that segregation of acceptor impurities followed by oxidation leads to the insulating type behavior at the grain boundary interface, that is, the increase of grain boundary resistivity. There have been some reports explaining the existence of acceptor segregation. Main Mn defect centers in oxidized MnO_2 doped $BaTiO_3$ are known to be $Mn^{3+}(3d^3)$ and $Mn^{4+}(3d^4)$ through the measurement of magnetic susceptibility¹³. Chiang et.al¹¹, observed the segregation of acceptor Mn through STEM analysis in $Ba_{1.00}Nb_{0.02}Ti_{1.00}Mn_{0.02}O_x$ and they said that this segregation is consistent with the majority being of 4+ valence and a minor fraction being in a more reduced acceptor state. Wakino et.al.¹⁴ confirmed that Mn ion in $BaTiO_3$ -PTCR ceramics acts as an acceptor which compensates the electron provided by Nb through the ESR analysis. The deeper interface level results from the severe oxidation treatment, leading to the formation of oxidized defect centers such as $Mn_{Ti}^{+}(Mn^{3+})$ or $Mn_{Ti}^{+}(Mn^{4+})$. In relation with the formation of deep trap centers in the grain boundary, it may be said that the competition between trap energy levels and trap populations influences strongly the PTCR property.

4. CONCLUSION

Long annealing in air contributed to both the increase of energy levels and the trap populations in the formation of the grain boundary interfacial traps in $(Ba_{0.76}Sr_{0.24})TiO_3$ based PTCR ceramics. The trap levels were evaluated as -0.36 eV, -0.43 eV and -0.46 eV below conduction band edge for the samples cooled down as 30°C/hr, 20 °C/hr and 15 °C/hr in air, respectively.

References

1. P.W.Haaijman, R.W.Dam, and H.A.Klasens, "Method of Preparation of Semiconducting Materials", Ger. Pat. No. 929350, June 1955
2. W.Heywang, "Barium Titanate as a Semiconductor with Blocking Layers", Solid-State Electronics, 3[1] 51-58(1961)
3. B.Kulwicki, in Advances in Ceramics Vol.1, edited by L.M.Levinson, P138-54 (1981)
4. T.Maeda and M.Takata, "Detection and Characterization of Trap Centers in ZnO Varistor by ICTS", Nippon Seramikusu Kyokai Ronbunshi, 97[10] 1119-28 (1989)
5. E.H.Han, M.C.Kim and S.J.Park, "Evaluation of Deep Trap Levels in Manganese Doped PTCR Ceramics by ICTS", J.Mat.Sci.Lett., 11[1] 1385-88 (1992)
6. H.Okushi, "Localized States in Semiconductors studied by Isothermal Capacitance Transient Spectroscopy"(in Japan), Electrochemical Laboratory research report No 867, 3-43 (1986)
7. W.Heywang, "Resistivity Anomaly in Doped Barium Titanate", J. Am. Ceram. Soc., 47[10] 484-90 (1964)
8. H.M. Al-Allak, A.W.Brinkman, G.J.Russel, and J.Woods, "The Effect of Mn on the Positive Temperature Coefficient of Resistance Characteristics of Doner Doped BaTiO₃ Ceramics", J. Appl. Phys., 63[9] 4530-35 (1988)
9. D.Y.Wang and K.Umeya, "Spontaneous Polarization Screening Effect and Trap-State Density at Grain Boundaries of Semiconducting Barium Titanate Ceramics", J.Am.Ceram.Soc., 74[2] 280-86 (1991)
10. S.B.Desu and D.A.Payne, "Interfacial Segregation in Perovskite: II, Experimental Evidence", J.Am.Ceram.Soc., 73[11] 3398-406 (1990)
11. Y.M.Chiang and T.Takagi, "Grain-Boundary Chemistry of Barium Titanate and Strontium Titanate:I, High Temperature Equilibrium Space Charge", J.Am.Ceram.Soc., 73[11] 3278-85 (1990)
12. J.Illingsworth, H.A. Al-Allak, A.W.Brinkman, and J.Woods, "The Influence of Mn on the Grain Boundary Potential Barrier Characteristics of Doner Doped BaTiO₃ Ceramics", J. Appl. Phys., 67[4] 2088-92 (1981)
13. H.Ihrig, "PTC Effect of BaTiO₃ as a function of Doping with 3D Elements", J.Am.Ceram.Soc., 72[1] 148-51 (1981)
14. K.Wakino, H.Takagi, H.Sano, K.Nishida, K.Tomono and Y.Sakabe, "Behavior of Mn-ion on Electrical Conductivity of Nb-doped TiO₂-based Ceramics", in Ceram. Trans., vol.32 P129-137 (1992)

ROLE OF POROSITY ON PTCR CHARACTERISTICS OF SEMICONDUCTING BaTiO_3 CERAMICS

Joon-Hyung LEE, Jeong-Joo KIM, and Sang-Hee CHO

Department of Inorganic Materials Engineering
Kyungpook National University, Taegu 702-701, Korea

ABSTRACT

Effect of porosity on PTCR characteristics of semiconducting Y-doped BaTiO_3 ceramics was studied. Porosity was controlled with the mixing of sieved PVA powder to calcined BaTiO_3 powders. Specimens were sintered in N_2 atmosphere after PVA burn out and then, heat treatment was carried out for various times in air at 1200°C. Defects concentrations of BaTiO_3 specimens around grain boundary were examined by Auger Electron Spectroscopy(AES). PTCR characteristics were improved with increasing of porosity and heat treatment time.

[Key Word] : PTCR characteristics, Porosity, Ti vacancy.

I. INTRODUCTION

Semiconducting donor-doped polycrystalline barium titanate, when properly doped with La_2O_3 or Y_2O_3 , yields a PTCR (Positive Temperature Coefficient of Resistivity) effect near the Curie temperature.^{1, 2)} It has been well established that anomaly of a grain-boundary resistivity with temperature triggers PTCR effect in barium titanate system.^{3, 4)}

Some plausible theoretical models have been proposed. Heywang⁵⁾ considered the grain boundaries as strong space-charge layers, which form n-type Schottky double barriers with the acceptors located on the grain boundaries. In this case, the species of acceptors are thought to be adsorbed oxygen on the grain boundaries and responsible for a sharp rise of barrier potential at Schottky double layer. On the

To the extent authorized under the laws of the United States of America, all copyright interests in this publication are the property of The American Ceramic Society. Any duplication, reproduction, or republication of this publication or any part thereof, without the express written consent of The American Ceramic Society or fee paid to the Copyright Clearance Center, is prohibited.

other hand, Daniels et al.^{6,7)} proposed that the acceptor-acting Ba vacancies appear along the grain boundaries during cooling process, and it can electrically compensates the donors around the grain boundaries and then, potential barriers form on the grain boundaries. They also found that the concentration of Ba vacancies depends both on the oxygen partial pressure during sintering and on the sintering temperature. Besides, according to previous studies, porous semiconducting BaTiO₃ ceramics are known to yield large PTCR effect.^{8,9)} It is thus believed that open pores can act as fast diffusion path of oxygen for oxidizing the grain boundaries. Anyway, it is supposed that the PTCR effect is strongly related to oxygen diffusion.

In this respect, we attempted to control the PTCR characteristics by changing of porosity in BaTiO₃ ceramics and also correlated the PTCR characteristics with the grain boundary oxidation during heat treatment.

II. EXPERIMENTAL

An n-type BaTiO₃ of composition (Ba_{0.996}Y_{0.004})TiO₃ was prepared from reagent-grade BaCO₃, Y₂O₃ and TiO₂ powder. Two mol% of excess TiO₂ was added to promote densification and homogeneous microstructure.¹⁰⁾ Powder mixtures were prepared by ball-milling for 12 hours with a polyethylene jar and ZrO₂ balls in ethyl alcohol. Dried mixtures were calcined at 1150°C for 1 hour, and then re-ground for 12 hours by ball-milling. For the formation of artificial pores in the compacts, poly vinyl alcohol(PVA #1500) powder sieved through #325 mesh was mixed with the calcined BaTiO₃ powder. Total porosity was controlled by the amount of PVA. The powders were isostatically pressed into a disk type (diameter in 10 mm height in 3 mm) with a pressure of 120 MPa. Compacts were heated at 550°C for 5 hours in air for PVA burn out, then sintered at 1380°C for 30 min with the heating rate of 300°C/h and nature cooled to room temperature in N₂. Heat treatment was carried out at 1200°C for various times in air. Heating and cooling rate for heat treatment was 400°C/h, respectively. The porosity and average grain size were determined by the water immersion method and linear intercept method, respectively. Also, Auger Electron Spectroscopy (Model Perkin Elmer PHI600SAM) was used to analyze the variation in atomic concentration across the grain boundaries. Samples were fractured in the AES instrument and analyzed inter-granular fractured part with

beam size of 7000\AA . The sputter rate was $68\text{\AA}/\text{min}$ with an Ar^+ ion beam accelerated through 3.5 kV. The PTCR characteristics of the specimens were examined after In/Ga electroding.

III. RESULTS AND DISCUSSION

The green density of compacts, the porosity, and the average grain size of sintered specimens are listed in Table 1. The green density was measured after PVA burn out. The samples were devided into 4 groups by PVA content. The green density decreased as PVA content increased due to large voids produced after PVA burn out. These large voids are hard to eliminate during sintering, and also lead to the decrease of sintered density. The average grain size was not significantly changed with PVA contents.

Table 1. Porosity and average grain size of sintered specimens.

	Green Density(%)	Porosity in Sintered Body(%)	Average Grain Size(μm)
Group 1	58.9 ± 1.6	4.0 ± 0.3	75.2
Group 2	54.1 ± 0.4	9.7 ± 0.3	73.7
Group 3	44.7 ± 0.4	20.4 ± 0.3	76.3
Group 4	40.5 ± 0.3	31.0 ± 0.2	77.8



Fig.1. Polished microstructures of specimens sintered at 1380°C for 30min. in N_2 atmosphere with different porosity; a)4%, b)10%, c)20% and d)31%.

Fig.1 shows the microstructures of sintered specimens as a function of PVA contents. Small pores are uniformly distributed throughout all the specimens regardless of the amount of PVA. However, the amount of large artificial pores increased with the amount of PVA.

Generally, when sintered density reaches about 92~93% of theoretical density, all pores in the specimen can be closed. In other words, open pores may be present when the total porosity is more than 7~8%.^{13,14)} Therefore, it can be supposed that the specimen as shown Fig.1(a) has only closed pores, on the contrary, the specimens as shown in Fig.1(b), (c) and (d) contain some open pores.

Fig.2 shows the atomic concentration profiles of specimen a) sintered at 1380°C for 30 min. in N₂ atmosphere and b) specimen heat treated at 1200°C for 1 hour in air. It was measured by AES from the grain boundary into the bulk of the specimens. In sintered specimen, any concentration variation of cation vacancy between grain boundary and grain interior could not be observed as shown in Fig.2(a). But, when the specimen was heat treated in air, large gradient of cation vacancy between grain boundary and grain interior was revealed. Especially, the concentration of Ti vacancy was higher than that of Ba in grain boundary region.

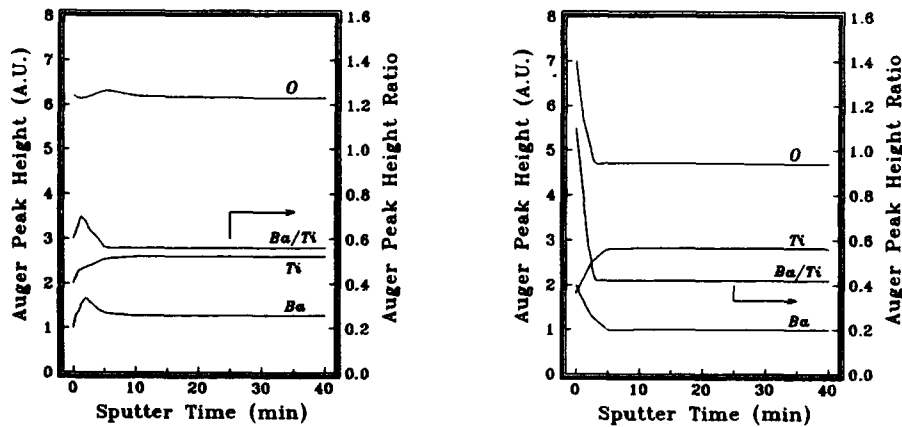


Fig.2. Atomic concentration profile of a)specimen sintered at 1380°C for 30 min. in N₂, and b) specimen sintered at 1380°C for 30 min. in N₂ and heat treated at 1200°C for 1h in air, measured by AES.

It was suggested that cation vacancies could be introduced in order to compensate donors in BaTiO_3 during oxidation (decreasing temperature and/or increasing oxygen partial pressure) by Daniels et al.^{6,7)} According to Daniels,^{6,7)} PTCR effect originates from Ba vacancy which compensates donors around grain boundary during grain boundary oxidation, and the concentration of the singly or doubly ionized Ba vacancies is proportional to the oxygen partial pressure of the sintering atmosphere and inverse proportional to temperature. However it is controversial whether Ba vacancy or Ti vacancy is formed.^{6,7,11,12)} In recent papers presented by Desu and Payne¹¹⁾ on the interfacial chemistry of BaTiO_3 system, they proposed that the Ti vacancy and acceptors were responsible for electron trapping on the grain boundary which was compared with each vacancy formation energies of Ba, Ti and O, respectively. In this study, it is confirmed that Ti vacancy variation is more significant around grain boundary.

Fig.3 shows the resistivity change of sintered specimens with temperature as functions of porosity and heat treatment time. The specimen contained relatively low porosity (4%), it revealed small PTCR jump. Besides, the resistivity of room temperature increased with heat treatment time, which could be explained by donor compensation with cation vacancy that was diffused from grain

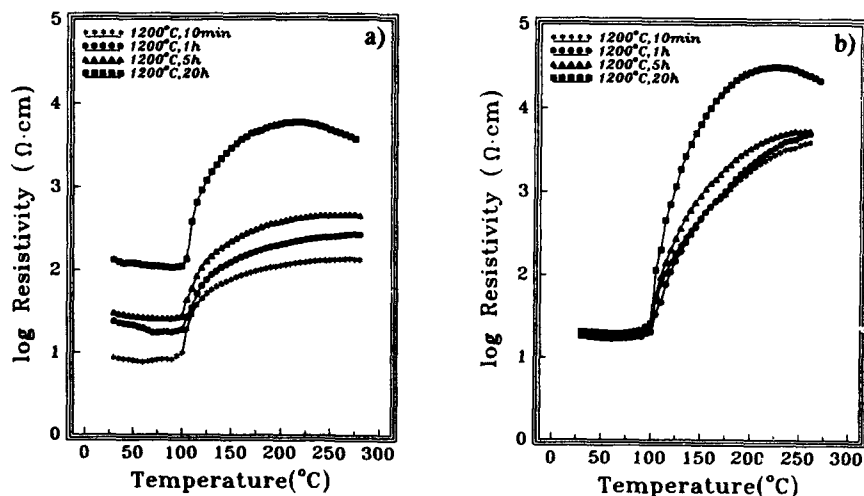


Fig.3. Temperature - Resistivity property as a function of heat treatment time, a) porosity is 4% and b) porosity is 31%.

boundary during heat treatment. Meanwhile when porosity is 31%, large PTCR jump was observed. The resistivity of room temperature was almost constant even though the increase of heat treatment time.

Fig.4 shows the PTCR jump [$\log(\rho_{\max}/\rho_{\min})$ value] as a function of porosity. For the specimens having open pores (10%, 20%, and 31% porosity), it showed the high value of $\log(\rho_{\max}/\rho_{\min})$ comparing with specimen which contains closed pores regardless of heat treatment time. The origin of PTCR effect is due to the formation of cation vacancy layer between grain boundaries, and the concentration of cation vacancy is closely related to oxygen partial pressure.^{6, 7, 10, 11)} Therefore it is believed that open pores could act as fast diffusion path of oxygen, as a result, which increase the grain boundary potential barrier with creation of Ti vacancies.

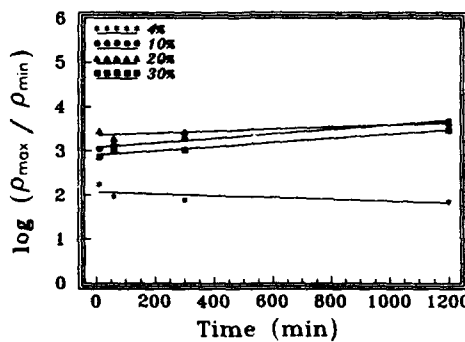


Fig.4. $\log(\rho_{\max}/\rho_{\min})$ value as functions of porosity and heat treatment time.

V. CONCLUSIONS

According to the experimental results, the PTCR effect was increased as porosity increased. It is believed that open pores act as fast diffusion path of oxygen for oxidizing the grain boundaries and enhance the creation of cation vacancies near grain boundaries. AES depth profiles showed the segregation of Ti vacancy on the grain boundary area.

REFERENCES

1. P.W.Haaijman, R.W.Dam and H.A.Klasens, German Patent 929, 350(1955)

2. W.Heywang, "Resistivity Anomaly in Doped Barium Titanate," *J.Am.Ceram.Soc.*, 47[10] 484-490 (1964)
3. G.Goodman, "Electrical Conductivity Anomaly in Samarium-Doped Barium Titanate," *J.Am.Ceram.Soc.*, 46[1] 48-54 (1963)
4. N.Nemoto and J.Oda, "Direct Examinations of PTC Action of Single Grain Boundaries in Semiconducting BaTiO₃ Ceramics," *J.Am.Ceram.Soc.*, 63[7-8] 393-401 (1980)
5. W.Heywang, "Barium Titanate as a Semiconductor with Blocking Layers," *Solid State Electron.*, 3[1] 51-58 (1961)
6. J.Daniels and R.Wernicke, "Part V, New Aspects of an Improved PTC Model," *Philips Res.Rep.*, 31, 544-559 (1976)
7. J.Daniels, K.H.Härdtl, and R.Wernicke, "The PTC Effect of Barium Titanate," *Philips Tech.Rev.*, 38[3] 73-82 (1978/79)
8. M.F.Yan and A.H.Heuer, Additives and Interfaces in Electronic Ceramics, *Advances in Ceramics Vol.7* (The American Ceramic Society, Inc., 1983), pp.137-145.
9. M.Kuwabara, "Effect of Microstructure on the PTCR Effect in Semiconducting Barium Titanate Ceramics" *J.Am.Ceram.Soc.*, 64[11] 639-644 (1981)
10. T.Fukami, "BaTiO₃ Ceramic Semiconductors by Liquid Phase Sintering," *Abstr. Trans. Inst. Electron. and Comm. Engrs. Japan*, 57[8] 31-32 (1974)
11. S.B.Desu and D.A.Payne, "Interfacial Segregation in Perovskite; I ~ N," *J.Am.Ceram.Soc.*, 73[11] 3391-3421 (1990)
12. Y.M.Chiang and T.Takagi, "Grain-Boundary Chemistry of Barium Titanate and Strontium Titanate: I, II," *J.Am.Ceram.Soc.*, 73[11] 3278-3291 (1990)
13. K.H.Härdtl, "Gas Isostatic Hot Pressing Without Molds," *Am.Ceram.Soc. Bull.*, 54[2] 201-207 (1975)
14. D.W.Budworth, "Theory of Pore Closure during Sintering," *Trans.Brit.Ceram.Soc.*, 69[1] 29-31 (1970)

Varistors and Conductors

INTERFACE STATES AT GRAIN BOUNDARIES AND THEIR EFFECTS
ON
THE I-V CHARACTERISTICS IN ZNO:PR VARISTORS
— THEORETICAL CALCULATION —

Kazuo Mukae and Koichi Tsuda
Fuji Electric Corporate Research and Development Ltd.
2-2-1, Nagasaka, Yokosuka, 240-01 JAPAN

ABSTRACT

Effects of the interface states on the applied voltage dependence of the double Schottky barrier(DSB) are theoretically discussed. Based on the simplified models of rectangular density distributions for the interface states, effects of the energy level, density of states, and the distribution width of the interface states on the applied voltage dependence of the DSB were quantitatively calculated. The I-V characteristics of DSB's were also calculated and the nonlinear I-V relations were discussed. The nonlinear exponent was found to be determined mainly by the barrier height and the total charge of the interface states. C-V characteristics are also theoretically simulated. The observed ICTS spectra of the ZnO varistor showed that the interface states were distributed monoenergetically and they fixed the Fermi level. These results agreed with the calculated results.

1. INTRODUCTION

Ceramic semiconductors are widely applied to electronic devices such as thermistors, varistors, capacitors and sensors. Key functions of these devices are often originated from the unique characteristics of the grain boundary. Recent investigations have indicated that the electric properties of the grain boundaries are related mainly to the double Schottky barrier(DSB) formed at the grain boundary.^{1, 2} Therefore it is important to understand the precise role of the grain boundaries for development and improvement of these devices. Although Heywang already explained the characteristics of PTC thermistors by the DSB model in 1964³, there are still some quantitative discrepancies between theoretical calculations and the observed results. The most important reason for the discrepancies is the negligence of the change in the interface charge by an applied voltage. The reported results of C-V characteristics of PTC thermistors showed the change in the interface charge and the presence of the interface states above Fermi level⁴. Therefore the precise analysis is important to understand the characteristics of a DSB. However few quantitative analyses have been reported about the

To the extent authorized under the laws of the United States of America, all copyright interests in this publication are the property of The American Ceramic Society. Any duplication, reproduction, or republication of this publication or any part thereof, without the express written consent of The American Ceramic Society or fee paid to the Copyright Clearance Center, is prohibited.

characteristics of the interface states and their influence to DSB properties. In this paper the quantitative analysis of the applied voltage dependence of the interface states in a DSB is carried out by simplifying the density distribution of the interface states and the calculated results are compared with the observed results.

2. DOUBLE SCHOTTKY BARRIER

2.1 Formulation of Double Schottky Barrier

At the grain boundaries of ceramic semiconductors, there are many imperfections such as crystal defects or inclusions. These imperfections often form the electronic states at the grain boundaries. When these interface states are acceptors, they capture electrons from each grain of both sides resulting in the negative charge of the interface of the grain boundaries. Because of the charge at the interface states, an electronic potential barrier is formed at the grain boundary as shown in Fig.1. When we denote $-Q_0$, N_d , l_0 and $-q$ as the charge density of the grain boundary, the donor concentration of the semiconductor grains, the width of the depletion layer of a grain and electron charge, respectively, the following equation can be obtained because the grain boundary charge should be compensated by that of depletion layers of both sides.

$$Q_0 = 2qN_d l_0 \quad (1)$$

The potential barrier can be expressed by the following equation if x is the position from the grain boundary and $|x| \leq l_0$.

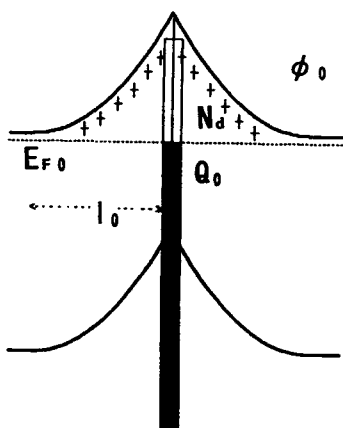


Fig.1 Band structure of double Schottky barrier.

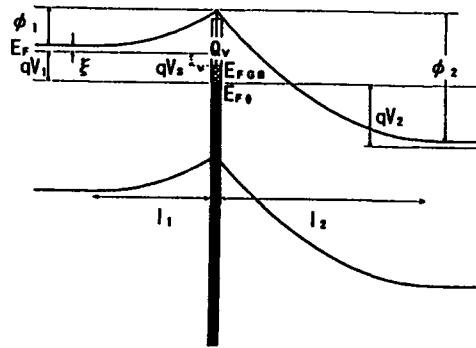


Fig.2 Band structure of DSB with an applied voltage.

$$\phi = \frac{q^2 N_d}{2\epsilon_s} (|x| - l_o)^2 \quad (2)$$

Since this electronic potential barrier is composed of two Schottky barriers symmetrically connected with each other, we call this double Schottky barrier(DSB). The barrier height at no applied voltage, ϕ_o , is expressed by the following equation.

$$\phi_o = \frac{q^2 N_d}{2\epsilon_s} l_o^2 = \frac{Q_o^2}{8\epsilon_s N_d} \quad (3)$$

If $D(E)$ is the distribution function of the density of the interface states, $f(E)$ is Fermi-Dirac distribution function, and E_{FGB} and E_{FGBo} are the Fermi level of the interface states and that when interface states are neutral, the interface charge, Q_o , is obtained by the integration of the following equation.

$$Q_o = q \int_{E_{FGBo}}^{E_{FGB}} D(E) f(E) dE, \quad (4)$$

where

$$f(E) = \frac{1}{1 + \exp\{(E - E_F)/kT\}}. \quad (5)$$

Therefore the actual DSB is determined by equations (2), (3), (4) and (5).

2.2 Applied Voltage Dependence of DSB

When a finite voltage is applied to a DSB regarding the left hand grain as negative region, the shape of DSB changes as shown in Fig. 2. Since electrons are injected into the interface states, the total depletion width becomes larger compensating the interface charge. The interface charge at V , Q_v , is obtained by the next eq. (6).

$$Q_v = q N_d (l_1 + l_2), \quad (6)$$

where

$$I_1 = \sqrt{\frac{2\epsilon_s \phi_1}{q^2 N_d}} \quad (7)$$

$$I_2 = \sqrt{\frac{2\epsilon_s \phi_2}{q^2 N_d}} \quad (8)$$

If we define S , qV_1 and qV_2 as ratio of Q_V to Q_o , decrease in ϕ_1 and increase in ϕ_2 , respectively, the following relations are obtained.

$$S = Q_V/Q_o = \frac{\sqrt{\phi_1} + \sqrt{\phi_2}}{2\sqrt{\phi_o}} \quad (9)$$

$$V = V_1 + V_2 \quad (10)$$

$$\phi_1 = \phi_o - qV_1 \quad (11)$$

$$\phi_2 = \phi_o + qV_2 \quad (12)$$

From the balance of electron injection and emission of the interface states, the Fermi energy of the left grain is derived as approximately the same as that of the interface states.

$$E_{FGB} = E_F \quad (13)$$

3. CALCULATION OF VOLTAGE DEPENDENCE OF BARRIER HEIGHT⁵

From the eqs.(9) ~ (12), the applied voltage dependence of ϕ_1 can be derived as the following simple equation.

$$\phi_1 = S^2 \left(1 - \frac{qV}{4S^2 \phi_o}\right)^2 \phi_o \quad (14)$$

Therefore if we know S as a function of V eq.(14) can be calculated. However in the actual case, dependence of S on V is rarely known because experimental

measurement of $D(E)$ is difficult. Therefore we will simplify the $D(E)$ and numerically simulate the applied voltage dependence of ϕ_1 in the following discussion.

3.1 $D(E)=0, E>E_{F0}$ (Heywang Model)

In this case, eq.(14) can be easily transformed to the next equation.

$$\phi_1 = \left(1 - \frac{qV}{4\phi_0}\right)^2 \phi_0 \quad (15)$$

This equation shows well known parabolic decrease in barrier height and disappearance of ϕ_1 at $V=4\phi_0$. Figure 3 shows this relation. Although ϕ_1 changes as V , it should be noted that the total depletion width, (l_1+l_2) , remains constant because of the constant interface charge. Consequently the capacitance of the DSB should be kept constant.

3.2 Rectangular $D(E)$

When $D(E)$ has a rectangular density distribution with a center at $E_0 + E_{F0}$ and $2\Delta E$ width as shown below, S can be also calculated as a function of V .

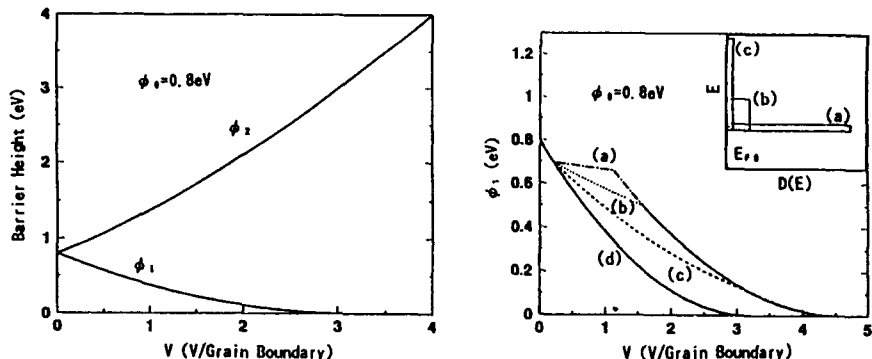


Fig.3 Dependence of ϕ_1 and ϕ_2 on applied voltage.
(Heywang Model)

Fig.4 ϕ_1 - V relation for $D(E)$.
 $\phi_0 = 0.8$ eV, $Q_0 = 6 \times 10^{12}$ q/cm^2 ,
 $D_0 =$
(a) 3×10^{13} eV/cm^2
(b) 6×10^{12}
(c) 2×10^{12}
(d) 0 (Heywang Model)

$$\begin{aligned} D(E) &= D_o, & (E_{F0} + E_o - \Delta E < E < E_{F0} + E_o + \Delta E) \\ D(E) &= 0, & (E < E_{F0} + E_o - \Delta E, \quad E > E_{F0} + E_o + \Delta E) \end{aligned}$$

Until the Fermi level meets the bottom of the rectangle, the interface charge does not increase similar to Heywang Model, but at $V=V_o$ where $E_F = E_{F0} + E_o - \Delta E$, electron injection into the interface states begins. In this case, V_o can be obtained as the following equation from eq.(9).

$$qV_o = 4[\phi_o - \sqrt{\phi_o \{\phi_o - (E_o - \Delta E)\}}] \quad (16)$$

When the Fermi level reaches the top of rectangle where $V=V_F$, the interface states are completely filled. Therefore, while $V_o < V < V_F$, the interface charge, Q_V , is expressed by the following equation.

$$Q_V = Q_o + qD_o \{qV_1 - (E_o - \Delta E)\} \quad (17)$$

Therefore, the following relation can be obtained from eq.(9).

$$qV = 4\phi_o [1 + \{qV_1 - (E_o - \Delta E)\} \frac{qD_o}{Q_o}]^2 - 4\sqrt{\phi_o} \sqrt{\{\phi_o - qV_1\}} [1 + \{qV_1 - (E_o - \Delta E)\} \frac{qD_o}{Q_o}] \quad (18)$$

Although solution of eq.(18) for V_1 as a function of V cannot easily be obtained, one can obtain $V_1 - V$ relation numerically. This numerical relation and eq.(14) enable simulation of $\phi_1 - V$ relation. Since the interface states are completely filled at $V=V_F$, the interface charge is kept constant above $V>V_F$. Therefore V_F and ϕ_1 are expressed by the following equations.

$$qV_F = 4\phi_o (1 + 2\Delta E \frac{qD_o}{Q_o})^2 - 4\sqrt{\phi_o} \sqrt{\{\phi_o - (E_o + \Delta E)\}} (1 + 2\Delta E \frac{qD_o}{Q_o}) \quad (19)$$

$$\phi_1 = S_F^2 (1 - \frac{qV}{4S_F^2 \phi_o})^2 \phi_o \quad (20)$$

$$S_F = 1 + \frac{2qD_o \Delta E}{Q_o} \quad (21)$$

Figure 4 shows 4 cases of this simulation where total quantity of the interface states is fixed as $1.2 \times 10^{12}/\text{cm}^2$ and the D_o and ΔE are changed. Figure 4 shows that decrease in ϕ_1 is retarded at V_o and recover the decreasing rate at V_F . The degree of retardation was larger as D_o increases. If D_o is extremely large, ϕ_1 is kept constant as $\phi_o - (E_o - \Delta E)$. This phenomenon is so called pinning of the Fermi level.

3.3 Monoenergetic $D(E)$

When the interface states are distributed monoenergetically, $D(E)$ can be expressed by the following equation if $\delta(E)$ is Dirac's δ function.

$$D(E) = D_o \delta(E_o) \quad (22)$$

In this case, change in ϕ_1 at $V < V_o$ is similar to that in the previous section. At $V = V_o$, electron injection into the interface states starts and finishes at $V = V_F$. Since Fermi level is pinned at $E_o + E_{F0}$ in this case, ϕ_1 is also kept constant as shown below.

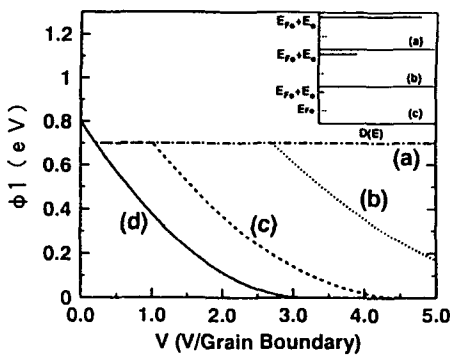


Fig.5 ϕ_1 -V relation for mono-

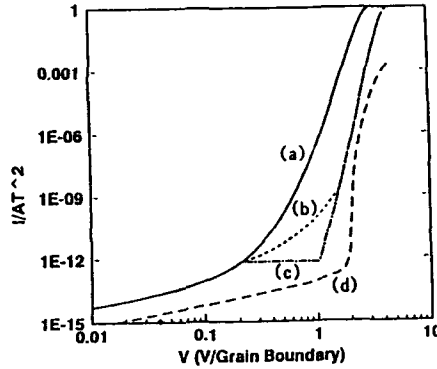


Fig.6 I-V characteristics of DSB.

- (a) Heywang Model.
- (b) Rectangular $D(E)$.
- (c) Monoenergetic $D(E)$.
- (d) Observed curve of ZnO:Pr varistor.

- (a) Heywang Model.
- (b) Rectangular $D(E)$.
- (c) Monoenergetic $D(E)$.
- (d) Observed curve of ZnO:Pr varistor.

$$\phi_1 = \phi_o - E_o. \quad (23)$$

$$qV_F = 4\phi_o S_F^2 - 4S_F \sqrt{\phi_o(\phi_o - E_o)} \quad (24)$$

Above V_o , ϕ_1 again decreases as V increases. Three typical changes in ϕ_1 are shown in Fig. 5.

In Table 1 calculated V_o and V_F in three cases are summarized.

Table 1. Calculated V_o and V_F

N_{gb} ($10^{12}/\text{cm}^2$)	S_F	D_o ($10^{12}/\text{eV/cm}^2$)	ΔE_F (eV)	V_o (V)	V_F (V)
1.2	1.2	2.0	0.3	0.207	3.28
1.2	1.2	6.0	0.1	0.207	1.57
1.2	1.2	30	0.02	0.207	1.12
0.6	1.1	6.0	0.05	0.207	0.824
1.2	1.2	6.0	0.1	0.207	1.572
3.6	1.6	6.0	0.3	0.207	6.382
1.2	1.2	1.2	0	0.207	1.016
3.0	1.5	3.0	0	0.207	2.710
6.0	2.0	6.0	0	0.207	6.813

4. CALCULATION OF I-V CHARACTERISTICS

Current-voltage characteristics are calculated numerically on the basis of the thermoionic process expressed by the following equation where A is Richardson constant and T is absolute temperature.

$$I = AT^2 \exp\left(-\frac{\phi_1}{kT}\right) \quad (25)$$

Equation (25) gives I-V curves for three typical cases discussed above as shown in Fig. 6 in which an observed I-V curve of ZnO:Pr varistor is also indicated. The theoretical nonlinear exponent, α , is obtained from eq. (24) as the following eq. (26) and (27). Equation (27) indicates that large ϕ_o and large total charge at the interface states will result in higher nonlinearity. All curves in Fig. 6 exhibit nonlinear characteristics. Calculated curves for rectangular and monoenergetic $D(E)$ have larger α of 22 than that for Heywang Model. However that of the

$$\alpha = \frac{qV}{2kT} \left(1 - \frac{qV}{4\phi_o S_F^2} \right) \quad (26)$$

$$\alpha_{\max} = \frac{\phi_o S_F^2}{2kT} \quad (27)$$

observed curve for a ZnO:Pr varistor was more than 80. Therefore the nonlinearity in ZnO varistor should be attributed other than fulfill of the interface states.

5. CALCULATION OF C-V CHARACTERISTICS

Voltage dependence of capacitance of ZnO varistors gives much information about the grain boundary. We have shown that the modified $1/C^2$ -V plot gives N_d and ϕ_o based on the assumption that the interface states fix ϕ_1 at initial value⁶. However if the interface states are distributed with a certain width or located above the Fermi level of ZnO grains as discussed before, this assumption is not correct. Therefore, in this section, C-V characteristics are theoretically calculated in the same cases as the preceding section and compared with the observed results.

From eq.(7), (8) and (9) the voltage dependence of the capacitance of a DSB per unit area is obtained by the following equation.

$$\begin{aligned} C/C_o &= 1/S = \frac{2\sqrt{\phi_o}}{\sqrt{\phi_1} + \sqrt{\phi_2}} \\ &= \frac{2\sqrt{\phi_o}}{\sqrt{(\phi_o - qV_1)} + \sqrt{\{\phi_o - q(V_1 - V)\}}} \end{aligned} \quad (28)$$

Again we use the previous rectangular distribution of the interface states to obtain numerically V_1 dependence on V . When the applied voltage is lower than V_F , there is no interface state to charge resulting in no capacitance change. Increase in the interface charge between V_o and V_F reduces the capacitance and above V_F the capacitance is again kept constant. The calculated result of eq.(28) is shown in Fig.7 in which the observed result is also shown. In Fig.7, three cases of rectangular interface distribution are shown. Since the observed curve begins to decrease at a small applied voltage, V_o of the ZnO varistor should be approximately zero. This situation means that the bottom of the interface states is located at the same level as the Fermi level of ZnO grains. Further numerical analysis showed that the Fermi level is fixed by the interface states because of their high density of more than $10^{13}/\text{cm}^2$.

6. ICTS MEASUREMENT

ICTS (Isothermal Capacitance Transient Spectroscopy) is an intensive method to investigate the interface states in ceramic semiconductors⁷. This method gives the peak not only for the bulk traps in the grains but also for the interface states at the grain boundaries. Figure 8 shows the observed ICTS peak of a ZnO:Pr varistor⁸ generated by various height of the applied pulses. Although the value of the applied pulses are different, the position of the peaks did not change. This result indicates that the Fermi level of the interface states does not change with the applied voltage. In addition, the calculated shape of the ICTS peak for monoenergetic interface states coincided with the observed peak. Consequently we can recognize that this observation agrees with the calculated results described above.

6. CONCLUSIONS

The applied voltage dependence of DSB was quantitatively simulated by simplifying the density distribution of the interface states. The calculated results are compared with the observed results of I-V and C-V characteristics and ICTS measurement to obtain the following conclusions.

(1) The interface states retard the decrease in ϕ_1 and extremely high density interface states will fix the Fermi energy and ϕ_1 .

(2) I-V characteristics are influenced not only by energy levels but also by their density and width of the energy distribution.

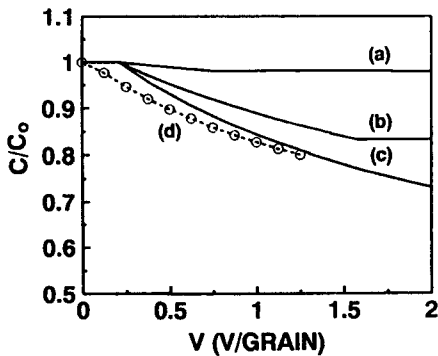


Fig. 7 Calculated C/C₀ - V curve for rectangular D(E).

$\Delta E = 0.1 \text{ eV}$, $E = 0.2 \text{ eV}$.
 (a) $D_0 = 0.6 \times 10^{12} \text{ eV/cm}^2$
 (b) 6.0.
 (c) 60.0.
 (d) Observed curve.

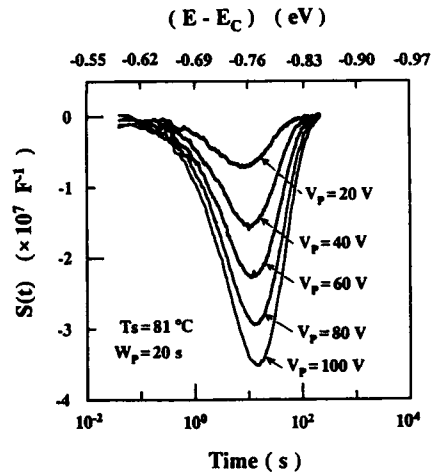


Fig. 8 ICTS spectra of ZnO varistor by various height of pulse.

(3) Although completion of electron charge into the interface states will produce steep rise in current, its nonlinear exponent, α , is confined to 22 and other mechanism is needed for explanation of ZnO varistor.

(4) C-V characteristics are theoretically calculated. Comparison with the observed result revealed that the interface states are located at the same level as Fermi level of ZnO grains and that they are pinning the Fermi level.

(5) ICTS measurement of ZnO:Pr varistor showed that the Fermi level of the ZnO grains is fixed by the interface states and that the interface states are distributed monoenergetically. These results agreed with the calculated results of the DSB structure.

7. REFERENCES

- 1 K.Mukae and I.Nagasawa, "Effect of Praseodymium Oxide and Donor Concentration in the Grain Boundary Region of ZnO Varistors", 331-342, "Advances in Ceramics, Vol.1", Ed., L. M. Levinson, Am. Ceram. Soc., (1981).
- 2 H.Ihrig, "Physics and Technology of PTC-type BaTiO₃ Ceramics", 117-127, "Advances in Ceramics, Vol.7", Ed., M. F. Yan and A. H. Heuer, Am. Ceram. Soc., (1983).
- 3 W.Heywang, "Resistivity Anomaly in Doped Barium Titanate", J.Am.Ceram.Soc., Vol.47, 484-90,1964.
- 4 P.Gerthsen and B.Hoffmann, "Current-Voltage Characteristics and Capacitance of Single Grain Boundaries in Semiconducting BaTiO₃ Ceramics", Solid-State Electron., Vol.16, 617-22,1973.
- 5 K.Mukae and K.Tsuda, "Effects of Interface States on Applied Voltage Dependence of Double Schottky Barrier(Part 1)", J.Ceram.Soc.Jpn., Vol.101, 1125-1130, 1993.
- 6 K.Mukae, K.Tsuda and I.Nagasawa, "Capacitance-vs-Voltage Characteristics of ZnO Varistors", J.Appl.Phys., Vol.50, 4475-4476, 1979.
- 7 T.Maeda and M.Takata, "Detection and Characterization of Trap Centers in ZnO Varistor by ICTS", J.Ceram.Soc.Jpn.,Vol.97, 1219-1227, 1989.
- 8 K.Tsuda and K.Mukae, "Characterization of Interface States in ZnO Varistors using Isothermal Capacitance Transient Spectroscopy", J.Ceram.Soc.Jpn, Vol.100, 1239-1244, 1992.

CRYOGENIC BEHAVIOR OF ZnO VARISTORS

Lionel M. Levinson and William N. Schultz
GE Corporate Research and Development
P.O. Box 8, Schenectady, NY 12301

ABSTRACT

By controlling the ZnO grain doping it is possible to fabricate ZnO varistors with good high-current nonlinearity at cryogenic (4.2 K) temperatures. We present here low-temperature current-voltage and capacitance-dissipation data measured on ZnO varistor ceramics having Al doping between zero and 1000 ppm atomic. Analysis of the data shows that adequate cryovaristor performance requires that the ZnO doping level exceed a donor doping concentration of about 10^{18} electrons/cm³ (50 ppm atomic Al). This doping level corresponds to the Mott critical concentration at which the activation energy for shallow donors tends toward zero; i.e., the donor impurity band overlaps the bottom of the conduction band.

1. INTRODUCTION

Metal-oxide varistors used in surge arresters are ZnO-based ceramic semiconductor devices with highly nonlinear current-voltage characteristics similar to back-to-back Zener diodes, but with much greater current, voltage, and energy-handling capabilities [1-4]. They are composed of ZnO (~95 mol%) plus a number of other oxide additives (~5 mol%) and are produced by a sintering process that gives rise to a microstructure consisting of conducting ZnO grains (room temperature resistivity $\rho \sim 1 \Omega \cdot \text{cm}$), 10 μm in size, surrounded by thin insulating barriers. The dc current-voltage characteristics of a ZnO varistor at 77 K and for a small range of temperatures near 300 K are shown in Figure 1. At very low applied electric fields, the varistor is highly resistive, and at room temperature (298 K) behaves essentially as a linear resistor of resistivity $\sim 10^{12} \Omega \cdot \text{cm}$. In this region and in the prebreakdown region that connects the linear characteristic to the highly nonlinear breakdown conduction process, the varistor exhibits a negative temperature coefficient of resistance; that is, as temperature increases, the effective resistance decreases, resulting in higher varistor current for a given applied voltage. The *I*-*V* characteristic in the prebreakdown and linear regions is often described by an activation energy

To the extent authorized under the laws of the United States of America, all copyright interests in this publication are the property of The American Ceramic Society. Any duplication, reproduction, or republication of this publication or any part thereof, without the express written consent of The American Ceramic Society or fee paid to the Copyright Clearance Center, is prohibited.

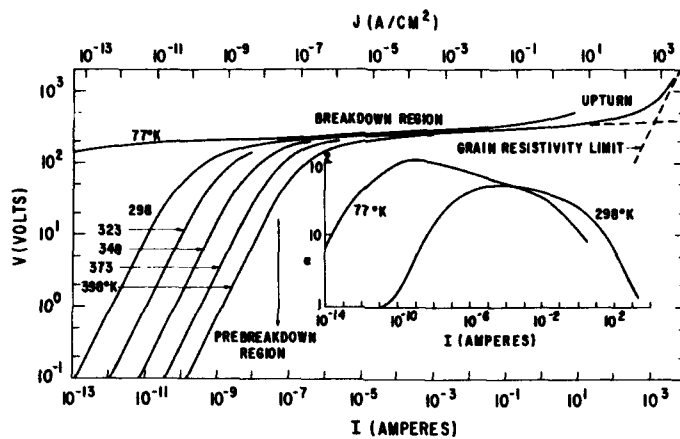


Figure 1. The current-voltage characteristics of a ZnO varistor at 77 K and for a small range of temperatures near 300 K. The varistor disc thickness was 0.19 cm. A simple extrapolation of the breakdown characteristic at 298 K is indicated by the dashed line. The room temperature grain resistivity limit is drawn for $\rho = 3.2 \Omega \cdot \text{cm}$. The coefficient of non-linearity $\alpha = d \ln I / d \ln V$ vs. I is shown in the inset.

$$I = I_0 \exp(-e\phi / kT), \quad (1)$$

where $e\phi \sim 0.7$ eV for many varistor formulations. At 77 K (liquid nitrogen temperature), the prebreakdown conduction takes place at currents too low to be measured by conventional instrumentation, $I < 10^{-14}$ A.

Significant conduction does not take place until the field across the varistor reaches a critical value, called the breakdown field, V_B , often defined as the varistor voltage at a current density of 1 mA/cm². Above this value, very small increases in voltage are accompanied by very large increases in current. The volt-ampere characteristic in the breakdown region is commonly characterized by an empirical power law

$$I = kV^\alpha, \quad (2)$$

where the exponent α can attain values of 50 or even 100 or more. This highly nonlinear behavior has permitted metal-oxide varistors to function as surge arresters for the protection of high-voltage ac and dc systems from the effects of transient overvoltages caused by switching surges and lightning strikes. In such devices, the varistors are normally stressed at voltages well below the breakdown region where the current drawn is very low. As the voltage from an incoming switching or lightning surge begins to increase, the varistor "clamps" the system voltage at the varistor breakdown voltage. The higher the exponent α , the lower the clamping voltage for a given current magnitude.

For very high currents an upturn occurs in the volt-ampere characteristic, associated with the finite resistivity of the grains themselves (Figure 1). This upturn derives from the voltage drop in the grains. The degree of upturn is of critical importance to the protective ability of the varistor material at high currents. The greater the upturn, the lower the exponent α and the poorer the protective level. Because the varistor grains consist of doped semiconducting ZnO, it is of interest to evaluate the temperature dependence of the varistor grain resistivity and its effect on varistor behavior at low temperatures.

2. CRYOVARISTORS

The initial measurements of the electrical response of varistor materials at cryogenic temperatures were made in our laboratory in the mid- to late-1970s. The first study [5] was performed to help understand varistor conduction behavior. This work also revealed that grain resistivity effects are enhanced at 4.2 K, severely limiting the low-temperature effectiveness of devices made with this early formulation.

A second study [6] quantitatively evaluated these low-temperature grain resistivity effects through measurements of the frequency dependence of the dielectric constant and dissipation factor. A loss peak and dispersion in ϵ were identified as resulting from the two-phase structure of the ZnO varistor (insulating grain boundaries and more conducting grains). We also were able to show that the grain resistivity in these early commercial varistors at 4.2 K, $\rho_{\text{ZnO}} \sim 10^6 \Omega\text{-cm}$, could be greatly improved by minor variations in the varistor formulation.

More recently Lawless et al. [7,8] measured the electrical and thermal properties of a cryovaristor sample and observed that the energy absorption capability of varistor materials could be dramatically improved by operating the varistor at cryogenic temperatures. They recognized that for certain applications such cryogenic operation was potentially practical and advantageous. They found that while the specific heat of varistor materials is small for $T < 100$ K, it becomes significant for temperatures above 100 K. Hence, the useful energy absorption capability is determined over a temperature range ($T_{\text{max}} - 100$) K, where T_{max} is the maximum temperature at which the varistor is operable after absorption of the surge.

Since our early work [5,6] showed that varistors did not function well at high currents and low temperatures because of the high ZnO grain resistivity at cryogenic temperatures, we have now evaluated the effect of varying the ZnO grain resistivity upon cryovaristor operation.

3. EXPERIMENTAL

Varistor samples were prepared for measurement at cryogenic temperatures by milling oxide powders, pressing, and sintering. Preparation details are as follows:

Varistor composition (mol%): $ZnO = 97$; $Bi_2O_3 = 0.5$; $Co_2O_3 = 0.5$;
 $MnO_2 = 0.5$; $NiO = 1.0$; $Sb_2O_3 = 1.0$; $CrO_3 = 0.5$

Sintering conditions: 1200 °C, 1 hour.

Varistor discs of diameter 0.75 inch and thickness 0.050 inch were pressed at about 4 kpsi and sintered in air in a muffle furnace. After firing, the varistors were electrode using an In-Ga eutectic alloy and characterized electrically at room temperature, 77 K and 4.2 K. The 77 K and 4.2 K data were obtained by immersing the devices in liquid nitrogen and liquid helium, respectively.

A series of varistor samples having the above composition and varying additional Al dopant content (added as the nitrate) were prepared. The ZnO powder used in the varistor preparation as well as undoped fired samples were characterized analytically using ICP emission spectroscopy to check for the possible presence of trace background donor dopants. Other than Al, the elements Ga and In are known donor dopants for ZnO [9]. The trace element analysis (Table 1) indicates a background donor dopant level of <10 ppm atomic for Al, Ga, and In. This value is modest compared with the range of intentionally added Al doping (10 to 1000 ppm atomic in our samples). For Al doping >>10 ppm we can have confidence that the ZnO donor doping is largely determined by the added Al.

Table 1. Trace Analysis of Some Dopants
(Data in ppm atomic; DL denotes detection limit)

	Al	Ga	In	Li	Na	K
"Pure" ZnO	<DL	<DL	7	<DL	3	<DL
ZnO varistor with no added Al	<DL	<DL	9	3	11	<DL
Detection limit (DL)	1	2	2	0.2	1	0.4

The current-voltage characteristic of the varistor samples was measured over a current range $10^{-9} A/cm^2 < I < 10 A/cm^2$. For currents over $3 mA/cm^2$ the data were obtained using a Velenex 360 pulse generator with all data measured $40 \mu s$ after pulse initiation. The values for $I < 3 mA/cm^2$ were obtained using dc methods.

We have also measured the capacitance-dissipation behavior of the samples for frequencies $10^2 Hz < f < 2 \times 10^6 Hz$. The data were obtained using HP 4274A and HP 4275A LCR meters.

4. RESULTS AND DISCUSSION

Figure 2 gives the dissipation ($\tan \delta$) vs frequency measured at room temperature, 77 K, and 4.2 K, for ZnO varistors with, respectively, no intentional Al-doping.

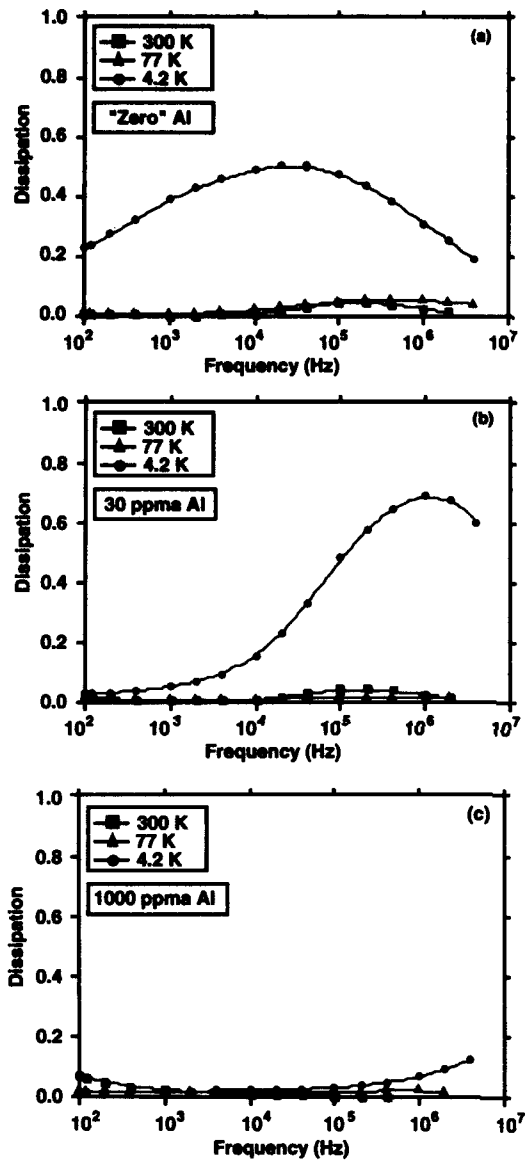


Figure 2. Dissipation ($\tan\delta$) vs. frequency at 300 K, 77 K, and 4.2 K for a varistor with (a) no intentionally added Al doping, (b) 30 ppm atomic added Al, (c) 1000 ppm atomic added Al.

30 ppm atomic Al doping, and 1000 ppm atomic Al doping. Al, Ga, and In are known trivalent dopants [9–11] that decrease the ZnO grain resistivity at room temperature. We have used Al doping to decrease the ZnO resistivity. The relative dielectric constant, ϵ , for the samples of Figure 2 is given in Figure 3.

Figures 2 and 3 at 4.2 K can be analyzed quite straightforwardly in terms of Maxwell-Wagner dispersion of a mixed phase. In this case, the more resistive phase is the ZnO grain boundary and the more conducting phase is the ZnO grain. This model is well known [12] and has been particularized for varistors [6]. Note the large magnitude of the peak of the dissipation factor ($\tan\delta \approx 0.6$) in Figures 2a and 2b. This Maxwell-Wagner peak is quite different in origin from other small peaks in $\tan\delta$ observed in ZnO varistors around room temperature [13,14].

To analyze the 4.2 K data of Figures 2 and 3 it is useful to quote some relations derived from the Maxwell-Wagner analysis for cryovaristors [6]:

The peak frequency in the $\tan\delta$ vs f curves is given by

$$f_{\max} = (d_1/d_2)^{1/2} (1/2\pi\epsilon_0\epsilon\mu_2) \quad (3)$$

where subscript “1” denotes the grain boundary and subscript “2” denotes the grain, and $\epsilon=8.5$ is the dielectric constant of ZnO.

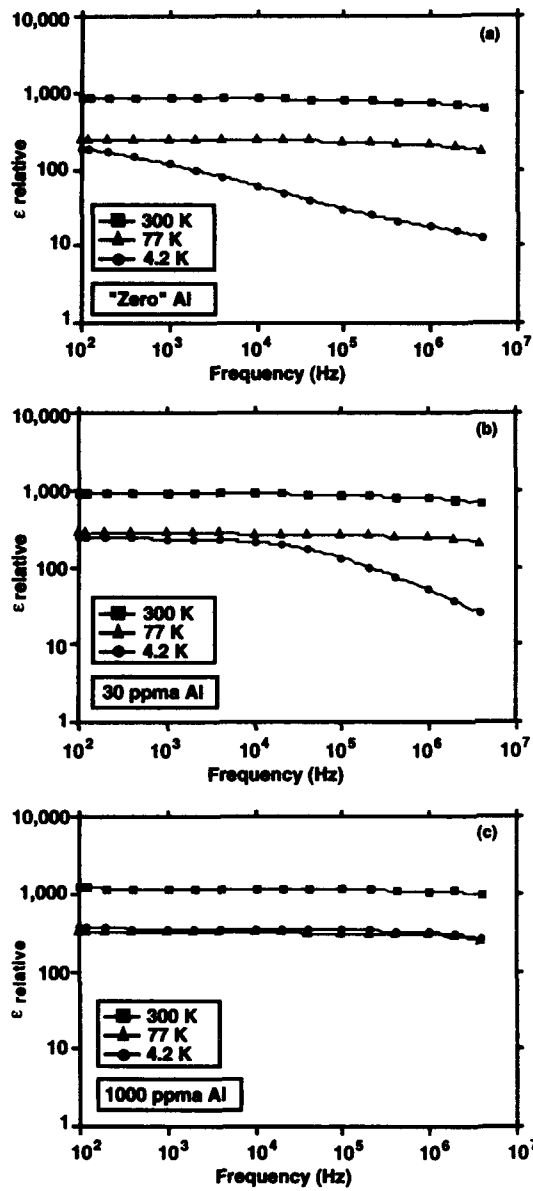


Figure 3. Relative dielectric constant ϵ vs. frequency for the samples of Figure 2; (a) no intentionally added Al doping, (b) 30 ppm atomic added Al, (c) 1000 ppm atomic added Al.

The ratio between the grain size and insulating grain boundary thickness d_2/d_1 is given by

$$\epsilon_s / \epsilon_\infty \approx d_2 / d_1 , \quad (4)$$

where ϵ_s and ϵ_∞ are the low-frequency (static) and high-frequency values, respectively, of the dielectric constant.

From Figures 3a and 3b, we crudely estimate $\epsilon_s / \epsilon_\infty = 20$, which is consistent with a grain dimension $d_2 \approx 10 \mu\text{m}$ and a (low-temperature) double depletion layer width at the grain boundary $d_1 \approx 0.5 \mu\text{m}$.

Using equation (3) and the data of Figures 2 and 3, as well as data from samples at other Al doping levels, we derive the resistivity values given in Table 2.

The resistivity values in Table 2 bear some discussion. At "zero" ppm atomic Al (i.e., no deliberate Al addition), the resistivity is in the meg-ohm region, which is in agreement with the data of Reference 5. The high value of ρ_2 is not unexpected, because the activation energy E_A (at

Table 2. Variation of ZnO Grain Resistivity ρ_2 with Al-doping at 4.2 K

Al Doping (ppm atomic)	f_{\max} (MHz)	ρ_2 (k Ω ·cm)
zero (<1)	0.03	1500
30	1	47
130	~10	~0.5
1000	>10	—

low concentrations) for most shallow donors in ZnO is in the 10- to 40-meV range [9], and thus these donor levels would be frozen out at 4.2 K. A doping level of 1 ppm atomic corresponds to 5×10^{16} electrons/cm³ (if completely activated). Li and Hagemark [15] similarly find that single crystals of ZnO with excess Zn doping at the $10^{16}/\text{cm}^3$ level have $\rho \sim 10^6 \Omega\text{-cm}$ at 4 K.

As the donor density increases, however, we expect a decrease in the effective donor activation energy. The decrease of the activation energy with increasing density of donors can be related to an increase in the overlapping of the wave functions of the bound electrons. The impurity band formed in this way becomes broader with increasing density of donors. The ionization energy of the donors vanishes when the impurity band reaches the lower edge of the conduction band.

We can estimate the critical concentration N_c at which the donor ionization energy is expected to go to zero using the criterion of Mott [16] that

$$N_c = \frac{3}{4\pi} \frac{1}{\lambda^3} \frac{1}{a_0}, \quad (5)$$

where λ is a constant approximately equal to 3, and a_0 is the Bohr radius of a hydrogen-like orbit of the electron in the coulomb field of the donor ion. Since

$$a_0 = \epsilon(m/m^*)a_H, \quad (6)$$

where m^* (=0.27 m) is the effective mass of the electron in ZnO [17], $\epsilon=8.5$, and a_H is the hydrogen atom Bohr radius = 5.3 nm, we obtain

$$N_c = 2 \times 10^{18} \text{ cm}^{-3}. \quad (7)$$

This value of N_c compares well with the data of Li and Hagemark [15], who find that the activation energy $E_A \rightarrow 0$ as the doping approaches $2 \times 10^{18}/\text{cm}^3$, and that $\rho \sim 10^3 \Omega\text{-cm}$ for single-crystal ZnO with excess Zn doping at the $10^{18}/\text{cm}^3$ level. Noting that a doping level of $10^{18}/\text{cm}^3$ corresponds to about 50 ppm atomic, the values of ρ_2 presented in Table 2 are consistent with the above.

We have also attempted to corroborate these estimates by pressing and sintering (at 1200 °C) the "pure" ZnO powder used to prepare all the varistors described here. Figure 4 gives the resistivity of the "pure" ZnO ceramic as a function of temperature and doping. Note that careful precautions were taken to avoid contamination of the ZnO with the other additives (in particular Bi_2O_3) usually added to varistors, and that the resistivity measurements were performed at a frequency of 10^6 Hz to avoid contact impedance effects.

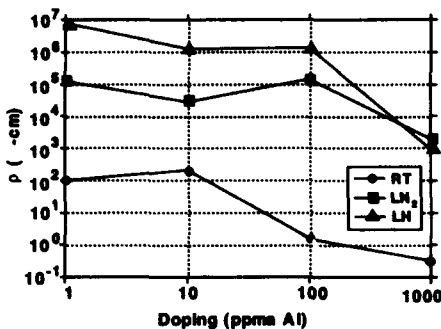


Figure 4. Variation with temperature and Al doping of the resistivity of "pure" ZnO ceramic material. Note that for 1000 ppm Al doping, cooling from liquid nitrogen to liquid helium hardly affects the resistivity.

The data of Figure 4 are in general agreement with the estimate of $N_c=2\times 10^{18}/\text{cm}^3$ shallow donor doping (Al=100 ppm atomic), as the level at which the activation energy E_A begins to tend to zero. Indeed, by the time the Al doping is 1000 ppm atomic, $\rho_{4.2\text{ K}}=\rho_{77\text{ K}}$ and $E_A=0$.

Figure 5 gives current density vs. applied field data for the samples of Figures 2 and 3.* As expected, the greater the Al doping, the less the upturn; i.e., the more nonlinear the behavior at high currents. It should be evident, however, that the resistivities of Table 2 are far too large to be consistent with the high-current data of Figure 5. For example, from Figure 5a ("zero" doping), at a current of 10 A/cm^2 the incremental field, ΔE , resulting from the upturn is about 3 kV/cm . (This estimate of ΔE is obtained by a rough linear extrapolation of the low-current data in the log-log plot to high currents.) Using this value of ΔE we would estimate a grain resistivity of $0.3\text{ k}\Omega\text{-cm}$, which is considerably less than the value in Table 2 for the "zero" doping sample.

The reason for this discrepancy is not clear at present. We presume it results from the basic difference between capacitance-dissipation data obtained at low applied fields and high-field effects arising during current-voltage measurements in varistors. These high fields could provide excess electrons in the ZnO grains, either via impact ionization or avalanche breakdown of neutral impurity levels, thereby decreasing the effective ZnO grain resistivity.

REFERENCES

- [1] For a review of these devices, see T.K. Gupta, *J. Am. Cer. Soc.* **73**, 1817 (1990); L.M. Levinson and H.R. Philipp, *Bull Am. Cer. Soc.* **65**, 639 (1986); H.R. Philipp and L.M. Levinson, 190 EOS/ESD *Symposium Proceedings EOS-2*, 26, 1981.

*Note that the pulse and dc data of Figure 5 are shifted in voltage because of effects such as the ac-dc shift and overshoot [18].

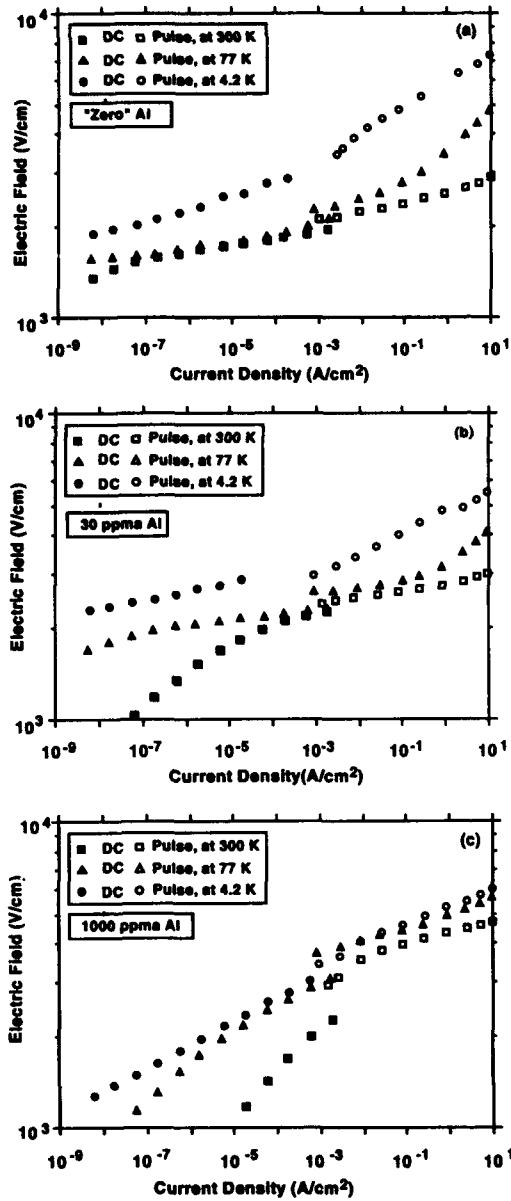


Figure 5. Current density vs. applied field at 300 K, 77 K, and 4.2 K for a varistor with (a) no intentionally added Al doping, (b) 30 ppm atomic added Al, (c) 1000 ppm atomic added Al.

- [2] E.C. Sakshaug, I.S. Kresge, and S.A. Miske, *IEEE Trans. Power App. Sys. PAS-96*, 1977, p. 647.
- [3] G.D. Mahan, L.M. Levinson, and H.R. Philipp, *Appl. Phys. Lett.* 33, 1978, p. 80.
- [4] G.D. Mahan, L.M. Levinson, and H.R. Philipp, *J. Appl. Phys.* 50, 1979, p. 2799.
- [5] H.R. Philipp and L.M. Levinson, *J. Appl. Phys.* 48, 1621 (1977).
- [6] L.M. Levinson and H.R. Philipp, *J. Appl. Phys.* 49, 6142 (1978).
- [7] W.N. Lawless, C.F. Clark, B.R. Patton, and F.S. Khan, *J. Appl. Phys.* 64, 4223 (1988).
- [8] W.N. Lawless and T.K. Gupta, *J. Appl. Phys.* 60, 607 (1986).
- [9] G. Heiland, E. Mollwo, and F. Stöckmann, *Solid State Physics*, Vol. 8, p. 193, F. Seitz and D. Turnbull, ed., Academic Press (1959).
- [10] T. Miyoshi, K. Maeda, K. Takahashi, and T. Yamazaki, *Advances in Ceramics*, Vol. 1, L.M. Levinson, ed., p. 309, American Ceramic Society (1981).
- [11] W.G. Carlson and T.K. Gupta, *J. Appl. Phys.* 53, 5746 (1982).
- [12] J. Volger in *Progress in Semiconductors*, Vol. 4, p. 207, A.F. Gibson, ed., Wiley, New York (1960).
- [13] L.M. Levinson and H.R. Philipp, *J. Appl. Phys.* 47, 1117 (1976).

- [14] L.M. Levinson and H.R. Philipp, *J. Appl. Phys.* **47**, 3116 (1976).
- [15] P.W. Li and K. I. Hagemark, *J. Solid State Chemistry* **12**, 371 (1975).
- [16] N.F. Mott and W.D. Twose, *Advances in Physics* **10**, 107 (1961).
- [17] A.R. Hudson, *Phys. Rev.* **108**, 222 (1957).
- [18] H.R. Philipp and L.M. Levinson, *Advances in Ceramics* **1**, 394 (1981).

MODELLING THE ELECTRICAL CHARACTERISTICS OF POLYCRYSTALLINE VARISTORS USING INDIVIDUAL GRAIN BOUNDARY PROPERTIES

Qingzhe Wen and David R. Clarke

**Materials Department, College of Engineering,
University of California, Santa Barbara, CA 93106**

1. INTRODUCTION

Since the original publication [1], by Matsouka in 1971, demonstrating that polycrystalline ZnO doped with additives, such as CoO, MnO, Bi₂O₃ and Sb₂O₃, can exhibit highly non-ohmic electrical characteristics, a voluminous literature has been generated. Although many of the essential ideas concerning the origin of the varistor behavior were introduced by Matsouka and others within a relatively short time, the literature has continued to grow. Much of it has been concerned with either detailing the electronic and defect mechanisms underlying the varistor behavior or with specific ceramic processing findings. In seeking an understanding of varistor behavior, the implicit assumption of much of this work has been that the electrical characteristics of a real, polycrystalline varistor can be determined by appropriate averaging once the characteristics of a single grain boundary are understood. However, observations of the microstructure, particularly at high spatial resolution, reveal that the microstructure can be quite complex. Second phases, such as spinel and various Bi₂O₃ polymorphs, each with a different thermal expansion coefficient and electrical conductivity, are usually present. Also, a bismuth-rich intergranular film has been reported at grain boundaries by many investigators as well as bismuth-rich segregation at other grain boundaries. In addition, experimental measurements of the current-voltage characteristics of individual grain boundaries reveal that there is a distribution in break-down voltage as well as variations in the non-linear, varistor exponent [2-6]. Furthermore, since zinc

To the extent authorized under the laws of the United States of America, all copyright interests in this publication are the property of The American Ceramic Society. Any duplication, reproduction, or republication of this publication or any part thereof, without the express written consent of The American Ceramic Society or fee paid to the Copyright Clearance Center, is prohibited.

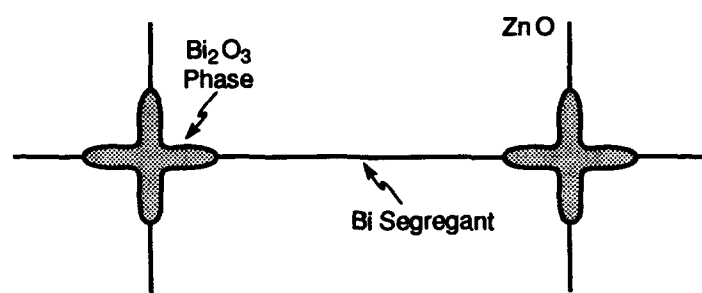
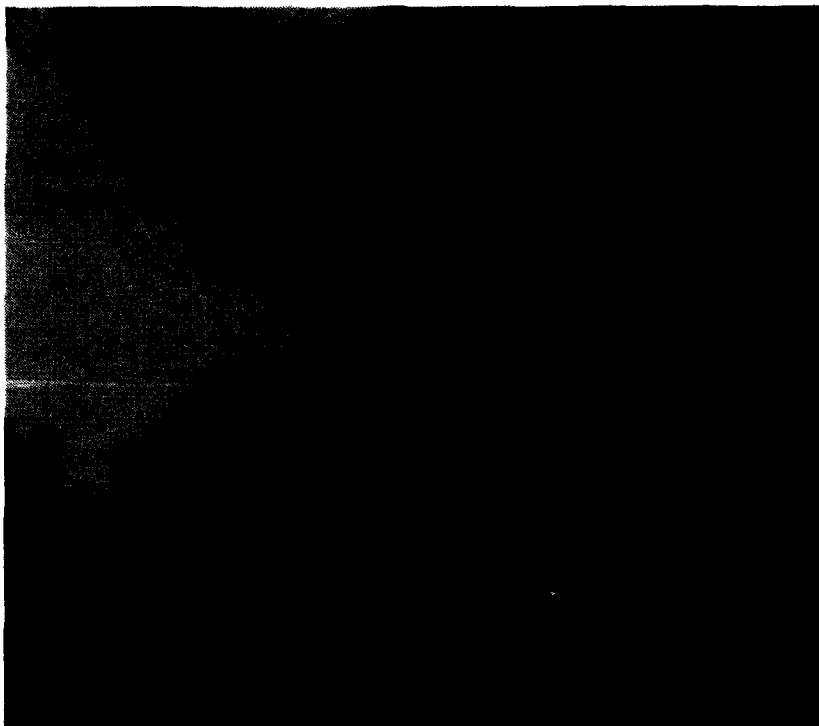


Figure 1 (a). Typical three-grain junction region in a commercial varistor. The Bi_2O_3 -rich second phase partially encroaches along the two-grain junctions thereby restricting current flow across the boundary. Transmission electron micrograph. (b) Representative microstructure of a varistor based on transmission electron microscopy observations.

features of the microstructure consist of ZnO grains wet along the three- and four-grain junctions by a bismuth oxide-rich phase with bismuth segregation along the majority of two-grain junctions [8-10]. This is illustrated with the transmission electron micrograph reproduced in figure 1a. Depending on the additives and the processing routes used, there may also be spinel second phases at the multiple grain junctions and the bismuth oxide rich phase may be partially crystallized to one or more of its polymorphs. The representative microstructure used to model these materials is shown in figure 1b and consists of equiaxed square grains with a second, insulating phase at each corner. The array of non-linear junctions which will be used to calculate the I - V characteristics of the material is the mathematical dual of this square array and is thus also square array. This relationship is shown in figure 2. Any number of grains can be included in the computation but present computer capacity limits us to microstructures of 30×30 grains.

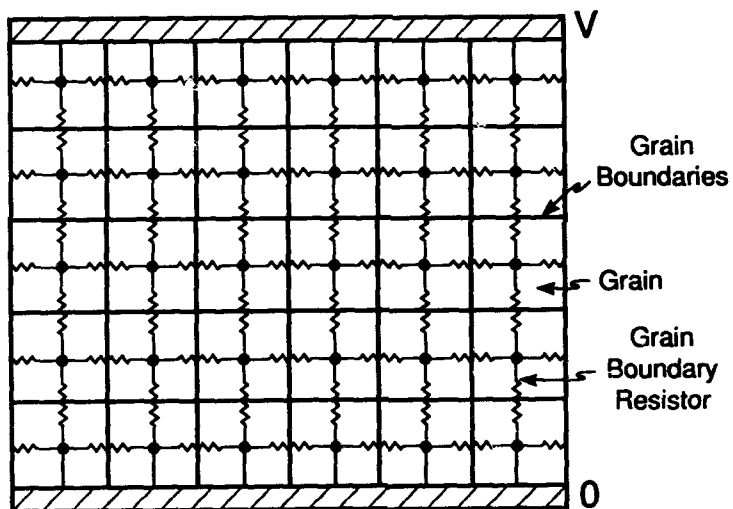


Figure 2. Network model used to compute the varistor characteristics. The array of grain boundary resistors is the topological dual of the microstructure of square grains. The electrical characteristics of the individual grain boundaries are described in the text and are selected at random again as described in the text.

Variations in the observed microstructures are incorporated in the model microstructure by varying the electrical characteristics of

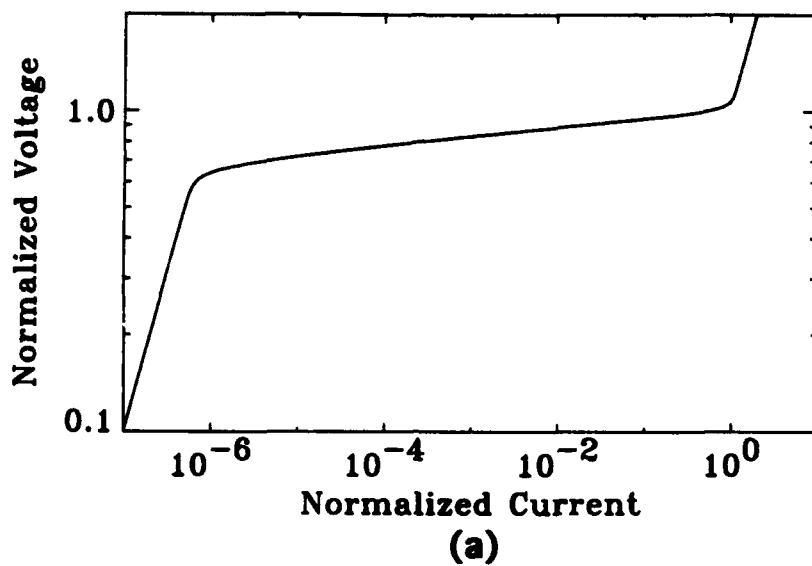
individual boundaries. For instance, the observation that different proportions of the grain boundary area are covered by the wetting phase at the multiple grain junctions, as shown in figure 1a, can be expressed by variations in the grain boundary resistance from one boundary to the next. Similarly, the crystallographic texture of the microstructure can be included by assigning the crystallographic orientation of each grain according to an appropriate rule. In the present scheme in which piezo-electric effects are neglected, the orientation of each grain is chosen at random. In the simulations reported here, the second phase is also assumed to have no effect on the electrical characteristics and the resistance of all the grains are fixed to the same value. In order to take into account the fact that the grain size of most ceramics is not uniform and that not every grain boundary has a Schottky barrier, a certain portion of the boundaries in the microstructure is assigned to be normal, linearly resistive grain boundaries. Therefore, an effective grain size is introduced to characterize the microstructure of our model polycrystalline system.

2.2. Single Boundary Characteristics

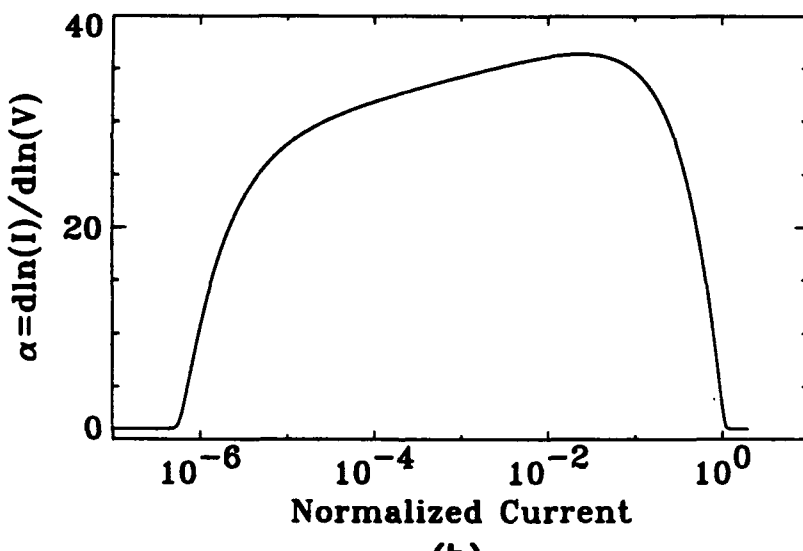
In accord with the reported electrical measurements of individual grain boundaries in varistors, two principal types of grain boundary junction are considered. One is a purely resistive, i.e. linear, boundary having a conductance that is the same as that of the grains themselves. (Setting the linear resistance to that of the grains also allows the proportion of linear boundaries to express variations in grain size, as will be described below). The second type of grain boundary is one having a non-linear, varistor characteristic. In our model these boundaries are treated, electrically, as shunted junctions having the following current-voltage characteristics:

$$I = V \sigma_s + V \sigma_g [1 + \tanh s (V_B - V) / V_B] \quad (1)$$

where σ_s and σ_g are the shunt and grain conductances respectively, V_B is the barrier voltage and s is a parameter that controls the numerical value of the dynamic conductance, α . Although this I - V characteristic is a phenomenological rather than a detailed physical description it does incorporate the essential physical features of models describing varistor grain boundaries. It is also relatively straightforward to program. The I - V characteristic of equation (1) is plotted in figure 3 (a) and the dynamic conductance derived from it is plotted in figure 3 (b).



(a)



(b)

Figure 3 (a). *I-V* characteristic of a single grain boundary and given by the empirical relationship of equation 1 in the text. (b) The corresponding dynamic conductance of the boundary as a function of applied current.

The latter may be compared with the nonlinear exponent as a function of junction voltage calculated by Mahan et al. from a modified back-to-back Schottky barrier model [11].

2.3. Calculation of the Polycrystalline I-V Curves.

In the third step, the overall electrical characteristics of the polycrystalline microstructure are calculated. First, however, each junction in the microstructure is assigned either a linear or non-linear electrical characteristic at random with a prescribed probability. Then, the barrier voltage of each non-linear junction is picked, again using a random number generator, from a Gaussian distribution chosen to represent the distribution of junction voltages observed in experiment. Having assigned the junction characteristics, current flow through the network of junctions is computed. This corresponds to a bond percolation model in which the individual bonds are either linear or non-linear resistors, as distinct from usual percolation models in which each bond is a linear resistor [12].

The current flow through the network at a constant applied voltage is computed subject to the constraint that current conservation is maintained at each node (figure 2). This is invoked by applying Kirchoff's law to each node:

$$\sum_j I_{ij} = 0$$

where the subscripts i denote the node and j the adjacent local nodes. Equivalently, Kirchoff's law may be expressed in terms of the voltages and conductances across each boundary:

$$\sum_j (V_i - V_j) \sigma_{ij} = 0 \quad (2)$$

The conductances of the individual boundaries are

$$\sigma_{ij} = \begin{cases} \sigma_g^{ij} & \text{for a resistive boundary} \\ \sigma_g^{ij} + \sigma_g^{ij} \cdot \frac{1}{2} \cdot \{1 + \tanh[s \cdot (1 - \frac{|V_i - V_j|}{V_B^{ij}})]\} & \text{for a nonlinear boundary} \end{cases} \quad (3)$$

In the computations, a voltage source is applied across the network with ohmic contacts being established at both the top and bottom ends of the network by assigning the first and last row of boundaries as being resistive. Periodic boundary conditions are also applied to the network in the direction perpendicular to the applied voltage. For a system of N grains there are N separate Kirchoff's equations, from which the electrical potential at each grain is solved numerically for each applied voltage across the varistor. The total current through the network is then calculated for each applied voltage. The dynamic conductance, or the nonlinear index, α , is then calculated according to the definition $\alpha = d\ln(I)/d\ln(V)$. In all the simulations reported here we have chosen the following values of the parameters in equation 3: $s=20$, the ratio of shunt to grain conductance, $\sigma_s/\sigma_g = 10^{-6}$, the average of V_B^{ij} , $V_B = 1$ and the conductance of the grains, $\sigma_g = 1$, i.e. voltages are normalized to V_B and currents are normalized to $\sigma_g V_B$.

3. RESULTS

3.1. Mixed Resistive and Non-linear Boundaries

We begin with a consideration of the effect of varying the proportion of grain boundaries that are simply resistive. Although this is a non-linear percolation problem, three limits are known apriori. Two are trivial and correspond to the extremes in which the resistors are either all linear resistors or all non-linear resistors. The third corresponds to the case in which the fraction of resistive bonds equals the percolation limit, P_c , which for a two-dimensional array occurs at 0.5. (In three-dimensions on a simple cubic lattice $P_c = 0.18$.) The computed I - V characteristics for these three cases are reproduced in figure 4. When the proportion of resistive boundaries is less than the percolation limit, the overall electrical response is non-linear and the shape of both the I - V curve and the dynamic conductance are altered. This is illustrated in figure 4 for a series of different concentrations of resistive junctions and is compared with that of a purely non-linear array. Both the maximum value of the exponent and the ohmic region conductivity are decreased from that exhibited by the homogeneous non-linear array, but the nonlinear character of the electrical response makes detailed comparison difficult. To aid comparison, we introduce the following parameters: α_m , the maximum value of the nonlinear index; V_m and I_m the voltage and current at which the non-linear index is equal to α_m ; ΔV_m , the voltage range with $\alpha > \alpha_m/2$; and R_L , the leakage

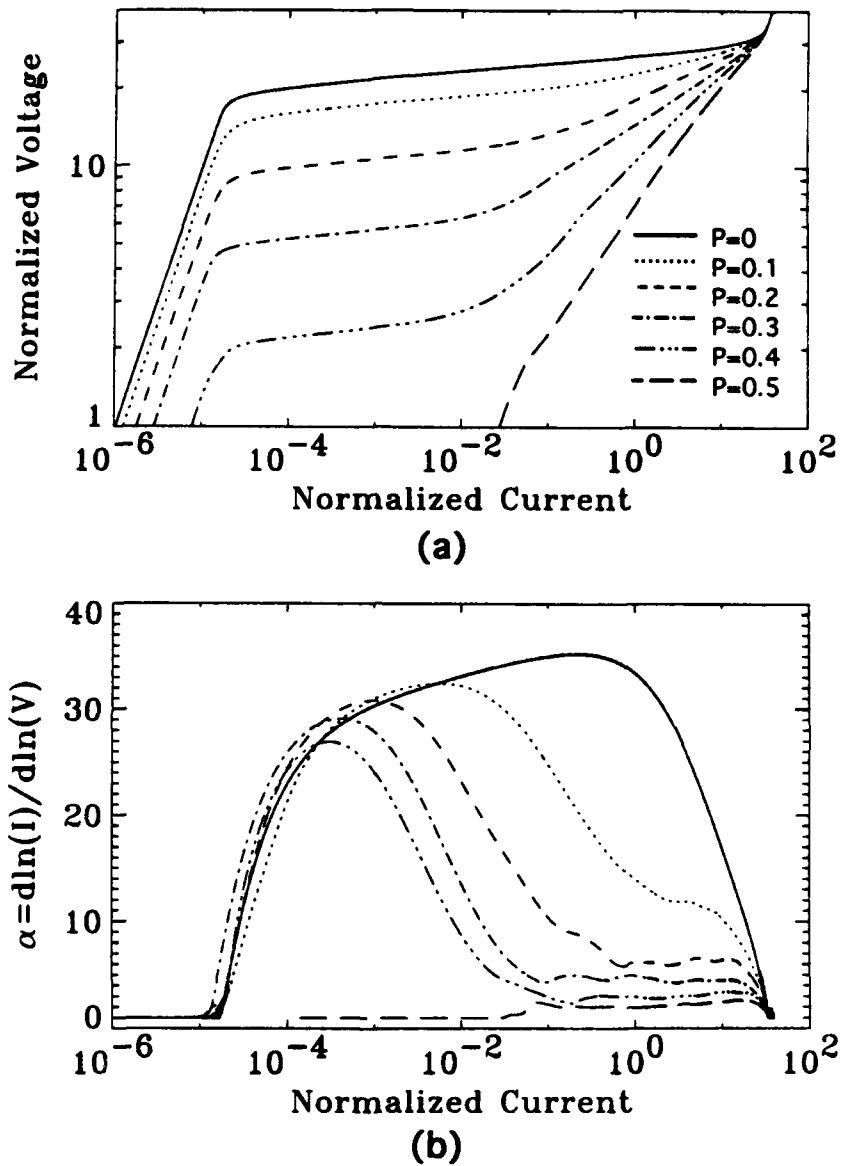


Figure 4 (a). Varistor characteristics as a function of the proportion, P , of linearly resistive grain boundaries. The curve for $P=0$ corresponds to a homogeneous array of identical non-linear boundaries whose individual I - V characteristic is shown in figure 3 (a). (b) The dynamic conductances as a function of applied current.

resistance. These parameters correspond to those often used in the characterization of actual varistors.

Because of our choice that the resistance of the linear boundaries is the same as that of the grains, the proportion of linear boundaries is also a measure of the effective grain size and the grain size distribution. Since the type of boundary is chosen at random, clusters of grains, each connected by resistive boundaries, are formed. The size and distribution of these clusters is a standard result in percolation theory of random grain assignments [12]. Thus, the effective grain size, d_{eff} , is defined as:

$$d_{eff} = \sqrt{\sum_v (n_v \bar{d}_v^2) / \sum_v n_v} \quad (4)$$

where n_v is the number of grains in the v -th cluster and \bar{d}_v is the average size of the cluster of grains. Each of these is a function of the proportion $P - P_c$, where P_c is the percolation limit. The average grain size as a function of the proportion of linear boundaries is shown in figure 5. The simulated results fit an empirical relationship:

$$d_{eff} = d_0 (P_c - P)^{4/3} \quad (5)$$

where d_0 has a value of 0.59, so that when $P = 0$ the effective grain size corresponds to the size of the grain size of the array.

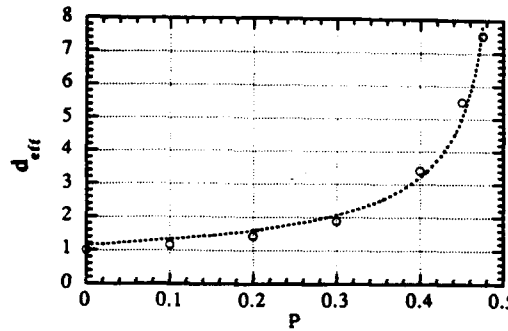


Figure 5. The effective grain size as a function of the proportion of resistive boundaries. Since the resistance of the linear grain boundaries is chosen to be the same as that of the grains, resistive boundaries are indistinguishable from the grains themselves. As a result the value of P also determines the grain size distribution.

From the simulations, the maximum dynamic conductance, α_m , is found to vary approximately linearly with the proportion of resistive boundaries, $P_c - P$. The origin of this dependence is not presently understood in detail but from images in which the current flow through the network is calculated at successively greater values of applied voltage, we believe that this is a direct consequence of the redistribution of current due to a self-adjusting behavior of the non-linear junctions.

One feature of the dynamic conductance curves of figure 4 is that when resistive boundaries are introduced into the network, the response at high currents is reduced but also flattens to a relatively low value of conductance. This is another consequence of combining nonlinearities with the underlying percolation structure of the problem, in essence creating a voltage modulated percolation system. The nonlinear boundaries in the system adjust their conductances in response to the applied voltages and hence the percolating structure of the system is also changing in response to the applied voltage. This effect is most pronounced above breakdown but before the final upturn region where the conductance corresponds to that of the grains themselves. We are not aware of whether this behavior has been reported but as it is past the peak in dynamic conductance it may hitherto have escaped notice.

3.2. Non-linear Boundaries with Distribution in Barrier Voltage

To account for the effect of a distribution of barrier voltages on the overall varistor behavior, the barrier voltage, V_B in equation (1) was chosen at random from a Gaussian distribution with a half-width of δV_B . By introducing a distribution in the barrier voltage, the degree of non-linearity of the overall array is seen to be lessened and so the dynamic conductance is decreased. In addition, the breakdown is made less abrupt and the leakage region conductance is decreased with increasing $\delta V_B / V_B$. These effects are illustrated in figure 6 for normalized distribution half-widths $\delta V_B / V_B$ from 0 to 0.3. The dependence of the maximum value of the dynamic conductance on the width of the distribution is shown in figure 7. Over the range of distribution widths explored, the maximum dynamic conductance results fit an exponential of the form:

$$\alpha_m = \alpha_m^0 \exp [-A (\delta V / V_B)^2] \quad (6)$$

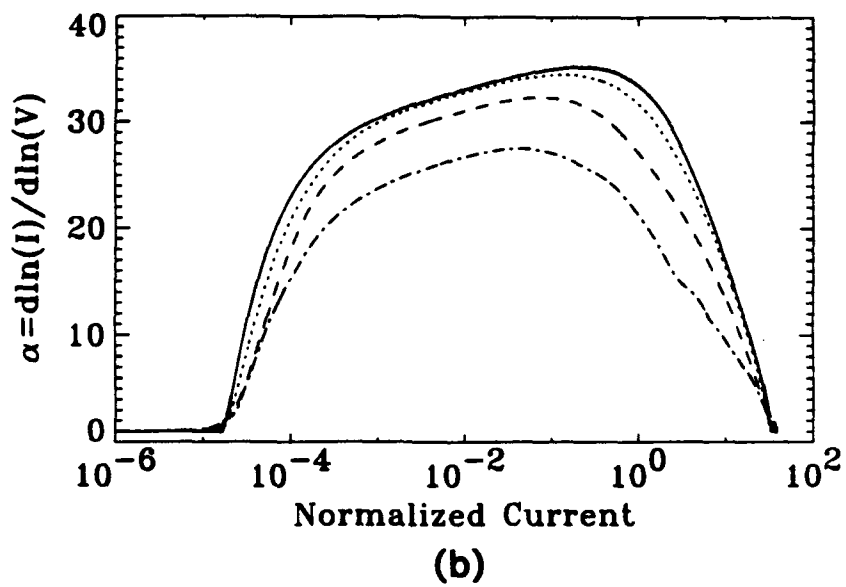
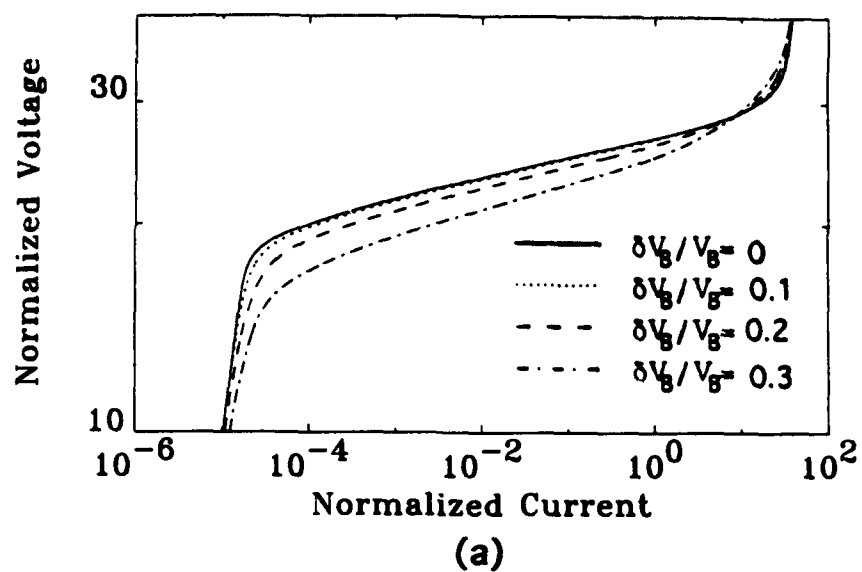


Figure 6. (a) Varistor characteristics as a function of the width in distribution of grain boundary breakdown voltage. (b) The corresponding dynamic conductances.

where A is a constant. A similar dependence is observed for the voltage at which the maximum conductance occurs. Although the numerical values of the constants vary according to the proportion of resistive boundaries, this exponential form fits all the simulation results we have obtained.

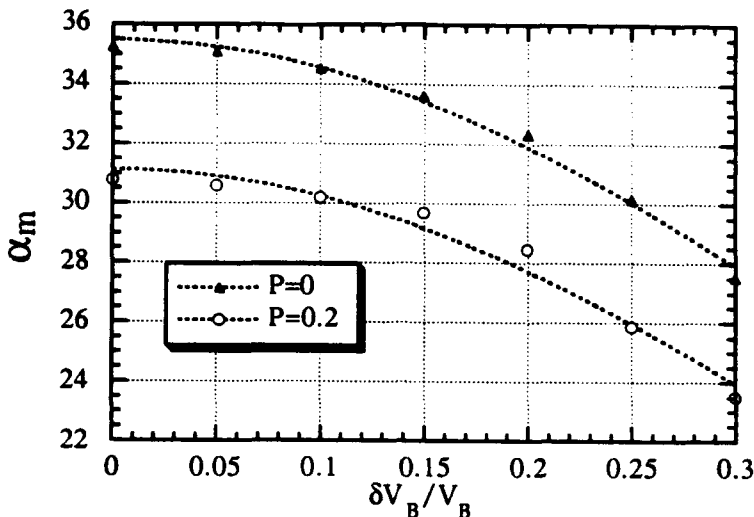


Figure 7. Variation in the maximum dynamic conductance with the boundary-to-boundary variation in breakdown voltage. The curves through the simulation results are the exponential function of equation 6.

4. DISCUSSION

Although we have investigated a particularly simple model to represent the behavior of varistors, the simulation of the I - V characteristics reveal a number of important inter-relationships between microstructure, individual grain boundary electrical characteristics and the variations in breakdown voltage. Perhaps the most striking inter-relationship concerns the effect of variations in grain size, represented by the proportion of linearly resistive grain boundaries. Grain size variations decrease the value of the breakdown voltage and also the range of current over which dynamic conductance has an appreciable value. The grain size variations also introduce an intermediate voltage "up-turn" before the on-set of an "upturn" given for a single grain boundary by the grain resistivity. A second inter-

relationship of importance to the design of varistors is the effect of variations in the break-down voltage, V_B , from one boundary to the next when the grain size is uniform. The simulations indicate that variations in breakdown voltage decrease both the value of the maximum dynamic conductance and the breakdown voltage making the on-set of non-linearity less abrupt. There is also a linear relationship between the maximum value of the dynamic conductance and the deviation of the proportion of linear boundaries from the percolation threshold.

Since the simulations presented are two-dimensional rather than three-dimensional, it is likely that some of the functional dependencies measured will differ from those presented here. However, in common with other percolation problems one can expect that the three-dimensional results will be related to those in two-dimensions through an appropriate scaling. Thus, grain size variations and variations in boundary-to-boundary breakdown voltage will still cause decreases in both the dynamic conductance and the polycrystalline breakdown voltage, but the numerical values will be different.

ACKNOWLEDGEMENTS

This work was supported by the Department of Energy under grant DE-FG03-91ER45447.

REFERENCES

1. M. Matsuoka, "Nonohmic Properties of Zinc Oxide Ceramics", Japanese Journal of Applied Physics, **10** [6] 736-746 (1971).
2. R. Einzinger, "Grain Junction Properties of ZnO Varistors", Applications of Surface Science, **3**, 390-408 (1979).
3. J. T. C. van Kemenade and R. K. Eijnthoven, "Direct Determination of Barrier Voltage in ZnO Varistors", Journal of Applied Physics, **50** [2] 938-941 (1979).
4. E. Olsson and G. L. Dunlop, "The Effect of Bi_2O_3 Content on the Microstructure and Electrical Properties of ZnO Varistor Materials", Journal of Applied Physics, **66** [9] 4317-4324 (1989).

5. M. Tao, B. O. Dorlanne and A. Loubiere, "Different Single Grain Junctions Within a ZnO Varistor", *Journal of Applied Physics*, **61** [4] 1562-1567 (1987).
6. J. Bernasconi, H. P. Klein, B. Knecht and S. Strassler, *Journal of Electronic Materials*, **5**, 473 (1976).
7. C. S. Nichols and D. R. Clarke, "Critical Currents In Inhomogeneous Triangular Josephson Arrays: A Model For Polycrystalline Superconductors", *Acta Metallurgica*, **39** [5] 995-1002 (1991).
8. W. G. Morris and J. W. Cahn, in *Grain Boundaries in Engineering Materials*, edited J. W. Walters et al. (Claitors Press, Baton Rouge, 1975).
9. D. R. Clarke, "Microstructural Location of the Intergranular Metal-Oxide Phase in a Zinc Oxide Varistor", *Journal of Applied Physics*, **49** [4] 2407-2411 (1978).
10. A. T. Santhanam, T. K. Gupta and W. G. Carlson, "Microstructural Evaluation of Multicomponent ZnO Ceramics", *Journal of Applied Physics*, **50** [2] 852-859 (1979).
11. G. D. Mahan, L. M. Levinson and H. R. Phillip, "Theory of Conduction in ZnO Varistors", *Journal of Applied Physics*, **50** [4], 2799-2812 (1979).
12. D. Stauffer and A. Aharony, *Introduction to Percolation Theory*, Taylor and Francis, Washington (1992).

VDR EFFECT IN Bi DIFFUSED SrTiO₃ BASED CERAMICS

N. Ichinose and M. Watanabe
Waseda University, Tokyo 169, Japan

ABSTRACT

VDR (voltage dependent resistor) effect in Bi diffused ceramics has been investigated. The semiconducting samples were prepared by reduction of sintered body in H₂-Ar atmosphere followed by partially reoxidizing in air and by diffusing Bi₂O₃ in air. The height of a double Schottky type potential barrier and the donor concentration in grains were estimated using capacitance - voltage characteristics. The barrier height had a similar tendency to VDR effect with the annealing temperature. The formation of energy barriers was studied by means of ICTS(Isothermal Capacitance Transient Spectroscopy) measurement. It is found from these measurements that there is a secondary phase in Bi diffused SrTiO₃ based ceramics. The VDR effect in this system may be explained by the SIS (Semiconductor-Insulator-Semiconductor) model.

1. INTRODUCTION

SrTiO₃ based ceramics have been widely used for electronic applications as the internal boundary layer capacitors having high apparent permittivity and a low dissipation factor. It has also been reported that sodium-thermally diffused SrTiO₃ based boundary layer capacitors have the non-ohmic behaviour of the voltage-current characteristics.¹⁻³⁾ The voltage-current relation is often described by the empirical formula of $I=KV^\alpha$, where α is the exponent of the nonlinearity and varies with the applied voltage. This non-ohmic behaviour is caused by the depletion layers near grain boundaries. Amongst various conduction mechanisms reported for the origin of the nonlinearity, the most prominent one is due to a double Schottky type potential barrier model.⁴⁾ Thus grain boundaries have play a significant role in determining the flow of electron current.

It is well-known that the voltage-dependent resistor (VDR) effect depends upon the firing conditions of the ceramics, particularly upon oxygen partial pressure. It has been reported that the energy barriers are closely related to

To the extent authorized under the laws of the United States of America, all copyright interests in this publication are the property of The American Ceramic Society. Any duplication, reproduction, or republication of this publication or any part thereof, without the express written consent of The American Ceramic Society or fee paid to the Copyright Clearance Center, is prohibited.

absorbed oxygen on grain surfaces, because the VDR effect is degraded by heating in a reducing atmosphere and restored by reoxidation.⁵⁾

In the present study, the relation between the electronic states at the grain boundaries and the VDR effect in the Bi-diffused SrTiO_3 based ceramics compared with that of non-diffused ones. The Bi-diffused and non-diffused SrTiO_3 based semiconducting samples were prepared by a reduction of sintered bodies in H_2 -Ar atmosphere followed by partial reoxidation in air as shown in Fig. 1.

The barrier height (ϕ_b) and donor concentration (N_d) in the grains were estimated from capacitance-voltage characteristics of the samples according to the double Schottky type potential barriers model. The interface states density (N_i) formed at grain boundaries were examined by means of isothermal capacitance transient spectroscopy (ICTS).

2. EXPERIMENTAL

Nb_2O_5 doped SrTiO_3 based ceramics were prepared by the conventional ceramic processing as shown in Fig. 1. The mixture was calcined at 1000°C for 3h in air, pelletized, pressed into disks of 18mm diameter x 3 mm thickness under 1 ton/cm², and then fired at 1460°C for 3h in air. The sintered samples were reduced at 1300°C for 3h in a H_2 /Ar=3:1 atmosphere. The samples were partially reoxidized (sample A) or Bi-diffused (sample B) at 900 - 1300°C for 1h in air.

The element distributions at the grains and grain boundaries of the sample were examined with the help of an energy dispersive X-ray microanalyzer (EDX). The samples were also examined by X-ray diffraction using $\text{CuK}\alpha$ radiation.

The In-Ga alloy was pasted on both surfaces of the samples to provide ohmic contact for the electrodes. DC voltage-current characteristics were measured by a 2-terminal method using a DC power supply. AC voltage-current characteristics were measured at 50Hz using a curve tracer. Complex impedance plots and capacitance-voltage characteristics were measured by means of an impedance analyzer. ICTS measurements were also performed using impedance analyzer at room temperature.

3. RESULTS AND DISCUSSION

Figure 2 shows the EDX spectrum for sample B. The secondary phase is identified as Bi-diffused SrTiO_3 . But for sample A, very little of secondary phase was found. Therefore the secondary phase for sample B is considered to be caused by the diffusion of Bi.

The semiconducting samples, as reduced in H_2 -Ar atmosphere, have low resistivities of about 2.0 - 2.5 $\Omega\text{-cm}$

and show ohmic behaviour. Partially reoxidized samples have higher resistivities and show more non-ohmic behaviour as shown in Fig. 3. Nonlinear coefficient α vs. annealing temperature is plotted in Fig. 4. Figure 5 gives complex impedance plots at room temperature for sample A reoxidized at 1000 - 1300°C for 1h in air. As shown in Fig. 5, the radii of the semicircles in these plots, which represent total impedance, become larger with increasing reoxidizing temperature. This indicates that energy barriers, corresponding to the insulating part in n-i-n structure, become larger in portion to the amount of insulating layer. It is found in Fig. 6 that the insulating or secondary phase is thicker than that of sample A. From these experiments, grain boundary structure for sample A and B may be described in Fig. 7.

Figures 8 and 9 show diffusion layer width for sample A and secondary phase width for sample B as a function of annealing temperature, respectively. They were calculated using apparent permittivity according to Maxwell-Wagner model of the mixed phase.

Annealing temperature dependence of barrier height ϕ_b is shown in Fig. 10. These curves are similar to those of α value in Fig. 4. Therefore, it is found in Fig. 11 that relation between barrier height (ϕ_b) and nonlinear coefficient (α) is linear. Figure 12 shows donor density N_d as a function of annealing temperature. On the other hand, interface states density N_i is calculated by using the following equation.

$$N_i = S(t) \dots \cdot K \cdot N_d$$

where, $S(t) \dots$ is the maximum value of ICTS signal and K is constant. Figure 13 represents annealing temperature dependence of interface states density. Using these data, N_i/N_d vs. annealing temperature is plotted in Fig. 14. These curves are also similar to those of α and ϕ_b values.

Influence of annealing temperature on grain boundary barrier for sample A and sample B is shown in Figures 15 and 16, respectively.

4. CONCLUSION

The conclusion is as follows ;

- (1) There is secondary phase in Bi diffused SrTiO_3 based ceramics
- (2) The VDR effect in this system may be explained by the SIS (Semiconductor-Insulator-Semiconductor) model
- (3) The barrier height (ϕ_b) and N_i/N_d ratio show the similar tendency to nonlinear coefficient (α) with the annealing temperature

REFERENCES

- 1) N. Yamaoka, M. Masuyama and M. Fukui ; Am. Ceram. Soc. Bull. 62 (1983) 698
- 2) D. Kaino, J. Funayama and N. Yamaoka ; Jpn. J. Appl. Phys. 24 Suppl. 24-3 (1985) 120
- 3) M. Fujimoto, Y-M Chiang, A. Roshko and W. D. Kingery ; J. Am. Ceram. Soc. 68 (1985) C-300
- 4) K. Mukae, K. Tsuda and I. Nagasawa ; Jpn. J. Appl. Phys. 16 (1977) 1361
- 5) Y. Nakano and N. Ichinose ; J. Mater. Res. 5 (1990) 2910

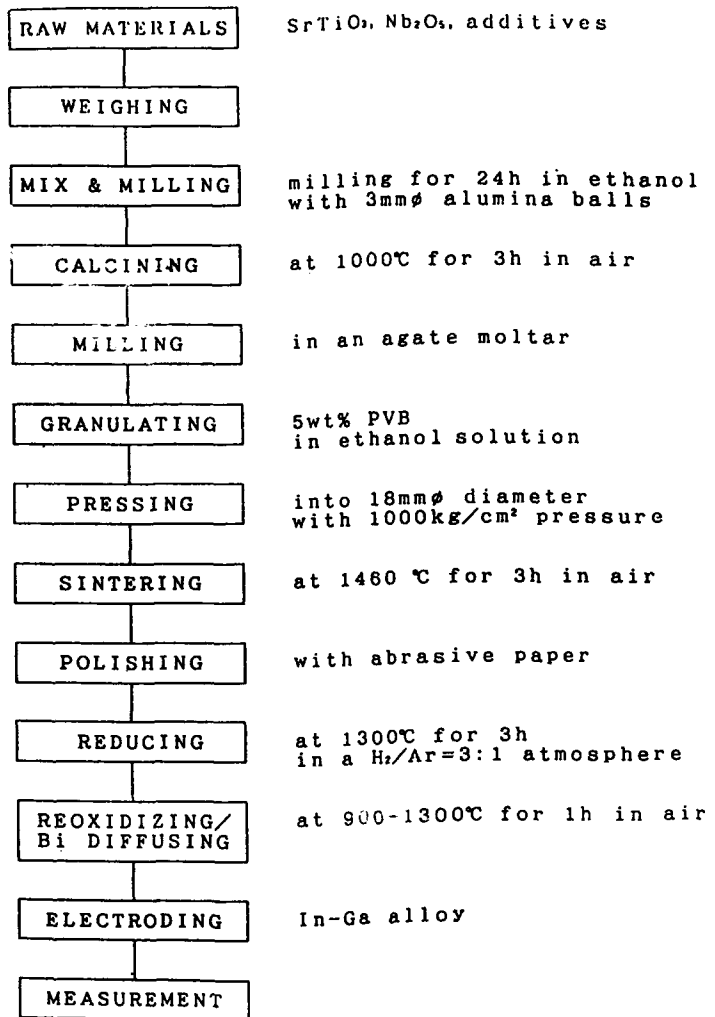


Fig. 1 Simplified flow diagram for fabrication SrTiO₃ based ceramics

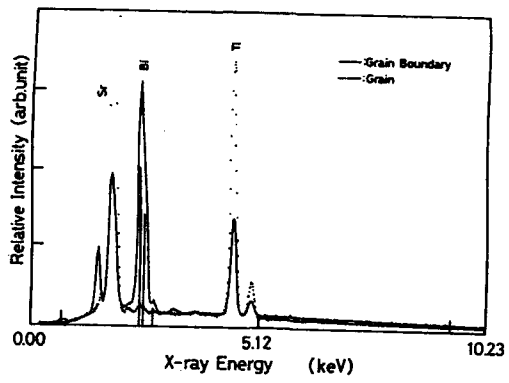


Fig. 2 EDX spectra of grain (broken line) and grainboundary (solid line)

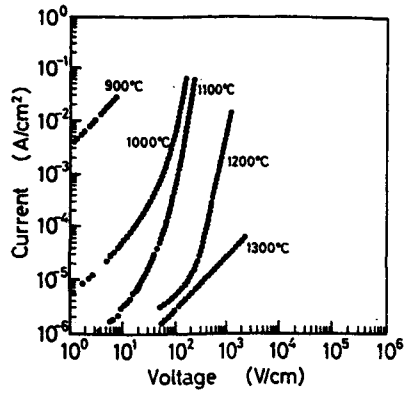


Fig. 3 d.c.V-I characteristics for Sample B

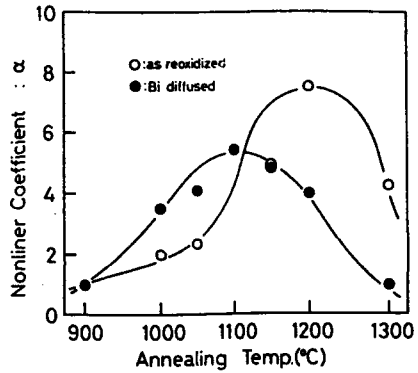


Fig. 4 Annealing Temperature dependence of Nonlinear Coefficient α

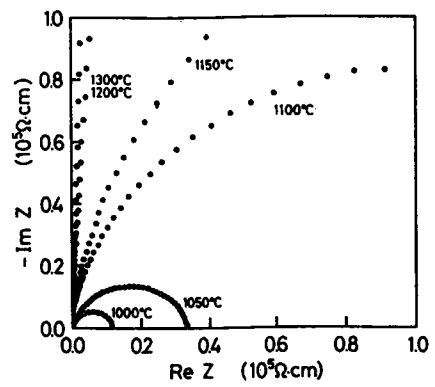


Fig. 5 Complex Impedance plots for Sample A
(Annealed at 1000-1300°C for 1h in air)

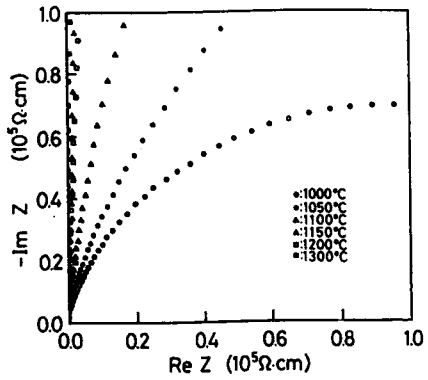


Fig. 6 Complex Impedance plots for Sample B
(Annealed at 1000-1300°C for 1h in air)

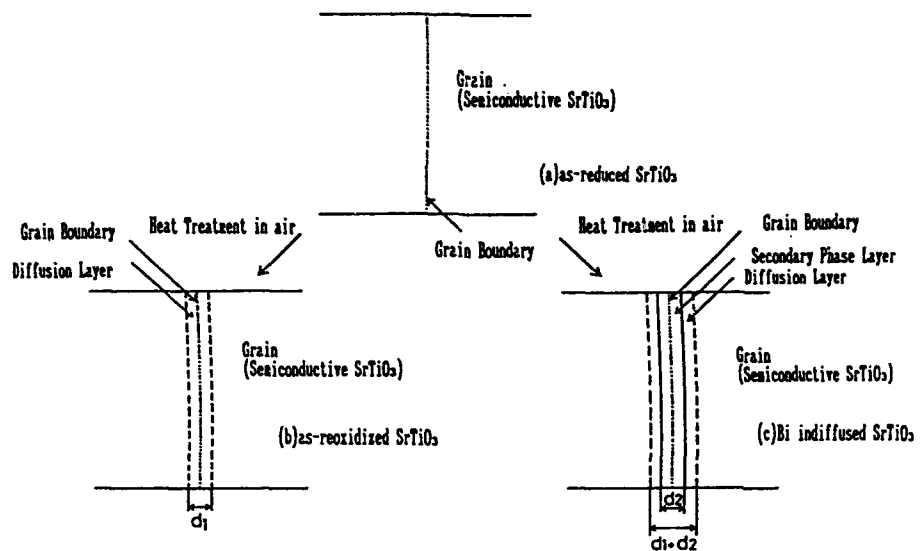


Fig. 7 Grain Boundary Structure for Sample A and Sample B
(after annealing)

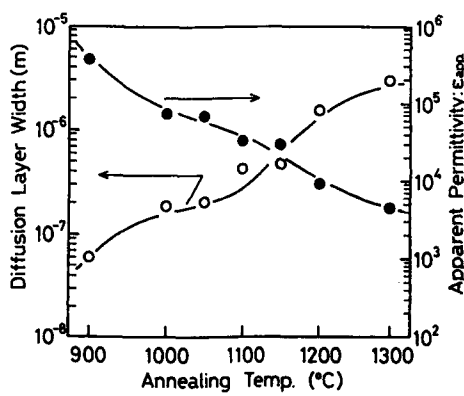


Fig. 8
Diffusion Layer Width as a function
of Annealing Temperature (Sample A)

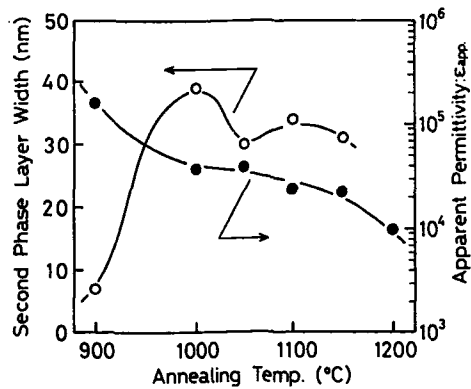


Fig. 9
Second Phase Layer Width as a function
of Annealing Temperature (Sample B)

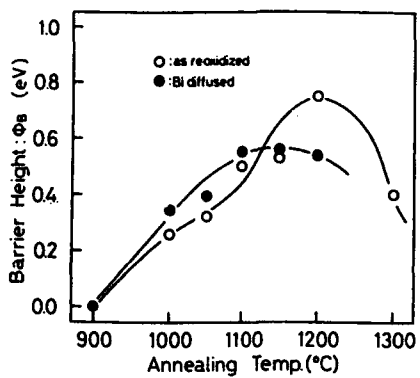


Fig. 10 Annealing Temperature dependence of Barrier Height ϕ_B

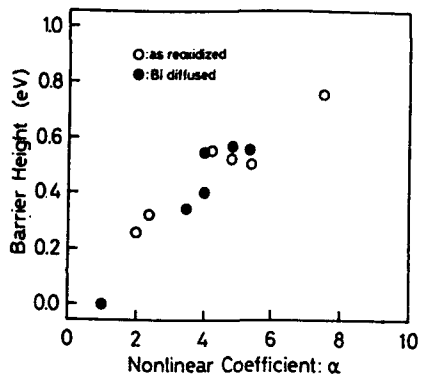


Fig. 11 Relation between Barrier Height and Nonlinear Coefficient

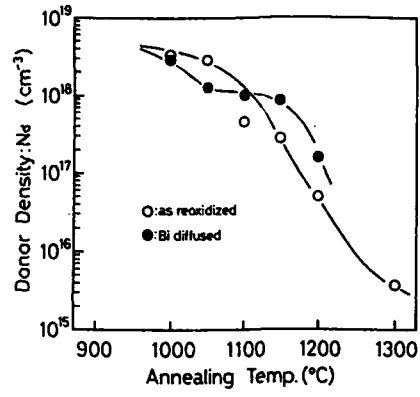


Fig. 12 Annealing Temperature dependence of Donor Density N_d

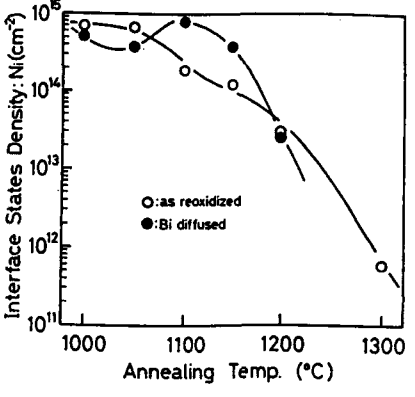


Fig. 13 Annealing Temperature dependence of Interface States Density N_i

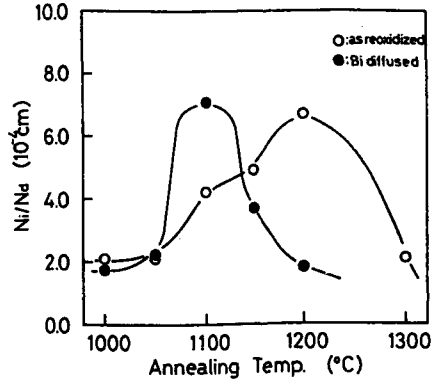


Fig. 14 Annealing Temperature dependence of N_i/N_d

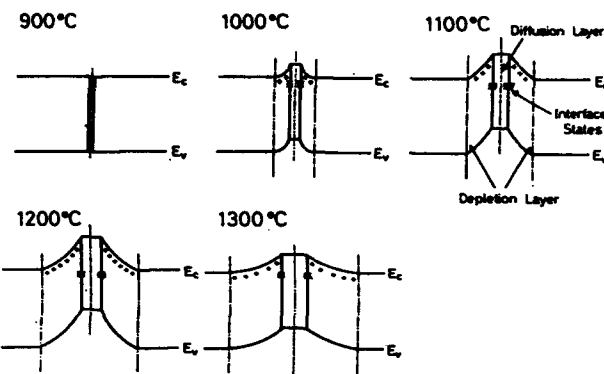


Fig. 15 Influence of Annealing Temperature on Grain Boundary Barrier
(for Sample A)

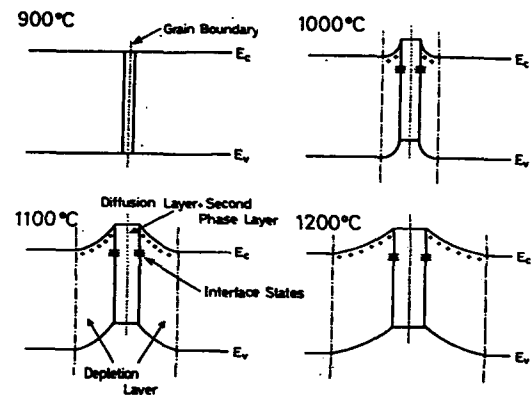


Fig. 16 Influence of Annealing Temperature on Grain Boundary Barrier
(for Sample B)

SUB-GRAINBOUNDARY PHENOMENON IN ZnO VARISTOR CERAMICS DURING SINTERING

Xiaolan Song Fuyi Liu

**Insulation Institute, Department of Electrical
Engineering, Xi'an Jiaotong University,
Xi'an, Shaanxi, P.R.C.**

Abstract

In this paper, the development of ZnO grains in ZnO varistor ceramics during sintering has been studied. It was found by scanning electron microscopy (SEM) that there is a sub-grainboundary phenomenon in the forming and development of ZnO grains. With sintering temperature rising, the size of ZnO grains increases, in the meantime, the sub-grainboundaries tend to disappear and ZnO grains develop gradually into complete crystals.

Introduction

Zinc oxide varistor ceramics have high nonlinearity and large energy absorption capability. The electrical characteristics of ZnO varistors are directly dependent on the microstructure. Other properties of polycrystalline ceramics also depend on the microstructure, so that it is important to understand the microstructural development of ZnO ceramics in a general sense.

To the extent authorized under the laws of the United States of America, all copyright interests in this publication are the property of The American Ceramic Society. Any duplication, reproduction, or republication of this publication or any part thereof, without the express written consent of The American Ceramic Society or fee paid to the Copyright Clearance Center, is prohibited.

Grain growth in pure ZnO has been extensively investigated. The isothermal rate of grain growth can be expressed by the phenomenological kinetic grain growth equation:

$$G^n = D t \exp(-E/RT)$$

where G is the average grain size at time t , D is a constant, n is the kinetic grain growth exponent, E is the apparent activation energy, R is the gas constant, and T is the absolute temperature. Nicholson[1] was the first who studied the grain growth in ZnO. He has reported that $n=3$. Subsequently, many investigators from different countries studied the grain growth in pure ZnO[2-4], the values of n reported in these studies were almost consistent, but the activation energies for grain growth ranged from 213 to 409 kcal/mol. Recently, the rate of grain growth in the ZnO-Bi₂O₃ system was studied. It was found that Bi₂O₃ increases the rate of ZnO grain growth[5]. Ying Chung[6] studied the influence of the valence state of cobalt on ZnO grain growth, Co³⁺ ions also increase the rate of grain growth. He suggested that ZnO grain growth is controlled by diffusion of zinc ions. The above investigations help to understand the law of ZnO grain growth during sintering.

In this paper, we describe the development of ZnO grains during sintering. It was found that there are irregular interfaces in ZnO grains, which are analogous to grainboundaries between grains, called sub-grainboundaries here. Based on the observation of sub-grainboundaries, an improved model of ZnO grain growth is proposed.

Experimental Procedures

The compositions used in this work are ZnO with additives such as Bi₂O₃, Sb₂O₃. The pure ZnO powder and additives were milled

by conventional techniques. Then, the powders were dried, granulated and pressed into disks of 20mm in diameter and 2.0mm in thickness. These pressed bodies were sintered at temperatures 900 °C, 1000 °C, 1100 °C and quenched in air directly.

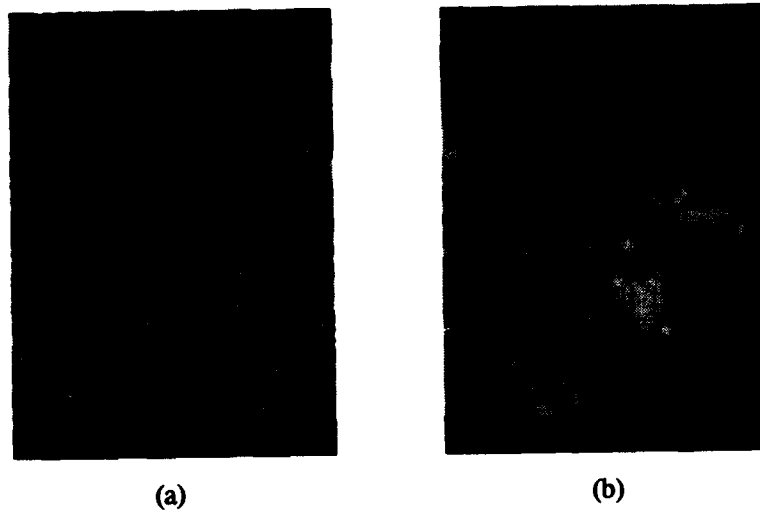
For microstructural observations, the surfaces of the sintered samples were lapped and polished to mirror like finish with fine abrasive papers and Cr₂O₃ paste on a wetted, rotating velvet. After cleaning, the specimens were etched in HF acid for an appropriate time. The development of ZnO grains during sintering can be observed by scanning electron microscopy, shown in Fig. 1. To investigate the microstructure of ZnO grains, the above specimens were observed again after having been etched in HCl acid for appropriate times. The results are shown in Fig.2.

Results and Discussion

By appropriate observation conditions, the results in Fig. 1 were obtained. The results illustrate that at 900°C, there are only small, original ZnO powders (<0.5μm) in the samples, not obvious ZnO grains. At 1000°C, the morphology of ZnO grains has been formed. However, ZnO grains are not crystals, there are many irregular interfaces in these ZnO grains, called sub-grainboundaries in this paper. When the sintering temperature increases to 1100°C, sub-grainboundaries tend to disappear.

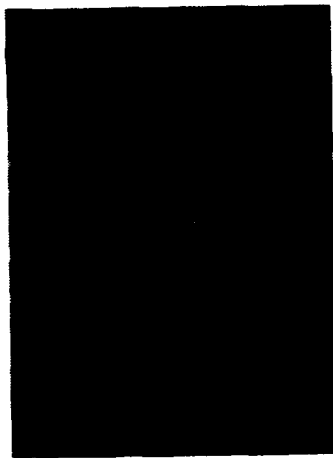
The three-dimensional morphology of ZnO grains is shown in Fig. 2. At 1000°C, it can be seen from Fig.2(a) that there are agglomerations of small grains. Therefore, it can be proposed that sub-grainboundaries are the interfaces between small grains. At 1100°C, small grains develop into large crystals, and many sub-grainboundaries disappear.

According to the above experimental results, ZnO grains are formed at some higher temperature, at the same time, there are



(a)

(b)



(c)

**Fig. 1 The Development of ZnO
Grains During Sintering**
(a) 900 °C (b) 1000 °C
(c) 1100 °C

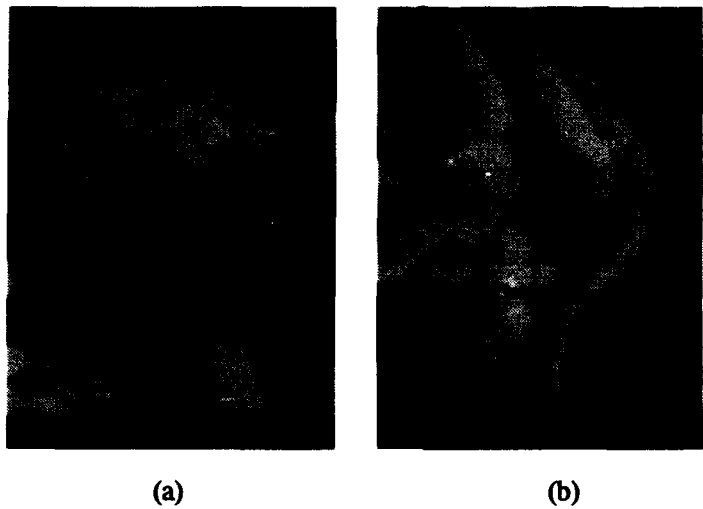


Fig.2 Three-dimensional Morphology of ZnO Grains
(a) 1000 °C (b) 1100 °C

sub-grainboundaries in ZnO grains. At the beginning of grain growth, original grains gathered together[7] under surface tension. With sintering temperature increasing, bigger grains absorb smaller ones in agglomerations, and develop into perfect crystals by ion diffusion. Since crystal orientations between grains are different, and there may be some additives between different grains, interfaces between small grains can't disappear as soon as the sintering temperature increases. This may result in the formation of sub-grainboundaries in ZnO grains.

Based on the above experimental results and discussion, the process of ZnO grain growth can be classified into two stages: one is agglomeration of small original grains, the other is grain growth.

The forming mechanism of sub-grainboundaries and the effects

of them on the electrical properties of ZnO varistors will be studied further.

Conclusion

By investigating the development of ZnO grains during sintering, it was found for the first time that there are sub-grainboundaries in ZnO grains. With sintering temperature rising, sub-grainboundaries tend to disappear. Based on the discovery of sub-grainboundaries, an improved model of grain growth in ZnO varistor ceramics is proposed in this paper, i.e., the development of ZnO grains can be classified into two stages: one is the agglomeration of small original grains, the other is grain growth.

References

- [1]. G.C.Nicholson, J. Am. Ceram. Soc. 48, 214(1965).
- [2]. S.K. Dutta and R.M.Spriggs, "Grain Growth in Fully Dense ZnO, J. Am. Ceram. Soc., 53[1], 61-62(1970).
- [3]. T.K.Gupta, "Inhibition of Grain Growth in ZnO", J. Am. Ceram. Soc., 54[8], 413-414(1971).
- [4]. T.Asokan and R.Freer, "Hot Pressing of Zinc Oxide Varistor", Br. Ceram. Trans. J., 89, 8-12, 1990.
- [5]. Tetsuya Senda and Richard C.Bradt, "Grain Growth in Sintered ZnO and ZnO-Bi₂O₃ Ceramics", J. Am. Ceram. Soc., 73[1], 106-114(1990).
- [6]. Ying-Chung Chen etc., "Grain Growth and Electrical Properties in ZnO Varistors with Various Valence States of Additions", Jpn. J. Appl. Phys., 30[1], 84-90(1991).
- [7]. Xiaolan Song and Fuyi Liu, to be published.

THE POLYNUCLEAR HYDROXY METAL CATIONS PILLARED ZIRCONIUM PHOSPHATES AND THEIR PROTON CONDUCTIVITY

Y. Ding*, J. Rozière, D. Jones
LAMMI, URA 79-CNRS, Université
Montpellier II, 34095 Montpellier, France

The treatment of alpha-zirconium hydrogenphosphate monohydrate with polynuclear metal cation sols in definite conditions resulted in the increase of the interlayer distance to 9-20 Å. The pillared novel materials have the proton conductivity as high as 10^{-2} Scm^{-1} at 20°C/100% RH. The structural and electrical characteristics were studied using XRD and conductivity measurement.

1. INTRODUCTION

One of the important route by controlled mixing of ceramic particles of nanometer scales has been used for developing new types of materials with desired functionality. Layered structured materials consisting of thin crystalline layers with a thickness of molecular scale can be regarded as the ideal composite matrix incorporating various inserted ceramic sols as well as polar organic molecules. The reactions to form such a layered composites are called intercalation reaction.

Zirconium phosphate, a two-dimensional layered materials, has been studied extensively in the intercalation chemistry. It was also used as the ceramic Nasicon precursor and gives the ceramics the higher sodium conductivity[1]. Two hydrates of zirconium monohydrogenphosphates, $\text{Zr}(\text{HPO}_4)_2$ are known: a monohydrate, α , and dihydrate, γ . The α -phase has a layer structure consisting of layers of metal atoms in a plane bridged by phosphate groups above and below the plane of the metal atoms with the P-OH groups pointing between the layers. Protons in the interlayer can be exchanged with smaller cations.

* To whom correspondence should be addressed. Present address: School of Chemical Engineering, Georgia Institute of Technology, Atlanta, Georgia 30332-0100, USA

To the extent authorized under the laws of the United States of America, all copyright interests in this publication are the property of The American Ceramic Society. Any duplication, reproduction, or republication of this publication or any part thereof, without the express written consent of The American Ceramic Society or fee paid to the Copyright Clearance Center, is prohibited.

Many metal cations are subject to hydrolysis because of a high electronic charge or high charge density. Initial products of hydrolysis can condense and polymerize to form polyvalent metal or polynuclear ions, which are themselves colloidal. These larger size ceramic sols can be exchanged with the interlayer cations of the zirconium monohydrogenphosphates by first propping the interlayer with larger organic polar molecules^[2]. The similar research has been conducted as the well known pillared clays which resulted in a new class of selective heterogeneous catalysts with stable structure by the calcination of the ceramic sols pillared clays^[3-4]. However, Conductivity of the pillared systems of these types has not previously been concentrated, though the likely high acidity of the galleried interlayer region offers excellent prospects of high ionic conductivity.

In this paper, we will brief out the intercalation reaction of several ceramic sols into the interlayer of α -ZrP and give the conductivity research of the materials.

2. EXPERIMENTAL

α -Zr(HPO₄)₂·H₂O was prepared by the method of Clearfield and Stynex^[5] using a 12 mol·dm⁻³ phosphoric acid solution as the reflux medium and refluxing for one week. The solid recovered was washed with distilled water, dried in air and stored without special precautions. Expansion of α -Zr(HPO₄)₂·H₂O was carried out using n-alkylamine of chain length between 4 and 10 carbon atoms(or aminocaproic acid). The resulting alkylammonium-intercalated phases are highly crystalline and have interlayer distance in agreement with literature values^[6].

Zr(IV) is known to be hydrolyzed even in very acidic aqueous solutions. Zirconium dichloride oxide aqueous solution, if not very diluted, gives rise to the predominant tetra zirconium species $[\text{Zr}_4(\text{OH})_8(\text{H}_2\text{O})_{16}]^{8+}$ [7-8](abbreviated as Zr₄). In a representative experiment, 0.1 M aqueous solution of ZrOCl₂·8H₂O is aged for 5 days at 50°C. Hydrolysis of aluminum trichloride was performed here using the alkylamine as that used to swell the phosphate layer. The PH of the aqueous solution of AlCl₃·6H₂O is adjusted 4.1 to give a limpid solution of Al:base ratio of 1:2 in which predominant species is so

called Keggion ions $[Al_{13}O_4(OH)_{24}\cdot 12H_2O]^{7+}$ (abbreviated as Al₁₃). The solution aged a week before use.

Ion-exchange of the alkylammonium ion in α -Zr(HPO₄)₂·H₂O for Zr₄ and Al₁₃ were carried out by suspending 1 g of the intercalation compound in a excess of above solution and refluxing respectively 4 and 5 days. The resulting materials were washed with distilled water three times and were air dried.

X-ray diffraction powder experiments were recorded by multiple scanning on an Philips diffractometer using Cu K α radiation.

Powder samples were pressed into pellets of about 1mm thick in a 13mm diameter steel die under a pressure of 5ton/cm². Pellets were stored in dessicators over reservoirs containing sulfuric acid of concentrations corresponding to relative humidities, where they were allowed to equilibrate for 4 days prior to use. The pellets were subsequently mounted between the two platinum electrodes of a sealed cell. ac measurements were performed in the frequency range 5Hz-13MHz using a computer controlled Hewlett Packard 4192 impedance analyzer using an oscillating voltage of 100mV. dc measurement were carried out at Chemistry Department of Exeter University with a voltage from 0 to 500 mV applied at room temperature across the pellet in 25mV steps, and the current noted when stability was reached. The sample was equilibrated with humidified hydrogen gas for 2 hours prior to the experiment.

3. RESULTS AND DISCUSSIONS

Pillaring of the aluminum Keggion ion into α -ZrP was first reported by Clearfield and Roberts in 1989[2]. Subsequently, Si sol was reported to be inserted into the interlayer of the phosphate[9]. The specific objective of them is to achieve pillared layered solids having high specific surface area. That was not a concern of the present research where, on the contrary, "stuffing" of the interlayer space with highly hydrated sols will contribute to the ionic conductivity. Jones, Leloup and Ding et al preliminary work[10] indicated that the hydrated Al species pillared α -structured metal(IV) hydrogen phosphate can greatly enhance the material conductivity. In their work, they found that the degree of crystallinity of the material formed after insertion depends on the reflux times. Longer reflux times reduce the

crystallinity and increase the conductivity. Usually, the crystallinity of the material prepared is not satisfactory. The interlayer distance varies and is dependent on the chain-length of the pre-swell agent.

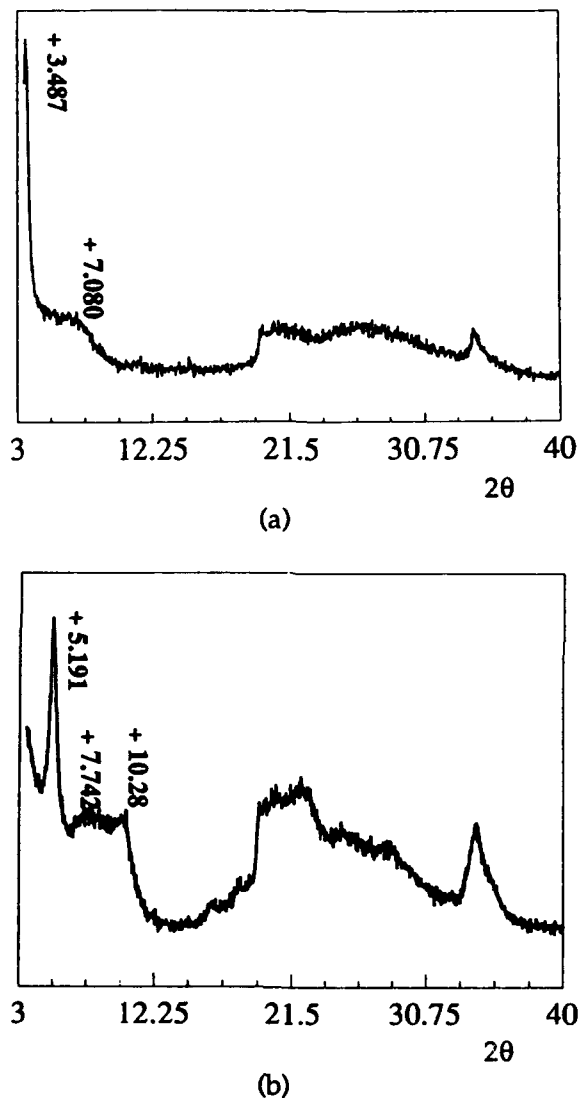


Fig.1. The XRD pattern of (a) $\{Zr_4(OH)_{14}(H_2O)_{10}\}^{2+}$ and (b) keggion ions pillared α -ZrP

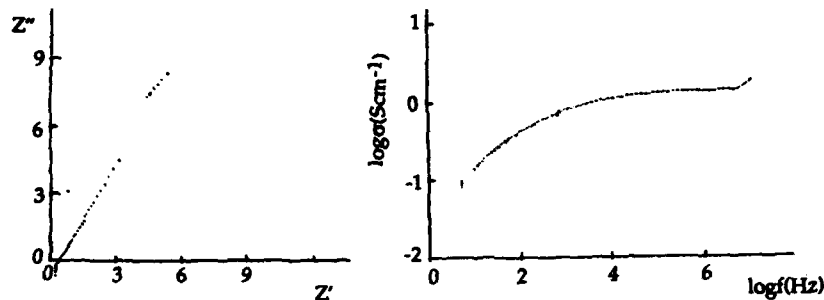


Fig. 2. Impedance spectra of $(\text{Zr}_4(\text{OH})_{14}(\text{H}_2\text{O})_{10})^{2+}$ pillared α -ZrP in conditions of 20°C and RH 100%

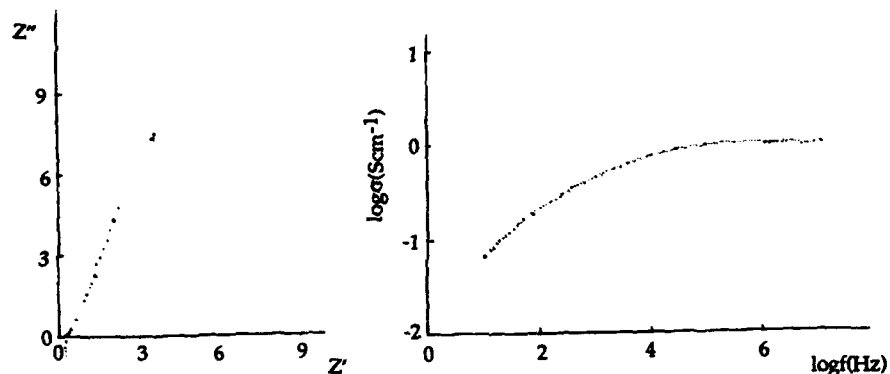


Fig. 3. Impedance spectra of keggion ions pillared α -ZrP (pre-swelled by aminocaproic acid) at 35°C and RH 100%

Fig. 1 gives the XRD pattern of the tetrameric species $[\text{Zr}_4(\text{OH})_8(\text{H}_2\text{O})_{16}]^{8+}$ and polynuclear hydroxyaluminum Keggion ions pillared α -Zr(HPO_4)₂. H_2O . The crystallinity of the material estimated from XRD pattern seems better than that reported in reference [2]. The existence of the Keggion ions in the layered solids was approved first time by the ^{27}Al MAS NMR[10]. XRD indicated the increase of the interlayer distance as compared with that of the α -ZrP, $d_{002}=6.7\text{\AA}$. The interlayer distance increase of the samples are respectively 17.3 \AA and 9.5 \AA which corresponding double Zr₄ and single Al₁₃ units respectively. Infrared spectroscopy showed the absence of any

remaining organic matter, the ceramic sols completely displace the alkyammonium ions.

Fig. 2-3 are respectively the impedance spectra of the above mentioned two kinds of the pillared α -ZrP. The relationship between relative humidity and ionic conductivity, and the relationship between conductivity and temperature of the Keggin ions pillared α -ZrP are schematically illustrated respectively in Fig. 4 and Fig. 5.

From Fig. 2-3, it can be seen that ac conductivity of ceramic sols pillared α -ZrP enhanced two magnitude higher as compared with pristine ZrP which has a typical value at 25°C/60% RH of $8 \cdot 10^{-6} \text{ Scm}^{-1}$. The Zr_4 pillared α -ZrP even show an ac conductivity of as high as $1.52 \cdot 10^{-2} \text{ Scm}^{-1}$ at 20°C/100% RH. Fig. 4 shows that the conductivity of the Al_{13} pillared phosphate sample depends greatly and increase with relative humidity. Fig. 5 shows the conductivity of the sample increases with the temperature in the definite region. No loss in conductivity due to the dehydration of the material up to 80°C. However, when the temperature is much higher, the conductivity decreases sharply for the lost of water in the interlayer and the ceramic sols become to the ceramic oxide. The interlayer distance also decrease when the sample is heated at higher temperatures. The d_{002} spacing 24 Å of $[\text{Zr}_4(\text{OH})_8(\text{H}_2\text{O})_{16}]^{8+}$ pillared α -ZrP decrease to 19 Å after the calcination of the sample at 300°C for 2 hours. Because of the higher conductivity of the ceramic sols pillared α -ZrP but not ceramic oxide pillared α -ZrP, potential application of it at low temperature direct methanol fuel cell and electrochemical devices will be anticipated.

dc measurement indicated that Al-ZrP showed an ohmic response under controlled voltage conditions. The current decayed rapidly to zero after applying 500mV potential which demonstrating no electronic conductivity. The dc conductivity measured is about the same as the ac conductivity which support the idea that the charge carriers are protons. Further proof is also given in reference[8]. The proton conduction origin from, after exerting electric field on the both side electrodes, the hydrolysis of the sols such as:



The different method prepared ceramic sols pillared α -ZrP often

gives the different characteristics. If the α -ZrP is pre-swelled by aminocaproic acid instead of alkylamine, the Al13 pillared phosphate shows a better crystallinity and much higher proton conductivity of the value $1.7 \cdot 10^{-2} \text{ Scm}^{-1}$ at $20^\circ\text{C}/100\% \text{ RH}$ (see Fig. 3) as compared with that of butylamine pre-swelled α -ZrP whose proton conductivity is $1 \cdot 10^{-3} \text{ Scm}^{-1}$ at $20^\circ\text{C}/100\% \text{ RH}$ condition (as shown in Fig. 4). The phenomenon contradict with the point that less crystallinity will increase the external surface area and will conducive to the increase in the conductivity. Even the age time of the sol solution and the

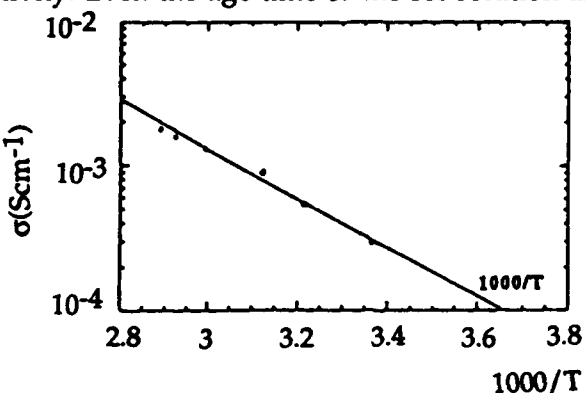


Fig. 4. Relationship of the conductivity of keggion ions pillared α -ZrP with the temperature at RH 65%

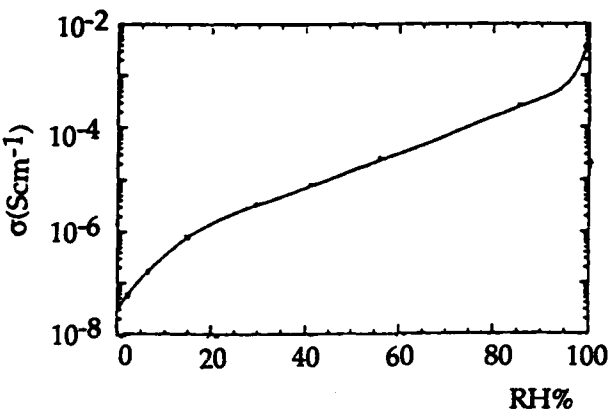


Fig. 5. Relationship of the conductivity of keggion ions pillared α -ZrP with the relative humidity at 20°C

refluxing temperature can greatly affect the crystallinity of the sample prepared. We once worked at precisely controlled conditions to get the very well crystallized Al₁₃ pillared α -ZrP[11]. The reasons for these are not clearly understand and are currently being investigated. Anyway, the weak basic characteristic of aminocaproic acid compared with alkylamine will make it be easier displaced by ceramic sols and probably plays an important role in the phenomenon. The aminocaproic acid preswelled α -ZrP is also successfully be used as the precursor for the intercalation of larger organic molecules[12].

4. CONCLUSIONS

The ceramic sols pillared α -ZrP shows a higher proton conductivity of as high as 10^{-2} Scm⁻¹ magnitude at 20°C/100% RH. The presence of closely packed and a highly hydrated acidic ceramic sols in the interlayer is suspected to supply a conduction way for protons.

Different method prepared ceramic sols pillared α -ZrP gives different conductivity. The samples prepared with the aminocaproic acid preswelled α -ZrP seems to give a better proton conductivity.

REFERENCES

- [1] A. Clearfield, P. Jerus and J. M. Troup, *Solid State Ionics*, 5(1981)301.
- [2] A. Clearfield and B. D. Roberts, *Inorg. Chem.*, 27(1989)3237.
- [3] F. Figueras, *Catal. Rev.*, 30(1988)457.
- [4] M. L. Occelli and D. H. Finseth, *J. Catalysis*, 99(1986)316.
- [5] A. Clearfield, R. H. Blessing and J. A. Stynes, *J. Inorg. Nucl. Chem.*, 30(1968)2249
- [6] U. Constantino, in *Inorganic Ion Exchange Materials*, ed. A. Clearfield(CRC Press, Boca Raton FL, 1982)p. 122.
- [7] Märtha Åberg and Julius Glaser, *Inorg. Chim. Acta*, 206(1993)53.
- [8] C. F. Baes, Jr and R. E. Mesmer, *The Hydrolysis of cations*, Wiley-Interscience, New York, 1976, P. 152.
- [9] L. Li, X. Liu, Y. Ge, L. Li and J. Klinowski, *J. Phys. Chem.*, 95(1991)5910.
- [10] D. J. Jones, J. M. Leloup, Y. Ding and J. Rozière, to be published in *Solid State Ionics*.
- [11] Y. Ding, D. J. Jones and J. Rozière, unpublished work.
- [12] Y. Ding, D. J. Jones and J. Rozière, to be published in *J. Chem. Soc., Chem. Commun.*.

LI DEINTERCALATION IN LITHIUM TRANSITION METAL NITRIDE, Li_3FeN_2

M.Nishijima, Y.Takeda, N.Imanishi and O.Yamamoto
Department of Chemistry, Faculty of Engineering, Mie University,
Kamihama-cho 1515, Tsu, Mie-ken, Japan

M.Takano
Institute for Chemical Research, Kyoto University,
Uji, Kyoto-fu 611, Japan

ABSTRACT

Li ion was easily deintercalated from Li_3FeN_2 with one-dimensional structure forming $\text{Li}_{3-x}\text{FeN}_2$ in a range of $0 \leq x \leq 1.0$ in a $\text{Li}/\text{Li}_3\text{FeN}_2$ cell. With increase of x , four kinds of phases ($x=0$, 0.5, 0.75 and 0.8–1.0) having orthorhombic symmetry sequentially appeared. Mössbauer spectra suggested that Li deintercalation oxidizes Fe^{III} to Fe^{IV} . The $\text{Li}/\text{Li}_3\text{FeN}_2$ cell showed a good reversibility suggesting to be a good candidate for an electrode for Lithium secondary battery.

INTRODUCTION

It is well known that Li_3N has a high Li ion conductivity of about $1 \times 10^{-2} \text{ Scm}^{-1}$ at room temperature, and numerous studies of this interesting material as a solid electrolyte has been performed for last 10 years (1–3). However, Li_3N has a low decomposition voltage (0.44V), which makes it difficult to be used as an electrolyte for solid lithium battery.

In the systems of Li–metal–nitrogen, a series of nitrides belonging to a general formula of $\text{Li}_{2n-1}\text{MN}_n$ (M: some elements of groups 3, 4 and some transition metals, n=2, 3) has been known for a long time (4–6). These nitrides show the

To the extent authorized under the laws of the United States of America, all copyright interests in this publication are the property of The American Ceramic Society. Any duplication, reproduction, or republication of this publication or any part thereof, without the express written consent of The American Ceramic Society or fee paid to the Copyright Clearance Center, is prohibited.

anti-fluorite type structure (5) where Li ions occupy the positions of fluorine in CaF_2 . As the fluorite structure has large lattice energy and shows high ionic conductivity, these nitrides make us expect the high stability and high Li ion conduction. In fact, Li-nitrides with 3rd and 4th group metals such as Li_3BN_2 (7,8), Li_3AlN_2 (9) and Li_3SiN_2 (10) show high ionic conductivity, whose structural and electrical properties have, therefore, been extensively studied as a solid electrolyte for solid Li secondary battery.

Studies of $\text{Li}_{2n-1}\text{MN}_n$ containing transition metals such as Mn (11), Fe (12), etc., have also been carried out, but these did not report the application for electrolyte but only pure physical properties of these interesting compounds. The introduction of transition metals might yield electron conduction which spoils the properties as an electrolyte. This disadvantage could be turned into an advantage if they should work as an electrode for lithium secondary battery. Possibly high lithium ion mobility originating in the fluorite structure and low reduction or oxidation potentials of transition metals may both facilitate Li deintercalation and subsequent Li intercalation in these nitrides. If such a reversibility can be realized, $\text{Li}_{2n-1}\text{MN}_n$ will be not only hopeful electrode candidates for Li secondary battery but also exotic materials containing transition metals in unusual oxidation states such as Fe^{4+} , Co^{4+} , which can not be prepared by other methods.

We tried to prepare this type of nitrides by reacting first transition metal nitrides M_xN_y ($\text{M}=\text{Ti, V, Cr, Mn, Fe, Co, Ni or Cu}$) and a lithium nitride Li_3N . We found that Li_3FeN_2 could be easily synthesized using a traditional ceramic method in a 1% H_2 -99% N_2 stream and that it showed extremely smooth Li deintercalation and intercalation.

EXPERIMENTAL

Li_3N and Fe_4N (kindly offered by Nihon-shin-kinzoku Co. Ltd.) were used as raw materials. Li_3N was prepared by a reaction of extra-pure lithium sheets and nitrogen at temperature between 80 and 150°C in a glass reactor, whose formation was confirmed by X-ray diffraction (XRD) measurements and by weight increase also. Mixtures of Li_3N and Fe_4N were pressed into tablets of 8 mm in diameter and 5 – 8 mm in thickness under a pressure of 3 MPa which were subsequently heated in an electrical furnace at 600°C for 12 hr in a 1% H_2 -99% N_2 stream. The heating rate was 10° C/min. Before firing, the furnace was evacuated with a rotary pump to remove moisture, oxygen and CO_2 . Powder XRD measurements were performed on Rigaku RAD-RC (12kW) using

monochromated CuK α radiation. As the products were very hygroscopic, they were protected against moisture during the XRD measurement by using a gas-tight holder filled with argon gas. A 7 μm thick aluminum window covered the sample holder plate in an arc.

For the electrochemical study aimed to obtain $\text{Li}_{3-x}\text{FeN}_2$ having various x values, single phase Li_3FeN_2 was ground and mixed with acetylene-black (electron conductor) and Teflon (binder), and the mixture was pressed into a tablet of 12 mm in diameter under a pressure of 1 MPa. A conventional Li-coin-type cell was assembled using this tablet as a cathode, a Li sheet as an anode and $\text{LiClO}_4/\text{PC}+\text{DME}$ as an electrolyte. Li ion was deintercalated by discharging the cell at 150 μAcm^{-2} .

All the treatments except for heating in a furnace and the discharge-charge experiments were carried out in an Ar-filled dry box.

Samples having various Li contents were measured by XRD. For a Reitveld analysis the intensity data were collected at each 0.02° step width for 2 or 3 seconds over a 2θ range from 10 to 100°. A computer program (REITAN) was used for a profile refinement calculation (13). ^{57}Fe Mössbauer measurements were performed at room temperature. The $^{57}\text{Co}/\text{Rh}$ source velocity was calibrated by using pure iron metal as the standard material.

RESULT AND DISCUSSION

1. Synthesis and Li deintercalation

Gudat et al. (12) reported that Li_3FeN_2 was prepared from Fe metal and molten Li in a N_2 stream. But this method requires high purity N_2 gas and a special furnace. As we wanted to use a conventional furnace, we chose Li_3N and Fe_4N as starting materials. We found that Li_3FeN_2 could be easily prepared from mixtures of Fe_4N and Li_3N powder in a 1% H_2 -99% N_2 gas stream. When commercial N_2 gas was used oxides and carbonates formed in stead of the nitride because of moisture, oxygen and CO_2 contained as impurities in the N_2 gas.

Starting mixing ratios, firing conditions and obtained phases are listed in Table 1. The starting molar ratio of 3.5:1 brings single phase Li_3FeN_2 . The XRD pattern agrees with that reported by Gudat et al. (12). Excess Li_3N might have evaporated during the reaction. Most of lithium-containing nitrides have been prepared from Li-excess mixtures as reported, for example, by Formont et al. (6). The fact that when the heating rate was below 2° C/min, single phase

could not be obtained even if the starting molar ratio was 3.5:1. It might be considered to have resulted from such an evaporation during heating. As discussed in the next section, however, we can not deny a possibility of Fe deficiency such as $\text{Li}_3\text{Fe}_{1-y}\text{N}_2$.

We tried to use Fe metal powder instead of Fe_4N , but single phase could not be obtained under any condition listed in Table 1. Oxides on the iron metal surface may hinder the reaction.

Figure 1 shows the closed circuit voltage (CCV) and open circuit voltage (OCV) curves of the $\text{Li}/\text{Li}_3\text{FeN}_2$ cell for the charge direction (Li deintercalation) at a current density of $150 \mu\text{Acm}^{-2}$. Both the CCV and OCV are very flat in

a wide range (the potential only increases by 30 mV from $x=0$ to 0.6), and the difference due to an overpotential is very small. These properties of Li_3FeN_2 are very characteristic and remarkable, and these are advantageous to practical use as an electrode for Li cell.

X-ray diffraction patterns for various Li contents, x , are shown in Fig. 2. The extraction of Li smoothly occurs up to $x=1.0$, however, in the range of $x>1.0$, the CCV suddenly increases, and XRD patterns become indistinct. These probably resulted from a decomposition of $\text{Li}_{3-x}\text{FeN}_2$.

Four distinct phases have been found to form for $x\leq 1.0$. All these phases have orthorhombic symmetry, *Ibam*. In order of appearance, they are named as α -, β -, γ - and δ -phases. Lattice parameters of each phase are listed in Table II, and the variation of these parameters with total Li content is shown in Fig. 3.

Table 1
Reacting condition and products in the $\text{Li}_3\text{N}-\text{Fe}_4\text{N}$ system.

Li:Fe	Rate (°C/min)	Temp. (°C)	Hold (hr)	Products
3.0:1	10	600	12	Li_3FeN_2 + NaCl-type
4.0:1	10	600	12	Li_3FeN_2 + unknown + Li_3N (trace)
5.0:1	10	600	12	Li_3FeN_2 + unknown + Li_3N (trace)
3.5:1	10	500	12	Li_3FeN_2 + unknown + NaCl-type
3.5:1	10	600	12	Li_3FeN_2
3.5:1	10	700	12	Melt
3.5:1	100	600	12	Li_3FeN_2
3.5:1	1	600	12	Li_3FeN_2 + NaCl-type + unknown

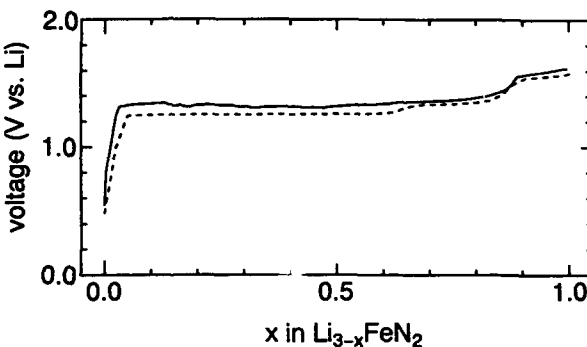


Fig. 1 Open circuit voltage and closed circuit voltage of $\text{Li}_{3-x}\text{FeN}_2$.
OCV;dot line, CCV:solid line ($150 \mu\text{Acm}^{-2}$)

The volume ratio of these phases was roughly estimated from the peak intensity as a function of total Li content as shown in Fig. 4.

Though the inhomogeneous reaction in the Li cell brings sometimes the coexistence of α , β and γ phases. A typical 2-phase reaction seems to occur on Li deintercalation up to $x=0.75$. For $x \leq 0.75$ each phase keeps its parameter values almost constant, and the each solid solution range seems to be very narrow: that is, $x=0$ for α -phase, $x=0.5$ for β -phase, $x=0.75$ for γ -phase. The lattice parameters, especially the b axis, decrease with a sequence of the phase transition.

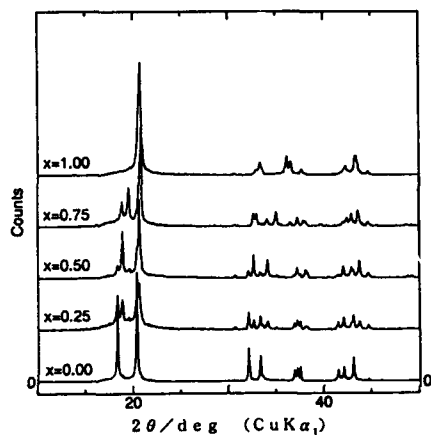


Fig. 2 X-ray diffraction patterns of $\text{Li}_{3-x}\text{FeN}_2$ for various charge depths.

Table 2

Lattice parameters of each phase

	a	b	c
α -phase	4.8630(3)	9.6318(5)	4.7833(2)
β -phase	4.830(3)	9.400(4)	4.714(3)
γ -phase	4.820(1)	9.100(3)	4.750(2)
d-phase	4.915(3)	8.604(7)	4.769(4)

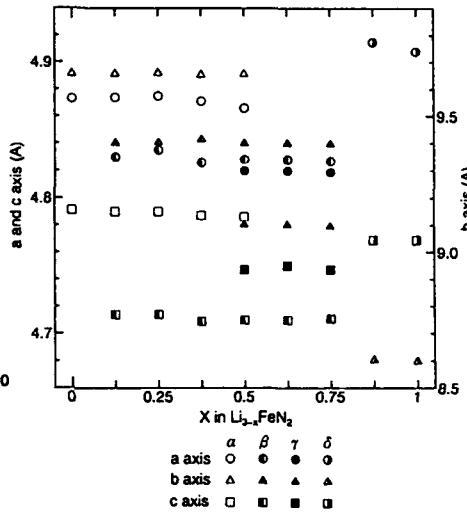


Fig. 3 Variation of the lattice parameters as a function of x in $\text{Li}_{3-x}\text{FeN}_2$.

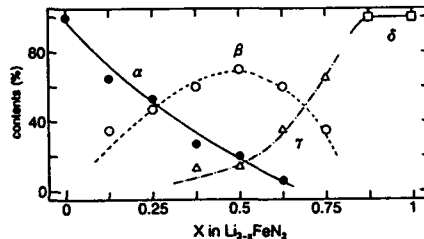


Fig. 4 Composition dependence of phase content for the $\text{Li}_{3-x}\text{FeN}_2$.

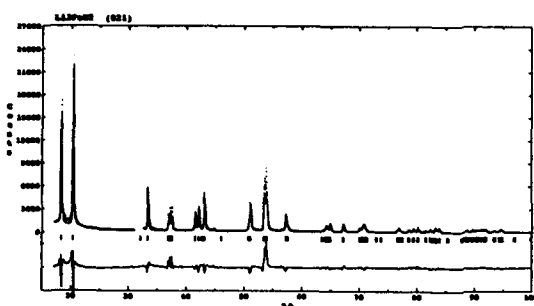


Fig. 5 Observed, calculated and difference plots of Li_3FeN_2 .

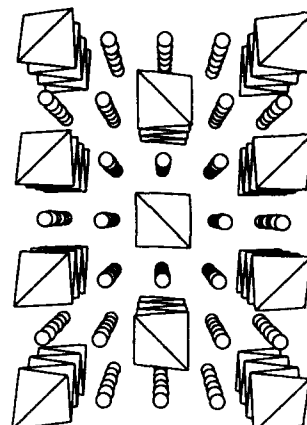


Fig. 6 Crystal structure of Li_3FeN_2 .

Table 3

Crystallographic data, atomic positions and displacement parameters of Li_3FeN_2 .

Space group	<i>Ibam</i>					
Lattice constants(A)	a=4.8630(3) b=9.6381(5) c=4.7833(2)					
D(gcm^{-3})	2.96					
Atom	Wyckoff position	Occupancy	x	y	z	$U_{\text{eq}}(\text{pm}^2)^a$
Li(1)	8g	1.0000	0.0000	0.7434(6)	0.2500	97(17)
Li(2)	4b	1.0000	0.5000	0.0000	0.0000	97(17)
Fe	4a	0.856(3)	0.0000	0.0000	0.2500	41(4)
N	8j	1.0000	0.2278(2)	0.8783(4)	0.0000	71(13)

2. Crystal structure and structure changes

To see the detailed structure changes, the XRD Reitveld refinement for each phase was tried.

Single phase Li_3FeN_2 assumes orthorhombic symmetry, space group *Ibam*. The XRD pattern for Reitveld refinement result is shown in Fig. 5 and the crystallographic data are given in Table 3. As shown in Fig. 6, Li_3FeN_2 crystallizes in a distorted anti-fluorite structure, in which Fe_4N tetrahedra sharing edges with each other form one dimensional chains to the c direction.

In the present work, the single phase of Li_3FeN_2 was synthesized from a mixture of Li_3N and Fe_4N at a ratio of $\text{Li:Fe}=3.5:1$, not $3:1$. As mentioned above, we first thought that the difference between the formal composition and the starting ratio was caused by evaporation of Li_3N during synthesis. Gudat et al. (12) also refined the structure by fixing the composition as Li_3FeN_2 . But in our structure refinement, the fixation of the molar ratio at $\text{Li:Fe}=3:1$ did not bring a reasonable value of the reliability factor (R). When the Fe site occupancy was varied, it converged to 0.86 with a low R factor. This value agrees well with the batch composition ($\text{Li:Fe}=3.5:1=3:0.857$), which suggests that the Fe site(4a) are considerably vacant or a substitution of Li for Fe at 4a site occurs rather than the Li evaporation.

Atomic distances shown in Table 4 agree well with Gudat's data, however, the composition of our sample is most likely different from the ideal one, Li_3FeN_2 .

The refinements for α , β and γ phases did not bring the reasonable R factors, because of the strong orientation and the existence as multiple phases. However, the phase changes have been considered as below based on the OCV, CCV and XRD results.

a). $\alpha - \beta$ ($0 \leq x \leq 0.5$)

The change in lattice parameters from α to β -phase is isotropic, though relatively large. In this stage, the OCV curve is perfectly flat suggesting that the difference in Gibbs Free energy is very low.

b). $\beta - \gamma$ ($0.5 \leq x \leq 0.75$)

As for the change from α to β , the a and b parameters decrease, while the c axis increases. Because of a larger change in Gibbs free energy than that of $\alpha - \beta$, the OCV has a step in this range.

c). $\gamma - \delta$ ($0.75 \leq x \leq 1.00$)

Though there is no change in space group, the a and c axes of the δ -phase largely increases and the b axis decreases in comparison with those of phase γ . Phase δ exists as a monophasic solid solution for $0.75 \leq x \leq 1.00$.

As seen in Fig. 3, the b axis monotonically decreases with phase changes from α -phase to δ -phase. This indicates that Li is deintercalated from $(0\ 0\ 4)$ planes, that is, $\text{Li}(1)$ is deintercalated dominantly.

Table 4

Selected interatomic distances (Å)

Fe-N	2.00(2)
Li(1)-N	2.09(4)
	2.13(4)
Li(2)-N	2.13(3)

As mentioned above, $\text{Li}_{3-x}\text{FeN}_2$ decomposes at $x > 1.0$. The decomposition also occurs when the current density is increased. If the overpotential was very high (if the current density was large), decomposition began at smaller x values. The decomposition voltage was estimated to be about 1.5V.

3. Mössbauer spectrum

Mössbauer spectra of $\text{Li}_{3-x}\text{FeN}_2$ with various Li contents measured at room temperature are shown in Fig. 7 and the Isomer Shift (IS) and quadrupole splitting (QS) are listed in Table V. For $x=0.0$, a single kind of quadrupole doublet (IS = 0.0525 mm/s, QS = 0.875 mm/s) assigned to Fe^{III} in low spin state is observed. With increasing x a new doublet with a more negative isomer shift and a smaller quadrupole splitting overlaps, and finally for $x > 0.75$ it becomes dominant.

The shoulder appearing at the right of the quadrupole peak for $x > 0.75$ has assigned yet, which may be attribute to the decomposed by product brought by overcharge. This suggests that Li deintercalation oxidizes Fe^{III} to Fe^{IV} . The computer peak fittings reveal that each phase has slightly different IS and QS value for both Fe^{III} and Fe^{IV} . The magnetic susceptibility measurement of Li_3FeN_2 by Gudat et al. (12) indicated that the Fe^{III} ions were in low spin state. The more negative value of IS (-0.22 mm/s) of Fe^{IV} in Li_2FeN_2 than the typical values of -0.0 mm/s measured for oxides likes in $\text{SrFe}^{4+}\text{O}_3$ (14), $\text{CaFe}^{4+}\text{O}_3$ (15),

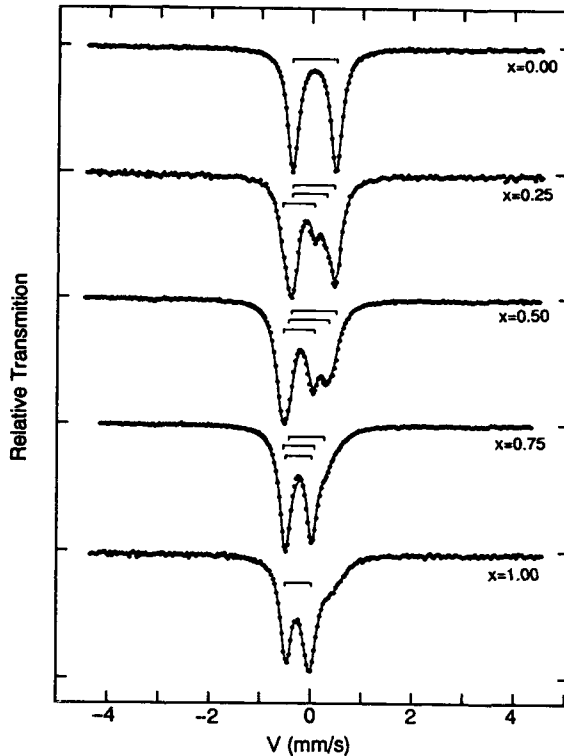


Fig. 7 Room temperature Mossbauer spectra of Li_3FeN_2 .

etc., is consistent with an assumption that the Fe^{IV} state in $\text{Li}_{3-x}\text{FeN}_2$ is in low spin state of d^6g^0 .

4. Li intercalation reaction

The discharge OCV and CCV curves for the samples charged to $x=1.0$ are shown in Fig. 9. The potential difference between the charge and discharge curves is small, indicating a high reversibility. In the XRD pattern of the fully discharged sample, only the original phase (α phase) was seen. Li_3FeN_2 has thus been found to have high capacity of 260 mAhg^{-1} .

CONCLUSION

Li_3FeN_2 was easily synthesized from a 3.5:1 mixture of Li_3N and Fe_4N by using a traditional ceramic method in a 1% H_2 -99% N_2 stream. Li could be deintercalated forming $\text{Li}_{3-x}\text{FeN}_2$ in a range of $0 \leq x \leq 1.0$. With increase of x , four phases sequentially appeared. The OCV and CCV curves for both charge and discharge directions were very flat and the overpotential was very low. Li_3FeN_2 has ideal properties as both a cathode and an anode for lithium secondary battery.

REFERENCES

1. A.Rabenau, *Solid State Ionics*, **6**, 277(1982).
2. T.Lapp, S.Skaarup and A.Hooper, *Solid State Ionics*, **11**, 97(1983).
3. P.M.Richards, *J.Solid State Chem.*, **33**, 127(1980).
4. R.Juza, H.H.Weber and E.Meyer-Simon, *Z.Anorg.Allg.Chem.*, **48**, 273(1953).
5. R.Juza and F.Hund, *Z.Anorg.Allg.Chem.*, **13**, 257(1948).
6. M.Fromont, *Rev.Chim.Niner.*, **259**, 447(1967).
7. H.Yamane, S.Kikkawa, H.Horiuchi and M.Koizumi, *J.Solid State Chem.*, **65**, 6(1986).
8. H.Yamane, S.Kikkawa and M.Koizumi, *J.Solid State Chem.*, **71**, 1(1987).
9. H.Yamane, S.Kikkawa and M.Koizumi, *Solid State Ionics*, **15**, 51(1985).
10. H.Yamane, S.Kikkawa and M.Koizumi, *Solid State Ionics*, **25**, 183(1987).
11. R.Juza, E.Anschutz and H.Puff, *Angew.Chem.*, **71**, 161(1959).
12. A.Gudat, R.Kniep and A.Rabenau, *J.Less-Common Met.*, **161**, 31(1990).
13. F.Izumi, *J.Mineral Soc.Jpn.*, **17**, 37(1985).
14. J.B.MacChesney, R.C.Sherwood and J.F.Potter, *J.Chem.Phys.*, **43**, 1907(1965).
15. Y.Takeda, O.Naka, M.Takano, T.Shinjo, T.Takada and M.Shinada, *Mat.Res.Bul.*, **13**, 61(1978).

POSITIVE HOLE-TYPE CHARGE CARRIERS IN OXIDE MATERIALS

Friedemann Freund*, Eun-Joo Whang**, and François Batllo***,

Department of Physics, San Jose State University
San Jose, CA 95192, USA

Lionel Desgranges and Corinne Desgranges,

Chimie-Physique des Solides, École Centrale Paris
92295 Châtenay Malabry, France

and Minoru M. Freund

Department of Physics, University of California
Berkeley, CA 94370, USA

ABSTRACT

Defect electrons on the O^{2-} sublattice, equivalent to O^- states, also known as oxygen-associated or positive holes, are electronic defects in otherwise insulating oxide materials. Though extensively studied as radiation-induced, paramagnetic defects in a wide range of materials at low temperature, little was known until now about the occurrence of O^- in the technologically more important range from 20–1000°C. We show that MgO single crystals of highest purity contain about 500 ppm peroxy-type (O_2^{2-}) defects, diamagnetic and electrically inactive, which release positive holes upon heating. We describe five experiments, each designed to address different aspects of the O^- defects: (1) electrical conductivity, (2) dielectric polarization, (3) magnetic susceptibility, (4) thermal expansion, (5) refractive index. O^- charge carriers appear between 200–400°C. Their mobility is low at first but increases rapidly above 450°C. They augment the dielectric polarization and give rise to a positive surface charge that increases between 450–750°C and then decreases. Between 200–300°C the O^- are still spin-coupled, probably in a bipolaronic state. Though the O^-/O^{2-} ratio is only 1:1000, the O^- cause a uniform increase of the thermal expansion without strain-induced broadening of the x-ray reflection. This suggests a high degree of delocalization of the O^- wave functions, equivalent to a decrease in the average electron density on O^{2-} anions and, hence, decreasing ionicity of the $Mg^{2+}-O^{2-}$ bond. This is corroborated by the increase of the refractive increase by ≈0.5% and recent chemical shift measurements of the ^{25}Mg and ^{17}O NMR signals which suggest increasing covalency of the $Mg^{2+}-O^{2-}$ bond with increasing temperature. O^- charge carriers may have far-reaching implications for the electric properties of otherwise highly insulating oxide materials.

* mailing address: NASA Ames Research Center
MS 239-4 Moffett Field, CA 94035

** now at the Department of Physics, Cornell University, Ithaca, NY 14853
*** now at INTA, 2281 Calle de Luna, Santa Clara, CA, 95054

To the extent authorized under the laws of the United States of America, all copyright interests in this publication are the property of The American Ceramic Society. Any duplication, reproduction, or republication of this publication or any part thereof, without the express written consent of The American Ceramic Society or fee paid to the Copyright Clearance Center, is prohibited.

I. INTRODUCTION

Our interest in MgO derives from the fact that it is well suited to serve as model material for the study of impurities and point defects in oxide materials in general. Specifically, we try to understand electronic defects that may occur in oxides and strongly affect their physical properties. Electronic defects in highly insulating, wide band gap oxide materials are generally believed to be always associated with transition metal impurities. However, electronic defects occur in such oxides that are not linked to transition metal impurities: defect electrons associated with the O_2^- sublattice. They have been variously called *positive holes*, *oxygen-associated positive hole centers*, or simply O^- states, and they have been known for years as radiation defects, introduced either intentionally or naturally by x-ray, γ -ray or α particle bombardment¹. Observable in many materials at low temperatures, primarily by means of electron spin resonance (ESR) spectroscopy², such radiation-induced O^- are unstable and generally anneal rather rapidly as the temperatures rise to room temperature or slightly above. The generation of such O^- may be considered a photoionization:



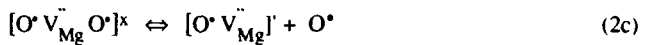
Eq. (1) implies that, in order to generate O^- , the energy of the incident photon has to exceed the band gap of MgO which is >8 eV³. It may therefore come somewhat as a surprise to many that O^- states can also be generated by simple heating to moderate temperatures. We shall show in this report that MgO crystals of the nominal highest purity grades generate O^- in the temperature interval 200–500°C. Obviously, these crystals contain some kind of dormant defects that release O^- without the help from ionizing radiation. The process is reversible upon cooling, suggesting that the O^- return to a dormant state. Defects that could potentially generate such O^- are self-trapped positive hole pairs, inactive at ambient temperature but dissociating upon heating according to:



Self-trapped positive hole pairs may also be described chemically as peroxy anions, O_2^{2-} . Since an Mg^{2+} vacancy is double negatively charged, two positive holes trapped on adjacent O_2^{2-} sites would compensate for these charges. Therefore, Mg^{2+} vacancies are favorable sites for trapping two positive holes, and an Mg^{2+} vacancy – peroxy anion aggregate represents a neutral defect. Using the Kröger point defect designation⁴ where $V_{Mg}^{\bullet\bullet}$ represents the Mg^{2+} vacancy and where superscript dot, prime and cross stand for positive, negative and neutral charges respectively, it is convenient to write eq. (2a) as follows:



Eq. (2b) indicates two positive holes decoupling their spins but remaining bound to the cation vacancy by Coulomb interaction: the initial step. If the dissociation proceeds further it becomes:



where the new species O^* represents an unbound positive hole. Such an unbound O^* is a hole state injected into the O 2p-dominated valence band⁵. The bracketed defects on the left and right hand sides of eq. (2c) correspond to the V_o and V^- centers, respectively, which have been known for some time from low temperature ESR studies of radiation-induced defects in the alkaline earth oxides¹. To our knowledge, self-trapped positive hole pair defects, adjacent to a divalent cation vacancy, have never been studied systematically, nor even proposed in the ceramic and material science literature. However, if they exist, they may have far-reaching consequences for the properties, electronic and others, of highly insulating oxide materials.

2. EXPERIMENTAL PROCEDURES

We have carried out five experiments, each designed to address different physical properties brought about by the O^* states. Specifically we have measured:

- (1) d.c. electrical conductivity,
- (2) dielectric polarization,
- (3) magnetic susceptibility,
- (4) thermal expansion by x-ray diffraction,
- (5) refractive index.

All measurements were done with nominally high purity MgO single crystals, grown by carbon arc fusion⁶ and obtained from W. & C. Spicer Ltd., England. 4N-grade (99.99%) crystals contain transition metal impurities at levels of ≈ 20 wt.-ppm (Cr+Mn+Ni), < 30 wt.-ppm Fe, plus < 50 wt.-ppm (Al+Si). The OH^- concentration (not included in the nominal purity rating) is $10-100$ per $10^6 O^{2-}$. The d.c. conductivity measurements of 4N- and 3N-grade MgO crystals, about $10 \times 10 \times 1$ mm, were carried out between $200-1000^\circ C$ in Ar, using Al electrodes in 2-electrode, 2-electrode + guard, and 2-electrode + 2-probe configurations, measuring currents and potentials with KEITHLEY 610C electrometers⁷. Below $500^\circ C$ the conductivity was measured in a Faraday cage to reduce ambient noise⁸. The conductivity σ can be written as the sum of all contributions from charge carriers i:

$$\sigma = \sum_i \sigma_{oi} \exp[-E_i/kT] \quad (3)$$

where σ_o and E are the preexponential factor and activation energy, respectively, while k and T have their usual meaning as the Boltzmann constant and the absolute temperature in Kelvin. For the dielectric polarization measurements a newly developed technique was used, Charge Distribution Analysis or CDA, which utilizes the effect that, when a dielectric is suspended, contact-free, in an electric field gradient along an axis z , a force F_z acts on it^{9,10}. This force depends upon the field gradient and the polarization P of the sample:

$$F_z = - \int_V P \cdot \nabla E_{ex} dV \quad (4)$$

where the volume integral contains the sample but not the sources of the field. P contains at least five contributions arising from the electronic polarizability, the ionic polarizability, any local defects that

may rotate in the electric field or change their polarizability, any space charges that are mobile in the externally applied electric field, and surface charges:

$$\mathbf{P} = \mathbf{P}_{\text{el}} + \mathbf{P}_{\text{ion}} + \mathbf{P}_{\text{local}} + \mathbf{P}_{\text{space}} + \mathbf{P}_{\text{surface}}$$

Bulk and surface contributions, F_{Σ} and F_{Δ} , can be separated by measuring the force upon field gradient reversal, F_z^+ and F_z^- . The sum $\mathbf{P}_{\text{el}} + \mathbf{P}_{\text{ion}} + \mathbf{P}_{\text{local}} + \mathbf{P}_{\text{space}}$ is invariant to reversal, while $\mathbf{P}_{\text{surface}}$ is not, we obtain expressions for the bulk and surface contributions, respectively:

$$F_{\Sigma} = \frac{1}{2}(F_z^- + F_z^+) = -\frac{\epsilon_0(\epsilon-1)}{4\pi} \int_V (\mathbf{P}_{\text{el}} + \mathbf{P}_{\text{ion}} + \mathbf{P}_{\text{local}} + \mathbf{P}_{\text{space}}) \nabla E_{\text{ext}} dV \quad (5a)$$

$$\text{and} \quad F_{\Delta} = \frac{1}{2}(F_z^- - F_z^+) = -\int_V (\mathbf{P}_{\text{surface}}) \nabla E_{\text{ext}} dV \quad (5b)$$

where ϵ is the bulk dielectric constant and ϵ_0 the permittivity of vacuum. The factor $\epsilon_0(\epsilon-1)/4\pi$ drops out in the derivation of eq. (5b) because F_{Δ} only refers to the surface charge layer. Using a PERKIN ELMER TGS-2 microbalance as a force measuring device and an axially symmetrical electric field gradient between a 2 mm diameter circular bias and a cylindrical ground electrode, 10 mm diameter, 10 mm high, F_z^- and F_z^+ were measured between 25–850°C during repetitive heating and cooling cycles in high purity nitrogen. The magnetic susceptibility was measured between 25–850°C with a PRINCETON APPLIED RESEARCH Vibrating Sample Magnetometer, Model 4500, equipped with a high temperature BN probe and a 5.4 KGauss electromagnet. The measurements were conducted with a 15.6 mm long, 4.8 mm diameter 4N-grade MgO crystal during heating/cooling at 4°C/min under a few millitorr of He¹¹. The intrinsic magnetic susceptibility of MgO, χ_{MgO} , is $-10.6 \cdot 10^{-6}$ emu/mole and that of paramagnetic impurities is given as:

$$\chi = \frac{N J(J+1) g^2 \mu^2}{3 k T} \quad (6)$$

where N is the number of paramagnetic species, g their Landé factor, and μ the Bohr magneton. O⁻ is a p⁵ ion with spin momentum $S = \frac{1}{2}$ and a magnetic momentum $L = +1$. Since the shell is more than half filled, $J = S+L = \frac{3}{2}$, and the Landé factor, $g = 3J(J+1) + S(S+1) = \frac{2J(J+1)}{2J(J+1) + 1}$, is 1.33. Assuming a paramagnetic transition metal concentration of 50 ppm, the contribution is $\approx 0.2 \cdot 10^{-6}$ emu/mole at 200°C, decaying as $\frac{1}{T}$. The thermal expansion measurements were conducted with a cleaved 4N-grade MgO plate, 10 x 10 x 0.2 mm, annealed at 800°C, followed by slow cooling. The measurements were done during heating to and cooling from 800°C at 1°C/min using a specially designed x-ray diffractometer at the École Central^e Paris, France, equipped with a position-sensitive, multichannel detector. For the refractive index measurements a large, optically clear 3N-grade MgO single crystal was cut and polished into a prism with a 39°55' angle. A 3N-grade crystal was chosen over one of the 4N-grade crystals because the latter tend to be cloudy due to minute cavities formed during cooling from the gas-saturated melt. The MgO prism was placed on an alumina support inside a tube furnace and heated in air. To minimize convection both ends of the tube were loosely closed with fused silica windows. The furnace was mounted on a 40 cm diameter goniometer, and the temperatures were adjusted manually between 25–800°C, using a Variac. The refractive index was measured at the He-Ne laser wavelength of 603 nm by the method of minimum deviation.

3. RESULTS

3. 1 Electrical Conductivity

Fig. 1 summarizes the electrical conductivity of MgO. The bold solid line traces the high-temperature (HT) conductivity where the activation energy is about 2.4 eV, due to ionic diffusion¹²⁻¹⁴. An electronic contribution may also be present, even in nominally pure MgO¹⁵, but no explanation has been offered except for the statement that the electronic charge carriers appear to be positive. While

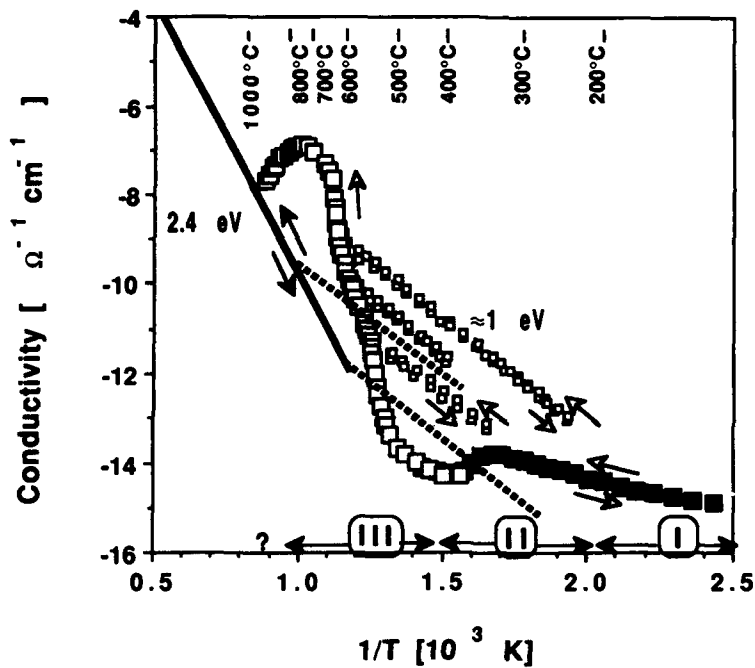


Fig. 1: The d.c. conductivity of MgO single crystals measured during heating/cooling cycles. Solid line: High temperature (HT) predominantly ionic conductivity (activation energy 2.4 eV); Dashed lines: low temperature (LT) conductivity during cooling, usually assigned to surface conduction (activation energy ≈ 1 eV); Large filled and open squares: conductivity during heating with a small but reproducible maximum in region II and a rapid increase in region III; Small squares: LT branches measured during intermittent cooling, indicative of the generation of charge carriers characterized by the same 1 eV activation energy.

the HT conductivity can be followed down to $\approx 600^\circ\text{C}$, provided the sample is cooled slowly, it always changes into a low-temperature (LT) branch indicated by bold dotted lines. Two LT branches are shown as examples. They are characterized by an activation energy of about 1 eV¹⁶⁻¹⁸

The filled and open squares in Fig. 1 combine conductivity data obtained during detailed studies of the LT region^{7,8}. Between 200–400°C, when the conductivity was still in the 10^{-15} – $10^{-14} \Omega^{-1}\text{cm}^{-1}$ range, a weak maximum occurred which was reproducible with a time-dependent hysteresis behavior. Above 450°C the conductivity rose steeply by several orders of magnitude, and a set of 1 eV branches were observed during intermittent cooling and reheating at 10°C/min. Upon cooling from above 900°C the conductivity followed approximately the bold solid and dotted lines. After annealing at room temperature the steeply rising section was reproduced. The 1 eV activation energy constant slope branches obtained during intermittent cooling suggest that they are caused by charge carriers that are generated in increasing number.

The disadvantage of conductivity measurements is that it is not possible to determine the sign of the charge carriers. Hall effect measurements^{19,20} are not possible with MgO single crystals, at least not in the temperature region of interest here, due to their low conductivity. Thermopotential measurements which suggested positive charge carriers in the HT region¹⁵, proved inconclusive in the LT region. Because MgO is an insulator, mobile electronic charges are predicted to diffuse to the surface, causing the surface to acquire a distinct charge⁵. However, at the time when the conductivity measurements were made^{7,8}, no method existed to detect suchsurface charges.

3.2 Dielectric Polarization

In response to the need to measure surface charges a new technique was developed: Charge Distribution Analysis. CDA provides unique information about bulk and surface charges as briefly discussed above and elsewhere^{9,21,10}. Fig. 2 shows the bulk dielectric polarization F_Σ (top) and surface charge contribution F_Δ (bottom) of a 4N-grade MgO single crystal as a function of temperature between 100–600°C, measured isothermally over 10 min at each of the indicated temperatures during stepwise heating at +50V and -50V. Three distinct regions can be identified which correlate with the regions I, II, and III in the d.c. conductivity plot in Fig. 1. Below 200°C F_Σ is temperature-independent such expected from the fact that the dielectric constant of a near-ideal dielectric is essentially temperature-independent. The MgO surface is slightly negative as is shown by F_Δ , consistent with thermodynamic arguments^{22,23} derived from the differences in the free energies of formation of cation and anion vacancies in an ionic material such as MgO²⁴.

Between 200–400°C F_Σ increases about 5-fold, very sluggishly at first, indicating that P_{local} begins to make a measurable contribution. Since there is only a minute increase in the d.c. conductivity as shown in Fig. 1, the contribution from P_{space} appears to be negligible. The increase in P_{local} implies that the MgO crystal contains defects which are either dipolar and orient in the externally applied field or undergo a significant increase in polarizability. F_Σ seems to reach a steady state value around 400°C. F_Δ tends ever so slightly towards positive values between 200–400°C, indicating the appearance of at least some positive charge carriers. The sluggishness with which the polarization reaches a steady state suggests that the the polarizable defects behave as a highly viscous jelly.

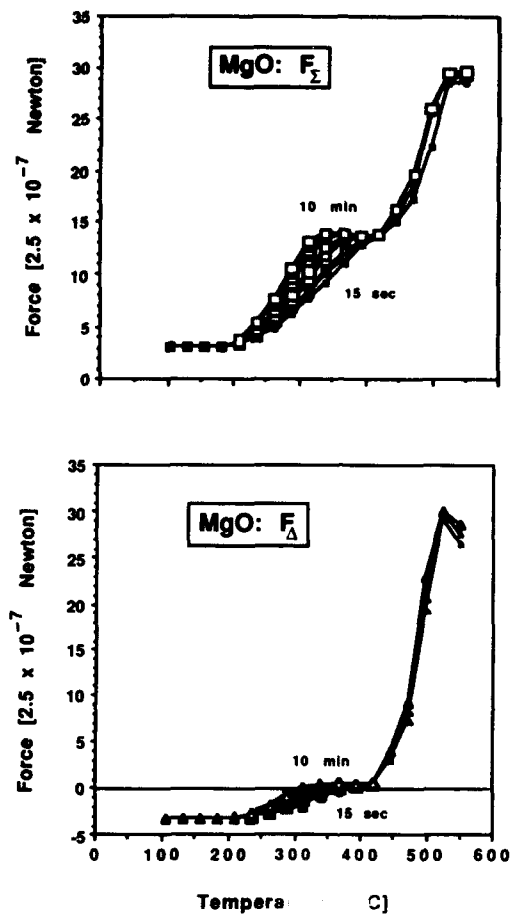


Fig. 2 **Top:** F_{Σ} , representative of the bulk polarization obtained from F^+ and F^- measurements at +50V and -50V bias respectively. F_{Σ} increases sluggishly between 200–400°C and more rapidly above 450°C, indicating the generation of mobile charges. Upon slow cooling the $F_{\Sigma}(T)$ curves are reversible, indicating that the mobile charges become re-trapped upon cooling. **Bottom:** F_{Δ} , representative of the surface contribution, shows that, below 200°C, the MgO surface is weakly negative, becomes weakly positive 200–400°C and strongly positive above 450°C. The charges which are generated in the bulk carry a positive sign.

Between 450–600°C F_{Σ} increases 2-fold over the steady state value at 400°C, e.g. 10-fold over the 20–200°C value. The response to the applied field is fast, suggesting highly mobile charge carriers which make a significant P_{space} contribution. Concurrently F_{Δ} becomes strongly positive, confirming that the charge carriers are positive. Around 600°C F_{Σ} reaches a value which remains approximately constant upon further heating to about 750–800°C. The decrease of F_{Δ} between 525–550°C, the highest temperature shown in Fig. 2 (bottom), is an artifact. Since the experimental procedure requires that F_{Σ} and F_{Δ} be measured sequentially, the mobility of the charge carriers has to be taken into account during data evaluation. In the case of a strong positive surface charge the response is faster under negative bias than under positive bias. For the data shown in Fig. 2 (bottom) this effect was not taken into account.

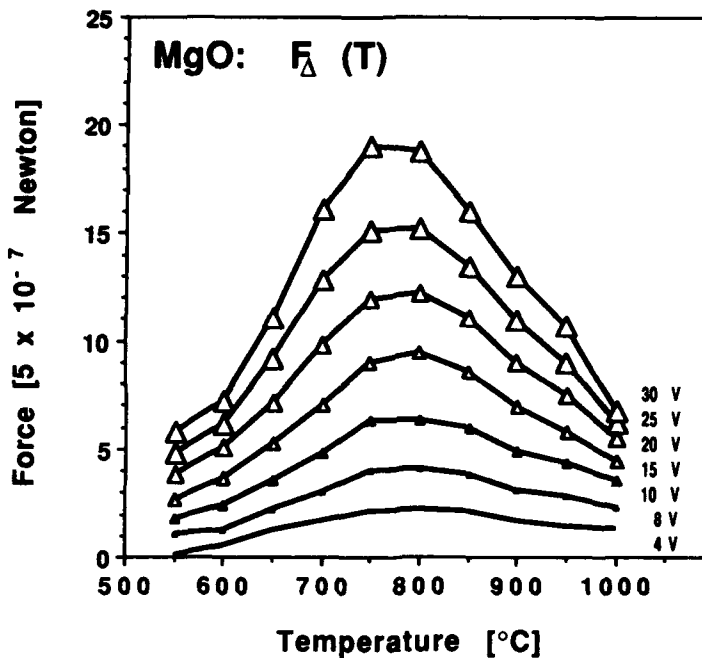


Fig. 3: F_{Δ} as measured in another CDA experiment with MgO using bias voltages between 4–30V: The positive surface charge continues to increase to about 750–800°C and then decreases upon further heating.

Fig. 3 depicts a set of $F_\Delta(T)$ values obtained in a separate run where F_Δ is shown to become increasingly positive up to 750–800°C and decreases only above 800°C. The decrease above 800°C is reversible, even during fast cooling at a rate of 10–20°C, provided that the sample was not heated for a very long time above 800°C. Below 750°C the reversibility upon cooling becomes rate-dependent. If cooling is fast, the positive surface charge may be frozen in, unless the crystal is annealed at temperatures above 200–400°C. Comparing the results from d.c. conductivity and dielectric polarization experiments suggests that the observed effects are caused by the same defects and/or charge carriers. The positive surface charge is consistent with the proposed appearance of O[−]-type charge carriers as formulated by eqs. 2a–c. However, in order to ascertain that these charge carriers are indeed positive holes, we need additional information such as may be obtained through improved high temperature magnetic susceptibility measurements.

3.3 Magnetic Susceptibility

The results of our magnetic susceptibility measurement are shown in Fig. 4. MgO is diamagnetic with $\chi = -10.6 \cdot 10^{-6}$ emu/mole, and its diamagnetism is temperature-independent²⁵. Any contribution from 50 wt.-ppm paramagnetic transition metal impurities is less than $+0.2 \cdot 10^{-6}$ emu/mole above 200°C, decreasing as $1/T$ as indicated by eq. (6)²⁶. A peroxy anion represents two tightly spin-coupled O[−] and is diamagnetic²⁷. The O[−]–O[−] bond is highly covalent, but not strong because the short (1.5 Å) bond distance results in a significant internuclear repulsion. Therefore, like the F–F bond in molecular F₂, the O[−]–O[−] bond easily dissociates. When this happens, the spins decouple. Therefore, if any paramagnetism appears which increases with temperature, it can only be due to paramagnetic states related to the O[−] sublattice. The only such species are O[−] states. The open circles in Fig. 4 show the paramagnetism measured during heating at 4°C/min. The data obtained during cooling are nearly identical. Paramagnetism appears around 300°C, increasing up to about 500°C reaching a value of nearly $+2 \cdot 10^{-6}$ emu/mole over the diamagnetic baseline at $-10.6 \cdot 10^{-6}$ emu/mole. Above 500°C the paramagnetism decreases approximately as $1/T$. The solid line with open triangles, which represents the contribution of paramagnetic species assuming no $1/T$ decrease, can be viewed as the generation curve as a function of temperature. Assuming that the orbital moment of O[−] in MgO is the same as that of free O[−] (an upper limit) the O[−] concentration has been estimated to be of the order of 1000 ± 500 at.-ppm¹¹.

Comparing the magnetic susceptibility measurements with the CDA results reveals a potentially interesting discrepancy. F_Σ , the bulk polarization, began to increase around 200°C, suggesting defects which become more polarizable. If we assume that 200°C mark the threshold for the dissociation of the self-trapped positive hole pair defects as described by eqs. 2a/b, the question is why the paramagnetic signal appears only around 300°C? A possible explanation is that, when the positive hole pair begins to break up, the spins of the O[−] still stay coupled, corresponding to a bipolaronic state where two spins remain paired and, hence, diamagnetic, even though they are no longer spatially close. Only when the mean thermal energy kT exceeds the spin–spin coupling will the bipolaron state break down and become paramagnetic. Eq. (7a) rewrites eq. (2b) with the electron spins. The left hand side represents the diamagnetic positive hole pair, while the center and the right hand side represent the progressive decoupling and transition to the paramagnetic state.

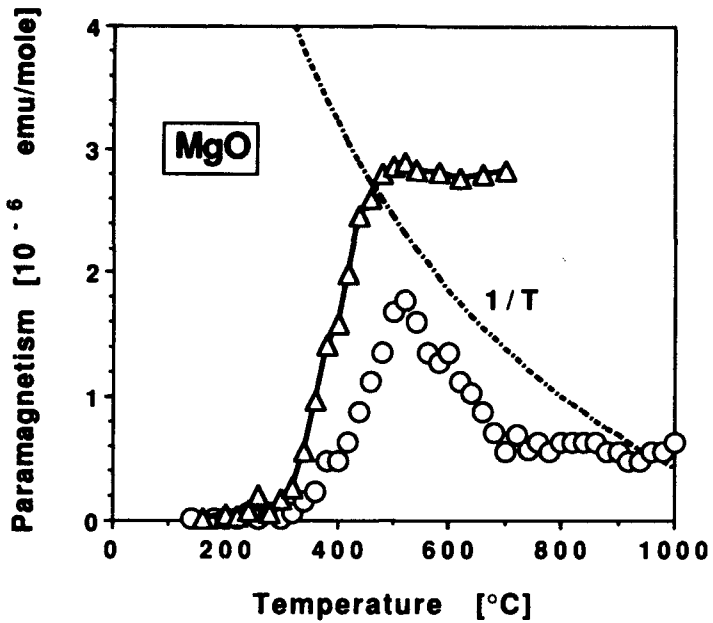
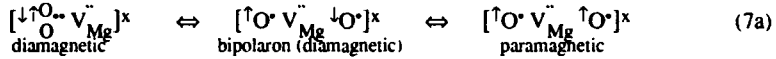
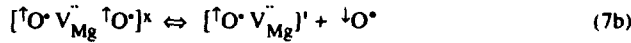


Fig. 4 Magnetic susceptibility χ of MgO, intrinsically diamagnetic at -10.6×10^{-6} emu mole $^{-1}$, measured with a Vibrating Sample Magnetometer. Open circles: Measured data indicating the appearance of paramagnetism between 300–500°C. Dashed line: $1/T$ decay of χ . Open triangles: Calculated concentration of paramagnetic centers reaching saturation at 500°C, consistent with positive holes, O^- , generated by peroxy dissociation.



The delay between the increase in the dielectric polarization, about 200°C, and the appearance of the paramagnetic signal, about 300°C, could therefore mean that the positive hole pairs remain spin-paired for about 100°C even though their chemical bond is already broken and their polarizability has increased. In fact, to account for the large increase in F_{Σ} between 200–300°C as shown in Fig. 2b, the polarizability of the O^- pairs must increase significantly, given that their concentration is probably less than 500 at.-ppm. Such a large increase suggests that a high degree of delocalization of the O^-

wave functions, even though the associated spins still remain paired. When the concentration of the paramagnetic centers reaches saturation around 500°C, all O²⁻-O²⁻ bonds are broken and their spins fully decoupled. This implies that the positive hole pairs are completely dissociated with the number of paramagnetic species remaining constant.



Eq. (7b) describes the generation of unbound O²⁻, e.g. O²⁻ that become mobile charge carriers⁵. This is consistent with our d.c. conductivity and CDA results indicating a generation of mobile charges above 450°C which make a large P_{space} contribution. As their mobility increases to 750–800°C, the MgO surface becomes ever more strongly positive.

3.4 Thermal Expansion

If there are defects in the MgO which undergo a sequence of dissociative transformations as described by eqs. (2a–c) and eqs. (7a/b), we should also see their effect in the thermal expansion behavior. We note that, crystallizing the face-centered cubic, densely packed NaCl-type structure with no phase transition, the thermal expansion of MgO must be monotonous²⁸. However, anomalies in the thermal expansion behavior of nominally high purity MgO crystals have already been reported earlier^{29,30}. With a dilatometer the expansion $\Delta l/l$, where l is the linear dimension of the sample, is the sum of the intrinsic lattice expansion plus any strain contribution that may arise from the presence of defects. By contrast, measuring the thermal expansion by x-ray diffraction gives the "true", intrinsic lattice expansion, while any strain contributions arising from defects lead to a broadening of the x-ray diffraction lines.

The results of our x-ray diffraction experiment are shown in Figs. 5a/b. The individual data points lie so close that they appear as a solid line. The results measured during heating and during cooling are nearly indistinguishable. Clearly, the thermal expansion behavior is anomalous between 200–500°C. Fig. 5b shows the expansion coefficient α which increases at 200°C, the same temperature at which the dielectric polarization starts to increase. It then rises to a maximum around 400°C and decreases to 500°C. Above 500°C α continues to increase but with a different slope than below 200°C. There is no indication for strain-induced broadening of the x-ray reflection. Since the temperatures at which the α anomaly begins and ends closely correspond to those identified in our d.c. conductivity, dielectric polarization and magnetic susceptibility measurements, we conclude that the bulk thermal expansion of the MgO is controlled by the same defects, e.g. the O²⁻ states.

This raises a very interesting question: How can defects which are present at a level of less than 10^{-3} give rise to a uniform lattice expansion? One would expect that, when the peroxy defects decouple their spins and expand, they cause local strains. If these strains are large and far-reaching, they may lead to x-ray line broadening. The absence of such broadening implies that a strain-free expansion. A possible explanation is that the wave function associated with O²⁻ is highly delocalized affecting a large lattice volume, maybe as many as 1000 O²⁻ sites. In this case, the thermal expansion increase around 200°C would mark a weakening of the ionic Mg²⁺-O²⁻ bond, due to a slight decrease of the effective electron density at the O²⁻ anions resulting from the delocalization of the O²⁻ wave function.

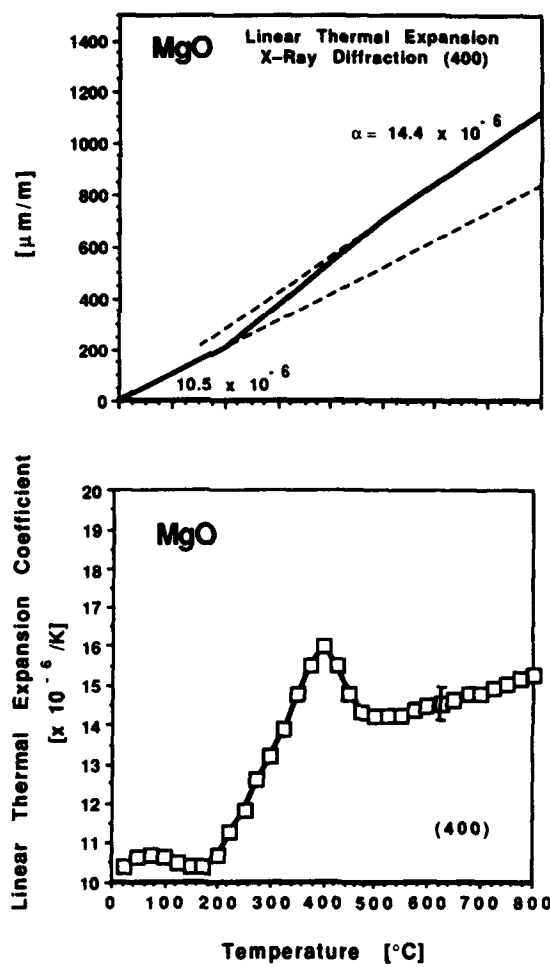


Fig. 5 **Top:** Thermal expansion of an MgO single crystal, measured by x-ray diffraction on the (004) line. **Bottom:** The linear thermal expansion coefficient undergoes a "wiggle" between 200–500°C. The absence of stress-induced broadening suggests uniform lattice expansion.

3.5 Refractive Index

In a non-absorbing medium the square of the refractive index is equal to the real part of the dielectric constant: $n^2(\omega) = \epsilon'(\omega)$, where ω is the frequency, $\approx 10^{16}$ Hz in the optical region of the spectrum^{19, 20}. Following the additivity rule for predominantly ionic materials, the sum of the polarizability of the anions and of the cations determines n ³¹. In MgO, the large, polarizable O^{2-} dominate over the small, less polarizable Mg^{2+} ³². If the electron density of the O^{2-} is decreased, due to O^{2-} delocalization, the O^{2-} polarizability and, hence, n will increase.

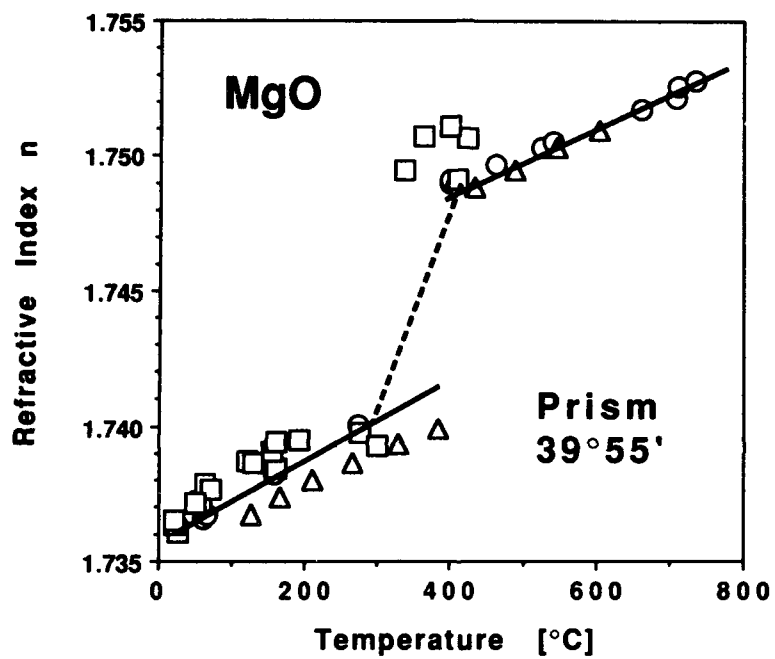


Fig. 6: At 300–400°C the refractive index, measured with an MgO single crystal prism, exhibits a sudden increase by as much as 0.5 %, suggesting an increase of the O^{2-} polarizability.

Fig. 6 depicts the results of three measurements of the refractive index of MgO between 20–730°C. The data shown by open triangles and circles were recorded during heating, those shown by open squares during cooling. The solid and dotted lines are drawn to aid the eye. Fig. 6 shows how sharply the refractive index increases between 300–400°C. The magnitude of the anomaly is about

0.5%, much larger than the error, estimated to be $\pm 0.05\%$. When the anomaly begins and ends has not yet been accurately determined, but it seems to coincide with the appearance of the paramagnetic signal (see Experiment #3). Since the paramagnetic signal was interpreted as caused by the decoupling of the O^- spins according to eq. (7b), we suggest that the increase in n is caused by the delocalization of the O^- wave function as discussed above.

4. DISCUSSION

The self-trapped positive hole pair in an oxide matrix such as MgO appears to be a very interesting defect. It can be described as a peroxy anion, O_2^{2-} , occupying two adjacent O^{2-} sites. If associated with an Mg^{2+} vacancy, it is a neutral defect and should therefore be energetically rather favorable. Tightly coupled and diamagnetic at ambient temperatures, the self-trapped positive hole pair - cation vacancy aggregates are point defects and unlikely to have any significant consequence for the bulk and surface properties of oxide materials in which they occur. At the same time, self-trapped positive hole pairs represent a fundamentally new type of defect. However, they seem to have escaped the attention of researchers in the many studies of MgO and other alkaline earth oxides.^{33-35, 24, 1}

The five independent experiments on which we report here provide evidence that, when the self-trapped positive hole pairs in MgO decouple their electron spins and dissociate in the temperature interval 200–500°C, they begin to have a significant effect on the bulk and surface properties of the material. They dominate the d.c. electrical conductivity below 800°C. They give rise to a strong positive surface charge, compensated by an internal negative space charge. They cause a magnetic anomaly. They cause a thermal expansion anomaly. They cause a refractive index anomaly. Considering the low O^- concentration of probably less than 1000 at.-ppm, their effect on the physical properties of MgO is quite remarkable. The underlying common cause seems to be that, when the self-trapped positive hole pairs decouple, the O^- wave functions spread out over a surprisingly large lattice volume, maybe as many as 1000 O^{2-} sites. This effectively lowers the electron density at each O^{2-} anion and thus decreases the ionicity of the $Mg^{2+}-O^{2-}$ bond. This conclusion appears to be corroborated by a recent report on the temperature-induced shift of the ^{17}O and ^{25}Mg nuclear magnetic resonance (NMR) frequency in a 3N-grade MgO single crystal up to 1300°C.³⁶ The NMR frequency is a sensitive measure of the electric field gradient at the site of the nucleus which, in turn, depends on the electron density in the outer shells of the atoms and ions. In predominantly ionic materials like MgO, one expects that the electric field gradient at the nuclei decreases with increasing temperature because, due to thermal expansion, the ions move apart. Hence, the ^{17}O and ^{25}Mg NMR frequencies should shift toward higher values. However, Fiske et al.³⁶ observe that the shift is in the opposite direction and suggest that this is due to an increase in the covalency of the $Mg^{2+}-O^{2-}$ bond with increasing temperature. Since only a few data points were recorded below 800°C, it is not possible at present to decide whether the shift reversal occurs in the 200–500°C interval.

Finally, we would like to point out that the study of the positive hole pairs in MgO, their transition from a tightly coupled to a dissociated state may shed light on hole-type charge carriers in other oxide materials, not the least in copper oxide-based ceramic superconductors. In this context the possibility of an intermediate bipolaronic state which is highly delocalized but spin-coupled and diamagnetic, certainly deserves further attention.

Acknowledgment: This work was partially supported by NASA through the Cooperative Agreements NCC 2-446 and NCC 2-572 with the SETI Institute, by the NATO Grant RG.896479, and by the Petroleum Research Fund of the American Chemical Society under Grant # 24335-ACS

REFERENCES

- 1 Henderson, B., and J. E. Wertz. *Defects in the Alkaline Earth Oxides*. (London: Taylor & Francis, 1977)
- 2 Griscom, D.L., "Electron spin resonance," *Glass: Sci. Technol.*, 4B (1990): 151-251.
- 3 Daude, N., C. Jouanin, and C. Gout, "Electronic band structure of magnesium and calcium oxides," *Phys. Rev. B* 15 (1977): 2399-2405.
- 4 Kräger, F.A., *The Chemistry of Imperfect Crystals*. (Amsterdam: North-Holland, 1971).
- 5 King, B.V., and F. Freund, "Surface charges and subsurface space charge distribution in magnesium oxide containing dissolved traces of water," *Phys. Rev. B* 29 (1984): 5814-5824.
- 6 Butler, C.T., B.J. Sturm, and R.B. Quincy, "Arc fusion growth and characterization of high-purity magnesium oxide single crystals," *J. Cryst. Growth* 8 (1971): 197-204.
- 7 Kathrein, H., and F. Freund, "Electrical conductivity of magnesium oxide single crystals below 1200 K.," *J. Phys. Chem. Solids* 44 (1983): 177-186.
- 8 Kathrein, H., U. Knipping, and F. Freund, "Atomic carbon in magnesium oxide. Part VI: Electrical conductivity," *Mat. Res. Bull.* 15 (1980): 1393-1399.
- 9 Freund, F., M.M. Freund, and F. Batillo, "Critical review of electrical conductivity measurements and charge distribution analysis of Magnesium oxide," *J. Geophys. Res.* 98 (1993): 22,209-22,229.
- 10 Freund, M.M., F. Freund, and F. Batillo, "Highly mobile oxygen holes in magnesium oxide," *Phys. Rev. Lett.* 63, Nov. 6, 1989 (1989): 2096-2099.
- 11 Batillo, F., R.C. LeRoy, K. Parvin, F. Freund, and M.M. Freund, "Positive hole centers in magnesium oxide — correlation between magnetic susceptibility, dielectric anomalies and electric conductivity," *J. Appl. Phys.* 69 (1991): 6031-6033.
- 12 Wuensch, B.J., S.C. Semken, F. Uchikoba, and H.I. Yoo, "The mechanisms for self-diffusion in magnesium oxide," *Ceram. Trans.* 24 (1991): 79-89.
- 13 Sempolinski, D.R., and W.D. Kingery, "Ionic conductivity and magnesium vacancy mobility in MgO," *J. Amer. Ceram. Soc.* 63 (1980): 664-669.
- 14 Schmalzried, H., "Electrical conduction in magnesium oxide," *J. Chem. Phys.* 33 (1960): 940.
- 15 Sempolinski, D.R., W.D. Kingery, and H.L. Tuller, "Electronic conductivity of single crystal MgO," *J. Amer. Ceram. Soc.* 63 (1980): 669-675.
- 16 Lewis, T.J., and A.J. Wright, "The electrical conductivity of MgO at low temperatures," *Brit. J. Appl. Phys.* 1 (1968): 441-447.
- 17 Mitoff, S.P., "Electrical and ionic conductivity in single crystal MgO," *J. Chem. Phys.* 36 (1960): 1383-1389.

18 Mitoff, S.P., "Electrical conductivity of single crystal of MgO." *J. Chem. Phys.* 31 (1959): 1261-1269.

19 Kittel, C., *Introduction to Solid State Physics*. (New York: J. Wiley & Sons, 1980).

20 Ashcroft, N.W., and N.D. Mermin, *Solid State Physics*. (Philadelphia, PA.: Holt-Saunders Publ., 1976).

21 Freund, M.M., "Highly mobile holes in wide band gap oxide insulators." Ph.D. Thesis, ETH, Zürich, 1990.

22 Kliewer, K. L., and J.S. Koehler, "Space charge in ionic crystals. I. General approach with application to NaCl." *Phys. Rev. A* 140 (1965): 1226-1240.

23 Lehovec, K., "Space-charge layer and distribution of lattice effects at the surface of ionic crystals." *J. Chem. Phys.* 21 (1953): 1123-1128.

24 Mackrodt, W.C., and R.F. Steward, "Defect properties of ionic solids: III. The calculation of the point-defect structure of the alkaline earth oxides and CdO." *J. Phys. C* 12 (1979): 5015-5036.

25 Cressy, N.F., and H.F. Hameka, "Theoretical principles of diamagnetism." *Theory and Applications of Molecular Diamagnetism*, ed. N.L. Mulay and E.A. Boudreux. (New York, NY: John Wiley, 1976) 29-58.

26 Mulay, L.N., and E.A. Boudreux, *Theory and Application of Molecular Diamagnetism*. (New York: Wiley, 1976).

27 Cremer, D., "General and theoretical aspects of the peroxide group." *The Chemistry of Functional Groups, Peroxides*, ed. ed. S. Patai. (New York, NY: Wiley & Sons, Publ., 1983) 1-79.

28 Reeber, R.R., and K. Goessel, "Thermal expansion and molar volume of MgO, periclase." *EOS Transaction Am. Geophys. Union* 74 [16] (1993): 162.

29 Wengeler, H., and F. Freund, "Anomalous thermal expansion behavior of arc-fused magnesium oxide." *Ceramic Forum Internat.* 58 (1981): 31-40.

30 Wengeler, H., and F. Freund, "Atomic carbon in magnesium oxide. Part III: Anomalous thermal expansion behavior." *Mat. Res. Bull.* 15 (1980): 1241-1245.

31 Pachalas, E., and A. Weiss, "Hartree-Fock-Roothan wavefunctions, electron densities, diamagnetic susceptibility, dipole polarizability, and antishielding factor for ions in crystals." *Theoret. Chim. Acta* 13 (1969): 381-408.

32 Shannon, R.D., and G.R. Rossman, "Dielectric constant of MgAl₂O₄ spinel and the oxide additivity rule." *J. Phys. Chem. Solids* 52.9 (1991): 1055-1059.

33 Chen, Y., and M.M. Abraham, "Trapped-hole centers in alkaline-earth oxides." *J. Phys. Chem. Solids* 51.7 (1990): 747-764.

34 Harding, J.H., "The calculation of free energies of point defects in ionic crystals." *Physica* 131 (1985): 13-26.

35 Sangster, M.J.L., and D.K. Rowell, "Calculation of defect energies and volumes in some oxides." *Phil. Mag.* 44 (1981): 613-624.

36 Fiske, P.S., J.F. Stebbins, and I. Farnan, "Oxygen diffusion and thermal expansion in MgO: A high T ¹⁷O NMR study." *EOS Trans. Amer. Geophys. Union* 73.43 (1992): 595.

CHARACTERIZATION OF ELECTROCONDUCTIVE TiN/Al-O-N COMPOSITES

J. L. Hoyer, J. A. Clark, and J. P. Bennett
U. S. Department of the Interior
Bureau of Mines
Tuscaloosa Research Center
P. O. Box L
Tuscaloosa, AL 35486-9777

ABSTRACT

TiN/Al-O-N composites were produced at the U. S. Bureau of Mines by mixing TiN (0 to 35 wt pct) with equal weight ratios of AlN and Al_2O_3 . Mixtures were densified by pressureless sintering at 1,850° C in a N_2 atmosphere. Crystalline phases after densification were TiN, AlN, and AlON. The critical volume fraction and the potential for a positive temperature coefficient of resistivity in TiN/Al-O-N composites has been investigated and related to percolation theory. Mechanical properties were also evaluated. Possible applications of these composites include switch contacts, compound sensors, and molten salt battery separators. Sample fabrication of some TiN/Al-O-N composites using electrical discharge machining may also be possible.

INTRODUCTION

The need for engineering ceramics with high hardness, high strength at elevated temperature, high toughness, and resistance to corrosion has led to development of particulate composites such as titanium nitride (TiN)/aluminum oxynitride (AlON) spinel materials. Some particulate reinforced composites are formed from conductive particulates within an insulating matrix which allows manipulation of the composites' electrical characteristics as well. Such electroconductive particulate composite systems studied include TiN in a SiAlON matrix¹, TiB_2 in a SiC matrix², and TiN in a Si_3N_4 matrix³.

An advantage of composites reinforced with an electrically conductive phase is the possibility of using electrical discharge

To the extent authorized under the laws of the United States of America, all copyright interests in this publication are the property of The American Ceramic Society. Any duplication, reproduction, or republication of this publication or any part thereof, without the express written consent of The American Ceramic Society or fee paid to the Copyright Clearance Center, is prohibited.

machining (EDM) to manufacture complex shapes. EDM can be applied to ceramics if the electrical resistivity is below $\approx 100 \Omega \cdot \text{cm}^4$. EDM is attractive for machining hard and brittle ceramics because no mechanical stress is placed on the workpiece. In addition, it gives an extremely fine surface finish. Materials tested for EDM applications include conductive Si_3N_4 , SiC-TiB_2 , and WC-Co composites⁴.

Limited information on the conductivity of materials in the $\text{TiN/AlN/Al}_2\text{O}_3$ system is available. Shibuta, Sakai, and Yoshizumi showed that conductivity of titanium oxynitrides increased with sintering temperature and varied with composition, generally changing with N/O ratio⁵. A composite formed at 1,400° C that was 98 pct TiN had a conductivity of approximately $10^4 \Omega^{-1} \cdot \text{cm}^{-1}$.

Al_2O_3 -TiN composites were prepared by an in situ reaction between TiO_2 and AlN by Mukerji and Biswas⁶. A composite formed from a 1:1 molar ratio of TiO_2 and AlN had a dc volume resistivity of $57 \times 10^6 \Omega \cdot \text{cm}$. They concluded that since the resistivity of the composite approaches that of TiN ($53.9 \times 10^6 \Omega \cdot \text{cm}$), the TiN phase is continuous and interconnected.

A general effective media equation has been used to describe a variable electrical resistivity phenomenon in non-ceramic composite systems by McLachlan and others⁷. Using both carbon and graphite in epoxy and black iron oxide (Fe_3O_4) in epoxy systems, this group demonstrated that composites consisting of conductive and nonconductive phases will exhibit a transition from more resistive to less resistive behavior between 1 and 60 vol pct. The point at which this transition occurs has been identified as the "critical (percolation threshold) volume fraction (Φ_c). At this threshold, the conductive material forms a conductive network throughout the insulating matrix. Increased loading of the conductive phase past this percolation threshold does not significantly improve the conductivity of the composite. This is important if one is developing a material for EDM and desires to add only as much electroconductive filler as necessary.

McLachlan and others also proposed that percolation may be induced or influenced by a change in environment which in turn causes stresses in the composite. These stresses would induce a percolation effect by changing the connectivity of the conductive phase which will in turn change the electrical properties of the composite. Applications for such materials include thermistors, chemical sensors, and piezoresistors (conductors). Groups in Europe and Japan^{2,3}, using a four probe dc technique, found that the resistivity of composites similar to the $\text{TiN/Al}_2\text{O}_3$ -N composites exhibited a marked increase when the loading of the conductive

phase was decreased between 40 and 20 vol pct. This generally agrees with the findings of McLachlan and others.

This paper presents the results of characterization of electroconductive TiN/AlON composites. Flexure strength, porosity, and hardness data were evaluated and the dc behavior of TiN/Al-O-N composite materials was examined. The presence of a positive temperature coefficient of resistivity (PTCR) in TiN/Al-O-N composites was studied and related to the percolation theory developed by McLachlan and others.

EXPERIMENTAL APPROACH

Five compositions (listed in table 1) were prepared for pressureless sintering by mixing 700 g batches of the TiN-AlN-Al₂O₃ powders* in isopropyl alcohol using a Bureau-developed turbomill previously described⁸. TiN content of the mixtures varied from 0 to 35 wt pct with a constant weight ratio of AlN to Al₂O₃. Billets were prepared by dry pressing the mixed powders into 8.25 diam pieces approximately 1.6 cm thick at 27.6 MPa, followed by isostatic pressing at 276 MPa and firing at 1,850° C for 2 h in 34.5 KPa N₂ using a graphite heating element furnace.

Table 1. Room temperature physical and mechanical properties of TiN/Al-O-N composites with varying TiN content after pressureless sintering at 1,850° C in a N₂ atmosphere

Sample ¹	Physical property				
	Bulk density, g/cm ³	True density, g/cm ³	Porosity, pct	Hardness, Gpa	MOR, MPa
0-50-50	3.07	3.50	12.2	11.89	ND
20-40-40	3.23	3.70	12.8	8.47	283
25-37.5-37.5	3.48	3.83	9.1	10.12	288
30-35-35	3.32	3.87	13.2	8.78	270
35-32.5-32.5	3.37	3.93	14.2	7.48	241

¹wt pct TiN-wt pct AlN-wt pct Al₂O₃

ND - Not determined

*Hermann Starck Grade B TiN and AlN and Baikowski CR6 Al₂O₃
Note: Reference to specific products does not imply endorsement by the U. S. Bureau of Mines.

Volume resistivity (ρ) was measured on 3.8 X 3.8 X 0.2 cm pieces cut from sintered billets. The measurement method used was based on ASTM D150, D257, and D1829. Samples were coated with gold that served as the conductive electrodes. The test apparatus was a guarded two probe configuration. The samples were then heated in air at 5° C/min and stabilized at the test temperature, a voltage was applied for 60 s and the current measured and heated to the next test temperature up to 316° C. Due to the effect of humidity and contamination below 100° C on ρ , data collection began at 116° C. Since the circuit configuration of the test apparatus limited the range of ρ measurements from 10^{14} to 10^{14} $\Omega\text{-cm}$, ρ of conductive samples was reported as $<10^{14}$.

Density, porosity, room temperature modulus of rupture (MOR) and hardness of the samples were measured. Bulk density of samples was determined using Archimedes' method (samples submerged in mercury). True density was determined by grinding samples to a powder (-325 mesh) to remove closed porosity, then determining the density of the powder using a He-pycnometer. Porosity was calculated using the bulk and true density as follows:

$$\text{Porosity, pct} = \frac{d_t - d_b}{d_t} \times 100$$

where d_t = true density (g/cm^3) and d_b = bulk density (g/cm^3).

Samples for hardness measurement and microstructure analysis were polished to a 1/4- μm diamond finish. Hardness was measured with a Vicker's indenter using a 500-g load. Five indentations were made on each sample and the results averaged. Samples for X-ray diffraction (XRD) analysis were prepared by grinding portions of each sintered material to pass through a 325 mesh screen.

RESULTS AND DISCUSSION

The physical and mechanical properties of the compositions are listed in table 1. Porosity values range from 9 to 14 pct for all compositions. The hardness of the sample with no TiN was higher than the values for other compositions. The room temperature MOR was in the mid 200 MPa range for all compositions containing TiN. Crystalline phases detected in all the sintered compositions were AlON and AlN. Crystalline TiN was present as such in all compositions containing TiN.

Data are listed for ρ in table 2. The volume pct of TiN in a sample was calculated based on the starting batch composition.

Porosity was included in the volume percent calculation because it was treated as a nonconductive phase in TiN/Al₂O₃ composites. Porosity increases the volume resistivity of the composites by preventing the development of the conductive TiN network. For the sample with 22.6 vol pct TiN, ρ was below the limits of the instrumentation, 4 log(Ω·cm) and is reported as < 4 log(Ω·cm). The samples with 19.4, 16.5, and 12.4 vol pct TiN were resistive, with ρ ranging from 10.78 to 10.94 log(Ω·cm). The sample which contained no TiN had a ρ of 12.55 log(Ω·cm).

Table 2. Volume resistivity of TiN/Al₂O₃ composites with varying TiN content, represented in both weight and volume percents, after pressureless sintering at 1,850° C in a N₂ atmosphere

TiN content		Volume resistivity at 116° C, log(Ω·cm)
Weight pct	Volume pct	
0	0	12.55
20	12.4	10.94
25	16.5	10.86
30	19.4	10.78
35	22.6	< 4

From this data, two observations can be made. First, Φ_c for this compositional area is between 22.6 and 19.4 vol pct TiN. This agrees with the observation of McLachlan and others who stated that this transition occurs between 1 and 60 vol pct loading of the conductive phase. Second, once the material becomes more resistive, ρ does not increase to a value equivalent to the sample with no TiN. This indicates that the presence of TiN influences the resistivity even when volumes are below Φ_c .

Figure 1 is a plot of log(ρ) versus temperature for the composites from 116° to 316° C. The sample containing 22.6 vol pct TiN was conductive over the entire temperature range. The ρ of the samples with 19.4, 16.5, and 12.4 vol pct TiN follow the same trend. The resistivity increases from 116° to 144° C, remains constant to 216° C, and gradually decreases to the value measured at 116° C as the temperature rises to 316° C. The maximum ρ of the sample containing 19.4 vol pct TiN was 11.2 log(Ω·cm) and the minimum was 10.7 log(Ω·cm). The sample with 16.5 vol pct TiN had a maximum ρ of 11.4 log(Ω·cm) and a minimum value of 10.8 log(Ω·cm). The increase in ρ starting at 116° through 144° C was more noticeable in the composite containing 12.4 vol pct TiN. It rose from 10.9

$\log(\Omega \cdot \text{cm})$ at 116°C to $11.6 \log(\Omega \cdot \text{cm})$ at 144°C . There was also a sharper change from 216° to 238°C followed by a gradual decrease to $11.1 \log(\Omega \cdot \text{cm})$ at 316°C . The ρ in the sample with no TiN vacillated about $12.75 \log(\Omega \cdot \text{cm})$.

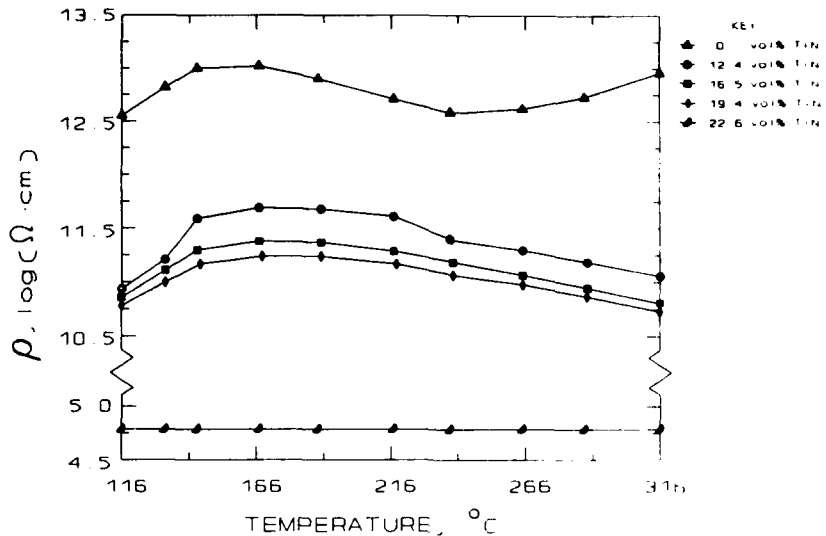


Figure 1. $\log(\rho)$ versus temperature for TiN/Al-O-N composites with varying TiN content after pressureless sintering at $1,850^\circ \text{C}$ in N_2 .

The increase in ρ with temperature in the sample containing 12.4 vol pct TiN, may indicate the presence of a second PTCR effect occurring between 0 and 12.4 vol pct TiN. McLachlan and others⁷ demonstrated that when volume fraction of Fe_3O_4 was near Φ_c , ρ of the Fe_3O_4 -epoxy composite decreased with the application of external pressure. They attributed this decrease in ρ to the variance in the relative volumes of the constituent phases which caused a change of Φ_c . Based on this concept, a PTCR transition was expected to occur in the 22.6 vol pct sample, but was not detected. Even though Φ_c for the TiN/AlON composites occurs between TiN loadings ranging from 22.6 to 19.4 vol pct, perhaps 22.6 vol pct the TiN was not close enough to Φ_c to trigger the PTCR effect over the temperature range evaluated. Also, the presence of porosity in the TiN/Al-O-N composite system may have contributed to the absence of this phenomenon.

Previous research⁸ has shown that TiN in pressureless sintered TiN/Al₂O₃-N composites sinters poorly. Most porosity in TiN/Al₂O₃-N composites is associated with the TiN phase. Table 3 lists accepted values for the coefficient of linear thermal expansion of the three crystalline phases identified in the TiN/Al₂O₃-N composites. TiN expands about 1.5 times faster than Al₂O₃. Therefore, it may be possible for TiN to preferentially fill the pore volume. If this were so, the relative volumetric composition of the TiN/Al₂O₃-N composite with 22.6 vol pct TiN would have been altered upon heating by creating a composite with less apparent porosity which would also have affected Φ_c . In addition, the low resistance in the TiN/Al₂O₃-N composite network could be maintained because TiN grains on the periphery of pores would enter the pore volume and connect with one another.

Table 3. Reference data for the major crystalline phases in TiN/Al₂O₃-N composites after pressureless sintering at 1,850° C in a N₂ atmosphere

Material	Density, g/cm ³	CLTE ¹ , (in/in) x 10 ⁻⁶ /°C	Source
TiN	5.42	8.0	J. Euro. Cer. Soc., v. 9, pp. 83-93, 1992
AlON	3.60	5.2	J. Amer. Cer. Soc., v. 71, No. 10, pp. 807-12, 1988
AlN (98 pct)	3.26	4.1	Ceramic Source, v. 8, p. TD27, 1992-1993

¹CLTE = coefficient of linear thermal expansion

Evaluation of samples with lower porosity is needed to determine if the thermal expansion differences influence the electrical properties of these materials. Additional research is necessary to determine the Φ_c and to investigate the possibility of a second PTCR transition in the TiN/Al₂O₃-N composites between 12.4 and 0 vol pct TiN.

SUMMARY

The resistivity of TiN/Al₂O₃-N composites was determined to be variable and dependent on the volume of TiN (conductive phase) used in their production. With strength values in the mid-200 MPa range, composites containing 35 wt pct or more TiN may be suitable for EDM applications. The critical volume fraction for these

composites appears to lie between 22.6 and 19.4 vol pct TiN. This result agrees with the theory of McLachlan and others which indicates that Φ_c should be located between 1 and 60 vol pct of the conductive phase.

A mild PTCR was detected in the composite loaded with 12.4 vol pct TiN. This may indicate the presence of a second PTCR in composites containing between 0 and 12.4 vol pct TiN. A PTCR was expected, but not detected, in the composite loaded with 22.6 vol pct TiN. Further research is necessary to determine Φ_c and to investigate the possibility of the occurrence of a second transition in the TiN/Al₂O₃ composites between 12.4 and 0 vol pct TiN.

REFERENCES

1. Hong, F., R. J. Lumby, and M. H. Lewis. TiN/Sialon Composites via In-Situ Reaction Sintering. *J. Euro. Cer. Soc.*, v. 11, pp. 237-239, 1993.
2. McMurtry, C., W. Boecker, S. Seshaadri, J. Zanchi and J. Garnier. Microstructure and Material Properties of SiC-TiB₂ Particulate Composites. *Am. Cer. Soc. Bull.*, v. 66, No. 2, pp. 325-9, 1987.
3. Bellosi, A., S. Guicciardi, and A. Tampieri. Development and Characterization of Electroconductive Si₃N₄-TiN Composites. *J. Euro. Cer. Soc.*, v. 9, pp. 83-93, 1992.
4. Petrofes, N. F. and A. M. Gadalla. Electrical Discharge Machining of Advanced Ceramics. *Am. Cer. Soc. Bull.* v. 67, No. 6, pp. 1048-1052, 1988.
5. Shibuta, D., Y. Sakai, and M. Yoshizumi. Sintering of Titanium Oxynitride Powder. *Ceram. Trans., Ceramic Powder Science II, Part B*, ed. G. L. Messing, E. R. Fuller Jr., and H. Hausner, *Am. Ceram. Soc.*, pp. 848-855, 1988.
6. Mukerji, J. and S. K. Biswas. Synthesis, Properties and Oxidation of Alumina-Titanium Nitride Composites. *J. Am. Ceram. Soc.*, v. 73, No. 1, pp. 142-145, 1990.
7. McLachlan, D. S., M. Blaszkiewicz, and R. E. Newnham. Electrical Resistivity of Composites. *J. Am. Ceram. Soc.*, v. 73, No. 8, pp. 2187-2203, 1990.
8. Hoyer, J. L., J. P. Bennett, K. J. Liles. Properties of TiAlON/Spinel Ceramic Composites. *Ceram. Eng. Sci. Proc.*, v. 11, No. 9-10, pp. 1423-1439, 1990.

High-Temperature Superconductors

GRAIN BOUNDARY DEGRADATION OF YBCO SUPERCONDUCTORS SINTERED IN CO₂-CONTAINING ATMOSPHERES

U. Balachandran, K. L. Merkle,[†] and J. N. Mundy[†]
Energy Technology Division, [†]Materials Science Division
Argonne National Laboratory, Argonne, IL 60439

Y. Gao
Department of Materials and Metallurgical Engineering
New Mexico Institute of Mining and Metallurgy
Socorro, NM 87801

C. Zhang, D. Xu, and G. Selvaduray
Department of Materials Engineering
San Jose State University, San Jose, CA 95192

ABSTRACT

The transport critical current density (J_c) of YBCO superconductors decreased with increasing CO₂ partial pressure in the sintering atmosphere and ultimately reached zero, even though magnetization measurements showed that the bulk of the samples with zero J_c remained superconducting. The microstructure and composition of the samples was investigated by high-resolution transmission electron microscopy and secondary-ion mass spectroscopy (SIMS). Microbeam SIMS indicated carbon segregation at grain boundaries (GBs). Approximately 10% of the GBs was coated with a thin layer of a second phase, deduced to be BaCuO₂ and BaCu₂O₂. Near some grain boundaries, the structure was tetragonal within several tens of nm of the boundaries. Degradation of J_c is discussed in terms of the partial pressure of CO₂ and the processing temperatures. Detailed examination of GB microstructures is presented in this paper.

INTRODUCTION

A major limitation of bulk-processed YBa₂Cu₃O_{7-x} (YBCO) superconductor for practical applications is its very low value of the transport critical current density (J_c). A possible cause of this problem is blockage of the superconducting currents across grain boundaries. One type of blockage is structural discontinuity at grain boundaries [1,2]. Another possible blockage is the

To the extent authorized under the laws of the United States of America, all copyright interests in this publication are the property of The American Ceramic Society. Any duplication, reproduction, or republication of this publication or any part thereof, without the express written consent of The American Ceramic Society or fee paid to the Copyright Clearance Center, is prohibited.

presence of second phases at grain boundaries [3-5]. Nakahara et al. [6] reported the presence of a few-angstrom-thick second phase at grain boundaries. By using scanning Auger microscopy, Verhoeven et al. [7] concluded that the second phase is a BaCO₃ and that the carbon contamination was not a product of original processing, but a consequence of the environment.

The transition temperature (T_c), J_c , and the width of the superconducting transition of YBCO are influenced by atmospheric contaminants such as CO₂ and H₂O [4,5,8-10]. Two potential sources of CO₂ are present during YBCO processing. One source is the CO₂ contained in the oxygen gas used during sintering and/or annealing. Another source is the CO₂ derived from the decomposition of BaCO₃ during the calcination step. Each source affects the quality of the final product in different ways and can lead to a drop in J_c .

During calcination, the Y₂O₃, BaCO₃, and CuO powders react to form YBCO. When BaCO₃ decomposes, CO₂ is released. The localized concentration of CO₂ can quickly reach its equilibrium value, and stagnant regions of CO₂ can form, even in systems with flowing gases. This localized CO₂ pressure, depending on the temperature and other thermodynamic conditions, can start other decomposition reactions, thereby forming undesired phases, which, in turn, contribute to reduce the J_c of the final product. A dynamic low-pressure vacuum calcination technique has been developed by Balachandran et al. [11,12] to effectively remove CO₂ from the reaction chamber during calcination of precursors to form YBCO.

The reaction of YBCO with CO₂ present in the sintering atmosphere has been reported by several researchers [3-5,8,13]. Gallagher et al. [8] reported that, at 1000°C in a 1% CO₂/99% O₂ mixture, the YBCO phase was not decomposed, whereas in a 10% CO₂/90% O₂ mixture, the YBCO phase was completely decomposed to BaCO₃, Y₂Cu₂O₅, and CuO. Fjellvag et al. [13] studied the interaction between CO₂ and YBCO in a 0.1% CO₂/99.9% O₂ mixture and reported that the reaction occurred in two steps: below 730°C the reaction products were BaCO₃, Y₂O₃, and CuO, whereas above this temperature, the products were BaCO₃, Y₂Cu₂O₅, and CuO.

Because of limitations of the X-ray diffraction (XRD) technique, neither Gallagher et al. [8] nor Fjellvag et al. [13] were able to study the spatial origin of the reaction between YBCO and CO₂, which may be very important to the low value of the J_c found in ceramic superconductors. Recently, Cooper et al. [14] used in-situ electrical conductivity measurements to study the kinetics of YBCO decomposition in a flowing 5% CO₂/95% O₂ atmosphere at 815°C.

In this paper, we report on the degradation of the J_c of YBCO sintered in CO₂-containing atmospheres. The grain boundary microstructures and compositions of the samples were investigated by transmission electron microscopy (TEM), analytical electron microscopy (AEM), and secondary ion mass spectroscopy (SIMS). The relationships between the properties and the partial pressure of CO₂ are discussed in terms of microstructural changes.

EXPERIMENTAL

Phase-pure orthorhombic powders of YBCO were prepared by mixing and grinding stoichiometric amounts of Y_2O_3 , $BaCO_3$, and CuO and then calcining in flowing oxygen at a reduced total pressure of ~2 mm Hg at ~850°C; this was followed by low-temperature annealing in ambient-pressure oxygen [11, 12]. The reduced pressure used in this process ensured the efficient removal of the CO_2 gas generated during the formation of the YBCO phase and resulted in the production of phase-pure orthorhombic powders. These powders were pressed into small pellets and sintered for ~5 h in a flowing CO_2/O_2 gas mixture at ~1 atm. pressure. The portion of CO_2 in the mixtures was 0-5%. Four groups of samples were sintered at 910, 940, 970, or 1000°C. Transition temperatures were obtained by resistivity and magnetization techniques. A low-field rf SQUID magnetometer was used for the magnetization measurements. TEM specimen disks (3 mm in diameter) were cut from bulk samples and polished on 600-grid paper in methyl alcohol to a thickness of ~120 μm . The disks were dimpled from both sides to have a thin area ~25 μm thick at the center. The final TEM specimens were obtained by argon ion-thinning in a liquid-nitrogen-cooled stage. TEM observations and AEM analysis were performed with a Philips 420 at an operating voltage of 120 kV.

RESULTS AND DISCUSSION

The J_c values (at 77 K, self-field) decreased with decreasing sintering temperatures and increasing CO_2 content. The J_c finally becomes zero at a CO_2 partial pressure that is dependent on the sintering temperature. Resistivity measurements showed that the materials with $J_c = 0$ were semiconductive. Figure 1 summarizes these results and presents them in terms of the processing conditions, namely partial pressure of CO_2 and sintering temperature, that are necessary for the production of superconductors. The solid line separates the stability regions of superconductors and semiconductors. Magnetization measurements for samples with $J_c = 0$ indicated that the major phase of these samples was still superconducting. The onset of superconductivity was almost the same, ~90 K, for all samples. The presence of CO_2 was detrimental, despite the fact that the major phases were still superconducting.

Figure 2 shows an example of resistivity-vs.-temperature and magnetization-vs.-temperature curves for samples sintered at 940°C in pure O_2 and in a 0.5% $CO_2/99.5\% O_2$ mixture. Resistivity and magnetization measurements of samples with high and zero J_c suggest a strong blockage of superconducting current at the grain boundaries in the latter samples. A possible cause of the blockage could be a thin layer of a second phase at grain boundaries that formed during sintering because of the reaction between YBCO and CO_2 in the gas atmosphere. This hypothesis was checked by TEM examination of several samples. Because the grain interiors are not degraded, a sharp change in magnetization is seen at ~90 K (Fig. 2b) in the samples that showed semiconducting behavior in the resistivity measurements (Fig. 2a).

EXPERIMENTAL

Phase-pure orthorhombic powders of YBCO were prepared by mixing and grinding stoichiometric amounts of Y_2O_3 , $BaCO_3$, and CuO and then calcining in flowing oxygen at a reduced total pressure of ~2 mm Hg at ~850°C; this was followed by low-temperature annealing in ambient-pressure oxygen [11,12]. The reduced pressure used in this process ensured the efficient removal of the CO_2 gas generated during the formation of the YBCO phase and resulted in the production of phase-pure orthorhombic powders. These powders were pressed into small pellets and sintered for ~5 h in a flowing CO_2/O_2 gas mixture at ~1 atm. pressure. The portion of CO_2 in the mixtures was 0-5%. Four groups of samples were sintered at 910, 940, 970, or 1000°C. Transition temperatures were obtained by resistivity and magnetization techniques. A low-field rf SQUID magnetometer was used for the magnetization measurements. TEM specimen disks (3 mm in diameter) were cut from bulk samples and polished on 600-grid paper in methyl alcohol to a thickness of ~120 μm . The disks were dimpled from both sides to have a thin area ~25 μm thick at the center. The final TEM specimens were obtained by argon ion-thinning in a liquid-nitrogen-cooled stage. TEM observations and AEM analysis were performed with a Philips 420 at an operating voltage of 120 kV.

RESULTS AND DISCUSSION

The J_c values (at 77 K, self-field) decreased with decreasing sintering temperatures and increasing CO_2 content. The J_c finally becomes zero at a CO_2 partial pressure that is dependent on the sintering temperature. Resistivity measurements showed that the materials with $J_c = 0$ were semiconductive. Figure 1 summarizes these results and presents them in terms of the processing conditions, namely partial pressure of CO_2 and sintering temperature, that are necessary for the production of superconductors. The solid line separates the stability regions of superconductors and semiconductors. Magnetization measurements for samples with $J_c = 0$ indicated that the major phase of these samples was still superconducting. The onset of superconductivity was almost the same, ~90 K, for all samples. The presence of CO_2 was detrimental, despite the fact that the major phases were still superconducting.

Figure 2 shows an example of resistivity-vs.-temperature and magnetization-vs.-temperature curves for samples sintered at 940°C in pure O_2 and in a 0.5% $CO_2/99.5\% O_2$ mixture. Resistivity and magnetization measurements of samples with high and zero J_c suggest a strong blockage of superconducting current at the grain boundaries in the latter samples. A possible cause of the blockage could be a thin layer of a second phase at grain boundaries that formed during sintering because of the reaction between YBCO and CO_2 in the gas atmosphere. This hypothesis was checked by TEM examination of several samples. Because the grain interiors are not degraded, a sharp change in magnetization is seen at ~90 K (Fig. 2b) in the samples that showed semiconducting behavior in the resistivity measurements (Fig. 2a).

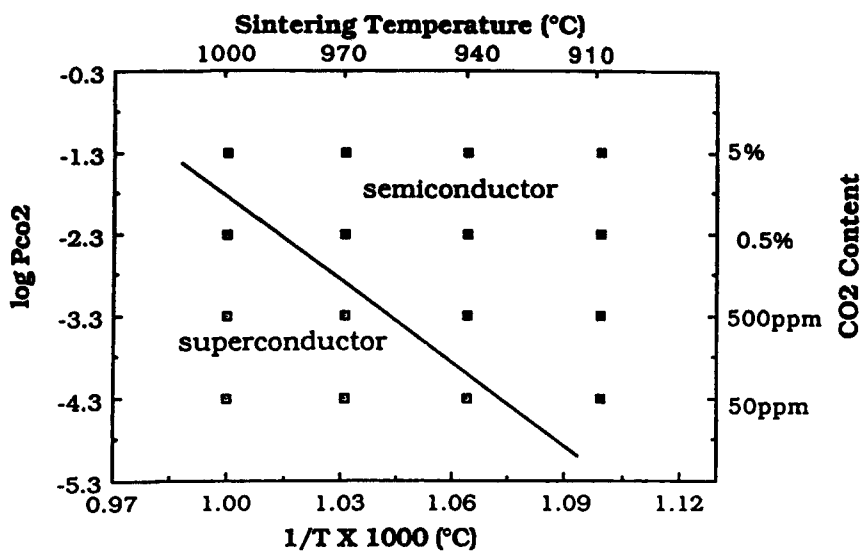


Figure 1 Stability of YBCO superconductor as a function of partial pressure of CO₂ (PCO₂) and temperature.

The compositions at and near grain boundaries in sintered samples were investigated by TEM in conjunction with energy dispersive spectroscopy (EDS). No evidence of second phases at grain boundaries was found in samples sintered in pure O₂. However, two distinct types of grain boundaries were observed in the samples that were sintered in 0.5% CO₂/99.5% O₂ mixture. Approximately 10% of the observed grain boundaries were found to be wet by a thin layer of a second phase, as shown in Fig. 3. EDS spectra obtained from locations along this boundary indicate that the composition of this layer was rich in Ba and Cu, but depleted in Y, and was likely to be BaCuO₂. At some locations, this layer was extremely rich in copper, and it is likely that the composition may be due to the eutectic reaction between BaCuO₂ and CuO, in accordance with the phase diagram [15]. The remaining boundaries (~90% of the boundaries) appeared quite sharp and contained no obvious evidence of second phases.

Because of the multitude of possible percolation paths, the value of J_c will not become zero if only 10% of the grain boundaries is coated with a second phase. Therefore, most of the grain boundaries must be resistive enough to block the flow of superconducting current across the boundaries. By careful study of high-resolution electron microscopy (HREM) images, we found that the structure near the sharp grain boundaries was not orthorhombic, but tetragonal, as shown in Fig. 4. The lattice fringes in the [001] direction were clearly observed, and it was found that the spacing c was 1.19 nm near the grain

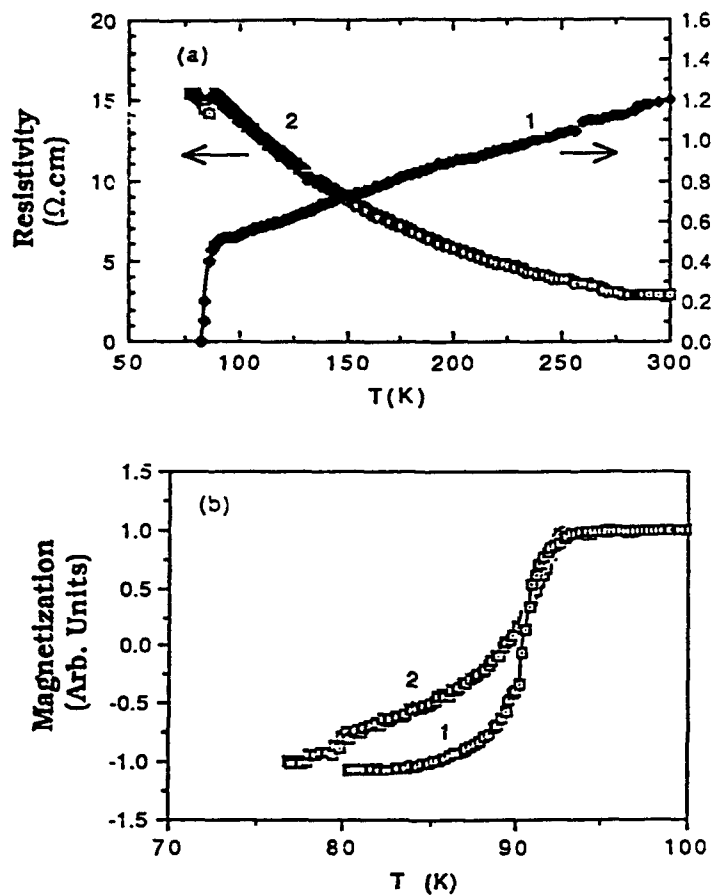


Figure 2 Resistivity vs. temperature (a), and magnetization vs. temperature (b), for two YBCO samples sintered at 940°C (Sample 1 sintered in pure O₂; Sample 2, in 0.5% CO₂/99.5% O₂).

boundary, whereas in the region far from the grain boundary c was 1.17 nm. From neutron diffraction data [16], we know that a structure with c = 1.19 nm is tetragonal and one with c = 1.17 nm is orthorhombic. Another indication of the presence of a tetragonal structure is the termination of the twin structure, as marked by PB (phase boundary) in Fig. 4. This can be taken as the signature of the demarcation line between the orthorhombic and tetragonal structures, because the tetragonal structure has no twins.



Figure 3 TEM photomicrograph of grain boundary (GB) in YBCO sample sintered at 970°C in 0.5% CO₂/99.5% O₂ atmosphere.

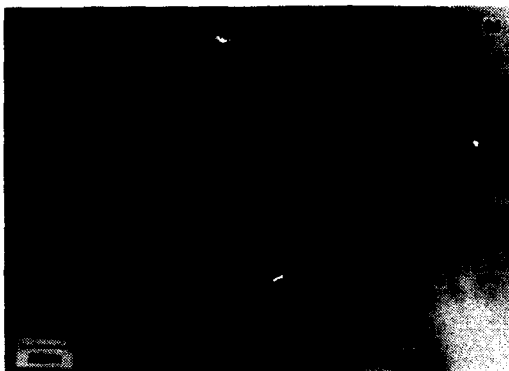


Figure 4 HREM image of grain boundary (GB) in YBCO sample sintered at 970°C in 0.5% CO₂/99.5% O₂ atmosphere. The structure with lattice fringes of 1.19 nm is tetragonal (T) and one with lattice fringes of 1.17 nm is orthorhombic (O). PB is the phase boundary between T and O structures.

A possible cause of the phase transformation from the orthorhombic to the tetragonal structure is the incorporation of carbon into the lattice because CO₂ is present in the sintering atmosphere [3-5]. Carbon diffuses into the lattice, and expells oxygen in the orthorhombic structure, thus forming a tetragonal structure. Secondary ion mass spectroscopy was used to detect the carbon

signal. The carbon maps obtained by SIMS show no carbon signal for the sample sintered in pure O₂, but a strong carbon signal at grain boundary regions of samples sintered in CO₂/O₂ mixtures [3]; Fig. 4 is a special example, with a particularly large tetragonal region. We observed, in most cases, that such tetragonal regions near grain boundaries vary from a few nanometers to several tens of nanometers. Therefore, they were very difficult to detect and are not readily identifiable in most boundaries. The width of these tetragonal regions is much larger than the coherence length of this material. Therefore, it is reasonable to conclude that these second phases block the passage of superconducting current.

EDS also revealed the presence of precipitates of Y₂BaCuO₅ in samples sintered in 0.5% CO₂/99.5% O₂ mixture, as shown in Fig. 5. Based on the findings here, and the fact that the samples were phase-pure before they were sintered in a CO₂-containing atmosphere, it can be concluded that YBCO decomposes in the presence of CO₂, yielding Y₂BaCuO₅, BaCO₃, BaCuO₂, and CuO. The decomposition products depend on temperature and partial pressure of CO₂ in the sintering atmosphere.

Our previous work indicates that the rate of reaction with CO₂ can differ greatly at various grain boundaries [4]. For example, in some cases, the reaction just started at some grain boundaries, as shown in Fig. 6a, whereas the reaction was complete at other grain boundaries, as indicated in Fig. 6b. The reaction rate may depend on grain boundary misorientation, or on grain boundary type. However, it is not clear at this time which aspects of grain boundary geometry or composition are controlling the nucleation and growth of second phases. At low partial pressures of CO₂ (up to a few hundred parts per million), only a fraction of the grain boundaries may be modified sufficiently by such reactions to cause interruption of the superconducting current. For samples sintered in 5% CO₂/95% O₂, the initial YBCO phase was completely decomposed and no superconducting transition was observed. Both EDS and XRD showed that the decomposition products were BaCO₃, CuO, and Y₂BaCuO₅.

CONCLUSIONS

YBCO samples react strongly with CO₂ in the sintering atmosphere, leading to a decrease in J_C. The tendency of the reaction depends on the sintering temperature, partial pressure of CO₂, and grain boundary structure. Increasing the sintering temperatures raises the equilibrium partial pressure of CO₂. Up to a certain value of the CO₂ partial pressure, the YBCO samples gradually lose their superconducting properties, although the major phase of these samples is still superconducting. The second phases formed at the grain boundaries as a result of the reaction of YBCO with CO₂ blocks the flow of superconducting currents. Carbon segregation near the grain boundary regions results in a transformation of the orthorhombic phase to the nonsuperconducting tetragonal phase. At a CO₂ level as high as 5%, the YBCO completely decomposed to BaCO₃, Y₂BaCuO₅, and CuO.



Figure 5 TEM photomicrograph of YBCO sample sintered at 970°C in 0.5% CO₂/99.5% O₂ atmosphere. The second phases, marked S, were identified to be Y₂BaCuO₅.

ACKNOWLEDGMENTS

Work supported by the U.S. Department of Energy, Energy Efficiency and Renewable Energy, as part of a program to develop electric power technology, Basic Energy Sciences-Materials Science, under Contract W-31-109-Eng-38; and the National Science Foundation (DMR88-09854) through the Science and Technology Center for Superconductivity.

REFERENCES

1. P. Chaudhari, J. Mannhart, D. Dimos, C. C. Tsuei, J. Chi, M. M. Oprysko, and M. Scheuermann, Direct measurement of the superconducting properties of single grain boundaries in YBa₂Cu₃O_{7-x}, *Phys. Rev. Lett.*, **60**, 1653-1656, (1988).
2. D. Dimos, P. Chaudhari, J. Mannhart, and F. K. LeGoues, Orientation dependence of grain boundary critical currents in YBa₂Cu₃O_{7-x} bicrystals, *Phys. Rev. Lett.*, **61**, 219-222, (1988).
3. Y. Gao, Y. Li, K. L. Merkle, J. N. Mundy, C. Zhang, U. Balachandran, and R. B. Poeppel, Jc degradation of YBa₂Cu₃O_{7-x} superconductors sintered in CO₂/O₂, *Mater. Lett.*, **9**, 347-352, (1990).
4. Y. Gao, K. L. Merkle, C. Zhang, U. Balachandran, and R. B. Poeppel, Decomposition of YBa₂Cu₃O_{7-x} during annealing in CO₂/O₂ mixtures, *J. Mater. Res.*, **5**, 1363-1367, (1990).

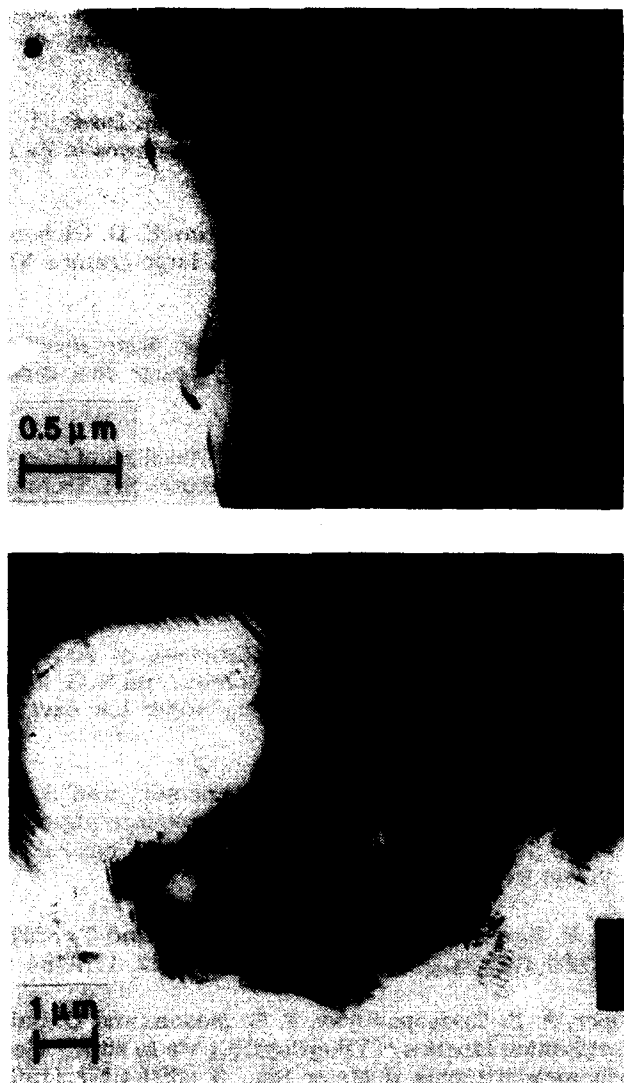


Figure 6 (a) Nuclei of secondary phases at a grain boundary in YBCO sample treated in CO_2/O_2 atmosphere for 0.5 h; (b) some grain boundaries are completely coated with second phases in the same sample as in (a).

5. G. Selvaduray, C. Zhang, U. Balachandran, Y. Gao, K. L. Merkle, H. Shi, and R. B. Poeppel, Effect of CO₂ on the processing of Y-Ba-Cu-O superconductors, *J. Mater. Res.*, **7**, 283-291, (1992).
6. S. Nakahara, G. J. Fisanick, M. F. Yan, R. B. van Dover, T. Boone, and R. Moore, On the defect structure of grain boundaries in Ba₂YCu₃O_{7-x}, *J. Crystal Growth*, **85**, 639-651, (1987).
7. J. D. Verhoeven, A. J. Bevolo, R. W. McCallum, E. D. Gibson, and M. A. Noack, Auger study of grain boundaries in large-grained YBa₂Cu₃O_x, *Appl. Phys. Letters*, **52**, 745-747, (1988).
8. P. K. Gallagher, G. S. Grader, and H. M. O'Bryan, Some effects of CO₂, CO, and H₂O upon the properties of YBa₂Cu₃O₇, *Mater. Res. Bull.*, **23**, 1491-1499, (1988).
9. E. K. Chang, E. F. Ezell, and M. J. Kirschner, The effect of CO₂ in the processing atmosphere of YBa₂Cu₃O_x, *Supercond. Sci. Technol.*, **8**, 391-394, (1990).
10. T. B. Lindemer, C. R. Hubbard, and J. Brynestad, CO₂ solubility in YBa₂Cu₃O_{7-x}, *Physica C*, **167**, 312-316, (1990).
11. U. Balachandran, R. B. Poeppel, J. E. Emerson, S. A. Johnson, M. T. Lanagan, C. A. Youngdahl, D. Shi, K. C. Goretta, and N. G. Eror, Synthesis of phase-pure orthorhombic YBa₂Cu₃O_x under low oxygen pressure, *Mater. Lett.*, **8**, 454-456, (1989).
12. U. Balachandran, R. B. Poeppel, J. E. Emerson, and S. A. Johnson, Calcination and solid state reaction of ceramic-forming components to provide single-phase superconducting materials having fine particle size, U.S. Patent 5,086,034, February 4, 1992.
13. H. Fjellvag, P. Karen, A. Kjekshus, P. Kofstad, and T. Norby, Carbonization of YBa₂Cu₃O_{6+x}, *Acta Chem. Scand.*, **A42**, 178-184, (1988).
14. E. A. Cooper, A. K. Gangopadhyay, T. O. Mason, and U. Balachandran, CO₂ decomposition kinetics of YBa₂Cu₃O_{7-x} via *in situ* electrical conductivity measurements, *J. Mater. Res.*, **6**, 1393-1397, (1991).
15. R. A. Laudise, L. F. Schneemeyer, and R. L. Barnes, Crystal growth of high temperature superconductors-Problems, successes, opportunities, *J. Cryst. Growth*, **85**, 569-575, (1987).
16. J. D. Jorgensen, M. A. Beno, D. G. Hinks, L. Soderholm, K. J. Volin, R. L. Hitterman, J. D. Grace, I. K. Schuller, C. U. Segre, K. Zhang, and M. S. Kleefisch, Oxygen ordering and the orthorhombic-to-tetragonal phase transition in YBa₂Cu₃O_{7-x}, *Phys. Rev. B36*, 3608-3616, (1987).

INTERFACE EFFECTS IN Bi-“2212”/Ag AND Bi-“2223”/Ag SUPERCONDUCTORS

S.J. Golden, T. Yamashita, A. Bhargava, J.C. Barry and I.D.R. Mackinnon, Centre for Microscopy and Microanalysis, The University of Queensland, Brisbane, Queensland 4072, Australia.

INTRODUCTION

The superconducting phases in the Bi-Sr-Ca-Cu-O system are some of the most promising materials for practical applications, especially for wire, tape and coil fabrication [1-3]. In the so-called powder-in-tube technology a precursor powder is packed into a Ag tube and given various thermo-mechanical heat treatments. Some of the wires with the highest critical current density, for example 5×10^4 A.cm⁻² at 77K and zero field [3], are made with a precursor to the “2223” phase which consists of the “2212” phase and non-superconducting phases. After processing the wire consists of a “2223” oxide core with a thickness in the range 40-100μm with a well-aligned texture, encapsulated by a Ag sheath. Thick films of the “2212” phase (10-60μm) on Ag are made by doctor-blading or painting. The “2212”/Ag thick films are melt processed, with the “2212” phase crystallising from the melt during slow cooling and forming well-aligned structures. Critical current densities of 2×10^4 A.cm⁻² (77K, 0T) and 3×10^5 A.cm⁻² (4.2K, 2T) have been measured for “2212”/Ag thick films made in this way [4].

The use of Ag fulfills several requirements in these materials. However, the precise role of the Ag/superconductor interface in the “2212”/Ag system and in the “2223”/Ag system is not well established. In a number of studies it has been concluded that the Ag/oxide interface plays a unique and important role with regard to “2212” texture formation in the melt-processed “2212”/Ag materials [5, 6]. However other studies indicate that the main function of the Ag is simply geometrical and that texture formation can be explained by considering anisotropic growth of “2212” in a quasi two-dimensional space [7, 8].

To the extent authorized under the laws of the United States of America, all copyright interests in this publication are the property of The American Ceramic Society. Any duplication, reproduction, or republication of this publication or any part thereof, without the express written consent of The American Ceramic Society or fee paid to the Copyright Clearance Center, is prohibited.

EXPERIMENTAL

A "2212" powder was fabricated using the standard co-precipitation process and subsequent heat treatments up to temperatures of 870°C for 10 h. Ag foil substrates were coated on both sides with the "2212" powder by a painting technique utilising an HPMC binder. Total thicknesses of up to 3 mm were deposited using a number of painting-drying repetitions. After a burn-out heat treatment at 400°C the thick films were melt processed by heating at 890°C for 30 min., cooling at 10°C/h to a temperature in the range 840°C-880°C where the sample is held for 10 h. The sample was quenched into oil at the end of the isothermal treatment. Thick layers on MgO single-crystals were also melt-processed. Scanning electron microscopy was carried out on cross-sections of the thick films in addition to X-ray diffraction on planes parallel to the substrate at varying distances from the substrate surface. A 1 µm diamond pad was used to remove the film from the upper surface.

For the study of the "2223"/Ag system a nitrate solution of cation composition Bi:Pb:Sr:Ca:Cu = 1.65:0.35:1.6:2:3 was made and an oxalate precipitate was formed using oxalic acid. The oxalate was heated at 800°C for 10 h with intermediate grinding and at 840°C for 2 h to produce a powder consisting of "2212", CuO, Ca₂PbO₄ and minor amounts of other phases. Thick films of this powder were deposited on Ag foil and {100}MgO substrates using the painting technique described above. The thick films were given isothermal heat treatments at temperatures ranging from 810°C to 880°C for 15 h. SEM and XRD were used to evaluate phase composition and microstructural variation as a function of distance from the substrate/film interface as described above.

RESULTS AND DISCUSSION

Melt-Processed "2212" on Ag and MgO Substrates

Thick films of "2212" on Ag and MgO were melt-processed using 890°C, a cooling rate of 10°C/h to 850°C, followed by an anneal at 850°C for 10 h and quenched to room temperature. The degree of c-axis orientation was measured by comparing the relative intensities of the (008) and (113) X-ray diffraction peaks from the "2212" layer.

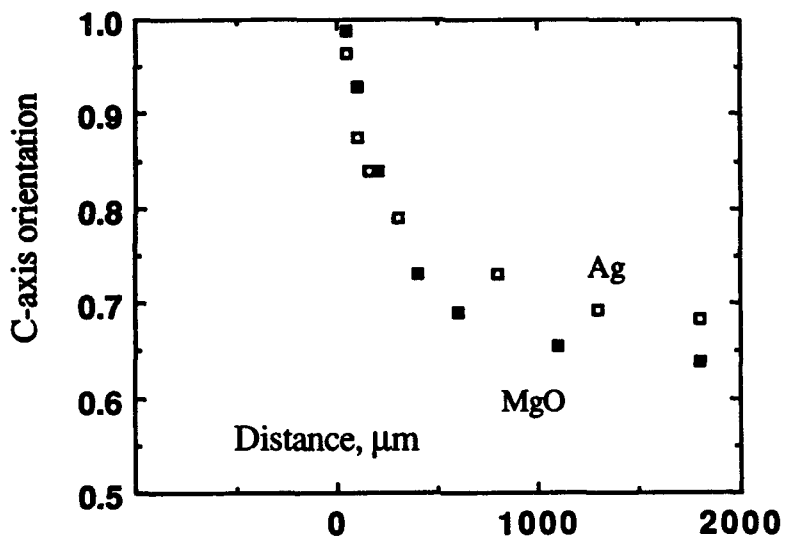


Figure 1 Variation of degree of c-axis orientation with distance from substrate interface in melt-processed "2212"/Ag and "2212"/MgO thick films.

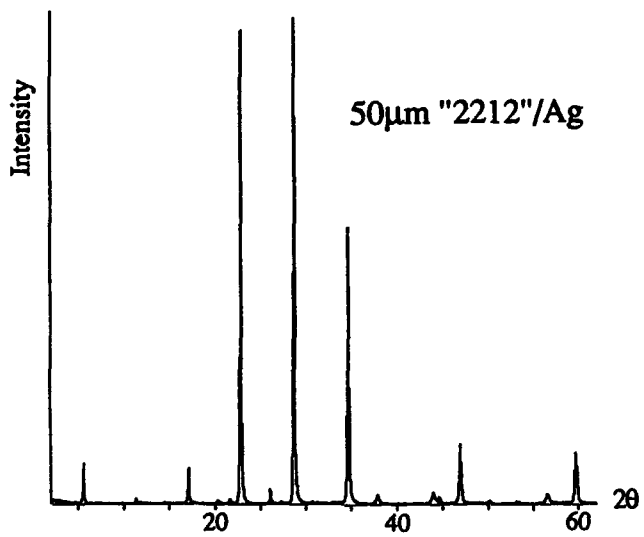


Figure 2 XRD trace of a 50μm thick layer of melt-processed "2212" on Ag showing the high degree of c-axis orientation.

It was found that there was a definite variation of texture with distance from the Ag/"2212" interface and MgO/"2212" interface as shown in figure 1. The region with good c-axis orientation (c-axis normal to the substrate/"2212" interface) is confined to a region of approximately 50 μ m adjacent to the interface. Figure 2 shows the XRD trace of the thick layer polished down to a thickness of approximately 50 μ m for the Ag substrate. The XRD trace for the MgO case (for the same thickness) resembled this one closely. Figure 3 shows an SEM image of the fracture surface of melt-processed "2212" on MgO, illustrating the high degree of orientation adjacent to the substrate. These results do not support the view that the Ag/"2212" interface plays a unique texturing role [5, 6].

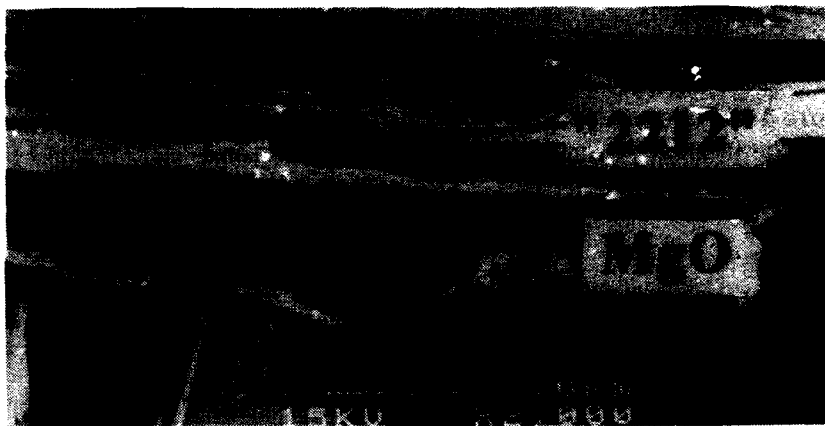


Figure 3 Fracture surface of the melt-processed "2212"/MgO showing the high degree of texture adjacent to the interface.

Formation of "2223" on Ag and MgO Substrates

The formation of "2223" from the precursor was studied for a range of heat treatment temperatures for Ag and single crystal MgO substrates. In particular the phase evolution and microstructure was studied as a function of distance from the substrate/film interface for each heat treatment. A comparison was made between the effect of the different substrates. Figure 4 shows the evolution of "2223" as a function of heat treatment temperature for material on MgO substrates.

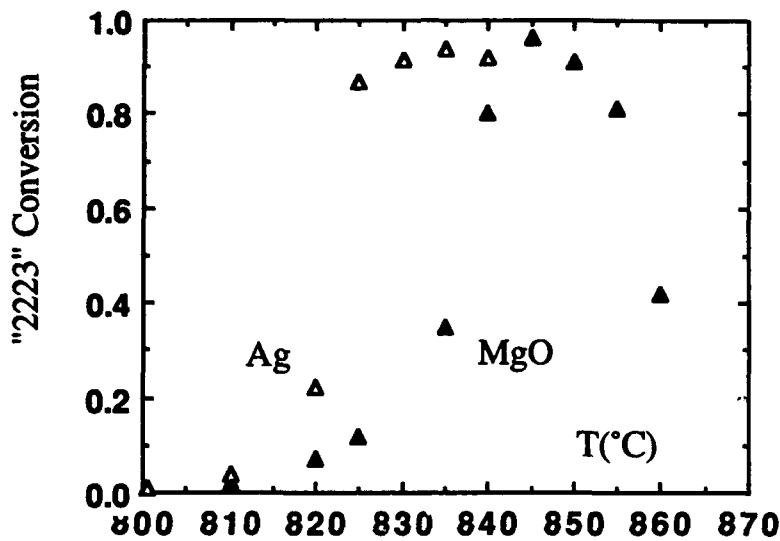


Figure 4 The variation of "2223" evolution vs. heat treatment temperature for MgO substrates ($t=15$ h). Also shown are the data for Ag substrates for a film thickness of $100\mu\text{m}$.

The data was obtained by carrying out XRD on the top surface of the thick film. It was found that there was little dependence between the phase evolution of "2223" and its microstructure and depth from the MgO/BSCCO interface. The measured amount of "2223" as a function of temperature, as shown in figure 4, was found to be independent of distance from the interface. It was found that in the case of MgO substrates there was no apparent bonding interaction between film and substrate, except for high heat treatment temperatures ($T>845^\circ\text{C}$), where there was large-scale decomposition of the "2223" phase which formed.

In contrast, the "2223" phase evolution on Ag substrates was strongly dependent on distance from the Ag/BSCCO interface at most of the heat treatment temperatures that were utilized. Figure 5 shows the distance-dependent "2223" phase formation as a function of heat treatment temperature. The amount of "2223" formation at large distances from the Ag interface were similar to those obtained on MgO (figure 4). However as the distance from the interface decreases there is a greatly enhanced "2223" evolution. This was observed for temperatures exceeding 820°C .

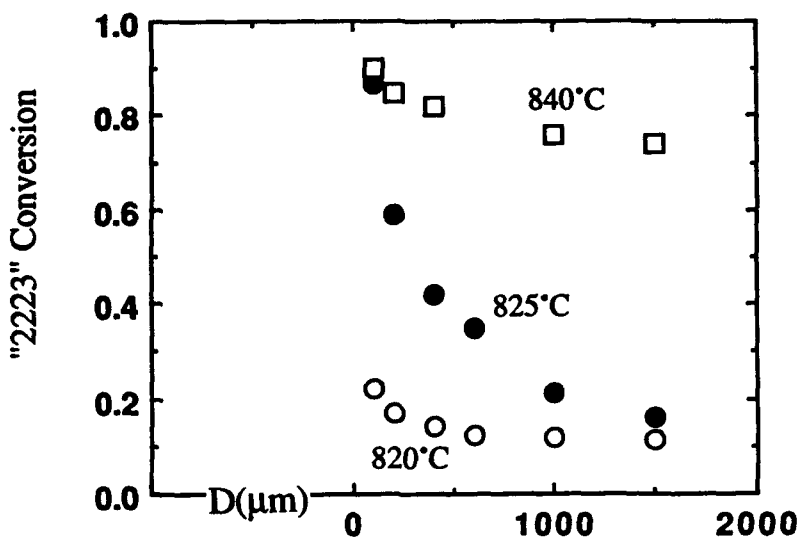


Figure 5 The variation of "2223" evolution vs. distance from substrate in the case of "2223"/Ag at different heat treatment temperatures.

Thick films on Ag heat treated at 820°C and lower showed no enhanced "2223" evolution relative to the MgO case. The "2223" formation (for a distance from the substrate interface of 100μm) vs. heat treatment temperature for the Ag substrate case has been plotted on figure 4. This clearly illustrates the effect of the Ag interface. There are two different temperature regimes with respect to "2223" formation adjacent to the Ag interface. The two temperature regimes, $T \leq 820^\circ\text{C}$ and $T \geq 825^\circ\text{C}$, can be explained by positing a temperature dependent Ag/BSCCO interaction at the interface. Electron microscopy studies of thick film regions near the interface revealed significant differences in microstructure and composition for samples heat treated at 820°C and at 825°C and above. In the latter case oxide regions near the Ag interface without a distinct crystalline morphology were rich in Cu relative to the "2223" type composition intermixed with some plate-like particles of a Sr-deficient "2201" phase. A typical region is shown in figure 6. In some of these regions a significant amount of Ag was also present

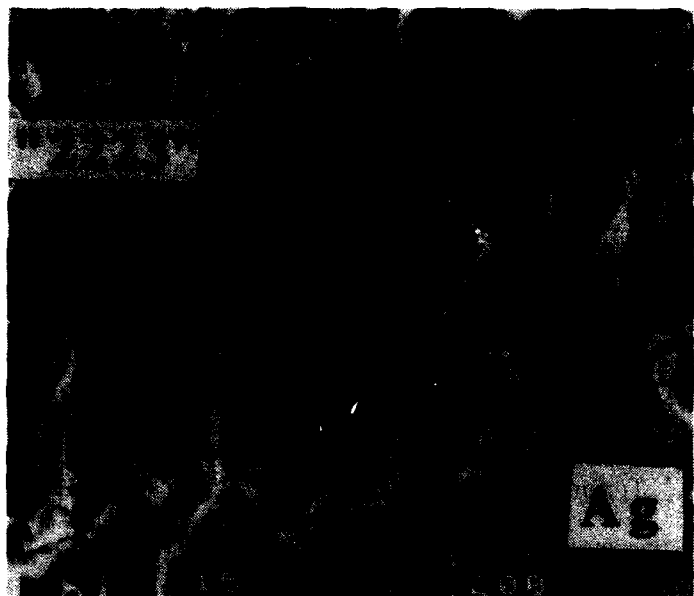


Figure 6 An SEM image of a region adjacent to the interface for a "2223"/Ag thick film heat treated at 825°C for 15 h.

In an earlier study strong evidence was presented for formation of a liquid at $\sim 822^\circ\text{C}$ between Ag and the Pb-doped Bi-2223 system which itself leads to the accelerated formation of the "2223" phase [9]. The enhanced formation of "2223" at the Ag/BSCCO interface at temperatures $\geq 825^\circ\text{C}$ found in this study is consistent with this liquid formation model. The Cu-rich regions found near the interface, in this study, might be from the liquid that has been quenched in to the sample.

CONCLUSION

The "2212" phase in melt-processed thick films on Ag and MgO shows a pronounced increase of c-axis orientation with decrease of distance from the "2212"/substrate interface. The thickness of the textured region is of the order of 50-100 μm . That this effect was observed in the case of MgO substrates argues against there being any unique texturing effect of the Ag/BSCCO interface. In the case of the formation of "2223" on Ag substrates, the Ag/BSCCO interface has a significant and unique effect on phase evolution. It is thought that at a temperature of 825°C

and above a liquid is formed as a result of an interaction between the Ag and some of the components in the BSCCO thick film which promotes the formation of the "2223" phase. This has significant ramifications for processing of "2223"/Ag powder-in-tube materials.

ACKNOWLEDGEMENT

This work was supported by Syndicated R&D investment funds through a partnership with Bankers Trust (Australia) and Comquest Pty. Ltd.

REFERENCES

- [1] *High-field critical current densities in $Bi_2Sr_2Ca_1Cu_2O_{8+x}/Ag$ wires*, K. Heine, J. Tenbrink and M. Thoner, *Appl. Phys. Lett.* 55 (1989) 2441-2443
- [2] *Phase alignment in Ag-clad Bi-Sr-Ca-Cu-O (2:2:1:2) wires*, R.D. Ray II and E.E. Hellstrom, *Appl. Phys. Lett.* 57 (1990) 2948-2950
- [3] *Microstructures and J_c -B characteristics of Ag-sheathed Bi-based superconducting wires*, M. Ueyama, T. Hikata, T. Kato and K. Sato, *Jpn. J. Appl. Phys.* 30 (1991) L1384-L1386
- [4] *Partial Melt Growth of $Bi_2Sr_2CaCu_2O_x$ Textured Tapes on Silver*, J. Kase, K. Togano, H. Kumakura, D.R. Dietderich, N. Irisawa, T. Morimoto and H. Maeda, *Jpn. J. Appl. Phys.* 29 (1990) L1096-L1099
- [5] *Textured thick films of $Bi_2Sr_2CaCu_2O_x$* , D.R. Dietderich, B. Ullmann, H.C. Freyhardt, J. Kase, H. Kumakura, K. Togano and H. Maeda, *Jpn. J. Appl. Phys.* 29 (1990) L1100-1103
- [6] *$BiSrCaCu/Ag$ Superconducting Composite Tapes*, H. Kumakura, K. Togano, D.R. Dietderich, H. Maeda, J. Kase and T. Morimoto, *Supercond. Sci. Technol.* 4 (1991) S157-159
- [7] *Texture formation in $Bi_2Sr_2CaCu_2O_x/Ag$ tapes prepared by partial melt process*, T.D. Aksenova, P.V. Bratukhin, S.V. Shavkin, V.L. Melnikov, E.V. Antipova, N.E. Khlebova and A.K. Shikov, *Physica C* 205 (1993) 271-279
- [8] *Important considerations for processing Bi-based high-temerature superconducting tapes and films for bulk applications*, E.E. Hellstrom, *Mater. Res. Bull.* XVII (1992) 45-51
- [9] *Use of a thermal gradient to study the role of liquid phase during the formation of Bismuth High Temperature Superconductors*, P.E.D. Morgan, J.D. Piche and R.M. Housley, *Physica C* 191 (1992) 179-184

FILM/SUBSTRATE THERMAL BOUNDARY RESISTANCE FOR Er-Ba-Cu-O HIGH-T_C THIN FILMS

P.E. Phelan, Y. Song*, and M. Kelkar

Department of Mechanical Engineering, University of Hawaii at Manoa, 2540 Dole Street, 302 Holmes Hall, Honolulu, Hawaii 96822 U.S.A.

ABSTRACT

The thermal boundary resistance between high-T_C thin films and their substrates is an important property for optimal thermal design of high-T_C devices. However, few measurements of this parameter have been conducted. In the present study, the thermal boundary resistance of two Er-Ba-Cu-O thin films—one deposited on MgO, and the other on SrTiO₃—is measured as a function of the substrate temperature. The results indicate a relatively large value of the resistance for the thicker film deposited on the SrTiO₃ substrate.

INTRODUCTION

The thermal boundary resistance (R_b) between the film and the substrate can strongly impact applications of thin-film high-T_C superconductors (HTS). Any impediment to heat flow from the thin film can lead to temperature excursions that take the film from the superconducting state to the normal state, which in many cases results in device failure. It has been demonstrated that the bolometric response of HTS to incident radiation depends on the magnitude of R_b , with regard to both the response time and the sensitivity [1,2]. This result has also been shown from numerical simulations of the voltage response [3], leading to the conclusion that R_b must be known for optimal thermal design of radiation detectors made from thin-film HTS [4]. The performance of other high-T_C applications, such as light-activated switches, interconnects, flux-flow transistors, etc., also requires knowledge of R_b for their optimal thermal design.

Very few direct measurements of R_b between high-T_C films and their substrates have been carried out. To the authors' knowledge, only two such experiments have been performed. The first measured R_b for a Y-Ba-Cu-O film on a LaAlO₃ substrate, and for several Y-Ba-Cu-O films on sapphire substrates, with intervening buffer layers of SrTiO₃, MgO, LaAlO₃, and/or CaTiO₃ [5]. Their measured R_b varied between 0.7×10^{-3} and $1.3 \times 10^{-3} \text{ K cm}^2 \text{ W}^{-1}$, and showed a weak or nonexistent dependence on temperature over

* Department of Physics and Astronomy, University of Hawaii at Manoa, 2505 Correa Road, Watanabe Hall, Honolulu, Hawaii 96822 U.S.A.

To the extent authorized under the laws of the United States of America, all copyright interests in this publication are the property of The American Ceramic Society. Any duplication, reproduction, or republication of this publication or any part thereof, without the express written consent of The American Ceramic Society or fee paid to the Copyright Clearance Center, is prohibited.

the temperature range 97 K to 177 K. More recently, R_b for a single Er-Ba-Cu-O film on an MgO substrate was determined to lie between 1×10^{-3} and $5 \times 10^{-3} \text{ K cm}^2 \text{ W}^{-1}$, over the substrate temperature range of 86 K to 244 K [6]. Those results showed that R_b tends to increase with increasing temperature.

The present study compares R_b measured for two Er-Ba-Cu-O films, of different thicknesses and T_c 's, and on different substrates. The experiments are restricted to temperatures where the films are in their normal state. The results indicate approximately an order of magnitude difference in R_b for the two films, with the thicker film deposited on the SrTiO₃ substrate having the higher value of R_b .

EXPERIMENT

Samples

Sample 1 is a 70-nm-thick Er-Ba-Cu-O film on an MgO substrate, and has a T_c of approximately 69 K. Sample 2 is a 300-nm-thick Er-Ba-Cu-O film on a SrTiO₃ substrate, and has a T_c of approximately 89 K. The substrate thickness in both cases is 1 mm. The films were deposited by ionized cluster beam codeposition [7]. The films were etched in the pattern shown in Fig. 1 using an etching solution of 1% H₃PO₄, and an etching time of 10 minutes for Sample 1, and 30 minutes for Sample 2.

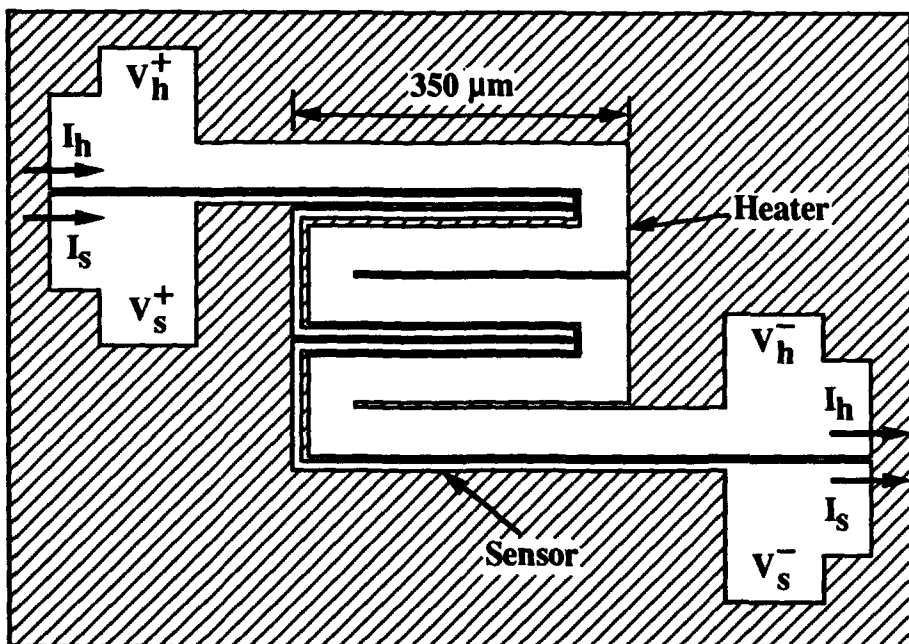


Figure 1 Two-strip etching pattern for measuring the thermal boundary resistance between the heater strip and the substrate. The width of the heater strip is 50 μm , that of the sensor strip is 10 μm , and the distance separating the strips is 5 μm .

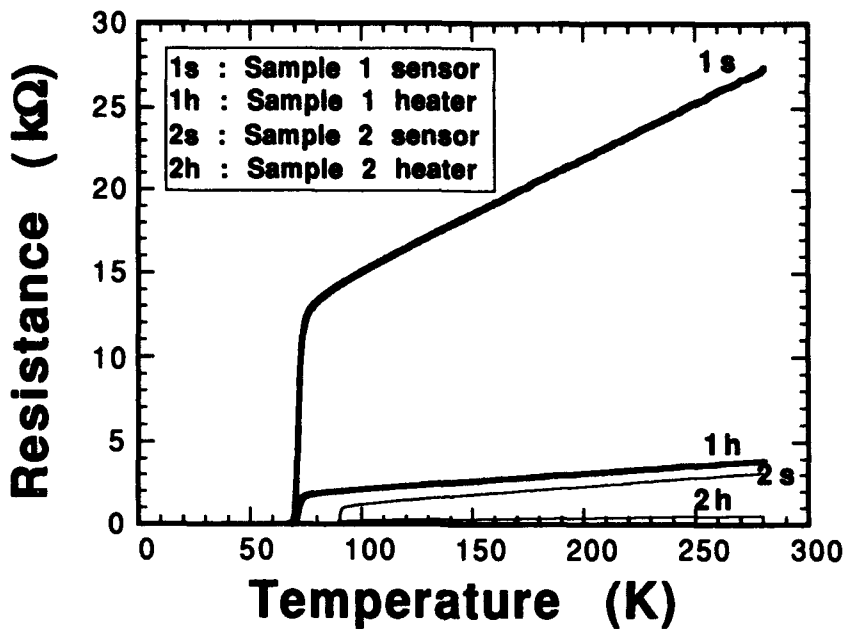


Figure 2 Electrical resistance calibration curves, taken under isothermal conditions.

Procedure

The experimental procedure is based on that described in [8], and has been fully described in [6]. In brief, a large bias current I_h is passed through the strip labeled 'heater' in Fig. 1, while a much smaller sensing current I_s is passed through the 'sensor'. Both strips are maintained in the normal state. The Joule heating generated in the heater results in a temperature difference between it and the substrate immediately below. On the other hand, since I_s is very small, the sensor temperature is nearly the same as that of the substrate. Therefore, using curves fitted to the electrical resistance calibration data in Fig. 2 enables us to determine the temperature drop between the heater and the substrate from the measured electrical resistances of the strips. The strips' electrical resistances are measured using the four-point method. After reaching steady-state, R_b is calculated from $R_b = \Delta T/q$, where q is the heat flux from the heater into the substrate, and $\Delta T = T_h - T_s$, where T_h is the heater temperature, and T_s is the sensor temperature.

The experiment was conducted for values of the heater current ranging from 8 to 20 mA dc. The sensor current source was a lock-in amplifier set at 47 Hz, and the current magnitude was typically about 5 μ A ac. The temperature during the electrical resistance calibration was measured with a diode sensor mounted on the Cu cold finger on which the sample was mounted. The experiments were carried out in a closed-cycle refrigeration system, and the data were recorded with a computer-controlled data acquisition system.

Uncertainty

The primary source of experimental uncertainty is the determination of T_h and T_s from the measured strips' electrical resistances. Due to slight scatter in the calibration data in Fig. 2, polynomial and linear curves are fitted to the data, and T_h and T_s are obtained from these curves. The uncertainty in ΔT , $\delta(\Delta T)$, is estimated from the standard deviation of the difference between the fitted curves and the calibration data points, yielding $0.27 \leq \delta(\Delta T) \leq 0.41$ K for Sample 1, and $0.06 \leq \delta(\Delta T) \leq 0.17$ K for Sample 2. Another potential source of error is the heat leak from the sample out through the electrical leads, but this is judged to be small. Finally, since the heater and sensor strips are separated by 5 μ m, there can be a small temperature drop in the substrate between the strips, so that T_s is not equal to the substrate temperature immediately beneath the heater strip. This error is also determined to be small, except for the very highest heat fluxes encountered in the data of Sample 1. The representative error bars drawn in the figures do not include this source of error.

RESULTS AND DISCUSSION

Figure 3 presents the measured temperature drop, $\Delta T = T_h - T_s$, as a function of the heat flux, q , for both samples. Although ΔT increases with q for both samples, which is to be expected, the rate of increase is very different between the samples. In general, the data of Sample 1 are more scattered than those of Sample 2. This scatter is also indicated in

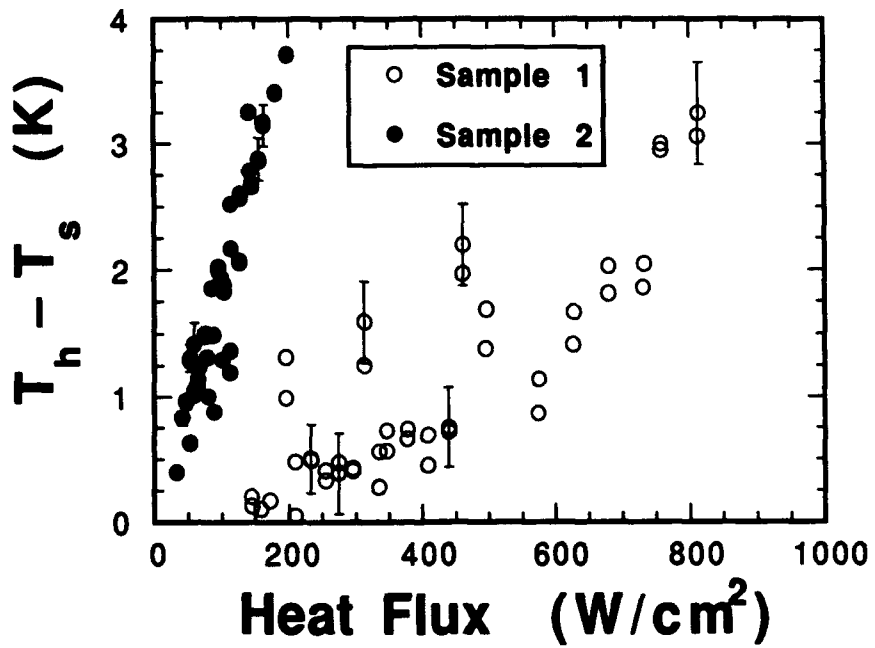


Figure 3 Temperature drop vs. heat flux. The error bars are calculated by considering the uncertainty in determining the temperature from the measured electrical resistances.

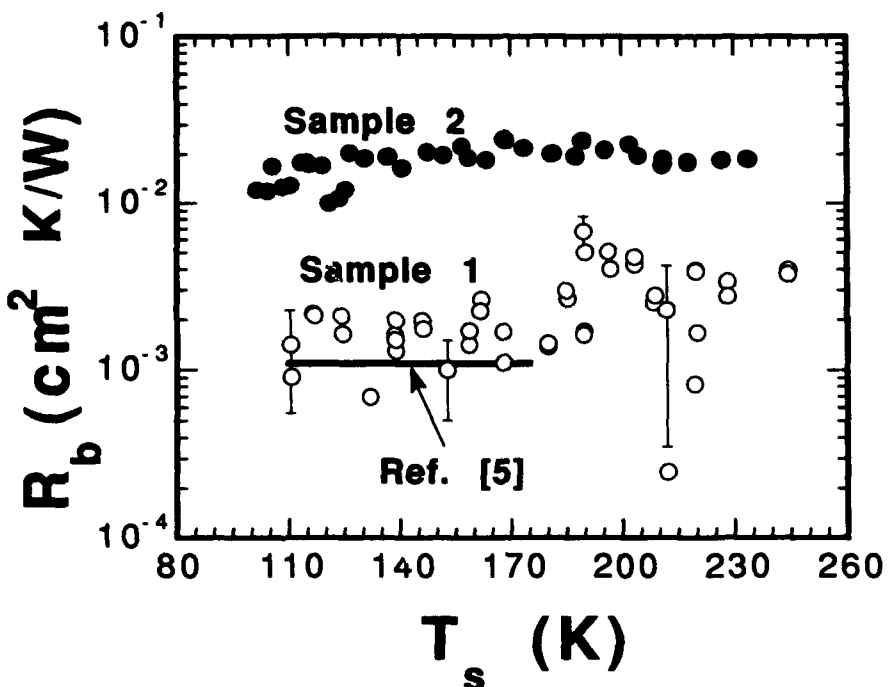


Figure 4 Thermal boundary resistance vs. substrate temperature. The error bars, which are too small to be visible for Sample 2, are calculated by considering the uncertainty in determining the temperature from the measured electrical resistances.

Fig. 4, which shows R_b as a function of T_s . Also included on this plot is one set of data from [5], which is for a $\text{YBa}_2\text{Cu}_3\text{O}_{7-\delta}$ film on a LaAlO_3 substrate. Clearly, R_b for Sample 2 is approximately one order of magnitude higher than R_b for Sample 1. The data for Sample 2 are almost flat with respect to T_s , while those for Sample 1 show a slight increase with increasing T_s . However, the greater uncertainty of the Sample 1 data makes this trend questionable.

It is conceivable that the higher R_b for Sample 2, as compared to that for Sample 1, could result from the greater film thickness, which is 300 nm for Sample 2, as opposed to 70 nm for Sample 1. The thermal resistance across the film can be estimated by d/k , where d is the film thickness and k is the thermal conductivity in the transverse direction (normal to the film/substrate interface). Assuming k of each film is about $2 \text{ W m}^{-1}\text{K}^{-1}$, the difference in film thickness cannot account for the order-of-magnitude difference in R_b . However, k for each film may be different, since the microstructure of thin films can be affected by the film thickness and choice of substrate. If so, this change in k should also be reflected in the films' electrical resistivities, which are plotted in Fig. 5. These resistivities are for transport in the ab plane, rather than in the c direction, but it is anticipated that the transport properties in one direction should correlate with those of the

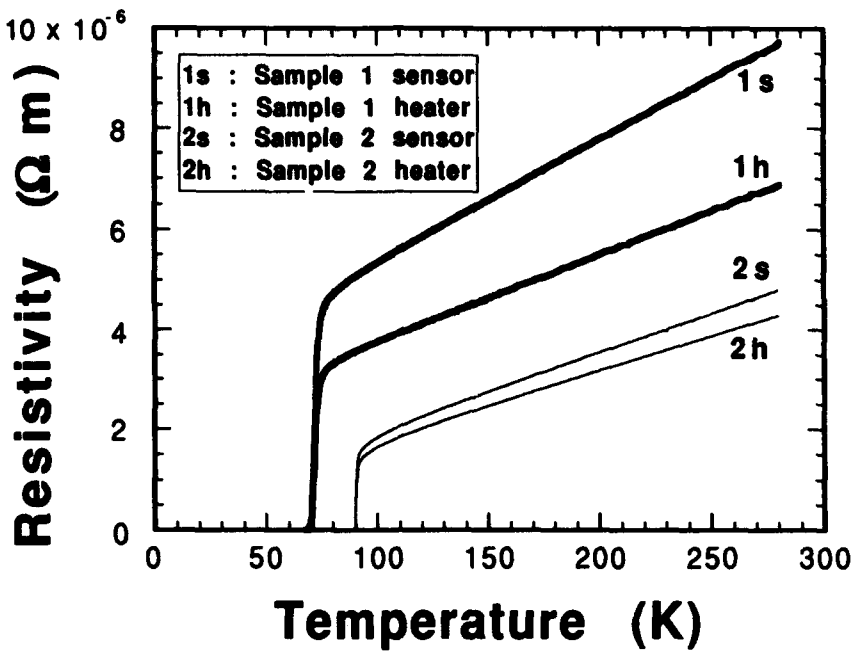


Figure 5 Electrical resistivity-vs. temperature, determined from the electrical resistance calibration curves.

other. It is apparent from Fig. 5 that the resistivity of Sample 1, the thinner sample, is considerably higher than that of Sample 2. Since the T_c of this film is also relatively low (69 K), this sample either has a greater oxygen deficiency, or contains more microstructural damage. Thus, k of Sample 2 should not be much different than k of Sample 1, and therefore the difference in R_b in Fig. 4 is most probably *not* due to the different film thermal resistances.

An interesting feature of Fig. 5 is that the electrical resistivities of the heater and sensor strips for Sample 1 diverge from each other with increasing temperature, while those for Sample 2 also diverge, but in general are much closer to each other. Since the strips in a given sample are made from the same film, the differences must be due to the etching process. The wider heater strips (50 μm in width) of each sample most likely provide a better indication of the actual film resistivity. The narrower sensor strips (10 μm in width) are more prone to damage induced by the etching process, and to the possibility that a grain boundary lies across the entire strip width. There may, therefore, be inhomogeneities along the sensor strips such that their electrical resistances, and the corresponding sensor temperatures, are not truly quantities that are averaged across the sample area, but rather reflect more local properties.

It is also noteworthy that the film having the higher T_c , Sample 2, exhibits the larger R_b . The oxygen deficiency and microstructure of Sample 1 may play a role in reducing R_b .

However, until more samples are measured, no conclusions concerning these effects on R_b can be made.

The predicted R_b from acoustic mismatch theory (AMT) [9] is about $10^{-5} \text{ cm}^2 \text{ K} \text{ W}^{-1}$ at 100 K, and decreases with increasing temperature. This large difference between the present data and AMT is consistent with previous measurements on other film/substrate systems, for temperatures higher than about 60 K [8]. Apparently, for the temperatures examined in this study, the phonon wavelengths are comparable to the lattice constants, so that the continuum assumption of AMT is invalid. At present, there is no existing theory which can predict R_b at such film/substrate interfaces at the moderate cryogenic temperatures applicable for HTS.

CONCLUSIONS

The film/substrate thermal boundary resistance R_b for two Er-Ba-Cu-O high- T_c thin films is measured as a function of the substrate temperature. All the measurements are carried out on normal-state films. The substrates and the film thicknesses differ between the two samples. The results indicate that R_b is in excess of $10^{-3} \text{ cm}^2 \text{ K} \text{ W}^{-1}$, and generally is constant or increases slightly with increasing temperature. The magnitude of R_b differs by approximately an order of magnitude between the two samples, with the film of greater thickness, higher T_c , and on a SrTiO_3 substrate exhibiting the largest value of R_b .

ACKNOWLEDGMENTS

This material is based upon work supported by the National Science Foundation under Grant No. CTS93-07753. The authors also owe their gratitude to H. Ito and colleagues at Mitsubishi Electric Co., along with Professor K. Hijikata of the Tokyo Institute of Technology, who furnished the high- T_c samples; Dr. Y. Kozono and colleagues at Hitachi Co., who patterned the samples; and Professor J.R. Gaines of the University of Hawaii at Manoa, who allowed us the use of his cryogenic laboratory facilities.

REFERENCES

- [1] Carr, G.L., Quijada, M., Tanner, D.B., Hirschmugl, C.J., Williams, G.P., Etemad, S., Dutta, B., DeRosa, F., Inam, A., Venkatesan, T., and Xi, X., "Fast bolometric response of high- T_c detectors measured with subnanosecond synchrotron radiation," *Appl. Phys. Lett.* **57**, no. 25, pp. 2725 - 2727 (1990).
- [2] Levey, C.G., Etemad, S., and Inam, A., "Optically detected transient thermal response of high- T_c epitaxial films," *Appl. Phys. Lett.* **60**, no. 1, pp. 126 - 128 (1992).
- [3] Chen, R.-C., Wu, J.-P., and Chu, H.-S., "Bolometric response of high- T_c superconducting detectors to optical pulses and continuous waves," ASME Paper No. 93-HT-7, *ASME National Heat Transfer Conf.*, Atlanta, Georgia, Aug. 8 - 11 (1993).
- [4] Zhang, Z.M., Frenkel, A., "Thermal and nonequilibrium responses of superconductors for radiation detectors," *ASME Winter Annual Meeting*, New Orleans, Louisiana, Nov. 28 - Dec. 3 (1993).
- [5] Nahum, M., Verghese, S., Richards, P.L., and Char, K., "Thermal boundary

resistance for $\text{YBa}_2\text{Cu}_3\text{O}_{7-\delta}$ films," *Appl. Phys. Lett.* **59**, no. 16, pp. 2034 - 2036 (1991).

- [6] Phelan, P.E., Song, Y., Nakabeppu, O., Ito, K., Hijikata, K., Ohmori, T., and Torikoshi, K., "Film/substrate thermal boundary resistance for an Er-Ba-Cu-O high- T_c superconducting film," submitted to *Journal of Heat Transfer* (1993).
- [7] Yamanishi, K., Yasunaga, S., Kawagoe, Y., Sato, K., and Imada, K., "Synthesis of superconducting Y-Ba-Cu-O thin films by ionized cluster beam codeposition," *Nuclear Instruments and Methods in Physics Research* **B37/38**, pp. 930 - 934 (1989).
- [8] Swartz, E.T., and Pohl, R.O., "Thermal boundary resistance," *Reviews of Modern Physics* **61**, pp. 605 - 668 (1989).
- [9] Little, W.A., "The transport of heat between dissimilar solids at low temperatures," *Can. J. Phys.* **37**, pp. 334 - 349 (1959).

EFFECT OF IMPREGNATION OF ZrO_2 ON THE CHEMICAL STABILITY AND THE SUPERCONDUCTIVITY OF Y- AND Bi-SYSTEMS

Masaaki MUROYA and Hideaki MINAMIYAMA

Osaka Electro-Communication University, 18-8, Hatsu-cho, Neyagawa, Osaka 572, Japan

The results are given concerning the influence of impregnation of Zr on chemical stability and superconductivity of $YBa_2(Cu_{1-x} \cdot Zr_x)_3O_{7-y}$ (123-system) and $Bi_{1.84}Zr_xPb_{0.34}Sr_{1.91}Ca_{2.03}Cu_{3.06}O_y$ (2223-system) superconductors, when the samples are contacted with the solutions of acid(pH3), distilled water(pH5.6) and base(pH9), where $x=0-0.35$.

It is concluded that the low chemical stability was found in the case of YBZCO, barium hydroxide and/or barium carbonate were precipitated into the solutions, even though mechanical strength was increased by impregnation of Zr, and the chemical stability of Bi-system is high compared with that of the Y-system.

1. Introduction

It is well known that Y-Ba-Cu-O(YBCO) and Bi-Pb-Sr-Ca-Cu-O(BPSCCO) system compounds are those of high-T_c superconducting materials. Numerous investigators have demonstrated the studies of preparation and the superconductive characterization of these materials. When these materials applied to various cases, such as wires coils, sensors, electronic devices and others, careful utilization of these materials is required to establish the laws of chemical stability.

It has been indicated by several workers that no chemical stability of Y- and Bi-system superconductors, when which were exposed to water, were reported[1-3]. Those works indicated that the Y-system compounds are sensitive to water and decompose in water to CuO , $Ba(OH)_2$ and Y_2BaCuO_5 , and then superconducting ability of the sample is down as a result of decomposition in superconducting phase. In the case of Bi-system, superconducting

To the extent authorized under the laws of the United States of America, all copyright interests in this publication are the property of The American Ceramic Society. Any duplication, reproduction, or republication of this publication or any part thereof, without the express written consent of The American Ceramic Society or fee paid to the Copyright Clearance Center, is prohibited.

grains were indeed stable, but nonsuperconducting grains were notably degraded polycrystalline which was caused by the dissolution of Sr and Ca from nonsuperconducting grains[4,5]. The mechanical strength of Y- and Bi-system superconducting materials was found to be reinforced by adding the ZrO_2 to those materials[6,7]. This result is in accord with expectations based on the chemical stability of the materials.

In this report, the chemical stability of the Y- and Bi-system compound prepared by our laboratory and the effect of impregnation of ZrO_2 on the chemical stability of these materials were detected by means of chemical approach, XRD, XPS and FT-IR techniques, and the activation energies of degradation in which these materials were obtained from the chemical process of solubility into water and solutions(acid and base).

2. Experimental

Preparation of the YBCO and BPSCCO compounds and doping ZrO_2 to these compounds were as follow. 1)Commercial special grade powders of Y_2O_3 , $BaCO_3$, CuO and ZrO_2 were weighed in mol ratio, $Y:Ba:(Cu_{1-x} \cdot Zr_x)=1:2:3$ ($x=0$, 0.02, 0.05, 0.08), and then mixed for 1h. These mixed powders were pre-heated at the temperature of $950^\circ C$ for 15h in air and compressed by $3200kg/cm^2$ for 20min after slowly cooled down under flowing 1 l/min in O_2 , respectively. Discoidal specimens, with 20mm diameter and about 3mm thickness, thus obtained from its procedure. These specimens were used for further heat-treated at $950^\circ C$ for 24h in air and then these specimens were cooled down under the condition of 1 l/min flow in O_2 , respectively. The specimens prepared by this procedure are so called as the YBCO($x=0$) and as YBZCCO($x=0.02-0.08$). 2)Commercial powders of Bi_2O_3 , PbO , $SrCO_3$, $CaCO_3$, CuO and ZrO_2 were weigh in mol ratio, $Bi:Zr_x:Pb:Sr:Ca:Cu=1.84:x:0.34:1.91:2.03:3.06$ ($x=0-0.35$), and then mixed for 1h. These mixed powders were pre-heat-treated at $800^\circ C$ for 12h in air and compressed by $3200kg/cm^2$ for 20min after slowly cooled down, and further crush and mixing of these treated specimens were carried out. Once again these powders were compressed by the pressure mentioned above. The discoidal specimens(20mm diameter and about 3mm thickness) were used for further heat-treated at $850^\circ C$ for 50h in air and then cooled down in air. These substances are so called as BPSCCO($x=0$) and as BPSZCCO($x=0.15-0.35$).

The discoidal specimens of Y- and Bi-systems were immersed to acid, neutral and base solutions, which were prepared with hydrochloric acid(pH3), distilled water(pH5.6) and sodium hydroxide(pH9), respectively. The temperature of the solution was kept at 25° , 35° and $45 \pm 1^\circ C$, through the all immersion experiments. The pH of the solutions was measured continuously for 200min after the sample was immersed to its solution, and

data was recorded with a pH meter.

Experimental procedures of X-ray diffraction(XRD), electrical resistance, X-ray photoelectron spectroscopy(XPS) and infrared spectroscopy(FT-IR) were same as reported described elsewhere[8]. Mechanical hardness of the sample was measured by using a shore type hardness tester.

3. Results and Discussion

3.1. Y-System.

A typical splitting X-ray diffraction lines due to the orthorhombic $\text{Ba}_2\text{YCu}_3\text{O}_{7-y}$ crystal phase were observed on the YBCO and also on the YBZCO($x=0.02-0.08$). It usually appears that the crystal growth of orthorhombic phase has not undergone inhibition by the ZrO_2 doping to the YBCO system compound. However, the superconducting properties of YBZCO specimens are not clear from only diffraction pattern.

The relationship between $T_{\text{c-end}}$ point temperature and Zr content for the YBCO and the YBZCO specimens were shown in the curve A of Fig.1. The critical endpoint temperature($T_{\text{c-end}}$) for the YBCO($x=0$) is detected at 91°K. When the YBCO is contained the ZrO_2 , the $T_{\text{c-end}}$ is shifted to lower side at 88-85K. It is thought that this effect results from the $\text{Cu}_{1-x}/\text{Zr}_x$ ratio was decreased with containing ZrO_2 and the formations of 211-phase(Y_2BaCuO_5) and BaZrO_3 in the 123-phase matrix.

The shore hardness of the specimens(YBCO and YBZCO) were measured, and the results were shown to be the relation of Zr content in the curve A of Fig.2. The addition of ZrO_2 results in an increase in hardness depending doped concentration. This is because they occasionally cause the packing

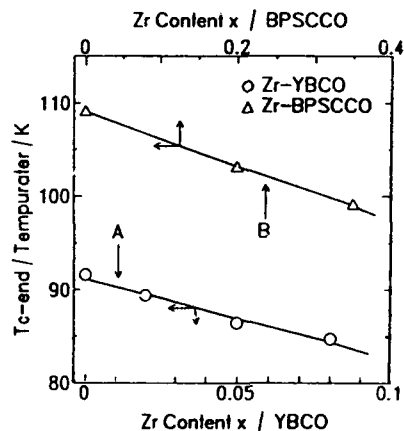


Fig. 1. Plot of the $T_{\text{c-end}}$ point temperature against Zr content.

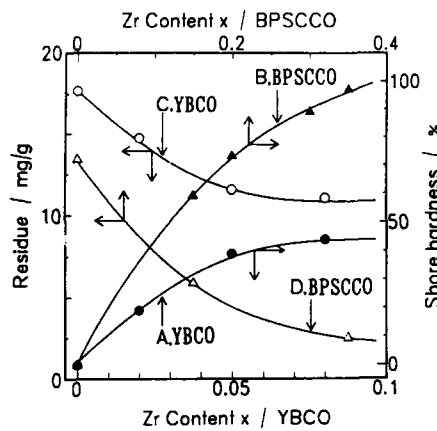


Fig. 2. Plot of the shore hardness and the residue against Zr content.

density of compressed sample becomes high by containing ZrO_2 since $BaZrO_3$ filled in porous regions present in 123-phase matrix[6,7]. Such effect can be expected to hold for chemical stability of the Zr -containing superconductor prepared in this work.

Fig.3 shows the variation of H^+ concentrations in the solutions (initial pH3, 5.6 and 9) which contain the YBCO sample as a function of elapse of the time. When the initial pH is 3, proton concentration of its solution decreases progressively from pH3 to about 4 with the passage of time until about 30min, the drastically decrease of proton concentration is indicated in time range from about 30 to 50min, and then the pH of its solution becomes almost constant at about 11 after converted to alkaline side. The decrease of proton concentration in the solution was also found on the cases of pH 5.6 and 9. Analogous pH curve was observed on the Zr -containing sample(YBCO), but the time of elevation in the pH was delay. Since the reaction is hindered by the added substance it is said to be a depressive material which is ZrO_2 . After the acidic solution converted to alkaline state, the precipitated product was produced in the solution for the both samples(YBCO and YBZCO). In the cases of any given pH value, the products of about 18-12 mg per unit sample weight, g, were determined to be the residue which was obtained by the heating at $170^\circ C$ 2h of the product. The quantity of product resulted from the YBZCO is less than that of comparative with the case of Zr -free sample. It is indicated that the YBCO and YBZCO specimens have been once accepted the chemical attack in those solutions. The magnitude of residue obtained from the precipitated product in pH3 solution against Zr -content was shown in curve C of Fig.2. When the

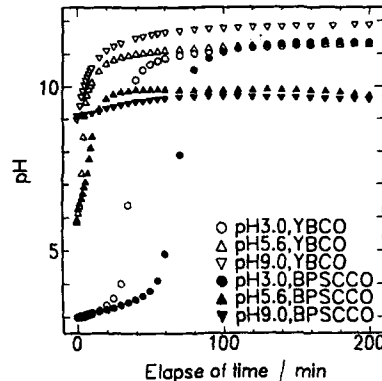


Fig.3. Time dependence of pH in the solutions contained the specimens such as YBCO and BPSCCO.

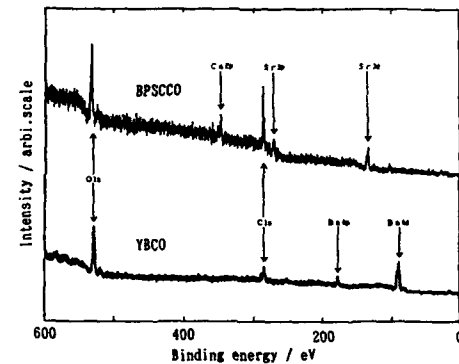


Fig.4. XPS spectra of the residues obtained from precipitated product.

Zr-free sample was contact with the solution, the magnitude of the residue is about 17.5mg/g. But the residue decreases with increasing Zr-content in the case of Zr-containing samples. It is suggested that the chemical stability of the specimen contained Zr is high compared with that of Zr-free specimen and doping of ZrO_2 to YBCO contribute to prevent drastically degradation of the superconductor.

In order to known the composition of product precipitated in the solution, XPS, XRD and FT-IR analysis of the residue were carried out. Fig.4 shows the XPS spectra for the residue produced from the YBCO specimens. Core signals of $Ba_{3d}(3/2, 5/2)$, Ba_{MNN} , Auger and O_{1s} were observed, it is indicated that products in the solution are barium hydroxide or barium carbonate. Same signals were also observed on the other pH and the Zr-containing specimens.

The techniques of FT-IR and XRD have been used to examine the composition of the product, and FT-IR spectra were shown in Fig.5. Clear absorption bands at 1462 and 857cm^{-1} were found on the YBCO specimen, and these absorption band are assigned to CO_3^{2-} in inorganic carbonate. These absorption bands were also observed on $YBZCO$ ($x=0.02-0.08$) specimens, and those wave numbers are in agreement with that of $BaCO_3$ powder. On the other hand, the XRD patterns of the product produced from the YBCO and the $YBZCO$ specimens are in agreement with that of $BaCO_3$. No existence of Cu-, Zr- and Y-compositions in products was revealed by the detailed XPS, FT-IR and XRD experiments. These results are indicated that the chemical species eluted from the specimens(YBCO and $YBZCO$) in the solution is mainly barium, which formed hydroxide or carbonate in the solution.

In the solutions, perhaps the reactions of ion exchange between proton and barium and then production of $Ba(OH)_2$ occurred to be resulting from a proton attack to barium site of YBCO and/or $YBZCO$. The reaction process may be expressed chemically as hereunder.

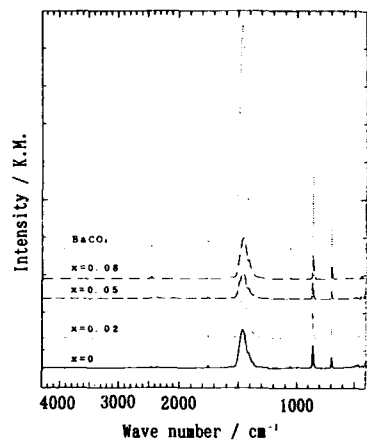
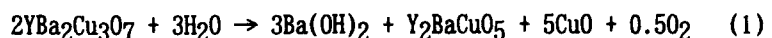


Fig.5. FT-IR spectra of the residues obtained from precipitated product.

Since the pH elevation reflects the elution of barium, the activation energy of this reaction can be determined by the experiments of temperature dependence in the chemical treatment. The activation energy, E , can be determined by Arrhenius's plot which is corresponded to the plot of $\log k$ versus $1/T$, where T is absolute temperature, and k is rate constant derived from reaction rate.

Fig.6 shows the Arrhenius's plot for the YBCO specimen. The slopes yield the E of 102(pH 3), 61(pH 5.6) and 16(pH 9) kJ/mol, and these activation energies, which depend on pH of the solutions, reported to data for the $\text{Ba}(\text{OH})_2$ production reaction. The plot of E against pH bear a linear relationship to each other, as shows in Fig.6. The activation energy in the case of initial acidic side is large than that of alkaline side. It is considered that the production reaction of $\text{Ba}(\text{OH})_2$ occurred most readily at alkaline side because of the concentration of OH^- ion is high in its solution.

The activation energy for the YBCO specimen was slightly large than that of the Zr-free specimen(YBCO). It is suggested that the influence of Zr-containing upon the chemical stability of Y-system is high. Moreover, the degradation process of Y-system compound in the solution is inhibited by the impregnation on ZrO_2 to its compound as find in Fig.2.

3.2. Bi-System

XRD and the temperature dependence of electrical resistance in the BPSCCO and the BPSZCCO specimens were measured, respectively. The diffraction pattern of BPSCCO specimen was indicated that the diffraction lines assigned to high-Tc(109K) phase of tetragonal crystal. When the sample(BPSCCO) is contained zirconium, Tc-end point at 109K was down to lower temperature side at 99K(BPSZCCO, $x=0.35$).

The hardnesses of the BPSCCO and the BPSZCCO specimens are shown in curve B of Fig.2. The hardness of the Zr contained specimen depend on the Zr concentration and was increased with increasing the amount of ZrO_2 , and Tc endpoint temperature was decreased as shown in curve B of Fig.1. When the BPSCCO is contained Zr and its compressed sample was heated in this experimental conditions, $M(\text{Sr},\text{Ca})\text{ZrO}_3$ is formed, and its $M\text{ZrO}_3$ filled in

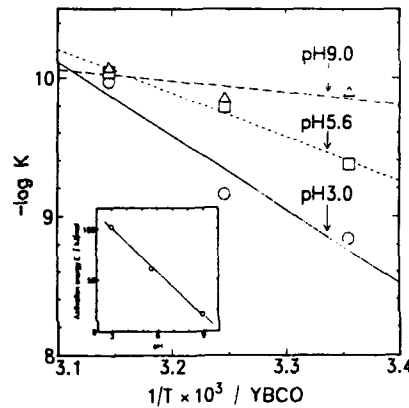


Fig.6. Arrhenius's plot of YBCO and pH dependency of activation energy.

porous regions present in 2223-phase matrix. Therefore, the decrease of molar ratio in Sr and Ca lead to down Tc-end point temperature, and the enhancement of mechanically hardness is derived from the decrease in porosity as resulting from $\text{M}\text{Zr}\text{O}_3$ was precipitated in pore.

pH of the solutions such as initial pH 3, 5.6 and 9 immersed BPSCCO specimen were detected for elapse of the time, and the results were shown in Fig.3. The drastic change of initial pH 3 to alkaline side was occurred, that is, pH rise rapidly from about 60 min after specimen immersed in the solution, and then pH of its solution becomes to approximately constant at 11.5. When the temperature of this solution is elevated to 35° and 45°C, starting point of elevation in pH was shifted to short time side. It is indicated that chemical process depend on the temperature. The change of the initial pH to alkaline side was also observed on the solution of pH 5.6. In both initial pH, the product was precipitated in the solution. On the other hand, pH of the solution in initial pH 9 is slightly increased with elapse of the time, but no large change of pH is observed. Furthermore, product was almost not precipitated in the solution of this pH. It is suggested that the chemical stability of the Bi-system superconductor is high compared with that of the Y-system.

In order to known the chemical composition of the product, XPS of the residue was measured, and its spectra were shown in Fig.4. The signals of $\text{Sr}(3\text{p},3\text{d})$, $\text{Ca}2\text{p}3/2$ and $0_{1\text{s}}$ were determined on the residue. Those results suggested that the products were precipitated in the solutions as resulting from proton attacked to Sr and Ca sites of BPSCCO specimen. The chemical composition of the product is presumably considered with hydroxide and/or carbonate of Sr and Ca.

When the BPSCCO specimen contain as other component a small amount of ZrO_2 , the amount of product in the solution was decreased compared with Zr-free sample, as shown in curve D of Fig.2. This means that the decrease of elution of Sr and Ca is derived from the sureface of the 2223-phase particles was coated with $\text{M}\text{Zr}\text{O}_3$ composition which is only slightly soluble in strong acid but insoluble in water. Therefore, the chemical stability of Zr contained BPSCCO is high compared with that of Zr-free.

It is considered that the chemical process of elution of Sr and Ca is that analogous mechanism in the case of Y-system, since Sr and Ca were same group as that of Ba. But the activation process of the reaction is second order, and such a treatment is actually valid only in acidic solution.

4. Conclusion

Superconductors of Y- and Bi-system were prepared by method of solid state reaction, and the chemical stability of those specimens was examined.

Critical temperature at 91 and 109K were detected on the Y- and Bi-system specimens, respectively. When these specimens were contained as other components a small amount of ZrO_2 , mechanical hardness of these specimens were enhanced, and T_c of these specimen were shifted to lower temperature side with few Kelvin degree. These were because they occasionally cause the molar ratio slightly changed with containing Zr and $M(Ba, Sr, Ca)ZrO_3$ filled in porous regions present in matrix.

The YBCO and BPSCCO specimens were too chemically unstable for distilled water and the solutions(acid and base). The chemical stability of the BPSCCO specimen was high compared with that of the YBCO. When the Y- and Bi-system specimens were contained as other components a small amount of ZrO_2 , the chemical stability of these specimens was enhanced as a results of the formation of $M(Ba, Sr, Ca)ZrO_3$ and the decrease of porosity, that is, the dense samples were produced.

The authors would like to thank Messrs. Kazuhiko Yaguchi, Harunobu Nakagawa, Takashi Ichikawa and Hideki Takei at Osaka Electro-Communication University, for his many comments and experimental help during the course of this work.

References

- 1)M.F.Yan,R.L.Barns,H.M.O'Bryan,Jr.,P.K.Gallagher,R.C.Sherwood,S.Jin,Water interaction with the superconducting $YBa_2Cu_3O_7$, *Appl.Phys.Lett.*, 51,532(1987).
- 2)R.L.Barns,R.A.Laudise, Stability of superconducting $YBa_2Cu_3O_7$ in the presence of water, *Appl.Phys.Lett.*, 51,1373(1987).
- 3)K.Kitazawa,K.Kishio,T.Hasegawa,O.Nakamura,J.shimoyama,N.Sugi,A.Ohtomo, S.Yaegashi, K.Fueki, Resistivity Anomaly Near Room Temperature of Y-Ba-Cu-O and Related Oxide as Created by the Surface Effect of Water, *Jpn.J.Appl.Phys.*, 26,L1979(1987).
- 4)K.Yoshikawa,M.Yoshida,M.Nakano, Degradation in Bi-Sr-Ca-Cu-O Thin Films Exposed to Water, *Jpn.J.Appl.Phys.*, 27,L2324 (1988).
- 5)W.Gao,J.Chen,C.Ow Yang,D.McNabb,J.Vander Sande, The stability of High- T_c BPSCCO/Ag superconducting microcomposites in water, some iorganic solutions and organic solvents, *Phys.C193*, 455(1992).
- 6)T.Oka,F.Ogasawara,Y.Itoh,M.Suganuma,U.Mizutani, Mechanical and Superconducting Properties of Ag/YBCO Composite Superconductors Reinforced by the Addition of Zr, *Jpn.J.Appl.Phys.*, 29,1924(1990).
- 7)S.W.Filipczuk, On the degradation of $YBa_2Cu_3O_{7-y}$ by ZrO_2 , *Phys.C*, 173, 1(1991).
- 8)M.Muroya,EFFECT OF OXYGEN CONTENT ON XPS SPECTRA OF $Ba_2YCu_3O_{7-y}$ Proceedings of Inter.Superconducting Electronic Conf.(ISEC'89),1989,p.139.

Processing and Characterization

COFIRE TECHNOLOGY: QUANTIFYING GLASS INFILTRATION IN THE CERAMIC-METAL INTERFACIAL REGION

K. S. Venkataraman, L. D. Martin, and D. A. Weirauch, Jr.
Chemical Systems Division
Electronic Packaging Center
Alcoa Technical Center
Alcoa Center, PA 15069

Abstract: Glass is a critical component in cofiring multilayer ceramic (MLC) packages for 1) improving the sintering/shrinkage compatibility of the ceramic and the circuit metal paste, 2) providing adhesion between the metal and the ceramic, 3) obtaining tighter dimensional control, and 4) providing hermeticity to the fired part. Quantifying the composition of the metal circuit lines in terms of glass, metal, and porosity as sintering progresses is a necessary prelude for understanding glass infiltration in the glass-ceramic interfacial region, and its influence on the macroscopic response—warpage of the part, for example—during sintering. This paper describes an image-analysis-based technique for quantifying the composition of the metal circuit lines in terms of glass, metal, and porosity in SEM pictures. Using the grey level differences among the three principal phases in the micrographs, the composition of the metal circuitry near, and away from, the ceramic-metal (C-M) interfacial region was quantified and compared in several partially and fully sintered samples. This technique, being repeatable and reproducible, offers opportunities for obtaining a greater insight into microstructure evolution during sintering and its relation to dimensional control of complex parts.

1. Introduction: The bulk of the multilayer ceramic (MLC) housings for silicon integrated circuits are made by sandwiching several layers of ~250- μm green ceramic tapes on which are screen-printed individualized ~20- μm electrical circuitry using metal powder-based thick-film inks. Upon sintering, both the ceramic and the metal powders in the multilayer package sinter and densify simultaneously. Hence the term “cofire technology.” Multilayer cofire technology employs a wide variety of inorganic and organic materials, some of which are transients necessary for building the parts, while others are functionally important in the final package. Examples of the transient materials: a) volatile solvents in the tape-making slurry and thick-film inks, and b) polymeric binders in the tape and the dried inks. Functionally important materials in the alumina-based packages are powders of alumina and glass or

To the extent authorized under the laws of the United States of America, all copyright interests in this publication are the property of The American Ceramic Society. Any duplication, reproduction, or republication of this publication or any part thereof, without the express written consent of The American Ceramic Society or fee paid to the Copyright Clearance Center, is prohibited.

glass-forming components, and tungsten and/or molybdenum powders providing the electrical circuitry.

The focus of this paper is on quantifying the different stages in the microstructural evolution of the alumina-tungsten system during sintering. Careful manipulation and control of the material system and its processing are essential for producing parts having tight dimensional control and having unique combinations of mechanical, electrical, and thermal properties. This combination makes ceramics the materials of choice in the majority of MLC applications (Tummala 1988).

During sintering, if the ceramic components and the refractory metal powders densify and shrink over temperature ranges and at rates that are widely different from each other, the fired multilayer parts are likely to develop camber (warpage), interlayer separations, or cracking within a layer. These defects, if severe enough, make the MLC parts unusable. The components of the material system in the MLC technology have different crystal structures and melting points. Some are metal while others are nonmetals. Consequently, they have widely differing atomic mobilities and diffusivities. Because of these differences, the functional components (metals and the ceramic) shrink/sinter over different temperature ranges, and at different rates. However, this incompatibility is typically compensated by kinetic effects such that it is still possible to make acceptable parts. For example, changing the particle size distributions (PSDs) of the inorganic components, or the glass contents in tapes and thick-film inks change the sintering/shrinkage kinetics. Such changes in the kinetic effects are often used to render the multicomponent material system more compatible during firing. These phenomena are well recognized in the literature [Chance (1970), Piper (1983), Hodgkins (1983), Majumdar et al. (1986), Bordia and Raj (1985), Pepin et al. (1989)].

Glass, an ubiquitous additive in thick-film inks and the tape, provides bonding and adhesion between the metal and the fired substrate [Cote and Bouchard (1988)], and prevents cracks and separations during sintering [(Pepin (1989), Vest (1990), Tummala (1988))]. Because of the importance of glass in the MLC technology, there is a need for a better understanding of the role of glass in 1) reducing the propensity for separations and camber, and 2) modifying the electrical properties of the circuitry (Gattuso, 1990). Despite this need, it appears that characterizing the ceramic-metal interfacial region as sintering progresses is not reported in the public literature, probably because of the time and efforts required, the uncertainty in obtaining definitive data, and the corporate reluctance to publish this information, even when available.

Towards filling this need, we developed and evaluated an image-analysis based technique discussed here for characterizing and quantifying the microstructure evolution in the metal circuitry during sintering. This tech-

nique should lead to a better understanding of the relationship of microstructural evolution to 1) tungsten PSDs, pore size distribution in the metal lines and extent of glass infiltration, and 2) how it relates to macroscopic responses (camber and electrical resistance) of the MLC parts.

2. Materials: Experimental tungsten-based thick-film inks (Binder: an ethyl cellulose) were prepared from metal powders with various PSDs and a range of glass contents. The particle size characteristics of the tungsten powders used in the inks are in Table 1. These powders were mixed in the proportions shown in Table 2 and made into 3 experimental circuit inks under otherwise standardized conditions. Additional inks were prepared in which 15 v/o of a proprietary glass powder (a Ca-Mg-Al-Mo silicate) having a median particle size of 1.5 μm was added in the ink formulation. The test pattern was a 3-layer laminate fabricated out of 250- μm thick proprietary alumina-glass green tape. The experimental circuit inks were screen-printed to ~25- μm thickness on the top layer of the 3-layer sandwich. These test parts were fired in a reducing H-N-O atmosphere up to 1350°C, 1450°C, 1550°C, and 1650°C with a 1-minute hold at the peak temperature. In addition, parts were soaked at 1650°C for 1 hour.

3. Sample Preparation for Image Analysis: The high porosity and weak mechanical strength of the samples sintered at temperatures below 1550°C made it difficult to prepare metallographic sections. To overcome this problem, the specimens were plated with electroless Ni before the polished sections were prepared. The plating filled most of the porosity in the metallization layer and assisted in the image analysis described later. The samples were mounted flat with the surface metallization at the bottom. Since the samples had cambered towards the ceramic side due to the greater extent of ceramic shrinkage, plane polishing into the bottom of the samples generated a polished section with the 10- to 14-micron thick metallization layer expanded to 200 to 600 microns from the ceramic-metal (C-M) interface to the free surface. This yielded results similar to the tapered sections employed by Pincus (1953) to examine ceramic-metal seals.

After the standardized diamond polishing steps (using progressively finer polishes up to 1- μm diamond dispersions), the specimens were polished/etched for 45 seconds using colloidal silica. Our experience was that the silica polishing/etching improved the quality of the images for analysis. The colloidal silica etches tungsten and highlights the interface between the glass and metal phases. Finally, the polished sections were gold-coated for enhancing the interfaces between the phases—especially porosity—and to generate a stronger signal for the SEM image. The samples were prepared in groups of six by firing temperature and time, ensuring that the plating and polishing within a single group would be the same.

4. The Image Analyzer: The phases in the SEM images were quantified using a Kevex Delta Class III microanalyzer. This system processed the images acquired through the ISI-DS130 scanning electron microscope. The Robinson back-scattered electron detector in the SEM utilized a variable potential on the collection scintillator to enhance low-energy electron signals. This allowed the use of a 10-keV operating voltage for the incident electron beam which was useful for distinguishing the glass phase from porosity in the presence of tungsten.

The combination of sample preparation procedure and the optimized instrument set points (operating voltage, beam current, spot size, sample tilt, the SEM's contrast and brightness, image density, image contrast, image acquisition, and time) were critical to the generation of images that could be analyzed easily and reproducibly.

5. Fields for Image Analysis: The two regions of interest within the 15- μm metallized layer in this study were the areas near the ceramic-metal (C-M) interface and the free surface. The C-M interfacial region is of interest for tracking the progress of glass infiltration into the metal layer, while the characteristics of the free surface are of interest for metal density, and the other downstream steps such as brazing and plating. Therefore two fields of view, one near the C-M interface, and the other near the free surface were chosen in each specimen for analysis. The images were taken at 2000X magnification with an approximate area of 2000 μm^2 . Each analyzed region was inspected to ensure that the fields chosen were representative of the specimen at large.

The SEM picture of the composite part is given for some of the specimens analyzed. The various phases were color-tagged for the image analysis: Nickel (void phase in the original sample) was highlighted in green, the glass phase in red, while the tungsten was tagged in blue. These phases show up as the darker areas (with varying degrees of grey levels) in the binary phases reproduced as black-and-white images in this paper. The image analyzer quantified the three phases in terms of area-% of the total pixels of the field of view. Using the principles of stereology, it can be shown that for a system in which the different phases are distributed randomly and isotropically, area-% is equivalent to volume-%.

6. Results and Discussion: The SEM micrograph of Figure 1A (upper left) is near the free surface of the M-20-M40 ink with no glass added, after a 1 hr hold at 1650°C. Individual phases are highlighted in Figures 1B to 1D. The darker phase of the binary images is Nickel (originally voids) in Figure 1B, glass in Figure 1C, and tungsten in Figure 1D. The distribution of the three phases near the free surface of the metallized layer using the same ink as shown in Figure 1, but with the firing conditions changed to only an 1-min hold at 1450°C is shown in Figure 2. As in Figure 1, the dark phases in

Figures 2B and 2D are Ni (originally void) and tungsten, respectively. Figure 2C is blank since no glass phase was detected in the specimen. The absence of glass indicates that under these firing conditions no glass has yet infiltrated into the free surface region from the C-M interface. By contrast, approximately 75% of the volume between the tungsten particles is filled with glass after a 1-hour hold at 1650°C (Figure 1C).

The effect of a finer tungsten PSD is shown in Figure 3. Comparison of Figure 3C (M-20 tungsten, 100% $< 7 \mu\text{m}$) to Figure 2C (coarser M-20-M-40 mixture, 100% $< 15 \mu\text{m}$) shows the differences in the microstructure—pore size distribution in particular—in the early stages of sintering (1-minute hold at 1450°C). The pore size distribution influences the capillary pressure, and consequently the glass infiltration kinetics.

The effect of a 15 v/o glass addition to the finer M-20 ink formulation is shown in Figure 4 for the specimen fired to 1450°C with 1-min hold time. A comparison of Figures 3 and 4 shows how glass addition to the ink formulated with the finer tungsten powder modifies the microstructure of the the circuit metal layer.

The infiltration of glass during firing as a function of tungsten PSD and preexisting glass in the ink was studied by comparing the image analysis results at the C-M interface to those at the free surface for the various firing conditions. This analysis was facilitated by reducing the phase composition to a void-free basis. This was necessary because the porosity of the circuit metal continuously changed during sintering on account of particle rearrangement and glass infiltration. Also, for quantifying changes in the glass content of the circuit metal lines when the circuit ink was glass-free (compared to when the ink was loaded with 15 v/o of glass) it was necessary to estimate the glass content of the circuit metal on a pore-free basis.

In Table III we see that for any given ink sintered to different temperatures, the tungsten and glass contents estimated in two fields (either close to the C-M interface or the free surface) are statistically identical. For example, for the ink based on the 100% M-20 powder with 15 v/o glass sintered at 1650°C with 1-min hold, the tungsten content near the free surface is 74 v/o & 72 v/o, and glass content is 23 v/o & 22 v/o. For all other conditions also, the estimated composition in the two fields showed similar or even better agreement. This strongly suggested that the technique was repeatable, and hence the numbers are reliable and therefore, can be used for quantifying the composition of the microstructure of the metal layers as sintering progressed.

7. Summary: Image analysis offers an elegant technique for quantifying the microstructure evolution in the liquid-phase sintering of high-temperature cofired systems. As described, this technique helps to study changes occurring in the volumetric compositions —alumina, glass, tungsten, and voids in the

specimen—as sintering progresses. As an accessory to the work-horse SEM with x-ray mapping capability, the image analyzer offers opportunities for expanding our horizon of understanding of microstructure evolution during sintering. The technique we presented here is general enough for use in many other multicomponent powder metallurgical and ceramic systems.

8. Acknowledgements: The authors acknowledge the support they received from Dr. Robert DiMilia of Alcoa Electronic Packaging, Inc., San Diego, and Dr. Tapan Gupta and Mr. Larry King of Alcoa Technical Center, PA.

9. References:

Bordia, R., and R. Raj, "Sintering Behavior of Ceramic films Constrained by a Rigid Substrate," *J. Am. Cer. Soc.*, vol. 68(6), 1985.

Chance, D. A., "Refractory Metallization of Green Ceramic," *Metall. Trans.*, vol 1, pp. 685-694, (1970)

Cote, R. E., and R. J. Bouchard, "Thick Film Technology," Chapter 8 in Electronic Ceramics, Editor L. M. Levinson, Marcel Dekker, New York, 1988.

Hodgkins, C. E., "Delaminations in Multilayer Ceramic Capacitors," pp. 195-205, National Materials Advisory Board Report No:400, 1983.

Majumdar, S., T. Claar, B. Flandermeyer, "Stress and Fracture Behavior of Monolithic Fuel Cell Tapes," *J. American Ceramic Society*, vol. 69[8], 628-33, (1986)

Parfitt, G. D. (1981), in Dispersion of Powders in Liquid, Chapter 1, "Fundamental Aspects of Dispersion," Section on Wetting, pp. 4-11, Allied Science, Englewood, N.J. (1981).

Pepin, J. G., W. Barland, P. O'Callaghan, and J. S. Young, "Electrode-Based Delaminations in Multilayer Ceramic Capacitors," pp. 2287-91, *J. Am. Cer. Society*, vol. 72(12), (1989).

Piper, J., "Physical Defects in Multilayer Ceramic Capacitors," pp. 19-39, National Materials Advisory Board Report No:400, 1983

Pincus, A.G., "Metallographic Examination of Ceramic-Metal Seals," *J. Am. Cer. Soc.*, vol 36(5), pp. 152-58, (1953).

Tummala , R. R., "Ceramics in Microelectronic Packaging," *Ceramic Bulletin* 67(4)752-758, 1988

Vest, R. A., "Materials Aspects of Thick Film Technology," Chapter 8 in Ceramic Materials for Electronics (Processing and Applications) 2nd Edition, Editor: R. C. Buchanan, Marcel and Dekker, New York, 1990.

Table 1. PSD of the tungsten powders used to make the circuit ink.

Parent Tungsten Powder	D ₁₀ (μm)	D ₅₀ (μm)	D ₉₀ (μm)
M-40*	2.20	5.0	9.2
M-20*	0.80	2.2	4.3
M-10*	0.33	0.9	2.1

* Product names of Osram-Sylvania, Towanda, PA, 18848.

Table 2. Blends of tungsten powders used to make 3 experimental circuit inks.

	M-10	M-20	M-40
Ink 1	-	50%	50%
Ink 2	10%	45%	45%
Ink 3	-	100%	-

Table 3. The tungsten and glass contents (void-free basis) of the metal layers.

	Near Free Surface	Sintered at 1450°C 1 min
	% Tungsten	% Glass
Ink: 100% M-20 Ink No Glass:		
Field 1	100	0
Field 2	100	0
Ink: 100% M-20 ink with 15 v/o glass:		
Field 1	87	13
Field 2	86	14
	Near C-M interface	Sintered at 1550°C 1 min
	% Tungsten	% Glass
Ink: M-40:M-20:M-10 = 45:45:10 No glass:		
Field 1	88	12
Field 2	91	9
Ink: M-40:M-20:M-10 = 45:45:10 with 15 v/o glass:		
Field 1	83	17
Field 2	85	15
	Near Free Surface	Sintered at 1650°C 1 min
	% Tungsten	% Glass
Ink: 100% M-20 Ink No Glass:		
Field 1	78	22
Field 2	78	22
Ink: 100% M-20 ink with 15 v/o glass:		
Field 1	74	26
Field 2	72	28
	Near C-M interface	Sintered at 1650°C 1 min
	% Tungsten	% Glass
Ink: M-40:M-20:M-10 = 45:45:10 No glass:		
Field 1	77	23
Field 2	78	22
Ink: M-40:M-20:M-10 = 45:45:10 with 15 v/o glass:		
Field 1	70	30
Field 2	74	26

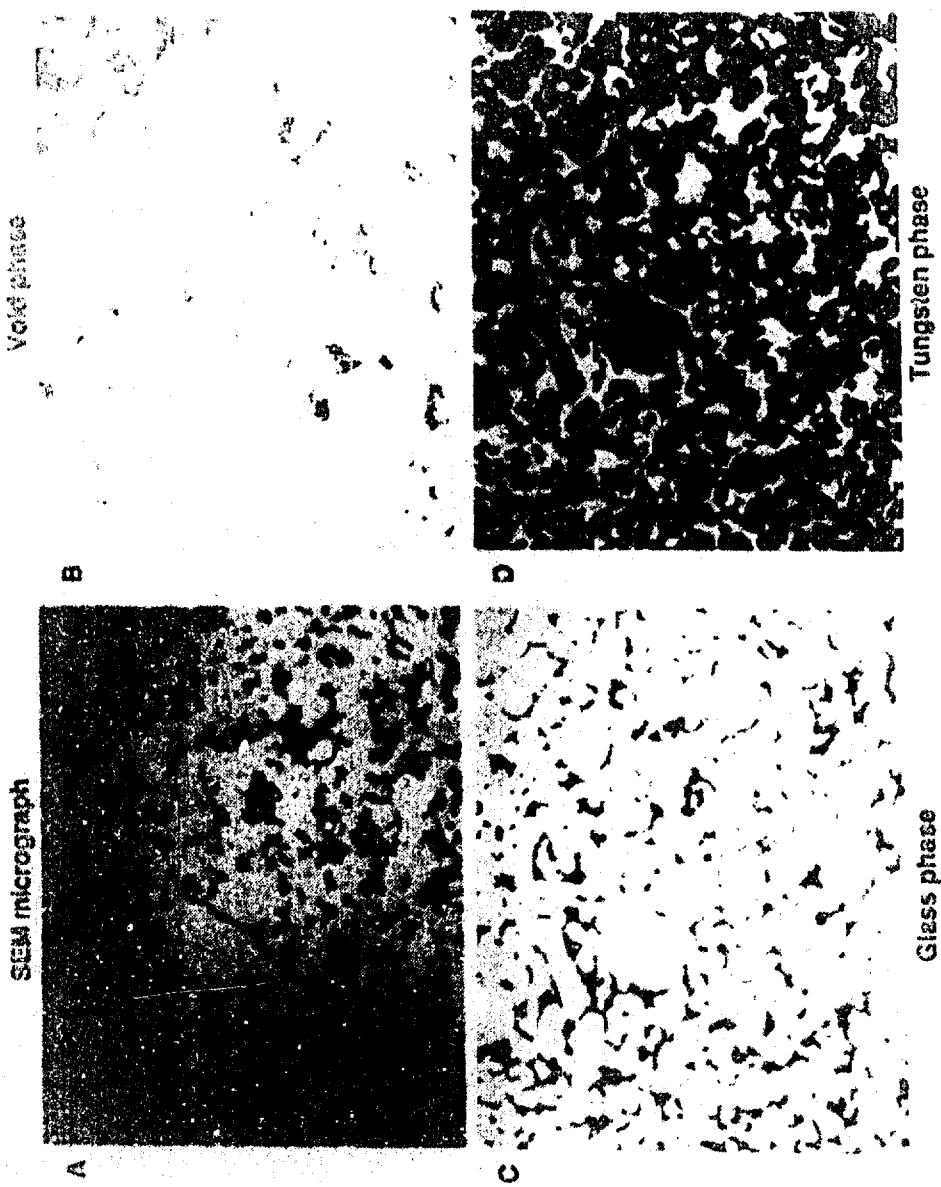


Figure 1: Ink 1 Fired to 1650°C 1 Hour

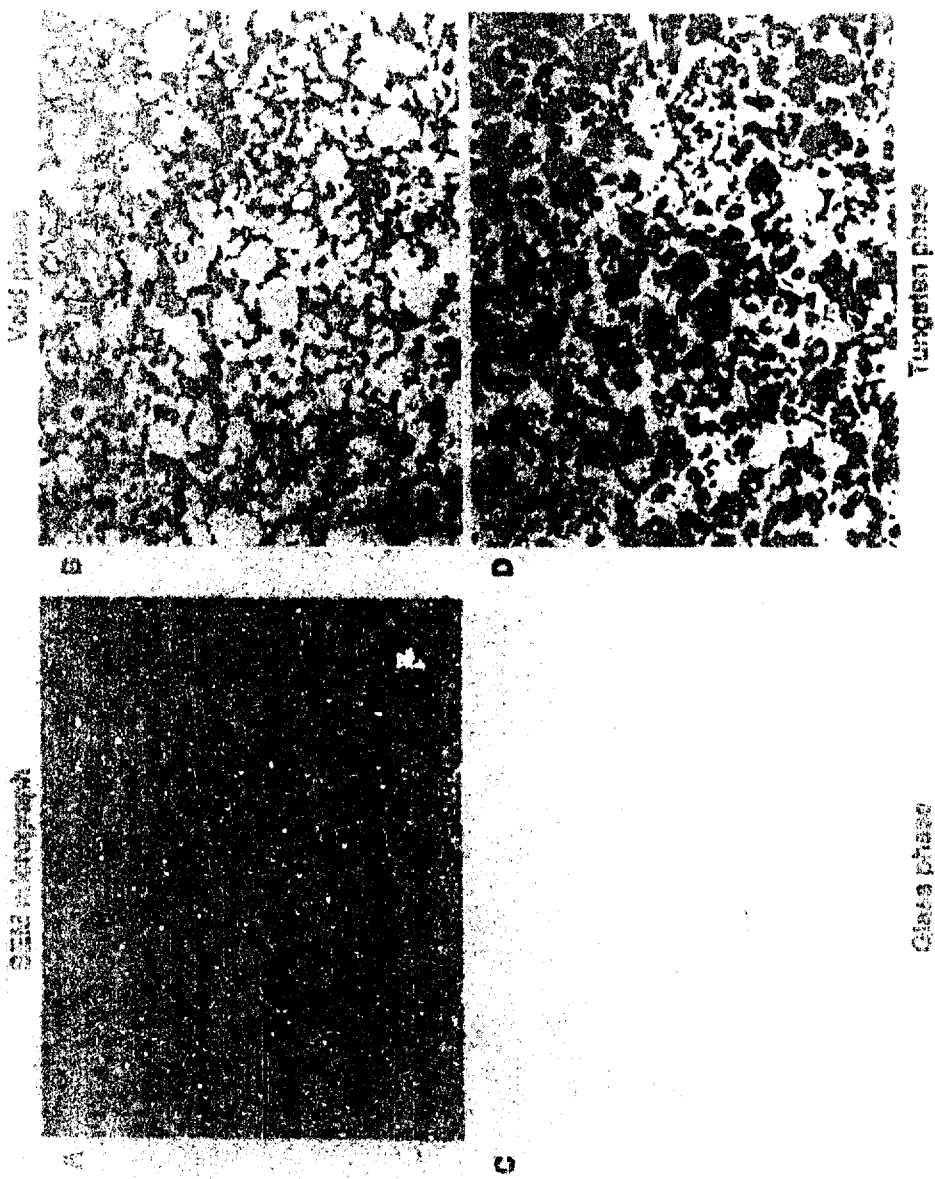


Figure 2: Ink 1 Fired to 1450°C 1 min.

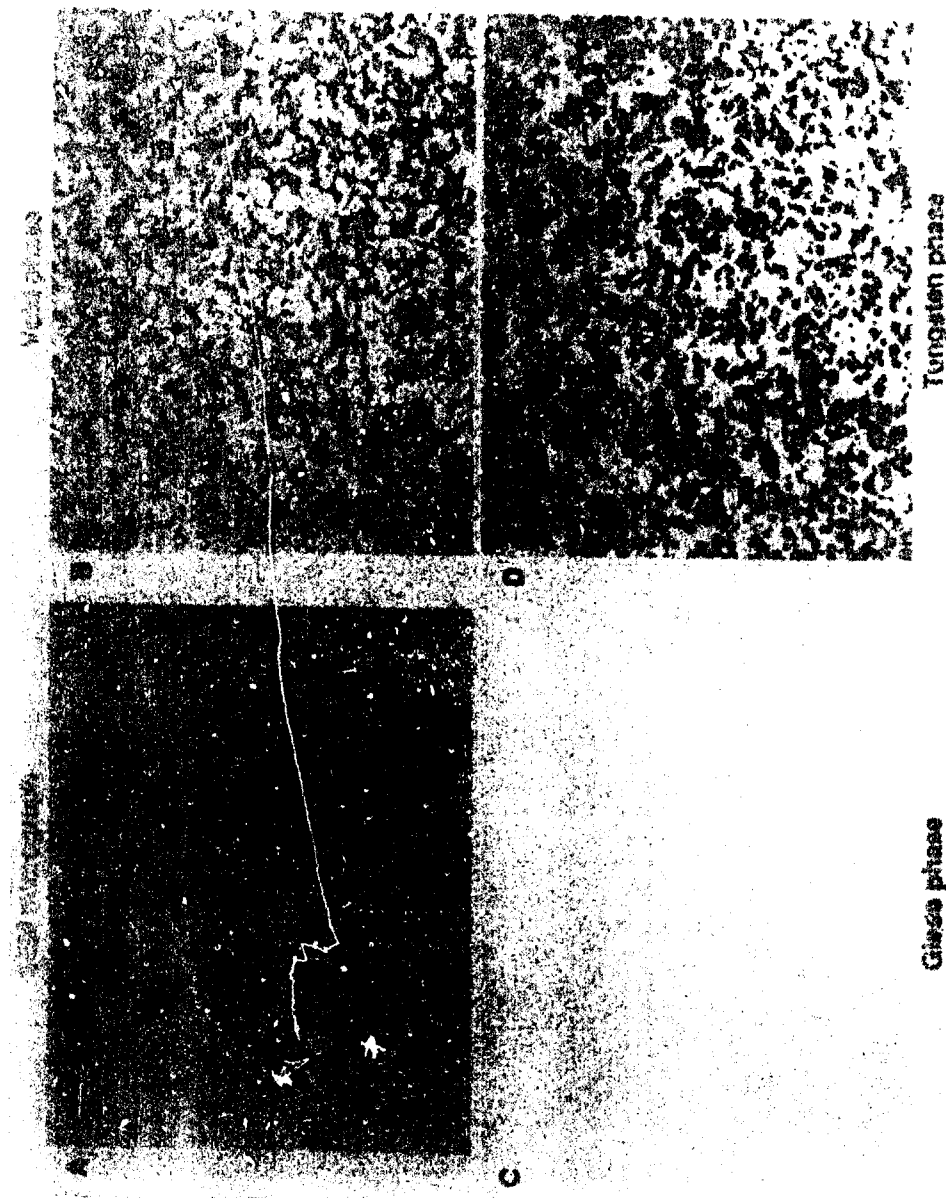


Figure 3: Inga 3 sintered to 1450°C 1 min.

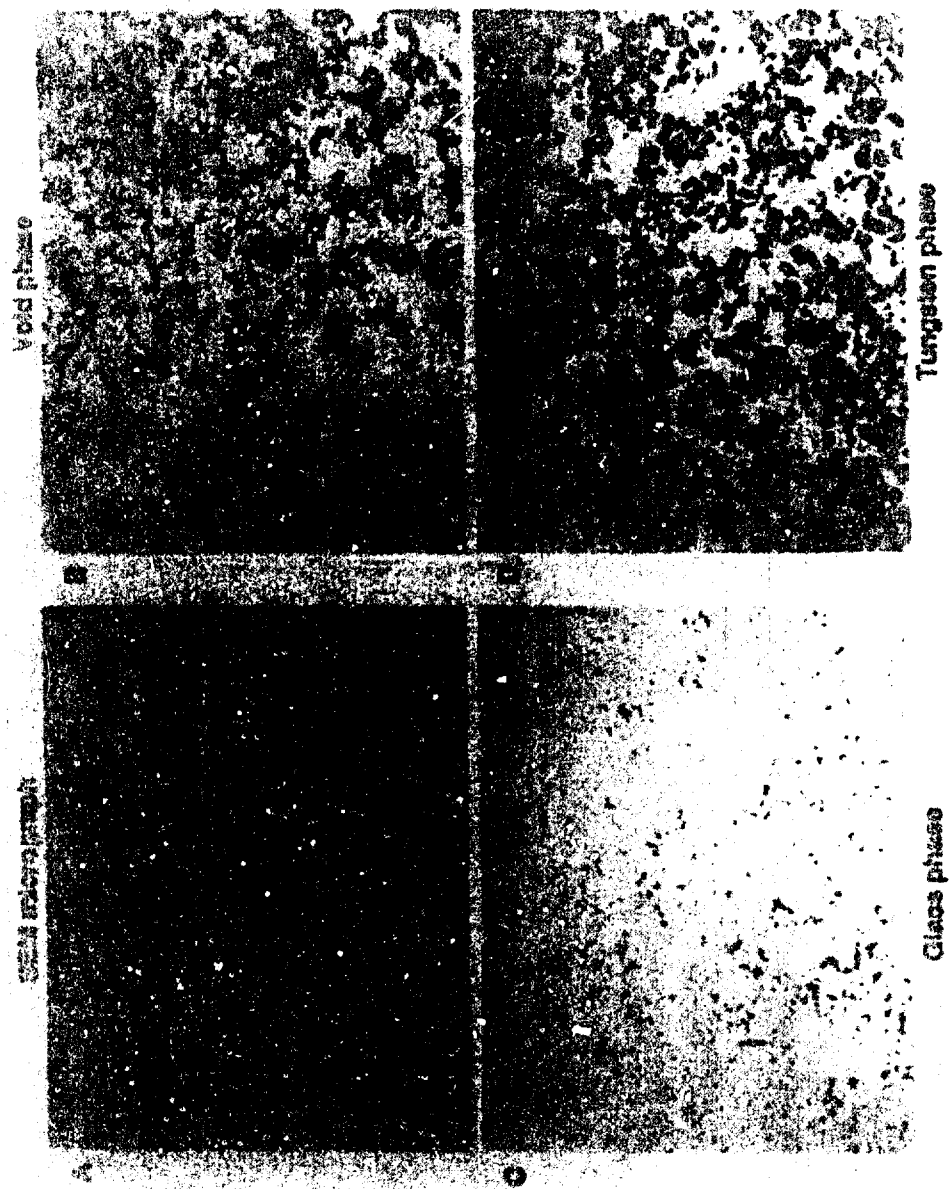


Figure 4: Ink 3 with 15 v/o Glass Fired to 1450°C 1 min.

ZIRCONIA HYDROGEL CASTING OF PZT CERAMICS

T.E. Petroff, S.A.M. Hesp and M. Sayer

Departments of Chemistry and Physics,
Queen's University, Kingston, Ontario, Canada, K7L 3N6.

ABSTRACT

Zirconium hydrogels have been used as a dispersing agent and binder for slip casting zirconia based ceramic powders. The method is capable of producing large, complex shapes with green body compacts which are tough enough for pre-sintering machining or finishing. The technique is extended to lead zirconate titanate, where the hydrogel minimises changes to the grain boundaries. The hydrostatic figure of merit ($g_a d_b$) for the slip cast, fired ceramics lie between 500 and $1300 \times 10^{-15} \text{ m}^2/\text{N}$.

INTRODUCTION

Inorganic additives may be used to enhance the properties and processing of structural ceramics [1]. The advantages of such inorganic dispersion aids and binders are that they do not require burning out and that they are compatible with the base ceramic. One such system is the addition of peptized, boehmite and amorphous alumina to alpha alumina [1]. This results in excellent sintered zirconia ceramics with exceptional toughness and strength. The unsintered bodies also display enhanced toughness to the point where machining is possible.

Another promising additive is zirconium hydrogel, polymeric $\text{Zr}(\text{OH})_4$, when slip casting zirconia or partially stabilized zirconia [2]. The additive behaves as an electrosteric stabilizer to enhance the dispersion of the ceramic powder and is then able to react with the ceramic and itself to act as an effective binder. Figure 1 displays the proposed structure of the zirconium hydrogel. In solution, this material is able to either adsorb or chemisorb onto the surface of a ceramic particle as depicted in Figure 2a. Upon removal of the solvent, the chemisorption of the binder is accelerated, and the gel is able to react with itself via condensation reactions (Figure 2b). Removal of the solvent condenses the

To the extent authorized under the laws of the United States of America, all copyright interests in this publication are the property of The American Ceramic Society. Any duplication, reproduction, or republication of this publication or any part thereof, without the express written consent of The American Ceramic Society or fee paid to the Copyright Clearance Center, is prohibited.

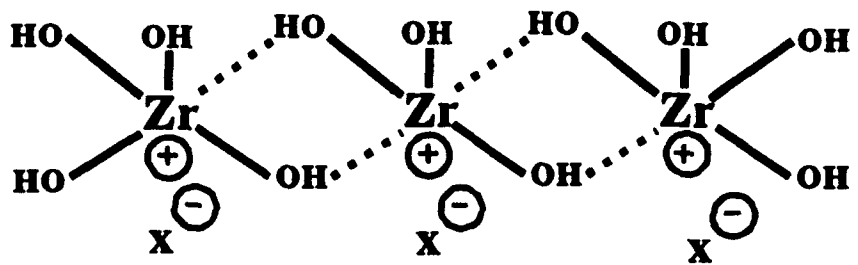


Figure 1: Proposed structure of zirconium hydrogel

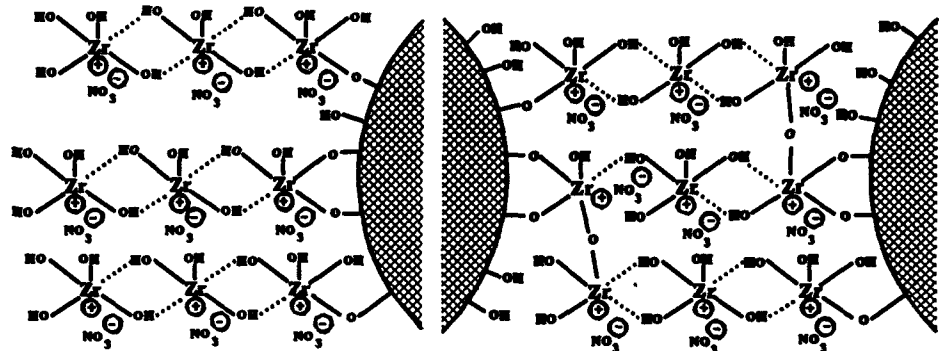


Figure 2a. Chemisorption of hydrogel onto a particle.

Figure 2b. Gelation of the hydrogel to form a continuous matrix.

hydrogel to form a continuous matrix providing mechanical strength to the pre-sintered body. During sintering the hydrogel crystallizes at the grain boundaries to become part of the final body.

It is of interest to apply this technique to lead zirconate titanate (PZT) ceramics. This paper defines a fabrication method to obtain large bodies of PZT ceramics via a slip casting process. The results show clear success in slip casting large, complex PZT

shapes which are piezoelectric on poling. While the full density has not yet been achieved, the electrical properties are characteristic of a strongly bonded 3-0 composite, and this results in a hydrostatic response which is significantly improved over that of the fully dense ceramic.

At present, most PZT ceramics are produced by pressing powders into shapes which are then consolidated by sintering. A typical process involves mixing PZT powders with a polymeric binder such as polyvinyl alcohol and uniaxially pressing the mixture into simple shapes. The resulting bodies are burned out to remove the organic binder and are then heated to sintering temperatures. The final ceramic shape can be obtained by cutting or machining the crude, sintered material into the desired shape, electroding and poling. It is possible to cast PZT by conventional slip casting, but such methods often involve adding large amounts of organic additives which have to be distilled out of the material prior to sintering. It is therefore often difficult to produce large but uniform ceramic bodies of complex shape using slip casting, and often significant post-sintering machining is required.

The objective of this work was to make large ceramic PZT bodies without sacrificing the piezoelectric response of the material. The ceramics were produced using a modified slip casting method which utilizes inorganic, polymeric zirconium hydroxide as both the dispersing agent and binder. The green body shapes produced have enough green body strength to allow for some pre-sintering machining or finishing.

BACKGROUND

In a typical slip casting operation ceramic powders are dispersed into an aqueous solvent and the resulting dispersion is milled for 24 to 48 hours. Dispersing agents are added to facilitate the break up of soft agglomerates and to promote dispersion. A binder such as polyvinyl alcohol or hydroxy methyl cellulose is added to give the cast, pre-sintered body some handling robustness. The resulting mixture or slip is transferred to a porous mould which serves to wick the solvent away and to give the body its shape. Removal of solvent results in the consolidation of the powder at the mould wall. The thickness of the body is determined by the length of time the slip is allowed to stand in the mould. Excess slip is then poured away and the resulting body is removed when dry. In solids casting, slip is not removed from the mould and the body dries as a solid shape. The final ceramic is obtain in both cases by heating the body to sintering temperatures.

It has been observed that the toughness of the sintered ceramic is greatly enhanced when using inorganic additives. Kindl has reported that the alumina bodies prepared with additions of peptized, boehmite and amorphous alumina are so tough that it is difficult to cut the material with a diamond saw [3]. The fracture surfaces reveal that the cracking

is intergranular as opposed to transgranular as is normally observed in alumina. Enhanced toughness is also observed with the zirconia work of Petroff et al [2,4]. These results imply that the gel modifies crack propagation at the interface and that the added toughness can be attributed to an amorphous layer which is chemically bonded to the crystalline ceramic. The presence of this layer may or may not affect the electrical properties of electric ceramics.

EXPERIMENTAL

The experiment was carried out in three stages. This paper focuses on the first two stages. The initial action was to determine the amount of zirconium hydrogel required to successfully slip cast PZT. The second was to modify the chemical composition of the PZT powder, if necessary, to identify and eliminate any processing problems. The final step is to produce large, complex shapes of commercial quality.

Two different zirconium hydrogels were used. One was an experimental zirconium hydrogel produced by Haldor Topsoe A/S of Copenhagen, Denmark; the conditions of its preparation are proprietary. The other was produced at Queen's by the coprecipitation of $ZrCl_4$ and $Zr(CO_3)_2$. The PZT powder used was attrition milled BM 400 provided by B.M. HiTech Inc. of Collingwood, Ontario.

PZT powder was mixed with varying amounts of Haldor Topsoe A/S and Queen's hydrogels. PZT powder, hydrogel and water were charged into a polyethylene bottle and the pH adjusted by the addition of ammonium hydroxide or nitric acid. Grinding media was added and the samples were allowed to mill for 1 hr. The grinding media was removed and the resulting slip was poured into a plaster of paris mould in the shape of a 2.5 cm diameter by 5 cm cylinder. The green body (of density 4.1 g/cm³) was removed from the mould within 20 min and allowed to dry over night in air. Finally, the sample was burned out at 900°C for 10 hr and then fired at 1260°C with a 1 hr soak. The best perceived composition was scaled up to 1 kg PZT powder batches and the material was cast into a variety of shapes and sizes.

Cylinders from the second stage were cut into slices. The surfaces of some of the slices were viewed by an ElectroScan Model E-3 environmental scanning electron microscope. The others were silvered, poled at 35 KV/cm at 130°C in oil and their electrical properties determined.

RESULTS AND DISCUSSION

The hydrogels were approximately 7 wt % solids for the Haldor Topsoe A/S material and 14 wt % for the Queen's as determined by thermal gravimetric analysis. The zirconium

content was approximately 55 % by dry weight of the gel by neutron activation analysis for both. The dry weight ratio of hydrogel added to PZT was 4.3 wt % resulting in an increase of 0.36 at % in the zirconium content for the bulk powder.

There was no noticeable difference in the processing of the PZT slips at pH 4, 7 and 10. Therefore all subsequent samples were cast at pH 7 to reduce the likelihood of deleterious chemical reactions with the plaster of paris mould. The ceramic loading of the slip that produced the best results was 70 % by weight. The cast samples could be removed from their moulds within 20 min of casting. This time is short when compared to traditional slip casting where the green body sits in the mould overnight.

Both the Haldor Topsoe A/S and the Queen's hydrogel produced green bodies that were robust enough to allow some green state sanding or grinding. However, the samples prepared using the Haldor Topsoe A/S hydrogel became soft and powdery after stage I irrespective of the amount of gel added. Therefore the material appears to be ineffective as a binder for PZT even though it behaves as a dispersing aid and is able to form good green bodies. Therefore these samples were not fired. The samples prepared using the Queen's hydrogel, on the other hand, produced calcined bodies that were similar to those in the green state but with enhanced toughness to the point where they could be carved with a metal paint scraper. These samples were sintered to obtain the final ceramics.

Samples for electrical measurements were obtained by slicing up a slip cast and sintered cylinder into discs 2.5mm thick using a diamond wheel cutter and electroding by silver screen print. No problems were encountered on poling at 35 KV/cm.

The following electrical data was taken: dielectric constant ϵ and loss at 1 KHz; radial coupling factor k_r determined from the radial resonant and anti-resonant frequencies; d_{33} measured using a Berlincourt-type meter; and hydrostatic voltage coefficient g_s using a Sensor Technology (Collingwood, On) apparatus, Model 8809HE. The g_s values were calibrated against standard samples of known value of g_s . The data measured for both a uniaxial pressed and sintered ceramic (reference) and the slip cast and sintered material (slip cast) is listed in Table 1. d_s was calculated from $g_s \times \epsilon_0$.

The density of the sintered samples prepared by the slip casting process varied from 5.60 to 6.80 g/cm³. This compares unfavourably to the theoretical density of PZT of 7.60 g/cm³. Environmental scanning electron microscopy revealed a large number of voids in the sintered ceramic possibly due to insufficient de-airing of the slip during casting thereby reducing the density of the material.

Table 1. Summary of the Electrical Data for the PZT Samples.

	Reference	Slip Cast		
		Sample 1	Sample 2	Sample 3
Density (g/cm ³)	7.40	6.80	6.00	5.60
Dielectric Constant (unpolarized material)	1239	1064	749	793
Dielectric Constant (polarized material)	1064	727	691	651
Radial Coupling Factor	0.61	0.30	0.29	0.18
Dielectric Loss	0.004	0.011	0.011	0.011
Charge co-efficient d_{33}	285	217	234	187
g_h (10 ⁻³ V.m/N)	4.0	8.4	9.0	15.0
$g_h d_h$ (10 ¹⁵ m ² /N)	150	450	500	1300

The bulk electrical properties are shown in Table 1. They are not comparable with those of pressed ceramic, however the hydrostatic figure of merit is significantly improved. It is of interest that the electrical parameters are close to those expected for a 3-0 composite where single grains are strongly bonded. The high values of the hydrostatic coefficient would be expected in such a structure.

Figure 3a compares the microstructure of the ceramic prepared by slip casting with that (Figure 3b) of similar material prepared by uniaxial pressing. Compared with the pressed sample, the grain growth in the slip cast sample is suppressed. Energy dispersive X-ray analysis of the cut samples performed on a scanning electron microscope indicate that there is no significant chemical difference between samples prepared by uniaxial pressing and by slip casting, and between their grain boundaries and their bulk. There was also no difference in the crystal structure of the bulk material as indicated by X-ray diffraction analysis. There is no deleterious affect of the addition of the hydrogel on the grain structure of the material apart from the suppression of the grain growth.

The most significant outcome of this research is that very large PZT bodies (over 200 g) can be cast in near net shape and that the major part of the final shaping can be performed on the green body. This can significantly reduce the amount of post-sintered

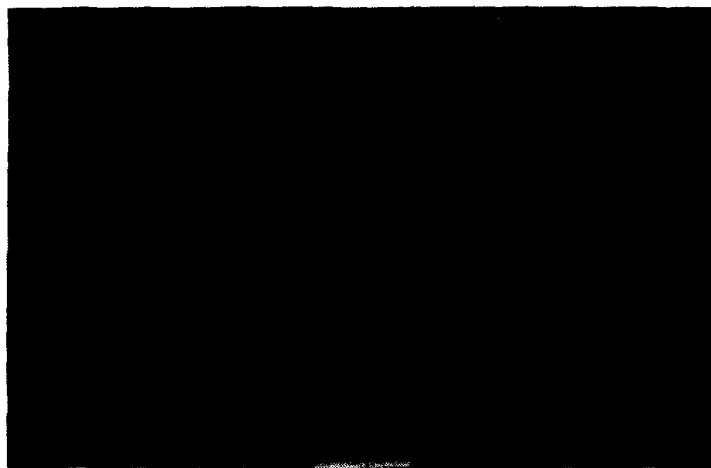


Figure 3a. Micrograph of a cut surface of a PZT sample prepared using the modified slip casting technique.

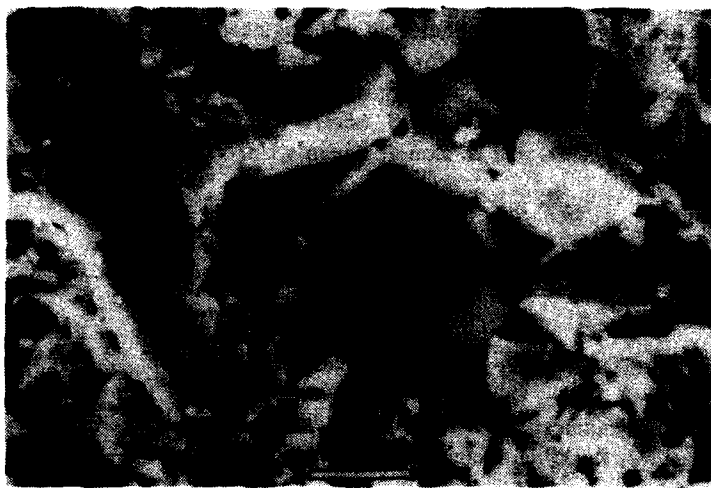


Figure 3b. Micrograph of a cut surface of a PZT sample prepared by uniaxial pressing.

machining necessary. For example in conventional processing, large, hollow hemispheres are obtained by uniaxial pressing a PZT disc to the appropriate size, sintering it and then machining the piece until the desired shape is obtained. Using the modified slip casting method, large, hollow hemispheres are obtained easily and in relatively short time.

CONCLUSIONS

Large complex shapes of PZT can be fabricated using a modified slip casting method. No organic additives are required to form high strength green bodies. The density of the initial samples prepared in this work have not been optimized and the bulk electrical constants are therefore inferior to fully dense PZT. However significant levels of piezoelectric activity have been observed under normal poling conditions. The dielectric strength of the sintered ceramic was sufficient to allow reliable poling at 35 kV/cm. It should be possible to increase the final density by subjecting the slip to reduced pressure or sonification. The hydrostatic figure of merit of these materials is 2-4 times higher than that of dense PZT and the method may be important for this reason.

ACKNOWLEDGEMENTS

The authors thank B.M. HiTech Inc., Collingwood, Ontario, Haldor Topsoe A/S, Copenhagen, Denmark, Industrial Ceramics Ltd., Milton, Ontario, the Ontario Centre for Materials Research, the Natural Sciences and Engineering Council of Canada and the Xerox Research Centre of Canada for funding, materials and facilities. Experimental assistance is appreciated from Dr. E.S. Prasad and K.I. Morton of B.M. HiTech Inc., D. Misale of Industrial Ceramics Ltd., S. Sherrit and Dr. B. Mukherjee of the Royal Military College of Canada, and L. Zou of Queen's University.

REFERENCES

- [1] B. Kindl, D.J. Carlsson, Y. Deslandes and J.M. Hoddenbagh, *Can.Ceram.Soc.*, **60** (1991) 53.
- [2] T.E. Petroff, M. Sayer and S.A.M. Hesp, *Colloid.Surf.*, **78** (1993) 235.
- [3] Private communications with B. Kindl, Danish Ceramic Centre, Risoe National Laboratory, Roskilde, Denmark, (1993).
- [4] T.E. Petroff, M. Sayer and B. Kindl, *J.Can.Ceram.Soc.* **61** (1992) 194.
- [5] M.I. Miller and T.A. Henriquez, *Proc. 1983 Ultrason. Symp.* (1983) 977.

INTERFACE AND MICROSTRUCTURE DEVELOPMENT OF COATED ALUMINA POWDERS DURING HEATING

H. Yokoi* and W. D. Kingery
Department of Materials Science and Engineering
University of Arizona, Tucson, AZ 85721

ABSTRACT

Alumina powders coated with precursors of various metal oxides were prepared. To characterize their interface and microstructure development during heating, powder compacts quenched from elevated temperatures were examined by analytical transmission electron microscopy and field emission scanning electron microscopy. The EM studies revealed that the alumina particle surfaces act as sites for heterogeneous nucleation. The final structure of the alumina simultaneously doped with cupric oxide and titania was reached in the presence of a liquid phase but a large shrinkage occurred before the liquid formed. This phenomenon was explained from the viewpoint of a solid state reaction during heating.

INTRODUCTION

Powder coating is an attractive powder preparation technique because we can expect the fastest densification rate due to the maximized initial contact between the ultrafine additive phase particles and the matrix phase particles and the uniform distribution of secondary phases in the final structure. Precursor coatings of $TiO_2^{1,2}$ or $ZrO_2^{3,4}$ on alumina have been tested. However, the techniques for producing the uniform coating of the additive phase on individual particles of the matrix phase have not been

*Present address: NGK Spark Plug Co., Ltd., Central Research Center, 2808 Iwasaki, Komaki, Aichi 485, JAPAN

To the extent authorized under the laws of the United States of America, all copyright interests in this publication are the property of The American Ceramic Society. Any duplication, reproduction, or republication of this publication or any part thereof, without the express written consent of The American Ceramic Society or fee paid to the Copyright Clearance Center, is prohibited.

optimized, and also the nature and behavior of the coated phase have not been fully characterized. Furthermore, there is no research concerning development of interfaces between the coating layers and the core particles and microstructures during heating.

In our laboratory, alumina powders coated with precursors of various metal oxides have been prepared by controlled hydrolysis of metal alkoxides in a slurry of alumina. In this paper, the sintering behavior and microstructure development during heating of the systems of $\text{Al}_2\text{O}_3\text{-TiO}_2$ and $\text{Al}_2\text{O}_3\text{-CuO-TiO}_2$ are reported.

EXPERIMENTAL PROCEDURE

A high-purity (> 99.99%) alumina with an average particle size of ~0.2 μm was used. The alumina powder coated with a precursor of 10 mol% TiO_2 (A10T) was prepared by hydrolysis of $\text{Ti}(\text{OPr})_4$ in a suspension of alumina using a water/isopropanol solution (1/10 by volume). The alumina powder coated with precursors of 5 mol% TiO_2 and 5 mol% CuO (A5C5T) was prepared by coprecipitation from $\text{Cu}(\text{NO}_3)_2$ and $\text{Ti}(\text{OPr})_4$ in a suspension of alumina using a basic solution. Copper nitrate was used as a starting material for CuO , since the dissolution of the copper alkoxides into common organic solvents was difficult.

The prepared powders were die-pressed under a compaction of 98 MPa into pellets. The powder compacts were heated at $600^\circ \sim 1400^\circ\text{C}$ for 1 h in a furnace and rapidly quenched into liquid N_2 . The thickness of the specimen was thin enough (0.2 mm) to satisfy Newtonian cooling in which the temperature gradients within the specimen were negligible. Liquid N_2 was selected as a quenching medium because it gives a rapid initial cooling rate, but then slows the quench due to gas film formation around the specimen.⁵ Therefore, thermal shock fracture was not a problem in this study.

The prepared powders and the sintered-quenched specimens were examined by TGA, DTA, XRD, XPS, FE-SEM, and analytical TEM.

RESULTS AND DISCUSSION

Figures 1 and 2 are FE-SEM micrographs showing morphology of "as-prepared" A10T and A5C5T powders. In the A10T powder, individual



Fig. 1. FE-SEM micrograph of "as-prepared" A10T powder.



Fig. 2. FE-SEM micrograph of "as-prepared" A5C5T powder.

alumina particles were uniformly coated with a 10-15 nm layer of very fine precursors, while in the A5C5T powder, homogeneous mixing was achieved, but each alumina particle was not completely coated as shown in Fig. 2. The heterogeneous deposition of precursors on individual alumina particles from metal alkoxides can be attributed to the presence of electronegative alkoxy groups and positive metal atoms. The metal atoms are consequently susceptible to adsorption by oxygen atoms on the surface of alumina in the suspension. In the subsequent hydrolysis process, the metal alkoxides on the surface of alumina are nucleophilically attacked by water. The hydrolysis may contain steps of partial hydrolysis to form monomer \rightarrow polycondensation, finally resulting in external layers of precursors.

The DTA curve of the A5C5T powder is illustrated in Fig. 3. An endothermic peak corresponding to liquid formation was observed at 925°C. On the other hand, the eutectic temperature of the Al_2O_3 - TiO_2 is high. Thus, a liquid phase is not operative in the A10T powder during sintering.

Figure 4 shows the shrinkage behavior of pure alumina (100A), the A10T, and the A5C5T powders. Since the green densities of the coated powders were lower than that of pure alumina, larger shrinkage occurred in the coated powders. The shrinkage of the 100A started around 1000°C. The sintering rate of alumina was accelerated by an addition of TiO_2 above 1100°C. The most important aspect in this figure is that the large shrinkage took place in the A5C5T before liquid formation, especially below 600°C (about 12 % at 600°C). The classic liquid phase sintering theory does not account for this low temperature process.

There are two critical points during heating in terms of microstructural change of alumina coated with the precursors of TiO_2 . The first point is the heterogeneous nucleation of rutile on the surfaces of alumina, resulting in breaking the precursor layers. This occurs below 900°C as shown in Fig. 5 (HREM). Referring to the densification curve given in Fig. 4, the second point is the start of accelerated densification which occurs at 1100°C. Rutile nucleated on the surfaces of alumina starts diffusing into the alumina grains at this temperature, which was confirmed by TEM-EDX. Consequently, the concentration of the rate determining defects, $[\text{V}_{\text{Al}}'']$, is made higher. The grain coarsening rapidly occurred above 1200°C. The uniform spatial distribution of fine TiO_2 was achieved from the coated powders at a relatively low temperature.

The XRD patterns of the A5C5T specimens heated at various temperatures are depicted in Fig. 6. The broad peaks of CuAl_2O_4 were recognized in the specimen sintered at 600°C, and they almost disappeared above 1100°C. It is thought that it was consumed for the liquid formation. The rutile existed in the sintered specimens over the whole temperature

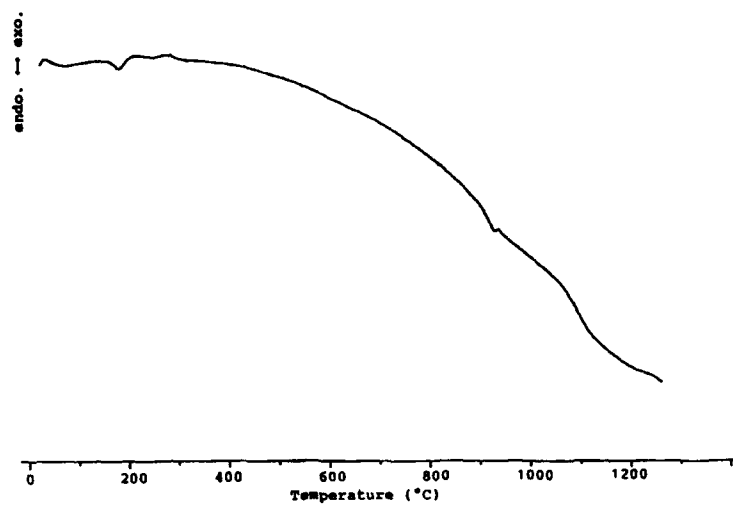


Fig. 3. DTA curve of the A5C5T powder.

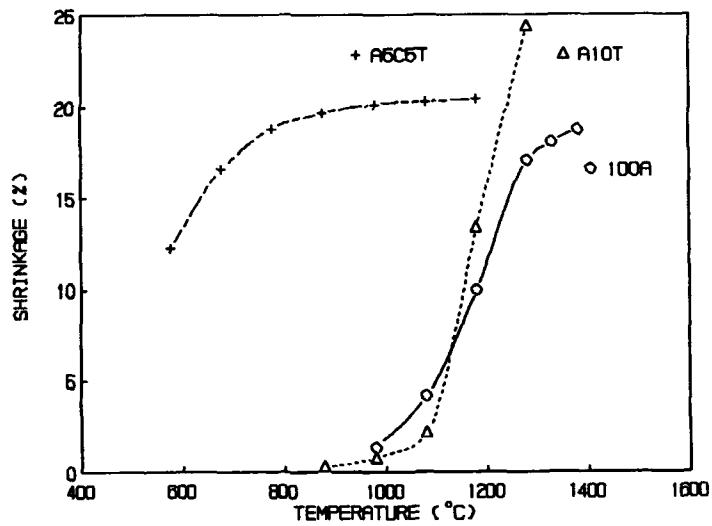


Fig. 4. Shrinkage behavior of pure alumina and the coated powders.

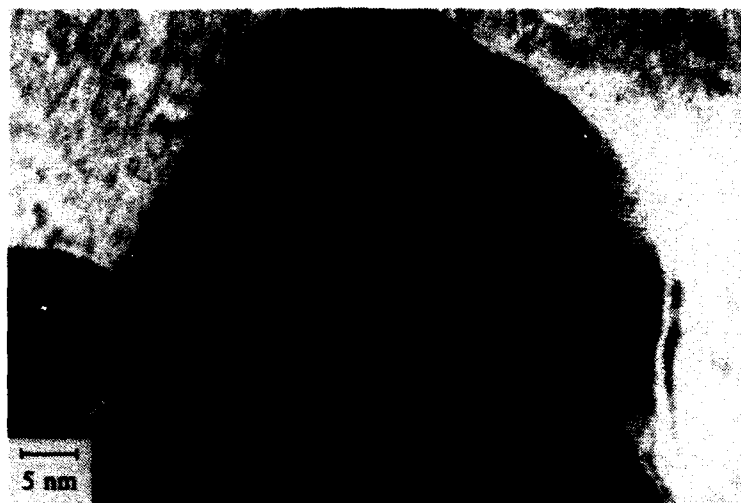


Fig. 5. Heterogeneous nucleation of rutile on the surface of alumina.

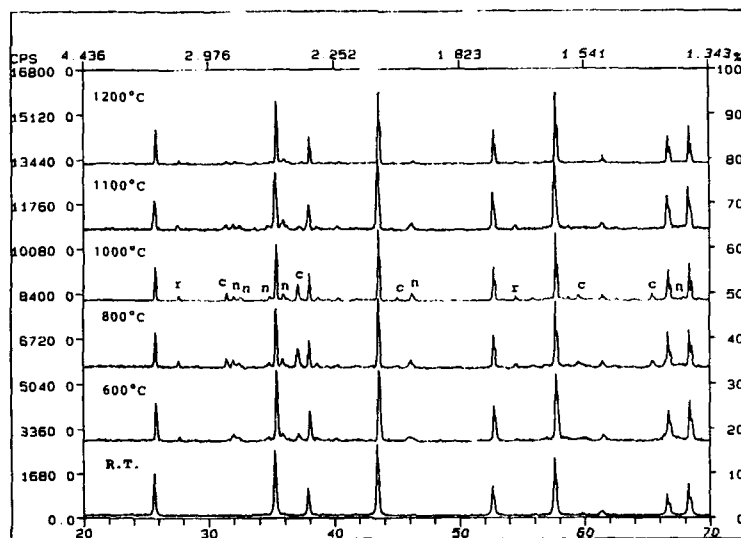


Fig. 6. XRD patterns of the A5C5T quenched from various temperatures. Rutile, CuAl₂O₄, and NaAl₂O₄ are denoted as r, c, and n, respectively.

range. This implies that rutile crystallizes below 600°C. This temperature is considerably lower than the reported crystallization temperature of rutile (900° ~ 1000°C).⁶ In addition, no anatase peaks were detected at this temperature in the XRD studies. Therefore, it was assumed that the amorphous precursors on the surface of alumina directly crystallized to rutile without the crystallization of anatase although other researchers have stated that the amorphous phase changes to the anatase crystal phase, then to rutile.^{1,2,6} The other very weak peaks in Fig. 6 were assigned to a NaAl_2O_8 phase. The origin of the impurity sodium was the basic solution used to precipitate $\text{Cu}(\text{OH})_2$.

The microstructure of the A5C5T sintered at 600°C is shown in Fig. 7. At this temperature, neck growth has occurred (71.7 % of theoretical

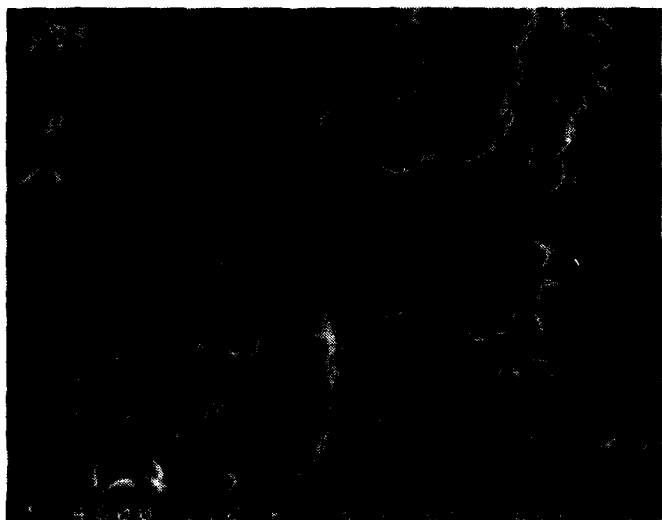


Fig. 7. FE-SEM micrograph of the A5C5T sintered at 600°C for 1 h.

density). Obviously, the classic model of the liquid phase sintering in which particle rearrangement in the first stage is explained by formation and penetration of a liquid phase cannot account for the sintering behavior of the A5C5T powder. In the very early stage of the sintering of the A5C5T, the amorphous $\text{Cu}(\text{OH})_2$ which was not adsorbed on the surface of alumina may exhibit superplastic character to allow sliding and repacking of the alumina particles. In order for the neck formation and growth to occur, matter must be transferred to the neck region. The XRD evidence showed that the solid

state reaction yielding CuAl_2O_4 occurred between Al_2O_3 and CuO below 600°C. For this reaction, it is clear that matter was transferred by diffusion; the formation of crystalline, CuAl_2O_4 requires that there be mobility of Al^{3+} in the system. This is also required for sintering. It is known that oxygen diffuses much faster than aluminum does and that the diffusion coefficient in a polycrystalline ceramic is much larger than that in a single crystal. Therefore, in this specimen at 600°C, it is thought that grain boundary diffusion of Al^{3+} has been enhanced.

CONCLUSIONS

- (1) A uniform coating of precursors of various metal oxides on individual alumina particles was achieved by controlled hydrolysis of metal alkoxides in a slurry of alumina. The heterogeneous deposition of precursors on alumina particles from metal uniform alkoxides is ascribed to the electronegative characteristics of alkoxy groups. The precipitation of $\text{Cu}(\text{OH})_2$ from nitrates led to homogeneous mixing but not powder coatings.
- (2) There are two critical points during heating in terms of microstructural change of alumina coated with the precursors of TiO_2 . The first point is the heterogeneous nucleation of rutile on the surfaces of the alumina particles, resulting in breaking the precursor layers. This occurs below 900°C. The second point is the start of accelerated densification at which TiO_2 nucleated on the surfaces of alumina begins diffusing into the alumina grains, and thereby, the rate determining defects, $V_{\text{Al}}^{''''}$ increases.
- (3) The alumina powder simultaneously doped with CuO and TiO_2 showed very rapid densification behavior before liquid formation (925°C). This rapid sintering at low temperatures was attributed to enhanced diffusion evidenced by solid state reaction to form CuAl_2O_4 .

REFERENCES

- ¹H. Okumura, E. A. Barringer, and H. K. Bowen, "Preparation and Sintering of Monosized Al_2O_3 - TiO_2 Composite Powder," *J. Am. Ceram. Soc.*, **69** [2] C-22-C-24 (1986).
- ²P. A. Brugger and A. Mocellin, "Preparation of Composite Al_2O_3 - TiO_2 Particles from Organometallic Precursors and Transformation during Heating," *J. Mater. Sci.*, **21**, 431-35 (1986).
- ³B. Fegley, Jr., P. White, and H. K. Bowen, "Preparation of Zirconia-Alumina Powders by Zirconium Alkoxide hydrolysis," *J. Am. Ceram. Soc.*, **68** [2] C-60-C-62 (1985).
- ⁴P. Cortesi and H. K. Bowen, "Continuous Coating of Alumina articles

with Alkoxide-Derived Zirconia Particles," *Ceram. International*, **15**, 173-77 (1989).

⁵D. P. Birnie, III and W. D. Kingery, "Quenching of Solid Samples for High Temperature Equilibrium Measurement," *J. Mater. Sci.*, **20**, 2193-98 (1985).

⁶O. Yamaguchi and Y. Mukaida, "Formation and Transformation of TiO_2 (Anatase) Solid Solution in the System TiO_2 - Al_2O_3 ," *J. Am. Ceram. Soc.*, **72** [2] 330-33 (1989).

HIGH Q-FACTOR TRI-PLATE RESONATOR WITH AN INNER CONDUCTOR OF MELTED SILVER

M.Kobayashi, K.Kawamura, and K.Suzuki

TDK CORPORATION
570 Minami-hatori 2,Narita,Chiba,286 Japan

ABSTRACT

A tri-plate resonator has been developed, fabricated by a process in which the silver inner conductor is melted. The measured Q-factor was 240 at 1.9GHz using a dielectric with a QF product in the range of 2,000GHz. It is concluded that the Q-factor of the isolated silver conductor was 300 within 75% of the theoretical value. The reduction in Q is attributed to conductor loss associated with grain boundaries within the conductor. The melting conductor method has been extended to conventional microwave dielectrics to yield a maximum resonator Q-factor of 316 for a dielectric material of 2mm thickness.

INTRODUCTION

Recently, cellular mobile communication systems are spreading rapidly. In these systems, small size and high performance dielectric resonators are required. Currently most mobile telephones employ coaxial resonators with a Q-factor of approximately 280 at 1.9GHz. A typical size of such a resonator is 2.5x2.5x5.0mm causing the minimum size of a two pole band-pass filter to be greater than 2.5x5.0x5.0mm. A technological objective for the realization of small sized devices has been the proposed use of tri-plate structures with a high Q co-fired inner conductor. A development of a very high Q tri-plate resonator by a new conductor forming process is reported in this paper.

Q-FACTOR ANALYSIS OF TRI-PLATE RESONATOR

As a first step the theoretical Q of a quarter wavelength tri-plate resonator was calculated over the frequency range 1-5 GHz according to the incremental inductance rule.⁽¹⁾ The cross-section of a tri-plate resonator, shown in Fig.1, illustrates an inner conductor sandwiched by the dielectric layers. Top and bottom surfaces are shielded by ground conductors.

The Q of the tri-plate resonator is expressed as follows.

To the extent authorized under the laws of the United States of America, all copyright interests in this publication are the property of The American Ceramic Society. Any duplication, reproduction, or republication of this publication or any part thereof, without the express written consent of The American Ceramic Society or fee paid to the Copyright Clearance Center, is prohibited.

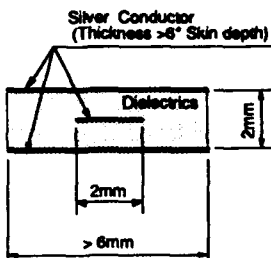


Fig. 1 Cross-section of resonator

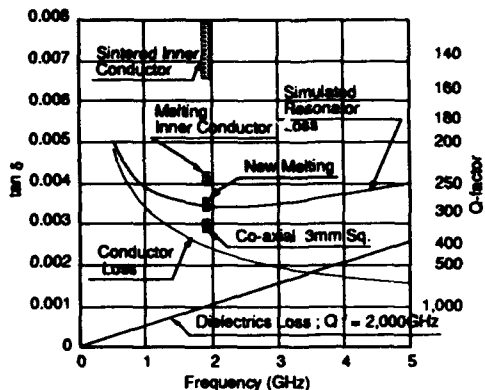


Fig. 2 Q-factor analysis

$(1/Q)$ Resonator = $(1/Q)$ Conductor + $(1/Q)$ Dielectrics ... (1)
 Q of the dielectric and conductor depend on frequency. Q of the conductor was calculated using the conductivity of bulk silver. A glass base material utilized in this simulation displayed a QF-product of 2000GHz, that is, the product of the material Q and its operating frequency in GHz is equal to 2000. The simulated Q of the resonator with dimensions given in Fig.1 is shown in Fig.2. This result shows that the maximum Q of the resonator, at 1.9GHz, is 300.

EXPERIMENTS

Resonator samples were made by green tape and thick film technology. Silver was selected as the inner conductor because of its high conductivity with respect to other metals. All of the tri-plate resonator samples were designed according to Fig.1 and the length adjusted to correspond to a quarter wavelength resonator at a specified frequency. The resonator Q was measured by a half power bandwidth method for a one port resonator.

MELTING CONDUCTOR METHOD

Improvements in resonator performance during this research are shown in Fig.3. At the outset we utilized conventional green tape and thick film technology using sintered inner conductors. These resonators had only half of the simulated Q value. A relatively small increase in Q was observed for an increase in sintering temperature up to the melting point of silver, abbreviated as m.p.. However, for samples sintered at the m.p. a remarkable increase of Q was observed. While the average Q was approximately 175, some of the samples had a Q greater than 190. This higher Q was considered to be related to the bulk like behavior of the melted inner silver conductor. Above the m.p., the average value of Q increased with the sintering temperature. More than half of the samples sintered at 1020°C had a Q higher than 200. Referring to Eq. (1), the contribution of the conductor to the measured Q of

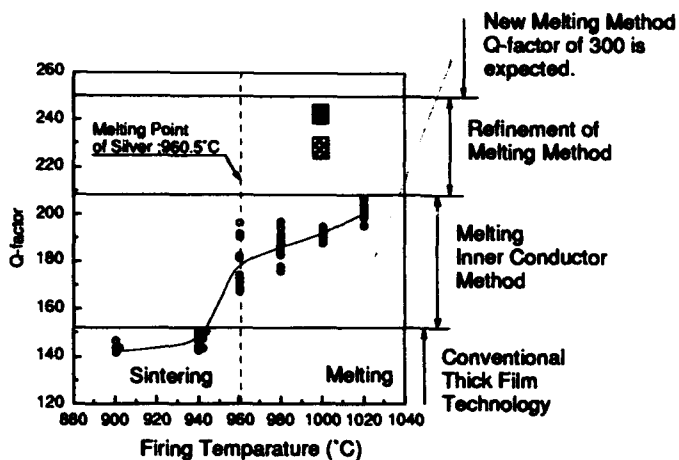


Fig. 3 Improvement of Q-factor by melting inner conductor method

200 was estimated to be 250 which was 60% of the simulated value of 400 in Fig.2. In order to refine this melting method, several material parameters for conductor paste were examined. Two important parameters were selected. The first was the size and the morphology of the silver powder and the second was inorganic additives. The metal content of the paste before the laminating process should be as high as possible, since, in the process of melting, the volume of the conductor is reduced. Thus, in the case of poor metal content paste, a certain number of voids will remain beyond the m.p. of the conductor causing disconnection or pinching of conductor. In a higher metal content paste, melted silver will fill the voids as if a bulk silver plate was inserted. It is apparent from Fig.4a that only the paste made from large silver particles displays both higher Q and smaller Q variation between samples.

The amount of inorganic additives had to be reduced since most of them in-

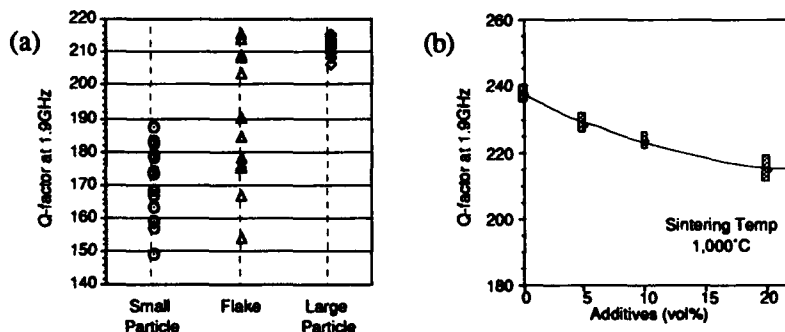


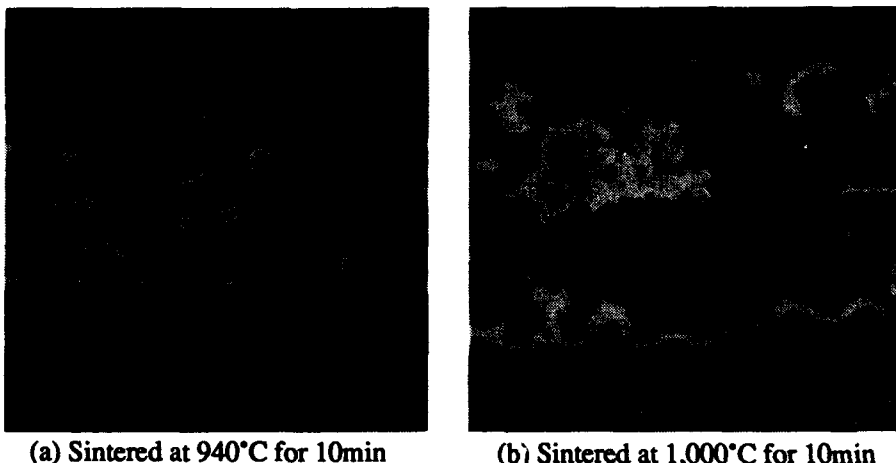
Fig. 4 Effect of conductor paste on Q-factor

(a) Particle size and shape (b) Additives

creased the resistivity of the conductor. Some additives increase the wettability of melted silver to dielectrics, and then they are expected to decrease the voids. In spite of this advantage, it was necessary to minimize the additive content. Fig.4b clearly shows that the Q increased with decreasing the additives.

With the refinements of the paste parameters mentioned above, the best characterized Q of the resonator was 240. This means that the Q of the conductor was about 300 corresponding to 75% of the simulated value of 400.

Fig.5 is SEM photograph of the etched conductors. For the conductors sintered below the m.p., grain boundaries remained within silver. When the sintering tem-



(a) Sintered at 940°C for 10min

(b) Sintered at 1,000°C for 10min

Fig.5 Etched conductors below and above the melting point of Silver

perature was increased above the m.p., no grain boundaries were observed. Although both conductors seemed to be sintered densely, only the conductors sintered above the m.p. of silver have shown higher Q . Thus, we concluded that the grain boundary is one of the most important causes of resistivity at higher frequencies.

The maximum conductor Q of 300 was achieved applying the melting method. The deviation from the theoretical value of 400 could be caused by the morphology of the melted inner conductor surface. Although the origin of the Q reduction was recognised, further refinement of the conductor surface was thought to be difficult.

EXTENSION FOR CONVENTIONAL MICROWAVE DIELECTRICS

Equation (1) indicates that a higher Q resonator can also be achieved with an increase of dielectric Q . Some extensions of this melting method to conventional microwave materials have been carried out. There are many high Q_F materials in conventional microwave dielectrics. Unfortunately, the sintering temperature of these dielectrics are much higher than the melting point of silver. In the sintering process for glass based materials the dielectrics are sintered before the melting of the conductor. Thus, melted silver will not penetrate into the dielectrics. The poor

wettability of melted silver for ceramics would not bring about the penetration of silver into the ceramics, which would be a serious problem if it occurred.

Fig.6a is SEM photograph of the inner conductor sintered at 1320°C. This dielectric composition was in the Ba-Nd-Bi-Ti system with $\epsilon=93$, QF=4000GHz. Although the dielectric started to sinter above 1150°C, melted silver did not penetrate into the dielectrics. The X-ray analysis, however, indicated the diffusion of silver as shown in Fig.6b. The X-ray count from the silver conductor was 12,000c/s, the silver concentration in the dielectrics close to the inner conductor was estimated to be 2.5wt%. This value suggests that a significant migration of silver under a high DC electric field will be observed in a lumped circuit element which would decrease the reliability of the element. However, in the case of distributed circuits element, such as a tri-plate, a grounded inner conductor will prevent the occurrence of DC field and there will be no migration. For the specific application of this method to a distributed circuit element, the diffusion of the silver would not be a serious problem. The calculated conductor Q of this resonator was 302 which is consistent with the Q obtained with the glass base materials.

Fig.7 is the relative dielectric constant vs. QF map of conventional microwave dielectrics. Very high QF materials up to 300,000GHz are known. By using mate-

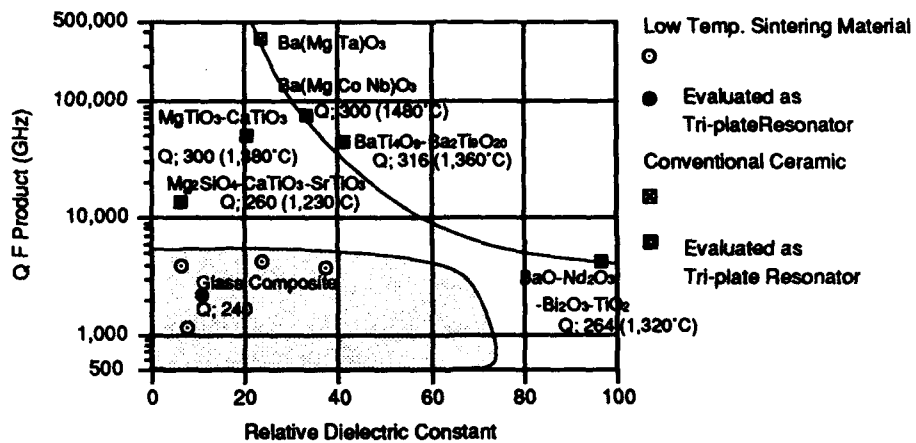


Fig. 7 Q-factor of tri-plate resonator with conventional dielectrics

rials having QF value higher than 10,000GHz, the contribution of dielectric loss will be almost negligible. Thus, the Q of tri-plate resonators with high QF materials of around 300 to 316 indicates that the Q values were defined only by the contribution of the conductor Q itself. A level of silver diffusion was observed in all materials, however, the concentration of silver near the conductor was at a much lower level than that of Fig.6b.

Sintering of Ba(Mg,Co,Nb)O₃ at 1480°C, which is 500°C higher than the m.p. of silver, has shown that the concentration of silver at the metal-ceramics interface was only 1/10 that in Fig.6b. This difference may depend on the dielectric composition, since the absence of bismuth in the later compositions may be a key factor.



(a) Etched conductor



1mm

(b) X-ray line analysis of Silver

Fig. 6 SEM image and characteristic X-ray analysis of conductor

APPLICATIONS

Some successful applications of the melting conductor method are presented in Fig.8a and 8b. By employing high Q resonators, a low insertion loss band-pass filter and very low consumption current VCO has been developed. Further development in refining this method will lead to enhanced performance and miniaturized microwave devices.

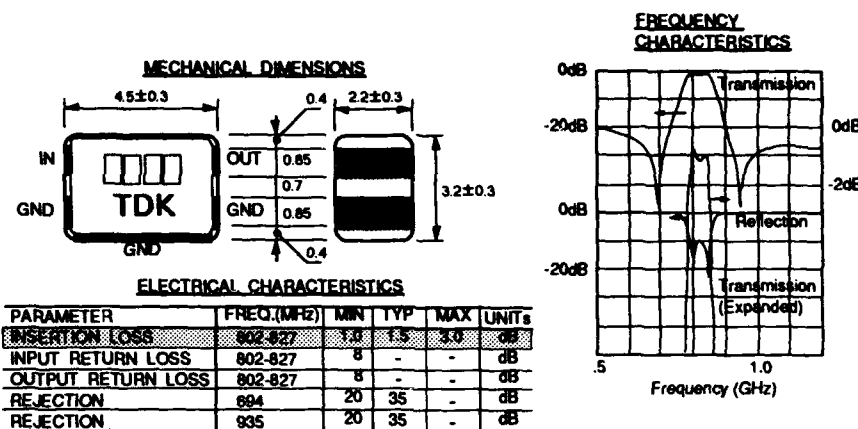


Fig. 8a Application of this method to a band-pass filter

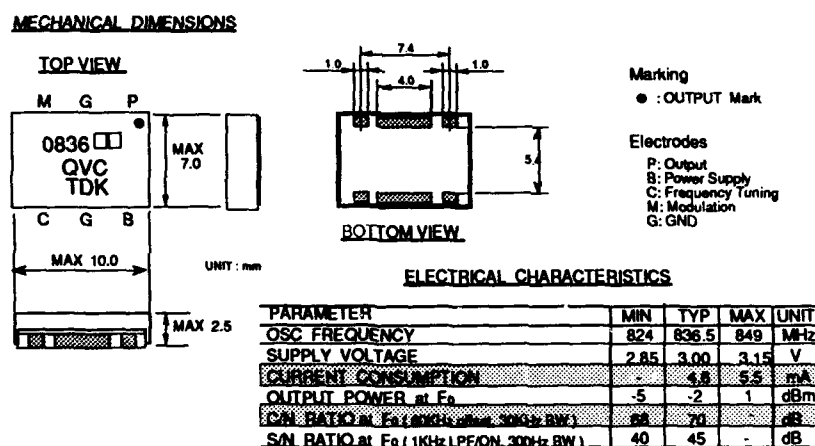


Fig. 8b Application of this method to a multilayer VCO

CONCLUSION

A series of firing temperatures from 900 to 1480°C were examined neglecting the melting point of silver. Resonators sintered at higher temperature than the silver melting point displayed higher Q-factor approaching that of the theoretical value. A maximum Q-factor of 316 was obtained using dielectric material of 2mm in thickness.

A microstructure observation by SEM showed that the bulk material like structure of the inner conductor was responsible for the higher Q-factor. A low loss band-pass filter and a low consumption current VCO, with a high C/N ratio, have been developed by employing a resonator fabricated by this method. A wide variety of applications of this method are expected in the development of low loss multi-layered integrated circuits.

ACKNOWLEDGMENT

The authors gratefully acknowledge Mr.T.Miura and Mr.T.Takahashi for their helpful discussions and microwave measurements. The authors also thank Mr.S.Nakai and Mr.H.Ninomiya for designing and preparing the devices.

REFERENCE

- (1) R.K.Hoffmann: *Handbook of Microwave Integrated Circuits*, Artech House, New York, 1983.

SINTERING AND MICROSTRUCTURE OF $\text{Sr}_{0.6}\text{Ba}_{0.4}\text{Nb}_2\text{O}_6$ CERAMICS

Junichi TAKAHASHI, Shiro NISHIWAKI and Kohei KODAIRA

Dept. of Applied Chemistry, Faculty of Engineering,
Hokkaido University, Kita-ku, Sapporo 060, JAPAN

ABSTRACT

Highly densified $\text{Sr}_{0.6}\text{Ba}_{0.4}\text{Nb}_2\text{O}_6$ (SBN:60) ceramics were fabricated by pressureless sintering above 1350°C. The grain growth was considerably inhibited for the SBN:60 samples sintered at 1350°C. Prolonged sintering at 1400°C drastically converted the microstructure of the sample from uniform and small-grained microstructure to coarse-grained and microcracked one. Duplex microstructure was also observed in the initial stage of abnormal grain growth. The temperature dependence of the dielectric constant for the SBN:60 ceramics was affected not only by microstructure inhomogeneity but also by lattice strain induced from compositional fluctuation in the solid solution.

INTRODUCTION

As has been extensively studied for BaTiO_3 ceramics[1-5], microstructure developed during sintering essentially affects the resulting dielectric properties of the product. It is, therefore, necessary to fully understand the relationship between the microstructure and ferroelectric properties for a selected material, and to establish the optimum procedure for obtaining a ferroelectric with the desired property.

$\text{Sr}_{1-x}\text{Ba}_x\text{Nb}_2\text{O}_6$ ($0.25 < x < 0.75$; SBN:x) is a ferroelectric with tungsten bronze structure. A limited number of studies have been done for the fabrication of the SBN ceramics[6-9], comparing with the SBN single crystals. Particularly, little is known on microstructure evolution during sintering and the resulting dielectric property change for the SBN ceramics. The purpose of this study is to elucidate the densification behavior and closely associated microstructure development of the SBN:60

To the extent authorized under the laws of the United States of America, all copyright interests in this publication are the property of The American Ceramic Society. Any duplication, reproduction, or republication of this publication or any part thereof, without the express written consent of The American Ceramic Society or fee paid to the Copyright Clearance Center, is prohibited.

ceramics. Furthermore, variations in the temperature dependence of the dielectric constant for the SBN:60 samples are correlated with the microstructure evolution and lattice strain involved.

EXPERIMENTAL PROCEDURE

Starting powders for sintering were prepared by mechanical mixing of Nb_2O_5 and carbonates of Sr and Ba(purity;99.9%). The mixed powders were calcined at 1000°–1300°C for 6h followed by grinding with satellite mill. The pressureless sintering of green compacts(CIPped at 100MPa) was conducted in air under various conditions. The density of a sintered product was measured by Archimedes method. X-ray powder diffractometry(Rigaku RINT2000) was used for phase identification, the calculation of lattice parameter at room and elevated temperatures and the estimation of lattice strain. The microstructure of the thermally etched surface was observed with SEM(JEOL JSM-35CF). The dielectric constant of the sintered sample was measured using a digital LCR meter(YHP 4274A) as a function of temperature.

RESULTS AND DISCUSSION

Microstructure evolution during sintering

Figure 1 shows the densification behavior of SBN:60 ceramics. Densified body with more than 95% of theoretical density can be obtained by heating above 1350°C. Isothermal density changes at 1350°C are indicated in Fig.2 as a function of sintering time.(It also includes some data obtained at 1400°C.) Rapid densification occurs in an initial period of the sintering and the densification of SBN:60 is almost completed after heating for 2h. Typical microstructure of the sintered SBN:60 samples is shown in Fig.3. Average grain sizes of those samples are estimated to be $\sim 8\mu\text{m}$ and $\sim 11\mu\text{m}$ for the (A) and (B) sample, respectively. The grain growth rate at 1350°C is considerably low and can be expressed by $D^s - D_0^s = Kt$, where D is the instantaneous diameter of the grains, D_0 the diameter at $t=0$, and K is constant. For the sample calcined at 1000°C, the uniform microstructure was drastically changed after heating for 24h.(Closed circles in Figs.1 and 2 show the occurrence of abnormal grain growth in the sintered sample.) More pronounced change in microstructure can be observed in sintering at 1400°C. As shown in Fig.2, heating at 1400°C for 2h results in the production of almost fully densified sample with uniform microstructure.

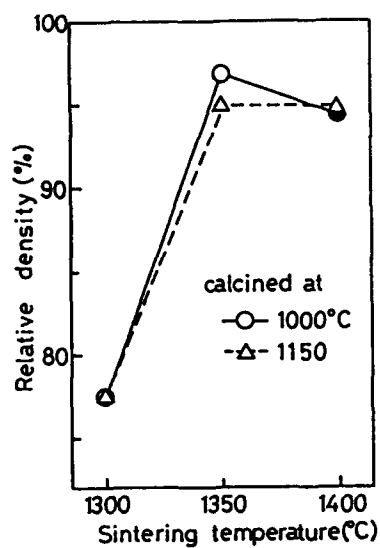


Fig.1 Density change of SBN:60 with sintering temperature(4h).

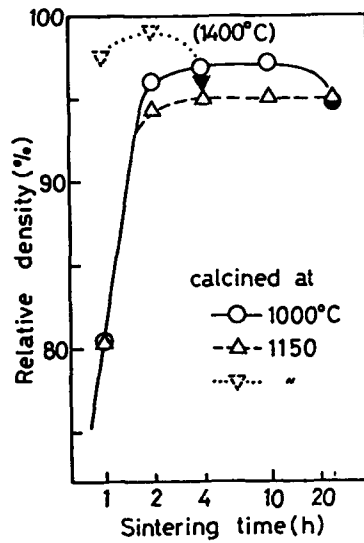


Fig.2 Isothermal densification behavior of SBN:60 at 1350°C.

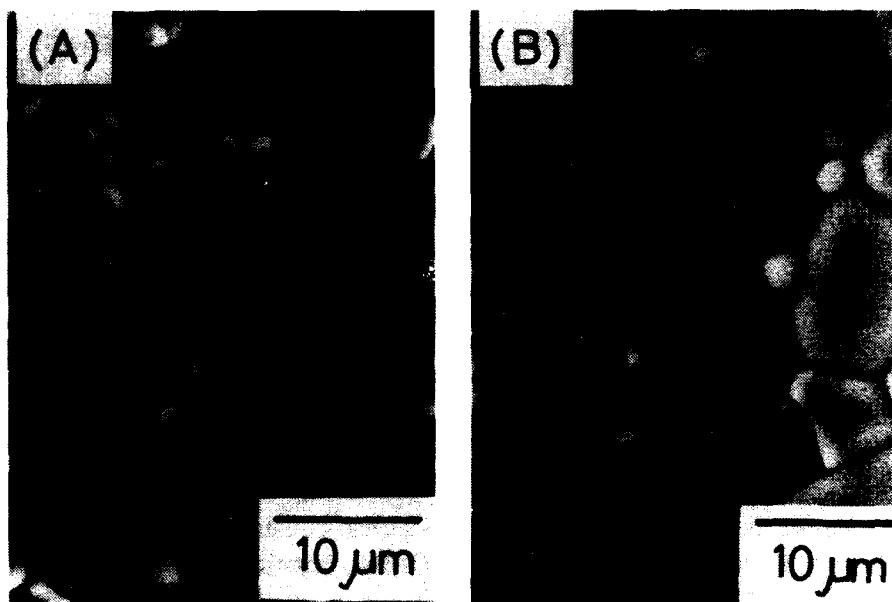


Fig.3 Microstructure of SBN:60 samples sintered at 1350°C for (A)4h and (B)24h(calcined at 1150°C).

Prolonged heating at 1400°C, however, converted the small-grained sample to that consisting of very largely grown grains with a number of microcracks via duplex microstructure. Figure 4 shows duplex structure observed in the SBN:60 sample sintered at 1400°C for 4h. Huge grains with pores entrapped inside the grains are embedded in a small-grained matrix. This kind of microstructure suggests that rapid grain growth such as coalescence initiates at very localized region and propagates fast through the sample. Gazza[10] explained the duplex structure observed in hot-pressing of LiAl_5O_8 as microstructure resulting from liquid-phase sintering produced by a residual inhomogeneous impurity distribution. In fact, the close relationship between duplex structure and the formation of liquid phase is confirmed in the present $\text{SrO}-\text{BaO}-\text{Nb}_2\text{O}_5$ system. Figure 5 shows the microstructure of samples which have compositions deviating from stoichiometry ($(\text{Sr}_{0.6}\text{Ba}_{0.4})\text{O}:\text{Nb}_2\text{O}_5=0.48:0.52$ and $0.53:0.47$ for the A- and B-composition, respectively) and were sintered at 1350°C for 4h. A phase diagram of the system $\text{SrO}-\text{BaO}-\text{Nb}_2\text{O}_5$ indicates the liquid phase formation at 1320°C for the A-composition. As expected, a similar duplex structure to that of Fig.4 can be seen in the microstructure of the A-composition.(Fig.5(A))

There is another evidence indicating that local inhomogeneity in composition might be responsible for duplex structure. Table 1 shows the phase(s) present in calcined powders and also the results of microstructure change with sintering time at 1400°C. It is found that a decrease in calcining temperature causes an appearance of duplex structure in a shorter period of sintering time. Because the powders calcined at 1000° and 1150°C are mixed-phase, they have much opportunity to yield local inhomogeneity in the composition on sintering. Probably, after the SBN:60 solid solution is formed with a simultaneous progress of sintering, a small amount of liquid phase which is derived from residual inhomogeneity in the composition and localized at some grain boundaries would cause inhomogeneous grain growth.

Variations in the temperature dependence of the dielectric constant

Figure 6 reveals changes in the dielectric constant accompanied with ferroelectric phase transition for the SBN:60 ceramics sintered at 1400°C. A small-grained sample with 99% of theoretical density(sample-S) has a maximum dielectric constant of about 4000 at $T_c=67^\circ\text{C}$. On the contrary, the samples having duplex structure(sample-D) and those consisting of abnormally grown grains(sample-L) exhibit substantially

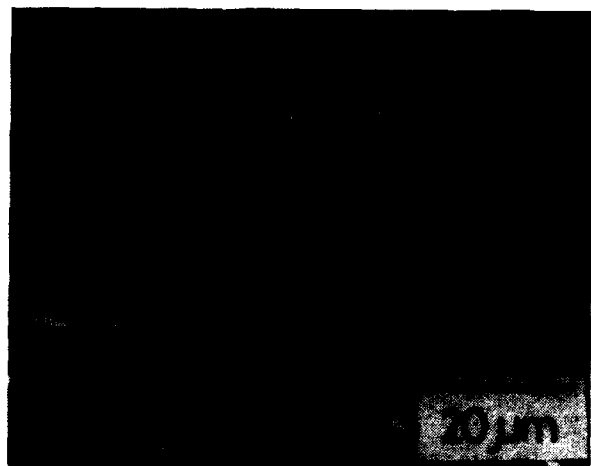


Fig.4 Duplex microstructure observed in the sample sintered at 1400°C for 4h.

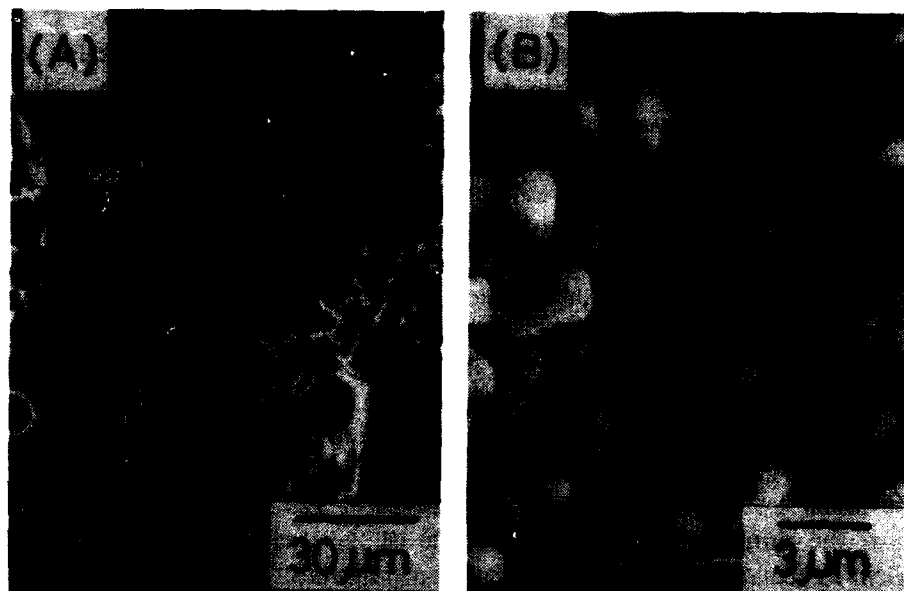


Fig.5 Microstructure of the ceramics with the composition of (A)(Sr0.6 Ba0.4)O:Nb2O5=0.48:0.52 and (B)0.53:0.47.

Table 1. Phase(s) present after calcining and microstructure development after sintering at 1400°C.

Calcining temperature(°C)	Phase(s)	Sintering at 1400°C			
		2h	4h	10h	24h
1000	SN>>SBN	N	DP	AB	-
1150	SBN>SN	N	N	DP	AB
1300	SBN	N	N	N	AB

SN;SrNb₂O₆ s.s. SBN;Sr_{0.6}Ba_{0.4}Nb₂O₆
 N;normal growth DP;duplex structure AB;abnormal growth

dielectric constant of the system. Information on the presence or absence of the second phase(s) on the grain boundary is required for further discussion.

Figures 7 and 8 show the effect of lattice strain accommodated inside the grains on the dielectric anomaly peak. Peak profiles of the samples which were calcined at 1000°C and then sintered at 1350°C for different duration, i.e., 2h and 10h, are given in Fig.7. A broadened and somewhat suppressed peak is for the sample sintered for 2h. Both samples have nearly the same micro-structure. Then an attempt to evaluate the lattice strain which might be induced from incompleteness in the formation of the solid solution was made for the samples calcined at 1000°C. In fig.8, $\beta \cos \theta$ is plotted against $\sin \theta$ where β is the line broadening of the specified X-ray diffraction peak at the Bragg angle θ (radians). Maximum error in calculating $\beta \cos \theta$ was estimated to be $\pm 0.2 \times 10^{-3}$. Obviously, those samples include different amounts of the lattice strain, although their crystallite sizes converge on the fixed value. As the sintering proceeds, the lattice strain due to the variation of the interplanar d spacing about its average value is lowered (indicated by decreasing gradient of the lines). The sample calcined at 1300°C for 6h has much less strain so that those sintered at 1350°C for 4h and 24h show the same temperature dependence of the dielectric constant. Thus calcining conditions are also one of the important processing parameters for fabricating the SBN:60 ceramics.

CONCLUSIONS

The SBN:60 ceramics were fabricated by pressureless sintering under various conditions. The densification of the ceramics became accelerated

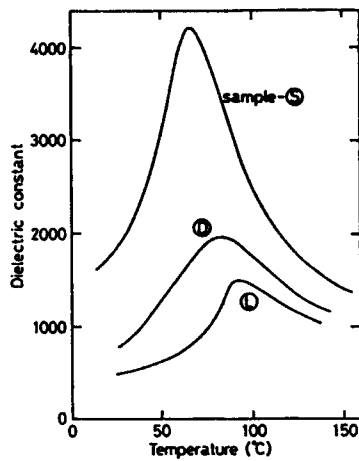


Fig.6 Temperature dependence of the dielectric constant for SBN:60.

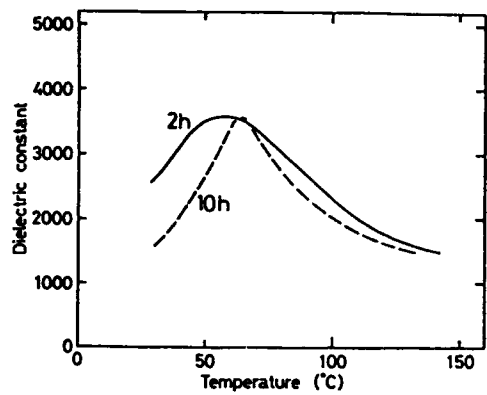


Fig.7 Dielectric anomaly peaks of the samples sintered at 1350°C.

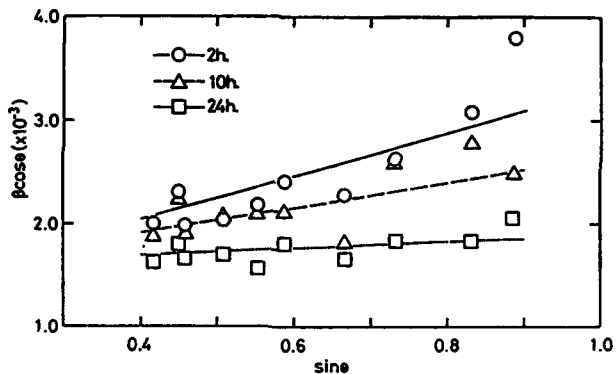


Fig.8 Estimation of lattice strain for SBN:60 samples sintered at 1350°C for different times.

by sintering above 1350°C, and a highly densified body with ~99% of theoretical density and uniform microstructure was produced by sintering at 1400°C for 2h. The microstructure evolution during sintering was strongly dependent on sintering temperature. Prolonged heating at 1400°C converted the sample with uniform microstructure to that consisting of abnormally grown grains and a number of microcracks, whereas the grain growth was considerably inhibited in the sintering at 1350°C. Duplex microstructure appeared in the initial stage of the abnormal grain growth.

The substantial lowering in the dielectric maximum at Curie temperature observed in the coarse-grained sample could be closely related to microcracking in the sample. Because lattice strain induced from the compositional fluctuation in the solid solution also affects the dielectric anomaly peak, an optimum calcining-sintering condition has to be selected to fabricate the SBN:60 ceramic with uniform microstructure and no compositional fluctuation.

ACKNOWLEDGMENTS

The authors wish to thank Y.Takano and T.Fujii for their experimental assistance. This work was partially supported by Tokuyama Science Foundation.

REFERENCES

- [1] G.H.Jonker and W.Noorlander, *Science of Ceramics 1*, ed. by G.H. Stewart, Academic Press, London(1962).
- [2] N.C.Sharma and E.R.McCartney, The Dielectric Properties of Pure Barium Titanate as a Function of Grain Size, *J.Austr.Ceram.Soc.*, **10**, 16-20 (1974).
- [3] G.Arlt, D.Hennings and G.deWith, Dielectric Properties of Fine-Grained Barium Titanate Ceramics, *J.Appl.Phys.*, **58**, 1619-25(1985).
- [4] A.J.Bell, A.J.Moulson and L.E.Cross, The Effect of Grain Size on the Permittivity of BaTiO_3 , *Ferroelectrics*, **54**, 487-90(1984).
- [5] Y.H.Hu, H.M.Chan, X.W.Zhang and M.P.Harmer, Scanning Electron Microscopy and Transmission Electron Microscopy Study of Ferroelectric Domains in Doped BaTiO_3 , *J.Amer.Ceram.Soc.*, **69**, 594-602(1986).
- [6] K.Nagata, Y.Yamamoto, H.Igarashi and K.Okazaki, Properties of the Hot-pressed Strontium Barium Niobate Ceramics, *Ferroelectrics*, **38**, 853-56(1981).
- [7] A.Watanabe, H.Haneda, S.Matsuda and H.Yamamura, Preparation of the Translucent $\text{Sr}_{1-x}\text{Ba}_x\text{Nb}_2\text{O}_6$ Ceramics, *Ceramic Transactions*, **1**, 926-31 (1988).
- [8] N.S.VanDamme, A.E.Sutherland, L.Jones, K.Bridger and S.R.Winzer, Fabrication of Optically Transparent and Electrooptic Strontium Barium Niobate Ceramics, *J.Amer.Ceram.Soc.*, **74**, 1785-92(1991).
- [9] S.B.Deshpande, H.S.Potdar, P.D.Godbole and S.K.Date, Preparation and Ferroelectric Properties of SBN:50 Ceramics, *J.Amer.Ceram.Soc.*, **75**, 2581-85(1992).
- [10] G.E.Gazza, Hot-pressing of LiAl_5O_8 , *J.Amer.Ceram.Soc.*, **55**, 172-3(1972).
- [11] T.Ota, J.Takahashi and I.Yamai, "Effect of Microstructure on the Dielectric Property of Ceramics," in *Electronic Ceramic Materials*, ed. by J.Nowotny, Trans Tech Pub., Switzerland, (1992)pp.185-246.

Interfacial Phenomena and Dielectric Properties of $Pb(Mg_{1/3}Nb_{2/3})O_3$ Ceramics with Excess PbO

K. H. Yoon, Y. S. Cho, D. H. Lee and D. H. Kang*
*Department of Ceramic Engineering, Yonsei University
Seoul 120-749, Korea*

Interfacial phenomena and dielectric properties of lead magnesium niobate ceramics have been studied as a function of excess PbO. With the addition of excess PbO up to 3 mol%, dielectric constant for the specimens sintered at 900°C increases due to increase in density and grain size by liquid phase sintering. Further additions of excess PbO bring PMN grains to rounded ones to reduce the interfacial energy, resulting in lower densities and inferior dielectric constant. These results can be attributed to the formation of PbO rich phases and Pb precipitates in the grain boundary regions.

INTRODUCTION

Generally, it has been known that for dielectrics, discontinuities, pore and inclusions will perturb cooperative long range ordering processes and hinder the development of dielectric displacements[1]. Also a grain size dependence of the dielectric constant of $BaTiO_3$ -related capacitors has been reported in terms of the internal stress generated at grain boundaries[2]. For $Pb(Mg_{1/3}Nb_{2/3})O_3$ (PMN) ceramics, the increase in dielectric constant with increasing grain size was explained mainly by the reduction of grain boundaries with lower permittivity[3]. Especially, as the beneficial effect of excess MgO or excess PbO on preparation and dielectric properties of PMN ceramics were widely investigated, microstructural features such as precipitates and solid second phase due to excess

* *Department of Electronic Materials Engineering, The University of Suwon,
Suwon 445-743, Korea*

To the extent authorized under the laws of the United States of America, all copyright interests in this publication are the property of The American Ceramic Society. Any duplication, reproduction, or republication of this publication or any part thereof, without the express written consent of The American Ceramic Society or fee paid to the Copyright Clearance Center, is prohibited.

MgO and PbO comprising either glossy or crystalline materials should be frequently associated with grain boundary which serves to emphasize the isolation of grains from one another[4]. Chen et al suggested that the pyrochlore phase had a minimal direct effect on the dielectric constant and the degradation of it may have been due to the presence of the semi-continuous secondary grain boundary phases[5]. In this study, dependence of PMN microstructure on excess PbO addition was investigated and especially, the grain boundary thickening effect on the dielectric properties was discussed.

EXPERIMENTAL PROCEDURE

Lead magnesium niobate powders were prepared by molten salt synthesis (MSS). Reagent grade oxides, PbO, MgO and Nb₂O₅, were altogether mixed with 0.635Li₂SO₄-0.365Na₂SO₄. The ratio of salt weight to raw materials weight was 0.5. It was determined experimentally as an optimum ratio in that with this ratio a maximum perovskite phase was formed in the range of 600°C to 850°C. The different amounts of excess PbO ranging from 0 mol% to 10 mol % were added before mixing. After milling with zirconia balls for 15h, the slurry was dried at 120°C to remove alcohol. The dried powders were fired in covered alumina crucibles at temperatures from 600°C to 850°C for 2h. Sulfates were then removed by washing with deionized water several times until no free SO₄²⁻ions were detected using a barium nitrate solution. The powders were finally dried at 120°C. After adding a 1.5 wt % polyvinyl alcohol (PVA) binder, the powders were pressed into disks at 1500 kg/cm². The pellets were buried in powders of the same composition to minimize PbO volatility and sintered in air at 900°C for 4h with a heating rate of 300°C/h. The fracture surfaces of specimens were examined by SEM (Scanning Electron Microscopy, DS-130, Akashi Co., Japan) equipped with an energy dispersive X-ray analyzer, and further analyzed by TEM (Transmission Electron Microscopy, CM-20, Philips, Netherlands). For dielectric measurements, specimens were polished with alumina powder (3μm) and then heat-treated at 750°C after electrodeing with silver paste (4102, Ferro Co., U.S.A). Dielectric constant and tan δ were measured at 1 kHz using an LCR meter (AG4303, ANDO Co., Japan) with a cooling rate of 2°C/min from 100°C to -80°C.

RESULTS AND DISCUSSION

Table 1 shows the effect of excess PbO contents on relative density (%), perovskite phase and maximum dielectric constant for the specimens sintered at 900°C for 4h. Compared to about 78.6% of the theoretical density for the specimens sintered at 900°C for 4h without excess PbO, about 97% with 3 mol% excess PbO was obtained. The apparent decrease in relative density and perovskite phase content were accompanied by the further addition of excess PbO. These trends could be identified by observing the microstructure of the fracture surfaces of specimens as shown in Fig. 1. The specimens containing excess PbO showed a dense microstructure with enlarged grains compared to those of no excess PbO added specimens at the same temperature. This observation disagrees with the study of Wang et al[6]. They reported that the grain size of the PMN ceramics sintered at 1200°C for 4h in the precalcined columbite method hardly increased by the addition of excess PbO. They explained the opposite observation was due to the difference in processing methods, i.e., calcining of mixed oxides method and columbite method. In fact, it should be considered the different sintering temperature as well as the different methods. At a low temperature of 900°C, excess PbO as a sintering aid increased grain size and density. While at 1200°C, it may bring no significant effect on grain size and density because 1200°C is near the saturation temperature.

Table 1. Characteristics of PMN ceramics sintered at 900°C, 4hr as a function of excess PbO.

PMN Composition	Relative Density	Perovskite Phase	Maximum K
pure PMN	78.6%	96%	4700
3 mol% excess PbO	97%	97%	15000
5 mol% excess PbO	95%	97%	12000
10 mol% excess PbO	90.9%	95%	8700

However, with further additions of excess PbO, PMN grains were changed to rounded ones to reduce interfacial energy between liquid and solid phase, due to the presence of much PbO liquid phase, resulting in separating PMN grains having smaller size as shown in Fig. 1 (D).

Energy dispersive spectroscopy (EDS) spectra for excess PbO-PMN specimens were studied to investigate compositional differences as shown in Fig. 2. Any difference in Pb/Nb intensity ratios between grain and grain boundary region was not observed for specimens with 3 mol% excess PbO. However, with further additions of excess PbO, these ratios became different. Furthermore, another precipitate was observed for the 10 mol% excess PbO PMN specimens. According to the EDS analysis, the precipitate contains Pb along with traces of Mg and Nb, and is probably PbO formed during cooling.

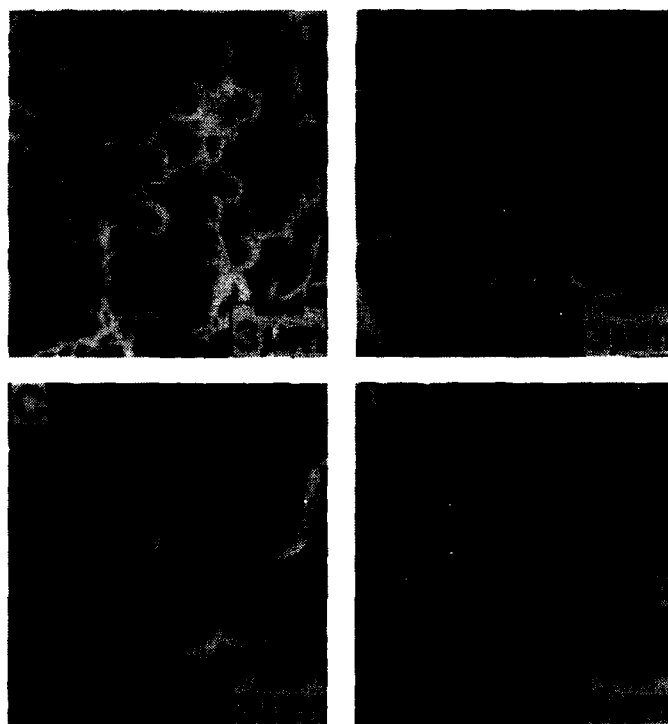


Fig. 1 SEM photographs for the fracture surfaces of (A) 0 mol% (B) 3 mol% (C) 5 mol% and (D) 10 mol% excess PbO-PMN sintered at 900°C for 4h.

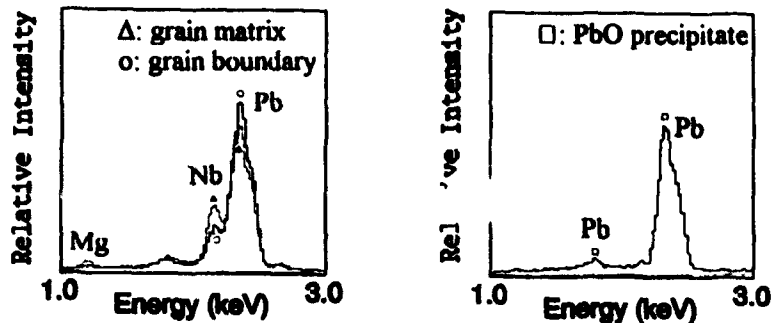


Fig. 2 EDS spectra for the 10 mol% excess PbO-PMN specimens sintered at 900°C for 4h. (Δ: grain matrix, o: grain boundary and □: PbO precipitate)

The addition of excess PbO influenced the dielectric properties of the PMN ceramics as shown in Table 1. When 3 mol% excess PbO added, the maximum dielectric constant increased significantly and reached about 15000 at 900°C. However, further addition of excess PbO led to the lowering of the maximum dielectric constant at the same sintering condition. These results indicate that an appropriate amount of excess PbO is necessary to optimize the dielectric properties of the ceramics. Especially, the increase in dielectric constant can be explained by the abrupt increases in grain size and density as reported by many investigators[3,4]. However, it's difficult to explain the difference of maximum dielectric constant between the 3 mol% excess PbO and 5 mol% excess PbO PMN specimens in terms of grain size, density and perovskite phase content due to their similar values as shown in Table 1 and Fig. 1. Therefore, one possible explanation is that intergranular phases are responsible.

Evaluation of dielectric constant as a function of grain boundary thickness were conducted using a simple series model and a logarithmic model for the mixing of high and low permittivity phases[1]. The results indicate that, for PMN ceramics, a series mixing model is more applicable and that other factors such as lattice impurities may be also important in dielectric property[5]. According to series mixing theory, the following equation can be applied:

$$D_s/K_s = D_g/K_g + D_{gb}/K_{gb} \quad (1)$$

where K_s is the dielectric constant of the sample, K_g the dielectric constant of the perovskite PMN grain, K_{gb} the dielectric constant of the PbO solid solution in the grain boundary, D_s the thickness of the sample, D_g the thickness of the PMN grains, and D_{gb} the thickness of the PbO grain boundary layers.

Compared to the temperature-independent K_{gb} of the PbO solid solution in the grain boundary, K_g of the PMN grain is temperature dependent. That temperature dependence can be calculated based on the compositional fluctuation model of Kirillov and Isupov[8]. Assuming $K \gg K_\infty$, the plot of the reciprocal dielectric constant($1/K$) versus $(T - T_0)^2$ as a function of excess PbO at 1 kHz are shown in Fig. 3. The nearly same slope for the given compositions indicates that the temperature dependence of the PMN grains is not changed by the excess PbO. It is suggested that the more excess PbO added, the thicker the grain boundary and the lower the dielectric constant. Assuming the K_g of the grains remains the same and is not changed by the excess PbO, the average thickness of the PbO layer can be estimated from Eq. (1), where K_{max} for PMN-STD and K_s for PMN with excess PbO. The K_{max} of 20000 for PMN-STD was used to calculate the PbO grain boundary layer in PMN ceramics[5,6]. If K_{gb} of 26 for PbO, and the grain sizes of 4 μm and 3.8 μm for PMN specimens with 3 mol % and 5 mol% excess PbO, respectively, are used in Eq.(1), the calculated thickness of the PbO layer is each 17.2 and 32 \AA . In fact, it was reported that despite of the stoichiometric PMN sintered at 1200°C, the grain boundaries did not contain very thin intergranular phases (10 to 20 \AA), undetected by TEM[5].

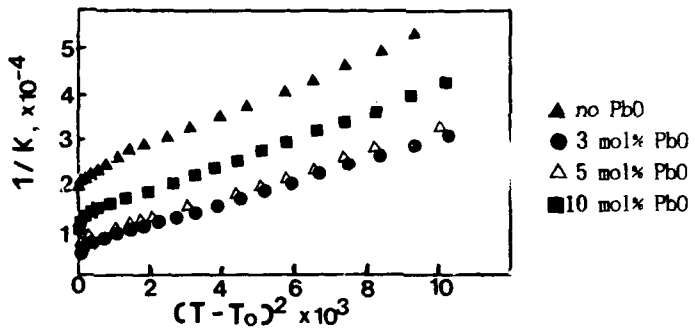


Fig. 3 $1/K$ vs. $(T - T_0)^2$ as a function of amount of excess PbO.

Also, for the 3 mol% excess PbO PMN, any intergranular phase was not detected by TEM analysis as shown in Fig. 4. Considering the thicker interlayer value of the 5 mol% excess PbO PMN, it can be thought that a degrading of the dielectric constant with 5 mol% excess PbO is related to the grain boundary thickening effect by PbO rich solid solution phase.

With further addition of excess PbO, the decrease of grain size was possibly related to the increase of boundary thickness, W , resulting in the decrease in grain boundary mobility, B , according to the following equations[8] :

$$B = (C_{gb}/kT) \cdot (\Omega/SW) \quad (2)$$

$$v = B \cdot F \quad (3)$$

where, C_{gb} is the grain boundary diffusion coefficient, Ω is the atomic volume, S is the boundary area, k is the Boltzman constant, F is the applied driving force and v is the boundary velocity. The decrease in grain boundary mobility brought a reduction in the boundary velocity and led to the inhibition of grain growth. Consequently, the increase of PbO-rich boundary thickness as well as the decrease of grain size resulted in the drastic decrease of dielectric constant for the 10 mol% excess-PbO PMN.

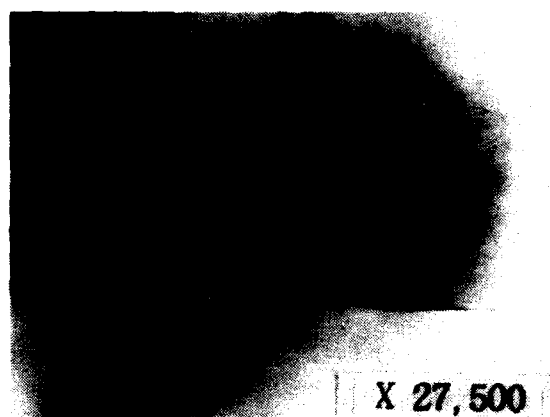


Fig. 4 TEM photographs of the 3 mol% excess PbO-PMN specimens.

CONCLUSION

With an addition of 3 mol% excess PbO in the MSS method, the PMN specimens sintered at 900°C for 4 hr, showing clean grain boundary and high density, had a dielectric constant of 15000 at 1 kHz. The further addition of excess PbO caused inferior sinterability and low dielectric constant. The resulting dielectric constant partially depended on the volume of intergranular phase with lower permittivity.

ACKNOWLEDGMENT

This work was supported by the Korea Science and Engineering Foundation.

REFERENCES

1. D. A. Payne and L. E. Cross, "Microstructure-Property Relations for Dielectric Ceramics," p.584-597 in Ceramic Microstructures '76, Edited by R. M. Fulrath and J. A. Pask, Westview Press, Boulder, CO, 1977.
2. W. R. Buessem, L. E. Cross, and A. K. Goswani, "Phenomenological Theory of High Permittivity in Fine-Grained Barium Titanate," *J. Am. Ceram. Soc.*, **49** (1) 33-36 (1966).
3. S. L. Swartz, T. R. Shrout, W. A. Schulze, and L. E. Cross, "Dielectric Properties of Lead-Magnesium Niobate Ceramics," *J. Am. Ceram. Soc.*, **76** (5) 311-315 (1984).
4. D. H. Kang and K. H. Yoon, "Dielectric Properties due to Excess PbO and MgO in Lead Magnesium Niobate Ceramics," *Ferroelectrics*, **87**, 255-264 (1988).
5. J. Chen, A. Gorton, H. M. Chan, and M. P. Harmer, "Effect of Powder Purity and Second Phases on the Dielectric Properties of Lead Magnesium Niobate Ceramics," *J. Am. Ceram. Soc.*, **69** (12) C303-C305 (1986).
6. H. C. Wang and W. A. Schulze, "The Role of Excess Magnesium Oxide or Lead Oxide in Determining the Microstructure and Properties of Lead Magnesium Niobate," *J. Am. Ceram. Soc.*, **73** (4) 825-832 (1990).
7. V. V. Kirillov and V. A. Isupor, "Relaxation Polarization of $Pb(Mg_{1/3}Nb_{2/3})O_3$ - A Ferroelectric with a Diffused Phase Transition," *Ferroelectrics*, **5**, 3-9 (1973).
8. W. D. Kingery, "Introduction to Ceramics," 2nd ed., p.452-486, John Wiley and Sons, New York, London, 1976.

CHARACTERIZATION OF BRIDGMAN CRYSTAL GROWTH USING RADIOGRAPHIC IMAGING

S.E. Sorokach*, R.T. Simchick*, A.L. Fripp, W.J. Debnam and P.G. Barber**
NASA Langley Research Center
Hampton, VA 23681

An x-ray imaging system was used to observe the melt-solid interface of semiconductor crystals during growth in a Bridgman furnace. X-rays penetrate the furnace and the crystal to reveal the shape and position of the interface as it grows. This technique has been verified using thermocouple temperature measurements. The two techniques will be compared and some of the inherent problems of thermocouple measurements will be discussed.

INTRODUCTION

It is well known to crystal growers that the shape of the solid-liquid interface and its position in the furnace affect the quality of the crystal. Semiconductor crystals grown in a vertical Bridgman furnace can undergo thermal stress caused by a non-flat interface. This stress can result in the formation of dislocations, which conglomerate and produce low-angle grain boundaries instead of the desired single crystal [1]. Therefore several methods have been used to characterize the shape and position of the interface.

One method used x-rays to penetrate the furnace and the crystal [2], but each image during the growth took about eight minutes to develop and needed image enhancement. However this method gave both interface position and shape. Another method involved taking a partially grown crystal and quenching it in water, which gave only one interface shape per run and was destructive to the crystal [3]. The Peltier pulsing technique [4] involved passing current through the sample during growth, which produced demarcation

*Lockheed Engineering and Sciences Co., Hampton, VA 23666

**Longwood College, Farmville, VA 23901

To the extent authorized under the laws of the United States of America, all copyright interests in this publication are the property of The American Ceramic Society. Any duplication, reproduction, or republication of this publication or any part thereof, without the express written consent of The American Ceramic Society or fee paid to the Copyright Clearance Center, is prohibited.

lines for each pulse. This procedure is very time consuming since the crystal has to be cut, polished and etched in order to see the lines, and the results are not always predictable. Also, the position of the interface within the furnace at each mark is not known. Ejim, Jesser and Fripp [5] used a technique which will be called "discontinuity in slope" to determine the position of the interface. They used a quartz tube with a capillary in the center which allowed them to run a thermocouple through the crystal. The temperature plotted versus distance gives a change (discontinuity) in slope at the solid-liquid interface. This method gives the position of the interface but not the shape, and it assumes a perfect thermocouple.

The newest method [6] uses x-rays or gamma-rays to penetrate the furnace and crystal and sends the image to a real time imaging system, which then sends the image to an image processor where it is seen on a standard television screen. This method gives both interface position and shape in realtime without disturbing or destroying the crystal. A schematic diagram of the realtime imaging system is shown in Fig. 1. The difference in densities between the solid and liquid phases shows up as a difference in image intensity. This system allows for the visual radiographic interface using the x-ray imaging system position to be compared to the position obtained by the discontinuity in slope, which will be referred to as the "thermal interface." The discontinuity is caused by the difference in thermal conductivity between the solid and liquid phases, which produces a change in temperature gradient. This paper will describe the x-ray imaging system, verify the ability to measure interface shape and position realtime, and compare the radiographic interface position to the thermal interface.

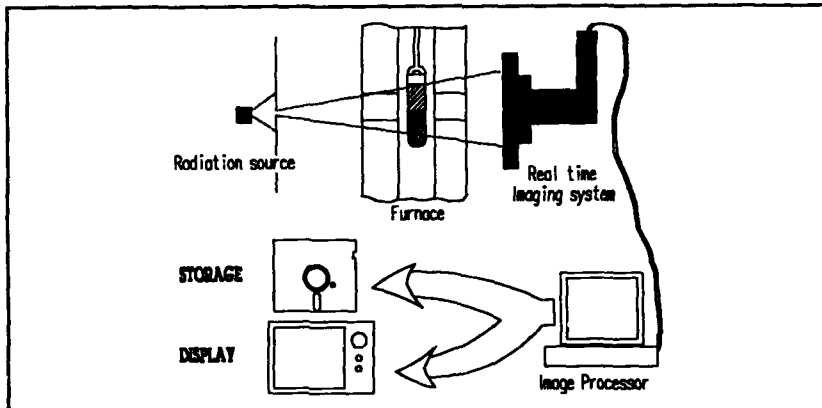


Figure 1. Realtime Imaging System.

EXPERIMENTAL PROCEDURE

The furnace used for the crystal growth experiments was a typical vertical Bridgman furnace as shown in Fig. 2. The top heater block is referred to as the hot zone and was heated to about 1000°C. The bottom heater is referred to as the cold zone and was heated to 600-800°C. The insulation zone was a block of compressed silica fiber which is transparent to the radiation used in these experiments. Isothermal liners are placed inside each zone to help keep the temperature uniform and to control the gradient between zones. The crystal material, either germanium or lead tin telluride, was heated in the hot zone to above its melting temperature and allowed to stabilize. The sample was then slowly translated into the gradient region (insulation zone) where the material solidified.

Two types of fused silica tubes were used to grow the crystals. The first tests used a standard tube as seen in Fig. 3a. Other tests were run with a tube that had a capillary at its center, such that thermocouples could be inserted into it and moved independently of the tube. This tube is illustrated in Fig. 3b. In both sets of tests the tubes were loaded with the material and vacuum pumped before sealing. Three 1 cm by 0.1 cm platinum rods spaced 1 cm apart were glued to the side of the tubes and used to indicate the position of the sample in the furnace. The placement of the platinum rods was based on a finished crystal of 6 cm long. Platinum sheathed type R thermocouples, 0.032" O.D. were used inside the capillary tubes. This type of thermocouple along with the platinum rods were chosen because platinum can be seen at the same x-ray intensity as the crystal material.

The experiments using the standard tubes began with the sample in the hot zone, either lead tin telluride (LTT) or germanium, where the material

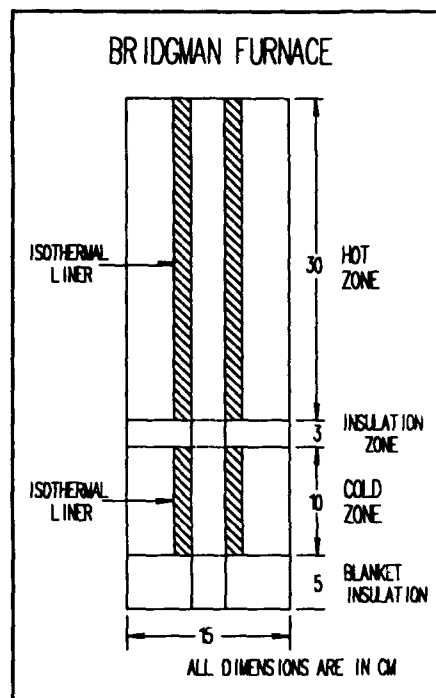


Figure 2. Crystal Growth Furnace

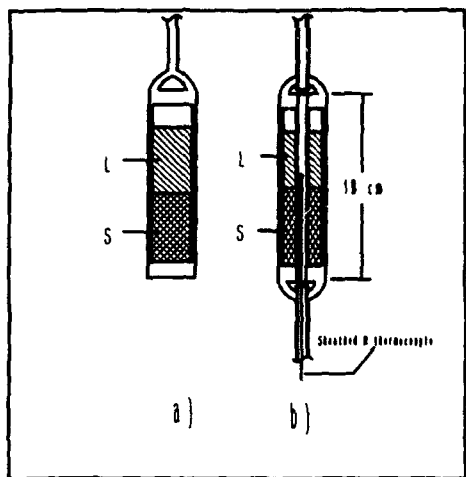


Figure 3. a) Standard Sample.
b). Capillary Sample.

melted and stabilized. X-rays were used with germanium and gamma rays were used with LTT, because stronger radiation was needed to penetrate the LTT material. The sample was then translated into the cold zone at 1 cm/hr until it solidified.

Data was recorded as follows. The images on the television monitor showing the interface shape and position were recorded at various times on floppy discs. These images could be recalled later and used for image enhancement. The images were also recorded on a VCR. Temperature data was taken on another computer using the Keithley Series 500 data acquisition system. The

position of the solid-liquid interface was determined vertically, with respect to a reference position in the insulation zone. Interface position was recorded by hand throughout the growth. If the interface was curved, the shape was obtained by measuring the position at various points.

The ability to measure interface shape as seen on the monitor was verified by using two different interpenetrating metal cylinders of different densities. A copper cylinder with a convex end was placed on top of a brass cylinder with a concave end. Both cylinders were machined to specific dimensions on each end. The set of cylinders was placed in the center of the insulation zone with the furnace at room temperature. Vertical position versus radial position data was taken with the x-ray imaging system, thus characterizing the shape of the copper and brass interface. Data was also taken with the interface moved both up 1 cm and down 1 cm from the center of the insulation zone. This procedure was repeated with the copper cylinder having a concave end on top of the brass having a convex end.

The realtime imaging system allowed the radiographic interface position to be compared to the thermal interface position using the capillary tube shown in Fig. 3b. Experiments were performed with germanium since it is a single element with a constant melt temperature of 937°C. The sample was moved into the cold zone such that half of it was solid and half liquid with the interface in the middle of the insulation zone. The sample was stationary throughout the test. Once the interface was established, the sheathed thermo-

couple was automatically moved to various positions across the interface region through the capillary. Thermocouple temperature and position data were recorded at each interval and plotted to obtain the thermal interface position. Two sets of data were taken with the sheathed thermocouple, one with the thermocouple exiting the hot zone and one with it exiting the cold zone. A long bare wire type R thermocouple was also run in the same crystal, with one end exiting the hot zone and the other exiting the cold zone. The thermal interface positions at the discontinuity in slope for the three sets of thermocouple data were compared. Previous measurements [7] with the thermocouple exiting the bottom have shown that thermal conductivity down the sheathed thermocouple would affect the measurements obtained from this method.

RESULTS

Fig. 4 is a photograph of a germanium sample as it is seen on the television screen. The interface shape is flat and its position in the furnace is determined by the position of the platinum markers, and relative to a fixed furnace position. The shape of the interface changes as the crystal grows. Normally, as the interface approaches the cold zone it becomes concave, when it is in the middle of the insulation zone it is flat, and as it approaches the hot zone it becomes more convex.



Figure 4. Realtime Image of Germanium Crystal

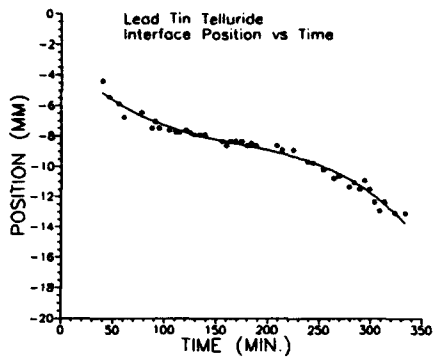


Figure 5. PbSnTe Interface Position vs. Time

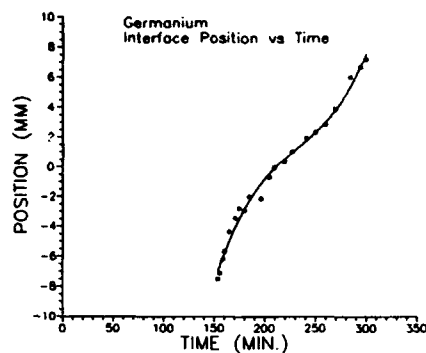


Figure 6. Ge Interface Position vs. Time

The interface movement relative to the bottom of the sample is the real growth rate, and the sample movement relative to the furnace is the pull rate. However, the interface movement relative to the fixed furnace position is the primary interest because this is the deviation of growth rate from pull rate. Fig. 5 shows position of the interface relative to a fixed position in the furnace during growth of lead tin telluride. If the interface was curved, the position at the middle was used. Note that the interface moves down with respect to the fixed furnace position. This means the growth rate was slower than the translation rate. Compare this data to Fig. 6, which shows the interface position of germanium moving up during growth, indicating that the growth rate was faster than translation rate. The actual growth rate can be calculated using the interface movement data and the translation rate. At one time it was assumed that the growth rate was equal to the translation rate, but these results prove this assumption to be false.

The results of the copper/brass interface tests are plotted in Fig. 7. These shapes obtained from the

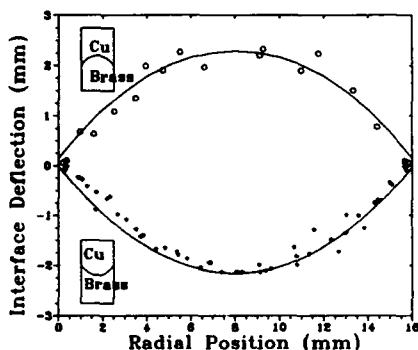


Figure 7. Interface Shapes of the Copper/Brass Cylinders

realtime imaging system compared favorably to the actual shapes of the cylinders. Therefore, the shapes seen on the monitor were verified.

Results from the capillary tube experiments are shown in Fig. 8, in

which the temperature measurements of the three different sets of experiments are plotted relative to the radiographic interface position. The interface temperatures for all three runs are very close to the melt temperature, as seen by the discontinuity in slope. However, the position of the interface, labels a,b,c, are not at the radiographic interface (which is at 0 mm.)

When the sheathed thermocouple is coming up from the cold zone it marks the thermal interface 7 mm above the x-ray interface, coming down from the hot zone it is 3.9 mm below the x-ray interface, and the bare wire thermocouple places it at 1 mm above the actual interface. These errors are due to thermal conductivity along the thermocouple, which acts as a heat source or sink.

When the thermocouple coming up from the bottom is at the interface it reads around 920°C instead of 937°C. In this case the thermocouple is acting as a heat sink. Coming down from the top, the thermocouple acts as a heat source and reads 939-943°C. The amount of error due to thermal conductivity depends on the total difference in temperature between the zone that the thermocouple exits and the melt temperature. In one case it is comparing 1000°C to 937°C and in the other it is comparing 937°C to 800°C. In these measure-

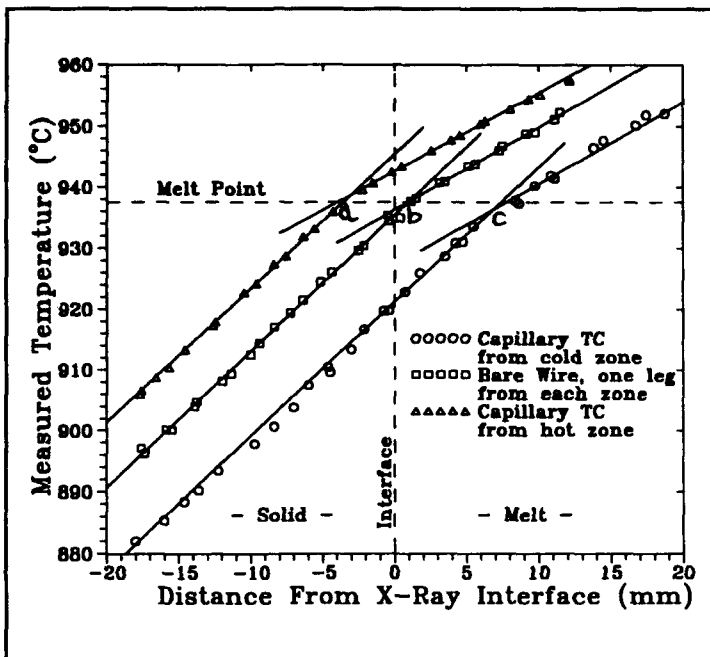


Figure 8. Thermal Interface for the Three Sets of Data

ments, the greater difference with the thermocouple exiting the bottom results in greater error in temperature reading.

DISCUSSION

The x-ray imaging system demonstrated that the interface position of semiconductor crystals could be obtained realtime. The position of the interface is used to calculate growth rate, and can now be calculated accurately using this method. Along with obtaining the position realtime, this method gave the shape of the interface, which was verified using the interpenetrating brass and copper cylinders.

It was discovered with this x-ray imaging system that the thermal interface position was in error due to thermal conductivity along the sheathed thermocouple. Also, the error was not the same with the thermocouple coming down from the top as it was coming up from the bottom.

REFERENCES

1. K. Kinoshita and K. Sugii, *J. Crystal Growth* 71 (1985) 283-288.
2. P.G. Barber, R.K. Crouch, A.L. Fripp, W.J. Debnam, R.F. Berry, and R.T. Simchick, *J. Crystal Growth* 74 (1986) 228-230.
3. Y. Huang, W.J. Debnam and A.L. Fripp, *J. Crystal Growth* 104 (1990) 315-326.
4. A. Murgai, H.C. Gatos and A.F. Witt, *J. Electrochem. Soc.* 123 (1976) 224.
5. T.I. Ejim, W.A. Jesser, and A.L. Fripp, *J. Crystal Growth* 69 (1984) 509-514.
6. R.T. Simchick, S.E. Sorokach, A.L. Fripp, W.J. Debnam, R.F. Berry and P.G. Barber, *Advances in X-Ray Analysis* 35 (1992) 1295-1300.
7. J.A. Hubert, A.L. Fripp and C.S. Welch, *J. Crystal Growth* 131 (1993) 75-82.

INDEX

Activation energy of degradation, 315
Additives, 111
Ag, 299
Al doping, 207
Alpha-zirconium hydrogen phosphate monohydrate, 245
Alumina powders, coated, 345
Analytical electron microscopy, 289
Atmospheric contaminants, 289

Ba(Cu_{0.5}W_{0.5})O₃, 161
Baek, K-K., 19
Balachandran, U., 289
Barber, P.G., 379
Barrier height, 231
Barry, J.C., 299
BaTiO₃, 129, 145, 153, 169
Batiño, François, 263
Begg, B.D., 169
Bennett, J.P., 279
Bhargava, A., 299
Bi-diffused SrTiO₃-based ceramics, 231
BiFeO₃, 161
Bi-Sr-Ca-Cu-O system, 299
Bi systems, 315
Binder, 337
Blairs, S., 169
BN, 145
Boundary migration behavior, 35
Bridgman furnace, 379
Buchanan, R.C., 153

Capacitor ceramics, 129
Carbon, 289
Cassidy, D.J., 169
Ceramic-metal interfacial region, 325
Charge carriers, 263
Chemical stability, 315
Chen, Chi-Jen, 101, 111
Chen, D.R., 129
Chiang, Yet-Ming, 3
Chip components, multilayer, 101
Cho, Y.S., 371
Cho, Sang-Hee, 145, 185

Clark, J.A., 279
Clarke, David R., 217
(Co,Fe)₃O₄ films, 93
Cofiring, 355
technology, 325
Compositional analysis, 161
Conductivity, 153
Cryogenic behavior, 207
Curie temperature, 145
C-V characteristics, 195

Debnam, W.J., 379
Desranges, Corinne, 263
Desranges, Lionel, 263
Dielectric constant, temperature dependence, 363
Dielectric properties, 371
Dielectric resonators, 355
Ding, Y., 245
Dispersing agent, 337
Dong, Dunzhuo, 161
Donor doping, 153
Dopants, 101
Double Schottky barrier, 195
Dynamic conductance, 217

Electrical characteristics, 245
Electrical conductivity, 53
Electrical discharge machining, 279
Electrically active boundaries, 19
Electroceramics, 3
Er-Ba-Cu-O, 307
Excess PbO, 371

Ferrite, 101
Freund, Friedemann, 263
Freund, Minoru M., 263
Fripp, A.L., 379
Fujimoto, Masayuki, 81

Gao, Y., 289
GBBLIC, 65
Glass infiltration, 325
Golden, S.J., 299

Grain boundary, 65, 161, 195, 289, 337
 layers, 119
 segregation, 3
 structure, 153
Grain growth, 363

Han, Sang Chul, 35
 Hesp, S.A.M., 337
High- T_c superconductors, 315
High- T_c thin films, 307
 Hirano, Shin-ichi, 93
Hollow particles, 53
 Homma, M., 119
 Hoyer, J.L., 279
 Hsu, Jen-Yan, 101
 Hu, C.T., 135
 Hur, Soo Hyung, 177
Hydrogels, 337

I-V characteristics, 195
 Ichinose, N., 231

Ikeda, Jeri Ann S., 3
Image analysis, 325
 Imanishi, N., 253
In-diffusion method, 19
Inductance, 81
Interface, 299
 development, 345
 migration, 35
 states, 195
Intergranular liquid films, 35
Isothermal capacitance transient spectroscopy, 195, 231
 Iwashita, S., 119

Jeon, Jae Ho, 35
 Jones, D., 245

Kaneko, Shoji, 161
 Kang, D.H., 371
 Kang, Suk-Joong L., 35
 Kawamura, K., 355
 Kelkar, M., 307
 Kikuta, Ko-ichi, 93
 Kim, J., 153
 Kim, Jeong-Joo, 185
 Kim, Myung Chul, 177

Kingery, W.D., 345
 Ko, Wen-Song, 101
 Kobayashi, M., 355
 Kodaira, Kohei, 363
 Koumoto, K., 53

Lattice strain, 363
Lead zirconate titanate, 337
 Lee, D.H., 371
 Lee, Joon-Hyung, 145, 185
 Levinson, Lionel M., 207
Li
 deintercalation, 253
 intercalation, 253
 secondary battery, 253
 Li₃FeN₂, 253
 Lin, I.N., 135
 Liu, C.S., 111
 Liu, Fuyi, 239

Mackinnon, I.D.R., 299
Magnetic properties, 81, 93
 Martin, L.D., 325
Mechanical properties, 279
Melt-solid interface, 379
 Merkle, K.L., 289
Metal circuit, 325
Metal oxides, 345
 MgO, 263
Microstructural analysis, 161
Microstructure, 81, 363
 development, 345
Microwave dielectrics, 355
 Minamiyama, Hideaki, 315
Minimum loss, 111
Mn-Zn ferrite, 111
Modeling, 217
Mössbauer spectra, 253
 Mukae, Kazuo, 195
 Mundy, J.N., 289
 Murakami, Kenji, 161
 Muroya, Masaaki, 315

Ni-Zn-Cu ferrite, low-temperature-fired, 81
 Nishijima, M., 253
 Nishiaki, Shiro, 363
Nonflat interface, 379

Nonlinear varistor characteristics, 217
 Non-ohmic electrical characteristics, 217
 Nowotny, J., 169
 Okada, M., 119
 Okada, Nagaya, 161
 Oxidative annealing, 177
 Oxide materials, 263
 Oxides, 35
 Pai, C.H., 53
 Park, Seh-Jin, 145
 Park, Soon Ja, 177
 Particle size, 169
 $\text{Pb}(\text{Mg}_{1/3}\text{Nb}_{2/3})\text{O}_3$, 371
 Pb/Sr ratio, 135
 $\text{PbTiO}_3\text{-TiO}_2$, 119
 $\text{Pb}(\text{Zr,Ti})\text{O}_3$ ceramics, 161
 Percolation theory, 279
 Permeability, 111
 Petroff, T.E., 337
 Phase separation, 93
 Phelan, P.E., 307
 PLZT, 65
 Polycrystalline ZnO , 217
 Polynuclear metal cation sols, 245
 Porosity, 185
 Porous ceramics, 53
 Position, 379
 Positive holes, 263
 Positive temperature coefficient of resistivity (PTCR), 135, 279
 ceramics, 119
 $(\text{Ba}_{0.76}\text{Sr}_{0.24})\text{TiO}_3$ -based, 177
 characteristics, 185
 effect, 145
 Power loss, 111
 Proton conductivity, 245
 Q-factor, 355
 Reaction rate, 289
 Reaction sintering, 53
 Representative microstructure, 217
 Roseman, R.D., 153
 Rozière, J., 245
 Sayer, M., 337
 Schultz, William N., 207
 Seebeck coefficient, 53
 Selvaduray, G., 289
 Semiconducting oxides, 19
 Semiconductor crystals, 379
 Semiconductor-insulator-semiconductor model, 231
 Seo, W.S., 53
 Shape, 379
 Shell-core structure, 129
 SiC, 53
 Simchick, R.T., 379
 Simulations, 217
 Sintering, 239, 325
 Slip casting, 337
 Sol-gel method, 93
 Solid-state reaction, 345
 Song, Xiaolan, 239
 Song, X.Y., 129
 Song, Y., 307
 Sorokach, S.E., 379
 Space charge, 3
 Spinodal decomposition, 93
 Strontium barium niobate, 363
 Structure, 169, 245
 changes, 253
 room temperature, 169
 Sub-grain boundaries, 239
 Suen, Meei-Lin 101
 Sung, Hsiao-Miin, 101
 Superconductors, 289, 299
 Surge arresters, 207
 Suzuki, K., 355
 Takahashi, Junichi, 363
 Takano, M., 253
 Takeda, Y., 253
 Theoretical calculation, 195
 Thermal boundary resistance, 307
 Thermal conductivity, 53
 Thermal design, 307
 Thermoelectric energy conversion, 53
 Ti vacancy, 185
 TiN/Al-O-N composites, 279
 TiO_2 , 3
 Trap levels, 177
 Tri-plate resonator, 355
 Tsai, T.D., 135

Tsay, M.J., 111
Tsuda, Koichi, 195
Tuller, H.L., 19
Tung, M.J., 111
Twin structure, 289

V-shape, 135
Vance, E.R., 169
Varistors, 217
VDR effect, 231
Venkataraman, K.S., 325
Volume resistivity, 279

Watanabe, M., 231
Weirauch, D.A., Jr., 325
Wen, Qingzhe, 217
Whang, Eun-Joo, 263

X-ray imaging system, 379
Xu, B.M., 65
Xu, D., 289

Y systems, 315
Yamamoto, Hiroshi, 93
Yamamoto, O., 253
Yamashita, T., 299
YBCO, 65
Yin, Z.W., 65, 129
Yogo, Toshinobu, 93
Yokoi, H., 345
Yoon, Duk Yong, 35
Yoon, K.H., 371

Zhang, C., 289
Zhao, M.Y., 65
Zirconia, 337
ZnO, 19
 grains, 239
 :Pr varistors, 195
 varistors, 195, 207, 239
Zr₂O doping, 315